A TWO-PHASE HEAT TRANSFER TEST FACILITY FOR AMMONIA: CONSTRUCTION AND TESTING

by

ERIK KELTNER

B.S., Kansas State University, 2002

A THESIS

Submitted in partial fulfillment of the Requirements for the degree

MASTER OF SCIENCE

Department of Mechanical Engineering
College of Engineering

KANSAS STATE UNIVERSITY
Manhattan, Kansas
2005

Approved by:

Major Professor
Dr. Bruce Babin
Department of Mechanical and Nuclear Engineering

ABSTRACT

Recent world events are motivating the United States Government to invest in the development of Directed Energy Weapons (DEW). One defense contractor developing the technology, Raytheon Missile Systems Company, is addressing the cooling requirements. To this end, Raytheon has proposed some two-phase (liquid and vapor) heat transfer devices capable of dispersing the high energy densities associated with DEW. The Kansas State University Mechanical and Nuclear Engineering Department has been contracted to characterize the performance of the devices using ammonia as the working fluid. To this end, an Ammonia Test Chamber was reconfigured to perform the experiments. The chamber is now configured to deliver liquid ammonia at saturation pressures ranging from 45 to 115 psia, a sub-cooled liquid temperature of -25^{o}C, and mass flow rates ranging from 0.01 to 0.03 kg/s. The Ammonia Test Chamber can absorb heat loads of up to 5000 W. Measurements of the Critical Heat Flux (CHF) of the device ranged from 173 W/cm^2 to 488 W/cm^2. This data agrees characteristically with published correlations of CHF values, however the correlations predict lower magnitudes.

TABLE OF CONTENTS

LIST OF FIGURES

LIST OF TABLES

ACKNOWLEDGEMENTS

First of all I want to thank my advisor Dr. Bruce Babin who allowed me to experience this once-in-a-lifetime opportunity where I was able to apply my engineering, presentation, and social skills on a higher level. I learned a tremendous amount from him and from the work that he had me do and I am forever grateful. Next I want to thank my thesis committee members Dr. Steven Eckels, Dr. Donald Fenton, and Dr. John Devore. I really appreciate the time they took to help me with any questions I had. Hans Brehm and Kevin deserve some thanks as well as they helped out a lot in obtaining data for me while I wrote my thesis. I also appreciate the help I received from Kyle Hildenbrand and Paul Lebin. I want to thank Kevin Lease for helping me get my masters degree started and Mo Hosni for being such a great leader for the Mechanical and Nuclear Engineering Department. I also want to thank Jason Selland for putting up with all of the work he did for me. I wouldn't have been able to do a whole lot without Sherry Donahey, Deb Stryker, Marcia Chacon, and Carol Konold either, thank you. Finally, I want to thank my future wife April Goodrich, my dad Gene, my mom Carol, and my sister Ashley for helping me through the good times and the bad, for supporting me in many different ways, and for their love.

NOMENCLATURE

C = constant defined by Equation 2.3
c_P = specific heat of liquid
d = diameter of an impinging jet
H_{fg} = latent heat of evaporation
Ja = Jakob number = $(\rho_l/\rho_v)*[(c_P*\Delta T_{sub})/H_{fg}]$
L = maximum distance away from jet on heated surface (in the case of the Slot Jet used here see Figure 3.3.11)
q_{co} = critical heat flux for saturated boiling
q_c = critical heat flux for subcooled boiling
ΔT_{sub} = subcooling temperature of jet = T_{sat} - T_{liq}
u = velocity of a liquid jet at the nozzle exit
ρ_l = density of saturated liquid
ρ_v = density of saturated vapor
σ = surface tension
T_{SJfi} = Slot Jet Fluid Inlet Temperature
T_{HNTM} = Heater Neck Top Middle Temperature
T_{HNBM} = Heater Neck Bottom Middle Temperature
T_{SJo} = Averaged Outside Heated Surface Temperature of Slot Jet
T_{SJi} = Inside Heated Surface Temperature of Slot Jet
T_{sub} = Subcooling
T_H = IR Camera High Temperature
T_L = IR Camera Low Temperature
PT = Pressure Transducer
x_{HN} = Distance Between Heater Neck Thermocouples
x_{SJ} = Thickness of Slot Jet Heated Surface
k_{Cu} = Thermal Conductivity of Copper
k_{Al} = Thermal Conductivity of Aluminum
q_{HN}" = Heater Neck Thermocouple Heat Flux
q_{EI}" = Energy Input Heat Flux
EI = Energy Input
HN_{height} = Heater Neck Height
HN_{width} = Heater Neck Width
q_{IR}" = IR Camera Heat Flux
h_{max} = Maximum Heat Transfer Coefficient

1 INTRODUCTION

Modern technological advances always carry on the additional problems of increasing energy density. Thermal engineers are continuously seeking ways to more efficiently dissipate heat from smaller areas. One of the more promising solutions to these problems is boiling heat transfer. Additionally, fluids with advantageous boiling properties are being proposed. This document describes the construction of a test facility to measure the boiling heat transfer properties of ammonia and the results of the measured data from this facility.

1.1 Application

The U.S. Department of Defense is interested in developing Direct Energy Weapon (DEW) technology to address the threat of a missile strike to the continental US. DEW are essentially high-powered LASER devices capable of disabling missiles from large distances. Raytheon Missile Systems Company has been tasked with developing the energy management system for these devices. According to Raytheon sources [10], energy densities in excess of 800W/cm^2 must be dissipated at a surface temperature of 20^{o}C in order for the devices to be viable. Thus, Raytheon is seeking to redefine the state of the art in high-density energy dissipation.

To this end, the Kansas State University Mechanical and Nuclear Engineering Department has been contracted to assist in the testing of Raytheon developed high-density energy dissipation devices. Specifically, Raytheon has requested the measurement of the surface energy dissipation of 2 devices (Evaporative Compact High Intensity Cooler (ECHIC) and Slot Jet) using ammonia. Due to the toxic and corrosive

properties of ammonia, Raytheon is not permitted to use pure ammonia at their plant site. Fortunately, KSU has a facility that was once developed specifically for testing the thermal properties of ammonia. Thus, the task addressed in this document is to re-configure this ammonia test facility to measure the heat dissipation rate for 2 devices developed by Raytheon Missile Systems Company.

1.2 Construction of an Ammonia Test Facility to measure Boiling Heat Transfer Coefficients

The success of this project was predicated on the ability to re-configure a test cell that once was used to measure the thermal properties of ammonia. The facility has not been used with ammonia in the past 5 years. To complete the construction of the Ammonia Test Facility, an assessment of the materials present in the facility and their compatibility with ammonia was required. All components, instruments, plumbing, o-rings, etc that were found incompatible with ammonia were replaced. All safety features of the facility had to be verified for functionality. Further, a thermodynamic assessment of the facility thermal management was performed to determine the ability of the facility to manage the heat addition requested by Raytheon. As currently configured, the test facility can absorb a maximum of 5000W. Other thermodynamic limitations of the facility include a test cell pressure range of 310-790 kPa, a minimum ammonia temperature of -25^{o}C (under no thermal load conditions), and a controllable ammonia liquid flow rate of 0.004-0.04 kg/s. The specifics of the Ammonia Test Facility are discussed in Chapter 3 of this document. A picture of the Ammonia Test Facility is shown in Figure 1.2.1.

Figure 1.2.1. Ammonia Test Facilty

1.3 Measurement of Surface Energy Dissipation Characteristics of Ammonia

Upon verification of the Ammonia Test Facility's ability to provide liquid ammonia at a specified thermodynamic state, the measurement of thermal energy dissipation rates for Raytheon's specific devices could be conducted. Two devices were tested: the ECHIC and the Slot Jet. It was initially desired to measure the boiling heat transfer coefficients as a function of ammonia flow rate, saturation pressure, and liquid subcooling for the ECHIC. Because the ECHIC device was intended to achieve very high heat transfer rates, critical heat flux (CHF) values at the point of surface dry out were not expected to be reached. Due to an error in the test plan, the ECHIC device was destroyed before any steady state data was collected. When replaced with the Slot Jet,

the desired data became CHF values by varying the same system parameters since dry out was expected with this device. It was tested for a total of 9 conditions. A summary of the test results are shown in Table 1.3.1. As shown in the table, the measured CHF values nominally agree with published correlations. It is significant to note that tests were not performed at varying liquid subcooled temperatures due to a malfunction of the Ammonia Test Cell chiller controller.

Table 1.3.1 Summary of Slot Jet Test Results

Slot Jet Inlet Pressure (psia)	Subcooled Inlet Fluid Temperature, T_{sub} (^{o}C)	Volumetric Flow Rate (gpm)	Mass Flow Rate (kg/s)	Measured CHF (W/cm^2)	Predicted CHF, q_{co} (W/cm^2)	Difference (W/cm^2)	Percent Difference of Correlation
341	-22.3	0.250	0.0104	173	120	53	31
339	-21.6	0.425	0.0171	249	156	93	37
339	-21.5	0.700	0.0287	289	210	80	28
444	-22.5	0.250	0.0098	231	134	97	42
446	-24.4	0.425	0.0172	280	191	89	32
439	-23.9	0.700	0.0293	313	257	56	18
792	-22.3	0.250	0.0102	262	175	87	33
781	-23.1	0.425	0.0171	275	244	31	11
769	-24.2	0.700	0.0288	488	335	153	31

1.4 Summary

To aid in the development of DEW cooling technology, KSU has been tasked by Raytheon to measure the surface energy dissipation rates of specific devices using ammonia. To this end KSU has re-configured an Ammonia Test Facility capable of performing the requested tests in a safe environment. Two distinct devices were tested in the facility. The ECHIC device was installed but failed before any data was recorded. The Slot Jet device was thoroughly tested and produced data that nominally agrees with published correlations.

2 BACKGROUND

Among the many tasks required to successfully complete an experimental investigation the most important is a thorough understanding of the results of previous investigations. The topics researched for this study can be broadly categorized as: ammonia safety considerations, ammonia material compatibility, construction of test facilities to perform CHF measurements, and predictions of CHF values for similar geometries and fluids. Each of these topics are discussed below.

2.1 Effect on Humans

Ammonia in its purest form is extremely toxic to humans. If liquid or high concentrations of vapor contacts the eyes ammonia can cause "painful, instant and possibly irreversible damage to tissue such as conjunctiva, cornea, and lens" [16]. Prolonged skin contact "can cause painful tissue damage, frostbite and serious chemical burns" [16]. If ammonia is inhaled it can obstruct breathing from laryngeal and bronchial spasm, to edema and severe damage to mucous membranes of the respiratory tract with possible fatal results. Latent edema and residual reduction in pulmonary function may occur." [16]. Tissue damage and chemical burns can also take place if ingested as well as nausea and vomiting. However, "ammonia is a gas under normal atmospheric conditions and ingestion is unlikely" and it is not a cumulative metabolic poison [16]. Thus, safety features must be integrated into the design of the Ammonia Test Facility. Proper ventilation is provided to minimize the effect of an ammonia spill within the confines of the facility. Further, safety procedures requiring the use of a gas mask and latex gloves to avoid skin contact with ammonia have been established.

2.2 Ammonia Material Compatibility

In general, pure ammonia is a corrosive chemical. Ammonia will corrode surfaces quickly, particularly in the presence of water.

A quick summary of ammonia material compatibility issues can be found by searching the internet. Two informative sites were identified (www.efunda.com [6] and www.airliquide.com [1]). Other information was gathered from literature distributed by the International Institute of Ammonia Refrigeration (IIAR) [12]. Lastly, the ASHRAE Refrigeration Handbook [2] was also referenced. A summary of the ammonia material compatibility information gathered from these sources is organized in Tables 2.1 and 2.2

Structural, or transport, materials usually consist of metal types which are much more rigid than sealing materials. Tubing, fittings, and valves are examples of components made of structural materials. Structural material ammonia compatibilities are summarized in Table 2.1. Sealing materials usually consist of rubber and/or plastic types of materials designed to be flexible such as o-rings and gaskets. Sealing material ammonia compatibilities are summarized in Table 2.2. Omissions from the tables are due to either conflicting or missing data regarding the specific table entry.

Table 2.2.1 Structural Materials

Transport Materials	Compatibility Description	
	airliquide.com	iiar
Aluminum	Fair	compatible
Brass	Poor	
Stainless Steel	Good (316)	compatible
Monel	Poor	
Copper	Good; Poor in presence of moisture	incompatible
Carbon Steel	Good, in presence of moisture; Poor in presence of oxygen	compatible
Zinc		incompatible
Copper-Based Alloys		incompatible

Table 2.2.2 Sealing Materials

Sealing Materials	Compatibility Description		
	efunda.com	airliquide.com	iiar
Kalrez	Good, both for static and dynamic seals		
Teflon, Virgin	Good, both for static and dynamic seals	Good	Highly compatible within temp. range of Teflon
Butyl	Good, both for static and dynamic seals	Insufficient Data	Acceptable between -20degF to 300degF
Ethylene-Propylene	Good, both for static and dynamic seals		Acceptable between -40degF to 300degF
Neoprene	Good, both for static and dynamic seals	Fair	Acceptable between -40degF to 175degF
Chemraz	Fair, usually OK for static seals		
Nitrile, Hydrogenated	Fair, usually OK for static seals		Not Recommended
Buna-N (Nitrile)	Fair, usually OK for static seals	Fair	
Silicone	Sometimes OK for static seals; not OK for dynamic seals		Acceptable between -65degF to 400degF
Fluorocarbon	Poor		
Styrene Butadiene	Poor		
Fluorosilicone	Poor		
Natural Rubber	Poor		Not Recommended
Polyacrylate	Poor		
Polyurethane, Millable	Poor		Not Recommended
Polysulfide	Poor		
Vamac	Poor		
Aflas	No Data		
Polyurethane, Cast	No Data		Not Recommended
Epichlorohydrin	No Data		
Hypalon	No Data		Acceptable between 0degF to 225degF
Kel-F		Good	
Viton			Not Recommended
Nylon		Insufficient Data	
Polyethylene		Poor	
PVC		Good	

2.3 Property Comparisons to Other Refrigerants

The benefits and disadvantages need to be known for ammonia in order to determine how and if it should be used as a working fluid. Here ammonia is compared to other typical fluids used as refrigerants or general working fluids and shown to be an excellent refrigerant mainly due to its low boiling temperature and high heat of vaporization.

2.3.1 Advantages Over Other Refrigerants

One advantage ammonia has over water is that it evaporates at much lower boiling temperatures as seen in Table 2.3.1. This allows two-phase ammonia flow loops to operate at much lower temperatures and pressures. Another advantage of ammonia is its much higher heat of vaporization than R-134a, as seen in Table 2.3.1, and most other refrigerants at the same conditions. Ammonia having a low viscosity seen in Table 2.3.1 is also an advantage when considering pressure losses through tubing and components because less pumping power is required.

2.3.2 Disadvantages Over Other Refrigerants

Ammonia evaporating at lower temperatures and pressures is also a disadvantage. This causes ammonia to evaporate instantly if there is a leak in the flow loop. This makes leak detection very difficult. The biggest disadvantage with ammonia is that, in its purest form, it is a very toxic fluid to humans and a leak in the system could create a very hazardous situation very quickly. The advantage of the low viscosity of ammonia also poses as a disadvantage. This property makes it more difficult to pump. The corrosive nature of ammonia on copper when moisture is present is another problem since copper is

a very common material used in constructing many refrigeration systems as it has one of the highest thermal conductivities of structural materials.

Table 2.3.1 Comparison of Ammonia to Other Refrigerants [19]

Saturated Properties @ 50 psia (345kPa & 267K)

	Ammonia	Water	R-134a
Heat of Vaporization (kJ/kg)	1300	2500	200
Density (kg/m^3)	650	1000	1300
Viscosity (kg/(m*s))	0.0002	0.002	0.0003
Boiling Temperature (^{o}C)	-5.7	138	4.6
Boiling Temperature @ Atmospheric Pressure (^{o}C)	-33	100	-26

2.4 Two-Phase Test Facilities with Ammonia

To aid in the development and construction of an evaporative ammonia two-phase flow loop, literature on previous ammonia two-phase facilities was reviewed. The literature review concentrated on the instrumentation methods, orientations, component types, the ammonia compatible materials used, and their corresponding results. All but one of the papers found utilized in-tube flow, horizontal and vertical. The one paper researched that did not utilize in-tube flow (Monde 1996) used an impinging jet evaporator. The correlation from this facility will be used for comparisons later, however, ammonia was not used as the working fluid.

2.4.1 Compatible Materials

As mentioned previously materials compatible with ammonia must be used when constructing an ammonia flow loop. Materials used in the facilities review included

steel, stainless steel, other alloy steels, and aluminium [3,13,26,29]. Also, sight glasses were made out of acrylic plastic and borosilicate glass [3,29].

2.4.2 Condensing

Condensers are needed to turn two-phase flow created by evaporators back to subcooled liquid flow. All of the papers reviewed had various ways of condensing ammonia. Some experimental setups had only one heat exchanger to accomplish this. However, others used two to condense and subcool the ammonia separately. The Kabelac facility condensed and subcooled the ammonia in this manner [13]. A diagram showing how the Kabelac condensing and subcooling section of the facility was setup is shown in Figure 2.4.1.

2.4.3 Pumping

A pump is needed in a two-phase flow loop to supply the test section with the working fluid being tested. This was accomplished in several different ways in the reviewed literature. Shah used conventional refrigeration compressors [26]. Chaddock's experimental setup pumped ammonia in an open loop circuit which consisted of two receivers, or large, pressureized reservoirs of ammonia. One of these receivers was at a high pressure and the other at a low pressure. The difference in pressure between these receivers caused the ammonia to flow through the test section [3]. Zurcher used a "magnetically driven gear type of pump (oil free)" [29]. The Zamfiresce facility did not even have a pump. The ammonia was circulated around this flow loop by gravity and the evaporation of the ammonia called "gravitationally generated (thermosiphon effect)" flow [28].

2.4.4 Pre-Heating (Conditioning)

Two-phase flow loops usually require a pre-heater, or conditioner, to control the conditions of the working fluid entering the test section. All of the facilities reviewed incorporated electrically powered pre-heaters except for the Shah facility. Since the Shah test section was so long it was used as the pre-heater as well [26].

2.4.5 Flow Visualization

Visualization of ammonia flow is required during charging of flow loops, for verifying two-phase flow, and for viewing of the flow regimes. Most of the experimental setups reviewed used tubular sight glasses before and after the test sections for flow visualization. However, the Shah and Zamfiresce experimental setups had tubular sight glasses placed within the test section. This was excellent for visualizing the flow while the ammonia was evaporating, however, where dry out (film boiling) occurred the sight glasses sometimes broke due to the increased temperatures [26,28]. The Zurcher experimental setup used sight glasses "for videotaping flow patterns at the exit" as well [29].

2.4.6 Flow Measurement

Flow measurement was needed to verify correct testing conditions for a flow loop and to perform heat transfer calculations. Flow rates were measured in a variety of ways. Orifice plate, membrane, coriolis, and ultrasonic meters were used. The more recent experiments used the ultrasonic [28] and coriolis [13,29] type meters.

2.4.7 Test Sections

The test section of a two-phase flow loop is used to either evaporate or condense the working fluid to obtain heat transfer measurements. In most of the literature reviewed, the test sections were horizontal tubular evaporators. Heating of these evaporative test sections was mostly done by electrical heating by heating elements coiled around the evaporator tube. However, the Shah experimental setup placed the heating elements parallel to the evaporator tube [26]. Two of the papers reviewed used fluids to supply energy to the evaporating ammonia. One used hot water [29] and the other used condensing ammonia in a separate loop [13].

To obtain heat transfer measurements at the test sections, wall temperatures of the evaporator tubes were measured by placing thermocouples on the outside of the tubes. Then the one-dimensional heat conduction equation [11] was used to find the inside wall temperatures. Usually several thermocouples were placed at one measurement point and the arithmetic mean of these was used as the local wall temperature [25]. One exception to this is that the Zamfiresce vertical test section only required one thermocouple per measurement point [28].

Pressure measurements from the reviewed papers were performed using manometers and pressure transducers. Pressure transducers were prominent in the more recent papers. One interesting application of pressure measurements was that the Zurcher experiments used the two pressure measurements on either side of the test section to find the local saturation pressure by linear interpolation. Using this value along with the vapor pressure curve of pure ammonia, the local saturation temperature was found [29].

2.4.8 Lies Test Facility

The Lies test facility is discussed separately here because it was the basis for constructing the current ammonia flow loop at Kansas State University. It was constructed specifically for testing ammonia. This test facility's purpose was "to measure in-tube, two-phase heat transfer coefficients and pressure drops" [17] as with the other facilities reviewed previously. However, the rest of Lies's facility construction is relevant to the KSU ammonia flow loop.

The main piece of equipment built for this ammonia test facility that allows the safe testing of ammonia is the environmental chamber. "Due to the toxic and flammable nature of ammonia, the entire test facility is enclosed within an environmental chamber that utilizes a ventilation hood to maintain a negative pressure environment" [17]. The chamber is 7 feet wide, 16 feet long, and 8 feet tall. This can be seen in Figure 2.4.2. Cinder block walls are on two sides and then there is a sheet metal wall and a plexi-glass wall. The plexi-glass wall has two panels that act as sliding doors to create an opening 8 feet wide. The sheet metal wall has an access panel built in so that valves and other equipment can be accessed without entering the chamber. There are also "five vents located around the base of the walls" to allow for make-up air [17].

The purpose of the ammonia loop originally built in this environmental chamber was "to provide ammonia to the test sections with a known inlet quality and mass flow rate" [17]. The primary components were "a pump, accumulator, filter, flow-meter, pre-heater, oil separator, heat exchanger, and sight glass" [17]. The pump was a magnetic drive gear pump with a charging valve positioned at its inlet. It could supply a flow rate of 2 gpm. The accumulator, attached to a dead end branch of tubing, at the pump outlet

controls the system pressure. Since the accumulator was on a dead end branch and ammonia testing would be performed down to temperatures of -20^{o}F the accumulator was wrapped in copper tubing for coolant to aid in its cooling. The flow meter used was a coriolis flow meter. The pre-heater regulates the quality of the ammonia at the inlet to the test sections by supplying desired amounts of energy to it. There are also tubular sight glasses at the end of each test section. There are two test sections in this ammonia loop because of the two different types of tubular evaporators. One is a smooth tube and the other is microfinned. Finally, the heat exchanger located before the pump was used to return the ammonia to a subcooled state [17].

Although this test facility was designed and constructed to be used with ammonia, it was not used with ammonia initially. It was initially operated with R-134a in the "ammonia" loop in order to verify its operation. However, the experiments done by Kelly [14] later with this facility did use ammonia. Measured data from these tests will be discussed later.

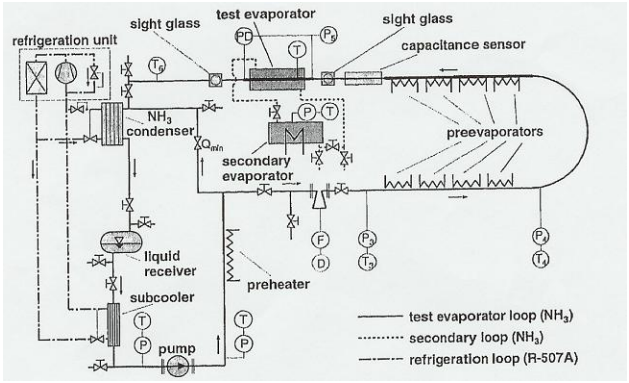

Figure 2.4.1 Kabelac Ammonia Two-Phase Test Facility [13]

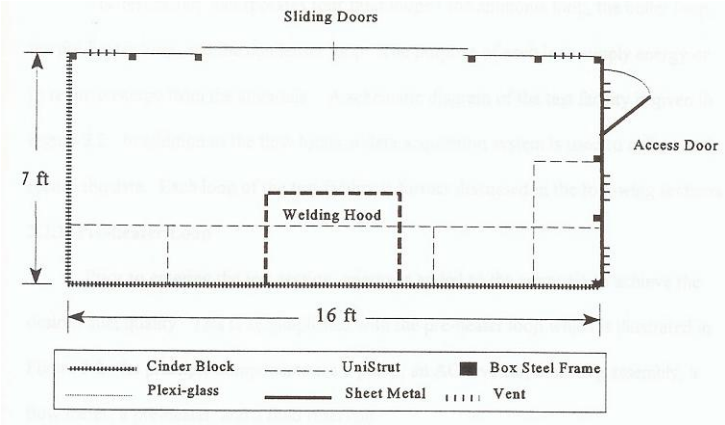

Figure 2.4.2 Lies Ammonia Chamber

2.5 Heat Transfer Calculations and Correlations

A heat transfer correlation was needed to verify the measured data from the current KSU ammonia flow loop presented later in this document. The correlations from the previously reviewed ammonia test facilities are for in-tube flow evaporators and are not applicable to the KSU ammonia flow loop. This is because the evaporator in the KSU ammonia flow loop is an impinging jet evaporator. Therefore the correlation discussed here from Monde is developed from a two-phase test facility with an impinging jet evaporator [18]. It will be used later to compare the experimental data found with the KSU ammonia flow loop. One of the drawbacks with this correlation is that it was not developed with ammonia. It was developed using water, R-113, and R-22. Another is that it was developed using circular cross section impinging jets and a circular heated surface. This is much different from the rectangular cross section jets and rectangular heated surface in the Slot Jet used with the KSU ammonia flow loop. Because of these differences this correlation is not expected to be very accurate. The correlation is as shown in Equations 2.1-2.4.

$$q_c = \{[1+(1+(4*C*Ja))^{1/2}]/2\}*q_{co} \qquad (2.1)$$

$$Ja = (\rho_l/\rho_v)*[(c_P*\Delta T_{sub})/H_{fg}] \quad (2.2)$$

$$C = (0.95*(d/L)^2*(1+(L/d))^{0.364}) \,/\, \{(\rho_l/\rho_v)^{0.43}*[(2*\sigma)/(\rho_l*u^2*(L-d))]^{0.343}\} \quad (2.3)$$

$$q_{co} = \rho_l*H_{fg}*u*0.221\ (\rho_l/\rho_v)^{0.645}*[(2*\sigma)/(\rho_l*u^2*(L-d))]^{0.343}*[1+(L/d)]^{-0.364} \quad (2.4)$$

Figure 2.5.1 shows the dimensions of the Slot Jet used with the Monde correlation. More importantly it shows the parameter "L" used in this correlation in Equations 2.3 and 2.4. This "L" parameter is called the maximum distance away from the jet on the heated surface.

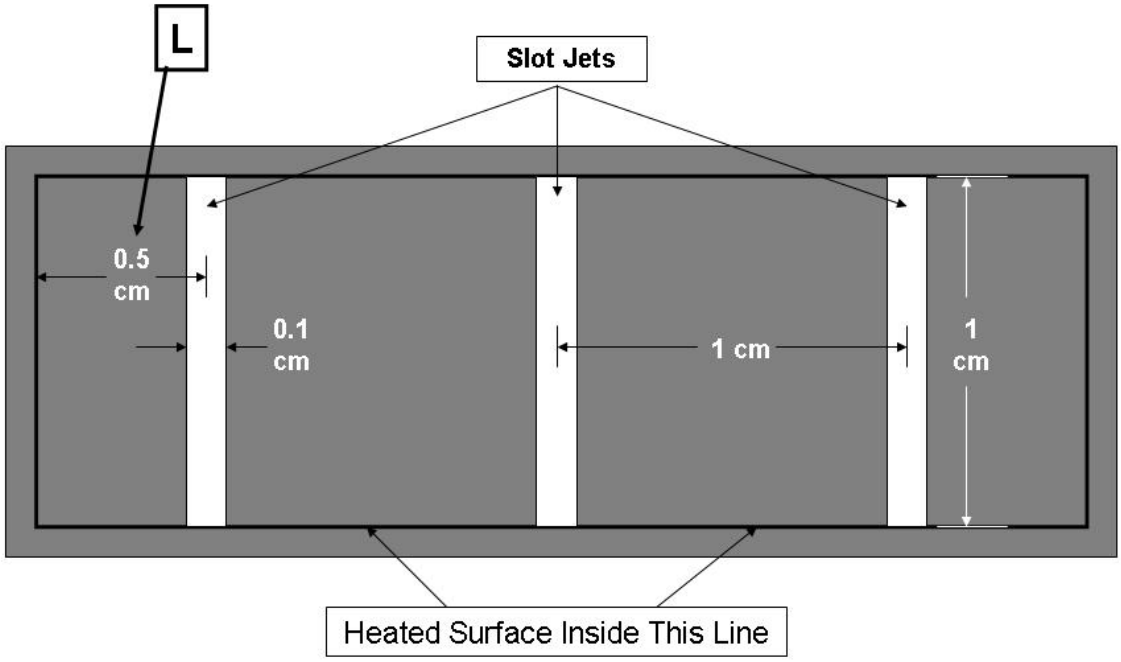

Figure 2.5.1 Slot Jet dimensions

2.6 Ammonia Data

Measured ammonia data is needed from reviewed literature to compare to the measured data from the KSU ammonia flow loop to verify its agreement, or superiority, to the literature measured data. The information discussed here mainly deals with plots of measured data concerning heat transfer coefficients from the various in-tube ammonia experimental setups from the previously reviewed literature.

There were several different trends seen in the reviewed literature measured data. The heat transfer coefficient increasing with increasing vapor qualities was observed in the data from Shah [27], Chaddock [3], and Zurcher [29]. Shah, Kabelac, and Kelly showed how heat transfer coefficients also increase with increased mass fluxes [13, 14,27]. It was also observed in the data from Sandru that heat transfer coefficients increase with increasing heat fluxes. This is shown in Figure 2.6.1 of heat flux versus the heat transfer coefficients.

Also seen in Figure 2.6.1 is a transition from single phase to two-phase heat transfer with the 630 kg/(sec)(m^2) mass flux between 10 and 20 kW/m^2 heat fluxes. The single-phase heat transfer region is where the plot is relatively horizontal due to a constant heat transfer coefficient. The two-phase heat transfer region is where the plot steadily rises do to increasing heat transfer coefficients with increasing heat fluxes. The measured data from Chaddock showed this transition as well with the 24000 lb/(hr*ft^2) mass flux in Figure 2.6.2 [3]. This trend was expected with the KSU ammonia flow loop measured data as well.

The same mass flux data in Figure 2.6.2 also shows a sharp decrease in the heat transfer coefficient at high vapor quality levels, around 80-90%. This trend is also seen

in the measured data from Kabelac [13]. This is due to dryout beginning to occur causing a greater resistance to heat transfer. A phenomenon similar to this is seen later with the KSU ammonia flow loop measured data as well where a sudden decrease in heat transfer occurs.

Figure 2.6.3 shows some experimental data from the Zurcher facility that can provide some useful data to compare to the data obtained from the KSU ammonia flow loop. From this Zurcher data the highest heat transfer coefficient recorded was approximately 21,000 W/m^2, or 2.1 W/cm^2. This was the highest of all two-phase in-tube evaporator ammonia experiments reviewed. However, for a better comparison to the KSU ammonia flow loop the mass flux ($kg/(m^2*s)$) in Figure 2.6.3 needed to be converted to mass flow rates in kg/s. The inside diameter of the tubular test section was needed for this conversion which was 0.014 m. This comparison is performed later.

The Kelly ammonia test facility was exactly the same as the Lies facility previously discussed, however, Lies did not use ammonia. Figure 2.6.4 shows a summary of resulting average heat transfer coefficients for evaporation of ammonia in a smooth and microfinned tube for the Kelly experimental setup. The highest recorded heat transfer coefficient here with a smooth tube was approximately 5500 $W(m^2-K)$. For the microfinned tube 9500 $W/(m^2-K)$ was approximately the highest recorded. Another important piece of information seen in measured data from other reviewed literature is the trend that as mass flux increases the heat transfer coefficients increase.

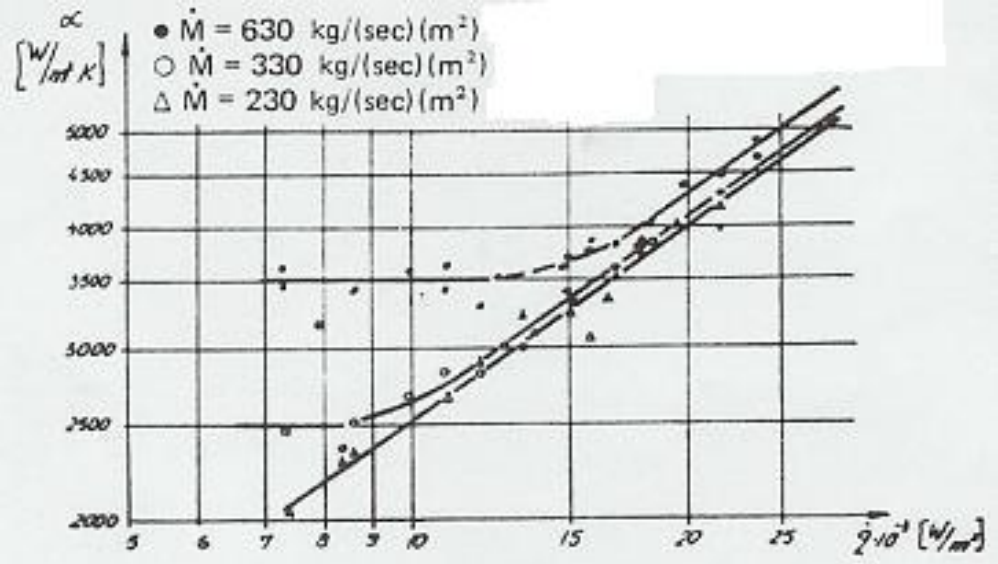

Figure 2.6.1 Sandru Results of Heat Transfer Coefficient vs. Heat Flux [25]

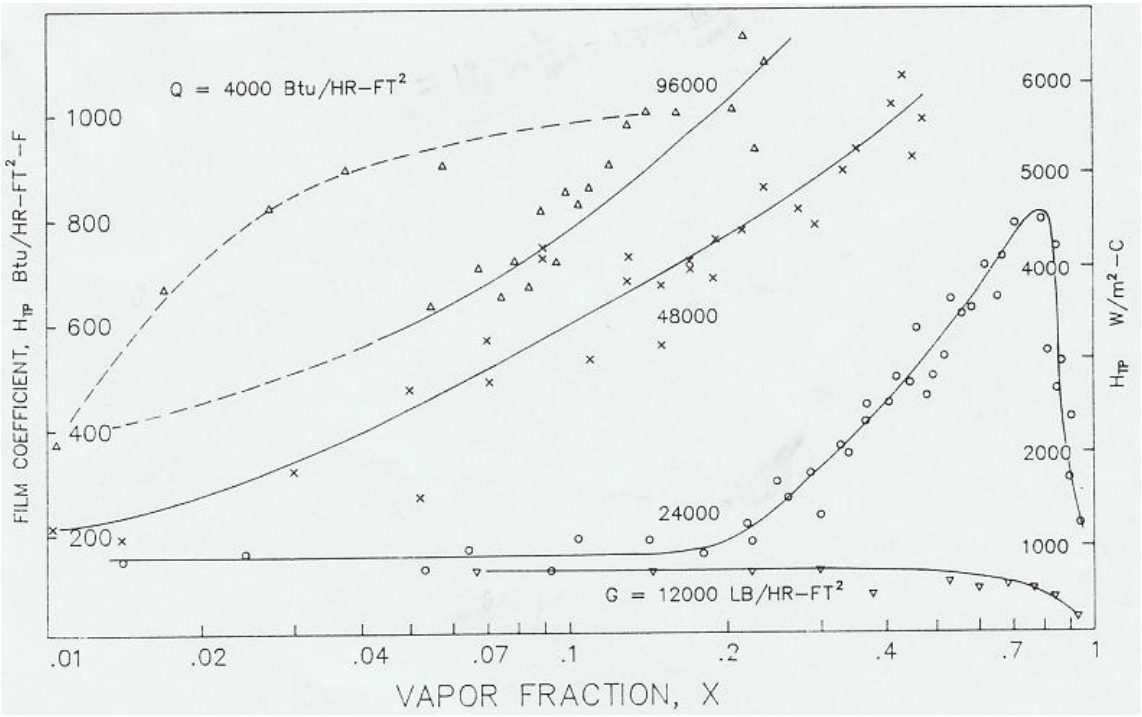

Figure 2.6.2 Chaddock Results of Heat Transfer Coefficient vs. Vapor Quality [3]

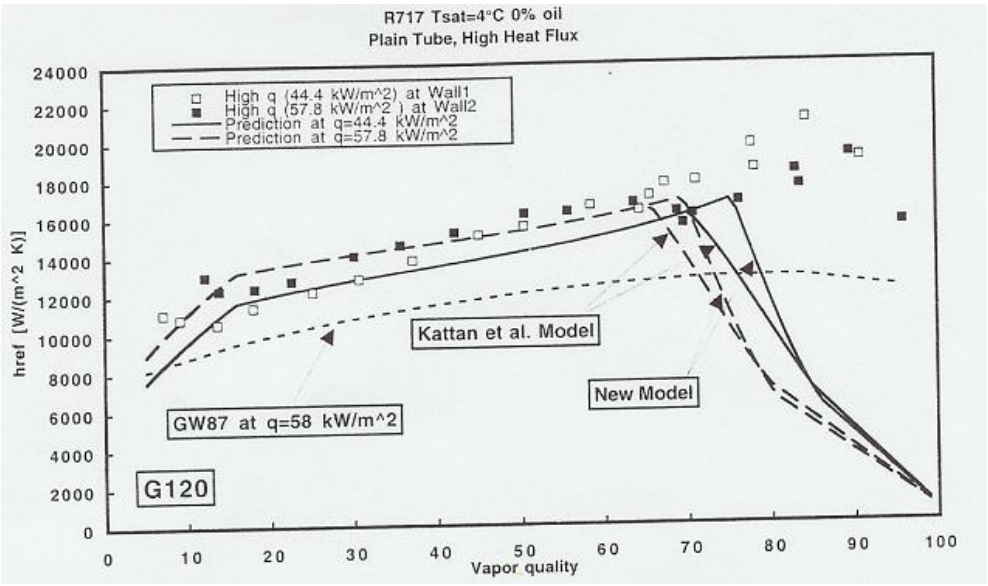

Figure 2.6.3 Zurcher Results of Heat Transfer Coefficient vs. Vapor Quality for Mass Flux of 120 kg/(m^2*s) [29]

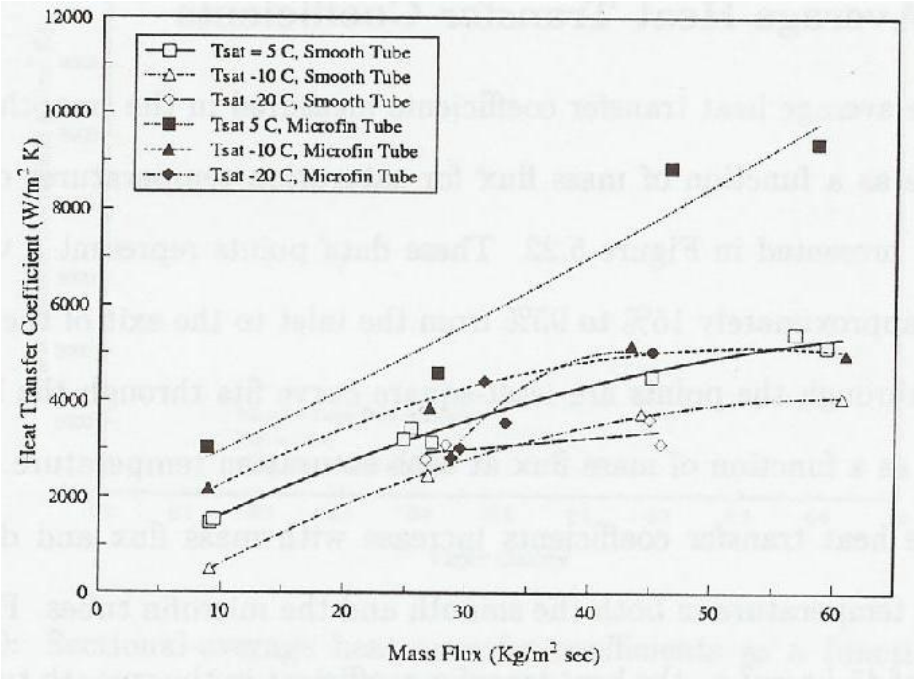

Figure 2.6.4 Kelly Results of Heat Transfer Coefficient vs. Mass Flux for Saturation Temperatures Using a Previous KSU Ammonia Test Facility [14]

2.7 Summary

Some common sealing materials compatible with ammonia include Kalrez, Teflon, Butyl, Ethylene-Propylene, and Neoprene. Most metals for use as transport materials are compatible with ammonia. Copper and copper based alloys are the main types to avoid.

For refrigeration purposes an advantage of ammonia over water is that it evaporates at much lower temperatures under the same conditions. Advantages of ammonia over other refrigerants include a much higher heat of vaporization and a lower viscosity. The disadvantages of ammonia include its toxicity to humans, its corrosiveness to some common materials, and its low evaporation temperature and viscosity.

A wide range of materials compatible with ammonia were used in the test sections and for other components of review facilities. Some of these included steel, stainless steel, aluminum, and acrylic plastic.

Several different ways of controlling ammonia flow loop temperature, pressure and flow have been observed. When condensing the ammonia after the evaporator one, or two, condensers can be used to condense and then subcool the ammonia for pumping again. Vapor and liquid separators were also used in conjunction with condensers. There was even an example of an open loop system that used two reservoirs at different pressures to flow ammonia. Several different pumps were used from conventional reciprocating compressors to magnetically driven gear pumps. For preheating all of the facilities discussed used some type of electrical heating.

Pressure measurements of the reviewed test facilities were done using manometers or by electronic means. A wide variety of methods for finding flow rates were used from orifice plates, membranes, Coriolis meters, and ultrasonic meters.

The methods of heating, or evaporating, the ammonia flow ranged from using electricity to separate fluid loops. The electrically heated test sections ran the heating elements parallel and spirally along the heated tubes. One of the methods of using a separate fluid loop to heat the test section simply passed hot water by the test section tubing. Another one used condensing fluid, ammonia, to heat the test section tubing in its own loop.

Temperature measurements at the test sections of review literature were measured on the outside of the evaporator tubes then the one-dimensional heat conduction equation was used to find the inside wall temperature. Most of these test sections used several temperature measurements at one point to obtain an average to be used as the wall temperature. Pressure measurements of the reviewed test facilities were done using manometers or by electronic means. A wide variety of methods for finding flow rates were used from orifice plates, membranes, Coriolis meters, and ultrasonic meters.

One of the trends observed in the data results of various experimental setups is that the heat transfer coefficients rise as the vapor quality increases. However, when high vapor qualities are reached, around 80-90%, film boiling begins to occur causing the heat transfer coefficients to suddenly drop. Other trends observed is that heat transfer coefficients rise with increasing mass fluxes and heat fluxes.

Some of the data from the experimental setups discussed here will be used for comparing to the KSU ammonia flow loop. However, due to its impinging jet evaporator, the ammonia flow loop being constructed here will likely produce much higher heat transfer coefficients under similar conditions.

So that the measured data from the KSU ammonia flow loop can be realistically compared to other literature the correlation by Monde developed for impinging jet boiling will be used. However, it is not expected to be very accurate due to the fact that it was developed from different geometries and working fluids.

3 TEST FACILITY

The purpose of the KSU Ammonia Testing Chamber is to provide a safe facility to test the boiling heat transfer properties of ammonia. The facility is located on the KSU campus in the basement of the Rathbone Engineering Building. A picture of the facility is shown in Figure 3.1.1. To successfully construct the facility, the following broad issues had to be addressed: ammonia compatibility, ammonia flow loop components, glycol flow loop components, specific cooling schemes to be tested, an analytical model of the ammonia test facility, and the facility operational characteristics. This chapter is a detailed discussion of all these topics.

3.1 Ammonia Properties Considerations

Due to ammonia's corrosive properties detailed in Chapter 2, the Ammonia Test Facility had to be thoughtfully constructed. In the event of an ammonia leak, the lab must have the capability to safely disperse the ammonia, minimizing the effect on the lab workers and the environment in general. In order to reduce the probability of an ammonia corrosion induced leak, the material used in the construction of facility had to be carefully controlled.

3.1.1 Test Chamber Safety

Test chamber safety is required to keep toxic ammonia from harming lab workers. Figure 3.1.1 shows the ammonia chamber that measures 16x7 ft. and is 8 ft. in height discussed in Chapter 2. In the event of a leak this chamber keeps the ammonia fumes from spreading throughout the lab and harming lab workers. There is a dedicated vent

and fan for it that expels the ammonia out over the roof of Rathbone Hall. This removes the ammonia fumes trapped in the chamber. The roof exit seen in Figure 3.1.2 extends above all other roof-top vents above Rathbone Hall so as to not interfere with any other air handling units.

One of the 16 ft. sides of the chamber has two sliding doors and is covered with Plexiglas for easy viewing into the chamber during experimentation. One of the 7 ft. sides is covered with sheet metal, but has a 2 ft. wide and 4 ft. tall access door for access into the chamber to manipulate and view components without entering the chamber. The other two sides are part of the walls of the ammonia chamber room (Rathbone 52B). The top is covered in sheet metal as well.

Other than the doors and access panel, there are penetrations in the chamber for electrical power, instrumentation, ventilation, and liquid cooling with propylene glycol that support the testing of ammonia in the chamber. Other refrigerants have been used in the chamber, but it was originally built with the intention of testing with ammonia. The capabilities with the electrical power, instrumentation, and liquid cooling with glycol in the ammonia chamber will be explained in more detail later. The exhaust vent for the chamber is continuously on so if there is an ammonia leak when no one is present in the lab the ammonia will still be vented out into the atmosphere. It is also continuously on so that someone wanting to manipulate the ammonia system in the chamber will not need to remember to turn it on. The amount of air that the vent can remove has been measured to be approximately 50 m^3/min (~1745 CFM) [21].

Another safety measure that is built into the ammonia chamber is a Manning Systems, Inc. Model 20 ammonia detector. A more detailed discussion of this detector is

given later in this chapter and the specifications of this detector can be found in Appendix A. It is connected to the data acquisition system discussed later where it is set to alarm above a certain ammonia concentration.

There is also a full faced mask supplied in the lab for lab workers to wear when inside the ammonia chamber. It uses special filters to filter out the ammonia from the air.

3.1.2 Material Compatibility Considerations

To ensure the structural integrity of the Ammonia Test Facility, all materials used within the facility were rated compatible according to the literature. The materials used are summarized Table 3.1.1. The only exception is one of the Raytheon high heat flux cooling devices has internal copper passages.

Although the literature clearly stated that ammonia and copper are not compatible, it was requested by Raytheon that we determine if the Ammonia Test Facility could be operated with the heated copper surface. As previously mentioned, the water content of the ammonia significantly enhances the corrosion of copper by ammonia. Thus all ammonia used in the facility must have less than 5 ppm of water [7]. The specific ammonia used in the test cell is supplied by Lampton Welding Supply out of Salina, KS and rated to 99.999% purity or less than 5 ppm of water.

To verify the compatibility of ammonia and copper in the Ammonia Test Facility, an exposure test was conducted. A schematic of the test configuration can be seen in Figure 3.1.3. A picture of the copper chamber is shown in Figure 3.1.4. This copper sample was exposed to ammonia within the flow loop for a total of 117 hours. During this time the ammonia mass flow rate was maintained at 0.015 kg/s. The test cell

temperature varied from 20 to –25°C which resulted in ammonia flow loop pressures varying from 930 - 480 kPa (120 – 55 psig). After 43 hours of exposure, the copper was removed from the ammonia flow and inspected for corrosion. As shown in Figure 3.1.5, the copper sample was not corroded. The copper was re-sealed in the chamber and tested further. The reinsertion of the sample also simulated a system isolation and repair event likely to occur during actual testing. Figure 3.1.6 shows the copper sample at the end of 117 hours of ammonia exposure. The sample does not show any signs of corrosion. Thus, the ammonia used in the KSU ammonia test facility is considered to be compatible with copper.

Table 3.1.1 Chosen Compatible Materials

Sealing Materials	Transport Materials
Kalrez	Stainless Steel (316)
Teflon, Virgin	Carbon Steel
Butyl	PVC
Ethylene-Propylene	Cast Iron
Neoprene	Hastalloy 'C'

Figure 3.1.1 Ammonia Chamber

Figure 3.1.2 Ammonia Chamber Exhaust Vent on Roof of Rathbone Hall

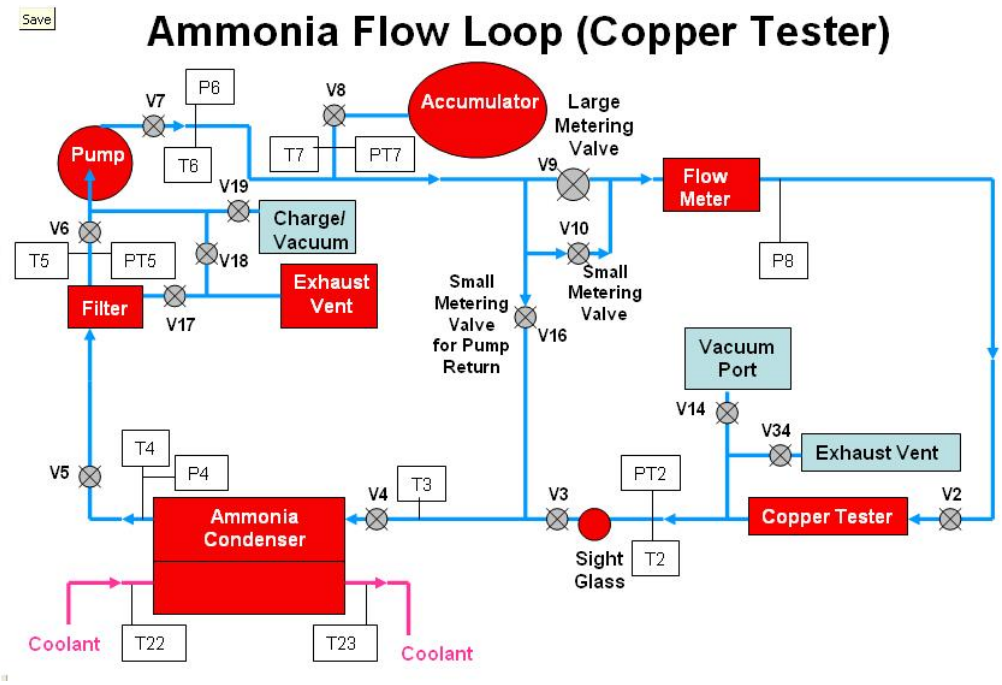

Figure 3.1.3 Schematic of Copper Corrosion Test Loop

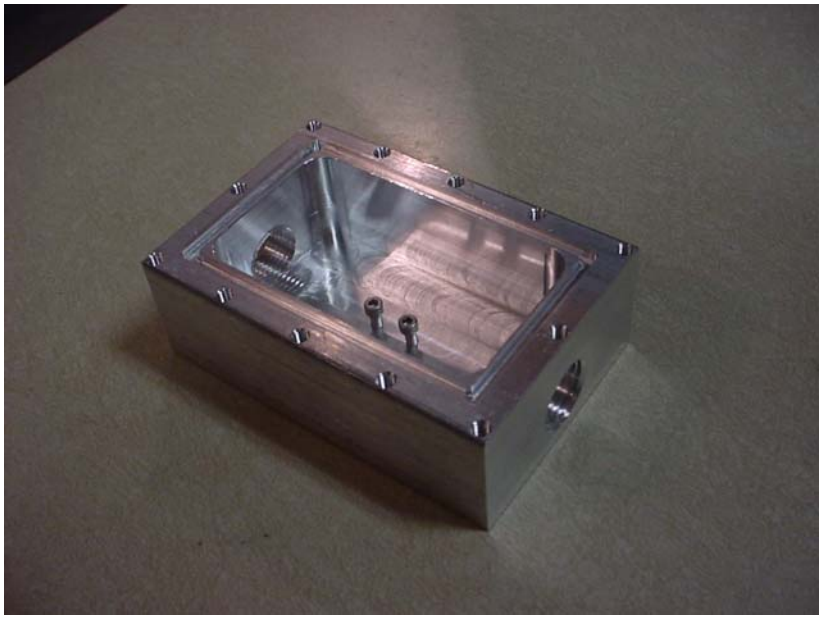

Figure 3.1.4 Copper Chamber

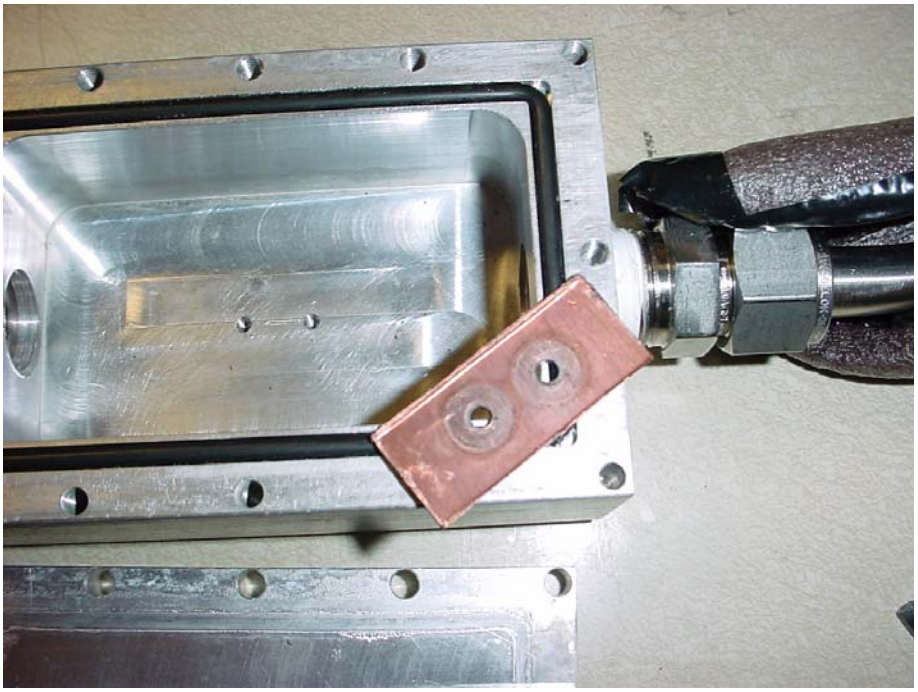

Figure 3.1.5 Copper Sample After 43 Hours of Exposure

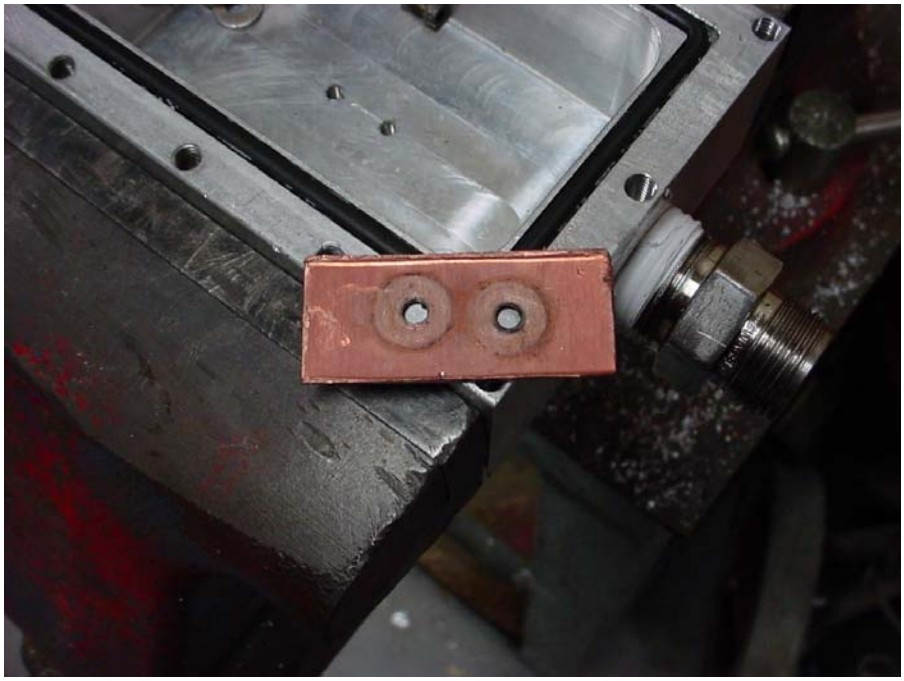

Figure 3.1.6 Copper Sample After 117 Hours of Exposure

3.2 Description of Ammonia Test Facility

The purpose of this Ammonia Test Facility is to deliver liquid ammonia to a test surface at a specific temperature and pressure in a safe laboratory environment. All components within the facility serve a specific purpose. This section is broadly divided into 3 sections: ammonia loop, glycol loop, and instrumentation.

3.2.1 Ammonia Loop

Clearly, the most important aspect of the chamber is how ammonia is processed. A schematic of all components associated with the ammonia flow is shown in Figure 3.2.1. Each of the components shown in the schematic will now be described.

3.2.1.1 Condenser

The condenser is the primary heat removal device for the ammonia flow loop. All energy introduced to the flow in the test section must be removed from the ammonia and transferred to the glycol. Because it is expected that a mixed liquid-vapor phase will leave the test section, the condenser must sufficiently condense the vapor phase and ensure that only liquid ammonia is allowed to exit the device.

The thermodynamic specifications of the condenser are summarized in Figure 3.2.2. The ammonia flow rate is dictated by the maximum flow rate to be considered within the test cell, 0.04 kg/s (~1gpm). The ammonia input conditions are dictated by the highest expected enthalpy of the ammonia as it leaves the test section. The ammonia output conditions are dictated by the lowest expected enthalpy of the ammonia subcooling to be considered for testing. The propylene glycol flow rate is estimated by the glycol pump curve from the pump manufacturer. The glycol pump is estimated to

supply 114 l/min (30 gpm) to all of the ammonia flow loop components using glycol. Most of this glycol is expected to be diverted to the condenser and conditioner discussed later. Therefore, it is assumed that there is a glycol flow rate of 57 l/min (15 gpm) to the condenser. The ammonia and glycol flow counter-current to each other.

Another significant design constraint for the condenser is that the structural materials be compatible with ammonia. It was desired to avoid copper in preference of a more ammonia compatible material such as stainless steel.

Many heat exchanger types were considered: concentric tubes, parallel plates, etc. Many vendors were consulted and supplied with the constraints discussed above.

The heat exchanger chosen for the Ammonia Test Facility was a Alfa Laval NB26-60H Stainless Steel Plate heat exchanger. The vendor supplied performance specifications for the device are listed in Appendix A. A picture of the device is shown in Figure 3.2.3.

3.2.1.2 Filter

Figure 3.2.4 shows a top view of the filter for the ammonia flow loop used to keep any particular contaminants in the system from being sent through the pump and all other components. This component was used for a previous experiment in the ammonia chamber so it was already available for use. It was reconfigured for use in the current ammonia flow loop.

Protecting the pump from contaminants was deemed most important. Therefore, since only pure liquid was wanted at the pump suction to protect the pump from pumping vapors, it was decided to also use the filter as a liquid/vapor separator as well. The outlet

of the filter, on the side of the cylindrical filter housing not seen in Figure 3.2.4, was pointed downward. This would allow gravity to help with only allowing liquid into the pump suction line after the filter in the event that there were vapors present inside the filter housing.

3.2.1.3 Pump

The pump was used to supply the Raytheon test cell with ammonia flow. One design constraint for the pump was the maximum required flow rate of the ammonia for the test cell which was 0.04 kg/s. A 138 kPa pressure drop, calculated from the previous flow loop in the ammonia chamber, was another constraint. Also, from a discussion with a thesis committee member [5] it was advised to purchase a magnetically-coupled gear pump due to their excellent ability to seal the working fluid from the outside environment. A Liquiflo 35R-MC magnetically-coupled gear pump was eventually chosen based on these constraints. The vendor supplied performance specifications for the pump are listed in Appendix A. A picture of the pump is shown in Figure 3.2.5.

The theoretical performance of the pump was required and, due to Liquiflo only supplying pump curves for water, pump curves for ammonia had to be calculated. Non-dimensional scaling factors were used to convert the water pump curves to ammonia [8]. A mass flow rate of 0.032 kg/s (0.77 gpm) at the 138 kPa pressure differential given to the pump manufacturer was calculated. The maximum theoretical mass flow rate calculated was 0.035 kg/s (0.85 gpm). This was less than the required 0.04 kg/s, however, these values were theoretical and it was decided to continue construction of the KSU ammonia flow loop with the purchased pump. After several tests had been performed it was found that the pump was actually able to obtain mass flow rates of over

0.04 kg/s. This is most likely do to the lower pressure drop around the loop than what was used in calculating the theoretical ammonia pump curve. Charts showing the given water pump curves and the calculated ammonia pump curves can be seen in Appendix A.

3.2.1.4 Accumulator

The accumulator, pictured in Figure 3.2.6, is the pressure setting device for the entire ammonia flow loop. It consists of a 1 gallon sized carbon steel outer tank, a rubber bladder that expands and contracts inside the outer tank, a valve at the bottom of the tank, the proper fittings and components for filling and venting the bladder, and copper lines coiled around the outer tank.

The outer steel tank contains the ammonia working fluid and is the main part of the accumulator to which all other components associated with it are attached.

The rubber bladder contains the inert gas (industrial grade nitrogen) used to pressurize and depressurize the system. The bladder can be ordered from the manufacturer in several different materials for different material compatibility situations. When the bladder is ordered it comes in a kit with all of the necessary seals for the rest of the accumulator components so that all of the rubber material in the accumulator is of the same material. The bladder is filled and vented by opening and closing a Schrader valve connected to the bladder which exits out the top of the accumulator outer tank.

Currently there is a valve on top of the accumulator that screws onto the bladder's Schrader valve to open and close it. This valve is connected to a header which also has a pressure gauge, venting valve, and a ball valve connected to it. The ball valve is where the source of the nitrogen comes from.

The ammonia comes in at the bottom of the accumulator outer tank. It comes through a valve that is normally open when both sides of the accumulator are pressurized. This valve is used to close off the accumulator from the ammonia when the bladder becomes too pressurized.

The last major component associated with the accumulator is the copper tubing coiled around the outside of it. This copper tubing has glycol running through it and the purpose of this is to cool the accumulator in order to condense most, or all, of the ammonia vapor that becomes present in the accumulator. The accumulator is not a flow-through device for the ammonia and another means is needed to keep the ammonia close to the temperature of the rest of the system to keep the ammonia vapor in the accumulator to a minimum. This is desired because it is easier to compress, or pressurize, liquid than vapor making it easier to control the pressure in the ammonia flow loop.

3.2.1.5 Flow Conditioner

Figure 3.2.7 partially shows the ammonia conditioner which is a heat exchanger located just before the test cell in the ammonia flow loop. It is used to set the state of the ammonia entering the test cell. Constructed as a three pass concentric tube heat exchanger it consists of three long sections of 316 stainless steel tubing that spans most of the length of the ammonia chamber. Special fittings are used at the ends to keep the glycol flowing through the annulus separate from the ammonia flowing through the inner tube.

Currently to control the outlet state of the ammonia, a metering valve at the inlet of the glycol fluid side is used. However, external electrical tape heaters after the

conditioner and/or more precise metering valves may be needed in the future in order to have more control over the state of the ammonia entering the test cell.

As mentioned in the Condenser section the glycol pump supplies roughly 114 l/min (30 gpm) of glycol to all of the components using it in the ammonia chamber. Since most of that flow rate is assumed to go to the condenser and the conditioner then an assumed glycol flow rate to the conditioner is roughly 57 l/min (15 gpm). Due to this rough assumption it was later decided to not use the conditioner as a system variable. The metering valve previously mentioned was left completely open allowing maximum glycol flow for all loop conditions tested for. Physical specifications for the conditioner are in Appendix A. The ammonia and glycol flowed counter-current to each other.

3.2.2 Glycol Loop

To provide a constant temperature source for the KSU Ammonia Test Chamber, a flow loop is used to circulate propylene glycol through the components in the ammonia flow loop used for cooling/condensing the ammonia. The ammonia flow loop components that are supplied with glycol have been discussed previously. A schematic of the glycol distribution is shown in Figure 3.2.8. This section applies to the control and supply of the glycol loop.

3.2.2.1 Pump

The location of the glycol pump in the glycol flow loop can be in Figure 3.2.8. It circulates glycol (pink antifreeze) in and out of the ammonia chamber and back into a large storage tank. While the glycol is in the ammonia chamber it travels to any one of the four components that need to be cooled in order to absorb the energy input into the

ammonia at the Raytheon test cell or to control the inlet condition to the test cell. These four components are the ammonia condenser, conditioner, accumulator, and the copper lines wrapped around the pump and pump suction lines after the condenser. A pump curve for the glycol pump can be found in Appendix A.

The glycol flowing through the condenser is used to condense the ammonia after part of it has become a vapor due to the energy input from the test cell. The glycol in the conditioner is used to create the desired state of the ammonia before it enters the test cell. As for the accumulator, the glycol flows in a coil pattern around it in order to keep ammonia vapor in the system pressure setting device to a minimum. This helps keep system pressures relatively steady. Finally, there is glycol running through copper tubes wrapped around the pump suction lines after the condenser. These glycol lines are used to create conditions in the ammonia lines, especially at start-up, to where there is all liquid ammonia present.

3.2.2.2 Storage Tank

The storage tank is used to store the glycol for controlling the temperatures of the ammonia in the chamber. It has a capacity of approximately 200 gallons [17]. The glycol temperature is controlled by pumps drawing glycol from the tank into the Liebert chiller, discussed next. These chiller pumps then circulate the glycol through the chiller's evaporators to cool the glycol. The glycol is then circulated back to the storage tank.

As mentioned previously the glycol in the storage tank is sent to the ammonia chamber by the glycol pump to various ammonia flow loop components which can be

seen in Figure 3.2.8. This is where the glycol from the storage tank absorbs energy that the chiller must control.

3.2.2.3 Chiller

The chiller is used to cool, or control the temperature of, the glycol coolant stored in the glycol storage tank. It consists of two separate cooling loops. The only thing that these two loops use in common is the glycol that they cool and their heat sink. This means that if one of the loops fails, or needs maintenance, the other loop is able to keep the glycol temperature under control.

The combined capacity of both of the chiller's cooling loops is 12 tons and they are made to run on R-502 refrigerant. This chiller also operates on its own, dedicated 480 volt, 70 amp circuit. The heat sink for the chiller is the building tap water supply. This tap water supply enters into the lab in the ammonia chamber room. After it passes through the chiller it is then diverted back up into the lab ceiling where it runs over into the main lab room and runs down to the large drain in the middle of the main room. More detailed specifications for the chiller are found in Appendix A.

The temperature controllability of this chiller was tested to see how well it was able to control the temperature of the glycol in the storage tank. After a few days of testing the results were inconclusive as the temperature profile, seen in Figure 3.2.9, over the testing period was very sporadic in its heating and cooling. No more time was allocated to continue to solve this problem so as of now testing in the ammonia chamber is done with the chiller set at its coldest temperature.

3.2.3 Instrumentation

Automated recording of the KSU ammonia flow loop parameters with various instrumentation equipment was done with thermocouples, pressure transducers, a flow meter, and an ammonia detector. This instrumentation was necessary for performing heat transfer and other calculations and for diagnosing unexpected events. Instrumentation for quick visual reference consisting if sight glasses and dial pressure gauges was also required to view flow loop status and to verify the automated instrumentation.

Table 3.2.1 shows the instrumentation and its corresponding channel that measure the ammonia flow loop parameters. All of these values shown above are read by a data acquisition unit and then recorded by the DAQ computer discussed later. The instrumentation from the list in Table 3.2.1 and other instrumentation that will be discussed here includes the sight glasses, pressure, temperature, flow, ammonia detection, and test cell instrumentation.

3.2.3.1 Data Acquisition Equipment

The data acquisition hardware for the ammonia test facility consisted of a Hewlett Packard 34970A Data Acquisition/Switch Unit seen in Figure 3.2.10 and a personal computer. The Data Acquisition/Switch Unit had a total of 60 channels available for voltage measurements on three separate cards for a total of 20 channels per card. Also on each of these cards were 2 channels for measuring current. This data acquisition unit was also configured to record temperature measurements with integrated temperature references on each of the three cards. The channels currently used in this data acquisition unit are shown in Tables 3.2.1, 3.2.2, and 3.3.1.

The data acquisition software on the personal computer (DAQ computer) was from National Instruments called LabVIEW 7.0. All of the thermocouple voltage conversions to temperatures were performed by the data acquisition unit and displayed only a temperature value in LabVIEW. Other instrumentation voltage and current signals had to be processed by LabVIEW. Channels were displayed real time on a monitor, as seen in Figure 3.2.11, and written to a file in approximately six second intervals.

3.2.3.2 Sight Glasses

The sight glasses like the one in Figure 3.2.12 were used at the inlet and outlet of the ammonia test section. Also, the sight glasses were instrumental in charging the ammonia flow loop since they were located at a higher point in the flow loop than most other components. Figure 3.2.13 shows the location of these sight glasses in the ammonia flow loop schematic.

3.2.3.3 Pressure

The pressure instrumentation recorded the pressure of the ammonia flow at various points throughout the flow loop. Both electronic pressure transducers and dial pressure gauges were utilized. The dial pressure gauges were in place for quick visual verification of pressure states. The location of the pressure transducers throughout the ammonia flow loop are shown by the highlighted purple rectangles in Figure 3.2.13 and are symbolized as "PT#." The dial pressure gauges are symbolized as "P#" and are shown in Figure 3.2.13 as well, but are not highlighted.

Dial pressure gauge P4 measured the pressure at the outlet of the condenser. Dial pressure gauge P6 measured the pressure at the outlet of the pump. Dial pressure gauge

P8 measured the pressure at the outlet of the flow meter. All dial pressure gauges had a range of 0-1480 kPa (0-215 psia).

Pressure transducer PT1 measured the pressure of the ammonia flow at the inlet to the test cell with an uncertainty of ±0.14% of reading. Pressure transducer PT2 measured the pressure of the ammonia flow at the outlet from the test cell with an uncertainty of ±0.07% of reading. Pressure transducer PT5 measured the pressure of the ammonia flow at the inlet to the ammonia pump with an uncertainty of ±1% of reading. Pressure transducer PT7 measured the pressure of the ammonia at the accumulator with an uncertainty of ±0.18% of reading. Pressure transducer PT8 measured the pressure of the ammonia flow at the ammonia inlet to the conditioner with an uncertainty of ±0.05% of reading. All pressure transducers were calibrated with a dead weight tester.

Pressure transducers PT1, PT5, and PT7 were calibrated up to 1480 kPa, but were rated to 3450 kPa (500 psia) or higher. However, pressure transducers PT2 and PT8 were only rated and calibrated up to 790 kPa (115 psia). Therefore, test conditions had to be limited to a maximum of 790 kPa so that pressure all readings were in range of all pressure transducers. More specific information regarding pressure transducer specifications is available in Appendix A. Additionally, the calibration plots for the pressure transducers are in Appendix B.

3.2.3.4 Temperature

The temperature instrumentation for the ammonia flow loop supporting the Raytheon test cell recorded all temperatures associated with the ammonia flow loop and glycol flow loop. It consisted of all T-type thermocouples. The locations of these

thermocouples, symbolized as "T#," are shown in Figure 3.2.14 by the highlighted purple rectangles. The full names of these abbreviated thermocouples in Figure 3.2.14 can be found on the instrumentation list for the ammonia flow loop in Table 3.2.1.

For the ammonia flow loop thermocouples T1 and T2 measured the inlet and outlet temperatures of the test cell. Thermocouples T3 and T4 measured the inlet and outlet temperatures of the condenser. Thermocouples T5 and T6 measured the inlet and outlet temperatures of the pump. Thermocouple T7 measured the temperature of the ammonia near the accumulator. Thermocouples T8 and T9 measured the inlet and outlet temperatures of the conditioner.

For the glycol flow loop thermocouples T20 and T21 measured the inlet and outlet glycol temperatures of the conditioner. Thermocouples T22 and T23 measured the inlet and outlet glycol temperatures of the condenser. The glycol storage tank temperature was also measured, by channel 120 in the data acquisition unit, but not shown in Figure 3.2.14.

No calibration was performed on these thermocouples. The uncertainty of these thermocouples in the ammonia and glycol flow loop supporting the test cell was $\pm 1.8^{o}C$ which was the maximum difference between all thermocouples at an average room temperature of $22.2^{o}C$.

3.2.3.5 Flow Meter

In order to measure the liquid ammonia flow through the system a coriolis type flow meter was used. The device is a Micromotion CMF025 meter with a corresponding Micromotion RTF9739 remote transmitter. Both the meter and the transmitter are

pictured in Figure 3.2.15. The location of the flow meter in the ammonia flow loop schematic is shown in Figure 3.2.16 by the highlighted green rectangle. The device was setup and monitored with a laptop computer using vendor specific software. The software allows the operator to manipulate/modify parameters of the flow meter in order to customize the flow meter's operation and outputs to suit the operator's specific requirements. It is measured by channel 121 in the data acquisition unit. Uncertainty for this device is ±0.1% of reading based on manufacturer specifications.

3.2.3.6 Ammonia Detector

A Manning Systems, Inc. Model 20 ammonia detector was used to record the concentration of ammonia in the chamber. It is located in the neck of the vent hood in the ammonia chamber where it can easily sense the amount of ammonia exiting the chamber. It is measured by channel 105 as seen in Table 3.2.1 by the data acquisition unit. In the DAQ computer it is set up to alarm when it senses a 400 ppm concentration of ammonia. Its range of maximum sensitivity is for 0-1000 ppm of ammonia concentration. More detailed specifications of this detector can be found in Appendix A.

3.2.3.7 Test Cell Instrumentation

Because multiple test configurations were to be considered, instrumentation for the test cell was distinct. The instrumentation common to both cooling devices, the ECHIC and Slot Jet, will be discussed here. It is used to measure and record data for the ammonia conditions close to the cooling device as well as other equipment supporting the use of the cooling device. Table 3.2.2 shows the test cell instrumentation and its corresponding channel.

The temperature instrumentation for the test cell consisted of K-type thermocouples and an infrared (IR) camera. As indicated in Figure 3.2.17 these thermocouples measure the cooling inlet and outlet ammonia fluid temperatures and the heater block top-left (HBTL) temperature, heater block top-right (HBTR) temperature, heater block top-middle (HBTM), and the heater block bottom-middle (HBBM) temperatures. Channels 201 and 202 measure the cooling device inlet and outlet fluid temperatures and the heater block temperatures are measured by channels 207-210. The exact location of these four thermocouples on the heater block can be seen in Figure 3.3.6. No calibration was performed on these thermocouples.

The IR camera overlooks the neck of the heater block from the main part of the heater block to where it interfaces with the cooling device. It is used to display a real time (IR) image on a television outside of the ammonia chamber and to store (IR) images to be analyzed later on a computer. Figure 4.2.4 shows a sample IR image. The image analyzing procedure to determine the heat flux into the heated surface can be found in Appendix E.

The pressure instrumentation specific to the test cell cooling device included 2 pressure transducers. The location of these can be seen in Figure 3.2.17. They included the cooling device inlet pressure transducer and the cooling device differential transducer which measured differential pressure across the cooling device. These pressures are measured on channels 215 and 212, respectively in Table 3.2.2. The cooling device inlet pressure transducer had a nominal range of 0-790 kPa and an uncertainty of ±1% of the reading [23]. As with the ammonia flow loop pressure transducers PT2 and PT8, this was another pressure transducer limiting the testing pressures to 790 kPa. The

differential transducer had a nominal range of 0-103 kPa (0-15 psid) and an uncertainty of ±0.5% of the reading [23]. These pressure transducers did not require a calibration because there was a correlation given by the manufacturer that was used.

The instrumentation not seen in Figure 3.2.17 is discussed next. Channels 203, 205, and 206 measure temperatures at various locations on the heated surface frame. Channel 204 measures the ambient temperature just a few inches away from the cooling device. Channels 213 and 214 are part of the pneumatic system pictured in Figure 3.3.2 and discussed later that measure pressures corresponding to the air cylinder pressing the heater block against the cooling device. Channel 216 measures the DC excitation voltage supplied to all pressure transducers on the test cell. The channels that measure energy input into the heater block are 217 and 218. Channel 219 measures the AC voltage where the electrical power lines for the energy input into the heater block plug into the test cell. Finally, channel 220 measures the AC voltage for the energy input into the heater block as well, but it does so at the watt transducers much farther away from the test cell. This is so electrical line losses for the wire powering the heater block can be calculated. These losses were calculated to be approximately 1% of the total reading from the watt transducers.

Table 3.2.1 Ammonia Flow Loop Instrumentation

Flow Loop Instrumentation	
Channel on HP 34970A	Component
101	Test Cell Inlet Pressure (PT1)
102	Test Cell Outlet Pressure (PT2)
103	Conditioner Inlet Pressure (PT8)
104	Pump Inlet Pressure (PT5)
105	(**High Alarm**) NH3 Detector
106	Accumulator Pressure (PT7)
107	Test Cell Inlet Temperature (T1)
108	Test Cell Outlet Temperature (T2)
109	Condenser Inlet Temperature (T3)
110	Condenser Outlet Temperature (T4)
111	Pump Inlet Temperature (T5)
112	Pump Outlet Temperature (T6)
113	Accumulator Temperature (T7)
114	Conditioner Inlet Temperature (T8)
115	Conditioner Outlet Temperature (T9)
116	Conditioner Glycol Inlet Temperature (T20)
117	Conditioner Glycol Outlet Temperature (T21)
118	Condenser Glycol Inlet Temperature (T22)
119	Condenser Glycol Outlet Temperature (T23)
120	Glycol Tank Temperature
121	Flowmeter Current Signal

Table 3.2.2 Raytheon Test Cell Instrumentation

Test Cell Instrumentation	
Channel on HP 34970A	Component
201	Cooling Device Fluid Inlet Temperature
202	Cooling Device Fluid Outlet Temperature
203	Gimbal Frame Temperature
204	Room Ambient Temperature
205	Test Cell Base Temperature
206	Middle Gimbal Temperature
207	Top-Left Heater Neck Temperature
208	Top-Right Heater Neck Temperature
209	(**High-Alarm**) Top-Middle Heater Neck Temperature
210	Bottom-Middle Heater Neck Temperature
212	Cooling Device Differential Pressure
213	Air Supply Pressure
214	(**High-Alarm**) Air Cylindar Pressure
215	Cooling Device Inlet Pressure
216	~9VDC Voltage Monitor
217	1000W Watt Transducer
218	2000W Watt Transducer
219	(**AC Voltage**) Heater Voltage @ Heater
220	(**AC Voltage**) Heater Voltage @ Watt Transducers

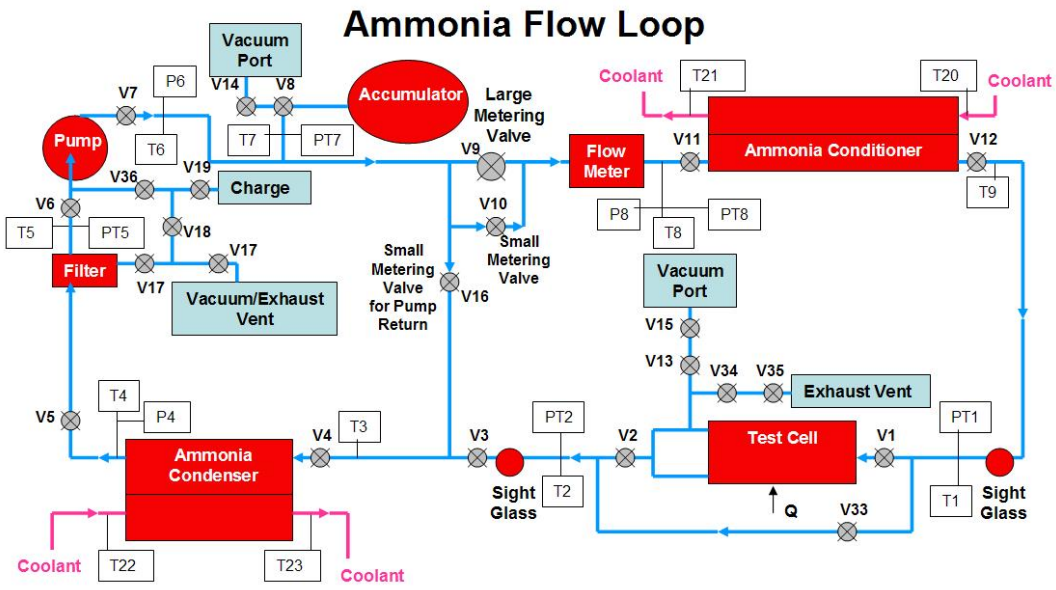

Figure 3.2.1 Ammonia Flow Loop

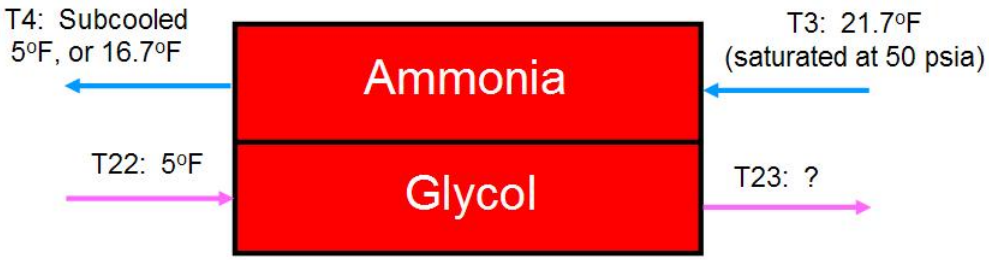

Figure 3.2.2 Ammonia Condenser Thermodynamic Specifications

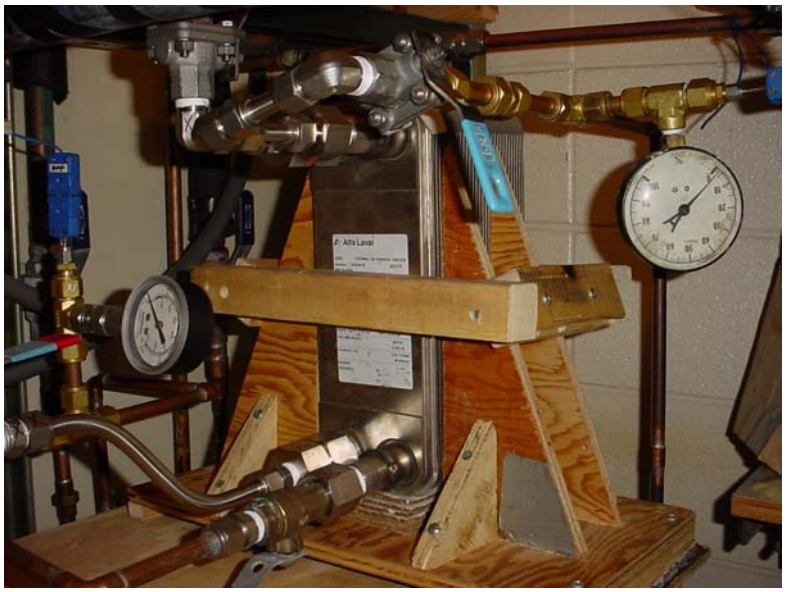

Figure 3.2.3 Ammonia Condenser Picture

Figure 3.2.4 Ammonia Flow Loop Filter

Figure 3.2.5 Ammonia Flow Loop Magnetically-Coupled Gear Pump

Figure 3.2.6 Ammonia Flow Loop Accumulator

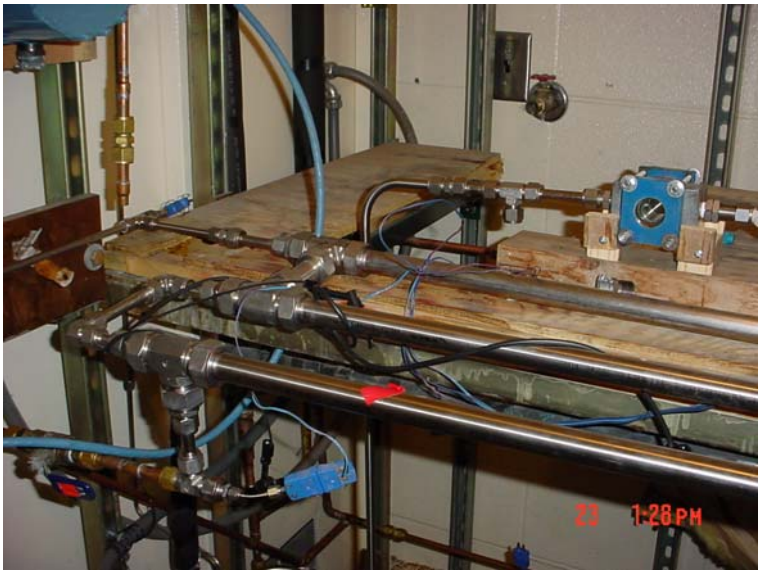

Figure 3.2.7 Ammonia Flow Loop Conditioner

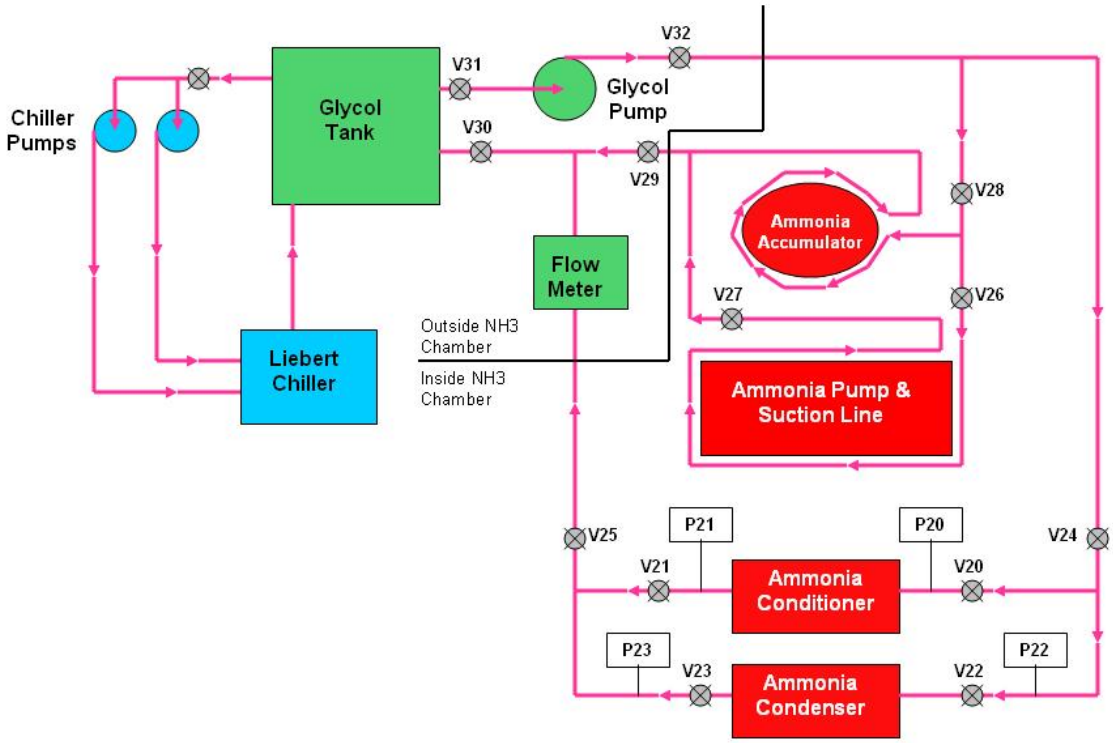

Figure 3.2.8 Glycol Flow Loop

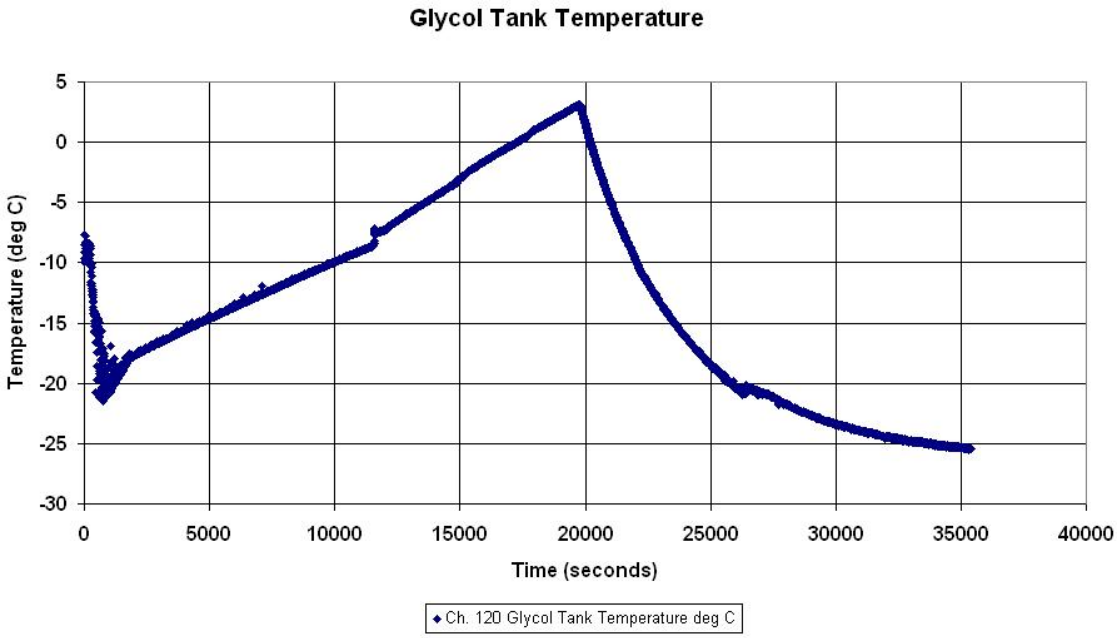

Figure 3.2.9: Glycol Tank Temperature When Testing Chiller Temperature Controls

Figure 3.2.10 Hewlett Packard 34970A Data Acquisition/Switch Unit

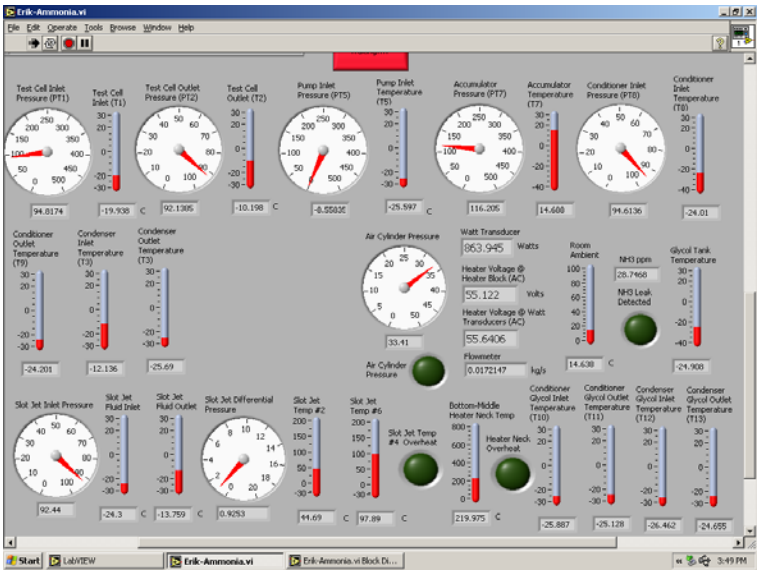

Figure 3.2.11 Data Acquisition Computer Screen (LabVIEW 7.0)

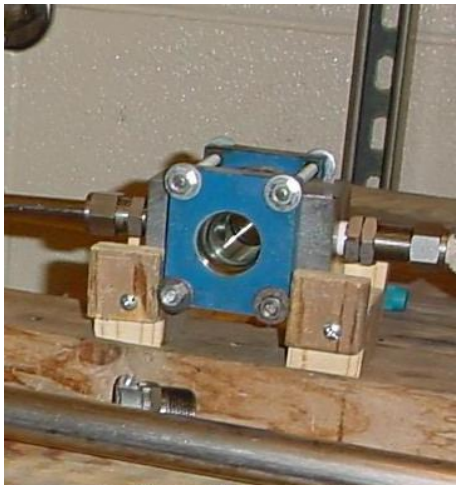

Figure 3.2.12 Ammonia Flow Loop Sight Glass

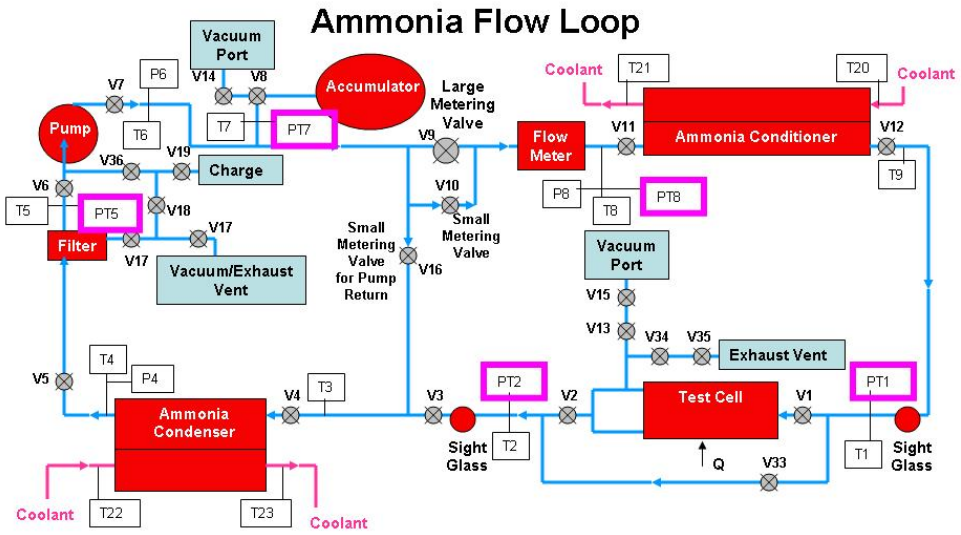

Figure 3.2.13 Ammonia Flow Loop Pressure Transducer Locations

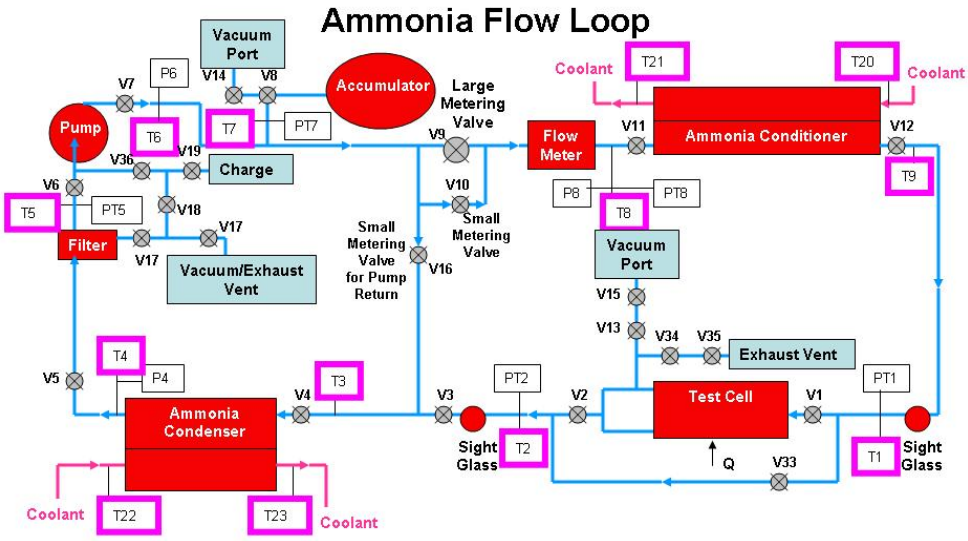

Figure 3.2.14 Ammonia and Glycol Flow Loop Temperature Instrumentation Locations

Figure 3.2.15 Ammonia Flow Loop Flow Meter

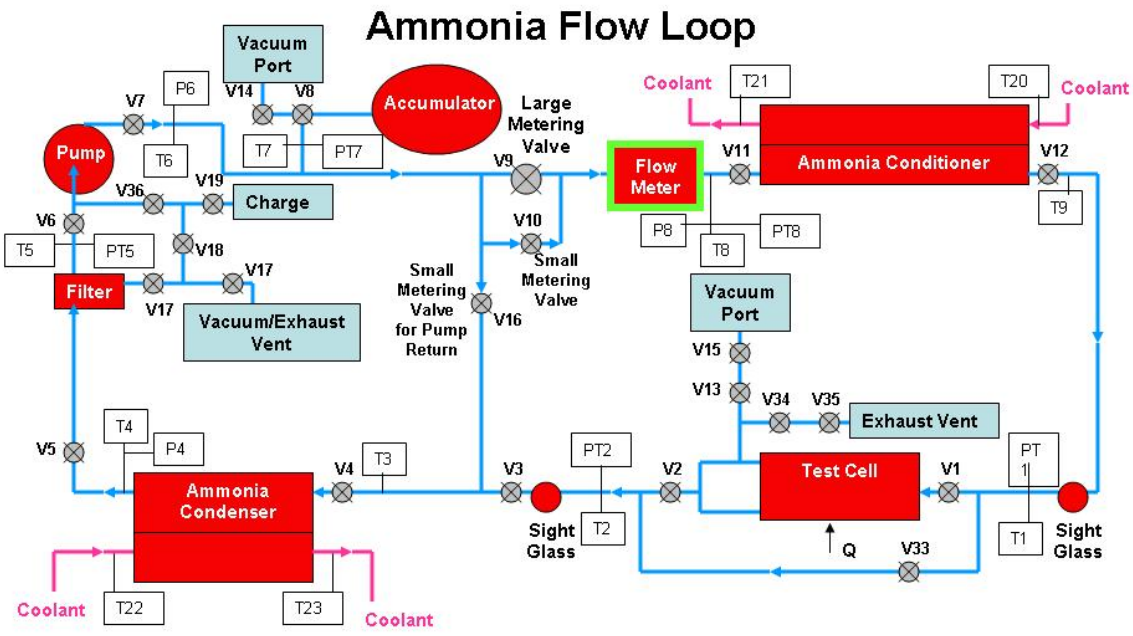

Figure 3.2.16 Ammonia Flow Loop Flow Meter Location

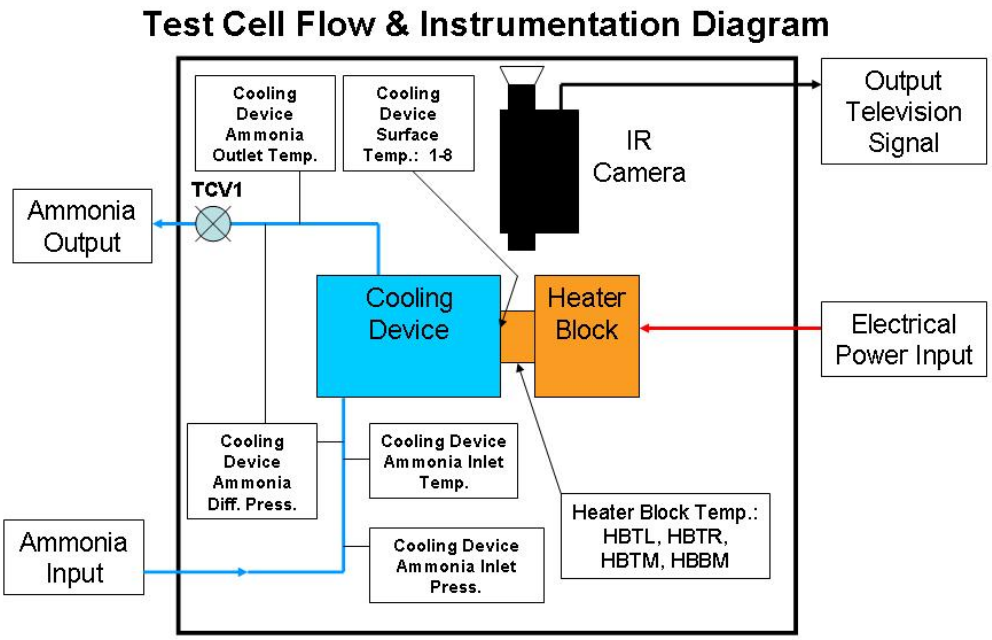

Figure 3.2.17 Raytheon Test Cell Instrumentation and Flow Diagram

3.3 Description of Raytheon Test Sections

There were two geometries considered, the ECHIC and the Slot Jet. Some of the supporting components were common to both geometries. These components and the specific test geometry will be discussed below.

3.3.1 Pneumatic System for Heater Block

The purpose of the pneumatic system, pictured in Figure 3.3.1, for the test cell was to seat the heater block neck onto the heated surface of the cooling device to ensure good mechanical and thermal contact. This was done supplying pressure to an air cylinder that would push on the back of the heater block opposite of the heater block neck. Compressed air was used as the pressure source.

The components of this pneumatic system consisted of the air cylinder, tubing, three solenoid valves, two pressure transducers, a pressure regulator, a metering valve, and a safety release valve. Figure 3.3.2 shows a schematic of the entire setup.

As discussed the air cylinder applied pressure to the heater block. The tubing supplied the air cylinder and other pneumatic components with the compressed air. One of the solenoid valves supplied the compressed air to the pneumatic system. The other two solenoid valves controlled the direction of the pressure applied by the air cylinder. The two pressure transducers were used to monitor the incoming compressed air pressure and the pressure inside the air cylinder. The air cylinder pressure could not exceed 50 psig as that was the maximum pressure the cooling devices were designed to handle. It was instructed by Raytheon to regulate the air cylinder pressure at 33 psig [10] which was performed with the pressure regulator. A metering valve placed in between the air cylinder and a solenoid valve controlled the rate at which the air cylinder retracted the heater block away from the cooling device. Finally, a safety release valve was placed on an air cylinder line to prevent over pressurizing.

3.3.2 Power Source

The maximum power required by the Raytheon test cell was 3000 watts [10]. The lab, able to supply 26 kW, was well equipped to handle this power requirement. One of the larger 7500 watt potentiometers in the lab powered the heater block on the Raytheon test cell. For the instrumentation to measure the output of the potentiometer there was not a single watt transducer able to handle the maximum required 3000 watt load for the heater block on the test cell. Instead two transducers were used in parallel. One of these

was the 0-2000 watt transducer and the other one was one of the 0-1000 watt transducers in the lab. These watt transducers and the potentiometer are shown in Figure 3.3.3. The potentiometers are the green boxes mounted on the side of the potentiometer shelf. The wiring diagram showing how these were used in parallel can be seen in Figure 3.3.4.

The two watt transducers were used in parallel by simply splitting the 6 AWG wires powering the test cell heater into two different wires of different sizes, a small diameter one and a larger one as shown in Figure 3.3.4. The small diameter wires were used to send power through the 0-1000 watt transducer and the larger ones sent power through the 0-2000 watt transducer.

Additional information on the electrical power supplies available in the lab is shown in Appendix A.

3.3.3 Heater Block

The heater block, seen in Figure 3.3.5, in the test cell is the component that supplies the energy input to the cooling device and to the entire ammonia flow loop. It is of a rectangular block design with a neck protruding from one side called the heater block neck. The end of this neck is what interfaces with the cooling device heated surface shown in Figure 3.3.6. The end of the neck is 1 cm tall and 3 cm wide making the heated surface area that interfaces with the cooling device 3 cm^2. During testing this neck is painted a flat black color with an approximate emissivity of 0.95 allowing the IR camera to more accurately measure the surface temperatures of this neck so that a heat flux can be calculated.

The main part of the heater block is where the heating elements, the actual source of the energy, are located. There are four of these heating elements and they are cylindrical in shape and fit into the four cylindrical holes machined out of the main part of the heater block seen in Figure 3.3.5. Each of the two leads of these heating elements are all joined together so that there are only two total leads to power the heater block heating elements. These elements are powered by the electrical energy source shown entering the heater block in Figure 3.3.6.

The instrumentation associated with the heater block, as previously discussed, consists of four K-type thermocouples recessed into the heater block neck on the opposite side that the IR camera views shown in Figure 3.3.6. These thermocouples measure the Top-Left, Top-Middle, Top-Right, and Bottom-Middle heater neck temperatures. The Top-Middle and Bottom-Middle temperatures were used to calculate the heat flux entering the cooling device.

Also shown in Figure 3.3.6 is where the pneumatic cylinder of the test cell pneumatic system attaches and pushes on the heater block to interface with the cooling device.

3.3.4 ECHIC Device

The copper ECHIC device in Figure 3.3.7 was the initial cooling device in the test cell. It was the initial reason for the requirement of very pure ammonia. The purpose of testing with the ECHIC device was to demonstrate the performance of many fluids dissipating a large amount of energy on a small surface.

The ECHIC had a heated surface of 3 cm^2. The ECHIC was designed to operate in two-phase flow. Its design diverted the fluid flow to take advantage of the two-phase heat transfer of any fluid flowing through it. Its design is proprietary to Raytheon. so its exact geometry is not known. A generalized schematic of its operating principle can be seen in Figure 3.3.8.

The instrumentation associated with the ECHIC device consisted of 20 E-type thermocouples all mounted to the outside edges of the heated surface on the outside of the ECHIC device. These thermocouple locations can be seen in Figure 3.3.9. E-type thermocouples were used because they have the highest voltage change per degree. The thermocouple locations with an "X" over them were defective.

3.3.5 Slot Jet Device

The Slot Jet device is pictured on the right in Figure 3.3.10. The picture on the left in Figure 3.3.10 is the actual piece that creates slot jets from the ammonia flow. The purpose of testing with the Slot Jet device was to also demonstrate the performance of many fluids, ammonia in this case, dissipating large thermal loads associated with DEW.

The energy input into the Slot Jet device is from the heater block previously mentioned in this section. Its heated surface is also 1 cm tall and 3 cm wide making a 3 cm^2 heated surface area. The geometry is shown in Figure 3.3.11. There are 3 slots 1 cm apart. The slots themselves are 1 cm tall by 0.1 cm wide. After the ammonia flow is passed through the slots and impacts the heated surface it exits through the small rectangular holes seen on the top of the Slot Jet in Figure 3.3.10.

Instrumentation was needed on the Slot Jet in order to perform heat transfer calculations. Table 3.3.1 shows the instrumentation and its corresponding channel for the Slot Jet. The location of the instruments on the Slot Jet listed in Table 3.3.1 can be seen in Figure 3.3.12.

All of the thermocouples on the Slot Jet device are T-type thermocouples. They were all made in the Heat Transfer Lab using a thermocouple welder. They are held onto the Slot Jet device using JB weld on the heated surface side of the Slot Jet, seen in Figure 3.3.13, and the sides as well. However, there is no JB weld present on the heated surface itself. The thermocouples just lay in the numbered thermocouple slots on the heated surface in Figure 3.3.12 without any adhesive. When the heater block neck is forced to contact the Slot Jet heated surface by the pneumatic cylinder the Slot Jet thermocouples are fixed in place.

Ensuring good thermal contact between the heated surface and the heater neck a thermally conductive paste, OMEGATHERM 201 [22], was used. The paste is rated at a maximum temperature of 200^{o}C. This maximum temperature was used to set the high alarm for Slot Jet thermocouple #6 as seen in Table 3.3.1.

Table 3.3.1 Slot Jet Instrumentation

Slot Jet Instrumentation	
Channel on HP 34970A	Component
302	SlotJet Temperature #2
303	SlotJet Temperature #3
304	SlotJet Temperature #4
305	SlotJet Temperature #5
306	(**High-Alarm**) SlotJet Temperature #6
307	SlotJet Temperature #7
308	SlotJet Temperature #8

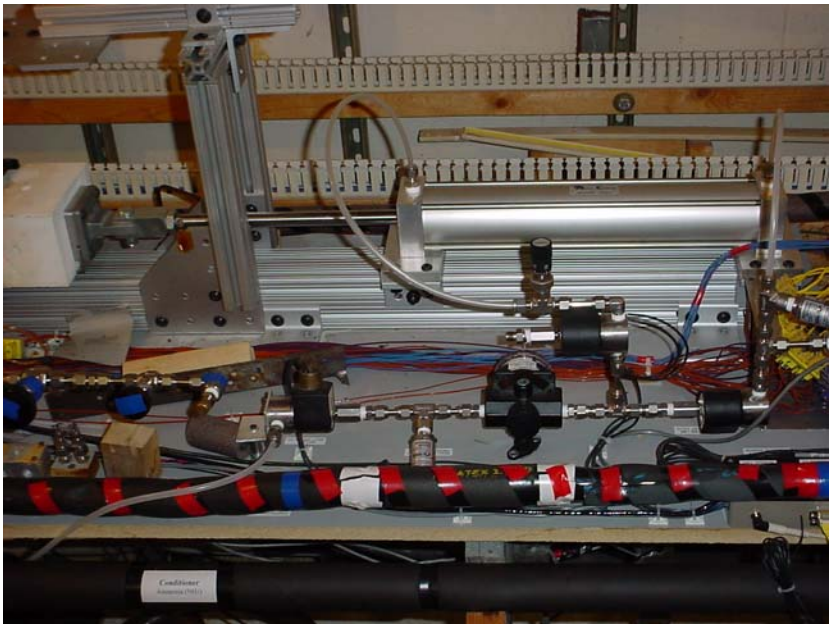

Figure 3.3.1 Picture of Raytheon Test Cell Pneumatic System

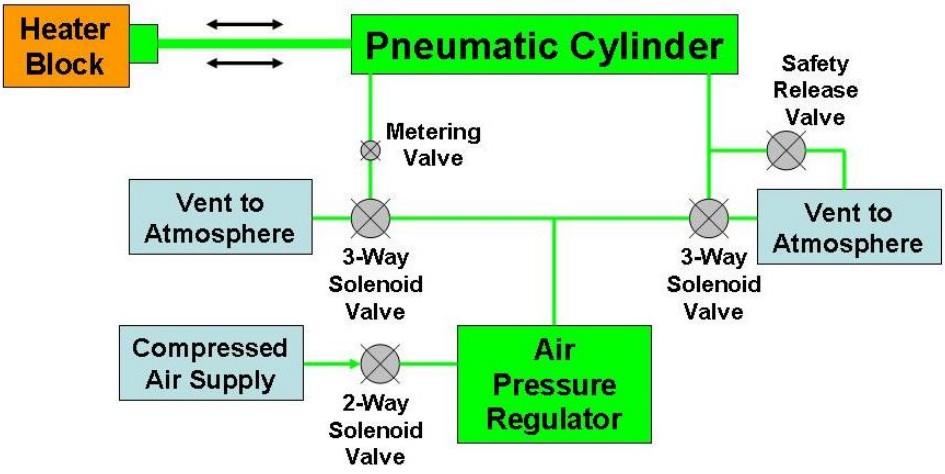

Figure 3.3.2 Raytheon Test Cell Pneumatic System

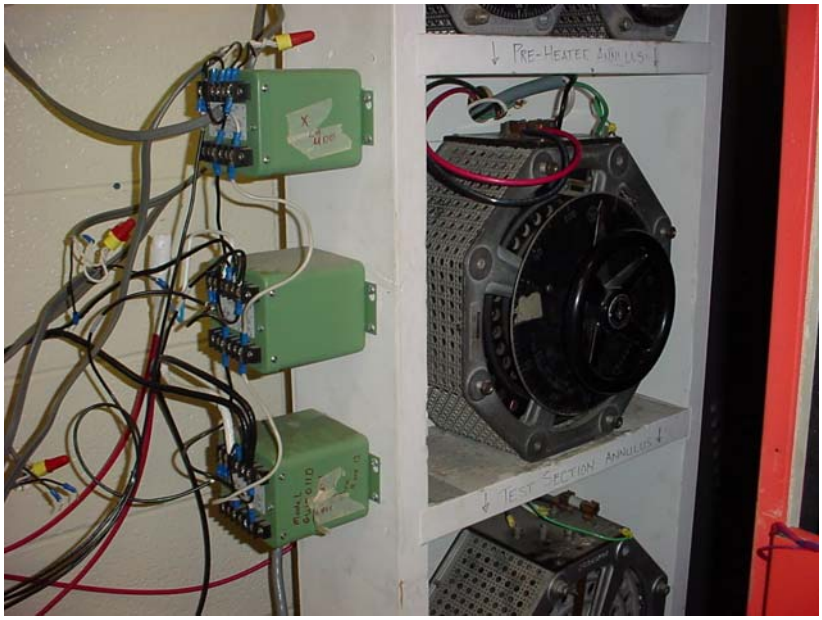

Figure 3.3.3 Test Cell Electrical Power Source and Instrumentation

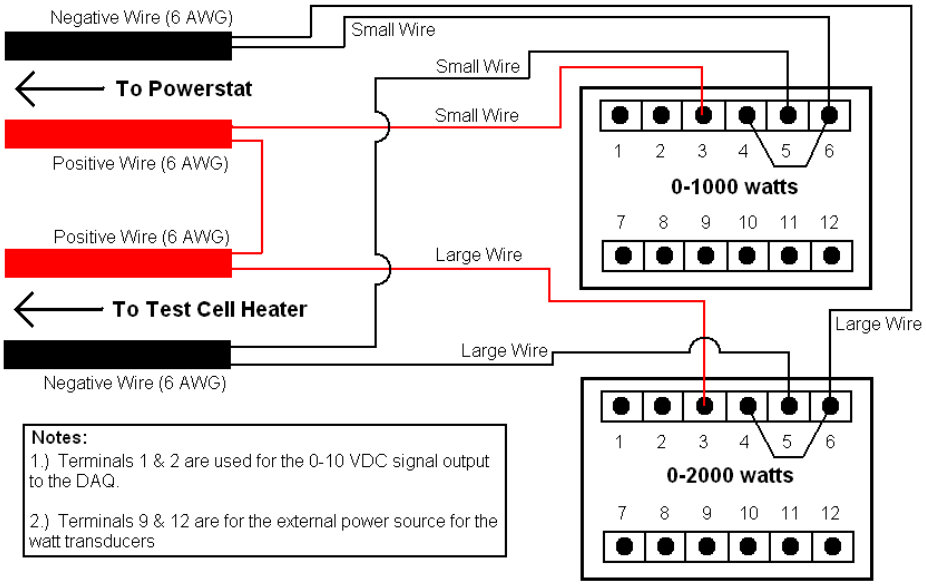

Figure 3.3.4 Wiring Diagram of Test Cell Electrical Power Source and Instrumentation

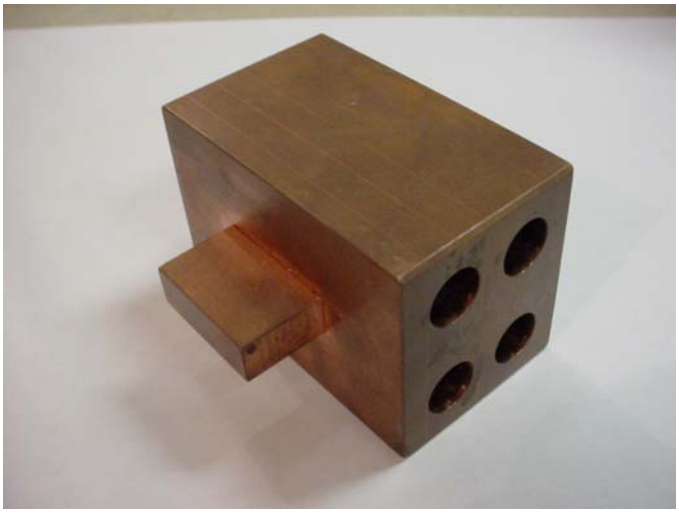

Figure 3.3.5 Heater Block

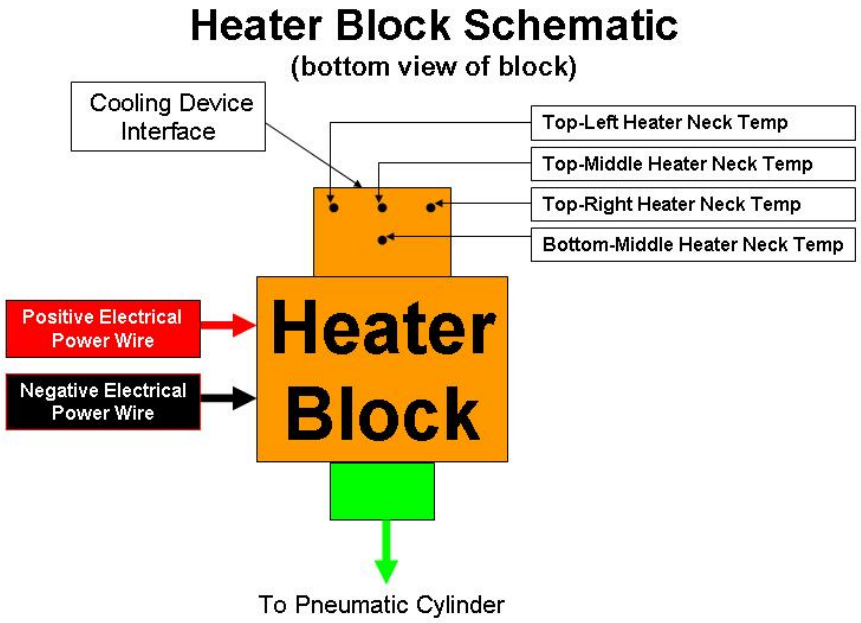

Figure 3.3.6 Heater Block Schematic

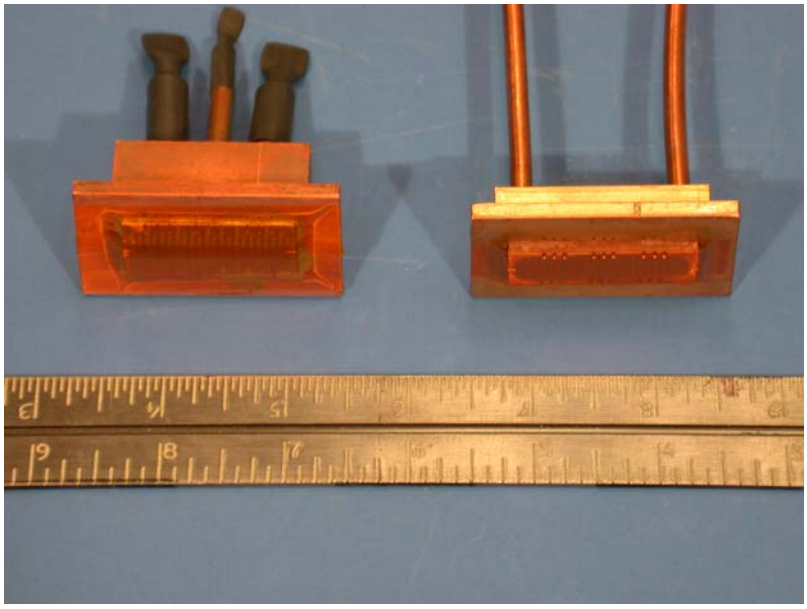

Figure 3.3.7 Picture of ECHIC Device (Left), a CHIC (compact high intensity cooler) Device in on the Right

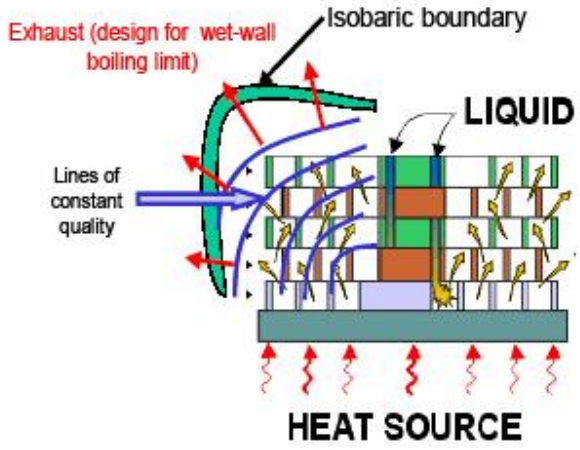

Figure 8. ECHIC theory of operation.

Figure 3.3.8 ECHIC Theory of Operation

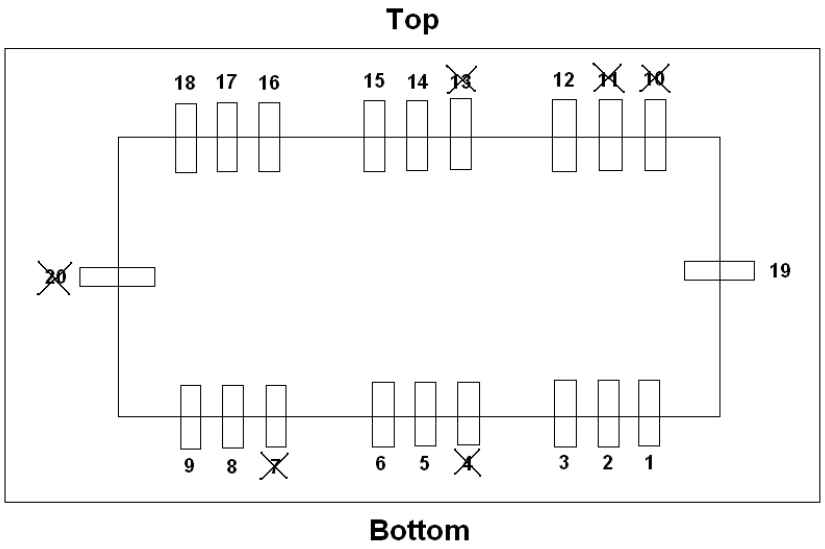

Figure 3.3.9 ECHIC Thermocouple Locations

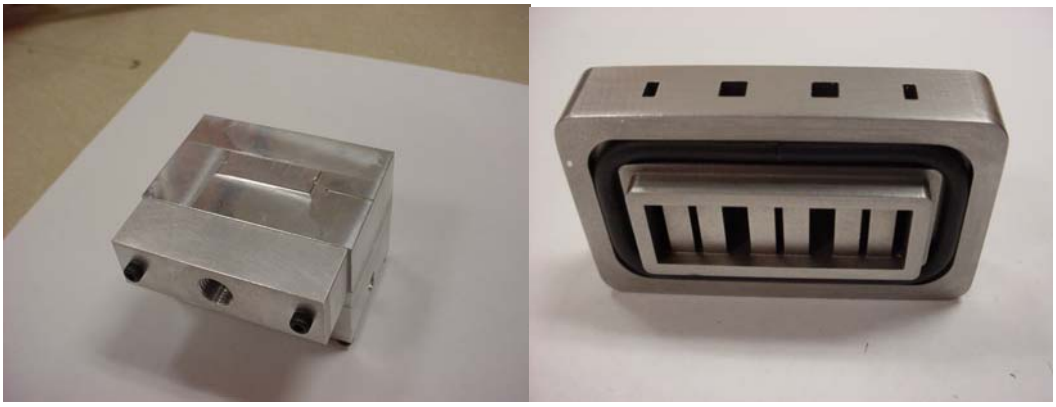

Figure 3.3.10 Slot Jet Device (Right: Entire Device, Left: Device Inside That Creates Slot Jets)

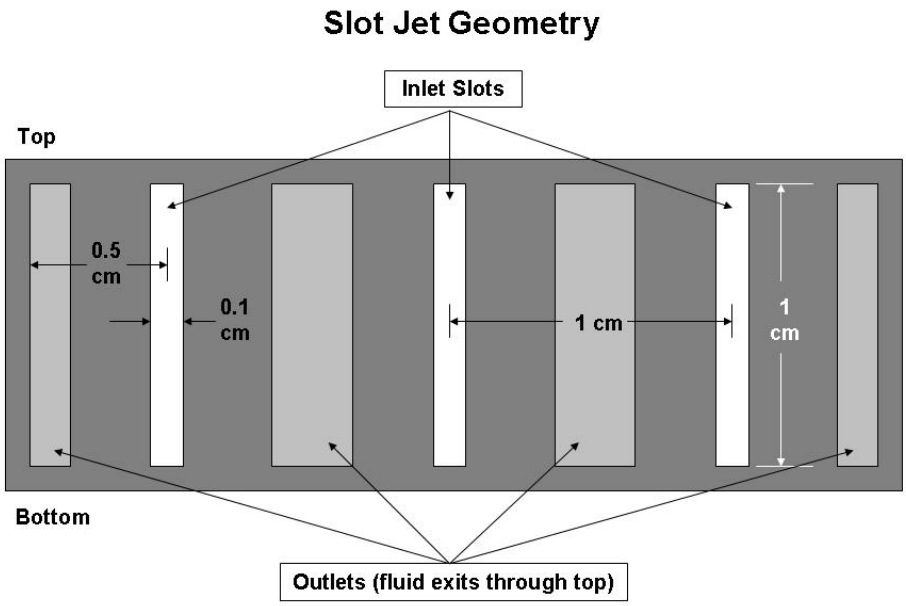

Figure 3.3.11 Slot Jet Geometry

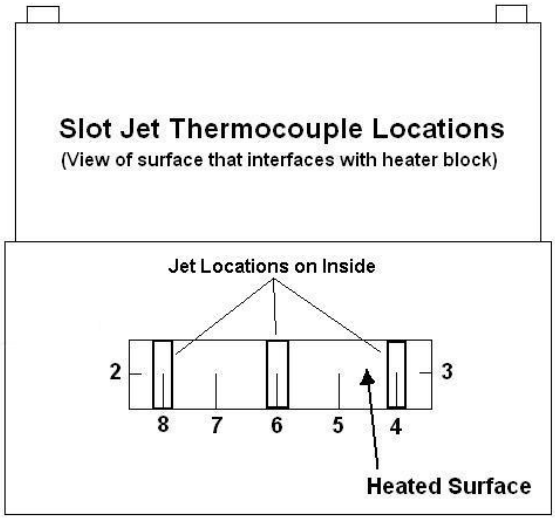

Figure 3.3.12 Slot Jet Thermocouple and Jet Locations

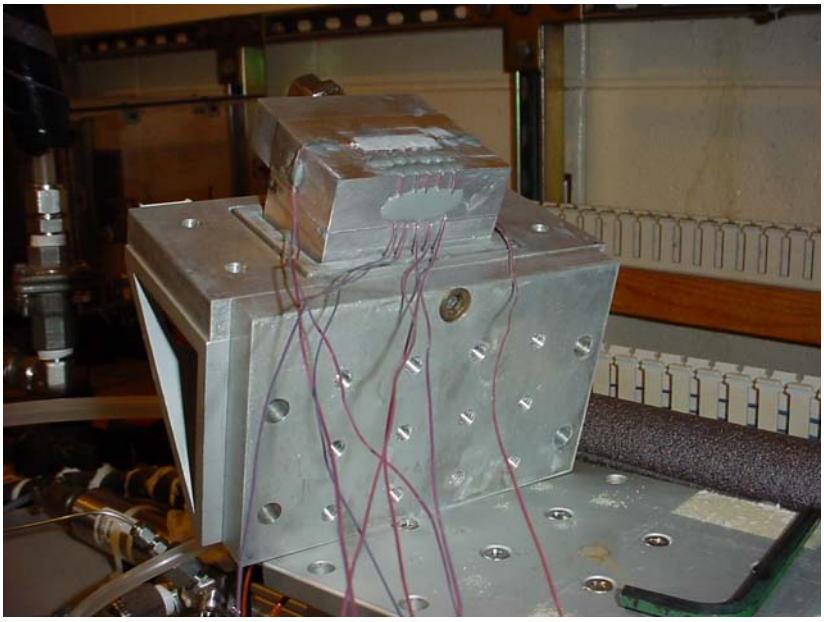

Figure 3.3.13 Slot Jet Device Mounted in Gimballed Structure Showing JB Weld Holding Thermocouples in Place

3.4 Thermodynamic Model of the Test Facility

To ensure proper operation of the Ammonia Test Chamber, a thermodynamic model of the ammonia loop was created. By considering the thermodynamic effect of each system component, predictions regarding the temperature and pressure at various points around the loop can be made.

3.4.1 General

Microsoft Excel was used to create this entire thermodynamic model. Design points used to construct the actual KSU ammonia flow loop were used to design this model. The calculations were broken up into different states of the ammonia throughout the loop. The manner in which the ammonia properties were incorporated into the model was via interpolation calculations from actual property tables using Microsoft Visual

Basic within Excel. All properties were from http://webbook.nist.gov/chemistry/fluid [20]. Measurements are performed with this model to compare to measured data.

3.4.2 Design Points

A simplified schematic was used to define important points around the KSU ammonia flow loop. The major components that affect the system thermodynamics, seen in Figure 3.4.1, include the test cell, condenser, pump, accumulator, and conditioner. Design points, or constraints, as seen in Figure 3.4.1 corresponding to these components then had to be established. The test cell is where the working fluid absorbs energy via single phase or evaporation heat transfer. The condenser is where most of the energy is removed from the working fluid via single phase heat transfer or condensation heat transfer. The pump, where the pressure rise in the system occurs, forces the working fluid through these components. The accumulator sets the system pressure to the desired test conditions. The conditioner removes energy from or adds energy to the working fluid to set its state as it enters the test cell.

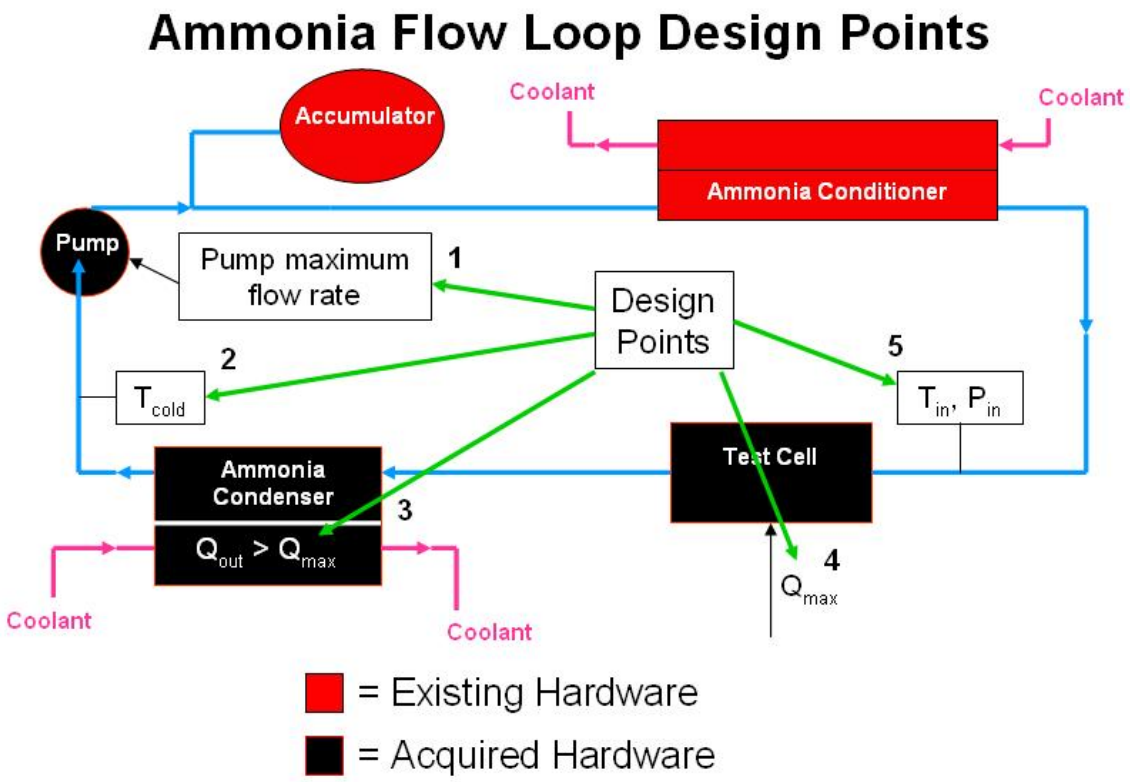

Figure 3.4.1 Ammonia Flow Loop Thermodynamic Model Design Points

The design points, or constraints, seen in Figure 3.4.1 of the model are the same as the actual ones used to construct the KSU ammonia flow loop. These constraints were not built into the model. Instead the operator knew the value of these constraints and once the model reached these values calculations ceased.

3.4.3 States

It was decided to characterize 10 states of the ammonia as it flowed around the loop based on the five major components in the ammonia flow loop in Figure 3.4.1. These states are shown in Figure 3.4.2 and make up the inlets and outlets of all of the major components. States 1 and 2 are the inlet and outlet of the test cell, respectively. States 3 and 4 are the inlet and outlet of the condenser, respectively. States 5 and 6 are

the inlet and outlet of the filter, respectively. States 7 and 8 are the inlet and outlet of the pump and metering valves section, respectively. States 9 and 10 are the inlet and outlet of the conditioner, respectively, where state 10 flows back into state 1 at the inlet to the test cell and the loop starts over again.

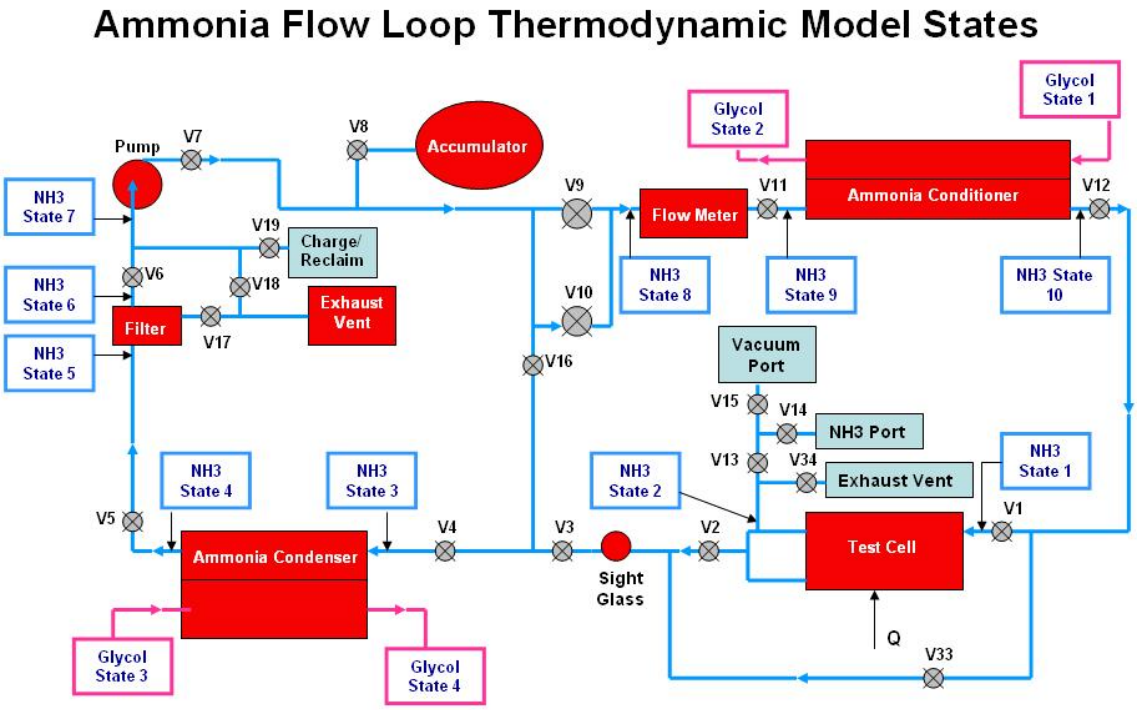

Figure 3.4.2 Ammonia Flow Loop Thermodynamic Model States

The pressure drop in this model was assumed to be of the smooth tube, single phase type for the liquid only parts of the ammonia flow loop and general L/D values were used for pressure drop through fittings [8]. For the two-phase parts of the ammonia flow loop the Friedel Correlation was used [4]. The thermodynamics of the system were analyzed on a system basis using inlet and outlet conditions of components. Also, the entire system was assumed to be perfectly insulated.

The process of finding the properties of the ammonia at each state was next. The given properties and conditions, previously mentioned, were started with first. Then the required properties of the states that were not set yet were done in numerical order of the states starting with state 2. With the ammonia flowing at 0.035 kg/s, a test cell energy input of 3000 watts, and state 1 set at 345 kPa and 0.6^{o}C subcooled state 2 had to be saturated. State 2 was also assumed to be at the same pressure as the ammonia in state 1. Since state 2 was saturated it had a quality associated with it which was calculated as well.

State 3 was assumed to have the same conditions as state 2 except that its lower pressure was calculated from the Friedel correlation previously mentioned. For state 4 two of the properties were already known, the temperature and the phase, because it was determined that the desired temperature would be 2.8^{o}C subcooled and the ammonia would be completely in the liquid phase. The pressure drop from state 3 to state 4 was calculated by correlating it to the pressure drop of the glycol flowing through the condenser.

State 5 was the same as state 4 except for the single phase pressure drop through line and fitting losses. State 6 was then the same as state 5 except for pressure drop through the filter. The filter manufacturer was contacted for this pressure drop. It was suggested that the pressure drop through the filter was 2 psi when running refrigerant R-22 through it at an energy capacity of 20 tons. This information was correlated to ammonia at a flow rate of 0.035 kg/s.

State 7 was the exact same as state 6 except for pressure drop through line and fitting losses. State 8, at the outlet of the metering valves, was assumed to be at the same

temperature as state 7. As for the pressure, this was the only point in the system where the pressure would rise due to the pump. This pressure for state 8 was calculated by simply adding up all of the other individually calculated pressure drops throughout the system and adding them to the pressure of state 7.

Finally, of the two states for the conditioner, state 9 & 10, state 9 was basically the same as state 8 except for, again, line and fitting pressure losses. The pressure of state 10 was also just a matter of line and fitting pressure losses from state 9. However, the temperature at state 10 was based on a subcooled liquid enthalpy from analyzing how much energy the ammonia lost to the glycol in the conditioner. This was done by simply subtracting the amount of energy that was added to the ammonia in the test cell from the amount of energy the glycol removed from the ammonia in the condenser. The result of this is the energy amount that needed to be removed from the ammonia in order for the ammonia to be brought back to the properties of state 1. Line and fitting pressure losses between states 10 and 1 were also considered.

3.4.4 Model Constraints and Limitations

Now that all of the states had been set there had to be some limitations to this model based on assumptions for simplification and property data limitations.

As far as the pressure drops were concerned the actual pressure drop in the system would always be higher than what would be calculated in this model. This is due to this model not accounting for the pressure drop across the metering valves, sight glasses, and the cooling device. The metering valves are located at the outlet of the pump and at the

outlet of the cooling device, the sight glasses are on either side of the test cell, and the cooling device is in the test cell.

The inputs and outputs for this model also qualify as limitations. For the inputs the user must include an ammonia flow rate in gpm, a test cell input pressure in psia, a test cell input subcooled temperature in ^{o}F, and a condenser ammonia outlet subcooled temperature in ^{o}F (usually left at 5^{o}F). These inputs are in English units because the model was initially designed with that unit system in mind. The model does convert all parameters to metric units. The outputs for this model include a saturated temperature based on the state pressure, a subcooled temperature, an actual temperature, and a corresponding density and enthalpy at each state. For the test cell states there is also an input for the test cell energy input and an output for the quality of the ammonia.

The ammonia properties at all of the different pressures and temperatures that these 10 states would be at needed to have a source. Based on the limitations previously mentioned ammonia property data tables were incorporated into the model. The ammonia saturation table in this model contains ammonia properties for saturation pressures between 140 kPa (20 psia) and 1380 kPa (200 psia). The other source of ammonia properties are tables containing subcooled liquid properties of ammonia from pressures of 140 to 1380 kPa as well. The model is limited to 16.7^{o}C (30^{o}F) of subcooling. Some of the subcooled liquid tables supported much more than 16.7^{o}C, but others did not so this subcooled amount became the standardized maximum amount.

3.4.5 Verification of Model

The only significant parameter that can be compared between the actual ammonia flow loop and the model created here is the pressure drop. The difference between the conditioner inlet pressure and the pump inlet pressure were used for the system pressure drop from the actual data set used in Table 3.4.1.

Table 3.4.1 shows a comparison of the pressure drop between the actual ammonia flow loop and the model. All other parameters in Table 3.4.1 are inputs for the model. As mentioned in the table the actual data was taken after steady state conditions were reached for a nominal test cell input pressure of 310 kPa (45 psia), a 15^{o}C (27^{o}F) subcooled test cell input temperature, a mass flow rate of 0.029 kg/s (0.7 gpm), and a test cell energy input of 800 watts. As can be seen in Table 3.4.1 the pressure drop values do not agree. This is believed to be due to the limitations discussed previously. One last parameter that should be mentioned, but not shown, is that the energy input from the surroundings could have affected this comparison by decreasing the pressure drop. This was not accounted for in the model as well.

After the ammonia flow loop was operated in the setup for copper corrosion testing mentioned previously in this chapter, a comparison between this data and the model was made as well. This comparison is shown in Table 3.4.2. These corrosion tests where only done in the single phase region because the test cell was completely bypassed. This meant that there was no energy input into the system other than from the outside environment. As with the previous comparison the only parameter that can be compared here is the pressure drop. Again, they do not match up due to the previously mentioned components and parameters not accounted for. The difference between the

accumulator pressure and the pump inlet pressure were used for the system pressure drop for the actual data set used in Table 3.4.2.

Table 3.4.1 Comparison of Slot Jet Test Data to Thermodynamic Model

Recorded Data: 310kPa, 15degC Subcooled, 0.029kg/s, 800watt data set		**Data From Model (Ammonia Flow Loop)**	
Slot Jet Inlet Pressure (kPa)	319.2	**Set:** Test Cell Inlet Pressure (kPa)	319.2
Slot Jet Inlet Subcooling (^{o}C)	14.3	**Set:** Test Cell Inlet Temperature (^{o}C)	14.3
Flow (kg/s)	0.0290	**Set:** Flow (kg/s)	0.0290
Test Cell Energy Input (watts)	800.2	**Set:** Test Cell Energy Input (watts)	800.2
Slot Jet Diff. Press. (kPa)	20.0	**Set:** Slot Jet Diff. Press. (kPa)	20.0
System Pressure Drop (kPa)	97.2	**Calculated:** System Pressure Drop (kPa)	46.2

Table 3.4.2 Comparison of Copper Corrosion Test Data to Thermodynamic Model

Recorded Data (Copper Test Loop)		**Data From Model (Copper Test Loop)**	
Accumulator Pressure, PT7 (kPa)	581.2	**Set:** Test Cell Inlet Pressure (kPa)	581.2
System Temperature (oC)	10.2	**Set:** Test Cell Inlet Temperature (oC)	10.2
Flow (kg/s)	0.0117	**Set:** Flow (kg/s)	0.0117
System Pressure Drop (kPa)	16.5	**Calculated:** System Pressure Drop (kPa)	2.0

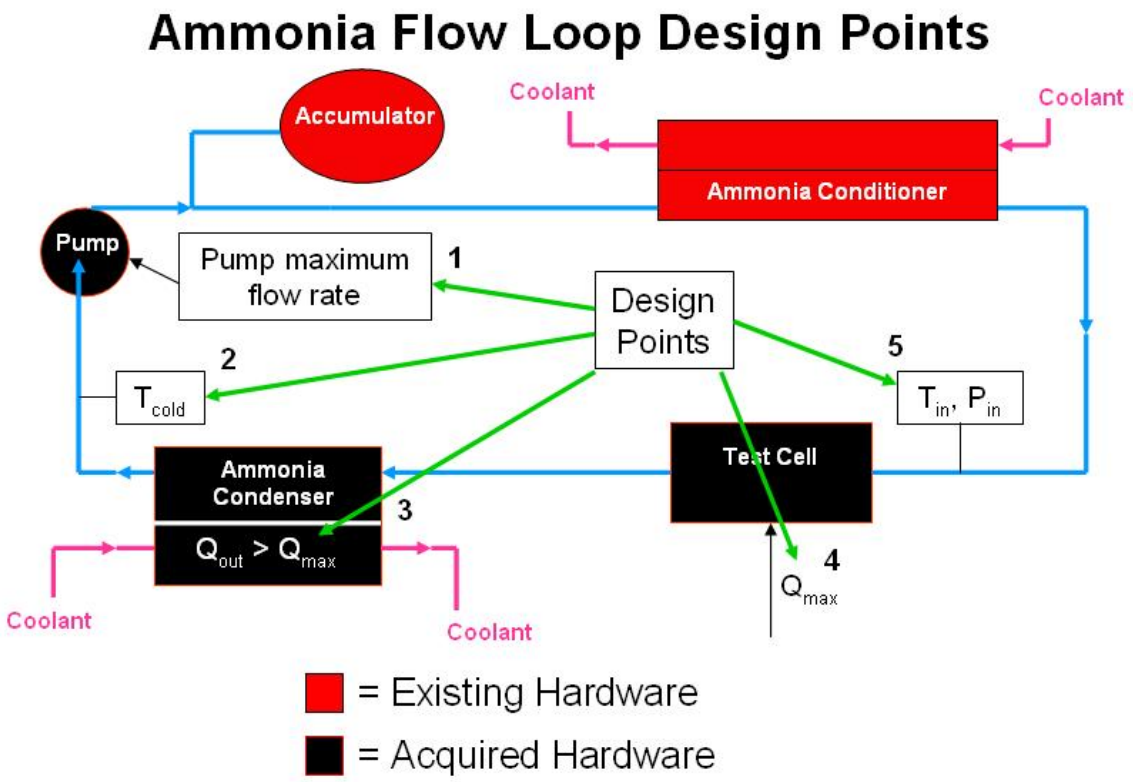

Figure 3.4.1 Ammonia Flow Loop Thermodynamic Model Design Points

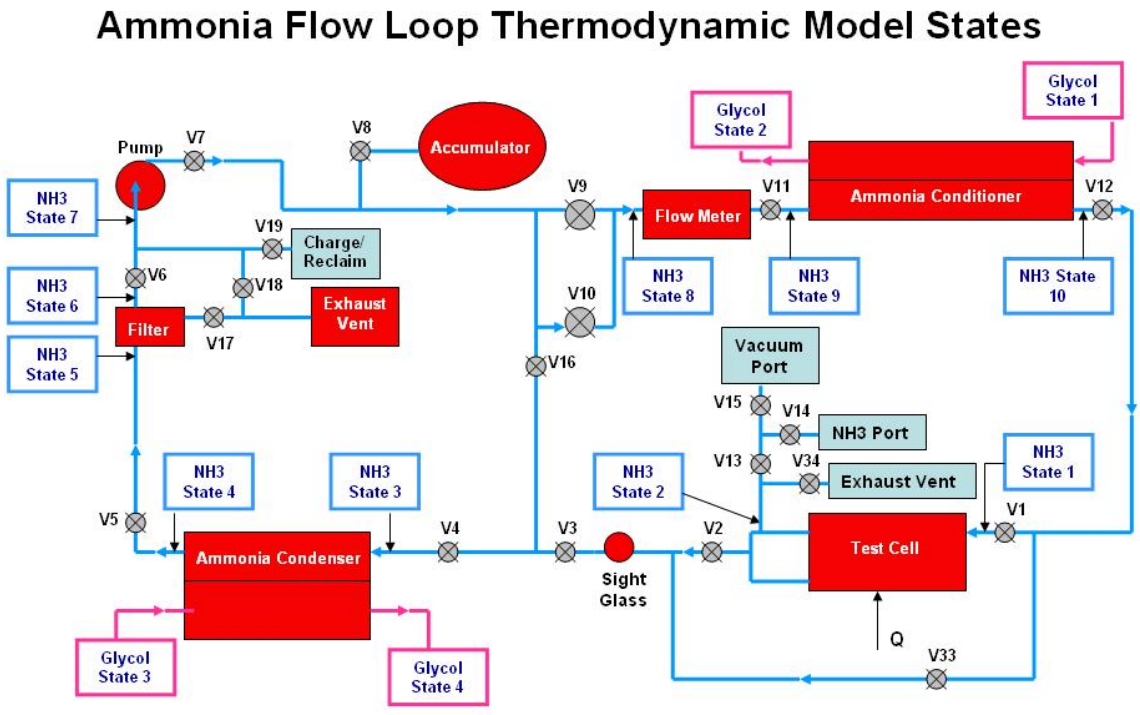

Figure 3.4.2 Ammonia Flow Loop Thermodynamic Model States

3.5 Test Facility Operational Considerations

The general operation of the test facility and the operational limitations are discussed here.

3.5.1 General Operating Procedure

The KSU ammonia flow loop was generally operated in the manner discussed here for obtaining measured data. First the initial thermodynamic state of the system was set except for adding energy to the cooling device. This consisted of first initiating the data acquisition system. The chiller was then powered up so that the glycol storage tank could be brought to testing temperatures. Then the glycol pump was started so that it would begin to bring the ammonia flow loop components to testing temperatures. Finally, the ammonia flow loop was started and adjustments were made to allow the ammonia loop to get to steady state where the inputs into the test cell matched the desired test conditions and did not change for at least an hour. This consisted of adjusting the accumulator pressure to set the system pressure and adjusting the ammonia flow rate. The desired amount of energy was then added to the cooling device.

After testing had begun, pressures and temperatures were monitored to ensure proper operation of the flow loop. The loop was then allowed to come to steady state for desired test conditions. Then an IR image was recorded. The next test condition in the test matrix was started by allowing the flow loop to continue to run while the data acquisition was restarted. Then the flow loop condition desired next in the test matrix was set. For each nominal system pressure and mass flow rate test condition energy was

added to the cooling device until one of the limits of the system components was reached. Test matrices developed for both cooling devices are discussed later in this document.

3.5.2 Operational Limits

The equipment limitations mentioned previously throughout this chapter for the ammonia test facility are summarized here. The knowledge of some of these limitations was gained only after operating the ammonia test facility. The first of these limitations was that the test cell inlet pressures were limited from 310 to 790 kPa. The only controllable temperature of the glycol coolant was approximately -25^{o}C, or -13^{o}F. Also, the condenser designed cooling capacity was 5000 watts and the ammonia pump's theoretical maximum mass flow rate was 0.035 kg/s.

3.6 Summary

Due to the toxicity of ammonia the Ammonia Test Chamber houses the entire ammonia flow loop. Ammonia compatible materials were used to build the ammonia flow loop.

Using most of the components of the ammonia flow loop a corrosion test of copper was done against the anhydrous ammonia that was supplied for the ammonia flow loop. The test was run for a total of 117 hours at varying temperatures and pressures. The copper test piece showed very little sign of corrosion, if any.

The major components comprising the ammonia flow loop were also discussed here. These included the condenser, pump, filter, accumulator, and conditioner. The condenser limited the maximum cooling capacity of the flow loop to 5000 watts and the

pump limited the maximum mass flow rate to a theoretical 0.035 kg/s. Also, the accumulator limited the minimum pressure of the flow loop to 310 kPa.

The glycol flow loop controls the temperature of the ammonia flow loop. The glycol loop consisted of a pump, storage tank, chiller for cooling the glycol, and the ammonia flow loop components that the glycol pump circulated glycol to and from. All of its components were outside of the ammonia chamber except for the tubing required to supply the ammonia flow loop components with glycol. The chiller limited the controllable temperature of the ammonia flow loop to -25^{o}C.

Instrumentation to record the ammonia states throughout the flow loop included sight glasses, pressure transducers, dial pressure gauges, thermocouples, the ammonia mass flow meter, and the ammonia detector. There are also diagrams showing where all of this instrumentation was located in the loop. All of the electronic instrumentation was controlled by a Hewlett Packard data acquisition/switch unit and National Instruments LabVIEW 7.0.

The description of the tested section included explanations of the pneumatic system, electrical energy source, heater block, instrumentation associated with the test section, and the ECHIC and Slot Jet cooling devices. The pneumatic system was used to keep the heater block interfaced with the cooling device. The electrical energy source powered the heater block. The heater block supplied energy to the cooling device for heat transfer measurements. The instrumentation recorded the data from the heat transfer that occurred. The ECHIC and Slot Jet cooling devices were interfaced with the heater block and supplied with ammonia to absorb the energy from the heater block.

The discussion of the thermodynamic model of the test facility included a general description, design points, the definition of the different states throughout the loop, the limitations of the model, and comparisons to actual data. There were a total of 10 states in the model with a state at the inlet and outlet of each of the major components starting with the test cell. One of the model limitations consisted of not accounting for the pressure drop across the metering valves and sight glasses. Further, some comparisons of this model to actual measured data were made during testing and from the copper corrosion test data. In both cases the model input parameters matched the measured conditions to compare pressure drop across the entire loop. The pressure drop calculated by the model was lower in both cases by at least 50%.

For the description of the test facility operation there was a general operating procedure for the test facility discussed. Discussed next was the operational limitations of the ammonia test facility. Pressure limitations consisted of both low (310 kPa) and high (790 kPa) limitations dictated by the accumulator and pressure transducers, respectively. There was a temperature limitation of -25^{o}C dictated by the chiller. The chiller could only control the glycol temperature at this temperature. The condensers designed cooling capacity of 5000 watts and the pump's theoretical maximum flow rate of 0.035 kg/s also limited the flow loop.

4 TWO-PHASE HEAT TRANSFER WITH AMMONIA

With a fully functional ammonia test facility, we can use it to measure boiling heat transfer coefficients of ammonia for specific geometries within the operational limit of the test cell. The following are two specific geometries tested.

4.1 Raytheon ECHIC Device

The Raytheon ECHIC Device is specifically designed to achieve a very high heat transfer rate. A picture of the device is shown in Figure 4.1.1. Although the specifics of the design are proprietary, we do know that it is an impinging jet type geometry with optimal jet nozzle sizes and spacing. The device is made of copper and intended to receive liquid coolant at the inlet and produce two-phase flow at the two larger outlets.

4.1.1 Measurement Procedure

The desired data to be obtained from the ECHIC device was the boiling heat transfer coefficient. Because the device was intended to achieve very high heat transfer rates, critical heat flux values at the point of surface dry out were not expected to be reached.

Before testing, a test matrix was negotiated with Raytheon. This preliminary matrix is shown in Table 4.1.1. At specific ammonia thermodynamic conditions at the test section inlet, the ammonia flow rate was to be varied in order to achieve specific test section output qualities. The measurement procedure is to set the desired thermodynamic properties and ammonia flow rate, as dictated by the test matrix, and then apply power to the heater. As the heater warmed the test surface, the transient data would be recorded

until steady state conditions were reached. The surface heat transfer rate would then be calculated from the steady state data.

4.1.2 Results

Unfortunately, no surface heat transfer coefficients were recorded with the ECHIC device. During testing of the first test matrix entry, an instrumentation error masked an excessively high applied heat loading. This, coupled with an error in temperature measurement observation, resulted in a structural failure of the ECHIC device. A report detailing the events that resulted in ECHIC failure was submitted to Raytheon and is included in Appendix D.

Although no surface heat transfer coefficients were measured, a significant amount of transient data was recorded leading up to, during, and after the ECHIC failure. The first plot, Figure 4.1.2, of this data shows the energy input into the ECHIC. The desired energy input to the ECHIC for the measurements was 600 watts. This plot illustrates the actual amount of energy applied, 1800 watts, and the shut-off time at approximately 300 seconds. The 1800 watts is determined by adding the two separate watt transducer signal magnitudes together. As shown on the plot, one signal was recorded as negative. The sum of the two signals produced the intended 600 watts, which was displayed on the data acquisition computer. Also indicated in the plot is the fact that when the data acquisition recording was started, the heat had already been applied for approximately 1-2 minutes.

Figure 4.1.3 shows the transient system pressures during the test. The rupture of the ECHIC device is indicated by the parallel decline in all pressures traces, starting at approximately 250 seconds.

Figure 4.1.4 shows the transient ECHIC inlet and outlet fluid temperatures. At approximately 100 seconds, the ECHIC inlet temperature and the outlet temperatures rise suddenly, although it is significant to note that one of the outlet temperatures increased much more than the other. This is likely due to the unequal flow rates going through each outlet tube. At about 250 seconds, the temperatures indicate a dramatic decline, further verifying the ECHIC rupture event.

Figure 4.1.5 represents the transient ECHIC outer surface temperatures. The top and bottom legend labels refer to average temperatures of the top and bottom groups of the ECHIC surface temperatures shown in Figure 3.3.9. These average temperature traces show a dramatic decline at approximately 250 seconds. It is anticipated that the rupture of the ECHIC caused the ammonia to leak onto the copper heater, resulting in efficient cooling of the surface by intercepting the heat before it reached the surface.

Figure 4.1.6 shows the mass flow rate of the ammonia during the failure of the ECHIC device. During the times that the ECHIC outer surface temperatures were increasing sharply through the rupture of the device (from approximately 100 seconds to 300 seconds), the mass flow rate is very scattered. This is likely due to fluctuating passage conditions causing sudden stops and starts to the flow as detected by the flow meter. Once ammonia was vented to atmosphere, the ammonia flow resistance from the pump decreased and resulted in a slightly higher flow rate.

Figure 4.1.7 shows a timeline of events as determined by an in depth analysis of the recorded data. All significant events discussed are indicated on the chart. For further specifics regarding these events and others please refer to Appendix D.

The physical results of the ECHIC can be seen in Figure 4.1.8. The top two pictures show the ECHIC as it sat in the test cell after the failure. The other four pictures show the ECHIC removed from the test cell with one showing how the damaged ECHIC compares to an undamaged one. The turquoise type color one the outside of the ECHIC is from the reaction of ammonia and water with copper. As seen in the bottom left picture most of the length of the inlet and outlet tubes for the copper ECHIC do not seem to have been exposed to this reaction. This is because they were sealed from the outside where the ammonia could not escape to the atmosphere, mix with the moisture in the atmosphere, and corrode this part of the ECHIC.

Table 4.1.1 ECHIC Test Matrix

	DESIRED/PREDICTED (First Set)											
Test Order	Air Cylinder Pressure (psig)	Subcooling (oC)	Test Cell Inlet Temperature (oC)	Heat Rate (W)	Heat Flux (W/cm2)	Test Cell Inlet Pressure (psia)	Outlet Quality (desired)	Flow (GPM), (desired)	Flow (kg/s), (desired)	Outlet Quality (predicted)	Flow (GPM), (predicted)	Flow (kg/s), (predicted)
1	33.3	9	-10	300	100	59.98	1	----------	----------	----------	0.006	0.00024276
2	33.3	9	-10	300	100	59.98	0.5	----------	----------	----------	0.012	0.00048552
3	33.3	9	-10	300	100	59.98	----------	0.85	0.0343907	0.007	----------	----------
4	33.3	9	-10	600	200	59.98	1	----------	----------	----------	0.012	0.00049513
5	33.3	9	-10	600	200	59.98	0.5	----------	----------	----------	0.023	0.000949
6	33.3	9	-10	600	200	59.98	----------	0.85	0.0350717	0.014	----------	----------
7	33.3	9	-10	900	300	59.98	1	----------	----------	----------	0.018	0.00072827
8	33.3	9	-10	900	300	59.98	0.5	----------	----------	----------	0.035	0.00141609
9	33.3	9	-10	900	300	59.98	----------	0.85	0.0343907	0.02	----------	----------

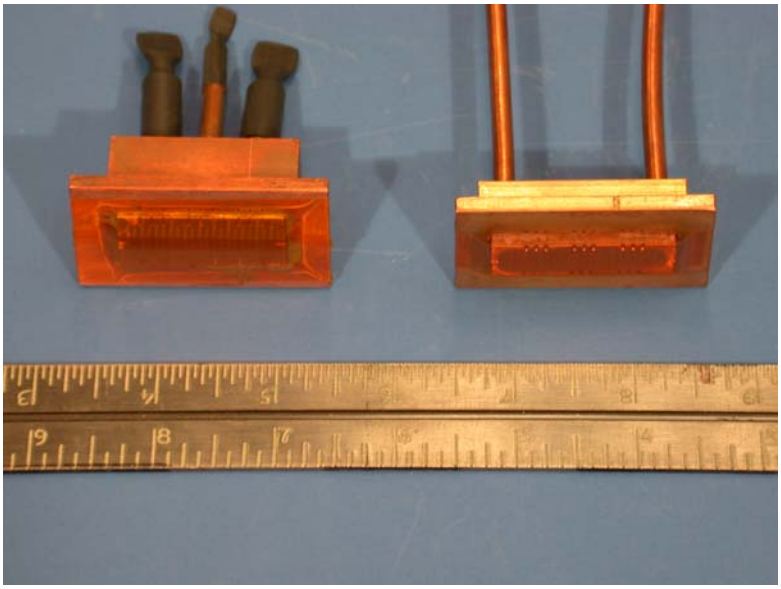

Figure 4.1.1 ECHIC Device (Left)

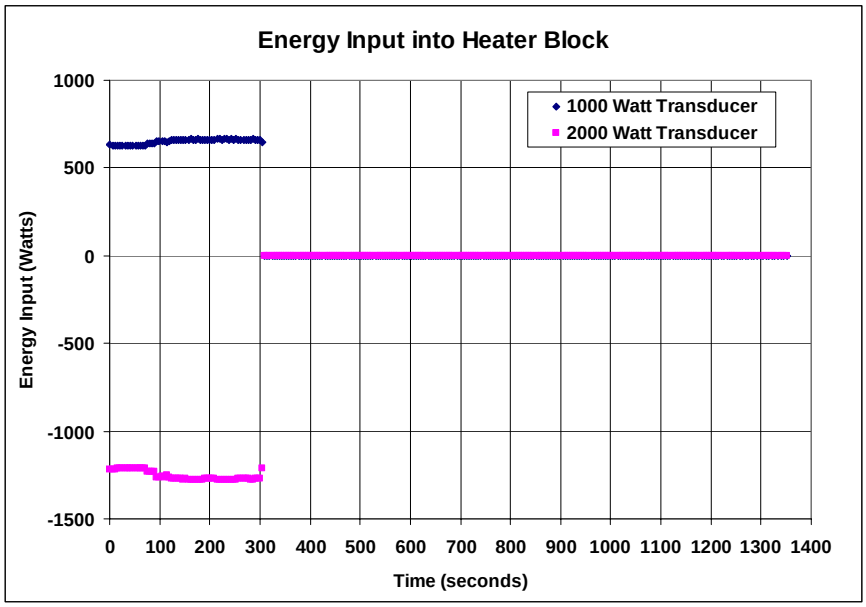

Figure 4.1.2 Energy Input into Heater Block

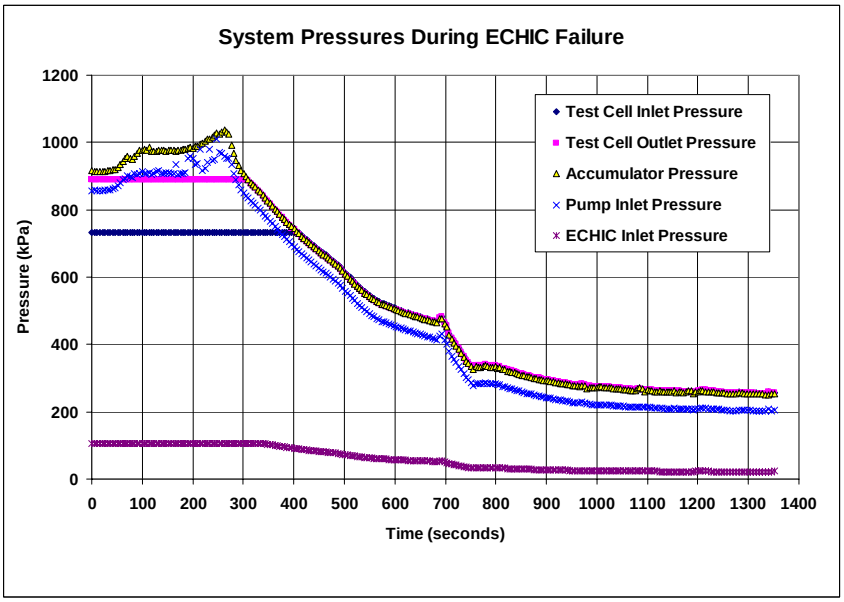

Figure 4.1.3 System Pressures

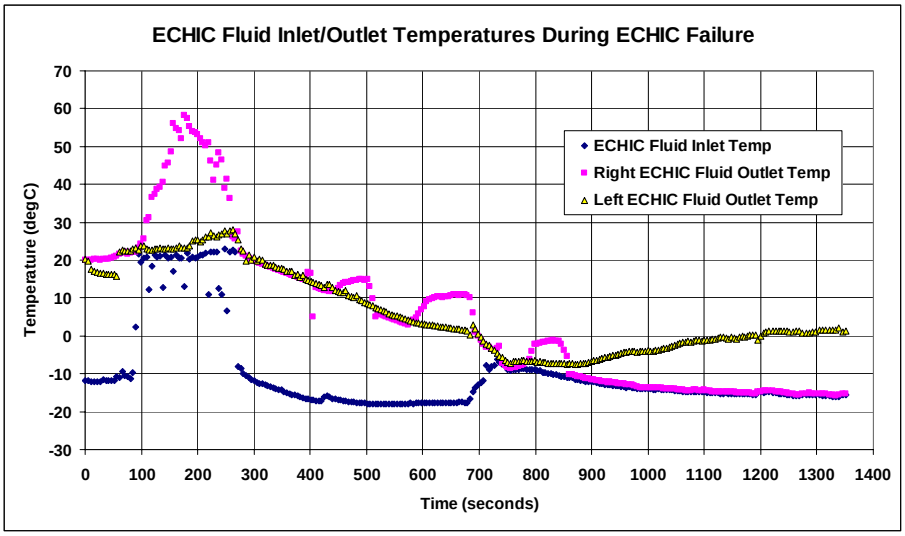

Figure 4.1.4 ECHIC Fluid Inlet and Outlet Temperatures

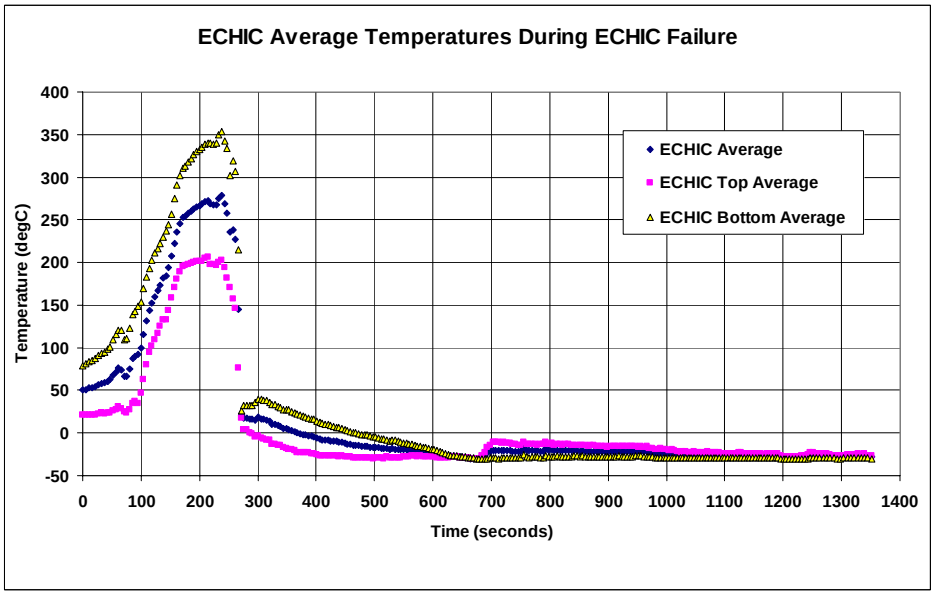

Figure 4.1.5 ECHIC Average Surface Temperatures

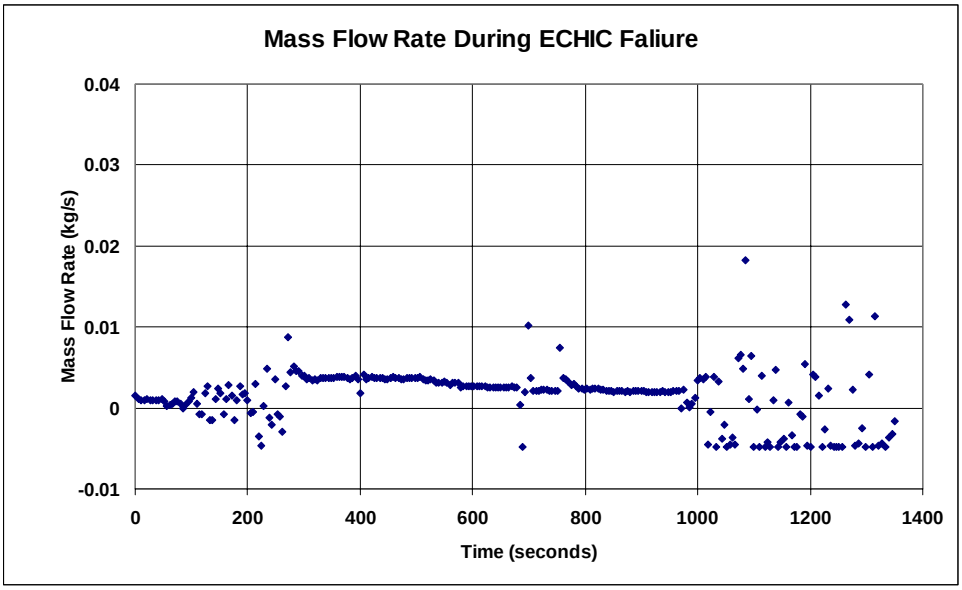

Figure 4.1.6 Ammonia Flow Loop Mass Flow Rate

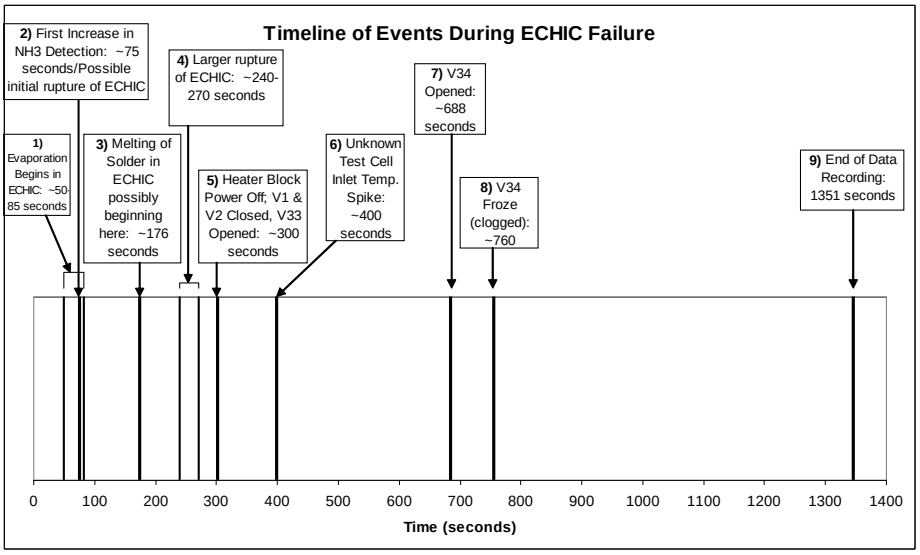

Figure 4.1.7 Timeline of Events During ECHIC Failure

Figure 4.1.8 Physical Results of ECHIC Failure

4.2 Raytheon Slot Jet Device

Another device Raytheon requested data from was the Slot Jet. A picture of the Slot Jet is shown in Figure 4.2.1. Raytheon's intent for the device was to provide a simple geometry with which to compare CHF and boiling heat transfer coefficients for various fluids. KSU was contracted to provide data using ammonia. Also, Figure 4.2.2 is shown here in order to easily refer to the layout of the Slot Jet heated surface thermocouple locations and where the impinging jets are in comparison to them.

In essence, KSU was to provide measured boiling curves, such as the one shown in Figure 4.2.3, as a function of ammonia flow rate and saturation pressure. A boiling curve consists of four major regions of heat transfer: single phase heat transfer, two-phase heat transfer (nucleate boiling), transition between nucleate and film boiling, and the vapor blanket phenomenon (film boiling). These flow regimes are illustrated on the plot.

4.2.1 Measurement Procedure

In order to obtain the desired boiling curve in Figure 4.2.3 a test matrix, shown in Table 4.2.1, has been developed. In this test matrix the ammonia flow loop system parameters and energy input rates, 50 – 1500 watts, are listed for the different test conditions where measured data was desired. As it was not known where the CHF would occur in any of these test conditions the energy input rates listed were preliminary and some of them could not be reached.

Based on reviewed literature it is expected that as the mass flow rates increase for each of the different test pressures the amount of energy the Slot Jet will be able to

absorb will increase and the CHF will increase. The same condition is expected as the test pressures increase.

The procedure for the measurement of data from the test matrix in Table 4.2.1 was to move from left to right for the flow loop conditions and then from top to bottom for the energy rates listed for each different test condition. That meant starting with the lowest test cell inlet pressure (310 kPa) the mid-level mass flow rate (0.017 kg/s) and the lowest energy input (50 watts). Once test conditions were set with a certain energy input the system would need a certain amount of time reach steady state. The measured data at steady state conditions was the data that was desired. Once enough data had been taken at steady state the data acquisition equipment was restarted and then next test condition was started. Also, once knowledge was gained about where CHF would occur for each test condition some of the lower energy inputs were skipped due to their lower level of importance

4.2.2 Results

The results of the tests performed from the test matrix in Table 4.2.1 are in the following sections. Examples of transient plots are shown and analyzed, examples of boiling curves are shown and analyzed, and CHF values and maximum heat transfer coefficients are calculated for each test condition from the measured data.

4.2.2.1 Data Collection

The best method of calculating the heat flux from the measured data is first discussed here. Then the results are shown and explained for transient data recorded due to a change in test cell energy input during typical and film boiling two-phase heat

transfer for various system conditions. Examples of CHF events and a Leidenfrost point occurrence are shown.

4.2.2.1.1 Comparison of Heat Flux Calculation Methods

Before the actual data can be discussed the methods of finding the heat flux entering the Slot Jet must be mentioned. There were three methods of finding the heat flux. One of the methods used the energy reading from the watt transducers and then simply divided that by the cross sectional area of the heater block neck, 3 cm^2. Another method was done by using two of the thermocouples in the heater block neck, the top-middle heater neck temperature and the bottom-middle heater neck temperature seen in Figure 3.3.6. These two temperatures were put into the one-dimensional heat conduction equation [11] along with the thermal conductivity of copper, 400 W/(m-K), and the known distance between the thermocouple probes, 0.635 cm (0.25 inches).

The IR camera was also used to find the heat flux entering the Slot Jet. It was used to collect data at the end of each test performed in the test matrix once steady state conditions had been reached. The data collected from the IR camera was the temperature profile of the heater block neck from the top (opposite the side of the heater block neck thermocouples) as shown in an example image in Figure 4.2.4. As seen in Figure 4.2.4, two lines were created using special software on the IR image where two temperature profiles across the heater block neck were found. From the heater block neck temperature profiles and knowing the length between the two lines the heat flux through the heater block neck could be calculated by, again, using the one-dimensional heat conduction equation [11]. A detailed explanation of the procedure to find these temperature profiles and heat fluxes from the IR images is in Appendix E.

Near the top of Figure 4.2.4 is the interface point between the heater block neck and the cooling device, the ECHIC in this picture. Near the bottom of the image is where the neck is attached to the main part of the heater block where the actual source of the heat, the heating elements, is located. This is the reason for the lighter colors near the bottom of the image, or the higher temperatures as seen in the temperature profile to the right.

Example comparisons of the results using the three different methods of heat flux calculations can be seen in Table 4.2.2 and Figure 4.2.5. The data for the two blank cells in Table 4.2.2 for the IR camera heat flux was not available. As can be seen in this table the IR camera method generally had the lower calculated heat flux value followed by the heater neck thermocouple method, then the energy input method. The heater neck thermocouple method was always slightly lower than the energy input method because the energy input method did not account for electrical line losses and losses to the surroundings at the heater block. Both of these losses not accounted for by the energy input method only became worse as the power increased. This can easily be seen in Figure 4.2.6 by the divergence of the two heat flux calculation methods of energy input and heater neck thermocouples.

Table 4.2.2 also shows that the IR camera heat flux calculation for the highest energy input decreased instead of increased. This is a small example of the inconsistency of the IR camera heat flux calculations that were eventually discovered after numerous calculations and comparisons. A much better example of this inconsistency is seen in Figure 4.2.6. More detailed examples of the inconsistency, or uncertainty, of the heat flux values from the IR images is in Appendix C. The main cause of the inconsistency

was that the top of the heater neck block would become dirty very easily and skew the temperature readings. This only got worse as time progressed as the neck became dirtier. This, along with the IR camera's inability to accurately read temperatures above 200^{o}C, caused the use of the method of using the IR camera to calculate heat fluxes to be cancelled. Also, another disadvantage of the IR camera is that it would only record images like the one in Figure 4.2.4, not video. This meant it was not able capture any transient data.

However, the IR camera was very useful as well. It was another check against temperature measurements in the heater block neck and on the Slot Jet heated surface. It was also useful in checking that the interface pressure between the heater block neck and the Slot Jet was relatively even across the interface surfaces. At the lower energy input levels where the heater neck temperatures were below 200^{o}C the IR camera could view the temperature distribution across the heater neck. If the distribution was even across the neck then the interface pressure was evenly spread across the interfaces surfaces.

It was only practical to use only one of these heat flux calculation methods to further evaluate the measured data to create boiling curves from the steady state values and to find CHF values and their corresponding heat transfer coefficients. There was no need to have two sets of these calculations as well. This lead to the decision to use the method of the heater block neck thermocouples. The previously discussed energy input method's lack of accounting for electrical and surrounding losses and the IR camera's inconsistency and lack of ability to record transient data were some of the reasons for this decision. Another important factor in this decision was that Figure 4.2.12 showed the change in energy input being put into the test cell as almost instantaneous and not

representative of how the system responded to changes. This meant that the heat flux values calculated from the method of using the energy input would not be representative of how the ammonia flow loop responded to changes. Figure 4.2.12 also showed the heat flux values calculated using the heater block neck thermocouples as time progressed. This method is much more representative of how the flow loop responds as seen by its gradual increase in heat flux.

Example boiling curves created by using the heater neck heat flux calculation method can be seen in Figure 4.2.37 and 4.2.38. The CHF values and corresponding heat transfer coefficients calculated with this heat flux method for each data set where film boiling occurred can be found in Tables 4.2.3 and 4.2.4.

4.2.2.1.2 Typical Data Set

The data set here in Figures 4.2.7 - 4.2.12 shows how a typical transient data set looks representing a point along the Slot Jet boiling curve in the two-phase heat transfer (nucleate boiling) region in Figure 4.2.3. For this test the energy input was change from 200 to 300 watts then the system was allowed to reach steady state. Typically, if the change in energy was not excessive, as in the change done for this set, the system reached steady state in 1 to 1.5 hours (3600 to 5400 seconds). Some data sets ran longer than this due to overnight testing or just due to the operator not being present in the lab.

Figure 4.2.12 shows the almost instant change in power near the beginning of the test at the time of zero seconds. This instant increase in power supplied to the test cell was the initial shock on the system that caused it to begin to reach a new steady state condition. After this happened there were the obvious responses that the system had as in the Slot Jet fluid outlet temperature increasing in Figure 4.2.8, the heater block neck

temperatures (used to calculate the heater block neck heat flux) increasing in Figure 4.2.11, the heater block neck heat flux increasing in Figure 4.2.12, and the Slot Jet surface temperatures increasing in Figure 4.2.10. The Slot Jet fluid inlet temperature remained steady as seen in Figure 4.2.8. Another system parameter that is shown in Figure 4.2.7 to be constant throughout the changes to other system parameters is the mass flow rate.

There are some other less obvious changes that occur in the system with the system pressures in Figure 4.2.9. It was not initially known what caused this to happen. It could have been that the increase in energy input into the test cell, and the entire ammonia flow loop, caused a slight decrease in the density of the liquid ammonia causing a system wide pressure rise. It could have also been that these types of typical data sets that were originally thought to be in the single phase region in the Slot Jet device were in fact in the two-phase region in the Slot Jet device. The latter of these possibilities, which ended up being the case, does make sense because when an increase in the amount of boiling occurs in any flow loop the pressure does rise throughout the entire system. This is due to the vapor occupying more volume than the liquid.

4.2.2.1.3 CHF Data Sets

The data sets discussed and shown here involve a typical CHF event where there is a distinct transition to film boiling and an inconsistent CHF event where the transition point to film boiling is difficult to distinguish.

4.2.2.1.3.1 Typical CHF

The data sets here in Figures 4.2.13 – 4.2.18 show what happens to various ammonia flow loop parameters when the Slot Jet reaches a CHF shown on the Slot Jet

boiling curve in Figure 4.2.3. First, Figure 4.2.18 shows that the energy being put into the test cell, or Slot Jet, is kept steady, even through the occurrence of the CHF at approximately 1100 seconds until the very end where it is shut off. Other figures show how other system parameters are kept constant also like the mass flow rate in Figure 4.2.13, the Slot Jet inlet fluid temperature in Figure 4.2.14, and the system pressures in Figure 4.2.15. However, the system pressures do rise very slightly, but do not clearly show the occurrence of the CHF event.

Figures 4.2.14, 4.2.16, 4.2.17, and 4.2.18 show system parameters that respond to the CHF event. Figure 4.2.14 shows how the Slot Jet outlet temperature decreases due to the decrease in heat transfer to the fluid once the CHF occurs and film boiling begins. The vapor blanket created with film boiling acts as an insulator between the heated surface and the fluid causing the fluid to absorb less energy. This makes the Slot Jet outlet temperature decrease. Figure 4.2.16 shows the reaction of the Slot Jet surface temperatures to the CHF event and how they continue to rise due to the film boiling. Figure 4.2.17 shows the reaction of the heater block neck temperatures to the CHF event. These temperature readings show the same trend as the Slot Jet surface temperatures. Figure 4.2.18 shows the reaction to the CHF event of the calculated heat flux through the heater block neck. The heat flux decreases due to the film boiling allowing less energy to transfer to the fluid. With all of these parameters changing and the constant energy input to the heater block some of the energy previously absorbed by the ammonia is now absorbed by the heater block shown by its increased temperatures.

4.2.2.1.3.2 Inconsistent CHF

This data set in Figure 4.2.19 – 4.2.24 shows a CHF event as the previously mentioned data set does. However, by looking at Figures 4.2.22 and 4.2.24 it is difficult to determine exactly when the CHF event occurred. Figure 4.2.22, showing the Slot Jet surface temperatures, shows all of the surface temperatures suddenly changing at various times instead of just once for a typical CHF event. At around 900 seconds some of the Slot Jet surface temperatures increase and some decrease while others stayed relatively constant. A slight CHF event might have occurred here with some film boiling, but it is not very defined because only two temperatures seemed to react, thermocouples 2 and 8. Thermocouple 2 suddenly decreased and thermocouple 8 gradually increased and then levelled off. Also, after this event thermocouples 2 and 3 diverged from each other beginning at around 1100 seconds and then converged again. Since the thermocouples for these two temperatures are on the far opposite sides of the Slot Jet heated surface with the rest in the middle it is unknown what happened here. The other Slot Jet surface temperatures should have reacted in some manner at this time as well.

At approximately 1650 seconds, once again, some of the temperatures increased and some decreased. However, here most of the changes were more dramatic. This seems to be where the actual CHF event occurred. There was also an event at around 2300 seconds that all of the temperatures seemed to react to as well. It is likely that a rewetting of the heated surface occurred for a short time and then film boiling suddenly continued again. This is shown by some of the temperatures slightly decreasing followed by a sudden reaction again. It is still inconclusive, though, what exactly happened at 1650 seconds, 2300 seconds, or any time between or after that. Some of the temperatures still exhibit inconsistent trends here.

It could be that instead of film boiling occurring everywhere on the heated surface it occurred only in certain spots. This could be due to the higher inlet pressure, and overall system pressure, of the liquid ammonia not allowing film boiling to occur everywhere on the heated surface. Also, as seen in Figure 4.2.22, the temperatures are always hotter on one side (the side with thermocouples 2, 7, and 8 seen in Figure 4.2.2) of the Slot Jet heated surface than the corresponding temperatures on the other side. That is, thermocouple 2 is always hotter than thermocouple 3, thermocouple 7 is always hotter than thermocouple 5, and thermocouple 8 is always hotter than thermocouple 4. These differences in the Slot Jet heated surface temperatures are most likely due to an unequal distribution of interface pressure between the heater block and the outside Slot Jet Heated surface. This interface pressure is supplied by the pneumatic cylinder. These two factors combined are believed to be the reason as to why film boiling would occur only on part of the heated surface. This would explain why some temperatures suddenly decrease instead of increasing at certain times as well. The creation of the vapor blanket from film boiling only on part of the heated surface could have pushed liquid ammonia on one side of the heated surface to the other side.

The Slot Jet fluid outlet temperature in Figure 4.2.20 is relatively constant up to 1650 seconds where it suddenly drops. This is another indication that the actual CHF event occurred here. However, there was a sudden change, as with the Slot Jet surface temperatures in Figure 4.2.22, at around 2300 seconds as well. This could be due to film boiling developing again after a short period of the heated surface being rewetted by liquid ammonia as discussed earlier. Figure 4.2.19 and 4.2.21, again, show consistent

pressures and a mass flow rate throughout the test. Figure 4.2.20 also shows the consistency of the Slot Jet fluid inlet temperature, once again.

When looking at Figure 4.2.23 showing the heater neck temperatures used in calculating the heater neck heat flux the CHF point is much more defined to happen at 1650 seconds. This is due to the sudden rise in these temperatures followed by a steady rise until the heat was shut off. Before that there is a much less defined rise at around 900 seconds shown with some of the Slot Jet surface temperatures as well. However, there was a break in the steady temperature rise after 1650 seconds at around 2300 seconds where, as discussed previously, a rewetting of the heated surface might have occurred for a short time.

The last figure, Figure 4.2.24, shows the energy input into the test cell and the calculated heater neck heat flux calculated from the heater neck temperatures in Figure 4.2.23. The energy input is shown to be constant until it was shut off by the operator. This, along with other constant parameters like the mass flow rate and the Slot Jet fluid inlet temperature, shows that the operator did not change any system parameters during this test. The heater neck heat flux, however, shows what happened with the system as with the Slot Jet surface temperatures and the heater neck temperatures. Again, at 1650 seconds a significant event occurred which is believed to be the actual CHF event discussed for Figure 4.2.23 and 4.2.24, due to the heat flux suddenly decreasing as in the data set showing a typical CHF event. However, this heat flux eventually returned to approximately its original value and stayed relatively steady until the possible rewetting event, previously discussed as well, happened at around 2300 seconds. After this

happened film boiling took over and the heat flux decreased again then levelled off for a short time until the energy input was shut off.

4.2.2.1.4 Film Boiling Data Set

The following Figures 4.2.25 – 4.2.30 show a data set where the Slot Jet reaches a CHF, as in the previous section, and experiences film boiling. However, here the operator adjusts the energy input into the test cell after the CHF event which happened at about the 200-300 second mark. The energy input adjustments are performed from 300 to 3000 seconds. This is done to bring the loop back to steady state while film boiling is still occurring. Steady state was then reached two more times using two more different energy inputs, slightly higher each time, which allowed the desired measurement of three different points along the Slot Jet boiling curve, Figure 4.2.3, in the film boiling region. The steady state points reached happened at approximately 5500, 7200, and 9600 seconds.

These changes in test cell energy input by the operator can be seen in Figure 4.2.30 by the different levels, or steps, of applied energy throughout the testing time. Adjustment of the energy input was done instead of allowing the system to come to steady state on its own in this data set, and most other data sets where a CHF event occurred, because otherwise the heater block and Slot Jet surface temperatures would become much too hot. So, as can be seen at the beginning of this data set in Figure 4.2.30, the heat rate was decreased by a considerable amount once the operator saw the symptoms of film boiling at the original power level of this data set which was 600 watts.

The parameters that were shown to not be affected by the CHF event, or the film boiling, are the mass flow rate and the Slot Jet fluid inlet temperature in Figures 4.2.25

and 4.2.26. In Figure 4.2.26 the Slot Jet fluid outlet temperature is, again, shown to react to the CHF event as discussed in the previous section. The effect the energy input changes during film boiling have on the Slot Jet fluid outlet temperature, though, is minimal. The reason that the Slot Jet fluid outlet temperature rises slightly over time is due to the operator increasing the energy input during the measurement of the film boiling points.

The pressures throughout the system shown in Figure 4.2.27 are only affected by the occurrence of the CHF event. After the CHF was reached the pressures became very steady, except for increasing slightly over time, and remained that way during the measurement of the film boiling points. All of the system pressures dropped once the CHF event occurred because of the decrease in two-phase heat transfer. Figure 4.2.9 in a previous section shows the system pressures rising when the heat rate is increased because there is more two-phase heat transfer, or more vapor is being created in the ammonia flow. Once this vapor creation in the flow decreases, as with film boiling, the system pressures decrease.

Figures 4.2.28, 4.2.29, and 4.2.30 show some system parameters that are affected by all of the changes that happened during this data set. These include the Slot Jet surface temperatures, the heater block neck temperatures, and the heater block neck heat flux. As discussed in the previous section the Slot Jet surface temperatures and heater block neck temperatures rapidly increased once the CHF event occurred and the heater block neck heat flux decreased. However, these parameters also showed the steadying of the system for each of the different film boiling points measured. The steadying of the system in Figures 4.2.28, 4.2.29, and 4.2.30 is shown by the horizontal parts of the data.

Film boiling region points were recorded for all of the tests at 310 kPa (45psia) and at 410 kPa (60psia) for the 0.01 kg/s (0.25 gpm) flow rate only. The steady state points for this data set shown here can be seen in Figure 4.2.38.

4.2.2.1.5 Leidenfrost Point Data Set

There was one data set, seen in Figures 4.2.31 – 4.2.36, during the Slot Jet data measurements of the film boiling points for the loop conditions of 310 kPa (45 psia) and 0.029 kg/s (0.7 gpm) shows that a Leidenfrost Point was possibly recorded. The Leidenfrost points is shown in the general Slot Jet boiling curve in Figure 4.2.3 and occurred in this data set at the very end around the 9000 second mark.

Figures 4.2.34, 4.2.35, and 4.2.36 show the symptoms of a Leidenfrost point. Figure 4.2.36 shows that the energy input into the test cell was held constant through the occurrence of the Leidenfrost point until around the 9500 second mark. Around the 9000 second mark in Figures 4.2.34 and 4.2.35 the sudden rapid decrease of the Slot Jet surface temperatures and heater neck temperatures can be seen showing that liquid ammonia began to finally break through the vapor blanket created by the film boiling. Figure 4.2.36 also shows the heater block neck heat flux rising at the 9000 second mark. This also shows that the liquid ammonia was finally beginning to break through the vapor blanket. When the liquid ammonia began to touch the heated surface it was able to absorb more heat flux than the vapor causing the heat flux to increase.

Figure 4.2.31 shows how the flow rate was once again kept constant throughout the measurements of this data. The same is shown with the Slot Jet fluid inlet temperature in Figure 4.2.32. Figure 4.2.32 also shows how the Slot Jet fluid outlet temperature reacted to the Leidenfrost point and to the CHF event also in this data. The

Slot Jet fluid outlet temperature increased at the occurrence of the Leidenfrost point because more energy was suddenly being transferred to the liquid ammonia. More energy was shown to be transferred to the ammonia by the increase in heat flux in Figure 4.2.36 as well. Figure 4.2.33 shows how the system pressures reacted to the CHF event and the Leidenfrost point as well. The pressures rose due to the Leidenfrost point occurrence because more two-phase heat transfer was occurring. This caused more vapor creation in the liquid ammonia due to the increase in heat flux.

4.2.2.2 Boiling Curve

The data in the plot of Figure 4.2.37 represents an actual example of the general boiling curve in Figure 4.2.3 that was desired from the measured test matrix data points in Table 4.2.1. Each of the points on the plot in Figure 4.2.37 are the result of the single steady state data points reached at the end of each test for each energy input tested. These single steady state data points are from the end of each of the transient plots as described previously for a complete set of tests done at the same test cell inlet pressure, subcooling, and mass flow rate. The data in Figure 4.2.37 consists of the subcooling versus the heat flux. The subcooling is calculated by subtracting the Slot Jet fluid inlet temperature from one of the Slot Jet outside surface temperatures. The data points that are enlarged in Figure 4.2.37 represent the CHF point and the Liedenfrost point. The locations of these points on the general Slot Jet boiling curve are shown in Figure 4.2.3.

Figure 4.2.38 was created to represent the data points of heat flux vs. subcooling for an entire series of tests done at the same system pressure and subcooling. Also, there are some data points in Figure 4.2.38 that are enlarged as well. These points represent the CHF values for each of the flow rates.

4.2.2.3 CHF/Heat Transfer Coefficients

The data in Tables 4.2.3 and 4.2.4 represent the CHF, the maximum attainable heat flux of the Slot Jet device, values and the corresponding maximum heat transfer coefficients in each of the system conditions tested. The CHF values in Table 4.2.3 mostly correspond to how the system should respond to increased flow rates and pressures. For the nominal Slot Jet inlet pressures the CHF value increased with increasing flow rate. This makes sense because when the liquid ammonia flow is at a higher flow rate it is more apt to contact the heated surface. The presence of liquid on the heated surface increases the cooling ability of the ammonia because it is at a lower enthalpy state than if it were a vapor. The same principle applies to the increase in Slot Jet inlet pressure. Therefore, in this case it also takes more energy input to the heated surface to reach the CHF point. However, there was one CHF point for 790 kPa and 0.017 kg/s that did not follow this trend. This is a testament to the difficulty in obtaining results from data of this sort due to all of the unforeseen parameters that cannot be controlled and skew results.

The CHF values and other heat flux values were calculated with one-dimensional heat conduction equation [11] of $q_{HN}" = k_{Cu} * [(T_{HNBM} - T_{HNTM}) / x_{HN}]$. The parameters involved in this equation are the temperature difference between the heater neck thermocouples Top-Middle (T_{HNTM}) and Bottom-Middle (T_{HNBM}), the distance between the heater neck thermocouples (x_{HN}), and the thermal conductivity of copper (k_{Cu}).

For the same reason the CHF values rise in Table 4.2.3, the corresponding maximum heat transfer coefficients should also rise in Table 4.2.4. However, this is only the case with the increasing mass flow rates for 310 kPa. For 410 kPa the exact opposite

happened. The maximum heat transfer coefficients decreased from 310 kPa to 410 kPa and as the mass flow rates increased. The maximum heat transfer coefficients for 790 kPa are inconsistent as well. These discrepancies, or inaccuracies, are most likely due to the large amount of uncertainty (see Appendix C) that is associated with calculating CHF values and even more so with the corresponding maximum heat transfer coefficients seen in Table 4.2.4. CHF values calculated here mainly involve uncertainties with only the thermocouple readings and the thermal conductivity of copper. The corresponding maximum heat transfer coefficients are calculated using these CHF values so they involve at least the uncertainties with those values. They also involve uncertainties with the thermal conductivity of aluminum, the Slot Jet surface thermocouple readings, and the Slot Jet fluid inlet temperature readings. Another factor in the discrepancy, or accuracy, of the heat transfer coefficients is that there were not multiple tests done at each flow loop condition.

These maximum heat transfer coefficients were calculated by using Newton's Law of Cooling [11], $h_{max} = q_{HN}" / (T_{SJi} - T_{SJfi})$, where the actual fluid temperature (T_{SJfi}) (as instructed by Raytheon [10]), surface (touching the fluid) temperature (T_{SJi}), and the heat flux ($q_{HN}"$) must be known. All of these parameters were known from the previously measured data and calculations except for the inside Slot Jet heated surface temperature (T_{SJi}) which was touching the ammonia fluid. This inside heated surface temperature was calculated by, once again, using the one-dimensional heat conduction equation [11] as $T_{SJi} = T_{SJo} – [(q_{HN}" * x_{SJ}) / k_{Al}]$. By using the corresponding CHF ($q_{HN}"$), the average outside Slot Jet surface temperature (T_{SJo}), the thermal conductivity of 7075-T6 aluminum (k_{Al} = 130 W/(m*K)), and the thickness of the aluminum at the

Slot Jet heated surface (x_{SJ} = 0.1905 cm) this inside temperature could be calculated. The average outside Slot Jet surface temperature was found by averaging Slot Jet surface temperature numbers 4 through 8.

The uncertainty associated with these CHF values and maximum heat transfer coefficients can be seen in Tables 4.2.5 and 4.2.6. The average uncertainty was a good representation of the uncertainties when compared to the maximum and minimum. Therefore it was as the representative uncertainty here. The CHF uncertainties are relatively all the same. However, the heat transfer coefficients, for the most part, increase as pressures and mass flow rates increase. This is another testament to the large variation in the Slot Jet temperatures at the higher pressures and mass flow rates compare to the smaller temperature variations at lower pressures and mass flow rates.

4.2.3 Comparison of Results to Literature

As mentioned earlier the results of the data taken with the ammonia flow loop constructed here would be compared to some of the in-tube flow boiling of ammonia results and an impinging jet correlation from literature. The in-tube flow ammonia boiling literature [29] should match for the measured maximum heat transfer coefficients. The impinging jet correlation will be used with the data taken here for comparisons between critical heat flux values of different operating conditions [18].

4.2.3.1 In-Tube Flow

In the background chapter it was mentioned that it is not practical to use an in-tube ammonia boiling correlation. Therefore, the only comparisons that can be made

here are with the final results calculated from the actual data from literature and from the KSU ammonia flow loop.

The only in-tube flow boiling of ammonia experimental setup that was run at flow rates comparable to the KSU ammonia flow loop is from Zurcher [29]. From these experiments shown in Figure 2.6.3 representing 120 kg/(m^2*s) (~0.018 kg/s) there was a maximum heat transfer coefficient recorded of approximately 21000 W/(m^2*K), or 2.1 W/(cm^2*K). This was with a heat flux of 44.4 kW/m^2 (4.44 W/cm^2), a saturation temperature of 4^{o}C (for saturation pressure or 500 kPa, or 72 psia), and the vapor quality was around 80%. After this point the heat transfer coefficient began to drop off as dryout began to occur.

An example of a series of tests from the KSU ammonia flow loop using the Slot Jet impinging jet evaporator seen in Table 4.2.7 with a mass flow rate of 0.017 kg/s (0.425 gpm) and a test cell inlet pressure of 410 kPa (60 psia) will be used for comparison. Just before film boiling began to occur the maximum heat flux obtained was 280 W/cm^2 with a maximum heat transfer coefficient of 6.66 W/(cm^2*K). The maximum heat transfer coefficient for the Slot Jet is higher than that shown earlier for this test condition due to the use of the ammonia saturation temperature instead of the actual temperature. This allows for proper comparison of the maximum heat transfer coefficients.

Dryout for in-tube evaporators is a much different mechanism than the film boiling that occurred with the Slot Jet. However, at both of these conditions each of the evaporators obtained a maximum heat transfer coefficient. This was the only applicable

way of comparing the maximum performance of each of these types of evaporators due to their different designs.

This comparison in Table 4.2.7 shows that for roughly the same operating conditions the Slot Jet impinging jet evaporator used in the KSU ammonia flow loop is superior in its ability to absorb energy compared to in-tube flow evaporators.

4.2.3.2 Impinging Jets

In the background chapter a correlation by Monde was shown for predicting the CHF for impinging jet boiling [18]. The measured data taken with the Slot Jet for each of the nine different test conditions is compared to this correlation in Table 4.2.8.

When comparing the measured and predicted CHF values the measured values from the Slot Jet are always higher. Also, the percentage difference between the correlation and the measured values was calculated. The average of this percentage was approximately 30%.

The fact that, as mentioned in the background, the correlation used here was developed using working fluids other that ammonia may account for some of the discrepancy between the measured and predicted CHF values. Also mentioned before was that this correlation was developed using different impinging jet and heated surface geometries. The impinging jets used for this correlation had a circular cross section and in order to used this correlation with the Slot Jet geometry hydraulic diameters had to be calculated. This is due to the rectangular jet cross sections of the Slot Jet.

Table 4.2.1 Slot Jet Test Matrix

Tinlet test cell	degC	-25	-25	-25	-25	-25	-25	-25	-25	-25
Pinlet test cell	kPa	310	310	310	410	410	410	790	790	790
Tsat @ test cell	degC	-8.4	-8.4	-8.4	-1	-1	-1	17.6	17.6	17.6
Mass flow rate	kg/s	0.017	0.010	0.029	0.017	0.010	0.029	0.017	0.010	0.029
Energy input	W	50	50	50	50	50	50	50	50	50
		100	100	100	100	100	100	100	100	100
		200	200	200	200	200	200	200	200	200
		300	300	300	300	300	300	300	300	300
		400	400	400	400	400	400	400	400	400
		500	500	500	500	500	500	500	500	500
		600	600	600	600	600	600	600	600	600
		700	700	700	700	700	700	700	700	700
		800	800	800	800	800	800	800	800	800
		900	900	900	900	900	900	900	900	900
		1000	1000	1000	1000	1000	1000	1000	1000	1000
		1100	1100	1100	1100	1100	1100	1100	1100	1100
		1200	1200	1200	1200	1200	1200	1200	1200	1200
		1300	1300	1300	1300	1300	1300	1300	1300	1300
		1400	1400	1400	1400	1400	1400	1400	1400	1400
		1500	1500	1500	1500	1500	1500	1500	1500	1500

Table 4.2.2 Comparison of Heat Flux Calculation Methods

Comparison of Heat Flux Calculation Methods (310 kPa, 15 degC Subcooled, 0.01 kg/s)			
Nominal Energy Input (watts)	Energy Input (W/cm^2)	Heater Neck Thermocouples (W/cm^2)	IR Camera (W/cm^2)
100.00	33	32	----------
200.00	69	65	60
300.00	101	93	88
400.00	137	127	113
500.00	171	158	165
550 (CHF)	184	173	----------
600 (CHF)	201	176	145

Table 4.2.3 CHF values for Each Test Condition

Critical Heat Fluxes, CHF (W/cm^2)

		Mass Flow Rate (kg/s)		
		0.010	0.017	0.029
Nominal Slot Jet Inlet Pressure (kPa)	310	173	249	289
	410	231	280	313
	790	262	275	488

Table 4.2.4 Maximum Heat Transfer Coefficients for Each Test Condition

Maximum Heat Transfer Coefficients ($W/(cm^2*K)$)

		Mass Flow Rate (kg/s)		
		0.010	0.017	0.029
Nominal Slot Jet Inlet Pressure (kPa)	310	4.54	4.89	5.36
	410	4.42	4.15	3.39
	790	3.21	2.83	4.14

Table 4.2.5 Average Uncertainty of Heat Flux During CHF Events at Each Test Condition and its Percent of the Actual Calculated Value

Average Uncertainty of Heat Fluxes (W/cm2)					**Percent of Measured Value**		
		Mass Flow Rate (kg/s)			Mass Flow Rate (kg/s)		
		0.010	0.017	0.029	0.010	0.017	0.029
Nominal Slot Jet Inlet Pressure (kPa)	310	19.07	26.66	29.92	11%	11%	10%
	410	24.79	29.02	32.66	11%	10%	10%
	790	26.71	27.88	49.47	10%	10%	10%

Table 4.2.6 Average Uncertainty of Heat Transfer Coefficients during CHF Events at Each Test Condition and its Percent of the Actual Calculated Value

Average Uncertainty of Heat Transfer Coefficients (W/(cm2*K))					**Percent of Measured Value**		
		Mass Flow Rate (kg/s)			Mass Flow Rate (kg/s)		
		0.010	0.017	0.029	0.010	0.017	0.029
Nominal Slot Jet Inlet Pressure (kPa)	310	0.98	1.24	1.50	22%	25%	28%
	410	1.02	1.73	1.92	23%	42%	57%
	790	0.47	0.81	2.74	15%	29%	66%

Table 4.2.7 In-Tube Measured Data Comparison to Slot Jet Measured Data

Data	Saturation Pressure (kPa)	Fluid Saturation Temperature (^oC)	Mass Flow Rate (kg/s)	Critical Heat Flux (W/cm^2)	Heat Transfer Coefficient ($W/(cm^2*K)$)
Zurcher	500	4	0.018	4.44	2.10
Measured	410	1	0.017	280	6.66

Table 4.2.8 Correlated CHF Values to CHF Values Calculated from Measured Data

Slot Jet Inlet Pressure (psia)	Subcooled Inlet Fluid Temperature, T_{sub} (^{o}C)	Volumetric Flow Rate (gpm)	Mass Flow Rate (kg/s)	Measured CHF (W/cm^2)	Predicted CHF, q_{co} (W/cm^2)	Difference (W/cm^2)	Percent Difference of Correlation
341	-22.3	0.250	0.0104	173	120	53	31
339	-21.6	0.425	0.0171	249	156	93	37
339	-21.5	0.700	0.0287	289	210	80	28
444	-22.5	0.250	0.0098	231	134	97	42
446	-24.4	0.425	0.0172	280	191	89	32
439	-23.9	0.700	0.0293	313	257	56	18
792	-22.3	0.250	0.0102	262	175	87	33
781	-23.1	0.425	0.0171	275	244	31	11
769	-24.2	0.700	0.0288	488	335	153	31

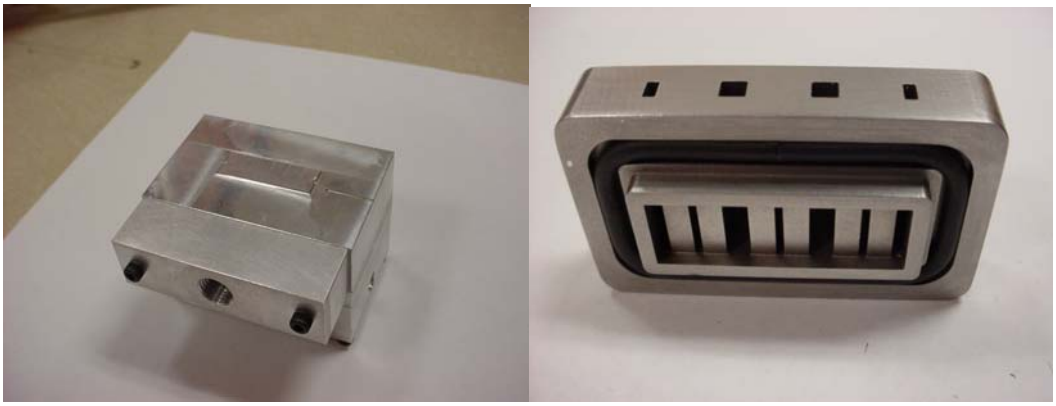

Figure 4.2.1 Slot Jet Device (Right: Entire Device, Left: Device Inside That Creates Slot Jets)

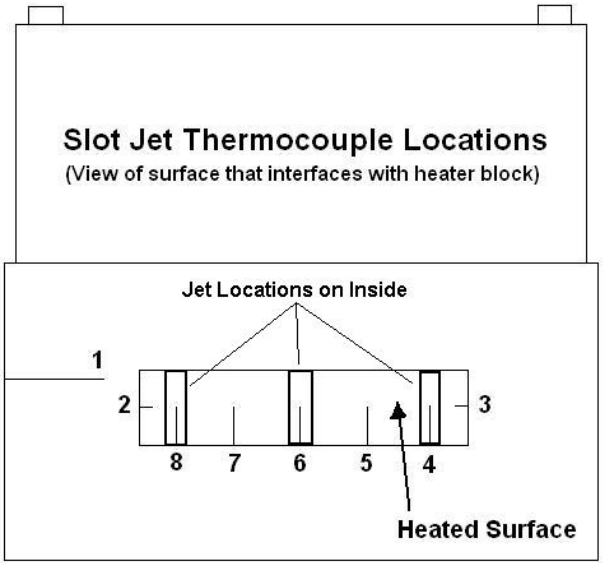

Figure 4.2.2 Slot Jet Thermocouple and Jet Locations

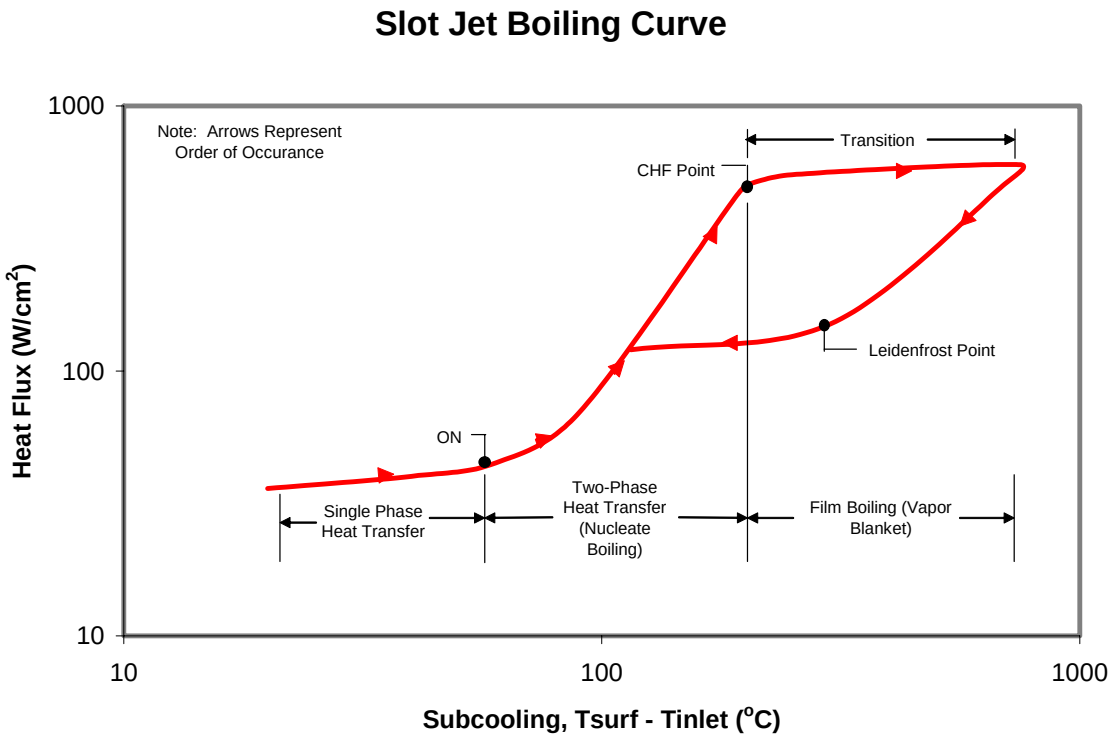

Figure 4.2.3 Slot Jet Boiling Curve

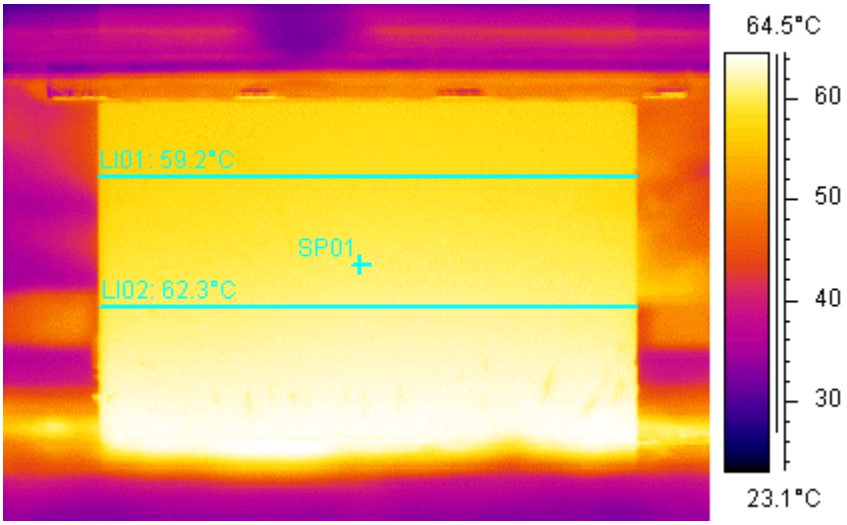

Figure 4.2.4 Example IR Image

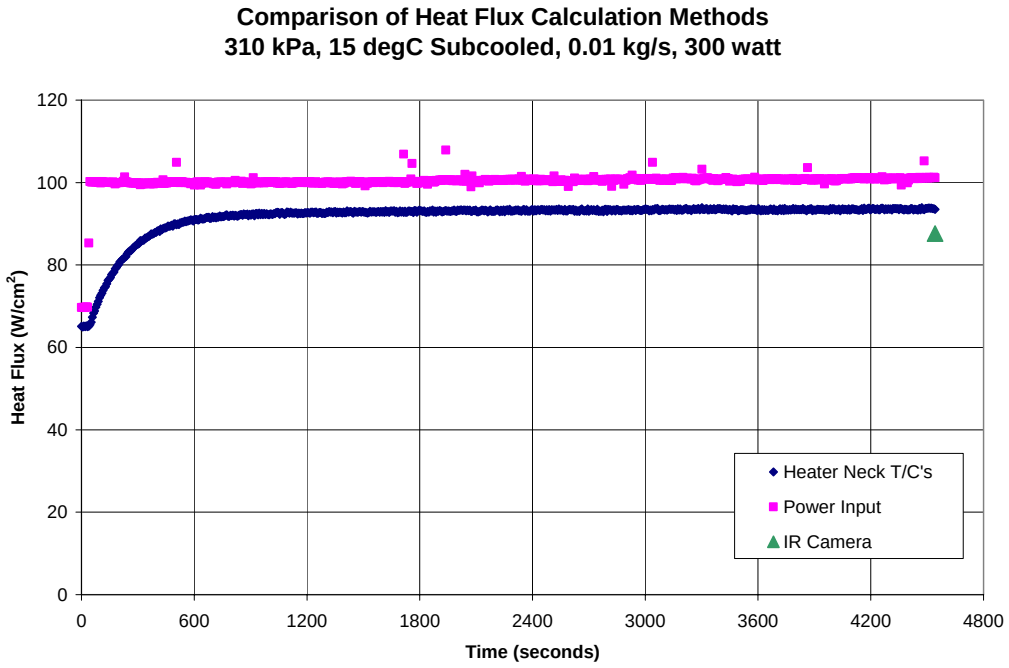

Figure 4.2.5 Plot of Comparison of Heat Flux Calculation Methods

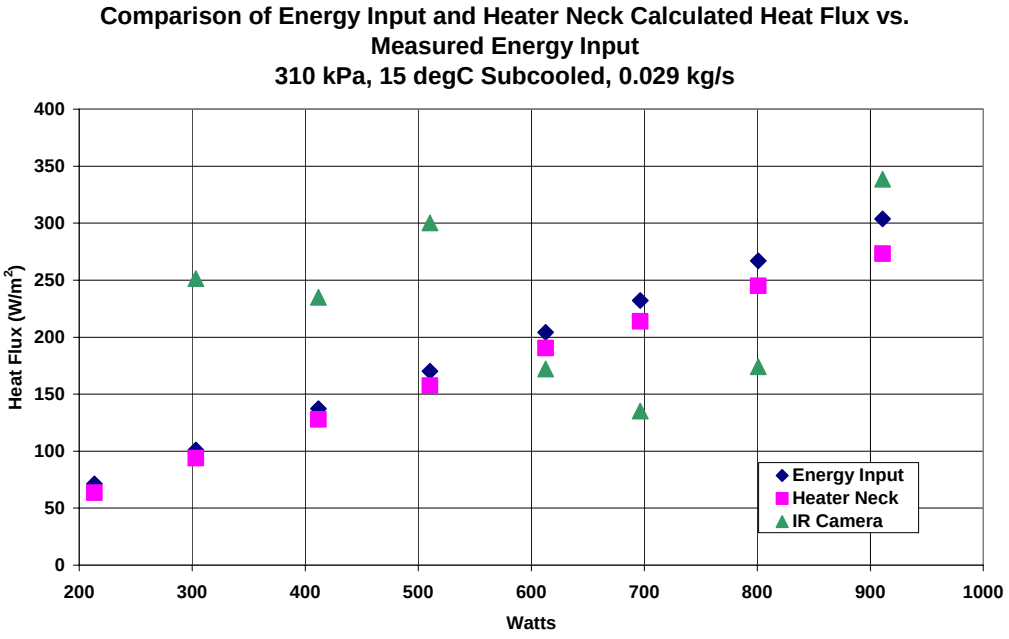

Figure 4.2.6 Comparison of Energy Input, Heater Neck, and IR Camera Calculated Heat Flux versus the Measured Energy Input

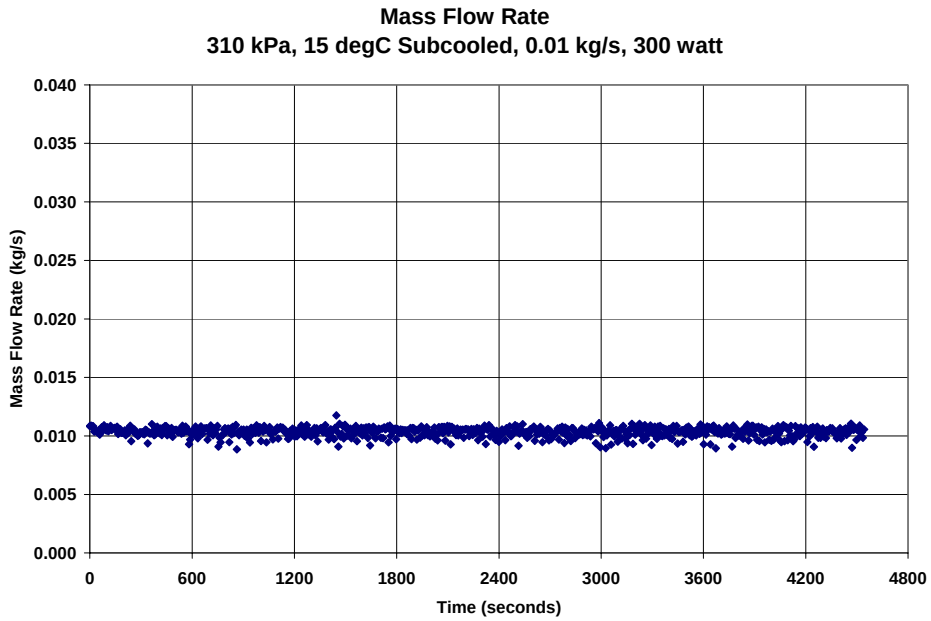

Figure 4.2.7 Mass Flow Rate for 310 kPa, 15 degC Subcooled, 0.01 kg/s, and 300 watt Test Conditions

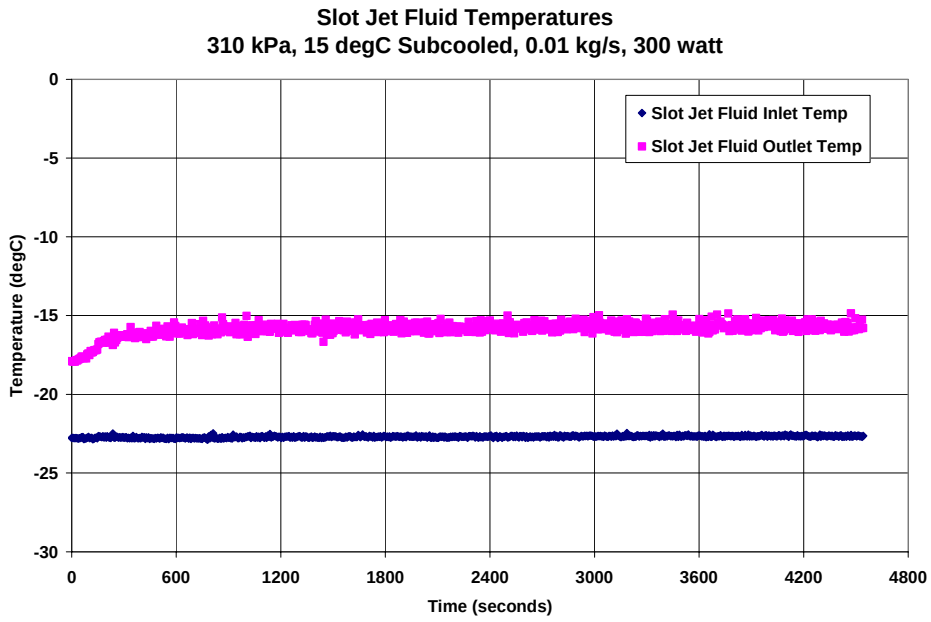

Figure 4.2.8 Slot Jet Fluid Temperatures for 310 kPa, 15 degC Subcooled, 0.01 kg/s, and 300 watt Test Conditions

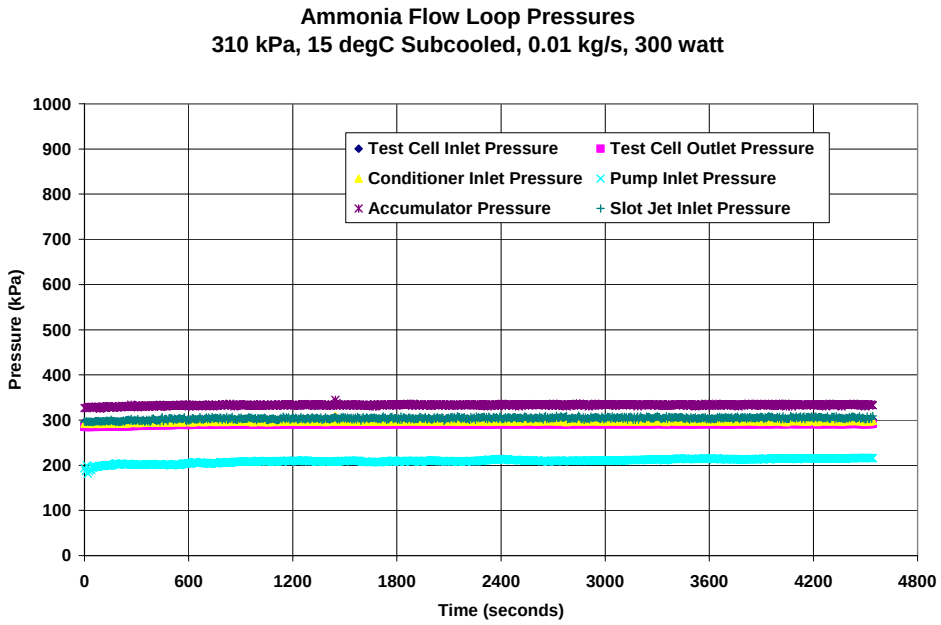

Figure 4.2.9 Ammonia Flow Loop Pressures for 310 kPa, 15 degC Subcooled, 0.01 kg/s, and 300 watt Test Conditions

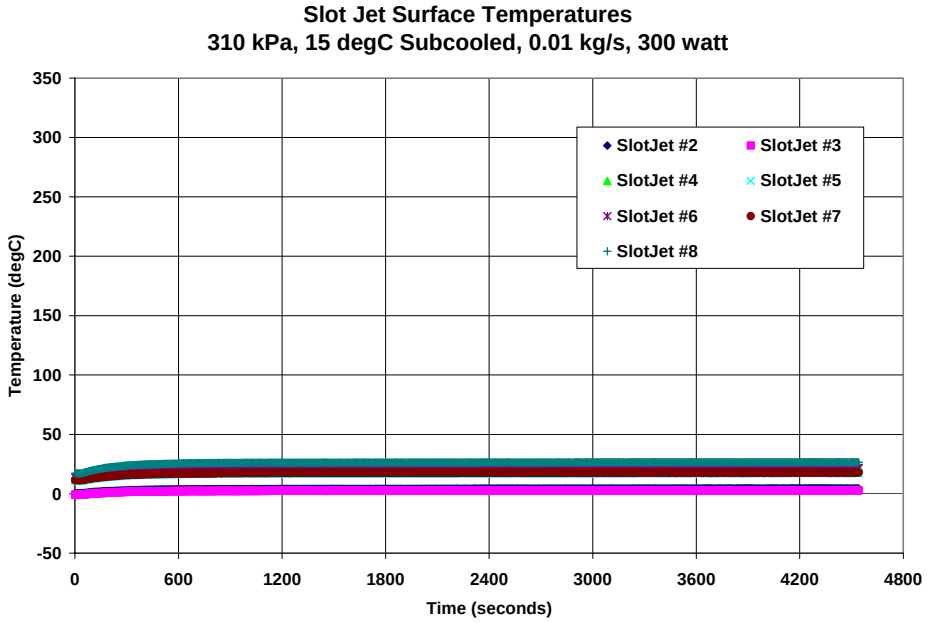

Figure 4.2.10 Slot Jet Surface Temperatures for 310 kPa, 15 degC Subcooled, 0.01 kg/s, and 300 watt Test Conditions

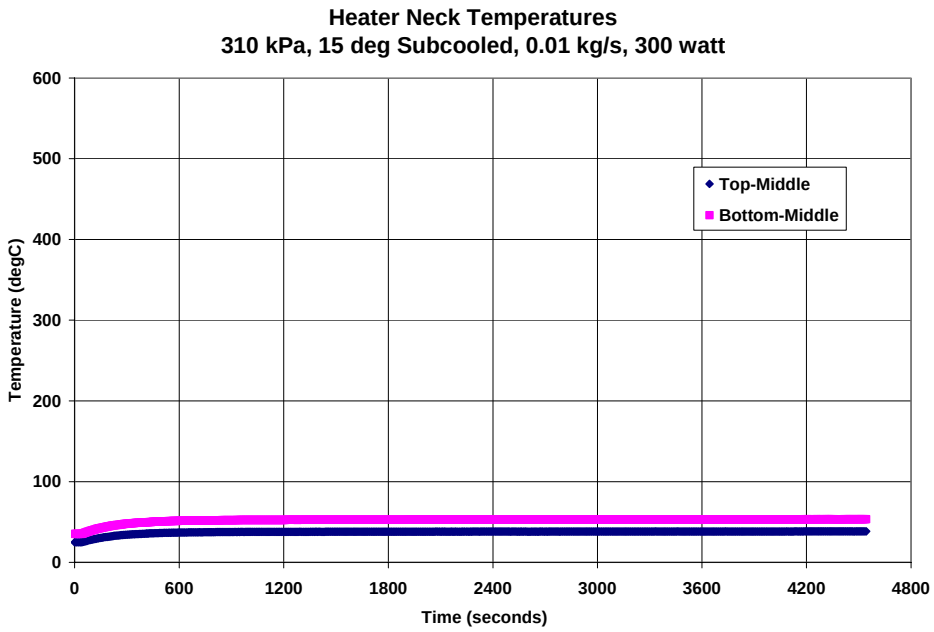

Figure 4.2.11 Heater Neck Temperatures for 310 kPa, 15 degC Subcooled, 0.01 kg/s, and 300 watt Test Conditions

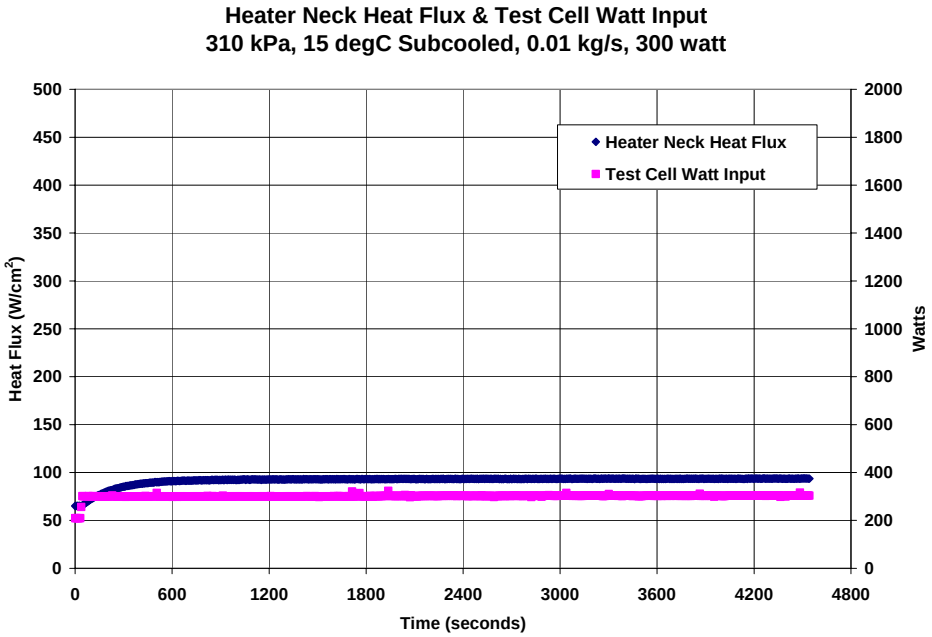

Figure 4.2.12 Heater Neck Heat Flux and Test Cell Energy Input for 310 kPa, 15 degC Subcooled, 0.01 kg/s, and 300 watt Test Conditions

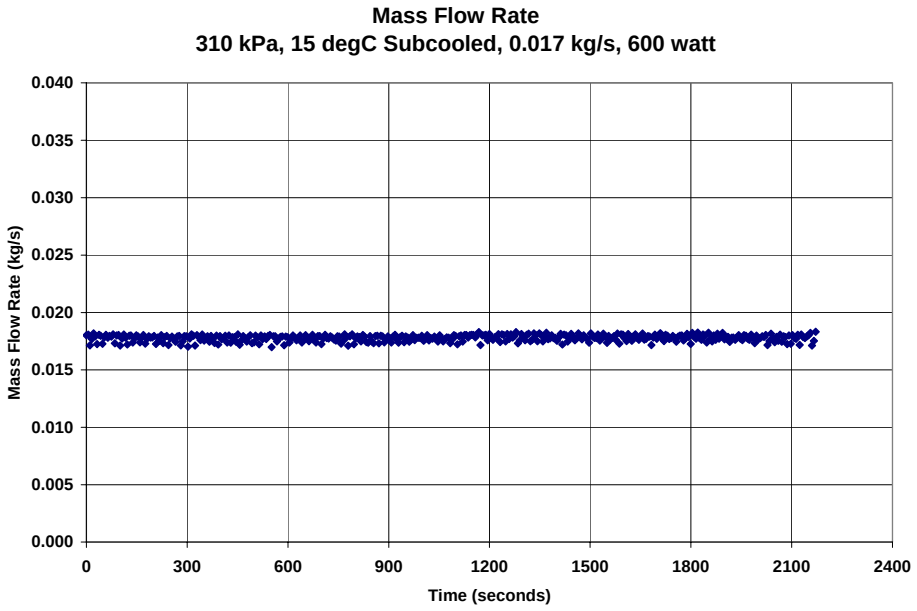

Figure 4.2.13 Mass Flow Rate for 310 kPa, 15 degC Subcooled, 0.017 kg/s, and 600 watt Test Conditions

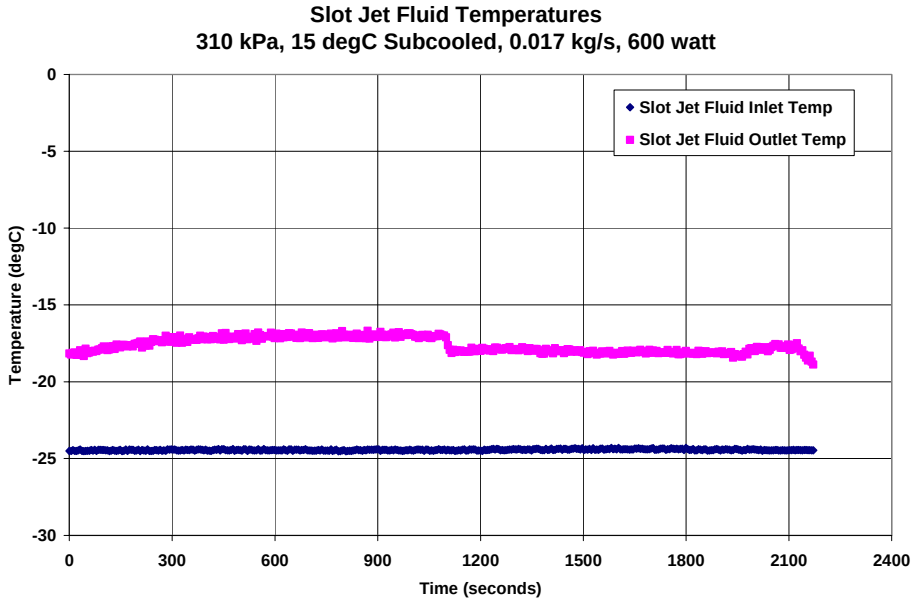

Figure 4.2.14 Slot Jet Fluid Temperatures for 310 kPa, 15 degC Subcooled, 0.017 kg/s, and 600 watt Test Conditions

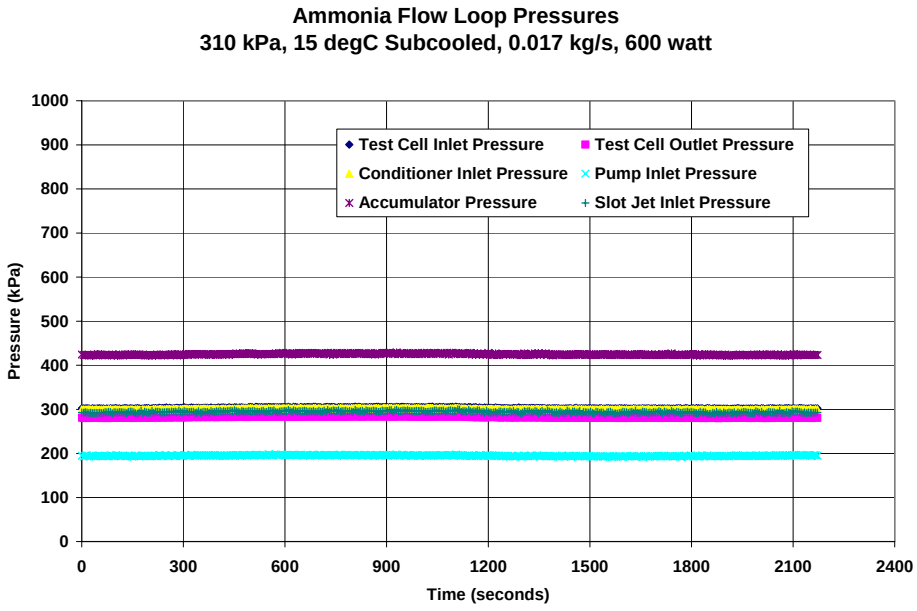

Figure 4.2.15 Ammonia Flow Loop Pressures for 310 kPa, 15 degC Subcooled, 0.017 kg/s, and 600 watt Test Conditions

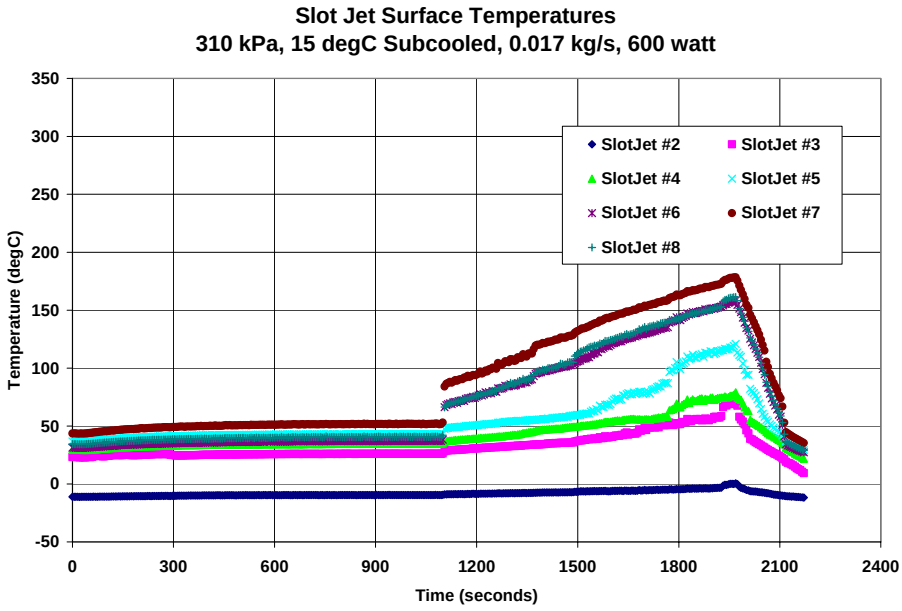

Figure 4.2.16 Slot Jet Surface Temperatures for 310 kPa, 15 degC Subcooled, 0.017 kg/s, and 600 watt Test Conditions

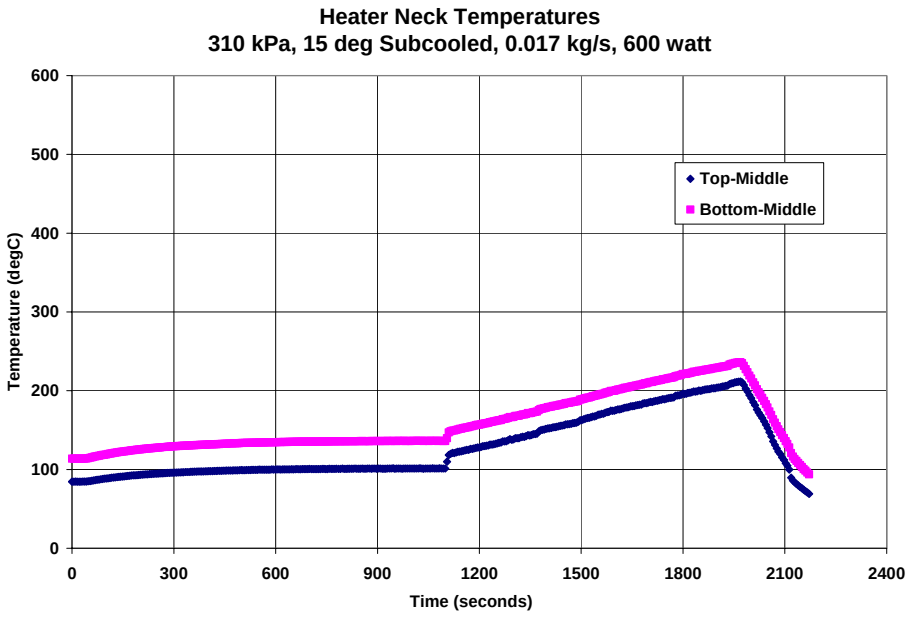

Figure 4.2.17 Heater Neck Temperatures for 310 kPa, 15 degC Subcooled, 0.017 kg/s, and 600 watt Test Conditions

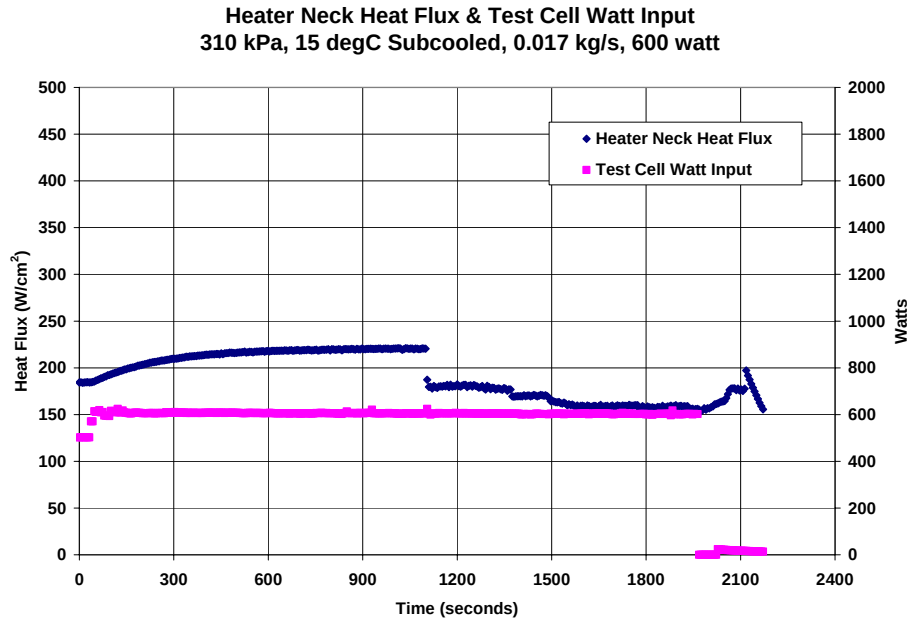

Figure 4.2.18 Heater Neck Heat Flux & Test Cell Energy Input for 310 kPa, 15 degC Subcooled, 0.017 kg/s, and 600 watt Test Conditions

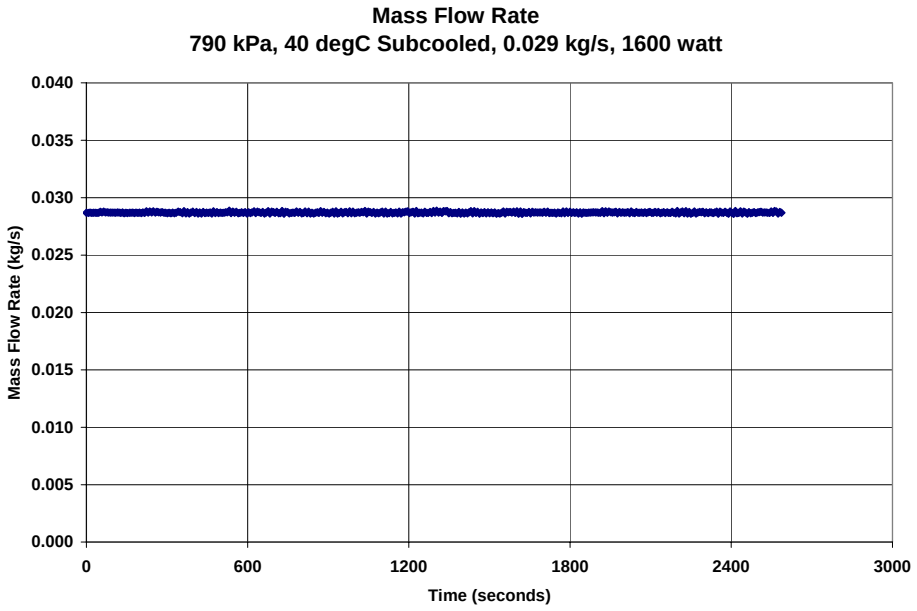

Figure 4.2.19 Mass Flow Rate for 790 kPa, 40 degC Subcooled, 0.029 kg/s, and 1600 watt Test Conditions

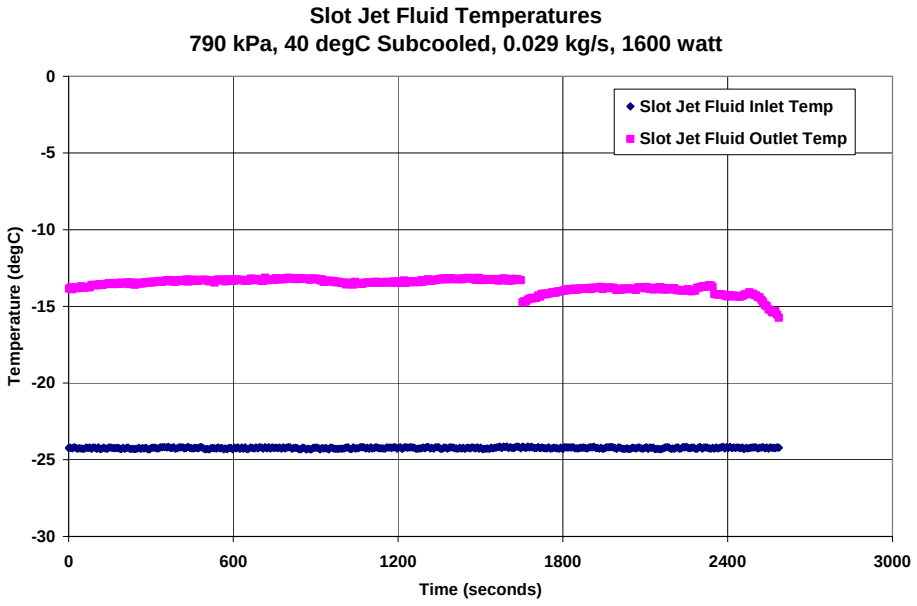

Figure 4.2.20 Slot Jet Fluid Temperatures for 790 kPa, 40 degC Subcooled, 0.029 kg/s, and 1600 watt Test Conditions

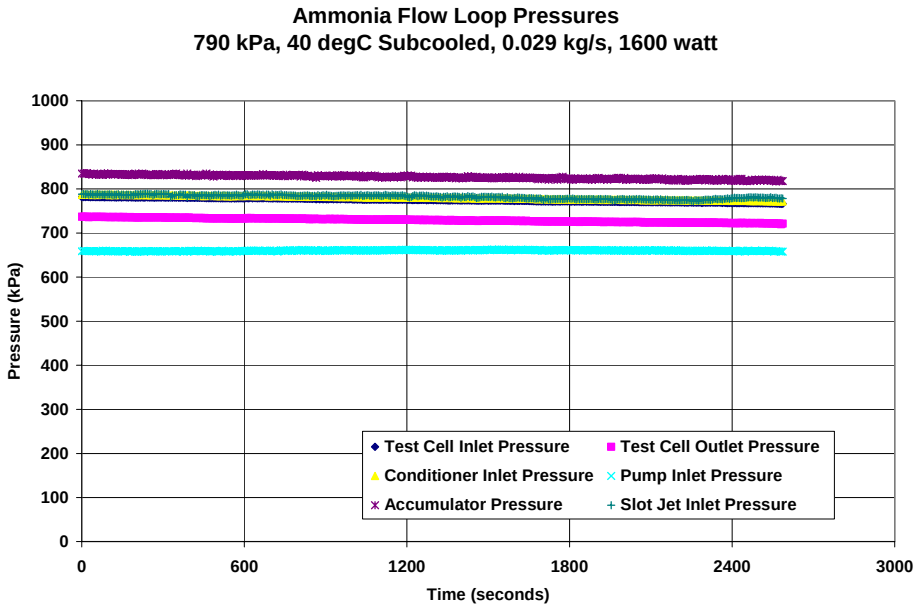

Figure 4.2.21 Ammonia Flow Loop Pressures for 790 kPa, 40 degC Subcooled, 0.029 kg/s, and 1600 watt Test Conditions

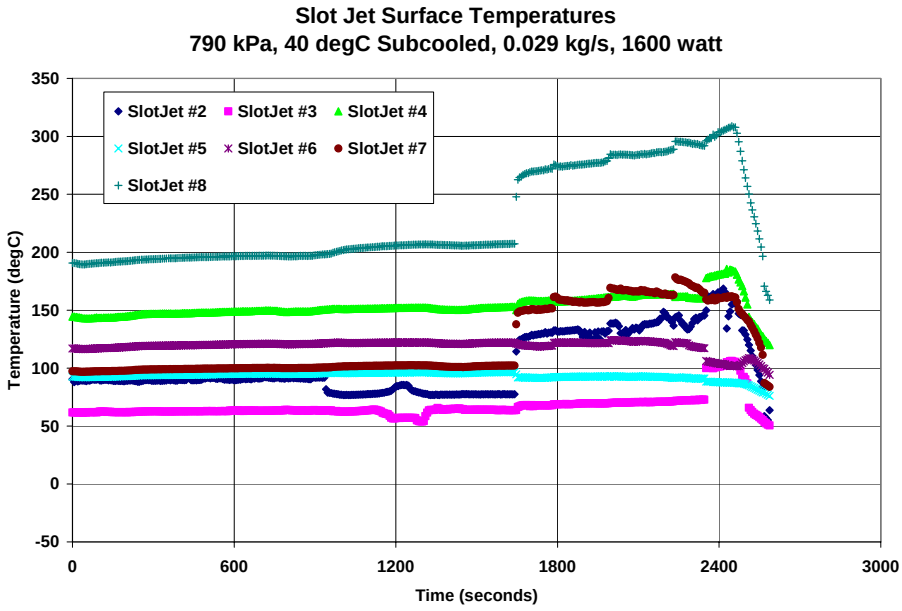

Figure 4.2.22 Slot Jet Surface Temperatures for 790 kPa, 40 degC Subcooled, 0.029 kg/s, and 1600 watt Test Conditions

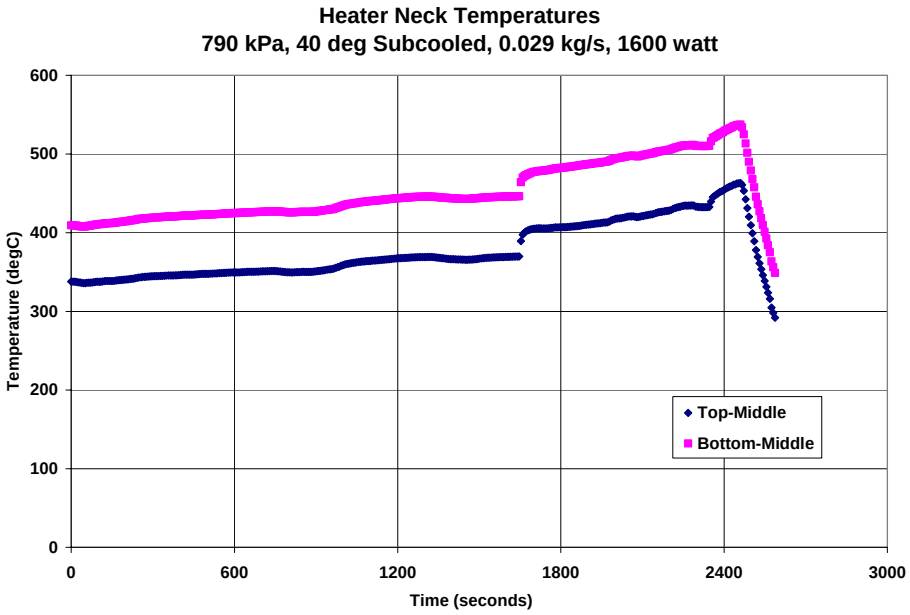

Figure 4.2.23 Heater Neck Temperatures for 790 kPa, 40 degC Subcooled, 0.029 kg/s, and 1600 watt Test Conditions

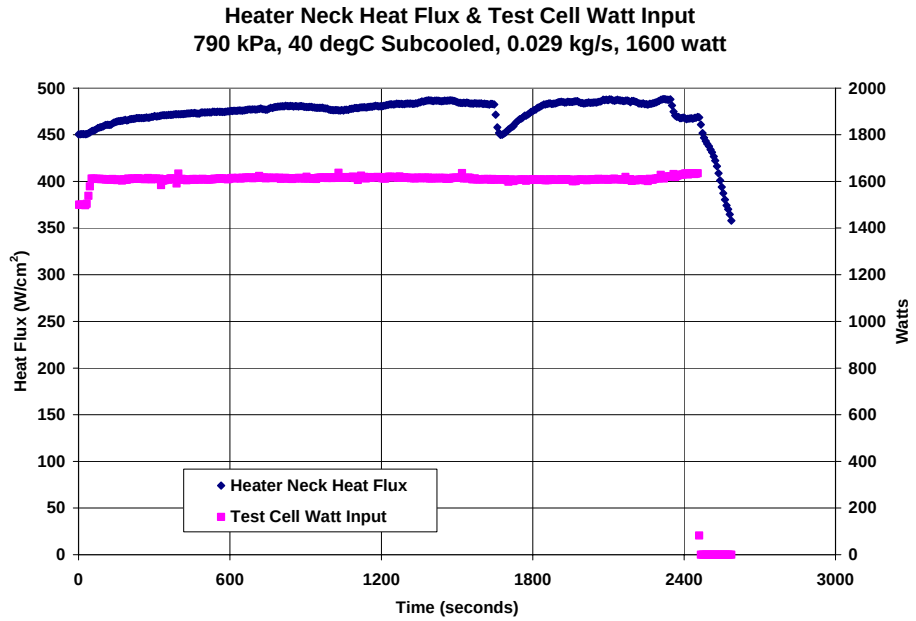

Figure 4.2.24 Heater Neck Heat Flux & Test Cell Energy Input for 790 kPa, 40 degC Subcooled, 0.029 kg/s, and 1600 watt Test Conditions

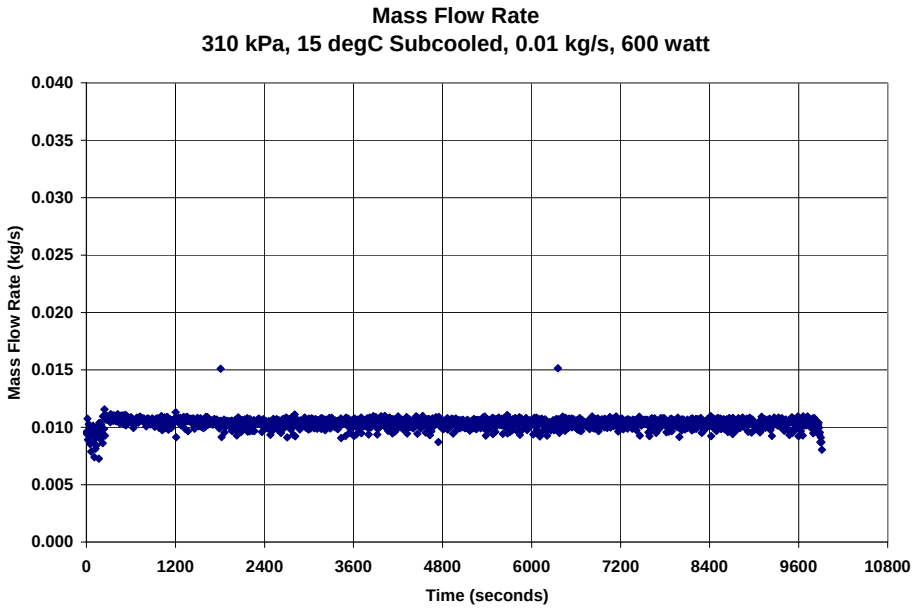

Figure 4.2.25 Mass Flow Rate for 310 kPa, 15 degC Subcooled, 0.01 kg/s, and 600 watt Test Conditions

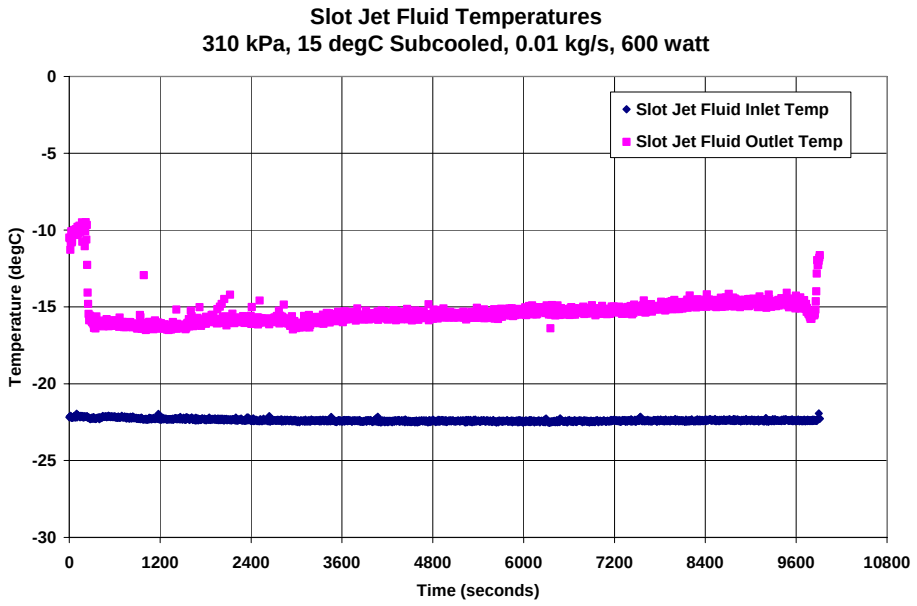

Figure 4.2.26 Slot Jet Fluid Temperatures for 310 kPa, 15 degC Subcooled, 0.01 kg/s, and 600 watt Test Conditions

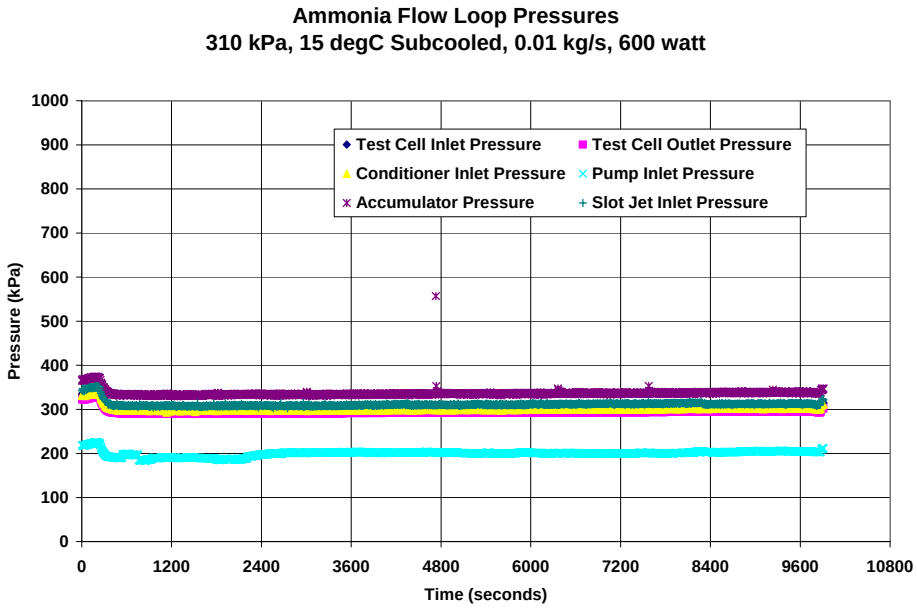

Figure 4.2.27 Ammonia Flow Loop Pressures for 310 kPa, 15 degC Subcooled, 0.01 kg/s, and 600 watt Test Conditions

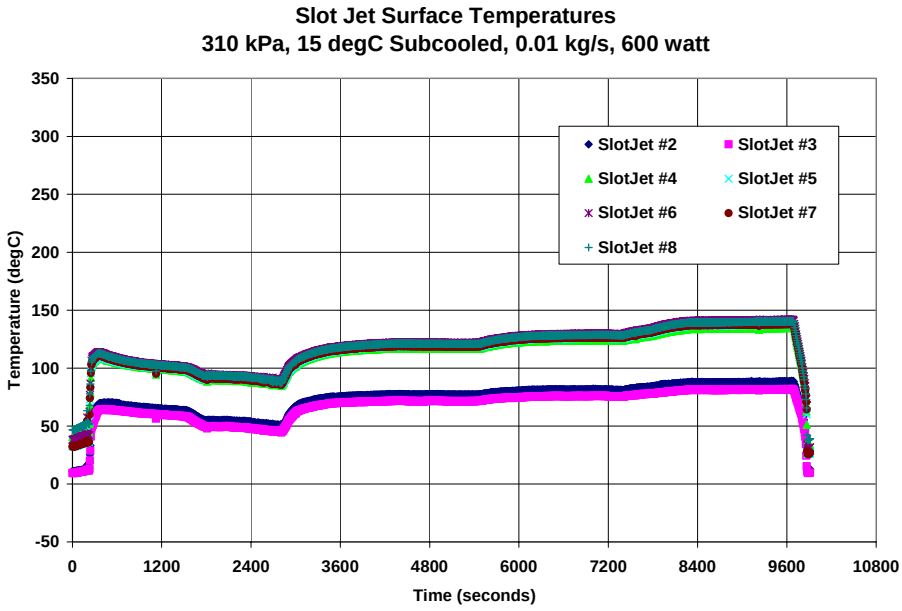

Figure 4.2.28 Slot Jet Surface Temperatures for 310 kPa, 15 degC Subcooled, 0.01 kg/s, and 600 watt Test Conditions

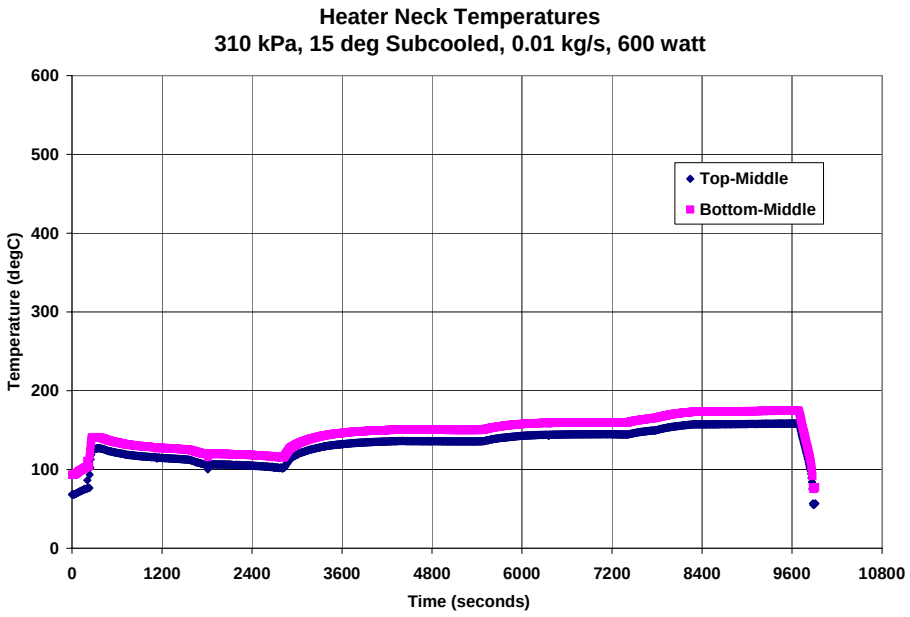

Figure 4.2.29 Heater Neck Temperatures for 310 kPa, 15 degC Subcooled, 0.01 kg/s, and 600 watt Test Conditions

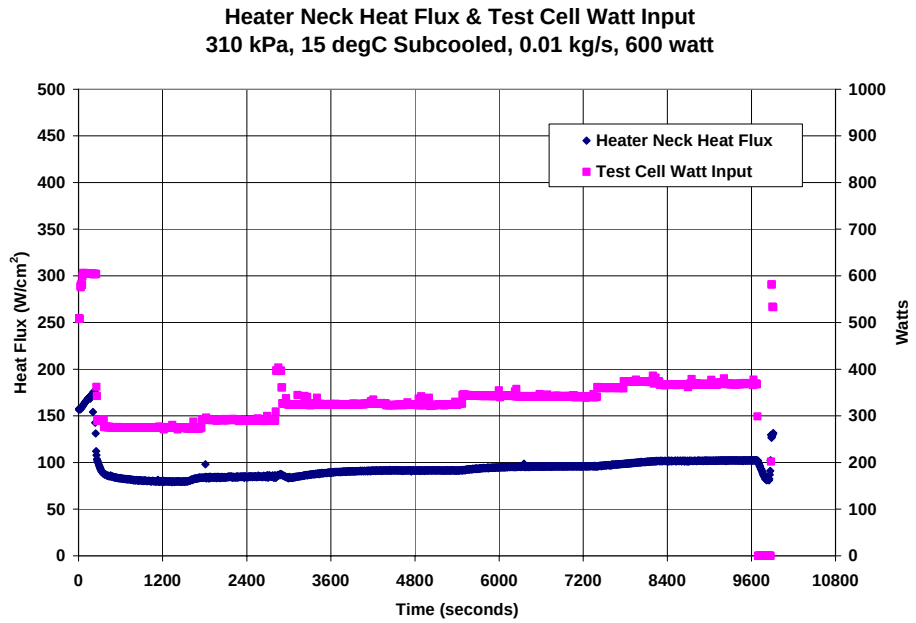

Figure 4.2.30 Heater Neck Heat Flux & Test Cell Energy Input for 310 kPa, 15 degC Subcooled, 0.01 kg/s, and 600 watt Test Conditions

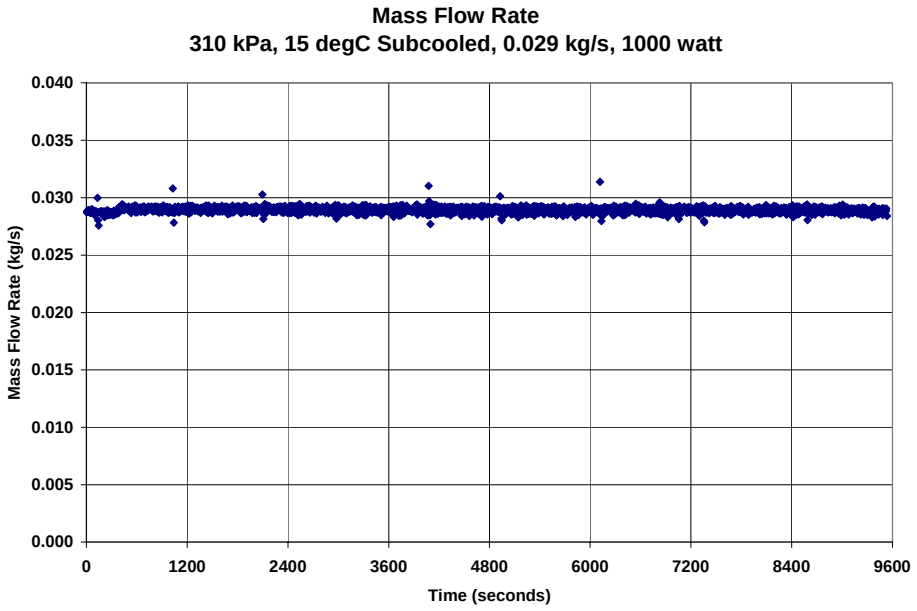

Figure 4.2.31 Mass Flow Rate for 310 kPa, 15 degC Subcooled, 0.029 kg/s, and 1000 watt Test Conditions

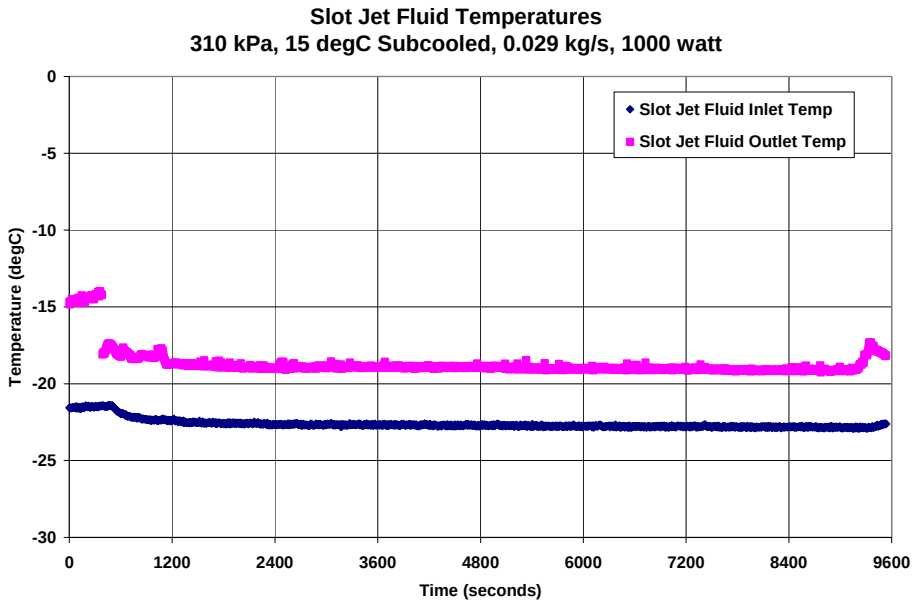

Figure 4.2.32 Slot Jet Fluid Temperatures for 310 kPa, 15 degC Subcooled, 0.029 kg/s, and 1000 watt Test Conditions

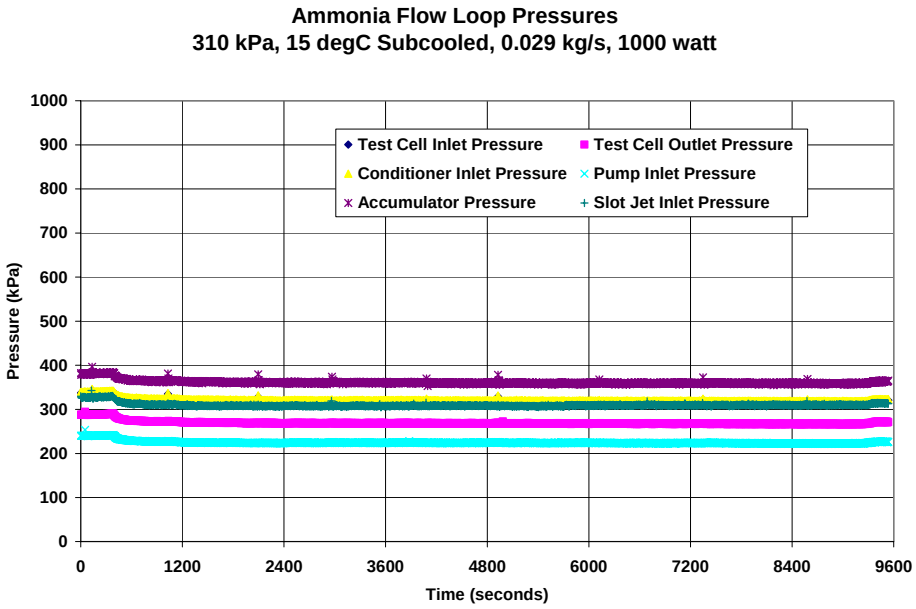

Figure 4.2.33 Ammonia Flow Loop Pressures for 310 kPa, 15 degC Subcooled, 0.029 kg/s, and 1000 watt Test Conditions

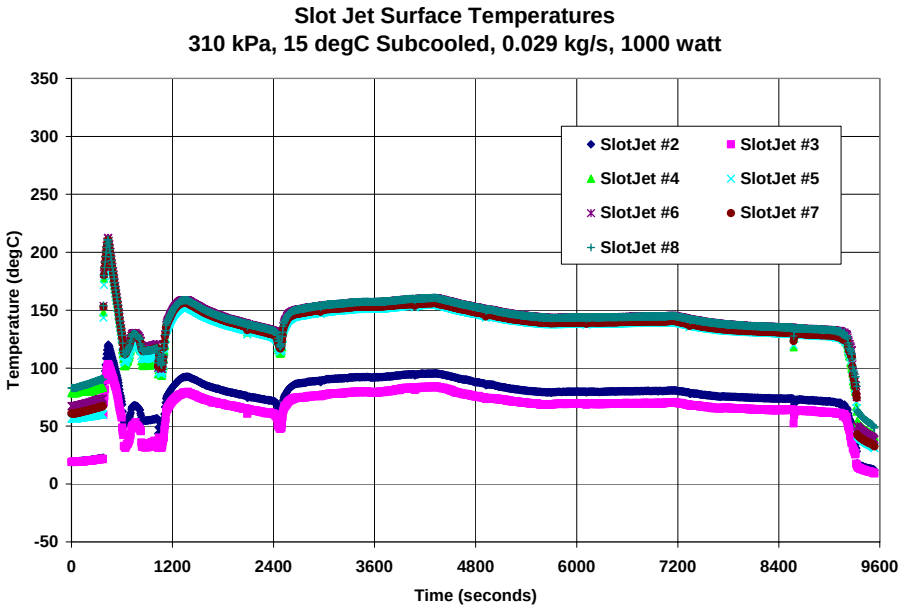

Figure 4.2.34 Slot Jet Surface Temperatures for 310 kPa, 15 degC Subcooled, 0.029 kg/s, and 1000 watt Test Conditions

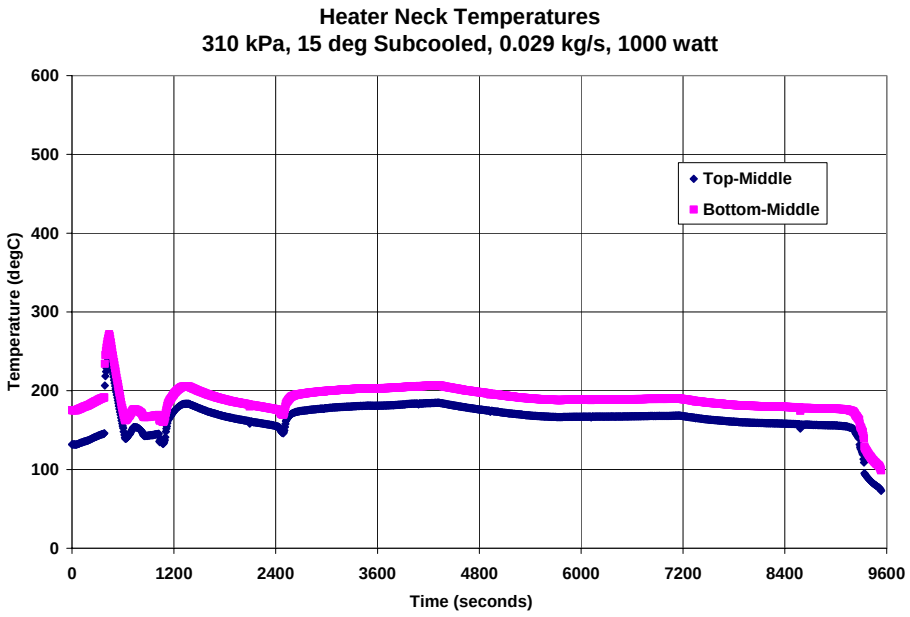

Figure 4.2.35 Heater Neck Temperatures for 310 kPa, 15 degC Subcooled, 0.029 kg/s, and 1000 watt Test Conditions

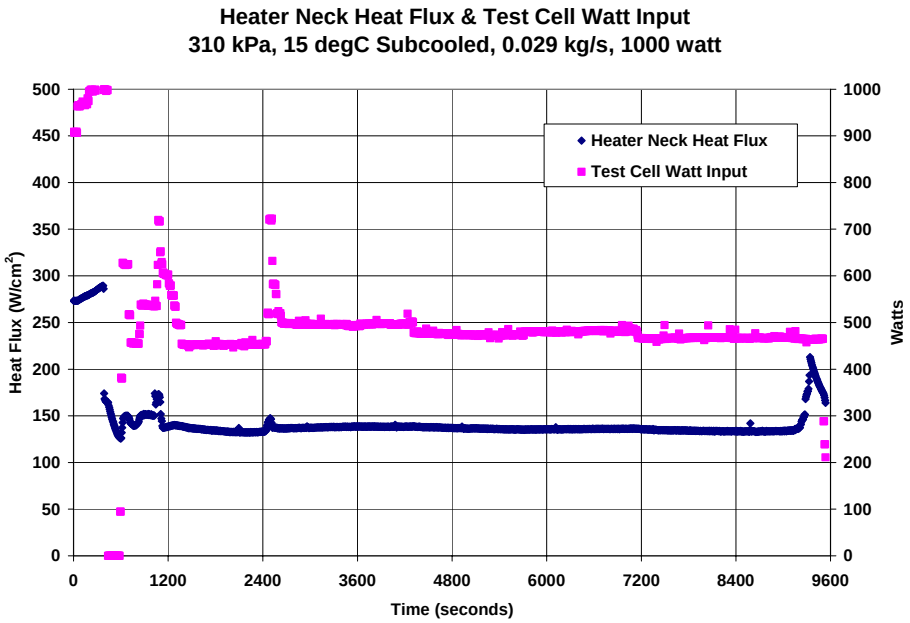

Figure 4.2.36 Heater Neck Heat Flux & Test Cell Watt Input for 310 kPa, 15 degC Subcooled, 0.029 kg/s, and 1000 watt Test Conditions

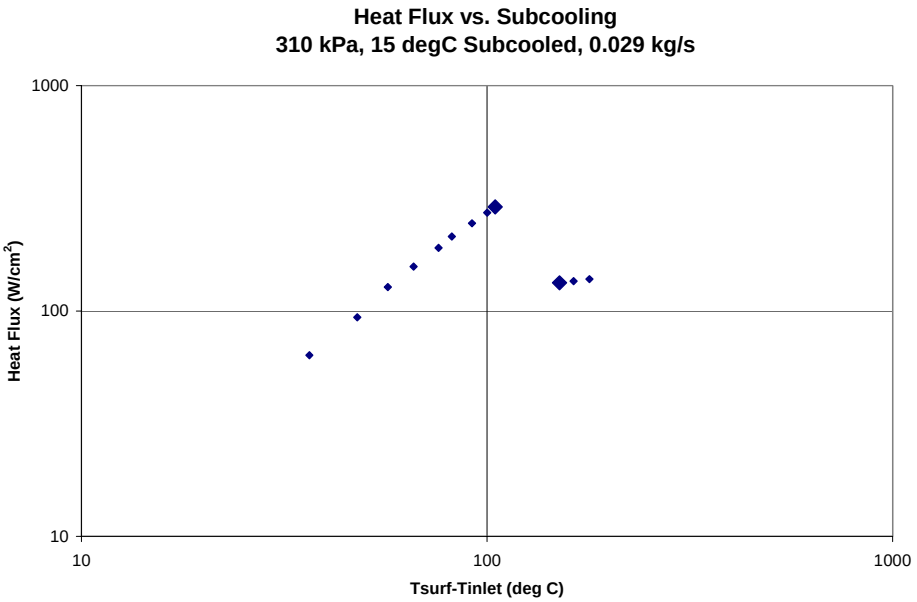

Figure 4.2.37 Actual Slot Jet Boiling Curve for 310 kPa, 15 degC Subcooled, 0.029 kg/s Test Conditions

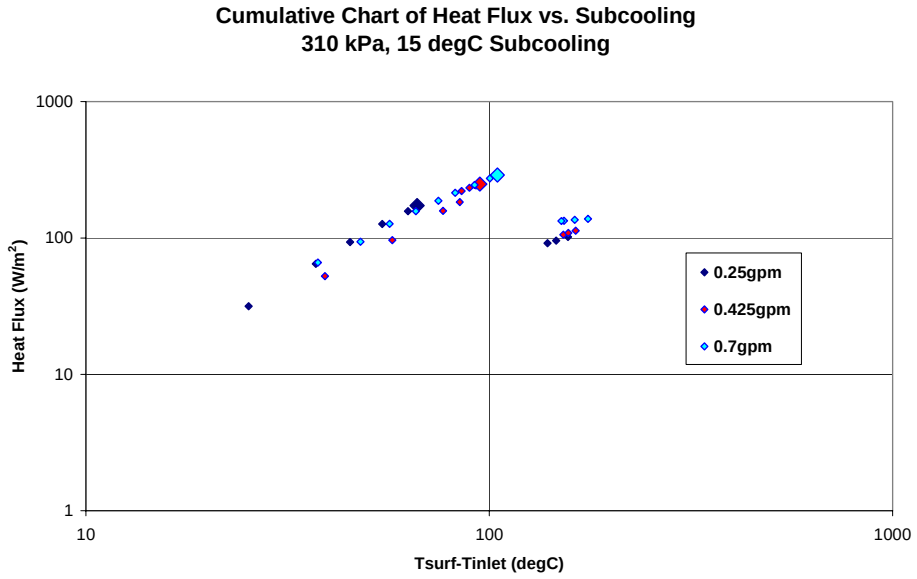

Figure 4.2.38 Actual Slot Jet Boiling Curves for 310 kPa and 15 degC Subcooled Test Conditions

4.3 Summary

The test matrix in Table 4.1.1 shows the desired measured data from the ECHIC. The measured data from this device never reached the maturity required to create any of the desired data. The ECHIC cooling device originally planned for taking data with the ammonia flow loop was exposed to conditions beyond its capabilities. This resulted in its failure on the first test run due to improper adherence to the test matrix and a lack of data acquisition equipment testing. The testing with the Raytheon ECHIC device was aborted. Appendix D has a more detailed discussion of its failure.

The lessons learned from this event are that adherence to test procedures is crucial, the instrumentation deficiencies were identified, and the physics of the ammonia flow loop are better understood. The corrective measure taken due to this event include a need to strictly adhere to a test matrix, an updated data acquisition system, and a test readiness review [24] presented to Raytheon before testing with the Slot Jet cooling device began.

A boiling curve representing the desired data from the Slot Jet, similar to the ECHIC, was shown in Figure 4.2.3 and discussed as well. In order to obtain the data to create this boiling curve a test matrix, Table 4.2.1, was developed and the manner in which it was designed to be used was explained.

There were three different methods to calculate the heat flux that the Slot Jet heated surface was exposed to. They included using the energy input, heater neck thermocouples, and the IR camera temperature readings. Before the measured data could be discussed only one of these methods had to be chosen to show different transient data

types and to calculate CHF values and their corresponding maximum heat transfer coefficients. The heater neck thermocouple method was chosen.

The first transient type of data that was discussed was a typical two-phase data set where only the energy input was changed. The system responses were shown to be a smooth exponential change at first followed by a gradual steadying of system parameters.

A typical CHF event was shown in the next data set discussed. Here the system parameters are shown to react the same as the typical data set except that when the CHF point is reached Slot Jet surface and heater neck temperatures suddenly begin to rise very quickly. The heater neck heat flux and Slot Jet fluid outlet temperatures suddenly drop also. This was caused by the occurrence of film boiling causing a decrease in heat transfer. There was also another data set mentioned here where an inconsistent CHF event occurred with the system operating at the highest system pressure and mass flow rate tested at. It was difficult to determine the point where CHF occurred due to the possibility of film boiling only occurring on part of the Slot Jet heated surface. This is shown by the inconsistent readings of the Slot Jet surface thermocouples.

The next type of transient data set mentioned was one where steady state measurements were made during film boiling after a CHF event had occurred. The steady state values of the Slot Jet surface and heater neck temperatures where much higher than in typical data sets. The steady state values of the heater neck heat flux and the Slot Jet fluid outlet temperatures were much lower than in typical data sets.

Finally a Liedenfrost point was possibly observed in another data set where the heat flux was reduced enough during film boiling to where the Slot Jet heated surface suddenly became rewetted again with no changes in energy input. This is shown by the

sudden drop in Slot Jet surface and heater neck temperatures and by the sudden rise in the Slot Jet fluid outlet temperature and heater neck heat flux.

The CHF values calculated from the measured data in Table 4.2.3 represent the correct trends that should be seen with increasing mass flow rates and system pressures. However, the corresponding heat transfer coefficients in Table 4.2.4, for the most part, do not. This is likely due to the large uncertainty associated with calculating heat transfer coefficients compared to CHF values.

The comparison of the Slot Jet measured data to literature in Table 4.2.5 was shown to be superior to an in-tube flow evaporator in its ability to absorb energy using ammonia in roughly the same operating conditions. Also, a correlation for finding critical heat flux with impinging jet boiling was used to predict the results of the measured data. This correlation consistently predicted lower critical heat fluxes than the measured data seen in Table 4.2.6 with an average difference of approximately 30%.

5 CONCLUSIONS AND RECOMMENDATIONS

An ammonia test facility was constructed to support the supplied Raytheon test cell to obtain CHF values and boiling heat transfer coefficients as applied to DEW. The KSU heat transfer lab allowed the construction of this ammonia test facility due to its available enclosed chamber, cooling capacity, electrical power, instrumentation, and other supporting equipment.

Background information needed before the construction of the ammonia test facility could begin included ammonia properties and material compatibility, reviewing other ammonia flow loops from literature, and reviewing results from these ammonia flow loops from literature. Material compatibility research showed different sealing and transport materials to use and not to use with ammonia. The most important compatibility issue with ammonia is that is should not be used with copper or copper-based alloys. All reviewed literature using ammonia consisted of in-tube flow evaporators. Reviewed literature for impinging jets where different working fluids were used suggested an impinging jet correlation that was used with the measured ammonia data collected here.

The construction of the ammonia test facility inside the enclosed chamber began by acquiring and purchasing the required components with materials compatible with ammonia. Once it was constructed a copper corrosion test was performed and the copper did not corrode. This allowed the use of the copper ECHIC cooling device from Raytheon in the Raytheon test cell.

The major components of the ammonia flow loop consist of a pump, conditioner, condenser, and filter to support the use of the Raytheon test cell. The glycol flow loop used to control temperatures in the ammonia flow loop consisted of a pump, storage tank, chiller, and the ammonia flow loop components. The instrumentation for the ammonia flow loop consisted of thermocouples, pressure transducers, a mass flow meter, sight glasses, and an ammonia detector to monitor the operations of the ammonia flow loop. This and other instrumentation was all controlled by a data acquisition/switch unit and a personal computer. The Raytheon test cell consisted of a pneumatic system, electrical energy source, heater block, instrumentation, the ECHIC and Slot Jet cooling devices, and other equipment to create and measure two-phase heat transfer.

A thermodynamic model of the ammonia flow loop was created. It consisted of 10 ammonia states throughout the loop with an inlet and outlet state for each major component. Some of its limitations were not accounting for pressure drop across some components and the ammonia property data that it used. When compared to actual data the pressure drops across the ammonia flow loop that the model calculated were about half or less of was obtain from actual data.

A general facility operation procedure for the ammonia flow loop was discussed including start-up, adjustments, and recording data for the facility. The operational limits of the ammonia test facility were also discussed.

The ECHIC cooling device originally planned for use with the Raytheon test cell was exposed to conditions beyond its cooling capabilities and failure resulted. Adherence to test procedures, thorough testing of instrumentation, and a better understanding of the physics of the ammonia flow loop were learned from this failure.

The Slot Jet then replaced the ECHIC as the cooling device for the test cell. Data recorded using the Slot Jet showed what happened to various system parameters under transient conditions for typical two-phase heat transfer, CHF events, film boiling, and a Liedenfrost point. Calculated CHF values matched changing trends in system conditions but the calculated maximum heat transfer coefficients did not due to the larger uncertainty involved in their calculations. When comparing the CHF values and maximum heat transfer coefficients measured here to in-tube flow evaporators, impinging jet evaporators are shown to be far superior. Calculated CHF values using the impinging jet correlation from literature were an average of 30% lower than measured data calculations.

One recommendation for the ammonia test facility is that the chiller be repaired in order to be able to control the glycol in the storage tank at higher temperatures. This will allow many more system conditions to be tested, specifically lower ammonia subcoolings at the test cell inlet. Another recommendation is the separate installation of flow meters for the glycol entering the conditioner and the condenser. This would allow better understanding of the heat transfer occurring in these components due to the knowledge of more accurate glycol flow rates. Replacing the plastic tubing in the test cell and acquiring pressure transducers able to read higher pressures allowing the testing of more system conditions with the Raytheon test cell is also recommended. Since there was only one way to accurately find the heat flux at the heater block neck more research could be done here to find other solutions as well. It would also be useful to incorporate an impinging jet correlation into the thermodynamic model used to better predict how the ammonia flow loop operated. Finally, it is recommended to further study the ammonia

measured data with the Slot Jet impinging jet evaporator to possibly develop a correlation. This would most likely be one of the first correlations of this type since there were no impinging jet correlations found in literature developed from ammonia data and it would be very beneficial to industry.

REFERENCES

[1] Air Liquide, www.airliquide.com

[2] ASHRAE Refrigeration Handbook 2002

[3] Chaddock J., Buzzard G., Film coefficients for in-tube evaporation of ammonia and R502 with and without small percentages of mineral oil, ASHRAE Transactions 1986; 92:222-40

[4] Collier, John G., Thome, John R., Convective Boiling and Condensation: Third Edition, Clarendon Press Oxford, 1996

[5] Eckels, Dr. Steven, Kansas State University Mechanical and Nuclear Engineering Department Professor, discussions September 2003 – June 2005

[6] efunda, Engineering Fundamentals, www.efunda.com

[7] Fenton, Dr. Donald, Kansas State University Mechanical and Nuclear Engineering Department Professor, discussions September 2003 – June 2005

[8] Fox, Robert W., McDonald, Alan T., Introduction to Fluid Mechanics: Fifth Edition, John Wiley & Sons, Inc.

[9] Goulds Pumps, http://www.goulds.com/pdf/C36{2f}3742.pdf

[10] Hopkins, Kevin, Raytheon Missile Systems Principal Engineer, conversations June 2003 – June 2005.

[11] Incropera, Frank P., DeWitt, David P., Fundamentals of Heat and Mass Transfer: Fourth Edition, John Wiley & Sons, 1996

[12] International Institute of Ammonia Refrigeration (iiar), Ammonia Data Book, Table 2-6, December 1992

[13] Kabelac, S. (Univ of Hannover); de Buhr, H.-J., Flow boiling of ammonia in a plain and a low finned horizontal tube, Source: International Journal of Refrigeration, v 24, n 1, Jan, 2001, p 41-50

[14] Kelly, John Eugene, "Evaporation of Ammonia in Smooth and Enhanced Tubes With and Without Miscible Oil," Kansas State University Department of Mechanical Engineering Thesis, 2000

[15] Kline, S. J., McClintock, F. A., Describing Uncertainties in Single-Sample Experiments, Mechanical Engineering 75: 3-8, 1953

[16] LaRoche Industries Inc., Material Safety Data Sheet # 4001: Anhydrous Ammonia, September 16, 2002

[17] Lies, Q. Shane, "Development of a Test Facility to Measure the Two-Phase Heat Transfer and Pressure Drop of Ammonia," Kansas State University Department of Mechanical Engineering Thesis, 1996

[18] Monde, M. and Mitsutake, Y., "Critical Heat Flux in Forced Convective Subcooled Boiling With Multiple Impinging Jets," Journal of Heat Transfer February 1996, Vol. 117, p. 241-243

[19] Moran, Michael J., Shapiro, Howard N.; Fundamentals of Engineering Thermodynamics: Fourth Edition; John Wiley & Sons, Inc.; 2000

[20] NIST Chemistry WebBook, Thermophysical Properties of Fluid Systems, http://webbook.nist.gov/chemistry/fluid

[21] OMEGA Engineering, Inc., OMEGA-FLO HHF300 Digital Anemometer, Serial #: 300-93-08352, KSU Property #: 428367ET, Supplied by Kansas State University Mechanical and Nuclear Engineering Measurements and Instrumentation Laboratory (Exhaust vent air velocity: 8.3 m/s (1634 ft/min)/Exhaust vent flow: 0.824 m^3/s (1745 CFM))

[22] Omega Engineering, www.omega.com

[23] Raytheon HS Small-Scale CHIC/ECHIC Test Bed Information, Raytheon Missile Systems

[24] Raytheon Test Readiness Review, March 2005

[25] Sandru E., Chiriac F., Heat transfer for the vaporization of ammonia during flow though horizontal pipe systems under conditions of low vapor concentration, Int. Chem. Eng. 18 (4) (1978) 692-699.

[26] Shah, M. M., "Heat Transfer and Pressure Drop in Ammonia Evaporators" 1974, ASHRAE Transactions, Vol. 80, Part 1.

[27] Shah, M. M., "Visual Observations in an Ammonia Evaporator" 1975, ASHRAE Transactions, Vol. 81, Part 1, pp. 295-306.

[28] Zamfirescu, Calin (Dept. Thermodynamics/Heat Trans., Technical University of Civil Eng.); Chiriac, Florea, Heat transfer measurements on ammonia forced convection boiling in vertical tubes, Source: Experimental Thermal and Fluid Science, v 25, n 7, January, 2002, p 529-534

[29] Zurcher, O. (Swiss Federal Inst of Technology-Lausanne); Thome, J.R.; Favrat, D., Evaporation of ammonia in a smooth horizontal tube: heat transfer measurements and predictions, Source: Journal of Heat Transfer, Transactions ASME, v 121, n 1, 1999, p 89-101

APPENDIX A COMPONENT SPEC SHEETS

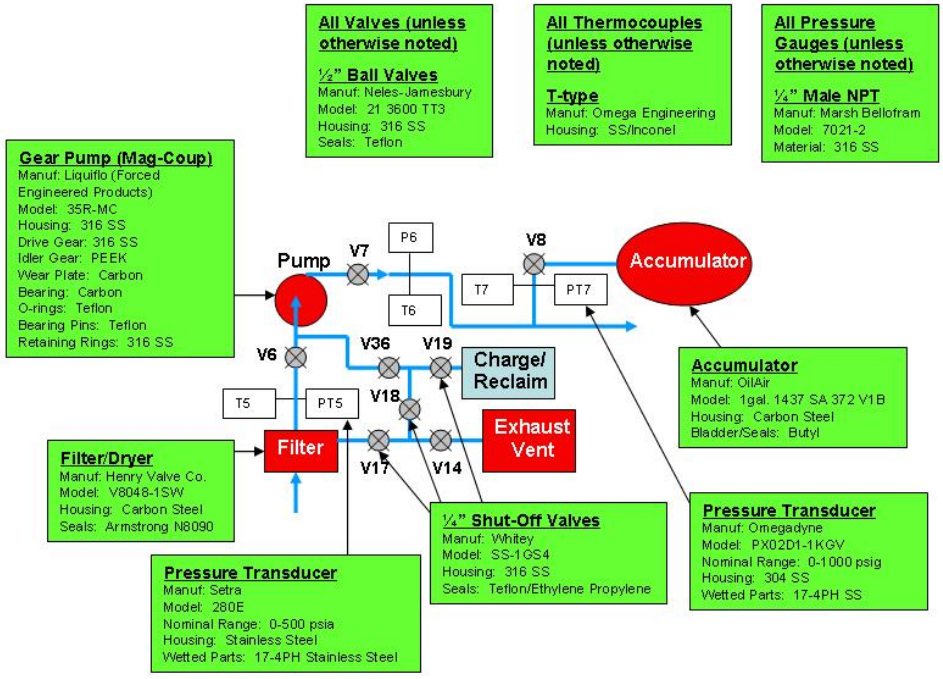

Figure A.1 Equipment Specifications for Part of KSU Ammonia Flow Loop

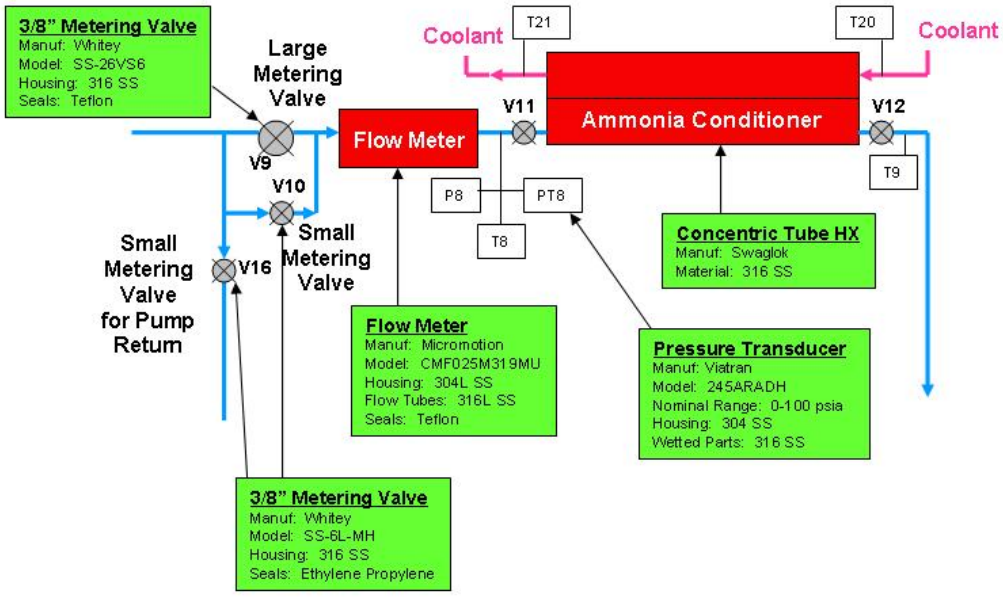

Figure A.2 Equipment Specifications for Part of KSU Ammonia Flow Loop

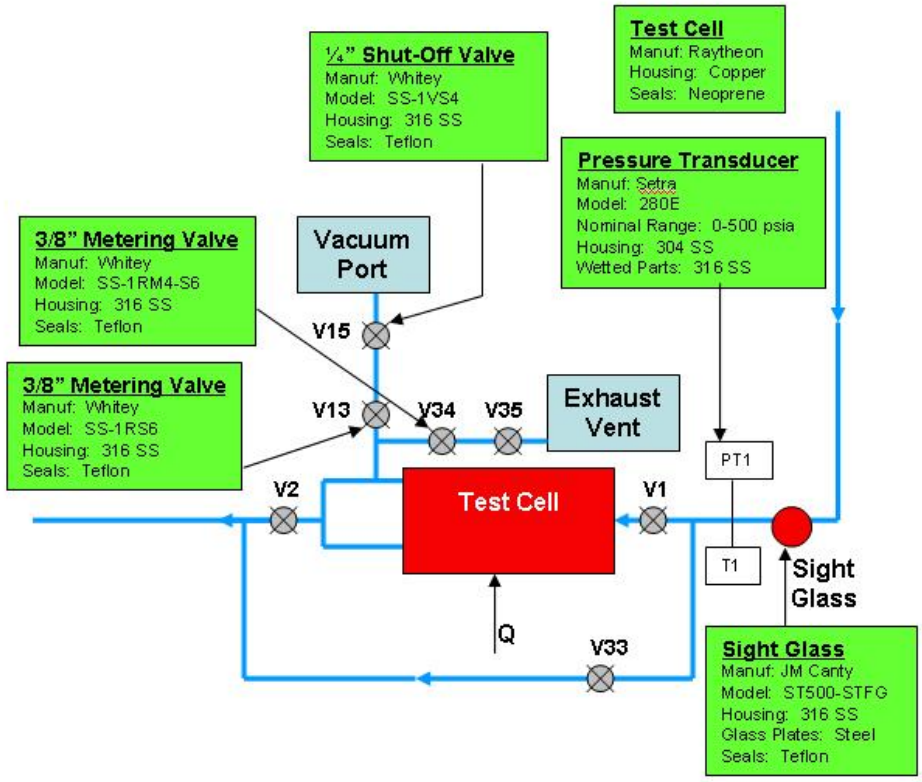

Figure A.3 Equipment Specifications for Part of KSU Ammonia Flow Loop

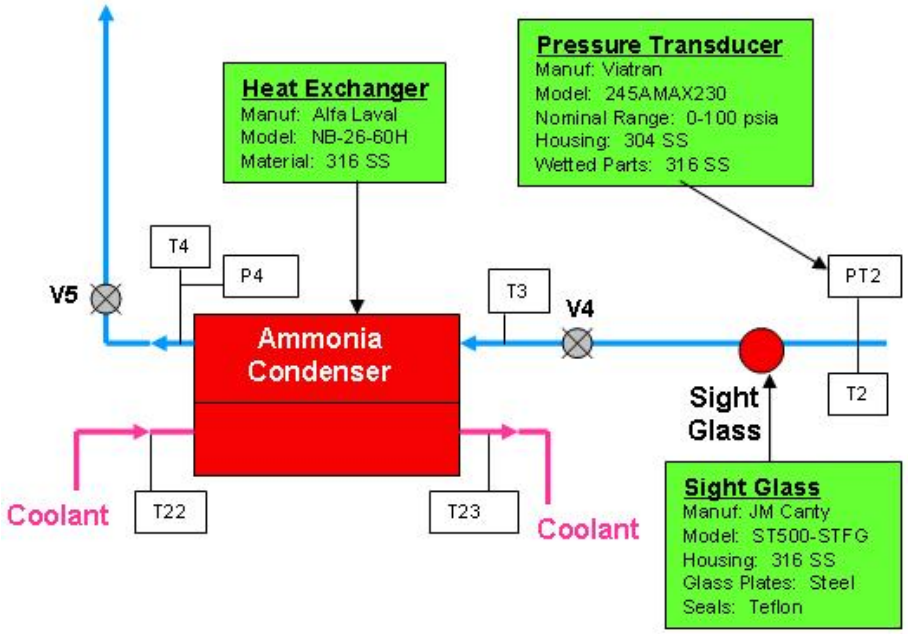

Figure A.4 Equipment Specifications for Part of KSU Ammonia Flow Loop

Ammonia Pump Assembly

Manufacturer: Liquiflo

Distributor: Force Engineered Products, Inc.
Suite 1415, 349 West Commercial St.
East Rochester, NY 14445

Specifications

Pump: Model: 35R-MC
Serial Number: 35FS6P22001000SS
Housing Material: 316 SS NPT
Drive Gear Material: 316 SS
Idler Gear Material: PEEK
Wear Plate Material: Carbon
Bearing Material: Carbon
Seal Type: 0.625" (56C)
Bearing Flush: Standard Housings
Shaft Coating: Ceramic
O-Rings: Teflon
Retaining Ring: Same as Housing
Bearing Pins: Teflon
Magnetic Coupling: 33in-ib
Options: Single Wall Can

Motor: Manufacturer: Baldor DC Industrial Motor
Fort Smith, AR
Cat. No.: CDP3330
Spec.: 33-2024Z122
H.P.: ½
Encl.: TENV
RPM: 1750

Frame: 56C

Type: PM3336P

Arm Volts: 90

Amps: 4.8

Insul.: F.F. 1.3

Brg/DE: 6203

Brg/ODE: 6203

Brush: 2/BP5011T01

Serial #: W0103150889

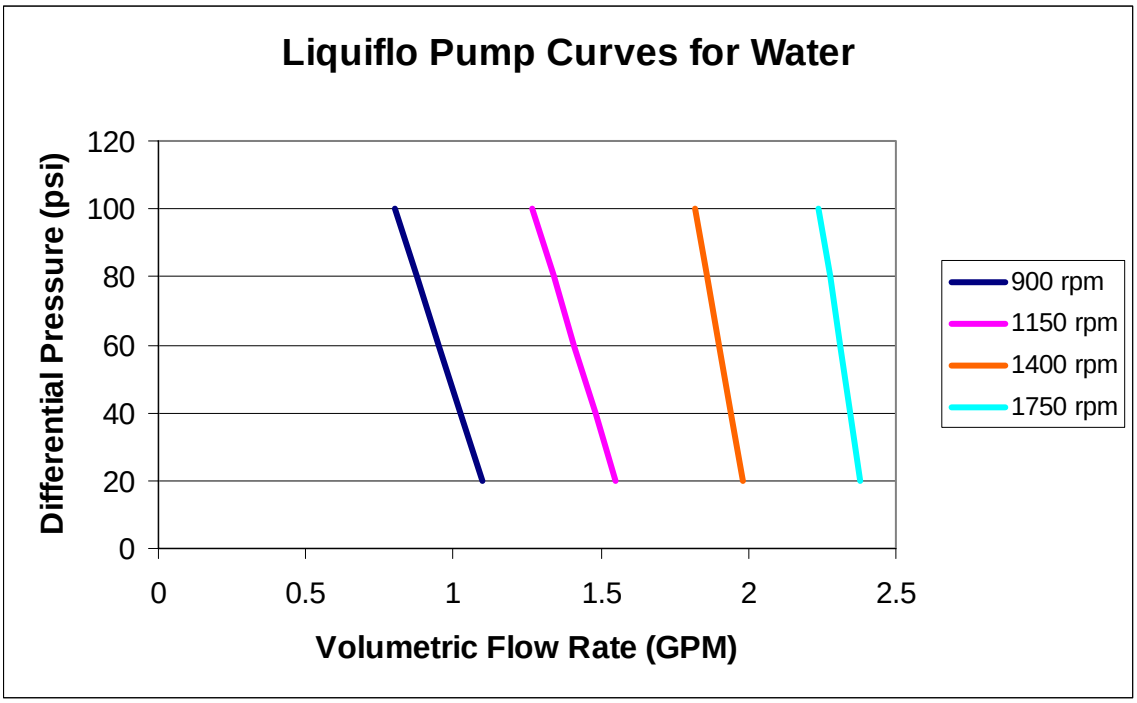

Figure A.5 Ammonia Pump Curve for Water

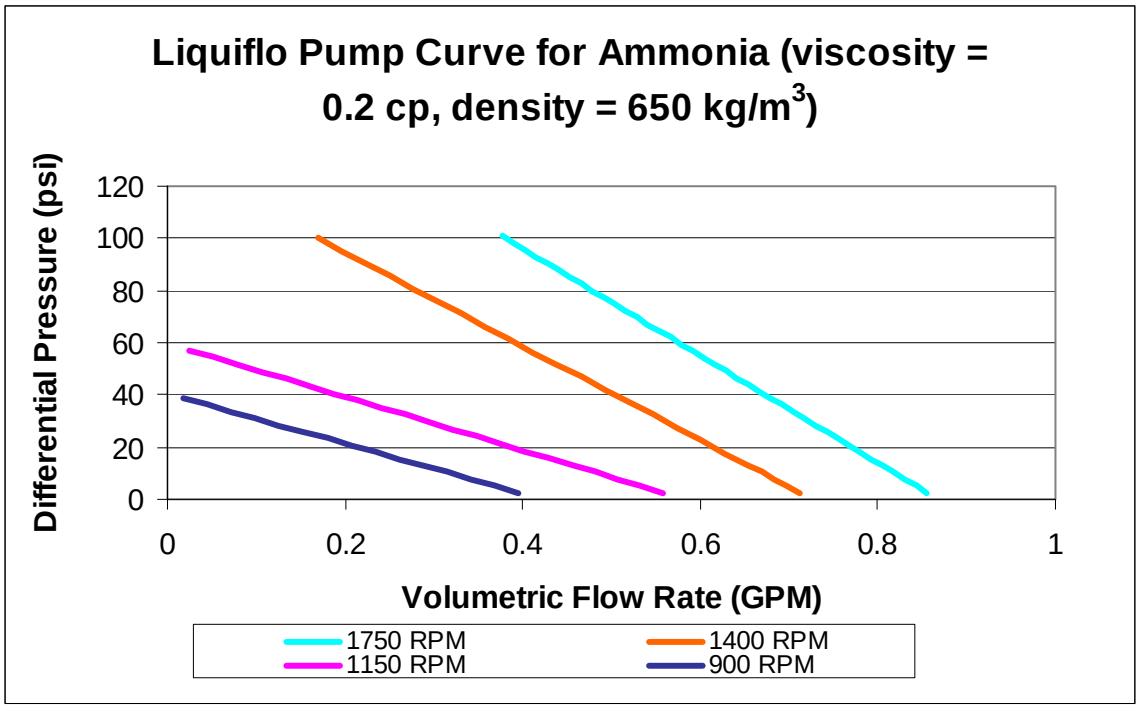

Figure A.6 Derived Ammonia Pump Curve for Ammonia from Water Pump Curve

Condenser (Flat Plate Heat Exchanger)

Manufacturer: Alfa Laval
5400 International Trade Dr.
Richmond, VA 23231
P: 804-222-5300
Contact: Peter Tran
P: 804-236-1358
F: 804-236-1360

Distributor: Chem-Slov, Inc.
6709 W. 119th Street; No. 451
Overland Park, KS 66209
P: 913-402-7417
F: 913-402-7418

Specifications:	Number: 5365418	
	Model: NB 26-60H (S3,S4: Threaded; S1,S2: Welded)	
	Design Press.:	S3,S4 => 290 psig
		S1,S2 => 261 psig
	Design Temp.:	S3,S4 => 752oF
		S1,S2 => 752oF
	Volume:	S3,S4 => 0.4 gallons
		S1,S2 => 0.38 gallons

Accumulator

Manufacturer: OilAir
11505 West Little York
Houston, TX 77041
P: 713-937-8900

Distrubutor: Berendsen Fluid Power
3727 West Dora
Wichita, KS 67213
P: 316-945-4455
F: 316-945-4342
www.bfpna.com
Contact: Tim Churchhill

Specifications

Steel Container: MDMT 40oF at 3000psi
Year 95 for OilAir Hyd.
1 Gal. 1437 SA 372 V1B

Bladder: MAWP 3000psi STAT 200oF
Butyl Material: BR1-101-B (says “#40” on bladder)

Chiller Specifications

Liebert CD-252G 12 ton Dual Compressor Chiller

Operates on a dedicated 480 volt circuit

Two Chiller Pumps Circulate Glycol Between Glycol Tank and Chiller3

Made for R-22 refrigerant

Sight Glasses

Manufacturer: JM Canty, Inc.
6100 Donner Road
Buffalo, N.Y. 14094
P: 716-625-4227
F: 716-625-4228
Contacts: Steve Smith x231
Colleen Canty x247

Distributor: Basic Controls of KC, Inc.
4224 S. Hocker Drive, Suite 120
Independence, MO 64055
P: 816-478-4799
F: 816-478-2390

Specifications

Sight Glasses: Model: SS-0.38-ST500-STFG
Max Press.: 500 psi
Max Temp.: 450oF
Material: 316SS
Heat #: ^13569

Flow Meter

Manufacturer: MicroMotion

P: 800-522-6277

Contact: Don x8246

Case No. 118735

Transmitter: Field Mount Type

Model: RFT9739E4SUJ

S/N: 1713944

Sensor S/N: 335864

Specifications: Model: CMF025M319NU

S/N: 335864

Flow Cal: 4.27744.75

DENS Cal: 06329074874.44

Inlet: ½" Swagelok compression fitting – pipe compression fitting w/ o-ring

Outlet: pipe compression fitting w/ o-ring - ½" Swagelok compression fitting

D1: 0.0012

D2: 0.99732

K1: 6330.351

K2: 7484.072

TC: 4.44

Temp. Range: -240 to 204oC

Tube: 1450 psig

Conn: 1450 psig

Case: 850 psig

O-rings: Teflon

Conditioner

Type: Concentric Tube Heat Exchanger

Sections: 3

Length of Each Section: 146 inches

Inner Tube OD: 0.5 inches

Outer Tube OD: 1 inch

Heat Transfer Area for Fluid in Inner Tube: 0.38 m^2

Heat Transfer Area for Fluid in Annulus: 0.442 m^2

Glycol Pump Curve

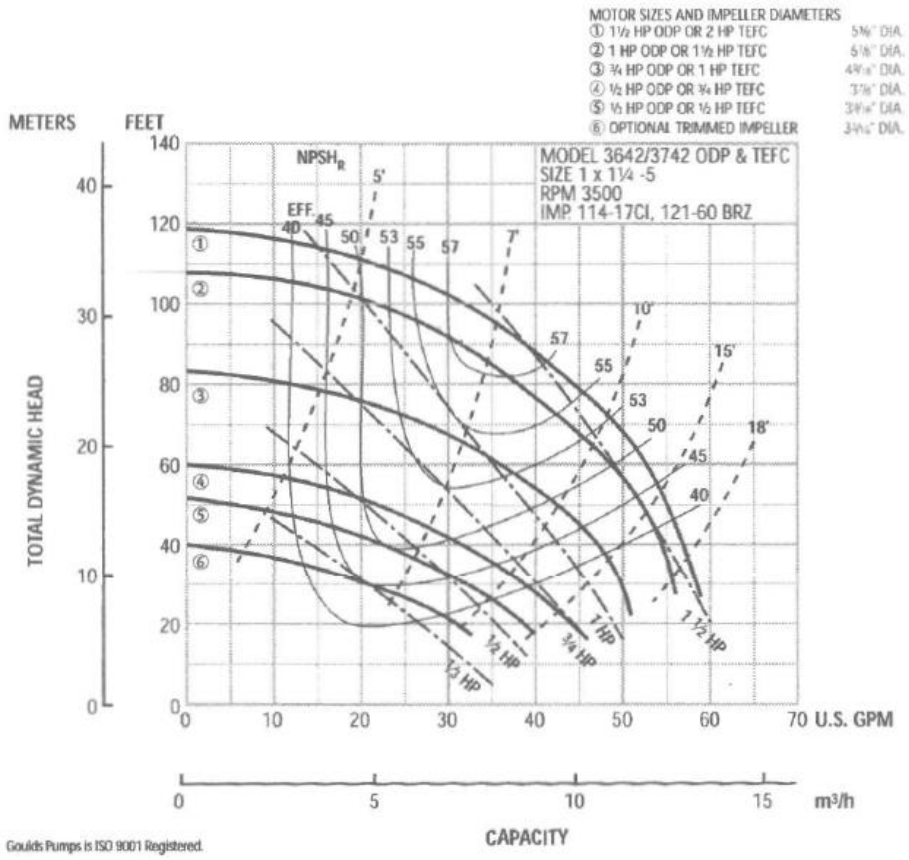

Figure A.7 Glycol Pump Curve (Use #2) [9]

Pressure Transducers

Transducer PT1: Manufacturer: Setra

Model: 280E

Nominal Range: 0-500 psia

Calibrated Range: 0-200 psig (5 psi increments)

Calibration Equation Error: 0.14% Max (30-100 psig) [45]

Calibration Plot: Figure B.1

Transducer PT2: Manufacturer: Viatran

Model: AMAX230

Nominal Range: 0-100 psia

Calibrated Range: 0-108 psig (5 psi increments from 0-105 psig and 1 psi increments from 105-108 psig)

Calibration Equation Error: 0.072% Max (30-100 psig) [45]

Calibration Plot: Figure B.2

Transducer PT5: Manufacturer: Setra

Model: 280E

Nominal Range: 0-500 psia

Calibrated Range: 5-190 psig (5 psi increments from 5-40 & 60-190 psig and 1 psi increments from 40-60 psig)

Calibration Equation Error: 0.987% Max (30-100 psig) [45]

Calibration Plot: Figure B.3

Transducer PT7: Manufacturer: Omegadyne

Model: PX02D1-1KGV

Nominal Range: 0-1000 psia

Calibrated Range: 0-200 psig (5 psi increments)

Calibration Equation Error: 0.18% Max (35-100 psig) [45]

Calibration Plot: Figure B.4

Transducer PT8: Manufacturer: Viatran

Model: 245ARADH

Nominal Range: 0-100 psia

Calibrated Range: 0-107 psig (5 psi increments from 0-105 psig and 1 psi increments from 105-107 psig)

Calibration Equation Error: 0.049% Max (30-100 psig) [45]

Calibration Plot: Figure B.5

Ammonia Detector

A Manning Systems, Inc. Model 20 is used. The range where it accurately measures the ammonia concentration is 0-1000 ppm and that concentration corresponds linearly to a 4-20 mA output current signal from the detector. Currently the output signal is read as a voltage with a known loop resistance (248 ohms) in order to calculate the current. With the known loop resistance for the output signal a correlation has been developed comparing voltage output to the ammonia concentration in the ammonia chamber. It can be seen in Figure B.7.

Electrical Energy Source

Potentiometers in Lab:

270V x 28A 7500 watts (Quantity of 2)

270V x 15A 4000 watts (Quantity of 2)

140V x 15A 2000 watts (Quantity of 1)

140V x 7.5A 1000 watts (Quantity of 1)

Total Electrical power: 26000 watts (with a total of 6 potentiometers)

Watt Transducers in Lab:

0-1000 watts (Quantity of 2)

0-2000 watts (Quantity of 1)

Total Electrical Power Measurability: 4000 watts (with a total of 3 watt transducers)

APPENDIX B CALIBRATION DATA

The calibration and correlation plots shown here are for various instrumentation used in the ammonia flow loop. The specifications and locations of the calibrated pressure transducers can be seen in Figures A.1 through A.4 in Appendix A.

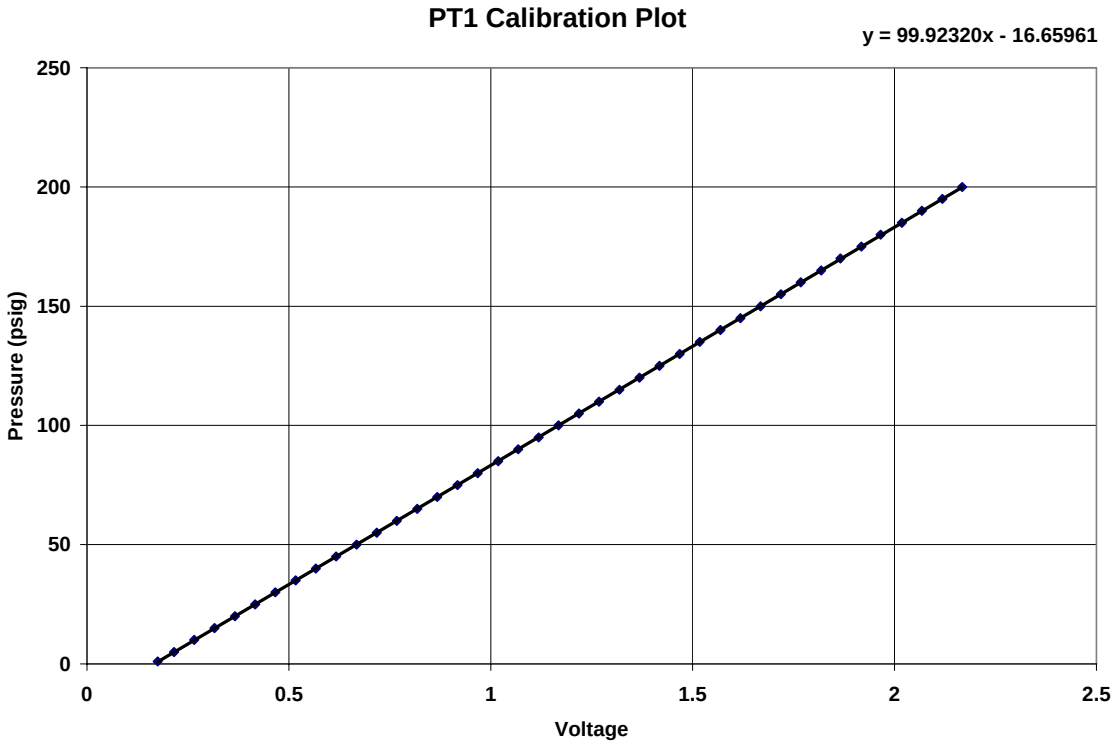

Figure B.1 Test Cell Inlet Pressure Transducer (PT1) Calibration

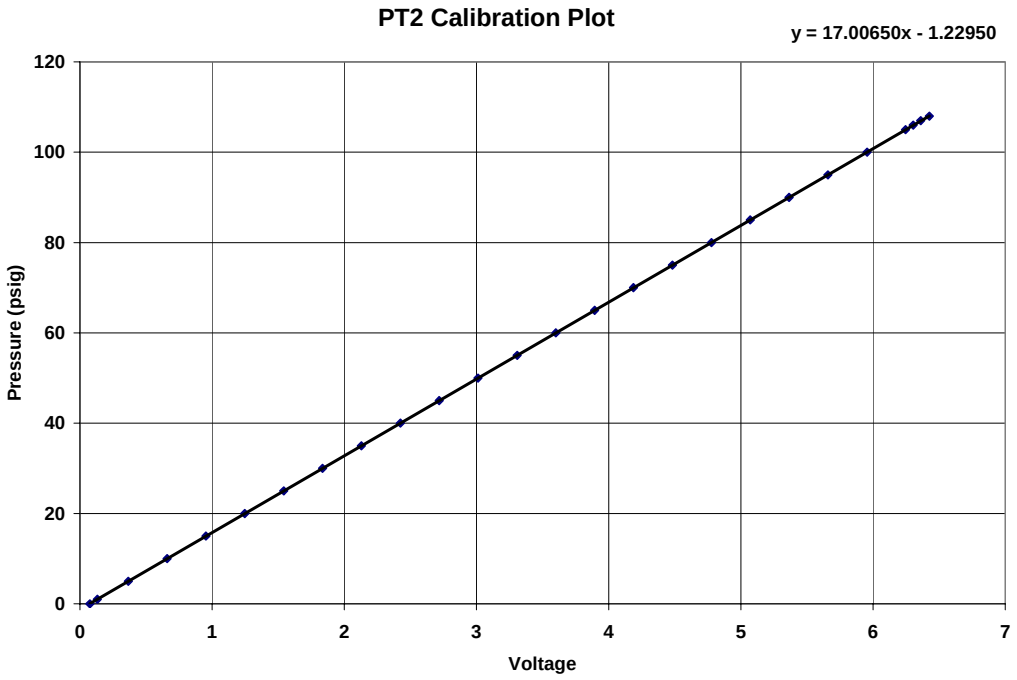

Figure B.2 Test Cell Outlet Pressure Transducer (PT2) Calibration

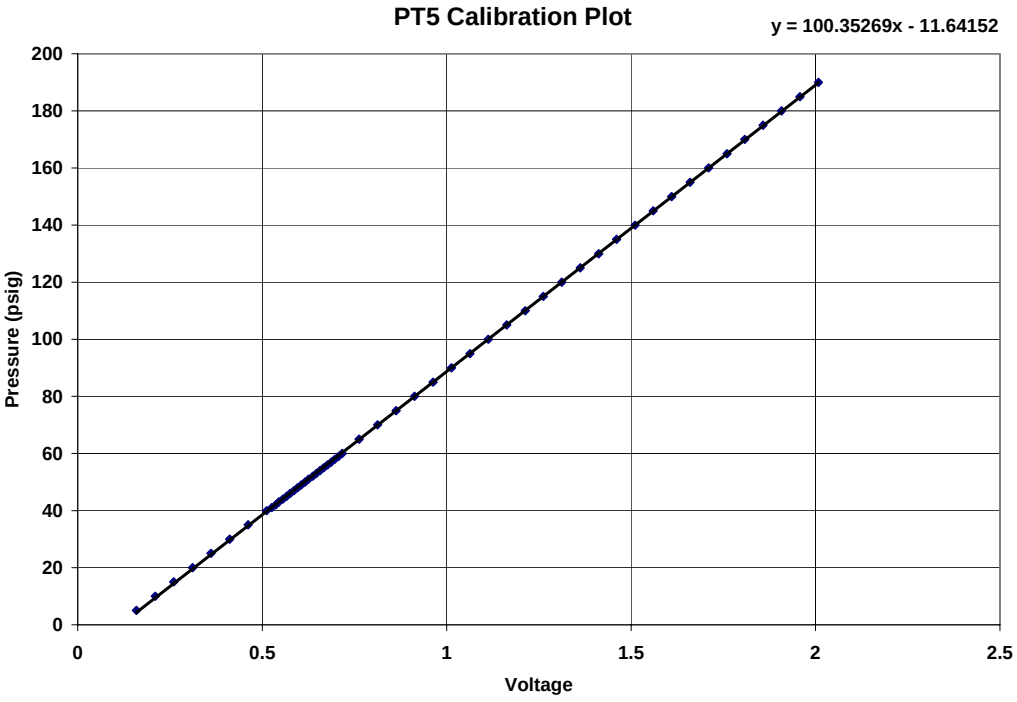

Figure B.3 Pump Inlet Pressure Transducer (PT5) Calibration

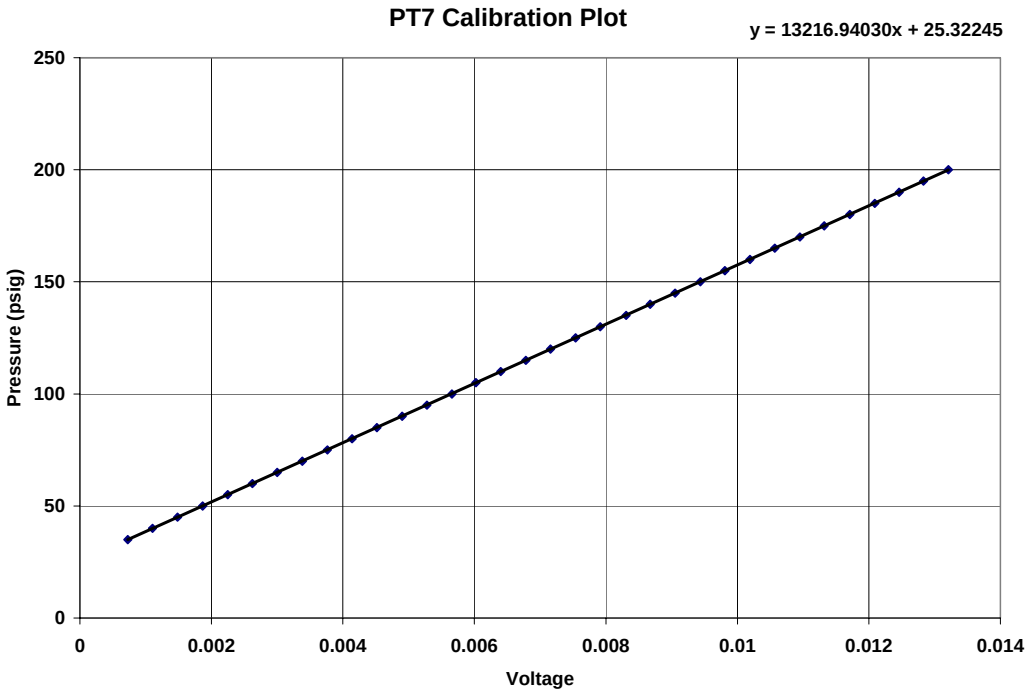

Figure B.4 Accumulator Pressure Transducer (PT7) Calibration

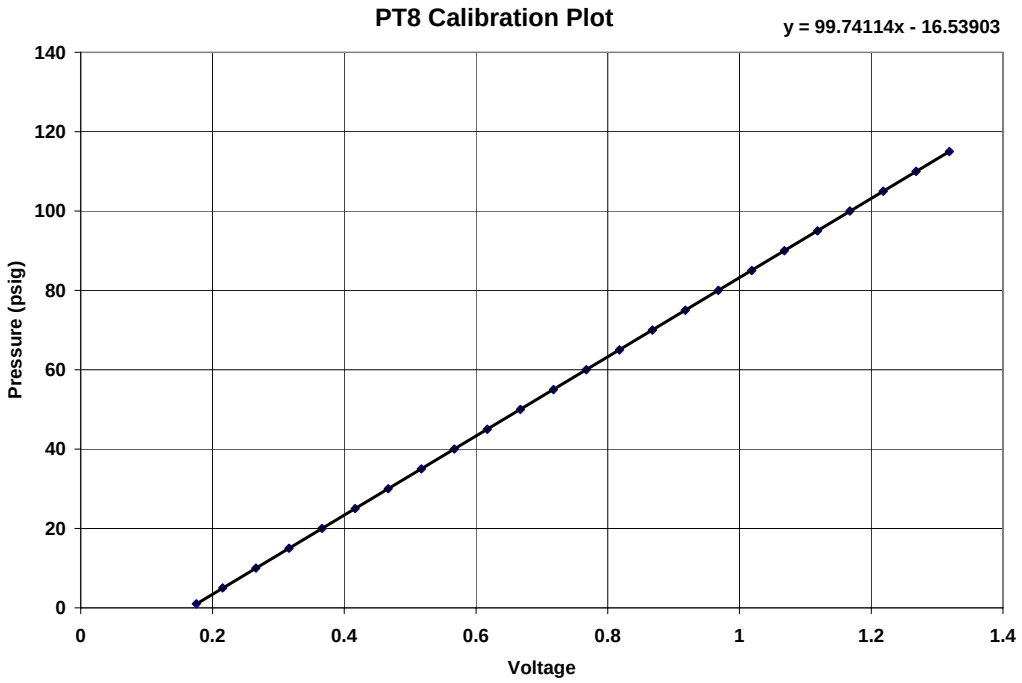

Figure B.5 Conditioner Inlet Pressure Transducer (PT8) Calibration

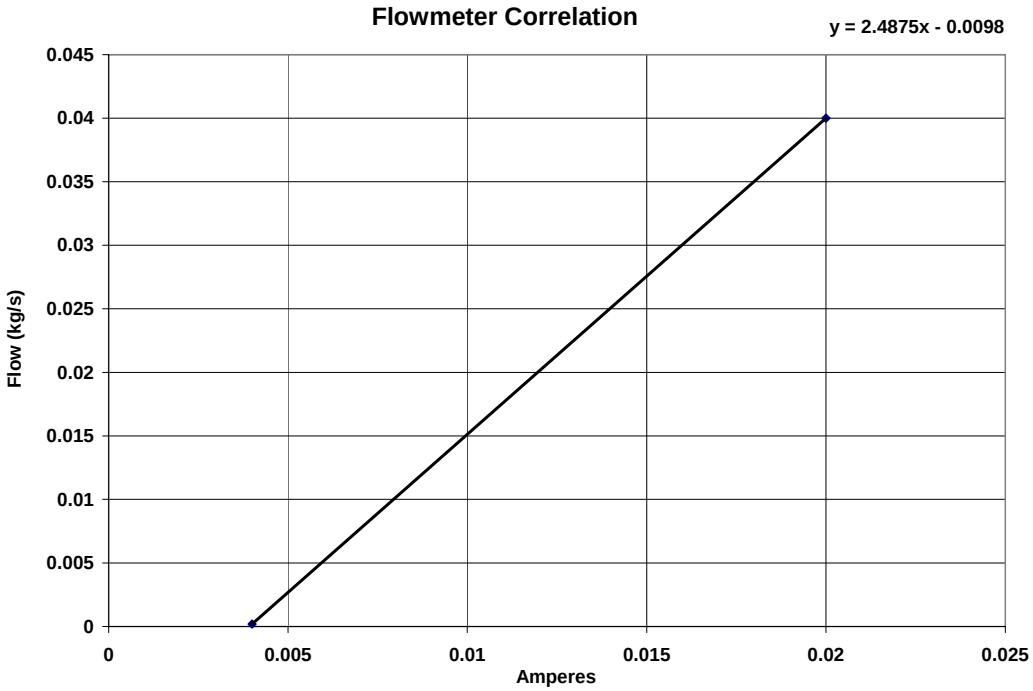

Figure B.6 Ammonia Flow Loop Flow Meter Correlation

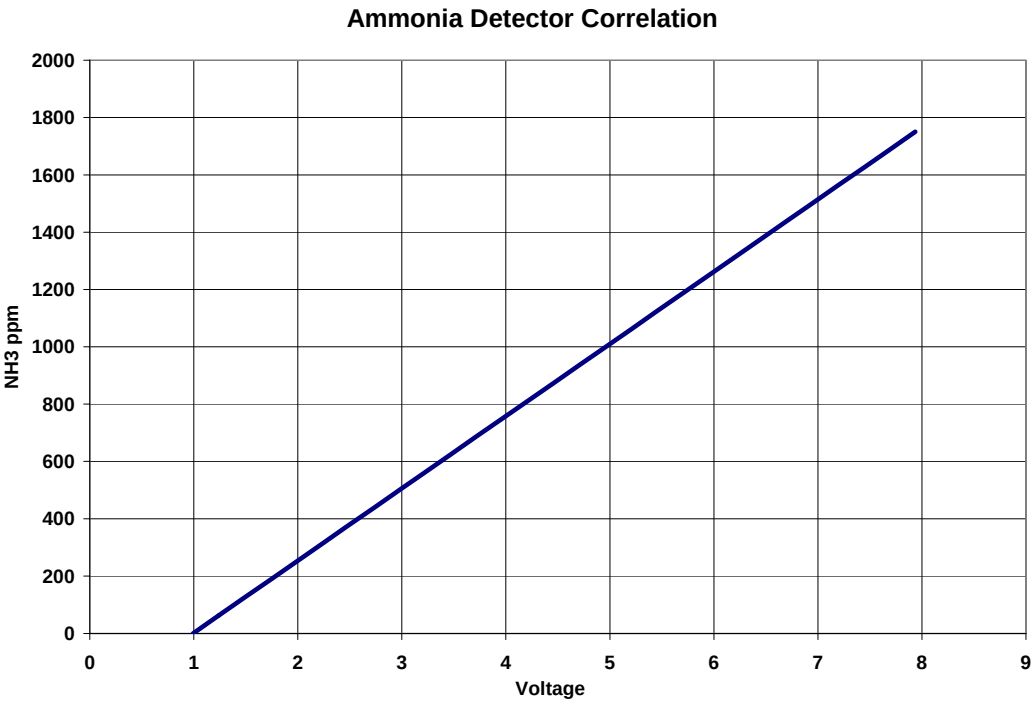

Figure B.7 Ammonia Chamber Ammonia Detector Correlation

APPENDIX C UNCERTAINTY ANALYSIS

C.1) Uncertainty of Measured Data

The uncertainties shown here are for the actual instruments used to record all of the measured data throughout all of the tests performed with the Slot Jet. Later some of these uncertainties will be used in the heat transfer calculations.

Ammonia Flow Loop Thermocouples (T-type)

The uncertainty of the ammonia flow loop thermocouples was determined from the maximum temperature variation recorded from these thermocouples at an average room temperature of 22.2^{o}C.

±1.8oC [24]

Test Cell Thermocouples (K-type)

The uncertainty of the test cell thermocouples was determined from the maximum temperature variation recorded from these thermocouples at an average room temperature of 22.3^{o}C.

±1 ^{o}C [24]

Used by these temperatures in heat transfer calculations: T_{SJfi}, T_{HNTM}, T_{HNBM}

Slot Jet Heated Surface Thermocouples (T-type)

At an average room temperature of 24.5 ^{o}C the temperature variation between these thermocouples was measured to be ±1.3 ^{o}C [24]. However, the uncertainty used for all

heat transfer calculations was the standard deviation of the Slot Jet heated surface thermocouples which varied greatly between test conditions. An example of these standard deviations at the point in time the CHF event occurred for each test condition is shown in Table C.1.

Table C.1 Standard Deviation of Slot Jet Surface Temperatures During CHF Events

Standard Deviation of Slot Jet Heated Surface Thermocouple Numbers 4, 5, 6, 7, & 8 at Points Where CHF Occurred (deg C)

		Mass Flow Rate (kg/s)		
		0.010	0.017	0.029
Nominal Slot Jet Inlet Pressure	310	6.48	10.03	12.14
	410	8.05	25.92	41.39
	790	15.38	25.94	77.24

Used by these temperatures in heat transfer calculations: T_{SJo}

Pressure Transducers

Theses ammonia flow loop pressure transducers had to be calibrated with a dead weight tester. The uncertainty listed for each transducer was the maximum percent difference between the calibration equation calculated pressure and the actual pressure applied.

PT1: ±0.14% (Maximum from 30-100) psig of reading

PT2: ±0.07% (Maximum from 30-100) psig of reading

PT5: ±1% (Maximum from 30-100) psig of reading

PT7: ±0.18% (Maximum from 35-100) psig of reading

PT8: ±0.05% (Maximum from 30-100) psig of reading

The uncertainty of these test cell pressure transducers was listed by the manufacturer as well as the correlation for converting their output voltages to pressures.

Slot Jet Inlet: ±1% of reading [23]

Slot Jet Differential: ±0.5% of reading [23]

Flow Meter

The uncertainty of the mass flow meter was listed by the manufacturer

±0.1% of reading

Watt Transducers

The uncertainty of the watt transducers was listed by the manufacturer

±0.2% of reading

Distance Between Heater Block Neck Thermocouples Top-Middle and Bottom Middle

The uncertainty is based the standard tolerance of 0.005 inches for drawings

$\delta(x_{HN}) = \pm 0.127$ mm

Thickness of Aluminum Slot Jet Heated Surface

The uncertainty is based the standard tolerance of 0.005 inches for drawings

$\delta(x_{SJ}) = \pm 0.127$ mm

Thermal Conductivity of Copper

Assume 10% of $k_{Cu} = 400$ W/(m*K)

$\delta(k_{Cu}) = \pm 40$ W/(m*K)

Thermal Conductivity of 7075-T6 Aluminum

Assume 10% of k_{Al} = 130 W/(m*K)

$\delta(k_{Al}) = \pm 13$ W/(m*K)

C.2) Uncertainty of Heat Transfer Calculations from Measured Data

The equations for uncertainty of the heat transfer calculations and the actual uncertainty of these heat transfer calculations is discussed here.

C.2.1) Equations for Uncertainty of Heat Transfer Calculations

The following are derived uncertainty equations for each of the values calculated for the analysis of the measured data from the tests performed with the Slot Jet. The method described by Kline and McClintock is used [15].

Heater Neck Heat Flux

Heater Neck Heat Flux Equation:

$$q_{HN}'' = k_{Cu} * [(T_{HNBM} - T_{HNTM}) / x_{HN}]$$

The Kline and McClintock suggested uncertainty equation:

$$\delta(q_{HN}'') = \{ [(\delta(q_{HN}'') / \delta(k_{Cu})) * \delta(k_{Cu})]^2 + [(\delta(q_{HN}'') / \delta(x_{HN})) * \delta(x_{HN})]^2 + [(\delta(q_{HN}'') / \delta(T_{HNTM})) * \delta(T_{HNTM})]^2 + [(\delta(q_{HN}'') / \delta(T_{HNBM})) * \delta(T_{HNBM})]^2 \}^{1/2}$$

The uncertainty equation becomes:

$$\delta(q_{HN}'') = \{ [((T_{HNBM} - T_{HNTM}) / x_{HN}) * \delta(k_{Cu})]^2 +$$

$$[((-k_{Cu} *(T_{HNBM} - T_{HNTM})) / x_{HN}^2) * \delta(x_{HN})]^2 + [(-k_{Cu} / x_{HN}) * \delta(T_{HNTM})]^2 +$$

$$[(k_{Cu} / x_{HN}) * \delta(T_{HNBM})]^2 \}^{1/2}$$

Energy Input Heat Flux

Energy Input Heat Flux Equation:

$$q_{EI}'' = EI / [(HN_{height}) * (HN_{width})]$$

The Kline and McClintock suggested uncertainty equation:

$$\delta(q_{EI}'') = \{ [(\delta(q_{EI}'') / \delta(EI)) * \delta(EI)]^2 + [(\delta(q_{EI}'') / \delta(HN_{height})) * \delta(HN_{height})]^2 +$$

$$[(\delta(q_{EI}'') / \delta(HN_{width})) * \delta(HN_{width})]^2 \}^{1/2}$$

The uncertainty equation becomes:

$$\delta(q_{EI}'') = \{ [(1 / (HN_{height} - HN_{width})) * \delta(EI)]^2 +$$

$$[(-EI / (HN_{height}^2 * HN_{width})) * \delta(HN_{height})]^2 +$$

$$[(-EI / (HN_{height} * HN_{width}^2)) * \delta(HN_{width})]^2 \}^{1/2}$$

Inside Heated Surface Temperature of Slot Jet

Inside Heated Surface Temperature of Slot Jet Equation:

$$T_{SJi} = T_{SJo} - [(q_{HN}'' * x_{SJ}) / k_{Al}]$$

The Kline and McClintock suggested uncertainty equation:

$$\delta(T_{SJi}) = \{ [(\delta(T_{SJi}) / \delta(T_{SJo})) * \delta(T_{SJo})]^2 + [(\delta(T_{SJi}) / \delta(q_{HN}'')) * \delta(q_{HN}'')]^2 +$$

$$[(\delta(T_{SJi}) / \delta(k_{Al})) * \delta(k_{Al})]^2 + [(\delta(T_{SJi}) / \delta(x_{SJ})) * \delta(x_{SJ})]^2 \}^{1/2}$$

The uncertainty equation becomes:

$$\delta(T_{SJi}) = \{ [\delta(T_{SJo})]^2 + [(-x_{SJ} / k_{Al}) * \delta(q_{HN}")]^2 + [((q_{HN}" * x_{SJ}) / k_{Al}^2) * \delta(k_{Al})]^2 + [(-q_{HN}" / k_{Al}) * \delta(x_{SJ})]^2 \}^{1/2}$$

Subcooling

Subcooling Equation:

$$T_{sub} = T_{SJo} - T_{SJfi}$$

The Kline and McClintock suggested uncertainty equation:

$$\delta(T_{sub}) = \{ [(\delta(T_{sub}) / \delta(T_{SJo})) * \delta(T_{SJo})]^2 + [(\delta(T_{sub}) / \delta(T_{SJfi})) * \delta(T_{SJfi})]^2 \}^{1/2}$$

The uncertainty equation becomes:

$$\delta(T_{sub}) = \{ [\delta(T_{SJo})]^2 + [-\delta(T_{SJfi})]^2 \}^{1/2}$$

Maximum Heat Transfer Coefficient

Maximum Heat Transfer Equation:

$$h_{max} = q_{HN}" / (T_{SJi} - T_{SJfi})$$

The Kline and McClintock suggested uncertainty equation:

$$\delta(h_{max}) = \{ [(\delta(h_{max}) / \delta(q_{HN}")) * \delta(q_{HN}")]^2 + [(\delta(h_{max}) / \delta(T_{SJi})) * \delta(T_{SJi})]^2 + [(\delta(h_{max}) / \delta(T_{SJfi})) * \delta(T_{SJfi})]^2 \}^{1/2}$$

The uncertainty equation becomes:

$$\delta(h_{max}) = \{ [\delta(q_{HN}") / (T_{SJi} - T_{SJfi})]^2 + [(q_{HN}" * \delta(T_{SJi})) / (T_{SJi} - T_{SJfi})^2]^2 + [(-q_{HN}" * \delta(T_{SJfi})) / (T_{SJi} - T_{SJfi})^2]^2 \}^{1/2}$$

C.2.2) Uncertainty of Heat Transfer Calculations

CHF/Heat Transfer Coefficient Calculations

The uncertainty of the CHF values calculated from the heater neck heat flux uncertainty equation and the corresponding maximum heat transfer coefficients discussed here. First the actual calculated CHF values and maximum heat transfer coefficients are shown in Tables C.2 and C.3 for reference.

Table C.2 CHF Values at Each Test Condition

Critical Heat Fluxes, CHF

		Mass Flow Rate (kg/s)		
		0.010	0.017	0.029
Nominal Slot Jet Inlet Pressure (kPa)	310	173	249	289
	410	231	280	313
	790	262	275	488

Table C.3 Maximum Heat Transfer Coefficients at Each Test Condition

Maximum Heat Transfer Coefficients (W/(cm2*K))

		Mass Flow Rate (kg/s)		
		0.010	0.017	0.029
Nominal Slot Jet Inlet Pressure (kPa)	310	4.54	4.89	5.36
	410	4.42	4.15	3.39
	790	3.21	2.83	4.14

Next, the average uncertainty for the calculated CHF values and maximum heat transfer coefficients are shown below in Tables C.4 and C.5. By looking at the percentage of the CHF uncertainties here, and for the maximum and minimum as well, they are all 9-11% of the actual calculated value which is very consistent. However, the results of the heat transfer coefficient uncertainty calculations are much different. For the most part the uncertainty increases as the mass flow rates and pressures increase.

Table C.4 Average Uncertainty of Heat Flux During CHF Events at Each Test Condition and its Percent of the Actual Calculated Value

Average Uncertainty of Heat Fluxes (W/cm2)					**Percent of Measured Value**		
		Mass Flow Rate (kg/s)			Mass Flow Rate (kg/s)		
		0.010	0.017	0.029	0.010	0.017	0.029
Nominal Slot Jet Inlet Pressure (kPa)	310	19.07	26.66	29.92	11%	11%	10%
	410	24.79	29.02	32.66	11%	10%	10%
	790	26.71	27.88	49.47	10%	10%	10%

Table C.5 Average Uncertainty of Heat Transfer Coefficients during CHF Events at Each Test Condition and its Percent of the Actual Calculated Value

Average Uncertainty of Heat Transfer Coefficients (W/(cm2*K))					**Percent of Measured Value**		
		Mass Flow Rate (kg/s)			Mass Flow Rate (kg/s)		
		0.010	0.017	0.029	0.010	0.017	0.029
Nominal Slot Jet Inlet Pressure (kPa)	310	0.98	1.24	1.50	22%	25%	28%
	410	1.02	1.73	1.92	23%	42%	57%
	790	0.47	0.81	2.74	15%	29%	66%

The maximum uncertainty for the calculated CHF values and maximum heat transfer coefficients are shown below in Tables C.6 and C.7.

Table C.6 Maximum Uncertainty of Heat Flux During CHF Events at Each Test Condition and its Percent of the Actual Calculated Value

Max Uncertainty of Heat Fluxes (W/cm2)					**Percent of Measured Value**		
		Mass Flow Rate (kg/s)			Mass Flow Rate (kg/s)		
		0.010	0.017	0.029	0.010	0.017	0.029
Nominal Slot Jet Inlet Pressure (kPa)	310	20.03	26.93	30.83	12%	11%	11%
	410	25.23	29.93	33.60	11%	11%	11%
	790	28.17	29.38	50.59	11%	11%	10%

Table C.7 Maximum Uncertainty of Heat Transfer Coefficients during CHF Events at Each Test Condition and its Percent of the Actual Calculated Value

Max Uncertainty Heat Transfer Coefficients (W/(cm2*K))					Percent of Measured Value		
		Mass Flow Rate (kg/s)			Mass Flow Rate (kg/s)		
		0.010	0.017	0.029	0.010	0.017	0.029
Nominal Slot Jet Inlet Pressure (kPa)	310	1.07	1.25	1.51	24%	26%	28%
	410	1.05	1.82	2.04	24%	44%	60%
	790	0.77	0.89	3.01	24%	31%	73%

The minimum uncertainty for the calculated CHF values and maximum heat transfer coefficients are shown below in Tables C.8 and C.9.

Table C.8 Minimum Uncertainty of Heat Flux During CHF Events at Each Test Condition and its Percent of the Actual Calculated Value

Min Uncertainty of Heat Fluxes (W/cm2)					Percent of Measured Value		
		Mass Flow Rate (kg/s)			Mass Flow Rate (kg/s)		
		0.010	0.017	0.029	0.010	0.017	0.029
Nominal Slot Jet Inlet Pressure (kPa)	310	18.06	26.41	29.25	10%	11%	10%
	410	23.62	28.27	31.76	10%	10%	10%
	790	25.72	26.00	46.74	10%	9%	10%

Table C.9 Minimum Uncertainty of Heat Transfer Coefficients during CHF Events at Each Test Condition and its Percent of the Actual Calculated Value

Min Uncertainty Heat Transfer Coefficients (W/(cm2*K))					Percent of Measured Value		
		Mass Flow Rate (kg/s)			Mass Flow Rate (kg/s)		
		0.010	0.017	0.029	0.010	0.017	0.029
Nominal Slot Jet Inlet Pressure (kPa)	310	0.62	1.22	1.48	14%	25%	28%
	410	0.96	1.59	1.59	22%	38%	47%
	790	0.30	0.76	2.32	9%	27%	56%

These tables of average, maximum, and minimum uncertainties for the maximum heat transfer coefficients for each of the nine test conditions illustrate a trend or event first discussed in the results of the measured data for the Slot Jet. The trend, mentioned earlier, is that as pressures and mass flow rates increase, so does the uncertainty of these values. This is due to the increase in the temperature difference between the Slot Jet heated surface thermocouples when the flow rates and operating pressures increase. However, there are a couple of uncertainties that violate this trend which are the two at the highest pressure and low and medium flow rates. A possible reason that these uncertainties do not match the trend is because the data used for these was measured after the Slot Jet had been disassembled a couple of times to replace seals. This could have

caused the heater block neck to not be interfaced in the exact same manner to the Slot Jet as in previous tests. Another observation made from the heat transfer coefficient uncertainty tables is that as the mass flow rates and pressures increase the difference between the average, maximum, and minimum uncertainties increase.

An example of this large difference in thermocouple temperatures is shown in Figure 4.2.22 in the Slot Jet results section. Another example of this is shown in the standard deviation of the Slot Jet surface temperatures for the CHF events in Table C.1. These differences in the Slot Jet surface temperatures could be caused by several things. One is that the interface pressure between the heater block neck and the Slot Jet might be more on one side of the Slot Jet heated surface than the other. This would allow more energy to travel into one side of the Slot Jet heated surface than the other causing temperature differences. Another thing that could cause these temperature differences is if some of the Slot Jet surface thermocouples were touching the hotter heater block neck and others were touching the cooler Slot Jet. One last thing that could cause this is if more liquid ammonia inside the Slot Jet is being diverted to one side of the Slot Jet heated surface more than the other.

The large differences in the Slot Jet surface temperatures can also be traced back to the smaller differences in the heater block neck temperature measurements of the top-middle, top-right, and top-left thermocouples. Examples of these steady state temperature differences, or the standard deviation, during low, medium, and high heat rates at a mass flow rate of 0.029 kg/s a Slot Jet inlet pressure of 115 psia with 40^{o}C subcooling are in Table C.10.

Table C.10 Heater Block Neck Temperature Differences at Same Depth of the Neck for Top-Left, Top-Right, and Top-Middle Temperatures

Description	Total Watts	Top-Left Heater Neck Temperature	Top-Right Heater Neck Temperature	Top-Middle Heater Neck Temperature	Standard Deviation
	Watts	deg C	deg C	deg C	deg C
End of Test	510	104	107	106	1.37
End of Test	996	207	210	211	2.26
End of Test	1496	335	334	338	2.22
CHF Event	1622	423	431	433	5.42

IR Camera Heat Flux Calculations

Table C.11 from the Raytheon Slot Jet results was used to introduce the large uncertainties experienced from the IR camera images. It is shown here again for reference.

Table C.11 Comparison of Heat Flux Calculations Methods for 310 kPa, 15 degC Subcooled, 0.01 kg/s

Comparison of Heat Flux Calculation Methods (310 kPa, 15 degC Subcooled, 0.01 kg/s)			
Nominal Energy Input (watts)	Energy Input (W/cm^2)	Heater Neck Thermocouples (W/cm^2)	IR Camera (W/cm^2)
100.00	33	32	----------
200.00	69	65	60
300.00	101	93	88
400.00	137	127	113
500.00	171	158	165
550 (CHF)	184	173	----------
600 (CHF)	201	176	145

Figures C.1 and C.2 show the IR camera calculated heat flux vs. the pixal position on the IR image across the heater block neck. As the pixal position numbers increase the Slot Jet surface temperatures move from #8 to #4 and the heater block neck temperatures move from the top-right to the top-left. One of the better looking IR camera heat flux

plots where the average IR camera heat flux of 165 W/cm^2 for 500 watts in Table C.11 was calculated, Figure C.1 still shows a large difference in the calculated heat fluxes. The standard deviation of the heat fluxes for this plot was 25 W/cm^2. Figure C.2 shows a more typical plot of the IR camera calculated heat fluxes where they vary greatly. The average IR camera heat flux of 145 W/cm^2 for 600 watts in Table C.11 was calculated from the data in this plot. The standard deviation here was found to be 87 W/cm^2. As can be seen from Figures C.1 and C.2, especially Figure C.2, is that these average IR camera heat flux values shown in Table C.11 do not have a lot of meaning since the standard deviations are so high. This is the reason that the heat flux calculate from the IR camera images was shortly ruled out

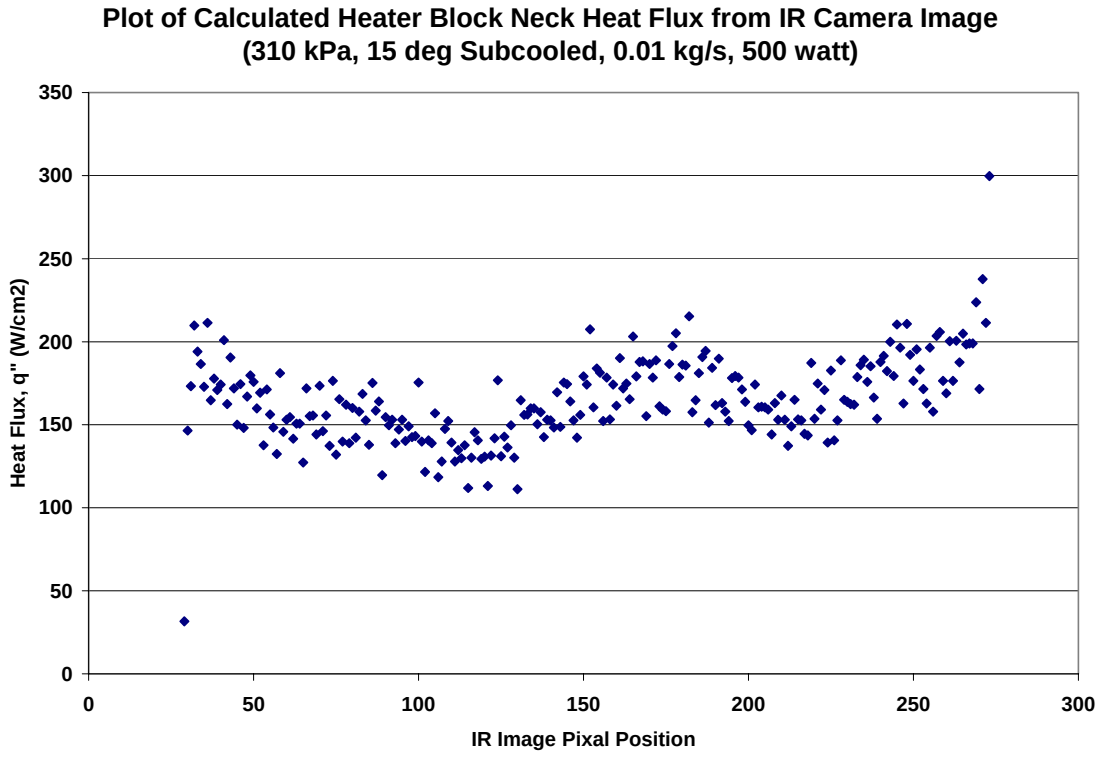

Figure C.1 Calculated Heater Block Neck Heat Flux from IR Camera Image for 310 kPa, 15 degC Subcooled, 0.01 kg/s, 500 watt

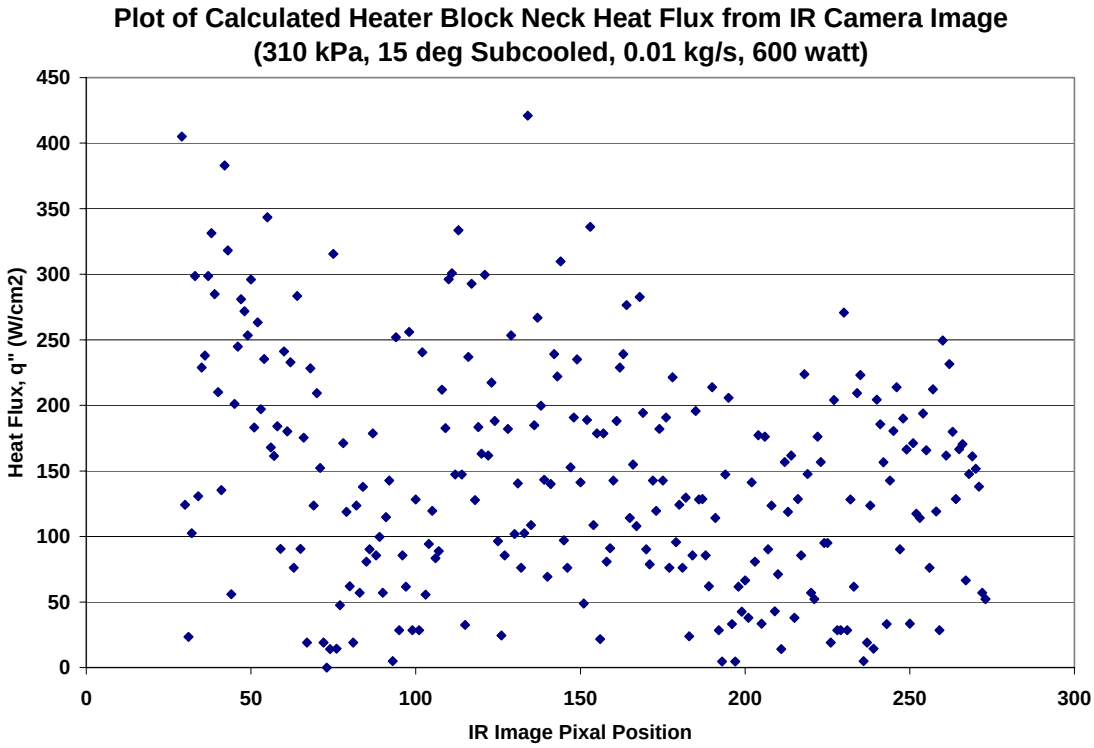

Figure C.2 Calculated Heater Block Neck Heat Flux from IR Camera Image for 310 kPa, 15 degC Subcooled, 0.01 kg/s, 600 watt

Energy Input Heat Flux Calculations

Using the uncertainty equation for this calculated heat flux the heat flux calculations done using the energy input in Table C.11 and others had a consistent uncertainty of approximately ±1.5%.

Subcooling Calculations in Boiling Curves

As seen in the equation for the uncertainty of the subcooling the Slot Jet heated surface thermocouples and Slot Jet fluid inlet thermocouple uncertainties were used. However, the uncertainty used here for the Slot Jet heated surface thermocouples was the one done at room temperature instead of the varying standard deviation of all five of the middle

surface temperatures. This is due to only one Slot Jet surface temperature, #4, being used throughout the calculation of the subcooling used for the boiling curves seen in Figures 4.2.37 and 4.2.38. Since these two temperature uncertainties used to calculate the subcooling uncertainty are constants, then the uncertainty of the subcooling must be a constant as well. This constant was calculated to be $\pm 1.64\ ^{o}C$.

APPENDIX D ECHIC FAILURE REPORT

Analysis of Data Recorded During ECHIC Failure on 1/20/2005

Kansas State University's Testing of Cooling Applications for Directed Energy Weapons Sponsored by Raytheon Missile Systems

The entire data recording period lasted 1351 seconds (22.5 minutes)

There is a timeline covering all of the major events (**Figure D.24**) at the end of this document.

Time Zero
Cold system (kept cold from night before)
Power input: 600 watts (supposedly)
System pressure: 118 psi at accumulator
Flow Rate: 0.001 kg/s
Not at steady state

System Schematic

System Pressures During ECHIC (Evaporative Compact High Intensity Cooler) Failure

Instruments Used:

- PT1 (test cell inlet pressure)
- PT2 (test cell outlet pressure)
- PT5 (pump inlet pressure)
- PT7 (accumulator pressure)
- ECHIC inlet pressure transducer not shown

(The locations in the ammonia flow loop of these instruments can be seen in **Figure D.1**)

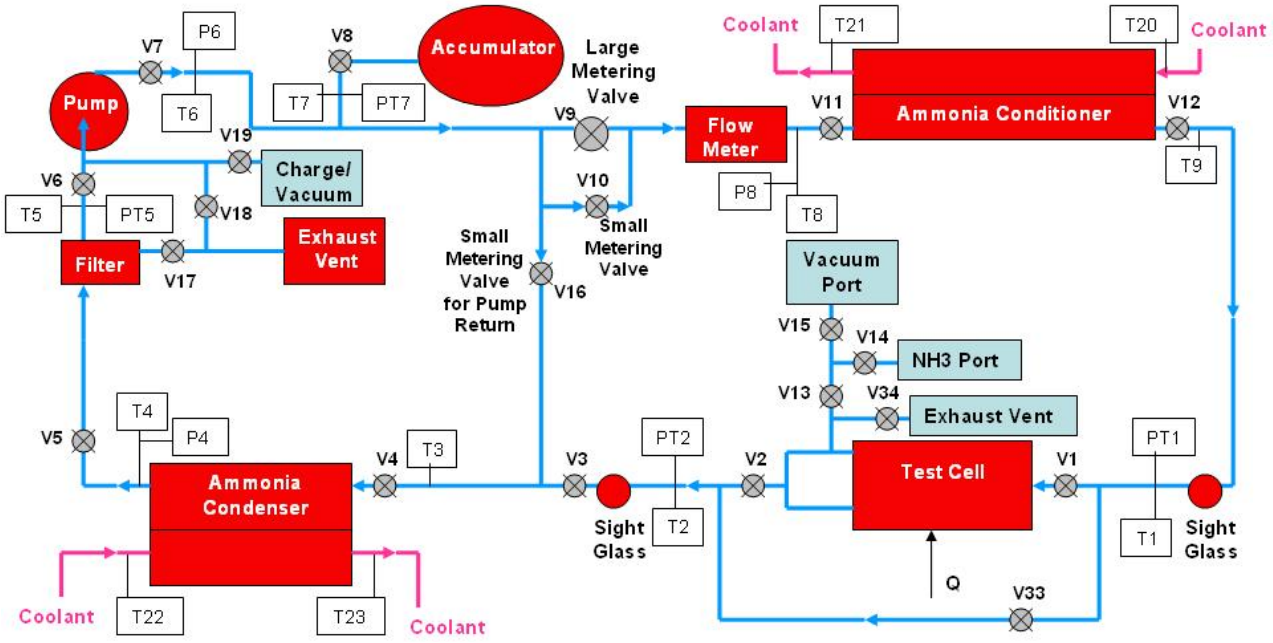

Figure D.1 Ammonia Flow Loop

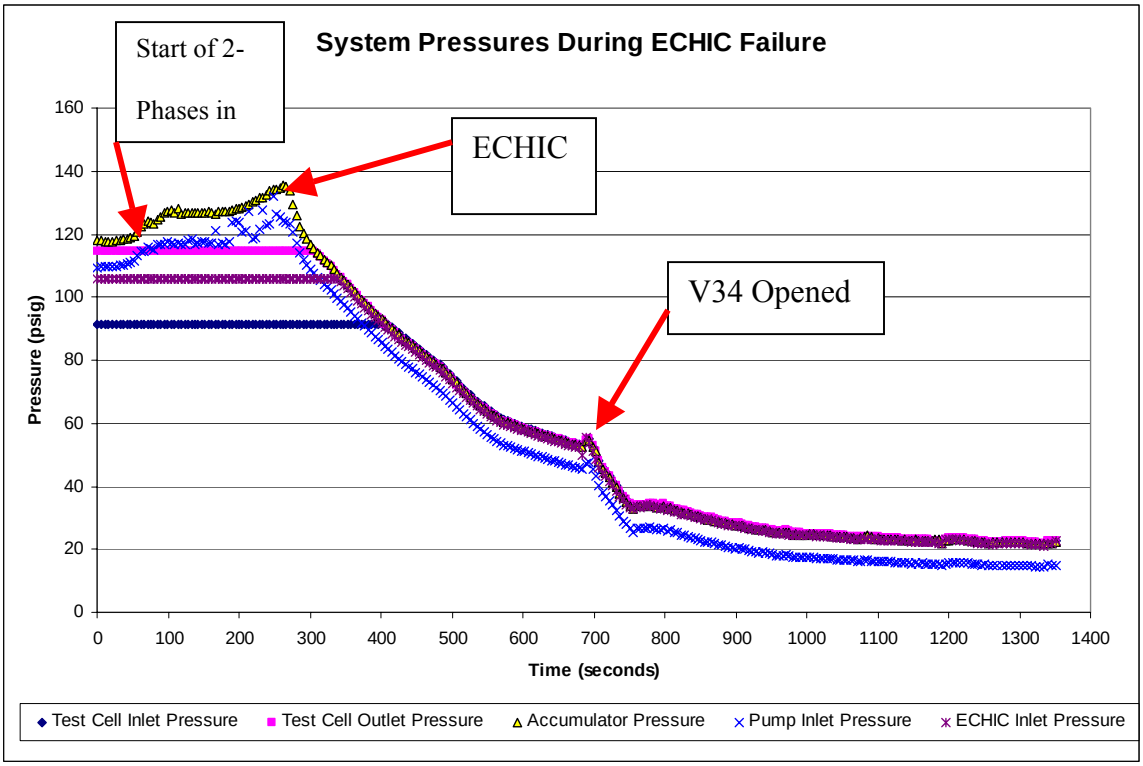

Figure D.2 System Pressures During ECHIC Failure

As can be seen in **Figure D.2**, all of the pressure transducers seemed to follow the same trend once their signal voltages become unsaturated (shown by the straight lines by some of the pressure signals) which means that they are all working correctly in that regard.

3 of the 5 pressure transducers output voltage were saturated (max pressure) at the time of ECHIC failure so only 2 were recording system wide pressure changes. The two that were still reading changes in pressure were the Accumulator Pressure Transducer and the Pump Inlet Pressure Transducer which can be seen in **Figure D.1** as PT7 and PT5, respectively. The other three pressure transducers measure the test cell inlet (saturated at 91 psig) and outlet (saturated at 114 psig) pressures and the ECHIC inlet pressure (saturated at 106 psig). The test cell inlet and outlet transducers can be seen in **Figure D.1** as PT1 and PT2, respectively. The ECHIC inlet pressure transducer is within the test cell and is not shown in **Figure D.1**.

Valve V2 seals failed which caused the ECHIC inlet pressure transducer readings to not differentiate from other pressures in ammonia loop. The entire loop was eventually evacuated because of this.

Events of Figure D.2

0-51 seconds:
Accumulator and Pump Inlet pressure were relatively constant at 118 and 110 psig, respectively.

51-113 seconds:
An increase of pressure occurred corresponding to an accumulator pressure that went from 118 psig to 127 psig. This pressure increase could have been due to the ammonia beginning to evaporate in the ECHIC.

113-190 seconds:
Accumulator and Pump Inlet pressure were then relatively constant again at 127 and 117 psig, respectively, more so with the accumulator pressure. The two-phase flow being produced could have momentarily stopped here due to the pressure increase or more liquid ammonia reaching the ECHIC again.

190-267 seconds:
Another increase of pressure occurred to where the accumulator pressure went from 127 to 135 psig. This was probably a continuation of two-phases being produced in the ECHIC.

267 seconds:
The ECHIC must have ruptured and started to release ammonia to the atmosphere in the ammonia chamber. This must be true due to the dramatic pressure drop that occurs in the entire system after this point in time.

267-300
The pump and accumulator pressures decrease at relatively the same rate here after the rupture.

300 seconds
The change in slope here could be due to the evening out of the rate of the ammonia escaping. It could also be due to the power being shut off to the heater block.

300-560 seconds:
The pressure continued to drop at the same rate around the entire.

560 seconds:
There is a slight decrease in the rate of change of the loop pressures. This was possibly due to some flashing of ammonia somewhere in the system since some of the temperatures around the loop match up with the pressures at this point to satisfy saturated conditions.

560-688 seconds:
All pressures continued to steadily decrease at the different rate

688 seconds:
There was a positive pressure spike of 2-3 psi from around 50 psig probably caused by valve V34, the test cell exhaust vent seen in **Figure D.3**, being opened.

688-760 seconds:
All pressures now drop at a higher rate due to the venting valve now being open.

760 seconds:
V34 probably froze up causing another, slight pressure spike before everything evens out again.

760-end seconds:
Transducer pressure readings now continue to all drop at the same steady rate at approximately the same pressures until the data recording stops.

NH3 Loop Temperatures During ECHIC Failure

Test Cell

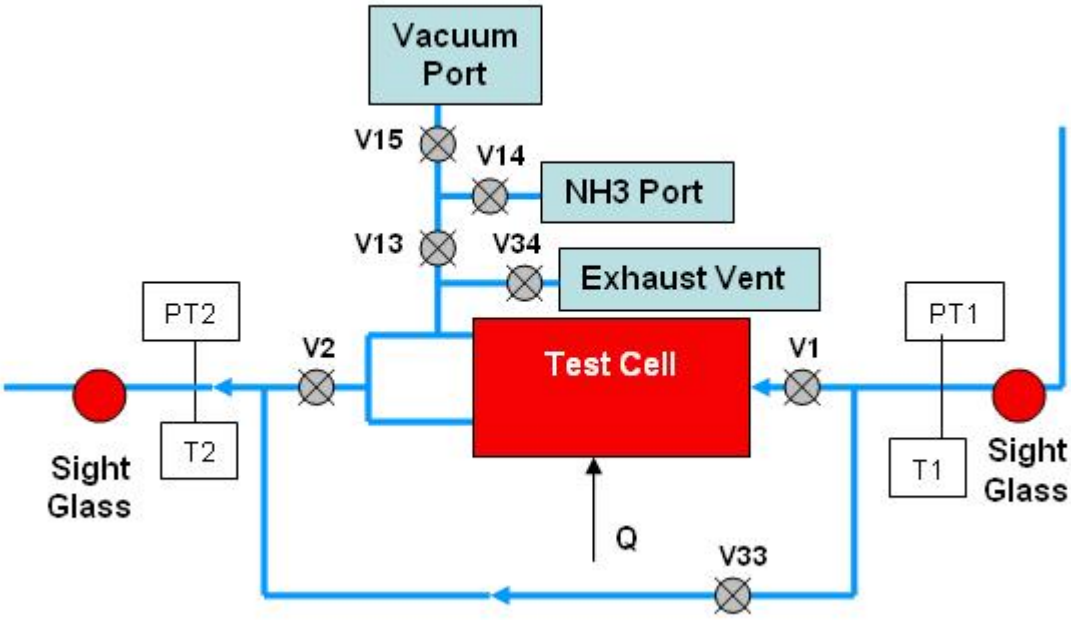

Figure D.3: Test Cell Section of Ammonia Loop

Instruments Used:

- T1 (test cell inlet temperature)
- T2 (test cell inlet temperature)

(The locations in the ammonia flow loop of these instruments can be seen in **Figure D.1** and **Figure D.3**)

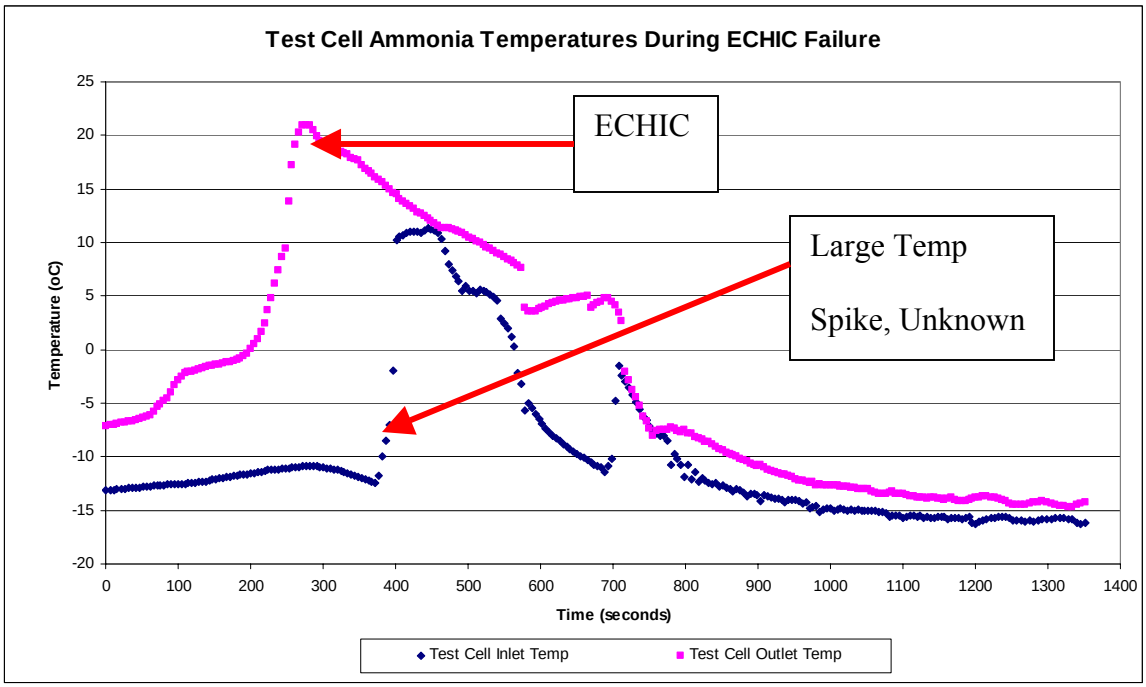

Figure D.4 Test Cell Fluid Temperatures During ECHIC Failure

Figure D.3 represents the component in the ammonia loop that the data in **Figure D.4** came from.

Events of Figure D.4

0-267 seconds:

The outlet temperature continues a steep increase

The inlet temperature remains relatively constant

267-end seconds:

Outlet temperature suddenly begins a decrease due to rupture of the ECHIC. Back flow of ammonia from the condenser might have caused this or just the fact that the ammonia was also rapidly decreasing in pressure might have caused it as well.

573-588 seconds:

A steep dip occurs here with the outlet temperature which could have been caused by a sudden burst of back flow from the condenser due to some ammonia in the system flashing or a sudden decrease in pressure from the test section venting valve being open.

693-760 seconds:

Same as 573-588 seconds for outlet temperature

267-372 seconds:

The inlet temperature remains relatively constant

372-405 seconds:
Inlet temperature increases at a very steep rate. The only thing that can be thought of that could have caused this is back flow of ammonia from the hot ECHIC, but this is not likely since other thermocouples in the area do not register this change so for now it is really **unknown**.

405-688 seconds:
Inlet temperature decreases relatively steadily representing what the system should be doing with the energy input shut off and ammonia still flowing and venting.

688-707 seconds:
Same as 372-405 seconds for the inlet temperature

707-end seconds:
Same as 405-688 seconds for the inlet temperature

Conditioner

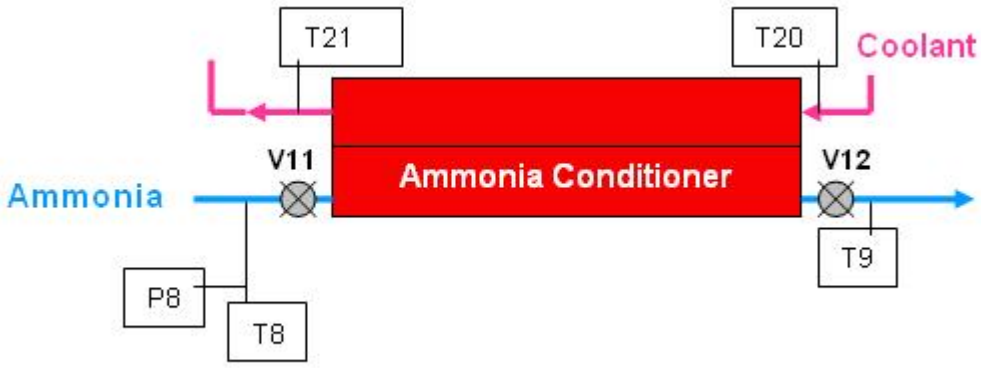

Figure D.5: Conditioner Section of Ammonia Loop

Instruments Used:

- T8 (ammonia conditioner inlet temperature)
- T9 (ammonia conditioner outlet temperature)
- T20 (ammonia conditioner glycol inlet temperature)
- T21 (ammonia condenser outlet temperature)

(The locations in the ammonia flow loop of these instruments can be seen in **Figure D.1** and **Figure D.5**)

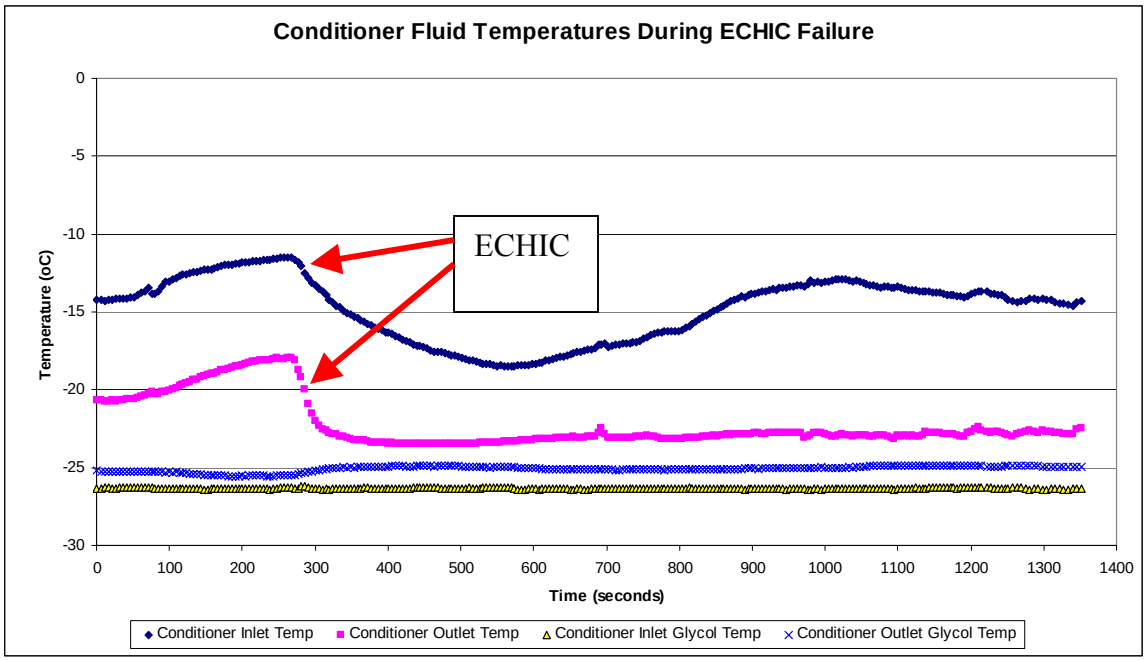

Figure D.6 Conditioner Fluid Temperatures During ECHIC Failure

Figure D.5 represents the component in the ammonia loop that the data in **Figure D.6** came from.

The glycol inlet and outlet temperatures are very constant with one colder than the other showing that energy is being absorbed from the ammonia.

Events of Figure D.6

0-267 seconds:

Both inlet and outlet temperatures are increasing steadily corresponding to the energy being put into the system from the heater block.

267-400 seconds:

The outlet temperature begins a steep dive which corresponds to the rupture of the ECHIC causing system pressure to decrease which affects the temperature in this way.

400- end seconds:

The outlet temperature stays constant for the remainder of the data recording

267-578 seconds:

The inlet temperature begins to dive as well due to the ECHIC rupture but not as steeply, probably because it was farther away from the ECHIC as far as the order of the ammonia loop goes. It was not affected by the ECHIC rupture as quickly as the outlet of the conditioner.

578-1018 seconds:
The inlet temperature begins to slowly increase again. The cause of this is **unknown**.

1018-end seconds:
The inlet temperature begins to slowly decrease again. The cause of this is **unknown**.

Condenser

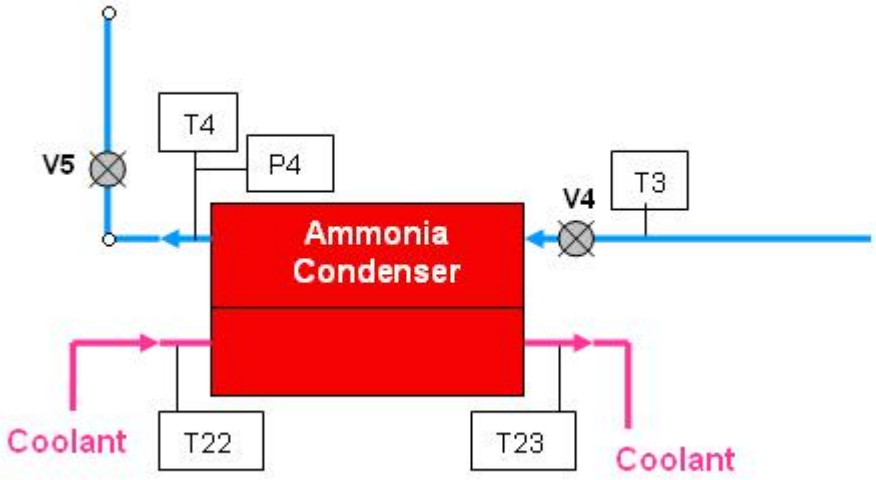

Figure D.7: Ammonia Condenser Section of Ammonia Loop

Instruments Used:

- T3 (ammonia condenser inlet temperature)
- T4 (ammonia condenser outlet temperature)
- T22 (ammonia condenser glycol inlet temperature)
- T23 (ammonia condenser glycol outlet temperature)

(The locations in the ammonia flow loop of these instruments can be seen in **Figure D.1** and **Figure D.7**)

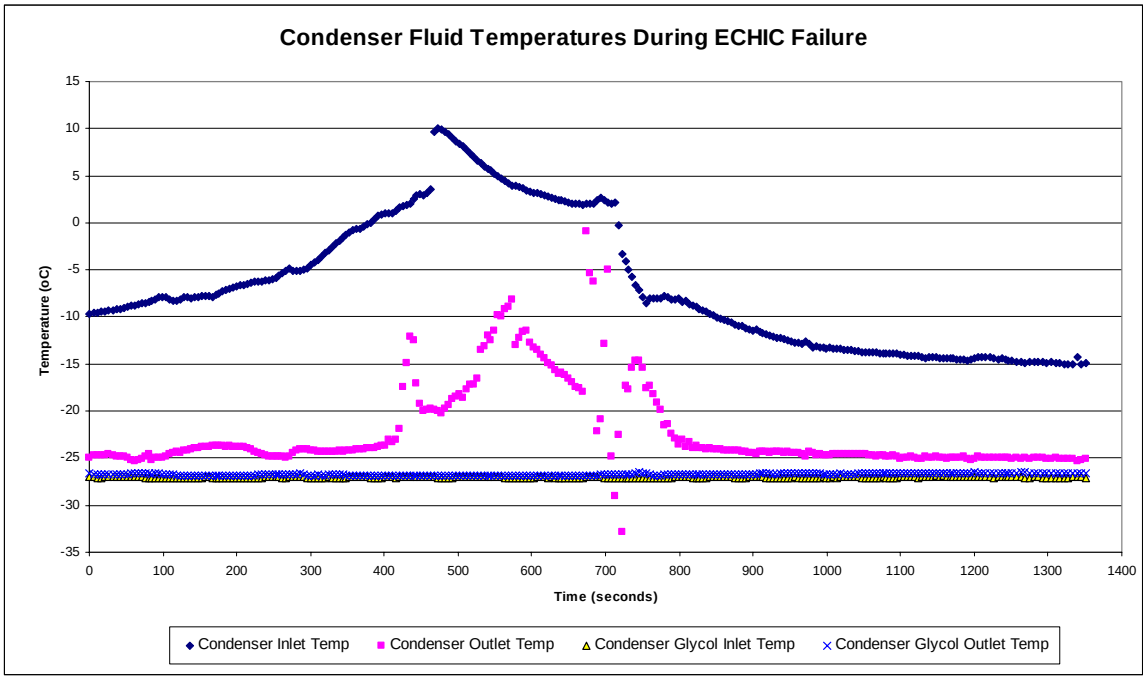

Figure D.8 Condenser Fluid Temperatures During ECHIC Failure

Figure D.7 represents the component in the ammonia loop that the data in **Figure D.8** came from.

The glycol inlet and outlet temperatures are very constant with one colder than the other showing that energy is being absorbed from the ammonia.

Events of Figure D.8

0-463 seconds:

The inlet temperature increases at a steady rate from about -10^{o}C to 3^{o}C corresponding to the energy that was being added to the system during most of this time. But there are no large spikes here that would indicate a rupture of the ECHIC.

463-472 seconds:

The inlet temperature has a large spike from 3oC to 10oC. It might have taken some time for the warmer ammonia from the ECHIC to reach the point in the loop so that is what this could be.

472-712 seconds:

The inlet temperature then begins a steady decrease from 10oC to 2oC representing what the system should be doing with the energy input shut off and ammonia still flowing and venting.

712-760 seconds:

A steep dip occurs here with the inlet temperature from 2oC to -8oC which could have been caused by a sudden burst of back flow of ammonia due to some ammonia in the system flashing or a sudden decrease in pressure from the test section venting valve being open. This corresponds with the Test Cell outlet temperature steep dive at this point

760-end seconds:
Inlet temperature drops at a steady level until it reaches a constant -15oC.

0-415 & 798-end seconds:
The outlet temperature is relatively constant here owning to the glycol and the condensers ability to cool down and stabilize the ammonia and cool it down from the inlet conditions.

415-798 seconds:
The outlet temperature is very sporatic here and it is really unknown what all of these different temperatures mean so it is really unknown what is going on here.

Pump and Accumulator

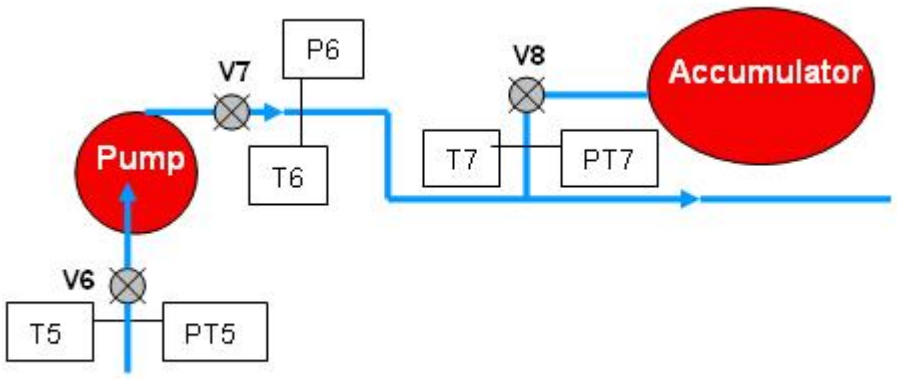

Figure D.9: Pump/Accumulator Section of Ammonia Loop

Instruments Used:

- T5 (pump inlet temperature)
- T6 (pump outlet temperature)
- T7 (accumulator temperature)

(The locations in the ammonia flow loop of these instruments can be seen in **Figure D.1** and **Figure D.9**)

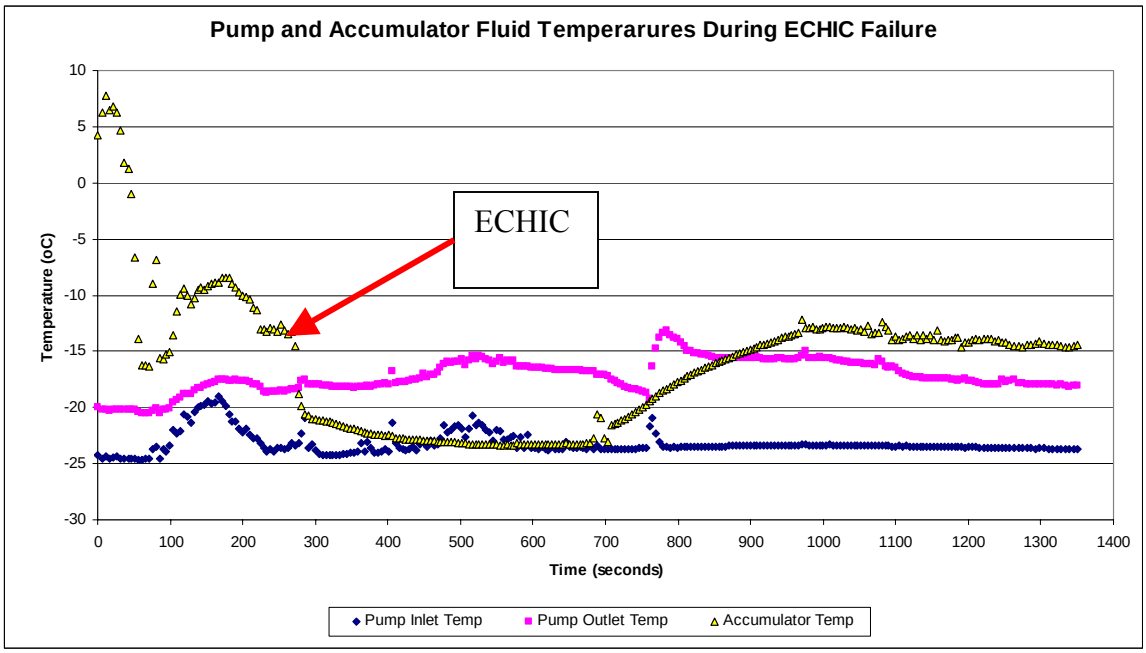

Figure D.10 Pump and Accumulator Fluid Temperatures During ECHIC Failure

Figure D.9 represents the component in the ammonia loop that the data in **Figure D.10** came from.

The accumulator changes temperature a lot here every time the system has a pressure change because that means liquid is either being drawn into or out of the accumulator to compensate for the pressure change. Since the fluid in the accumulator is kept cold and the ammonia in the loop is cold this thermocouple reads these temperatures when pressure changes. This can be seen very easily at around the 260 mark where the temperature drops suddenly because of the ECHIC rupturing. The temperature dropped dramatically because the ammonia that was previously being kept cold in the accumulator dropped down to the thermocouple reading the accumulator temperature.

The pump inlet and outlet temperatures remain relatively constant throughout this event except for a few small spikes here and there. Those could be caused by a vapor pocket being formed in the filter suddenly and increasing or decreasing the temperature. That is the only reason that is available right now since the liquid coming out of the condenser and into the filter should be consistently cold.

Test Cell Temperatures During ECHIC Failure

ECHIC Fluid Inlet/Outlet Temperatures

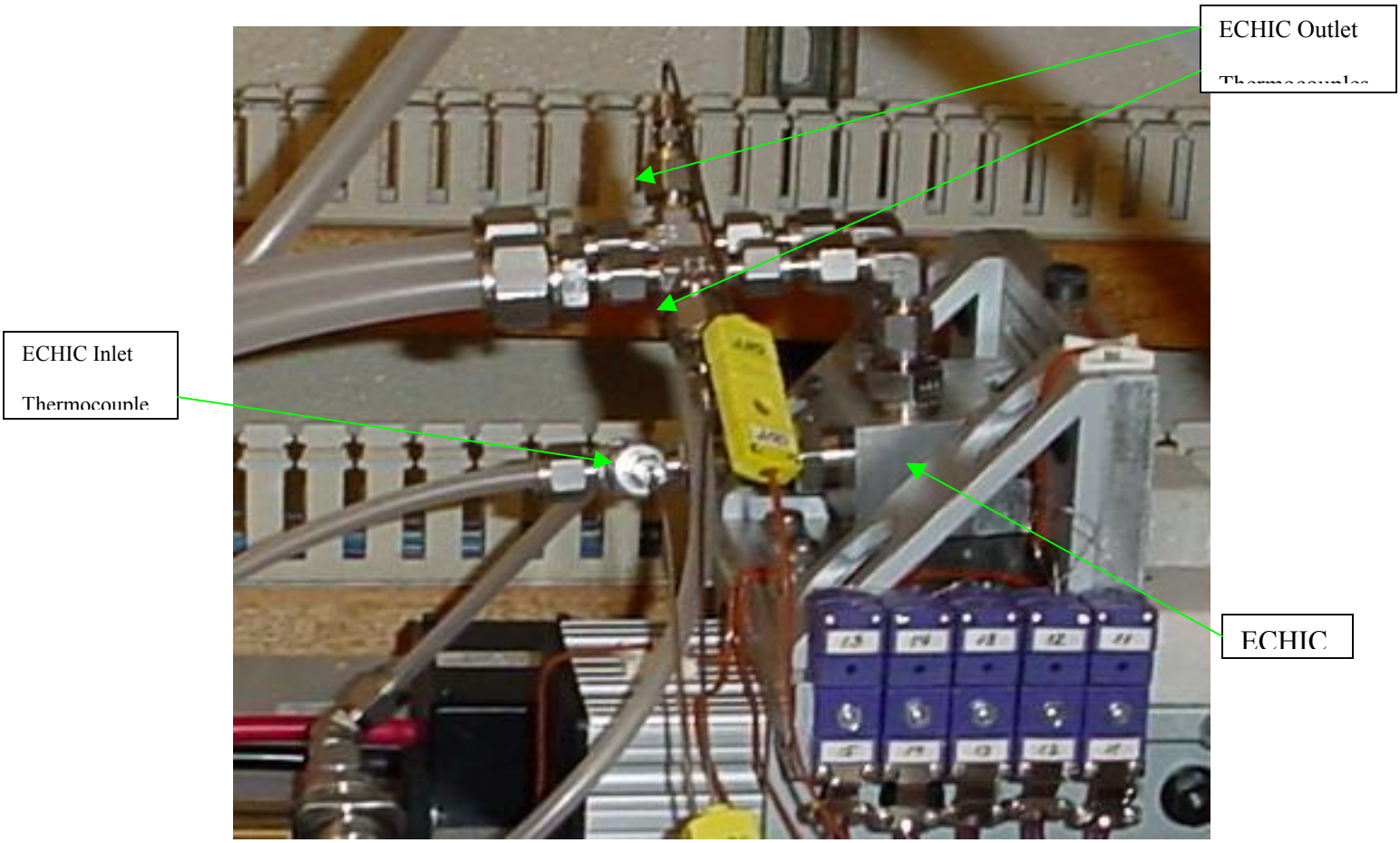

Figure D.11: ECHIC Hooked up to Test Cell

Instruments Used:
The inlet and the two outlet thermocouples to the ECHIC which can be seen in **Figure D.11** (not shown in **Figure D.1**)

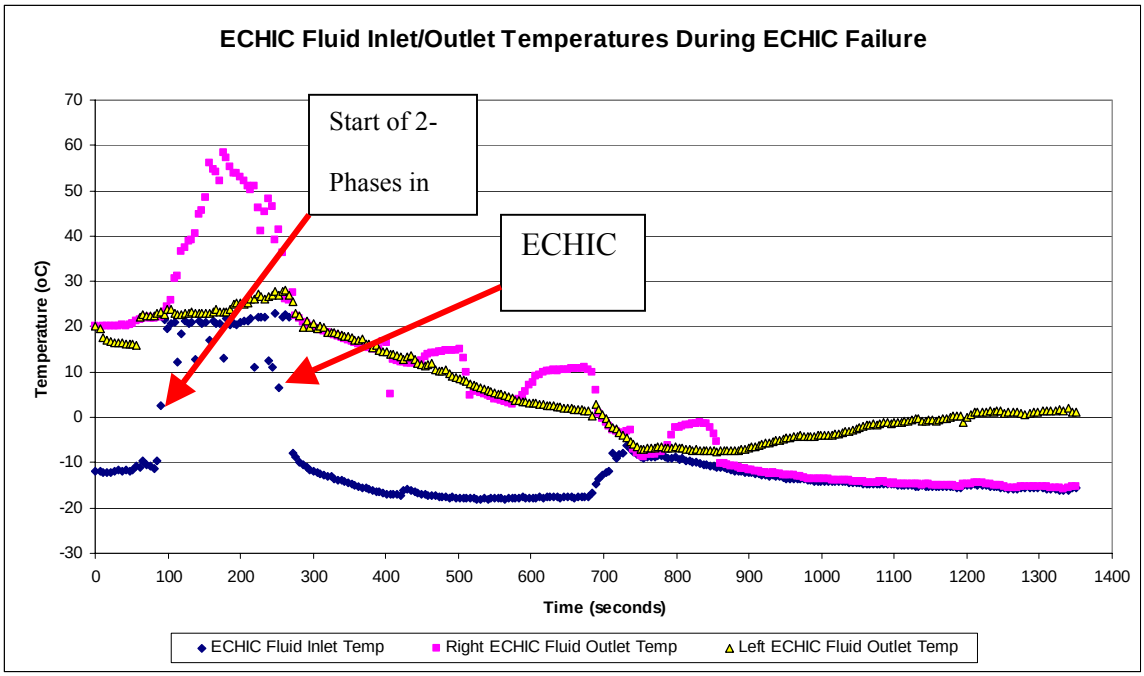

Figure D.12 ECHIC Fluid Temperatures During ECHIC Failure

Figure D.11 shows what the ECHIC actually looks like which show how close the inlet and outlet ECHIC thermocouple ports are to the actually ECHIC which probably caused the data in **Figure D.12** to be so jumpy.

Events of Figure D.12

0-85 seconds:

The inlet temperature remains very constant here at -11oC.

85-276 seconds:

The inlet temperature jumps suddenly to between 10 and 20oC during this time. It is believe that this happened due to the ammonia now evaporating from the energy input and back flowing back into this thermocouple.

276-683 seconds:

The inlet temperature suddenly drops down again to -10oC, tapers off and then stays at a relatively constant level at around -17oC. This is another indication that, at the beginning of this time period, this is when the ECHIC ruptured because the temperature suddenly drops. It probably dropped because when the ECHIC ruptured all of the ammonia vapor in the ECHIC escaped to the atmosphere and liquid ammonia started flowing at a much faster rate to the ECHIC since it was now able to escape to the atmosphere.

683-736 seconds:

Inlet increases from -17oC to -8oC which corresponds to the Test Cell inlet temperature increase around this time mentioned earlier.

736-end seconds:
Inlet steadily decreases again until a steady temperature of -16oC is reached.

0-99 seconds:
Outlet temperatures are close to same temperature of 20oC.

99-271 seconds:
Outlet temperatures vary a lot here between each other.

One reaches 27oC and the other one reaches 58oC.

This probably says that only one of the outlets allowed much more ammonia flow than the other.

The much warmer two-phase ammonia flow created in this time interval probably flowed through the one that became much warmer.

Although, the other outlet leg seems to have registered two-phase flow as well due to its similarity to the Inlet temperature profile.

These outlet legs are the highest point in the system so the different flow rates were probably due to a vapor or air pocket in one of the lines since air was previously introduced into the system by accident.

271-850 seconds:
With some strange spikes from one of the legs, the outlet temperatures seem to decrease at the same rate here from 25oC to -7oC.

This is probably due to the lack of two-phase flow now and ammonia from the rest of the system moving toward the ECHIC as it escapes to the atmosphere.

850-end seconds:
Outlet temperatures split off here with one rising again to 0oC and the other continuing to decrease down to -15oC. The cause of this is **unknown**.

Heater Neck Temperatures

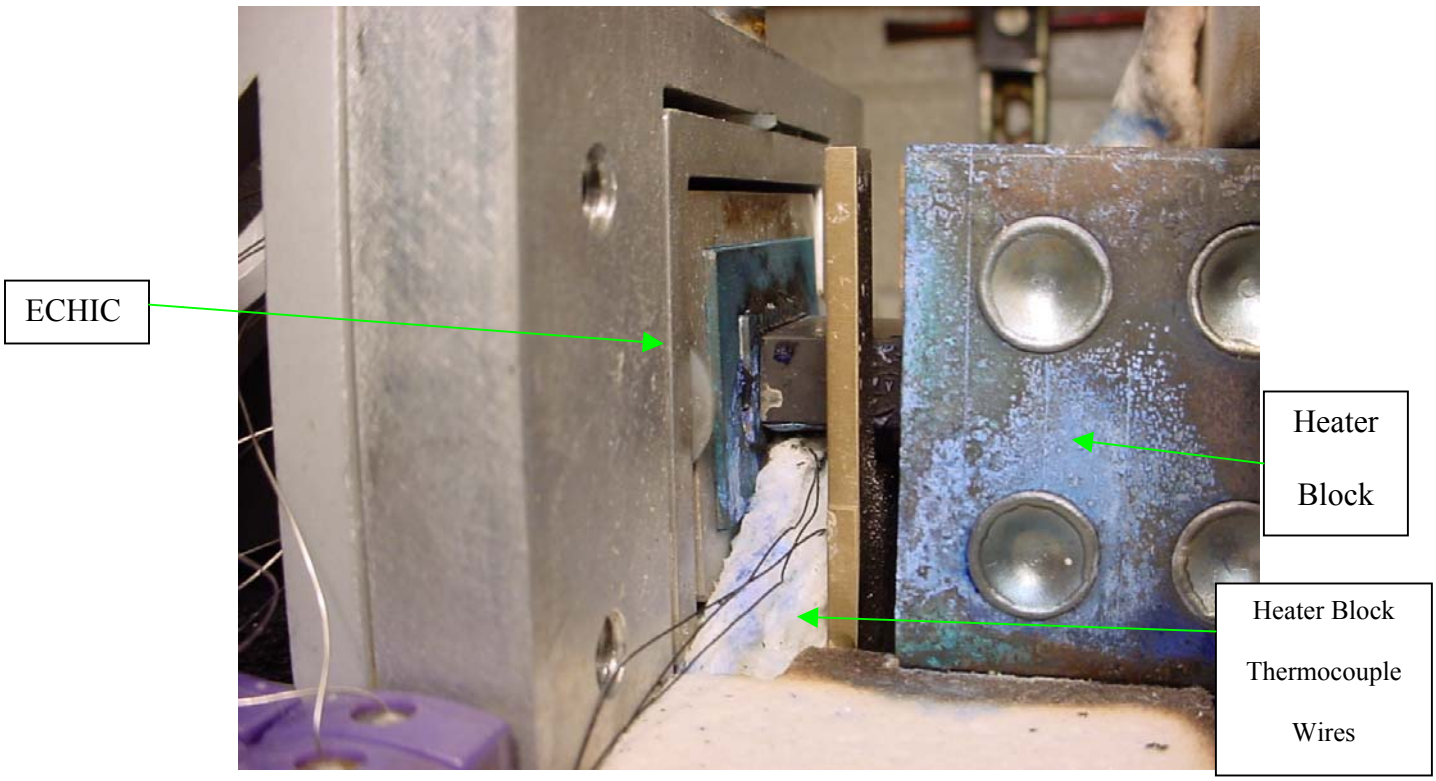

Figure D.13: Heater Block Interfaced with ECHIC

Instruments Used:
Three thermocouples connected to the heater block neck (not shown in **Figure D.1**)

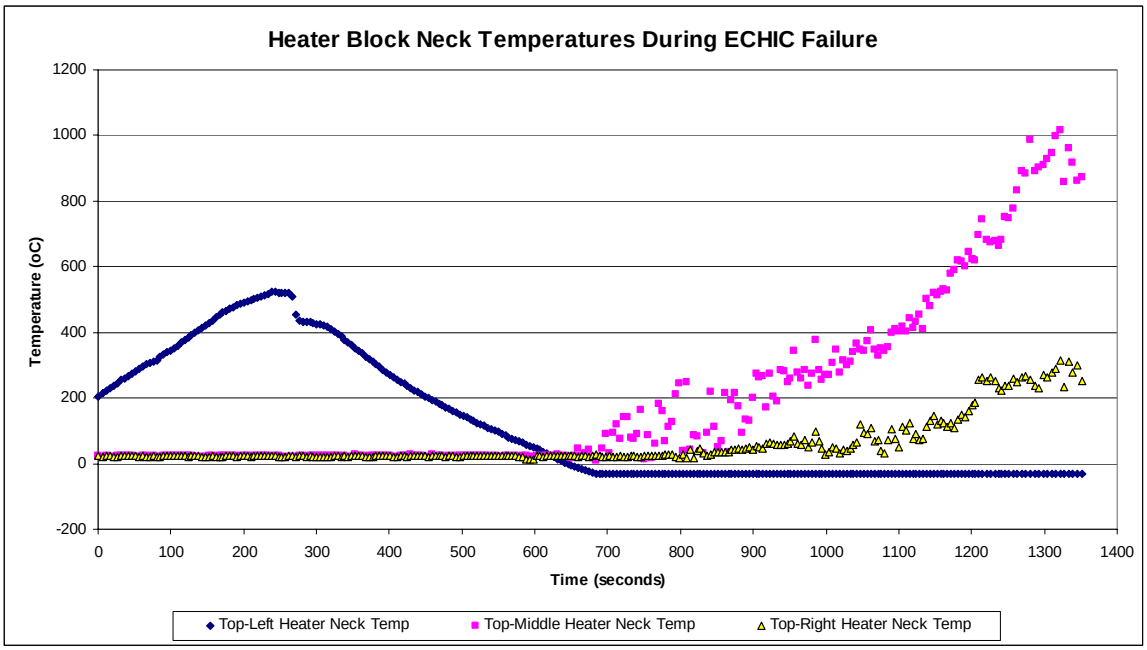

Figure D.14 Heater Block Neck Temperatures During ECHIC Failure

Figure D.13 shows how the heater block and ECHIC interface and the location of the thermocouple wires for the thermocouples that created the data in **Figure D.14**.

These trends these temperatures show do not match up at all with any of the other data recorded during this entire time period.

Due to this and the fact that the adhesive compound used to hold these thermocouples to the heater neck was damaged and they were partially removed from their holes these temperature readings will be disregarded.

ECHIC Temperatures During ECHIC Failure

A definite trend, or major event can be seen when looking at these plots.

ECHIC Surface Temperatures

Figure D.15: Damaged ECHIC

Instruments Used:
The 20 thermocouples connected to the surface of the ECHIC where the heater block interfaces with it. The locations can be seen in **Figure D.15** (not shown in **Figure D.1**).

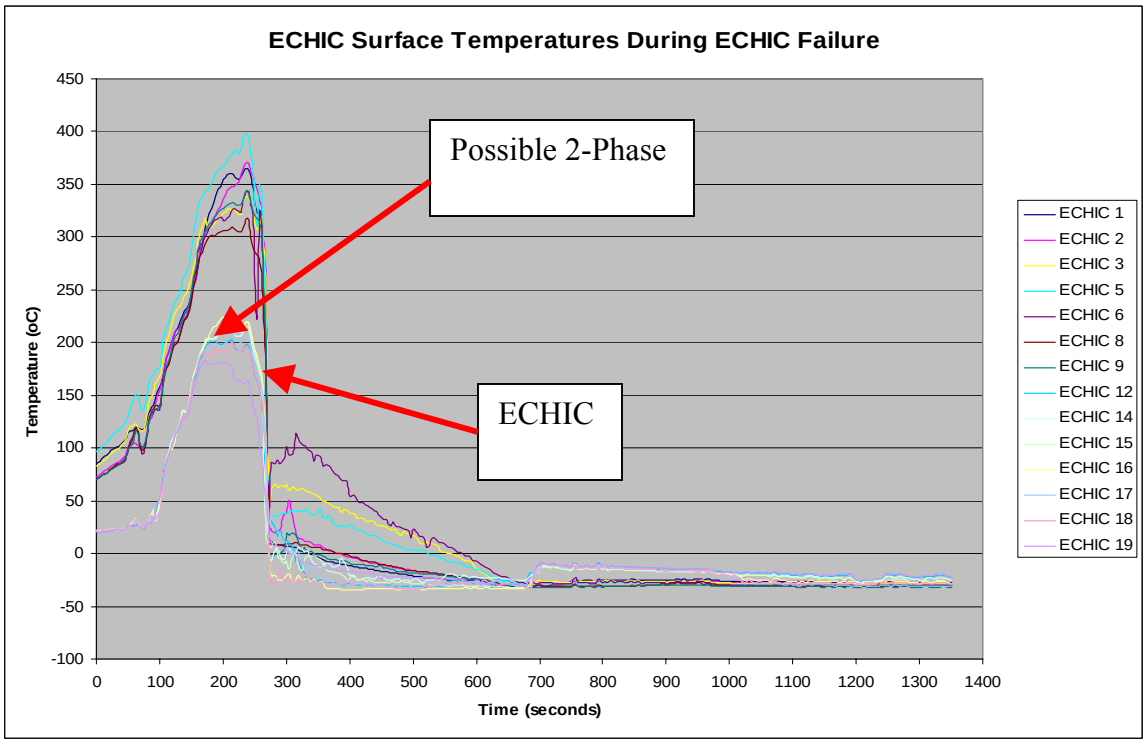

Figure D.16 ECHIC Surface Temperatures During ECHIC Failure

Not all 20 ECHIC thermocouples are shown in Figure 16 due to some of them giving data inconsistent with conditions and other ECHIC thermocouples. These ECHIC thermocouples that recorded inconsistent data include # 4, 7, 10, 11, 13, and 20. The locations of all of the ECHIC thermocouples can be seen in **Figure D.17.**

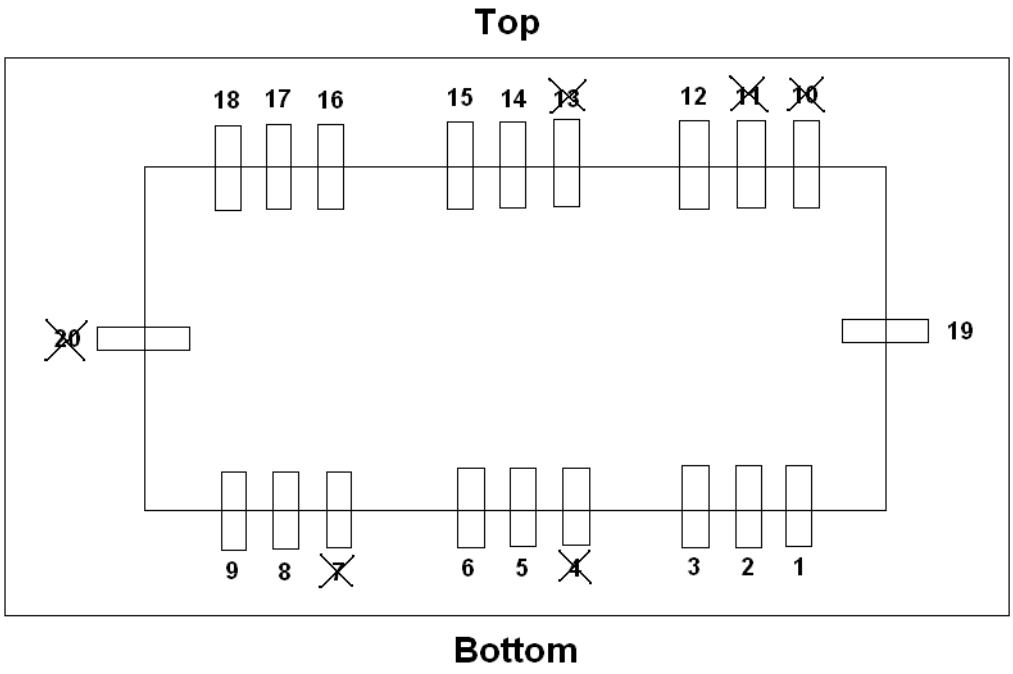

Figure D.17: ECHIC Surface Temperature Thermocouple Locations

Events of Figure D.16

0-176 seconds:

All ECHIC surface temperatures can be seen as steadily, and steeply, increasing from roughly 75oC to 275oC due to the energy being added to the ECHIC from the heater block.

176-238 seconds:

All of the ECHIC surface temperatures seemed to level out to some degree during this time. This could be due to ammonia evaporation beginning here instead of earlier as previously thought or the evaporation could have become more intense. This more intense evaporation could have caused these somewhat constant temperatures.

238-271 seconds:

All ECHIC surface temperatures suddenly drop from roughly 275oC to 50oC.

Out of all of the plots that show indications of when the ECHIC ruptured, this is the strongest indication due to the sharp temperature drop.

All of these temperatures dropped suddenly because when the ammonia finally began to escape to the atmosphere by evaporation it took a lot of energy with it. This, in turn, caused all of these ECHIC surface thermocouples to show sharp decreases in temperature.

271-end seconds:

From here on the ECHIC temperatures taper off, for the most part, to -25oC.

ECHIC Average Surface Temperatures

Instruments Used:
Same as for **Figure D.16**

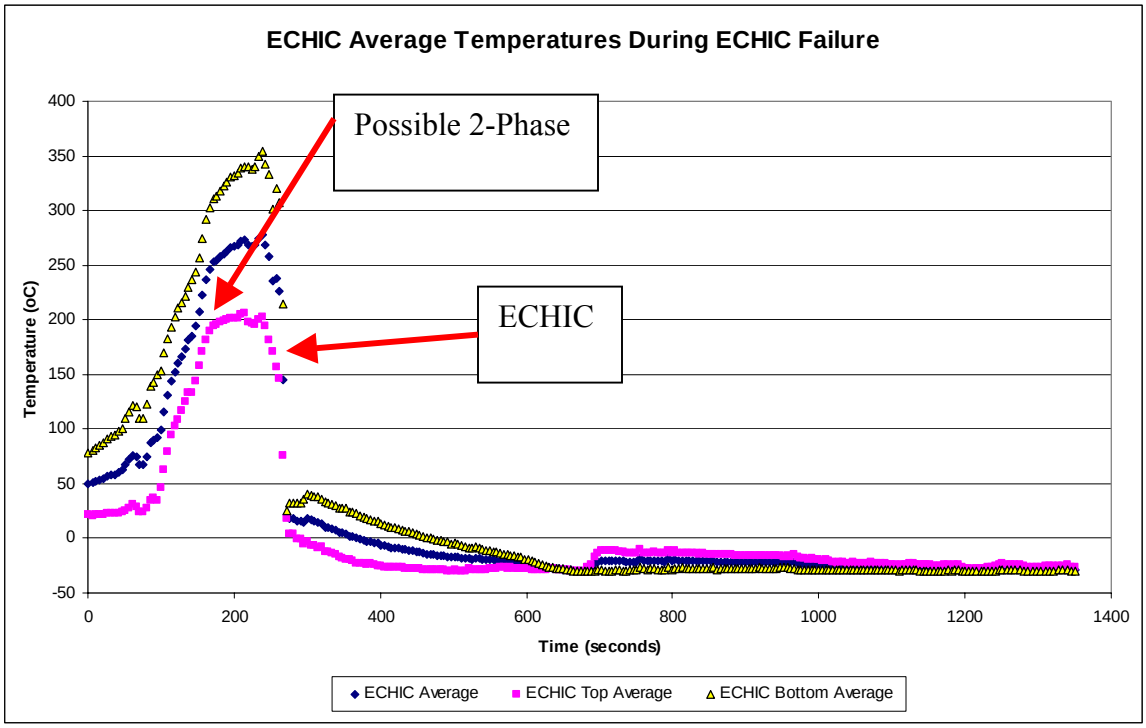

Figure D.18 ECHIC Average Temperatures During ECHIC Failure

Events of Figure D.18
This plot shows how the average temperatures of the top and bottom of the surface of the ECHIC device interfaced with the heater block vary significantly.

At the beginning of this plot the difference in temperature between the top and bottom is roughly 50oC. At peak temperatures the difference becomes roughly 150oC.

This shows that there was a definite difference in ECHIC/Heater Block interface pressure between the top and bottom of the ECHIC. The more pressure there was from the top to the bottom, the better the heat transfer from the heater block to the ECHIC. This is one definite problem that needs to be fixed or made sure that it is not repeated. Perfectly even heating of the ECHIC is the most desirable situation.

Energy Input into Heater Block

Instruments Used:
A 1000W watt transducer and a 2000W watt tranducer (not shown in **Figure D.1**). These measure the "Q" input into the Test Cell shown in **Figure D.1** and **Figure D.3.**

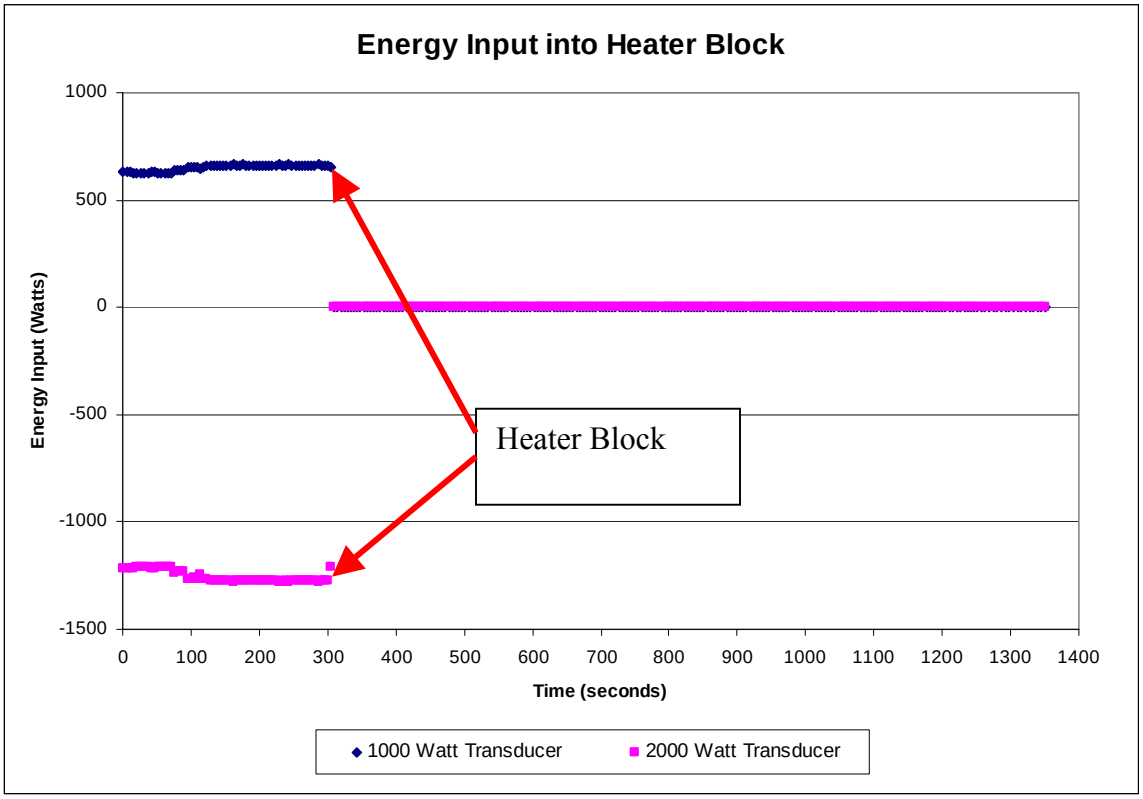

Figure D.19 Energy Input into Heater Block

Events of Figure D.19
This plot shows the definite negative value that one of the watt transducers was outputting to skew the total watt input value that was being read during the time of the experiment.

The only other information, but very important information, that this plot shows is the exact moment the energy to the heater block was shut off which happened just after the 300 second mark.

NH3 Concentration in Chamber During ECHIC Failure

Instruments Used:
Ammonia detector in the ammonia chamber (not shown in **Figure D.1**)

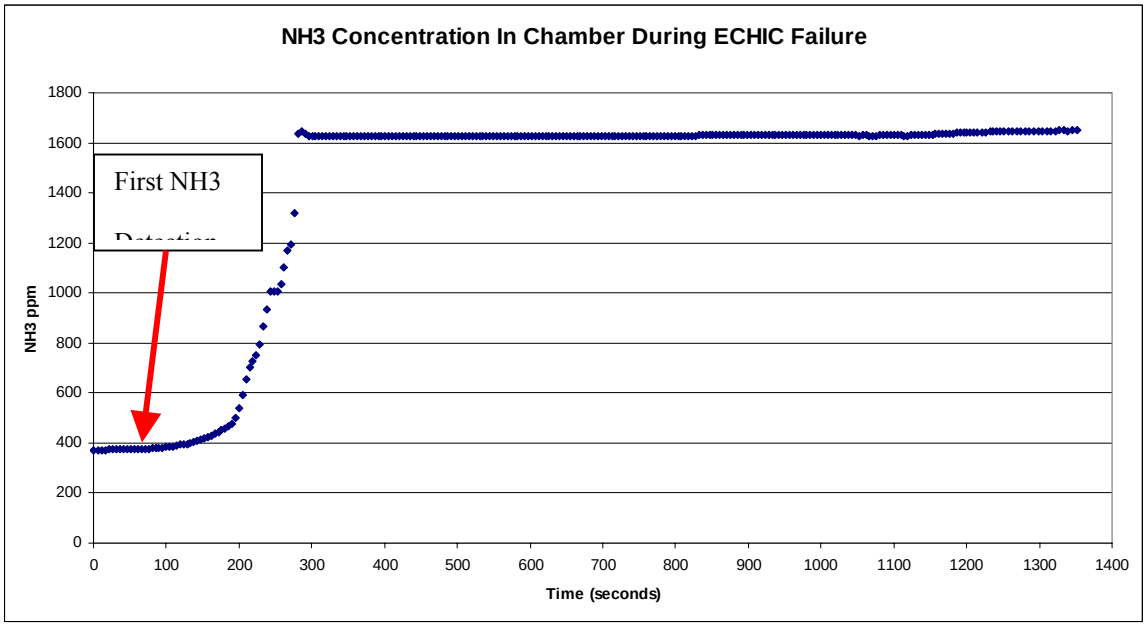

Figure D.20 NH_3 Concentration in Chamber During ECHIC Failure

Events of Figure D.20

0-75 seconds:

Ammonia concentration stays fairly constant at round 374 ppm.

75-295 seconds:

Ammonia concentration exponentially increases until the detector becomes saturated at 1627 ppm (The detector is only rated to 1000 ppm so the accuracy of this ppm amount is unknown).

The ammonia detector shows an increase in concentration well before all of the other data that show an ECHIC rupture roughly somewhere between 238 and 271 seconds.

This difference could have happened due to a small amount of ammonia vapor already escaping out of the ECHIC due to the high heat transfer taking place before the ECHIC finally, totally gave in to the temperatures and pressures it was being subjected to. As shown on other plots, 75-100 seconds is the time period when two-phase began to appear in the data.

Other than that it is **unknown** why the ammonia concentration began to increase sharply much before a rupture was shown in any of the other data.

295-end seconds:

Ammonia detector stays at this concentration of 1627 ppm for the remainder of the data recording period.

Ammonia Flow Rate During ECHIC Failure

Instruments Used:
Flow meter (shown in **Figure D.1**)

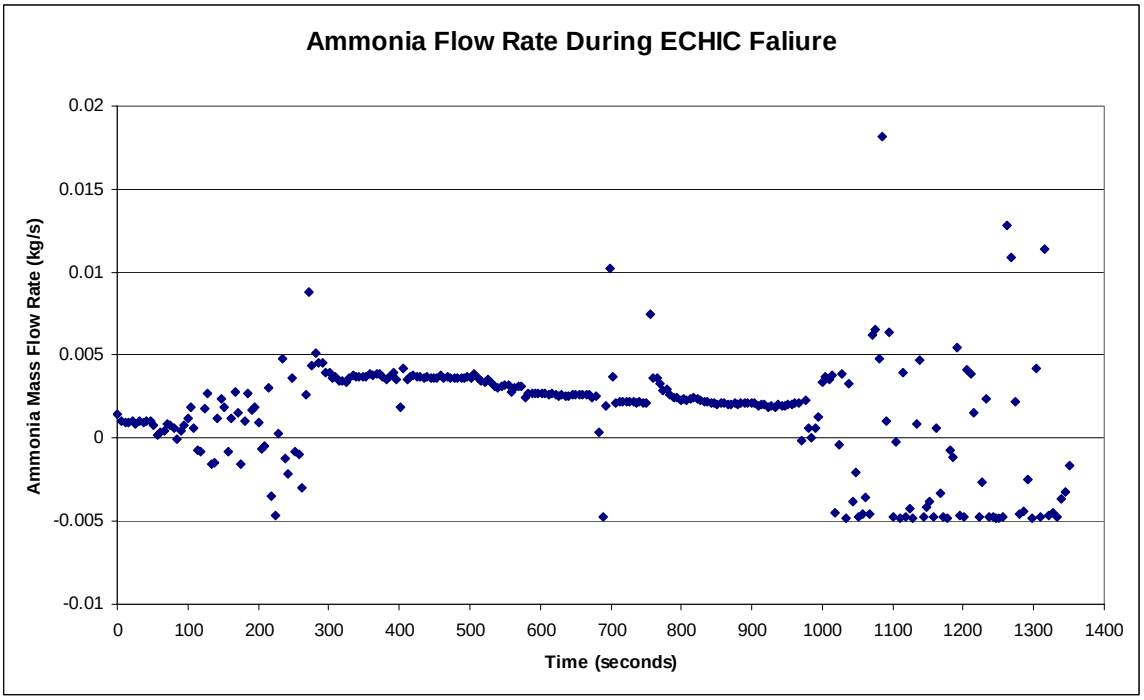

Figure D.21 Ammonia Mass Flow Rate During ECHIC Failure

Events of Figure D.21
0-80 seconds:
The beginning of this plot confirms the desired flow rate at beginning of the experiment.

80-310 seconds:
When the two-phase flow was thought to begin in the ECHIC the flow rate is very sporadic and the reason for this in **unknown**.

310-975 seconds:
When the rupture is thought to occur the flow rate steadies out showing a higher flow rate than what the pump was set at meaning ammonia was definitely being lost somewhere in the system.

975-end seconds:

The flow rate becomes very sporadic again. This shows that there are probably two-phases present in the entire system now. The flow is moving from positive to negative because of the liquid in the flowmeter being moved back and forth from all of the vapor pockets being created system wide.

Comparison of Test Cell Inlet/Outlet Temperatures During ECHIC Failure

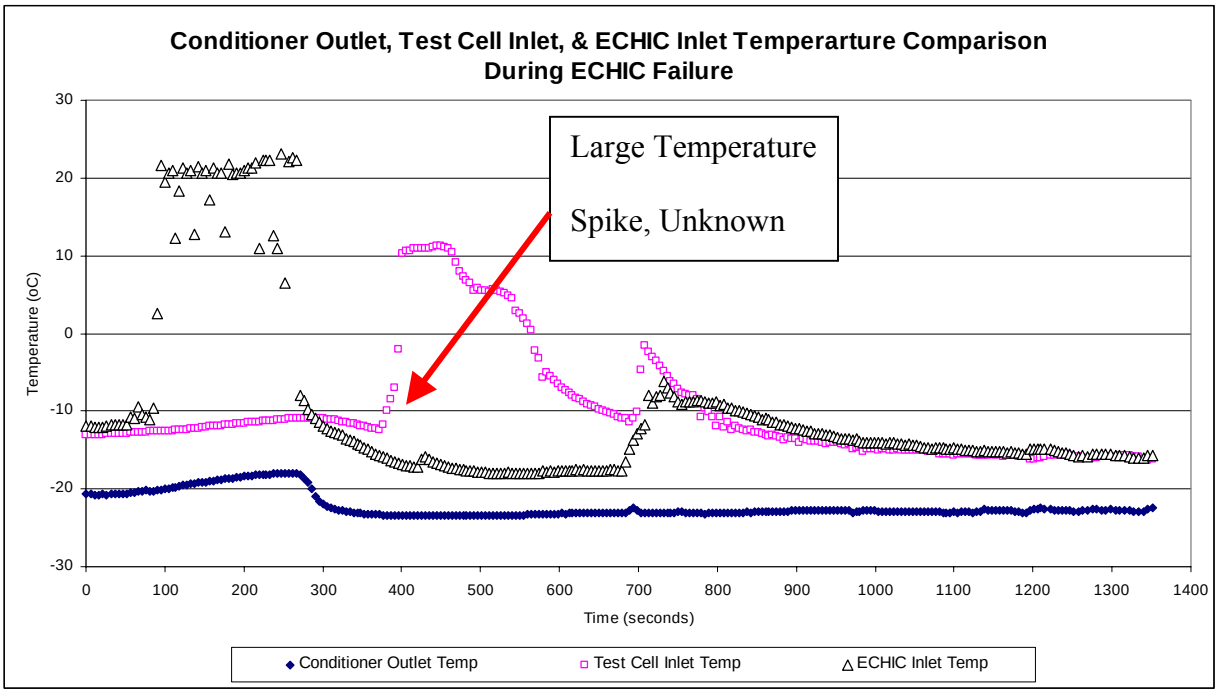

Figure D.22 ECHIC Inlet, Test Cell Inlet, & Conditioner Outlet Fluid Temp. Comparison During ECHIC Faiure

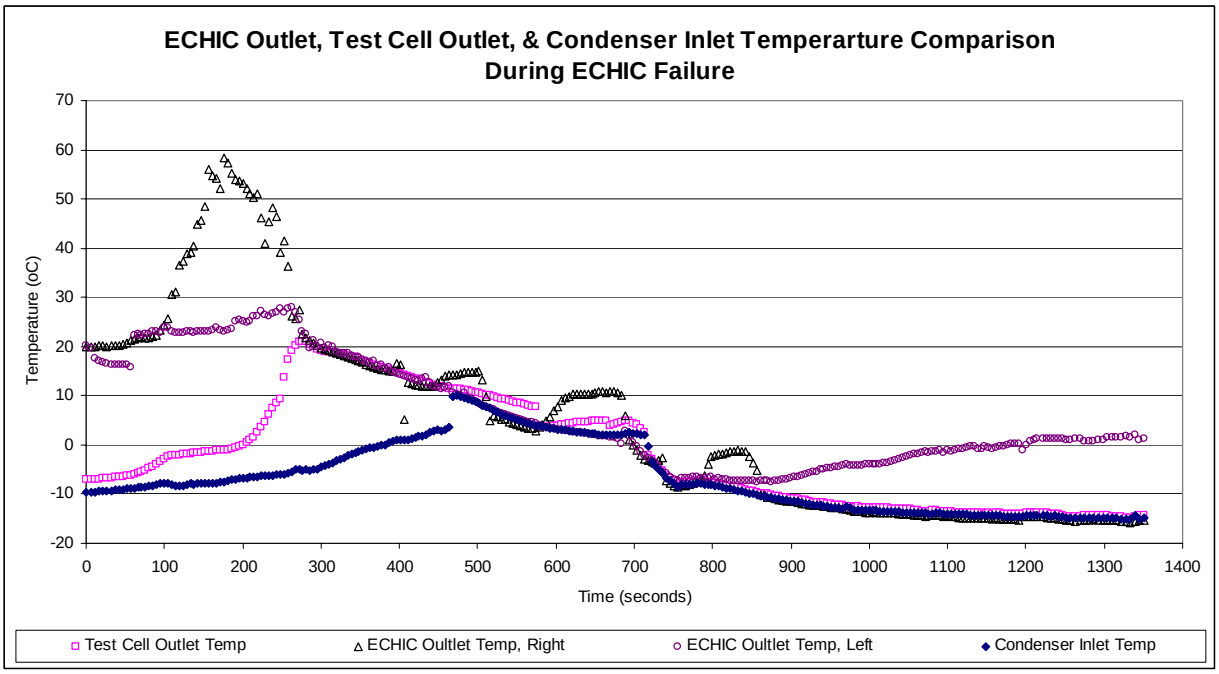

Figure D.23 ECHIC Outlet, Test Cell Outlet, & Condenser Inlet Fluid Temp. Comparison

During ECHIC Faiure

Instruments Used:
Same as mentioned in previous plots with these instruments

Events of Figures D.22 & D.23
These two plots in Figures 22 and 23 representing the inlet and outlet ammonia temperatures for the test cell were created for comparison of temperatures between different ammonia loop components. More specifically, they were created to possibly find if there was anything else happening in the system that could have caused the large temperature spike registered by the test cell inlet temperature at around 400 seconds (**red arrow in Figure D.22**). However, from looking at all of this data together there seems to be no explanation at all for this so for now the cause will remain unknown.

Time Line of Events

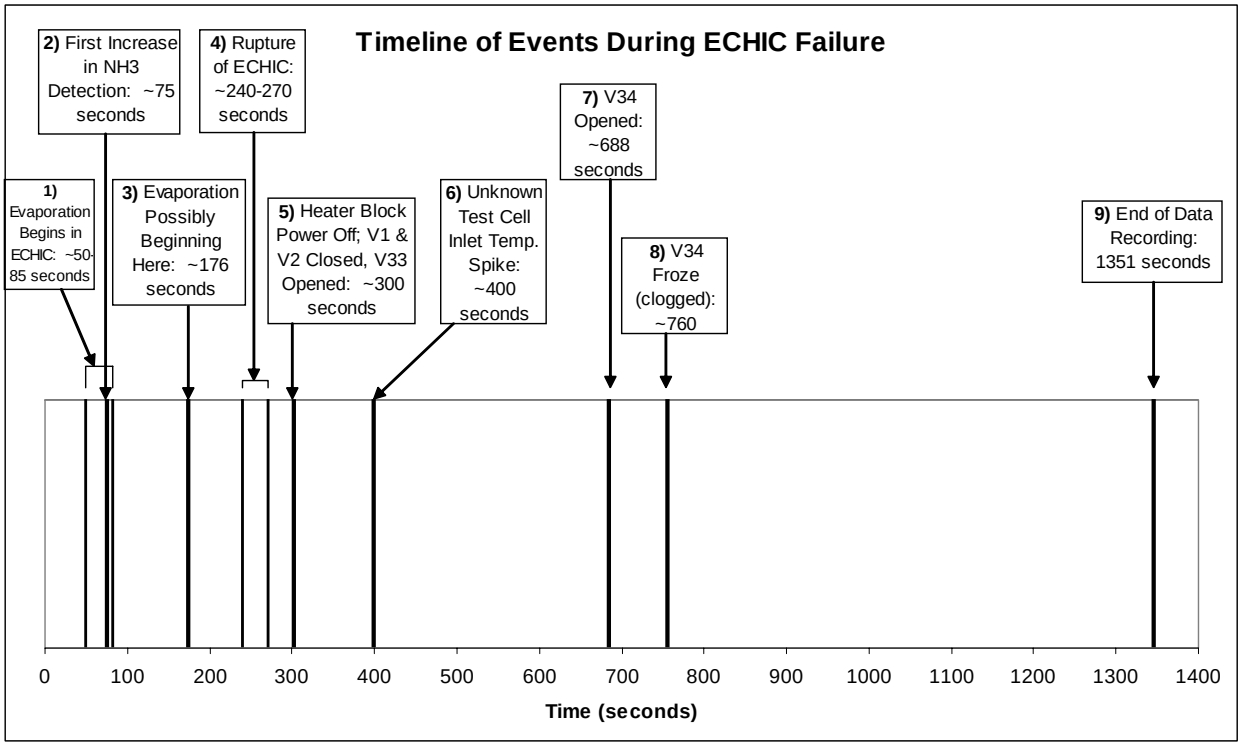

Figure D.24 Timeline of Events During ECHIC Failure

Figure D.24 shows the timeline of events during the testing when the ECHIC failed. These events are the major ones that, for the most part, affected the entire ammonia loop in one form or another. Each of these events are shown by more than one of the plots that have been previously analyzed. There are many other smaller, more local events that these previously analyzed plots show as well, however, many of them are relatively insignificant and/or their cause is **unknown**. A list of the plots that each of these events corresponds to is listed below.

Events and Corresponding Plots (Figures)

1) Figure D.2, D.12, D.21, & D.22
2) Figure 20
3) Figure 16 & 18
4) Figure D.2, D.4, D.6, D.10, D.12, D.16, & D.18
5) Figure D.19
6) Figure D.4 & D.22
7) Figure D.2 definitely, there are also other hints of this in almost every other plot
8) Figure D.2
9) Every Figure

APPENDIX E IR IMAGE ANALYSIS

IR Camera Operation

Storing an Image:

Make sure IR camera (FSI FLIR Systems Prism DS) is on and warmed up.

Make sure PCMCIA flash memory card is in slot in camera

When ready to record an image (refer to camera instruction manual for correct setup of camera) push the “STORE” button on the outside of the IR camera

Remove the PCMCIA flash memory card from the camera

Place it in a laptop computer with a PCMCIA slot

Transfer the IR image from the PCMCIA card to a 3.5” floppy disk

Use the 3.5” floppy disk to transfer the IR image to a computer with the correct software to analyze the image (Irwin OLE 1.1 in this case)

IR Image Analysis

Find Distance Between Pixels:

Open Irwin OLE 1.1 and the screen in Figure E.1 will be seen.

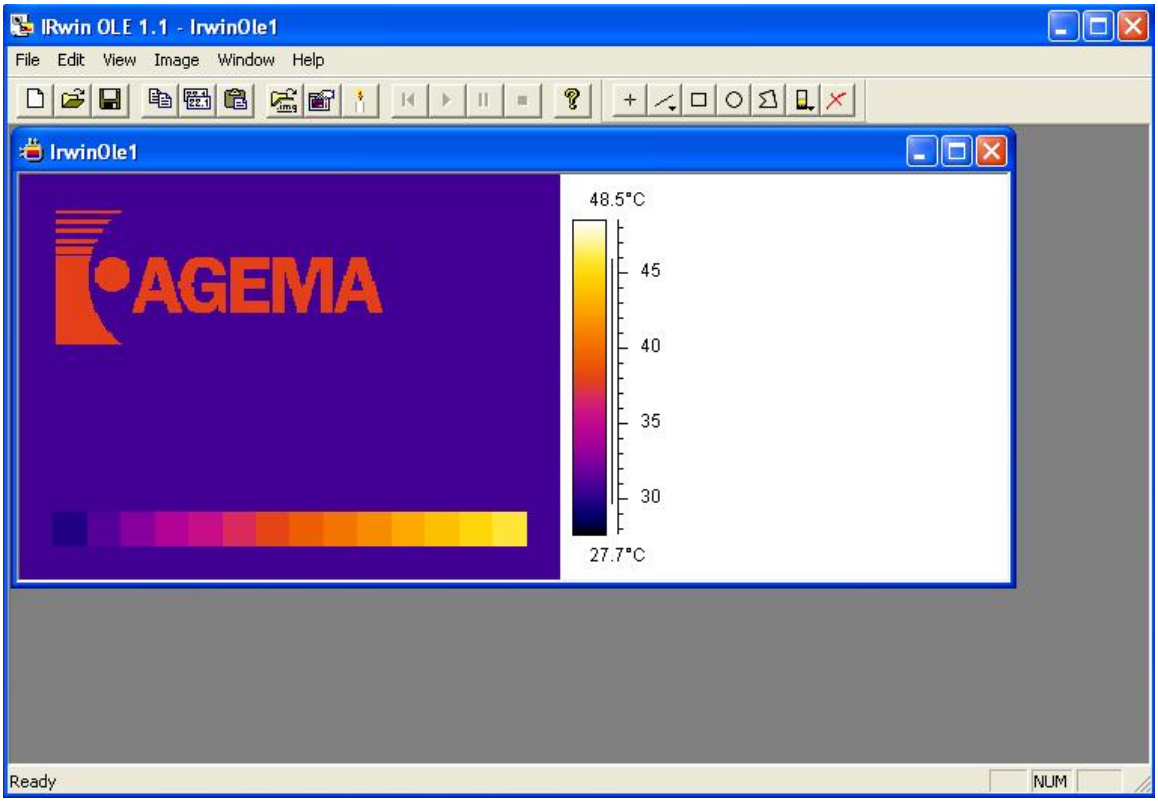

Figure E.2: IRwin OLE 1.1 Opening Screen

Under the Image Menu: select “Open…” as shown in FIGURE E.2 and a window called “Open Image” will pop up.

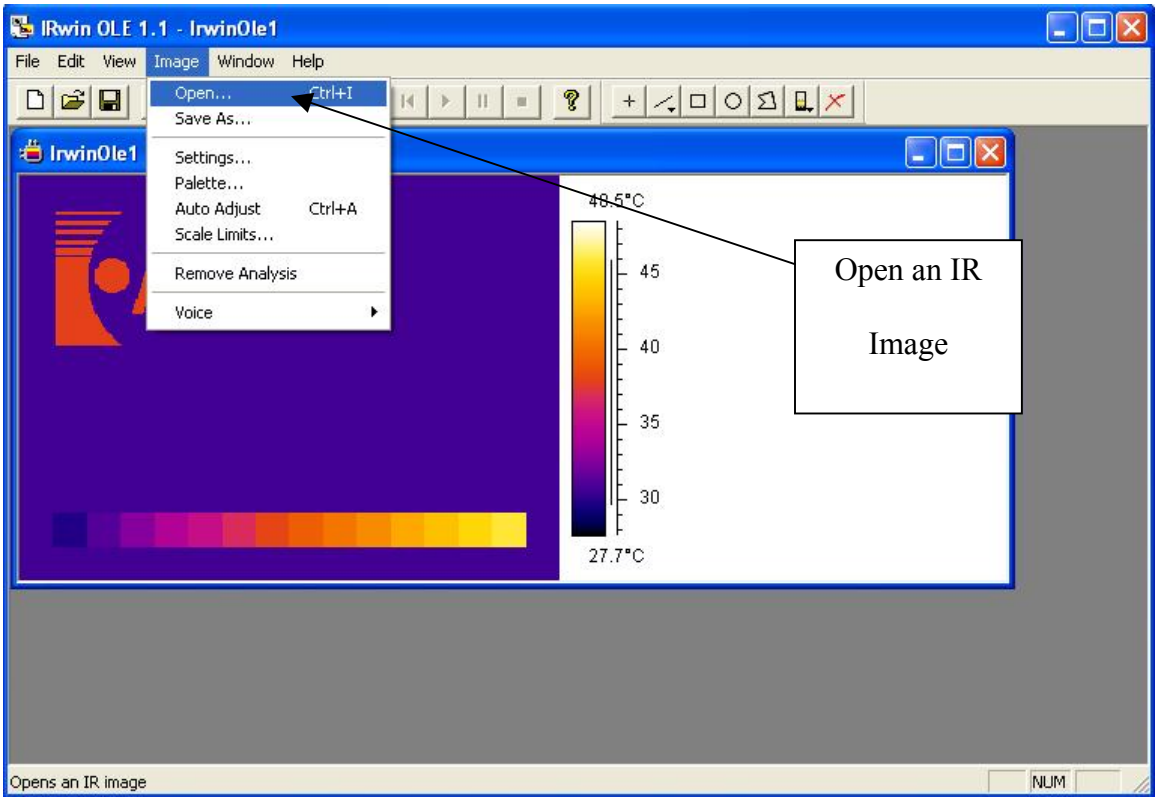

Figure E.3: Opening an Image in IRwin OLE 1.1

In the "Open Image" window click on the "…" button as shown in FIGURE E.3 and find the folder where the IR image is saved at. The file should end with ".ana" as seen in FIGURE E.3.

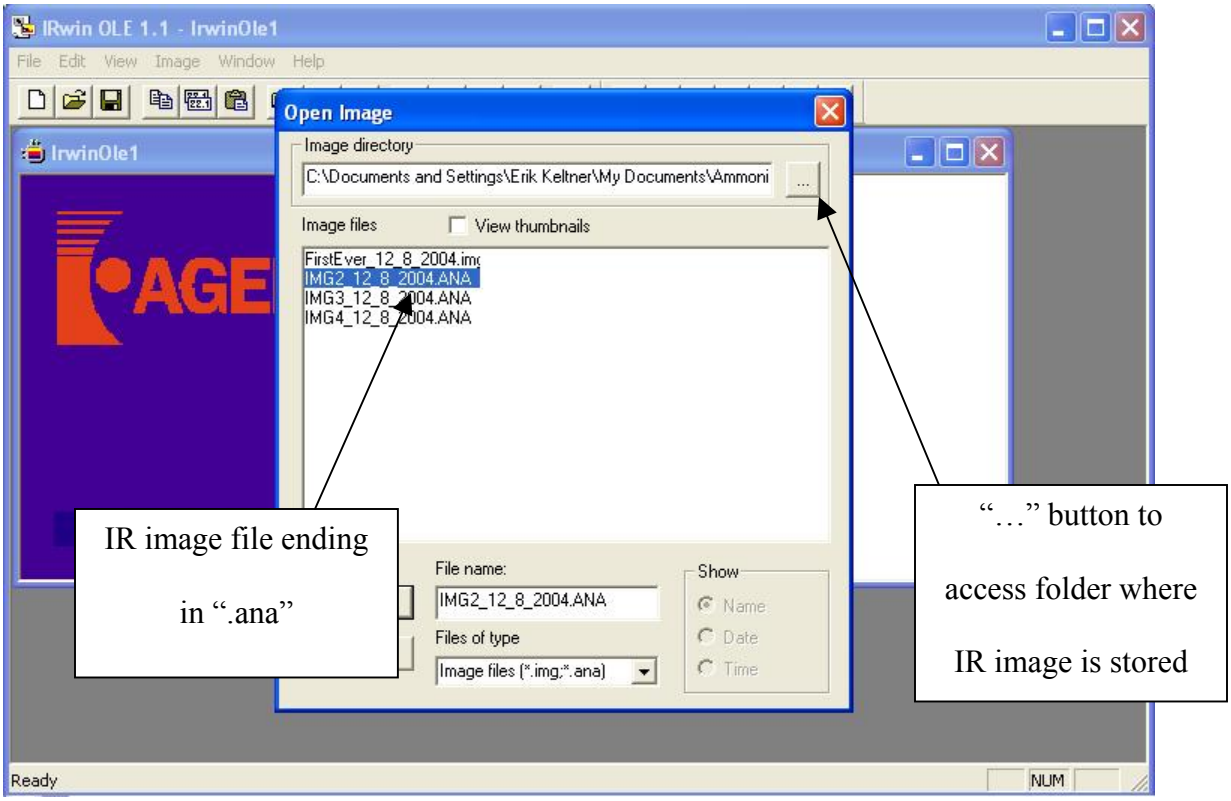

Figure E.4: Opening an Image in IRwin OLE 1.1

Open the file by clicking "OK" and now the screen should have an IR image appear as shown in FIGURE E.4.

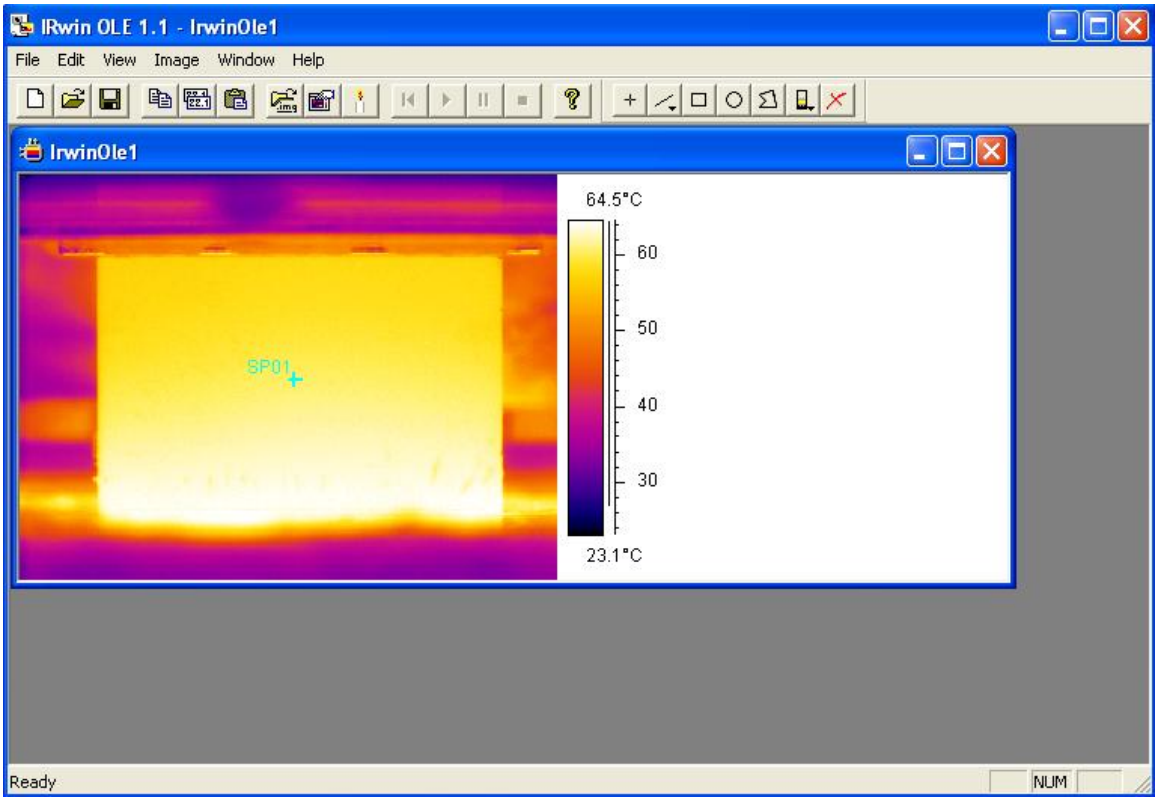

Figure E.5: Example IR Image

Click on the "Line or Cursor" button on the image toolbar as shown in FIGURE E.5.

Draw a line across a known distance based on dramatic color changes in the image (the line will be a turquoise color) as shown in FIGURE E.5.

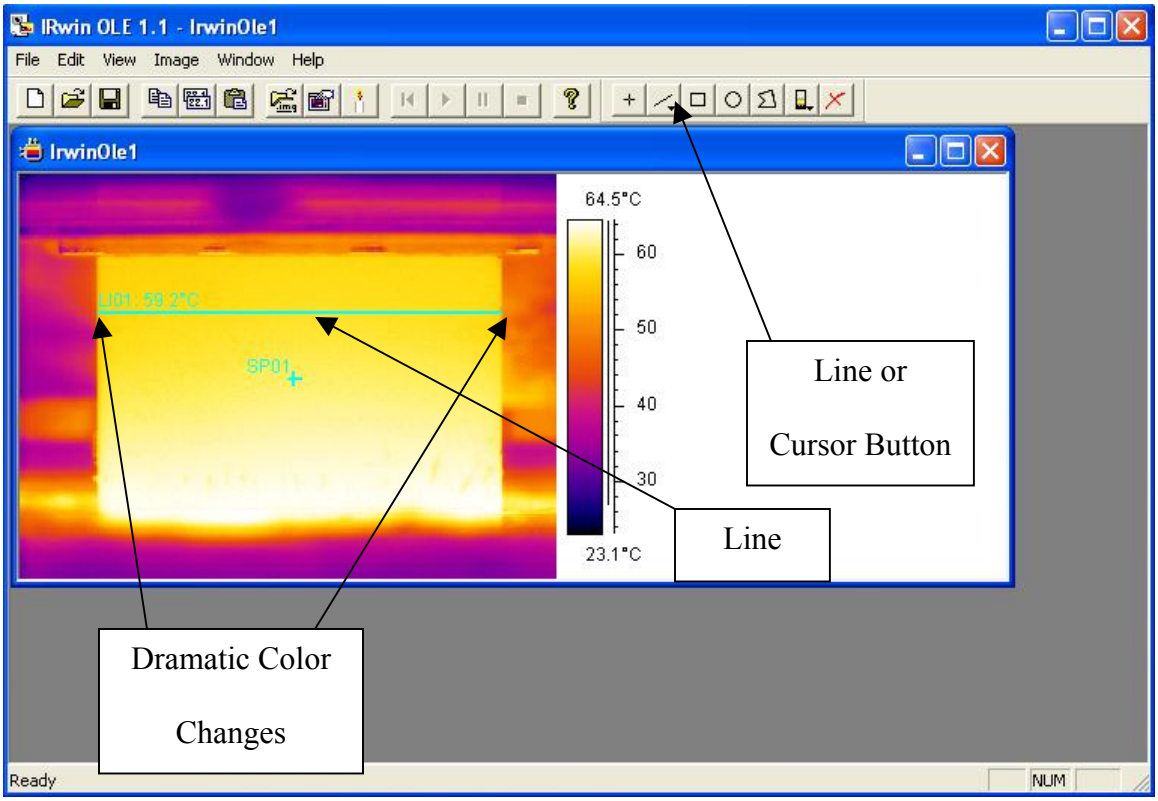

Figure E.6: Line Created on Example IR Image

Save the file.

Select the line (it should turn white).

Click on the "Copy Value" button shown in FIGURE E.6. A new window called "Copy Value" will now pop up.

Select "Line" as the object as shown in FIGURE E.6.

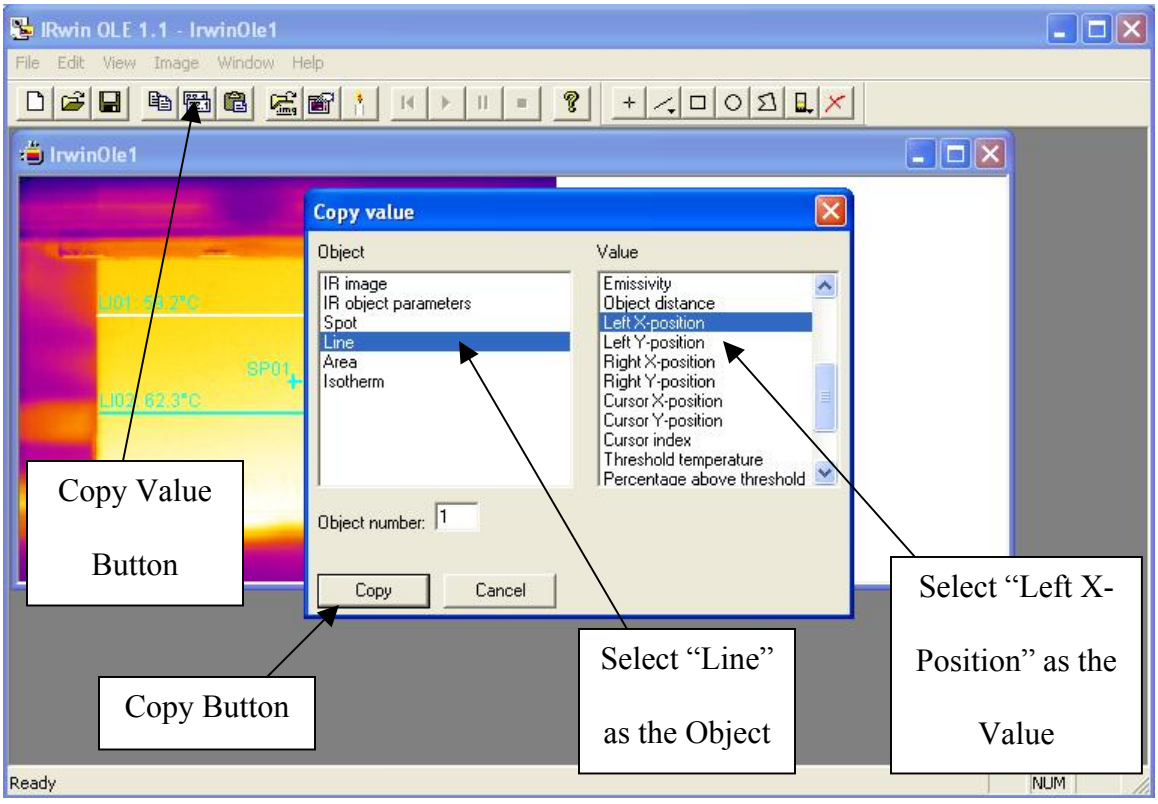

Figure E.7: Copying Left X-Position Value from Line in Example IR Image

Select "Left X-position" as the value as shown in FIGURE E.6.

Click on the "Copy" button as shown in FIGURE E.6.

Open Microsoft Excel

Paste the Left X-position of the line into the Excel file as shown in FIGURE E.7.

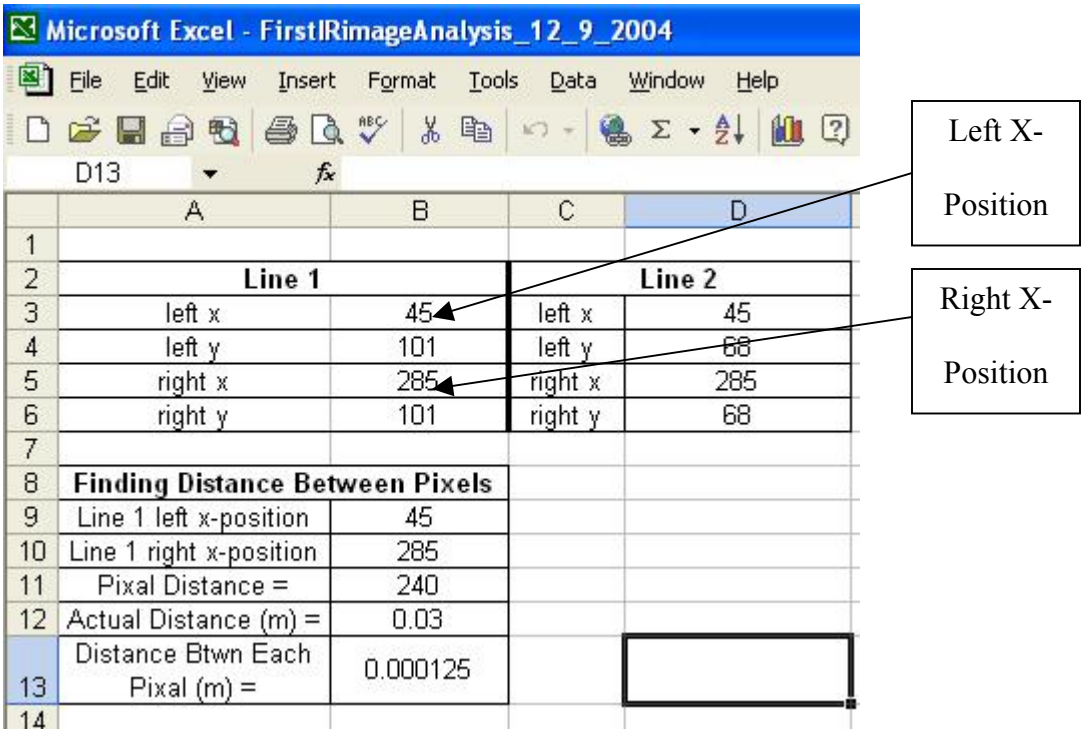

	A	B	C	D
1				
2	**Line 1**		**Line 2**	
3	left x	45	left x	45
4	left y	101	left y	68
5	right x	285	right x	285
6	right y	101	right y	68
7				
8	**Finding Distance Between Pixels**			
9	Line 1 left x-position	45		
10	Line 1 right x-position	285		
11	Pixal Distance =	240		
12	Actual Distance (m) =	0.03		
13	Distance Btwn Each Pixal (m) =	0.000125		
14				

Figure E.8: Copied Line Values from Example IR Image Pasted in Microsoft Excel

Go Back to Irwin OLE 1.1, click on the "Copy Value" button again

Select "Line" as the object as shown in FIGURE E.6 again.

Select "Right X-position" as the value.

Click on the "Copy" button again.

Paste the Right X-position of the line into the Excel file as shown in FIGURE E.7.

Repeat this copy and paste process for the left "y" and right "y" positions. These two values are found in order to confirm that the line is straight. These values are shown in FIGURE E.7 as well.

Using the left and right X-positions and the known, actual distance of the line, the distance between each pixel can be found by dividing the known length in the direction the line was drawn by the number of pixels in between that length. An example of the numbers representing this is also shown in FIGURE E.7 in the table labeled "Finding Distance Between Pixels".

Finding Temperatures Along a Line

Follow Steps 1-10 in the previous section of "Finding Distance Between Pixels."

Select "String Data" as the value as shown in FIGURE E.8.

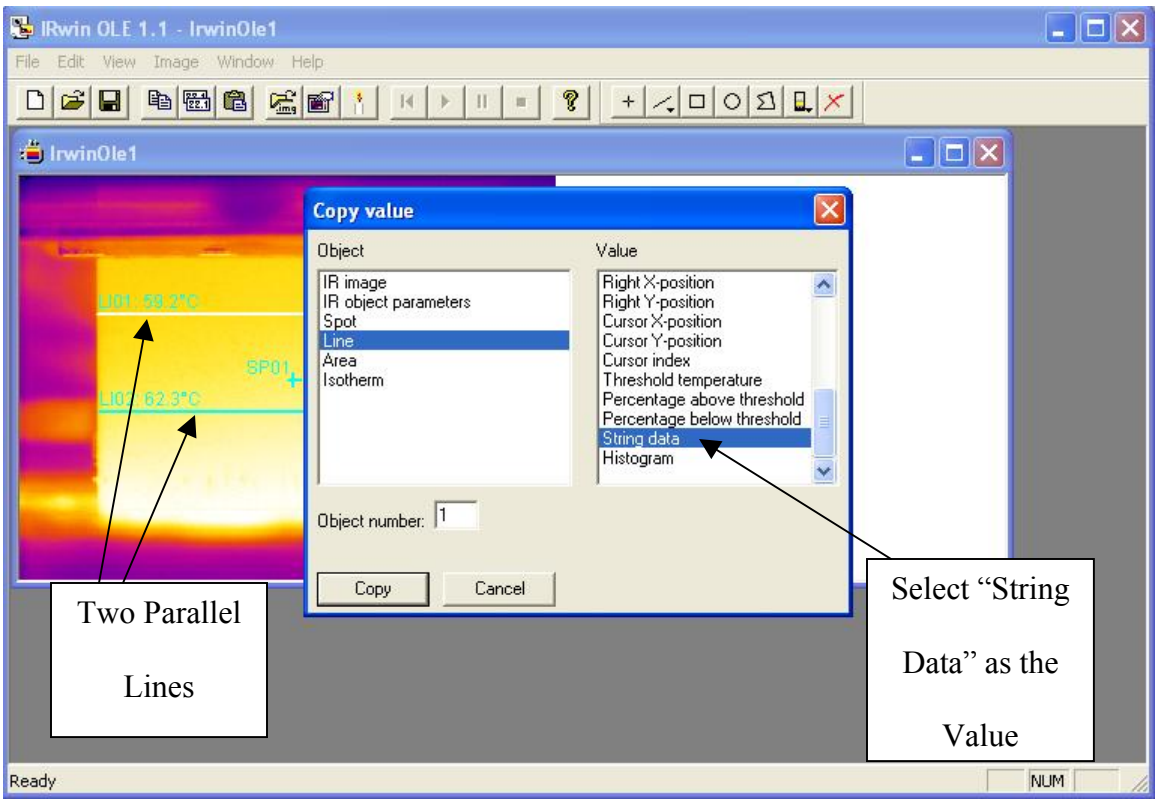

Figure E.9: Copying String Data Values from Line in Example IR Image

Click on “Copy”

Open Microsoft Excel

Paste the copied string data of the selected line in the Excel file. It should look something like what is shown in FIGURE E.9. The temperature value at each pixel along the selected line should appear in the Excel column where this data was pasted and the pixel numbers along that line correspond to each of these temperatures. The pixel numbers increase from left to right and top to bottom.

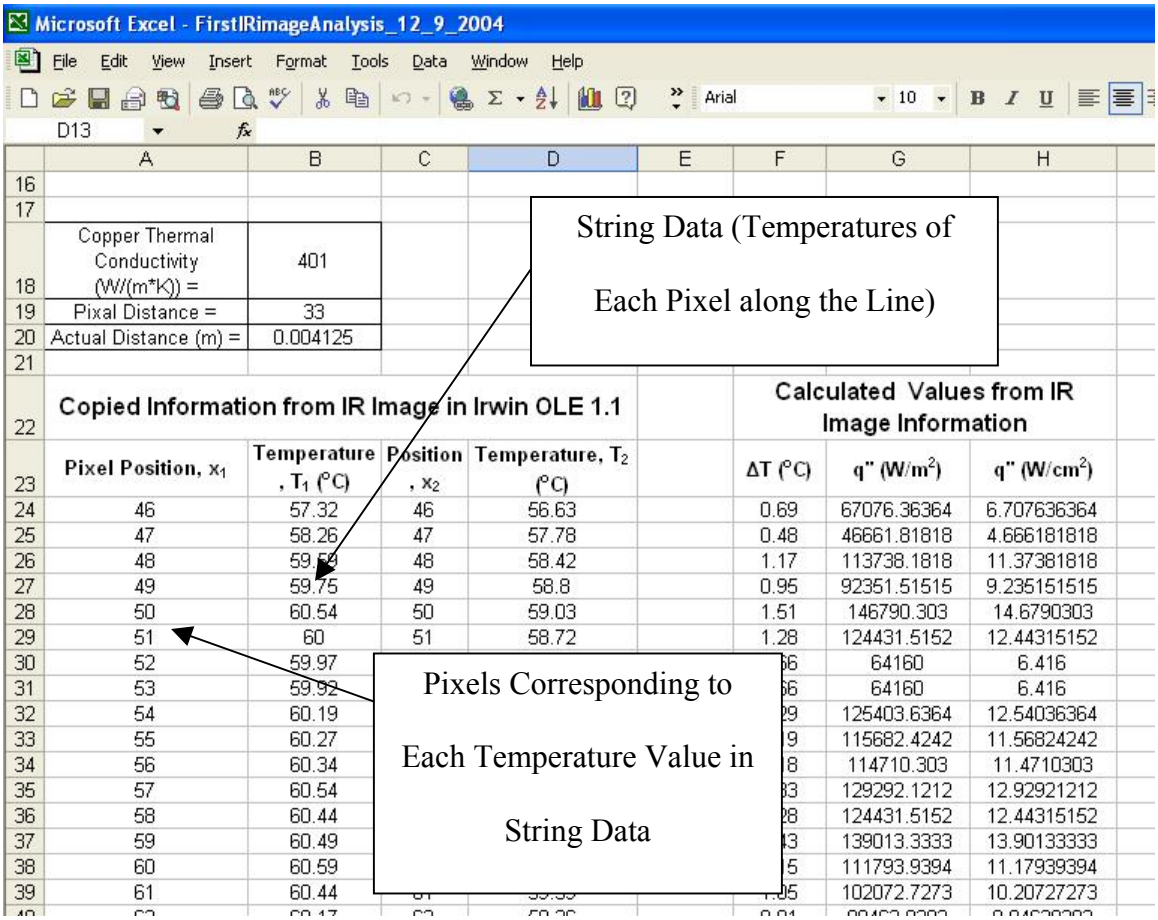

	A	B	C	D	E	F	G	H
16								
17								
18	Copper Thermal Conductivity (W/(m*K)) =	401						
19	Pixal Distance =	33						
20	Actual Distance (m) =	0.004125						
21								
22	Copied Information from IR Image in Irwin OLE 1.1					Calculated Values from IR Image Information		
23	Pixel Position, x_1	Temperature, T_1 (°C)	Position, x_2	Temperature, T_2 (°C)		ΔT (°C)	q" (W/m^2)	q" (W/cm^2)
24	46	57.32	46	56.63		0.69	67076.36364	6.707636364
25	47	58.26	47	57.78		0.48	46661.81818	4.666181818
26	48	59.59	48	58.42		1.17	113738.1818	11.37381818
27	49	59.75	49	58.8		0.95	92351.51515	9.235151515
28	50	60.54	50	59.03		1.51	146790.303	14.6790303
29	51	60	51	58.72		1.28	124431.5152	12.44315152
30	52	59.97				66	64160	6.416
31	53	59.92				66	64160	6.416
32	54	60.19				29	125403.6364	12.54036364
33	55	60.27				9	115682.4242	11.56824242
34	56	60.34				8	114710.303	11.4710303
35	57	60.54				33	129292.1212	12.92921212
36	58	60.44				28	124431.5152	12.44315152
37	59	60.49				13	139013.3333	13.90133333
38	60	60.59				5	111793.9394	11.17939394
39	61	60.44				05	102072.7273	10.20727273

Figure E.10: Pasted String Data from Example IR Image

Finding Heat Flux

Find the distance between each pixel (assuming it is the same in the "X" and "Y" directions). *See "Find Distance Between Pixels"*

Create two parallel lines, as seen in FIGURE E.8, which start and end at the same "X" or "Y" values depending on the direction of the lines (assuming they are vertical or horizontal only). For creating a line: *See "Find Distance Between Pixels"*

Find the temperature of each pixel within these two lines and paste this in Microsoft Excel as shown in FIGURE E.9. *See "Finding Temperatures Along a Line"*

Find the number of pixels that separate each temperature line. An example of the pasted positions of two horizontal lines in Microsoft Excel can be seen in FIGURE E.10.

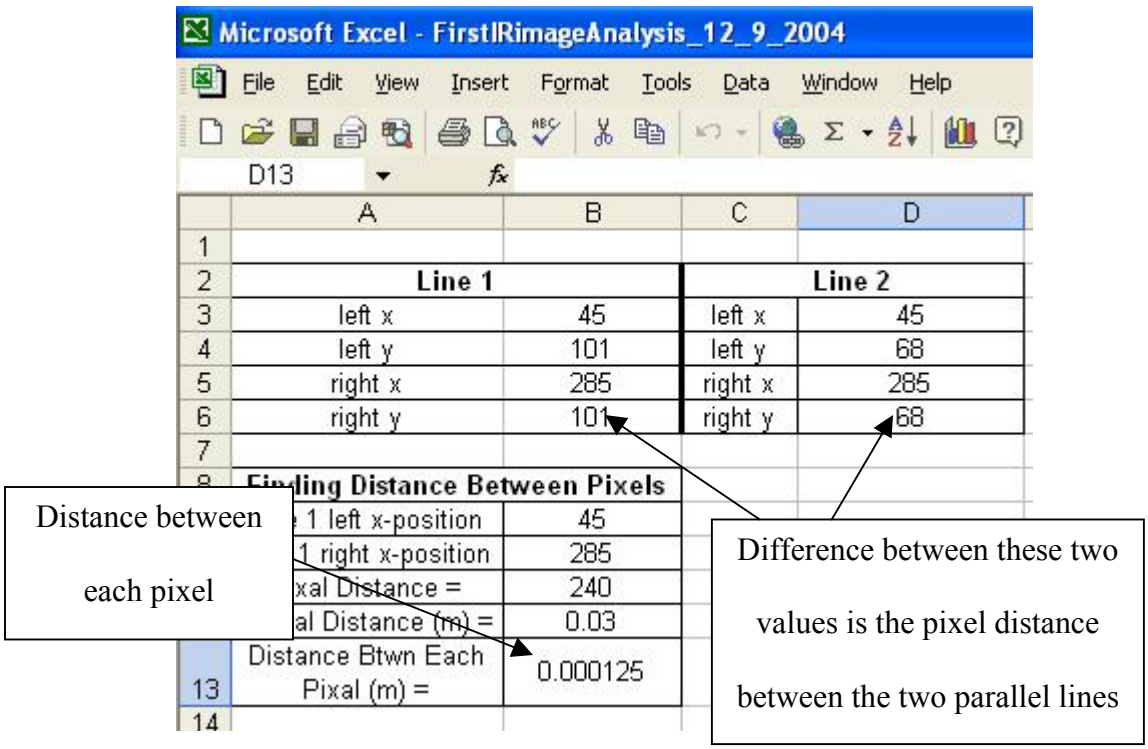

	A	B	C	D
1				
2	**Line 1**		**Line 2**	
3	left x	45	left x	45
4	left y	101	left y	68
5	right x	285	right x	285
6	right y	101	right y	68
7				
8	**Finding Distance Between Pixels**			
9	1 left x-position	45		
10	1 right x-position	285		
11	xal Distance =	240		
12	al Distance (m) =	0.03		
13	Distance Btwn Each Pixal (m) =	0.000125		
14				

Figure E.11: Copied Line Values from Example IR Image Pasted in Microsoft Excel

Find the actual distance between the lines by multiplying the number of pixels that separate these lines by the distance between each pixel. Both of these values can be seen in FIGURE E.10. This is the distance that will be used in the one-dimensional heat conduction equation to find the heat flux at each pixel along each of the temperature lines

Find the heat flux at each pixel along each of the temperature lines by using the following equation (one-dimensional heat conduction) for each pixel along both of the lines:

$$q'' = -k * [(T_1 - T_2) / (x_1 - x_2)]$$

"k" is the heat conduction coefficient of the material being considered

T_1 and T_2 are the temperatures at a certain pixel length along each line (this is represented by the "**ΔT (^{0}C)**" column in FIGURE E.9 under "Calculated Values from IR Image Information")

x_1 - x_2 is the actual distance between the lines, not the pixel distance (this value is constant and is found in step 5)

q" is the heat flux (represented by the "**q" (W/m^2)**" and "**q" (W/cm^2)**" columns in FIGURE E.9 under "Calculated Values from IR Image Information")

A plot of the heat flux values from left to right of the IR Image analyzed here can be seen in FIGURE E.11. The plot represents the data seen in FIGURE E.9.

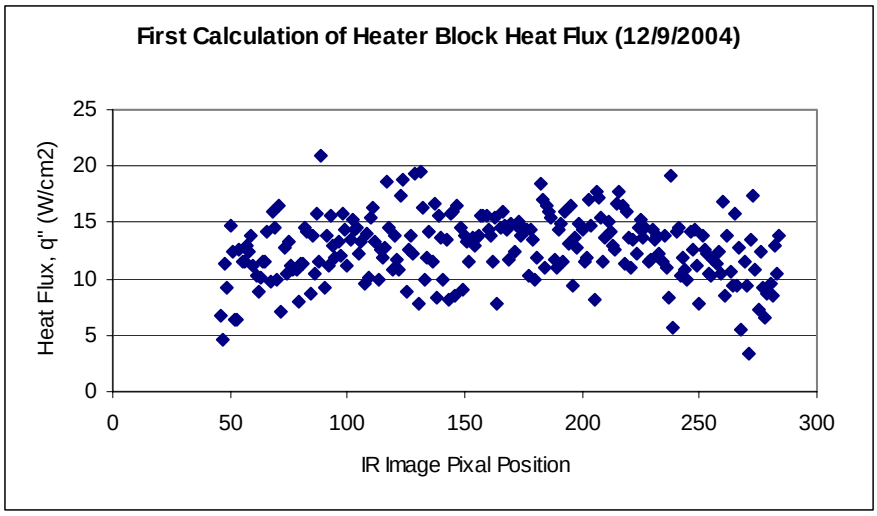

Figure E.12: Plot of Heat Flux from Left to Right of Analyzed IR Image

APPENDIX F MEASURED DATA

The representative transient measured data for each test performed with the Slot Jet is shown here. This representative data consists of six plots for each test. The first plot shows mass flow rate. The second plot shows Slot Jet fluid temperatures. The third plot shows the system pressures. The fourth plot shows the outside Slot Jet surface temperatures. The fifth plot shows the two heater neck temperatures used to find the heat flux through the heater block neck and into the Slot Jet. The sixth and final plot shows the heater block neck heat flux and the energy input.

The order of the tests shown will be from lowest to highest nominal pressure, then from lowest to highest nominal mass flow rate, and then from lowest to highest nominal energy input.

310 kPa, 15 degC Subcooled, 0.01 kg/s, 100 watt

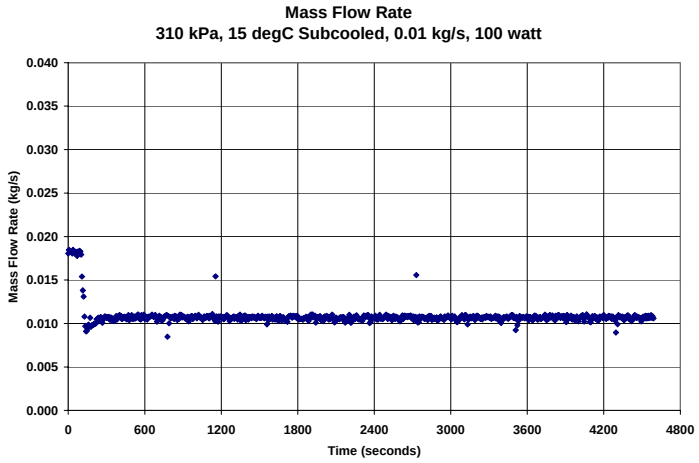

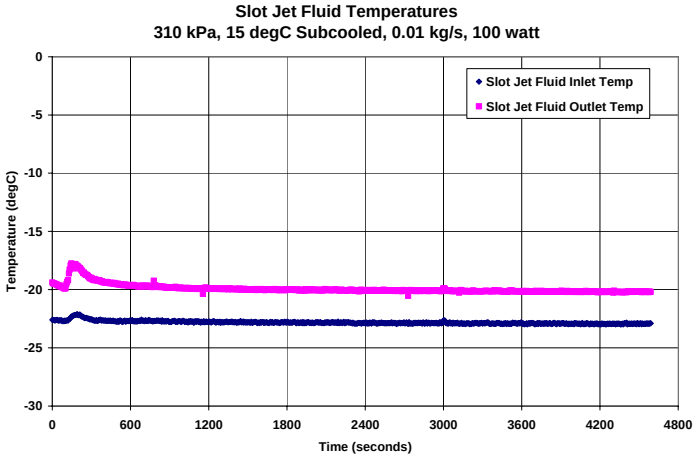

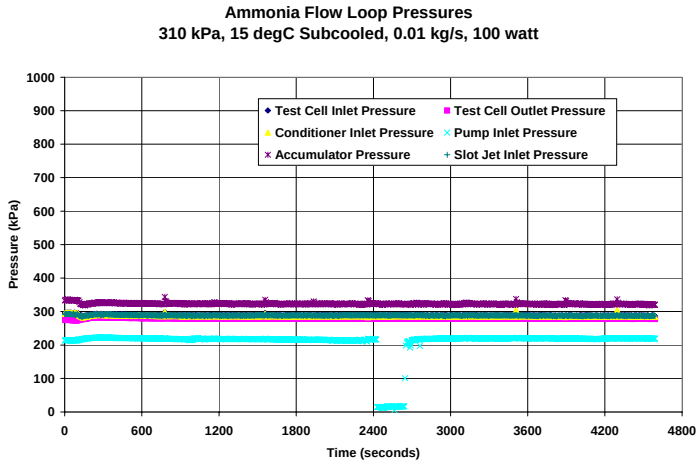

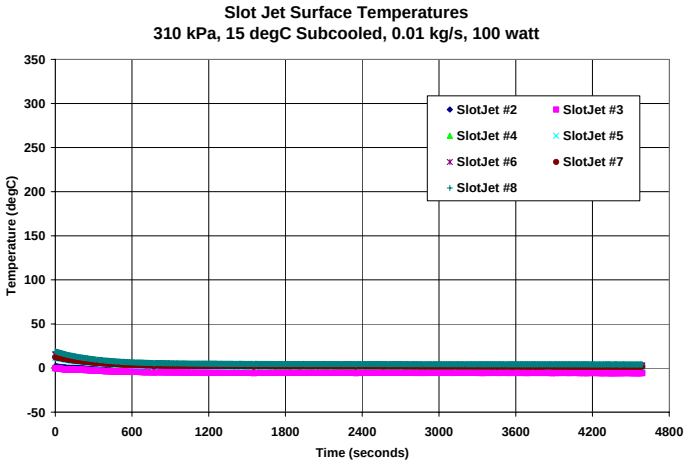

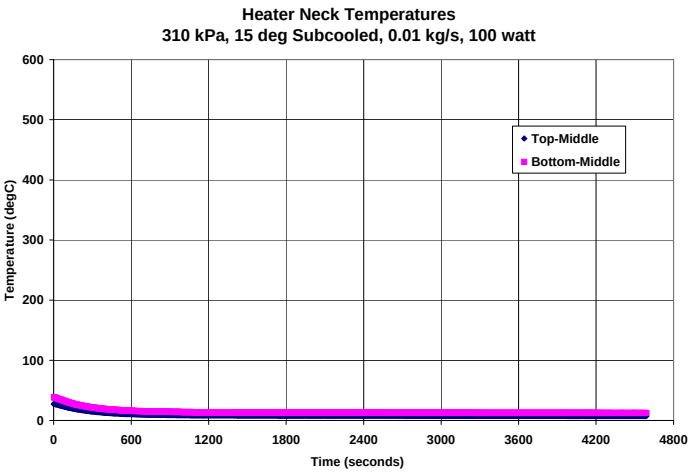

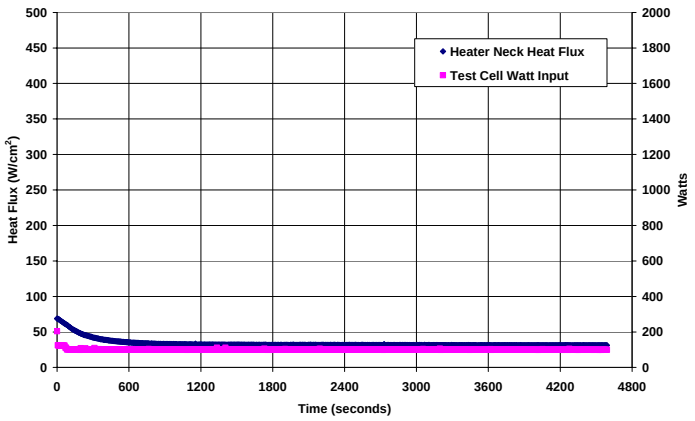

310 kPa, 15 degC Subcooled, 0.01 kg/s, 200 watt

Mass Flow Rate
310 kPa, 15 degC Subcooled, 0.01 kg/s, 200 watt

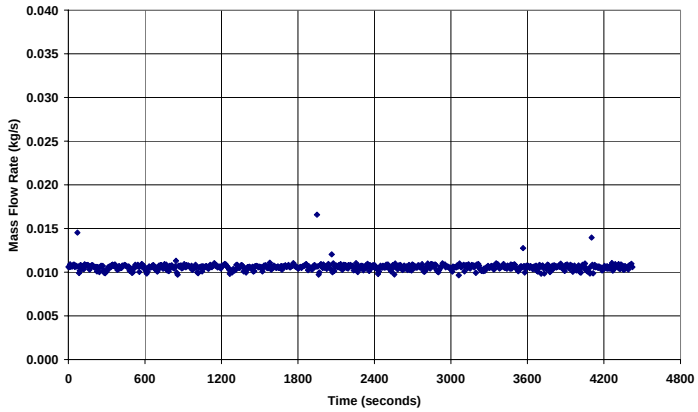

Slot Jet Fluid Temperatures
310 kPa, 15 degC Subcooled, 0.01 kg/s, 200 watt

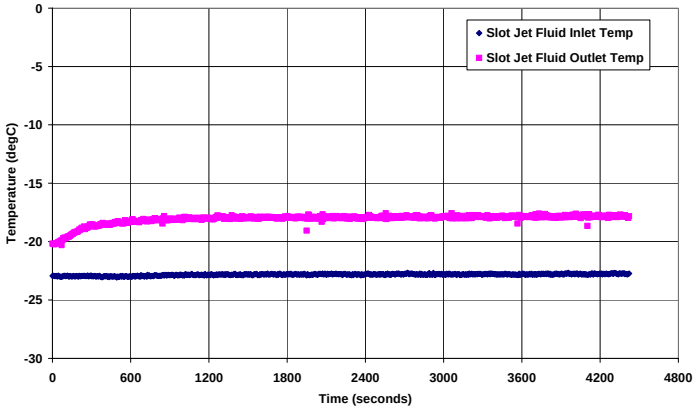

Ammonia Flow Loop Pressures
310 kPa, 15 degC Subcooled, 0.01 kg/s, 200 watt

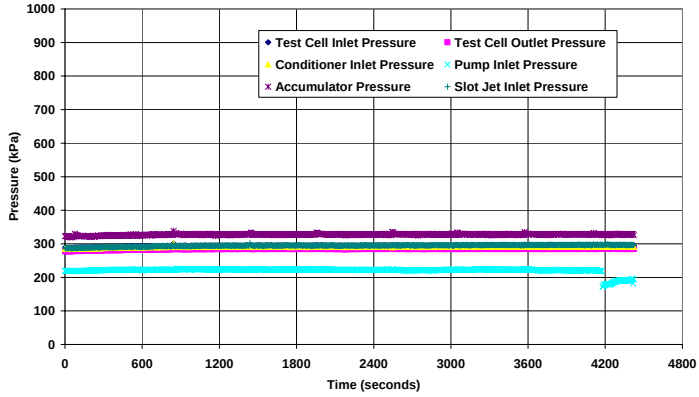

Slot Jet Surface Temperatures
310 kPa, 15 degC Subcooled, 0.01 kg/s, 200 watt

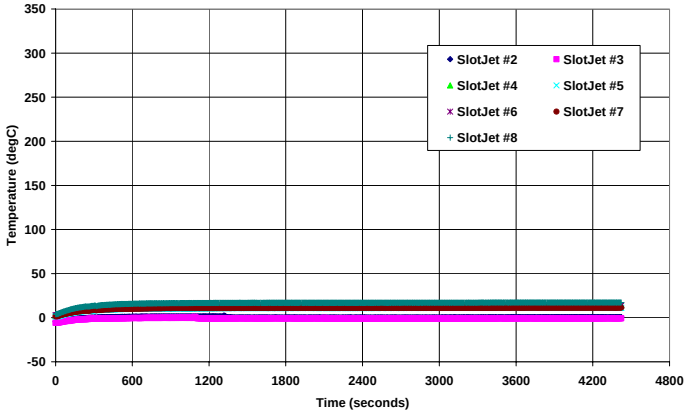

Heater Neck Temperatures
310 kPa, 15 deg Subcooled, 0.01 kg/s, 200 watt

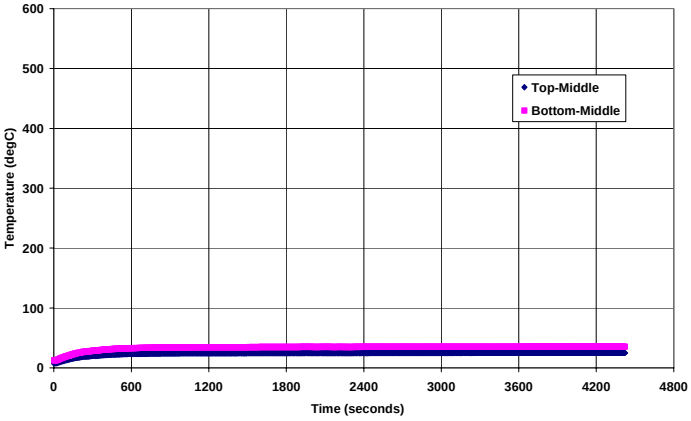

Heater Neck Heat Flux & Test Cell Watt Input
310 kPa, 15 degC Subcooled, 0.01 kg/s, 200 watt

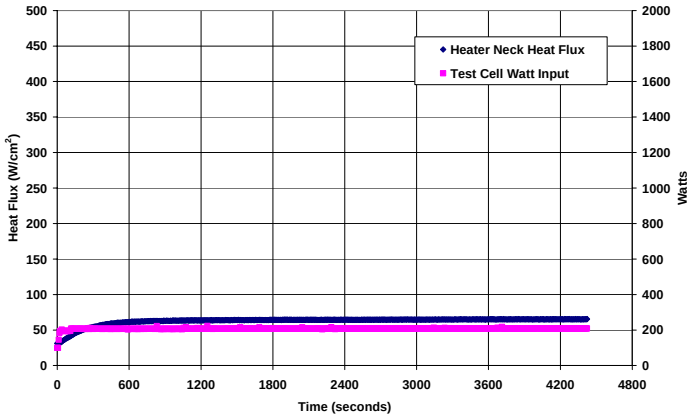

310 kPa, 15 degC Subcooled, 0.01 kg/s, 300 watt

Mass Flow Rate
310 kPa, 15 degC Subcooled, 0.01 kg/s, 300 watt

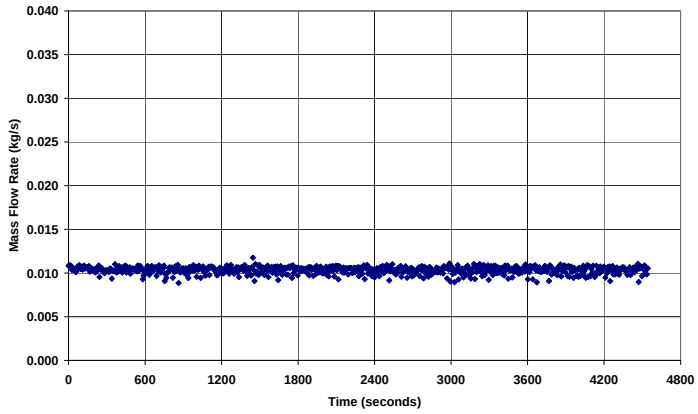

Slot Jet Fluid Temperatures
310 kPa, 15 degC Subcooled, 0.01 kg/s, 300 watt

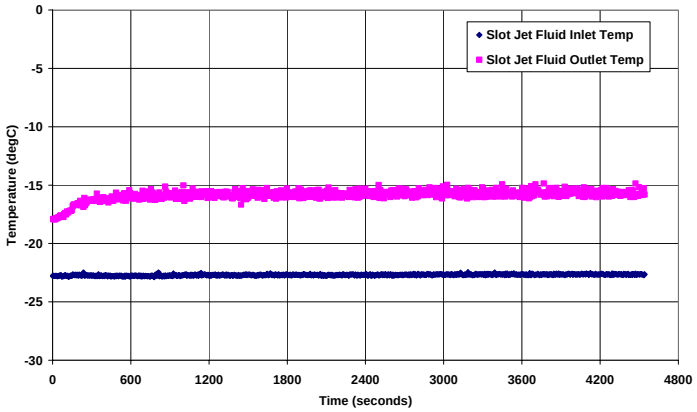

Ammonia Flow Loop Pressures
310 kPa, 15 degC Subcooled, 0.01 kg/s, 300 watt

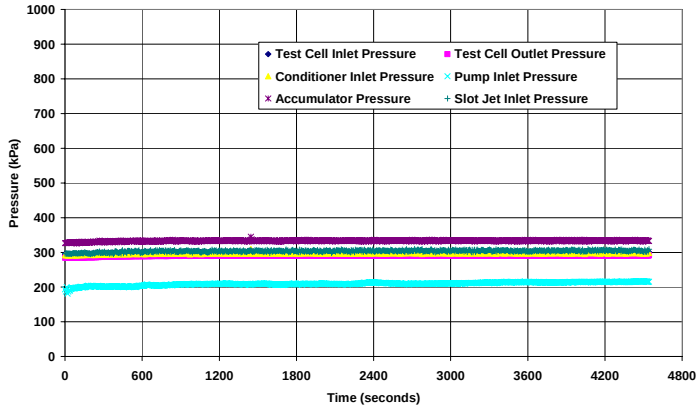

Slot Jet Surface Temperatures
310 kPa, 15 degC Subcooled, 0.01 kg/s, 300 watt

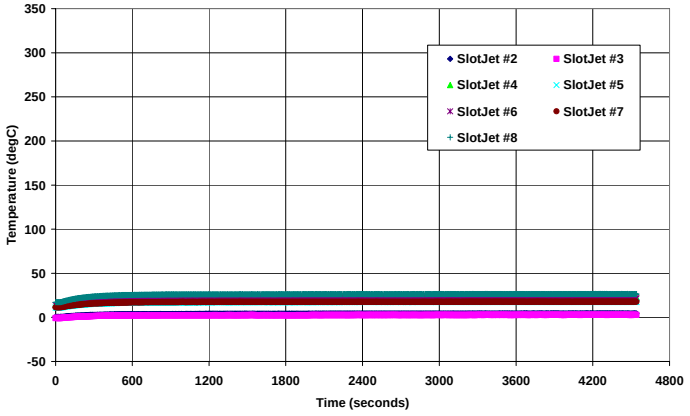

Heater Neck Temperatures
310 kPa, 15 deg Subcooled, 0.01 kg/s, 300 watt

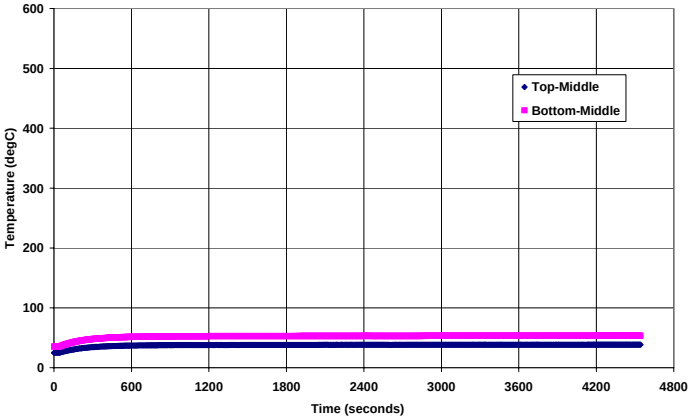

Heater Neck Heat Flux & Test Cell Watt Input
310 kPa, 15 degC Subcooled, 0.01 kg/s, 300 watt

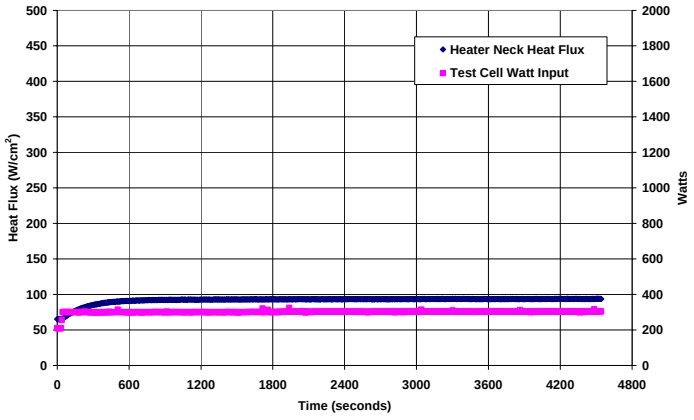

310 kPa, 15 degC Subcooled, 0.01 kg/s, 400 watt

Mass Flow Rate
310 kPa, 15 degC Subcooled, 0.01 kg/s, 400 watt

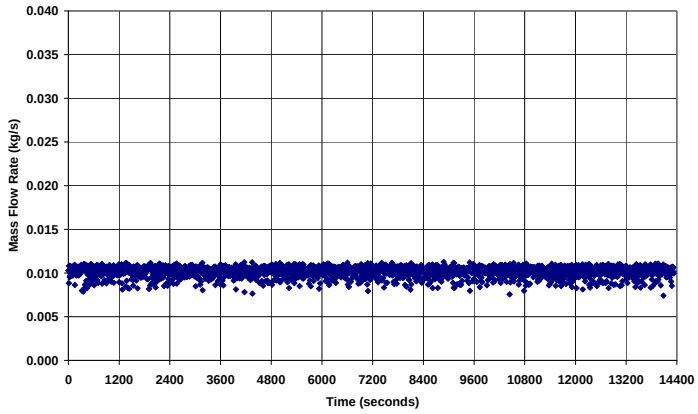

Slot Jet Fluid Temperatures
310 kPa, 15 degC Subcooled, 0.01 kg/s, 400 watt

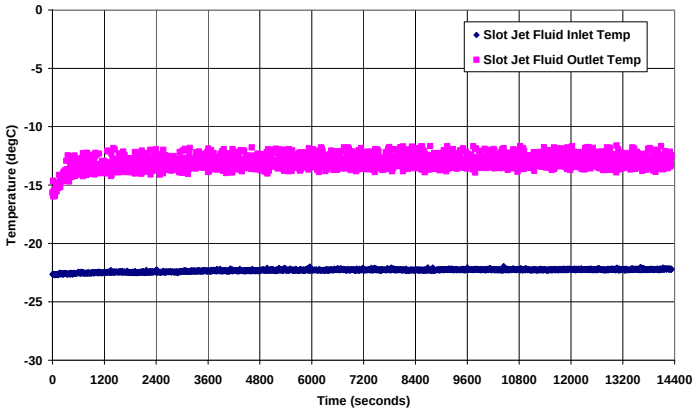

Ammonia Flow Loop Pressures
310 kPa, 15 degC Subcooled, 0.01 kg/s, 400 watt

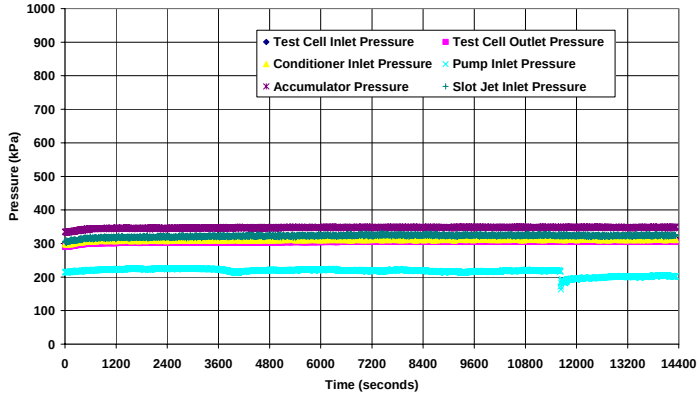

Slot Jet Surface Temperatures
310 kPa, 15 degC Subcooled, 0.01 kg/s, 400 watt

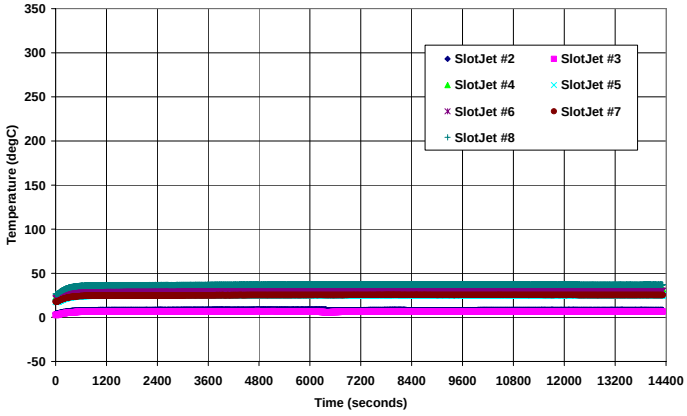

Heater Neck Temperatures
310 kPa, 15 deg Subcooled, 0.01 kg/s, 400 watt

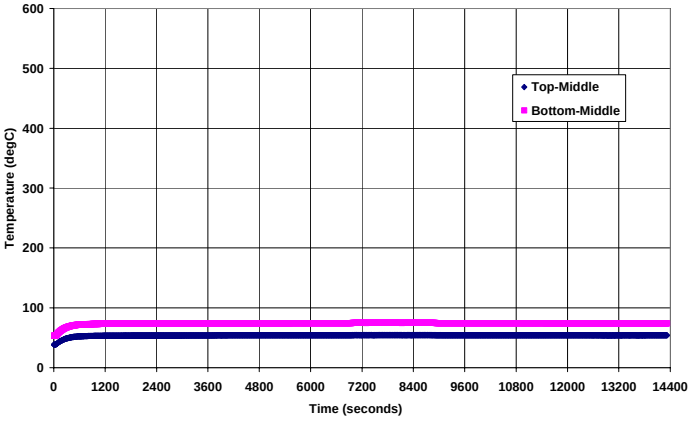

Heater Neck Heat Flux & Test Cell Watt Input
310 kPa, 15 degC Subcooled, 0.01 kg/s, 400 watt

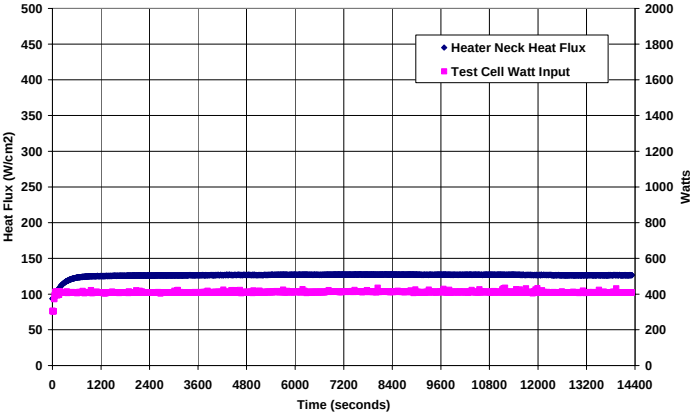

310 kPa, 15 degC Subcooled, 0.01 kg/s, 500 watt

Mass Flow Rate
310 kPa, 15 degC Subcooled, 0.01 kg/s, 500 watt

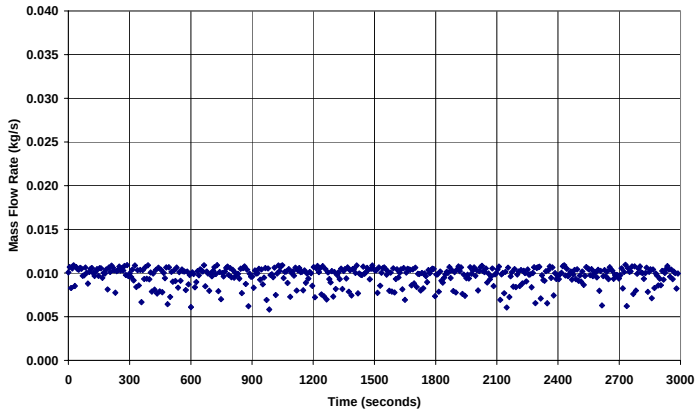

Slot Jet Fluid Temperatures
310 kPa, 15 degC Subcooled, 0.01 kg/s, 500 watt

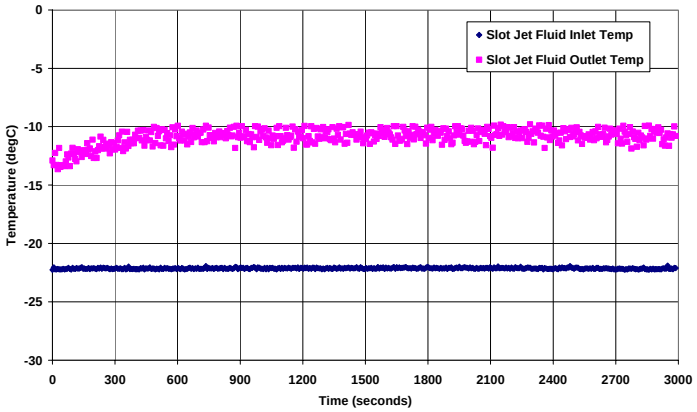

Ammonia Flow Loop Pressures
310 kPa, 15 degC Subcooled, 0.01 kg/s, 500 watt

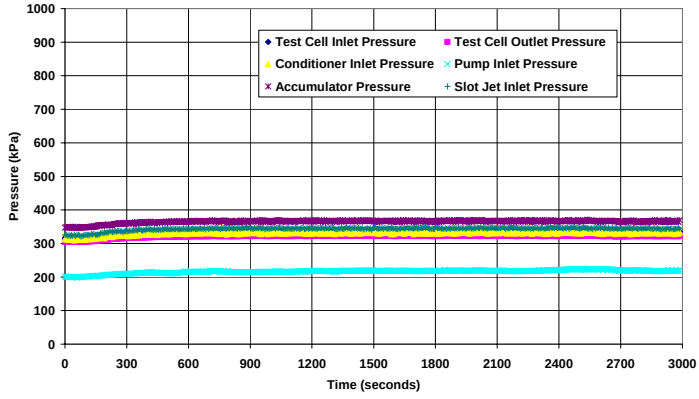

Slot Jet Surface Temperatures
310 kPa, 15 degC Subcooled, 0.01 kg/s, 500 watt

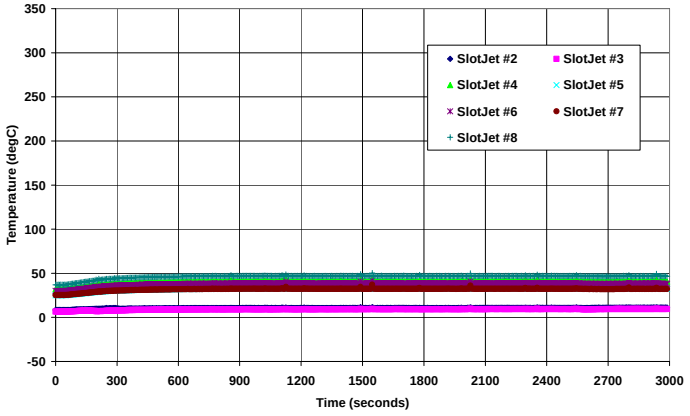

Heater Neck Temperatures
310 kPa, 15 deg Subcooled, 0.01 kg/s, 500 watt

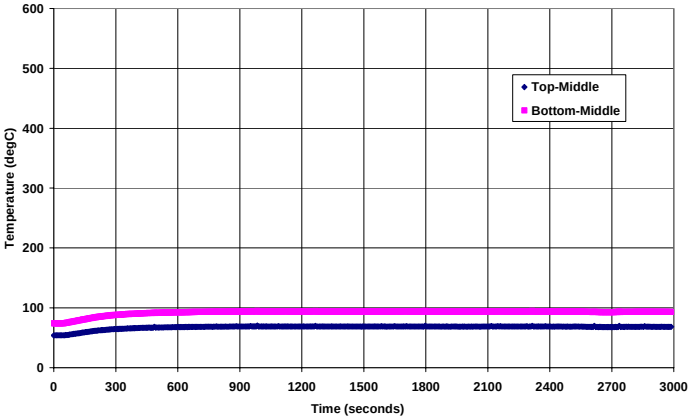

Heater Neck Heat Flux & Test Cell Watt Input
310 kPa, 15 degC Subcooled, 0.01 kg/s, 500 watt

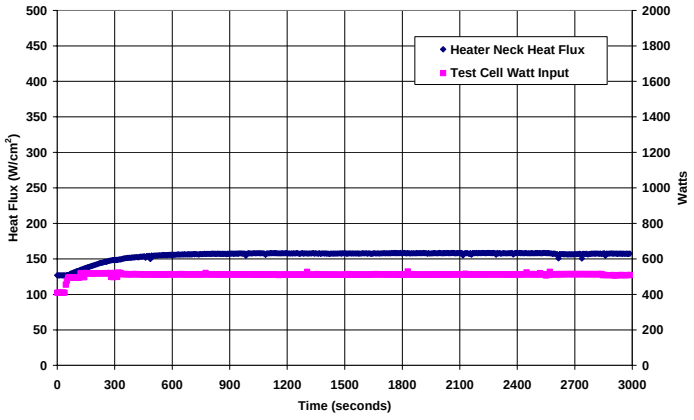

310 kPa, 15 degC Subcooled, 0.01 kg/s, 550 watt

Mass Flow Rate
310 kPa, 15 degC Subcooled, 0.01 kg/s, 550 watt

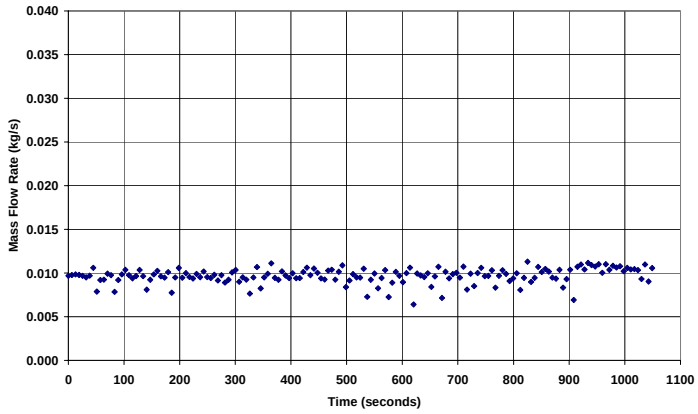

Slot Jet Fluid Temperatures
310 kPa, 15 degC Subcooled, 0.01 kg/s, 550 watt

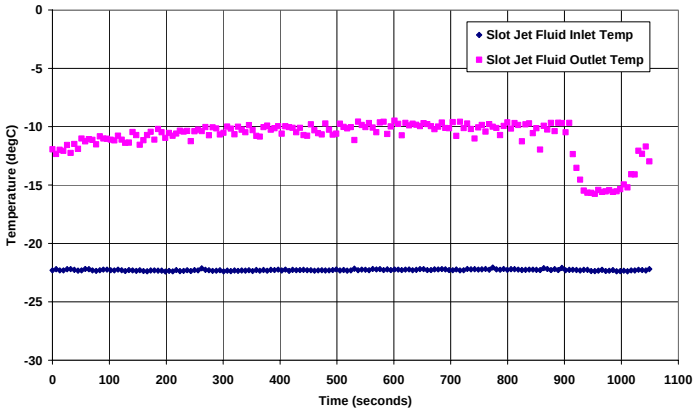

Ammonia Flow Loop Pressures
310 kPa, 15 degC Subcooled, 0.01 kg/s, 550 watt

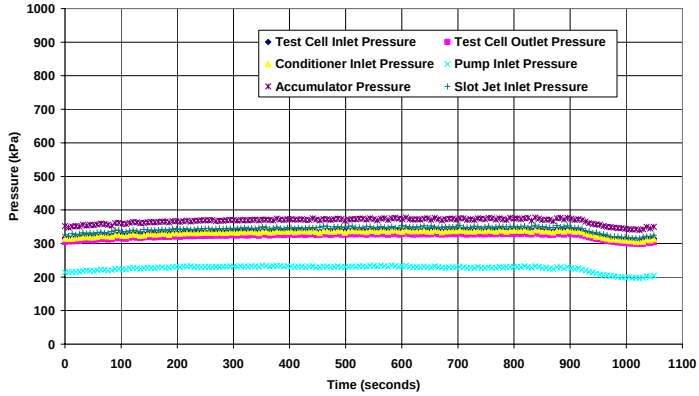

Slot Jet Surface Temperatures
310 kPa, 15 degC Subcooled, 0.01 kg/s, 550 watt

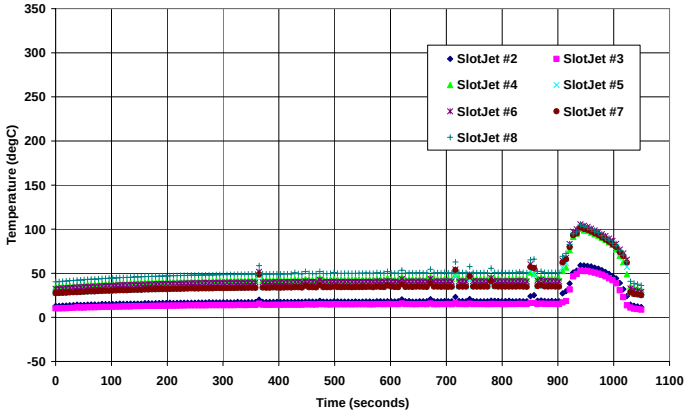

Heater Neck Temperatures
310 kPa, 15 deg Subcooled, 0.01 kg/s, 550 watt

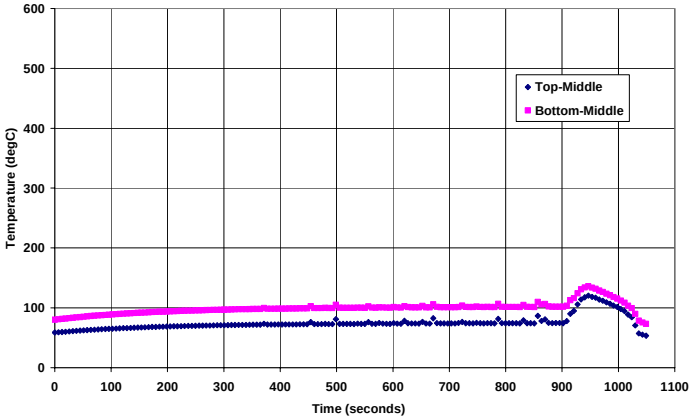

Heater Neck Heat Flux & Test Cell Watt Input
310 kPa, 15 degC Subcooled, 0.01 kg/s, 550 watt

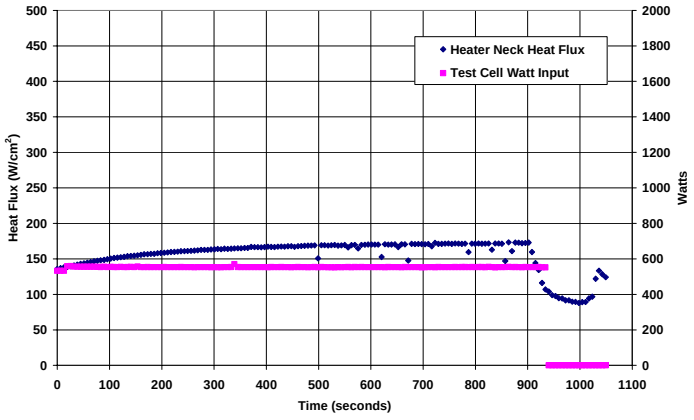

310 kPa, 15 degC Subcooled, 0.01 kg/s, 600 watt

Mass Flow Rate
310 kPa, 15 degC Subcooled, 0.01 kg/s, 600 watt

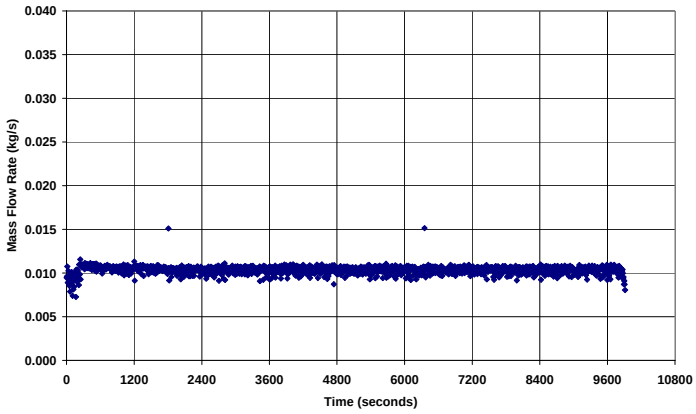

Slot Jet Fluid Temperatures
310 kPa, 15 degC Subcooled, 0.01 kg/s, 600 watt

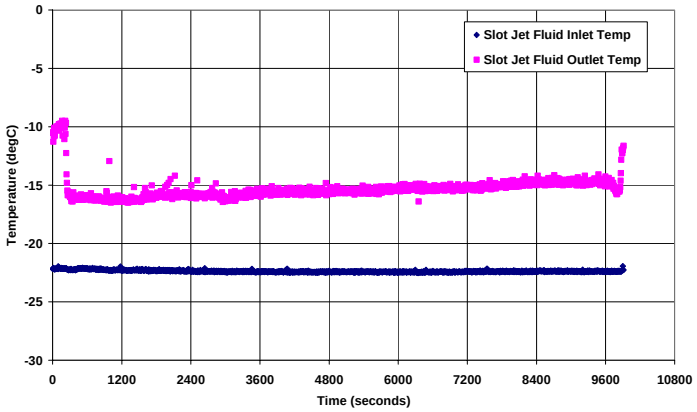

Ammonia Flow Loop Pressures
310 kPa, 15 degC Subcooled, 0.01 kg/s, 600 watt

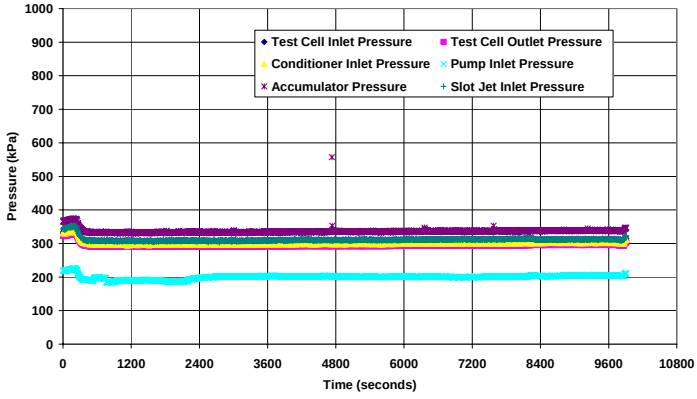

Slot Jet Surface Temperatures
310 kPa, 15 degC Subcooled, 0.01 kg/s, 600 watt

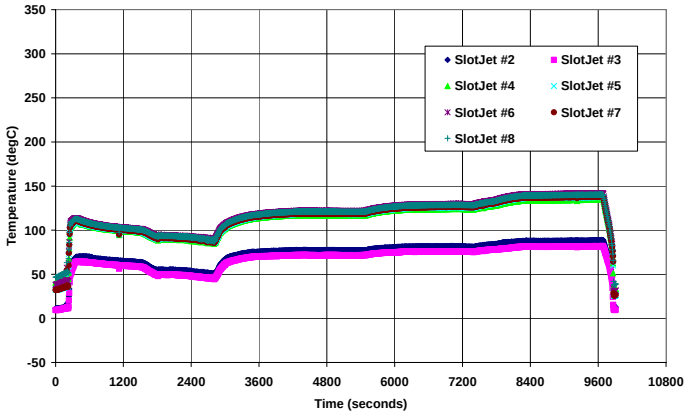

Heater Neck Temperatures
310 kPa, 15 deg Subcooled, 0.01 kg/s, 600 watt

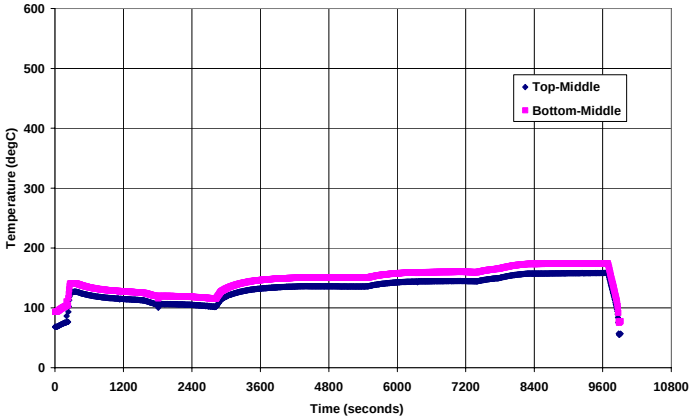

Heater Neck Heat Flux & Test Cell Watt Input
310 kPa, 15 degC Subcooled, 0.01 kg/s, 600 watt

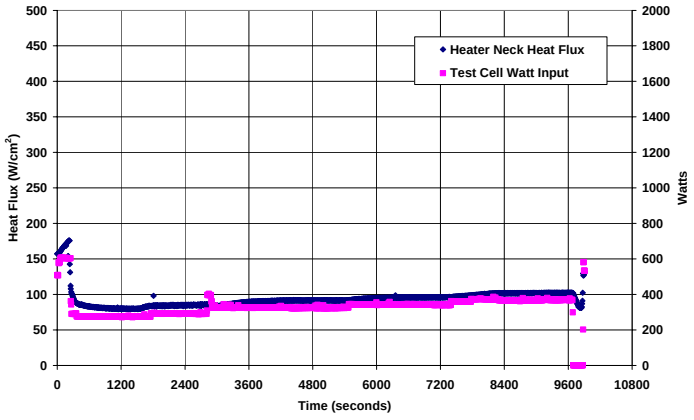

310 kPa, 15 degC Subcooled, 0.017 kg/s, 50 watt #1

Mass Flow Rate
310 kPa, 15 degC Subcooled, 0.017 kg/s, 50 watt #1

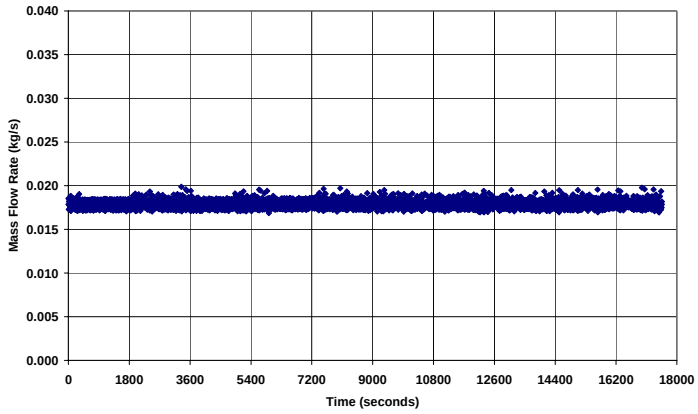

Slot Jet Fluid Temperatures
310 kPa, 15 degC Subcooled, 0.017 kg/s, 50 watt #1

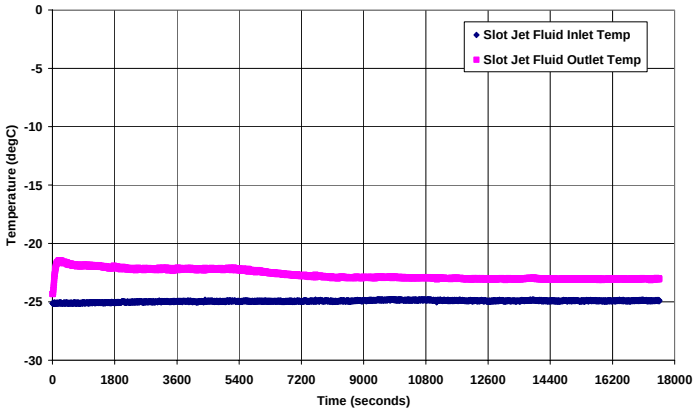

Ammonia Flow Loop Pressures
310 kPa, 15 degC Subcooled, 0.017 kg/s, 50 watt #1

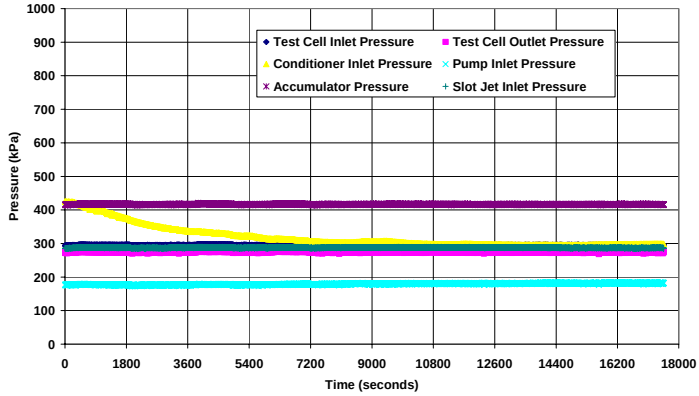

Slot Jet Surface Temperatures
310 kPa, 15 degC Subcooled, 0.017 kg/s, 50 watt #1

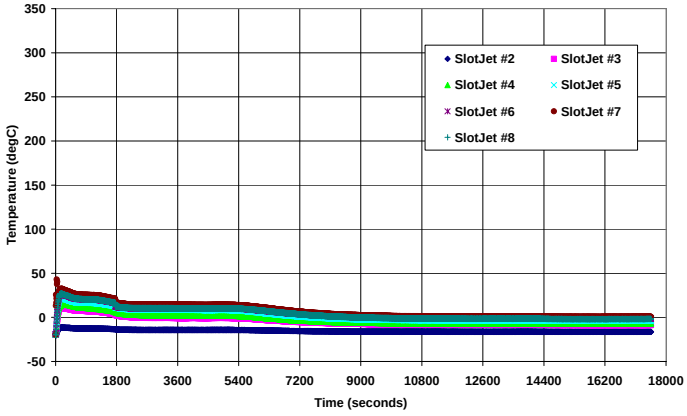

Heater Neck Temperatures
310 kPa, 15 deg Subcooled, 0.017 kg/s, 50 watt #1

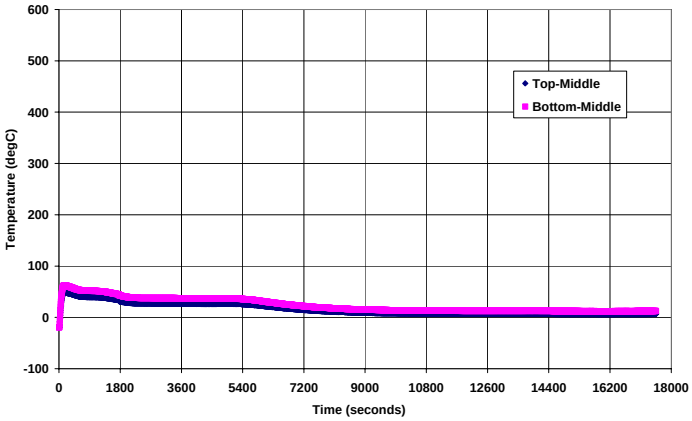

Heater Neck Heat Flux & Test Cell Watt Input
310 kPa, 15 degC Subcooled, 0.017 kg/s, 50 watt #1

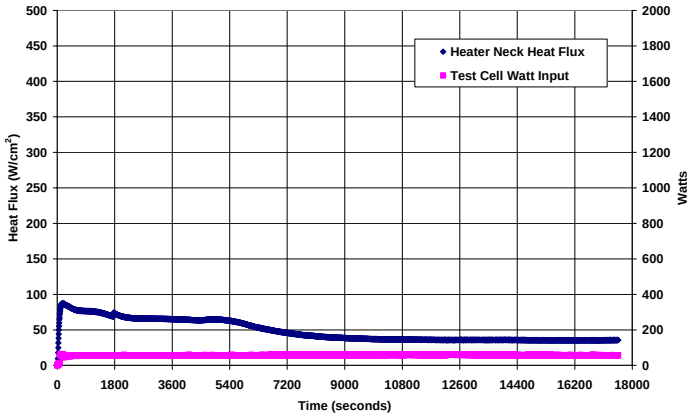

310 kPa, 15 degC Subcooled, 0.017 kg/s, 100 watt #1

Mass Flow Rate
310 kPa, 15 degC Subcooled, 0.017 kg/s, 100 watt #1

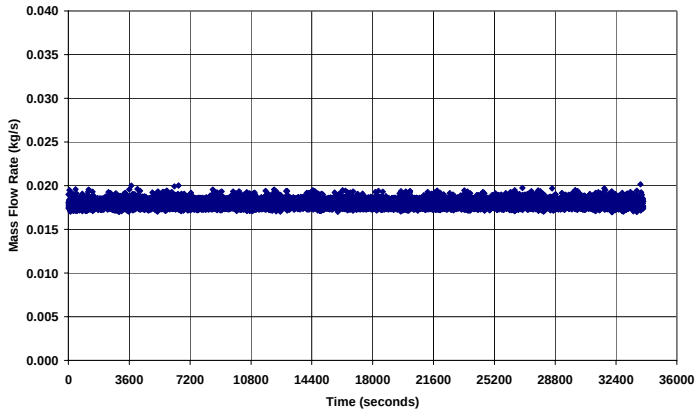

Slot Jet Fluid Temperatures
310 kPa, 15 degC Subcooled, 0.017 kg/s, 100 watt #1

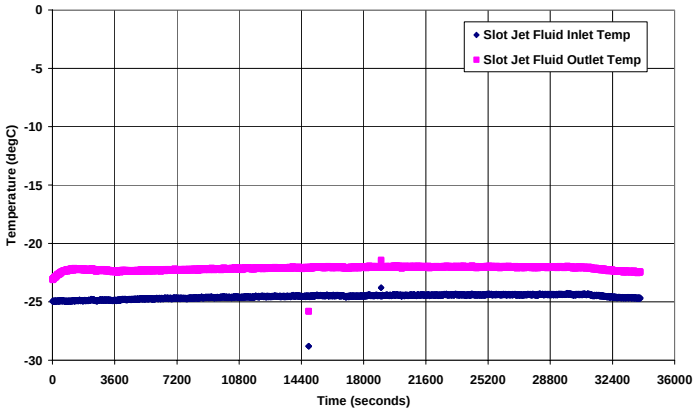

Ammonia Flow Loop Pressures
310 kPa, 15 degC Subcooled, 0.017 kg/s, 100 watt #1

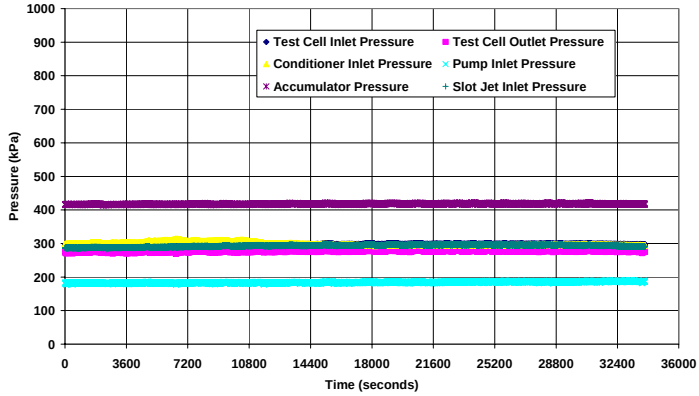

Slot Jet Surface Temperatures
310 kPa, 15 degC Subcooled, 0.017 kg/s, 100 watt #1

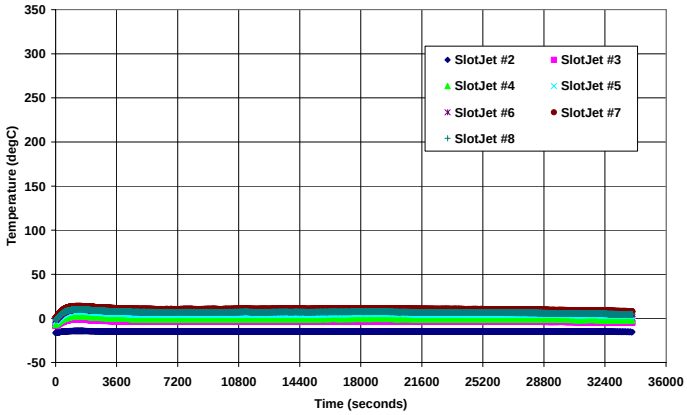

Heater Neck Temperatures
310 kPa, 15 deg Subcooled, 0.017 kg/s, 100 watt #1

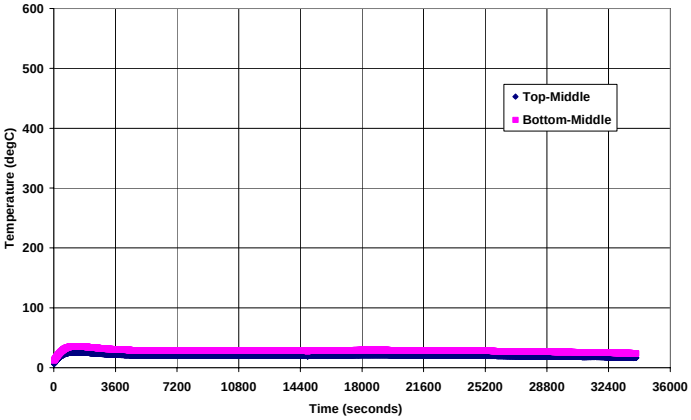

Heater Neck Heat Flux & Test Cell Watt Input
310 kPa, 15 degC Subcooled, 0.017 kg/s, 100 watt #1

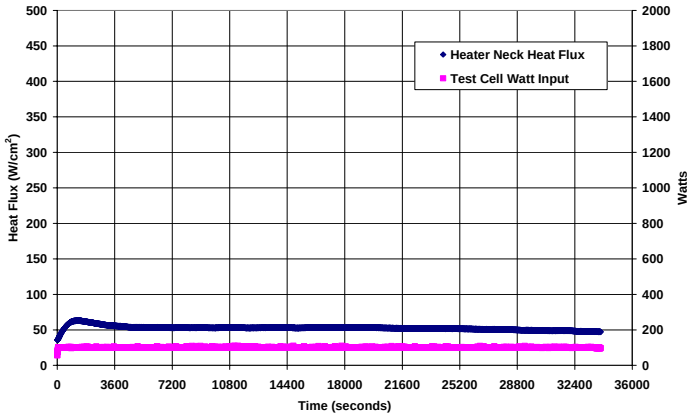

310 kPa, 15 degC Subcooled, 0.017 kg/s, 200 watt #1

Mass Flow Rate
310 kPa, 15 degC Subcooled, 0.017 kg/s, 200 watt #1

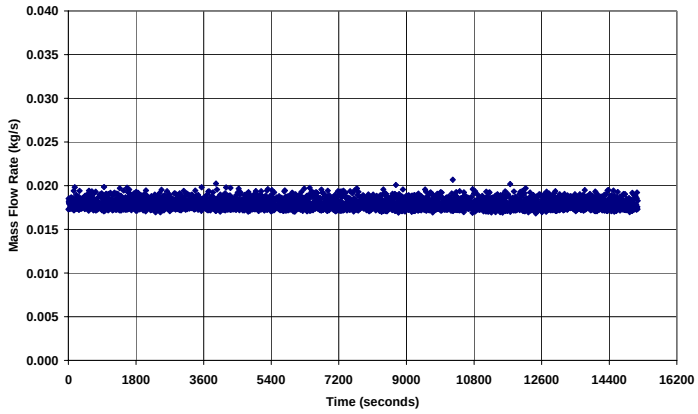

Slot Jet Fluid Temperatures
310 kPa, 15 degC Subcooled, 0.017 kg/s, 200 watt #1

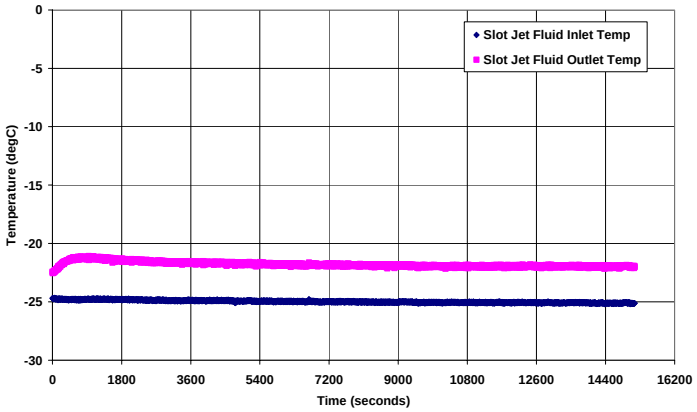

Ammonia Flow Loop Pressures
310 kPa, 15 degC Subcooled, 0.017 kg/s, 200 watt #1

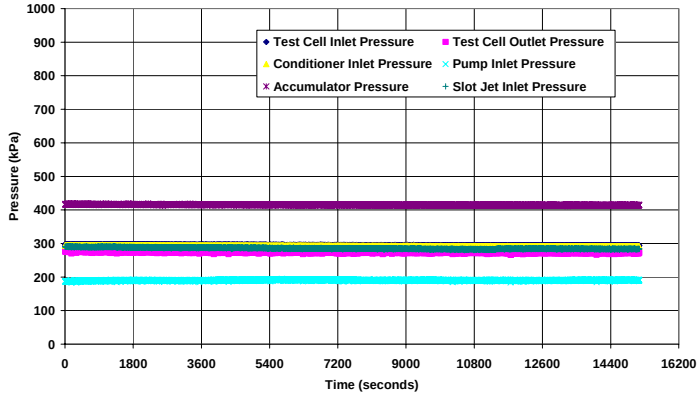

Slot Jet Surface Temperatures
310 kPa, 15 degC Subcooled, 0.017 kg/s, 200 watt #1

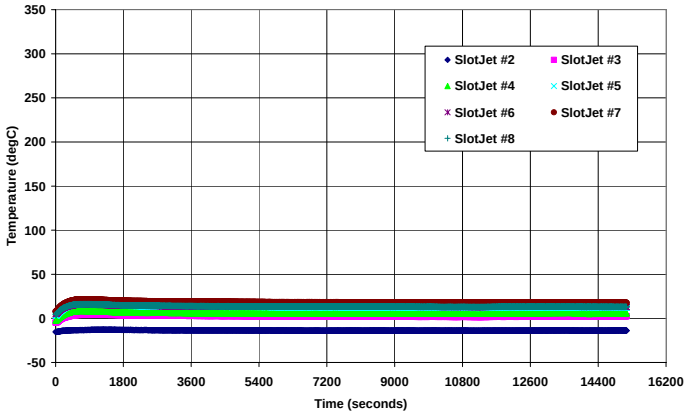

Heater Neck Temperatures
310 kPa, 15 deg Subcooled, 0.017 kg/s, 200 watt #1

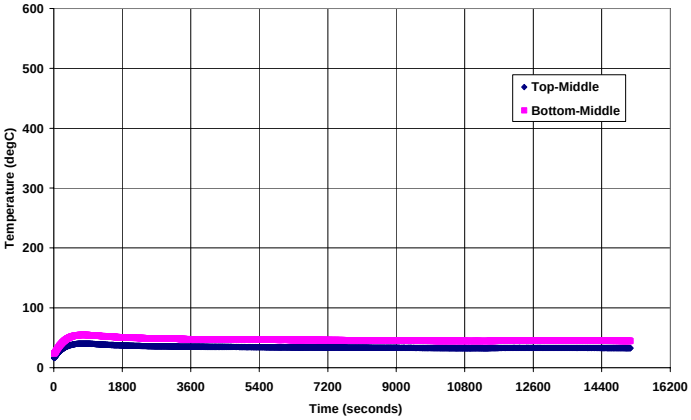

Heater Neck Heat Flux & Test Cell Watt Input
310 kPa, 15 degC Subcooled, 0.017 kg/s, 200 watt #1

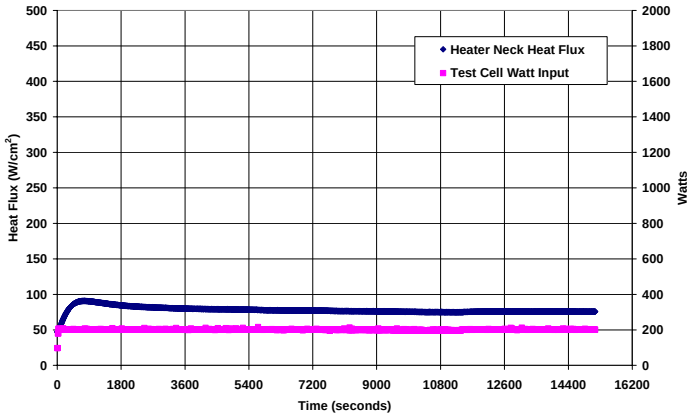

310 kPa, 15 degC Subcooled, 0.017 kg/s, 300 watt #1

Mass Flow Rate
310 kPa, 15 degC Subcooled, 0.017 kg/s, 300 watt #1

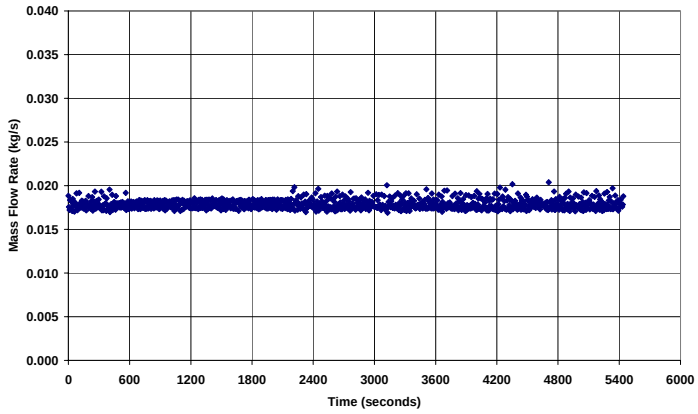

Slot Jet Fluid Temperatures
310 kPa, 15 degC Subcooled, 0.017 kg/s, 300 watt #1

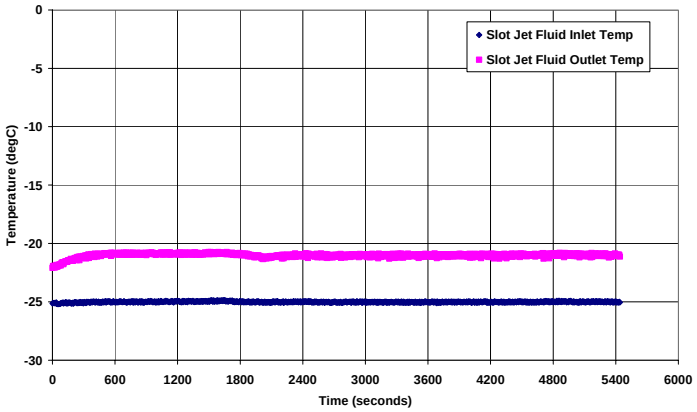

Ammonia Flow Loop Pressures
310 kPa, 15 degC Subcooled, 0.017 kg/s, 300 watt #1

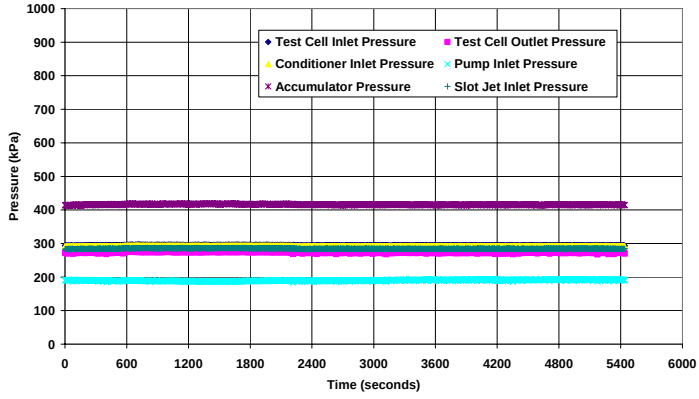

Slot Jet Surface Temperatures
310 kPa, 15 degC Subcooled, 0.017 kg/s, 300 watt #1

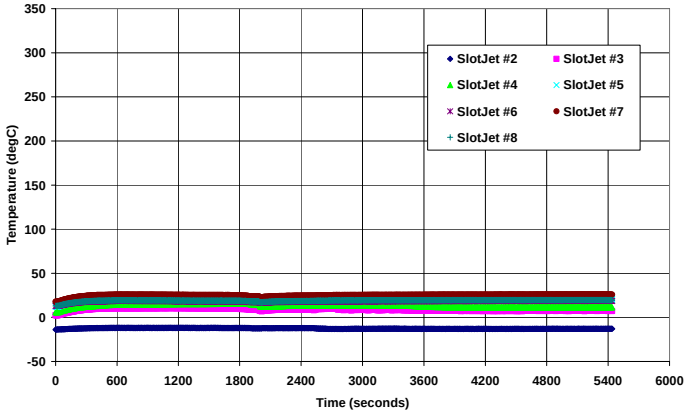

Heater Neck Temperatures
310 kPa, 15 deg Subcooled, 0.017 kg/s, 300 watt #1

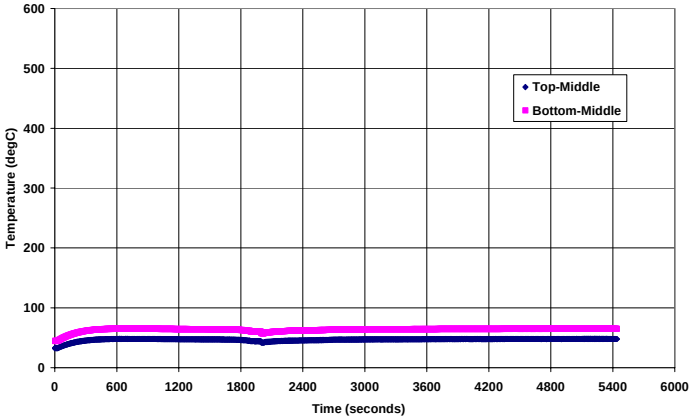

Heater Neck Heat Flux & Test Cell Watt Input
310 kPa, 15 degC Subcooled, 0.017 kg/s, 300 watt #1

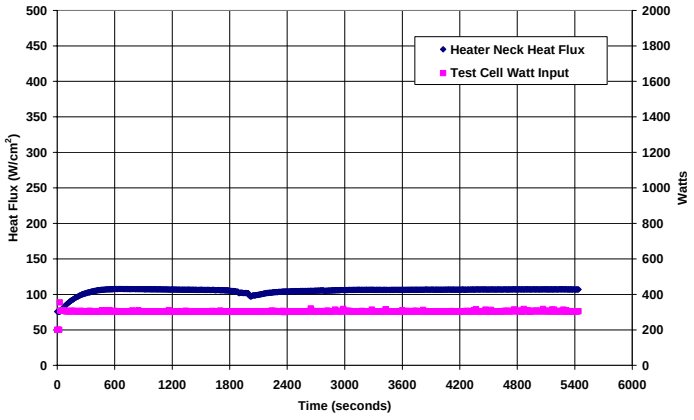

310 kPa, 15 degC Subcooled, 0.017 kg/s, 400 watt #1

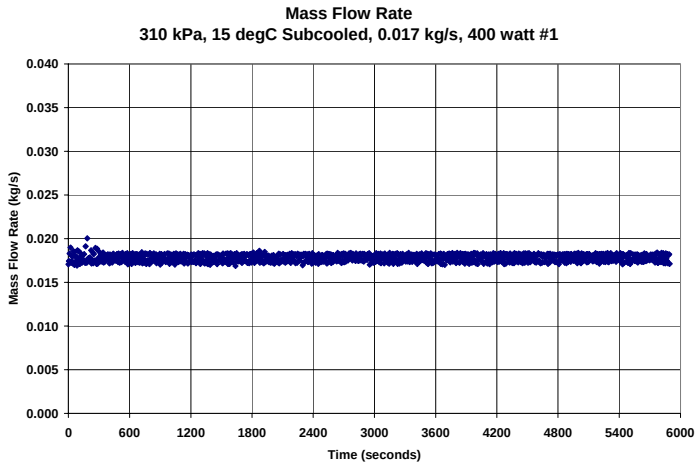

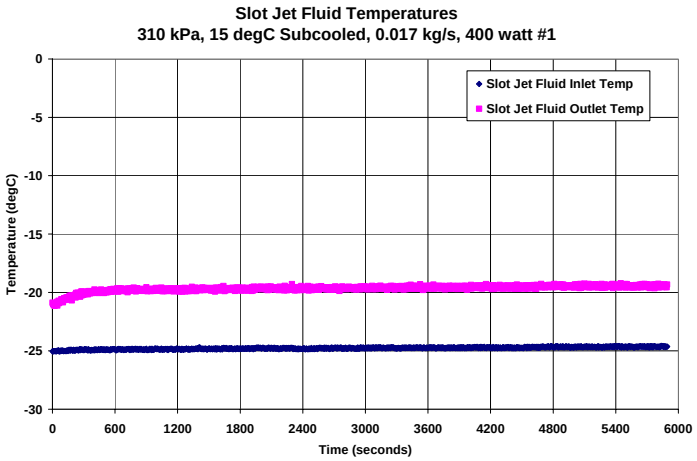

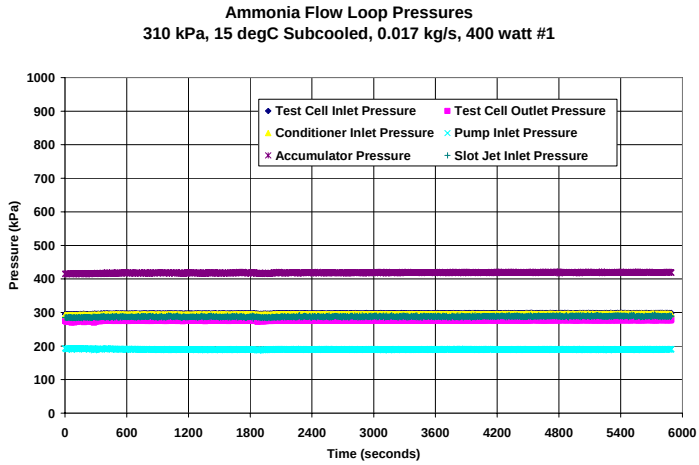

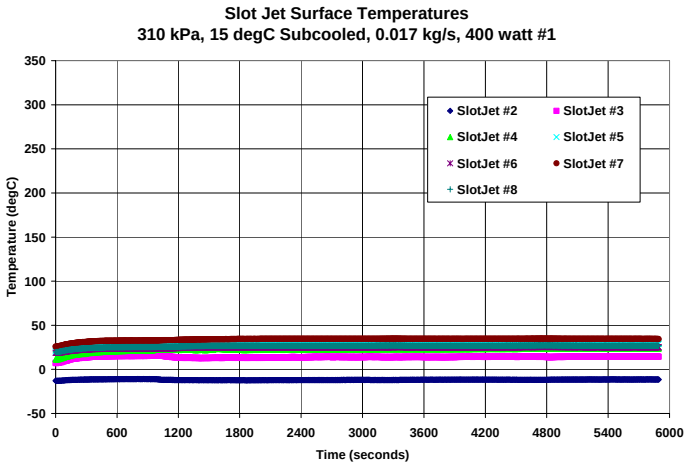

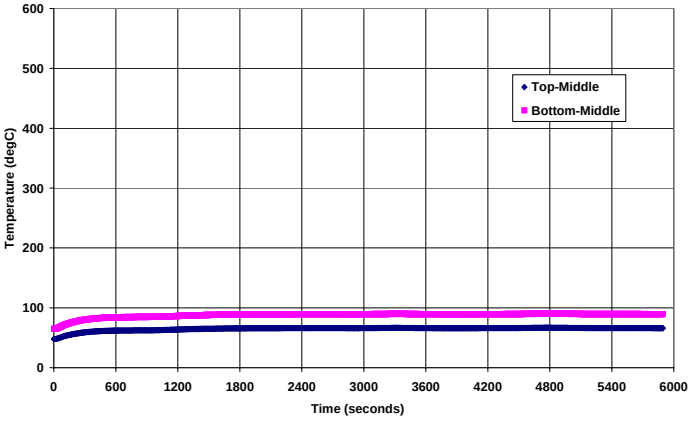

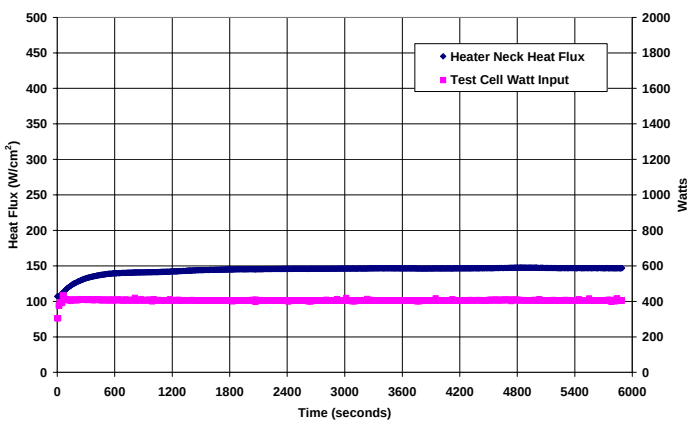

310 kPa, 15 degC Subcooled, 0.017 kg/s, 500 watt #1

Mass Flow Rate
310 kPa, 15 degC Subcooled, 0.017 kg/s, 500 watt #1

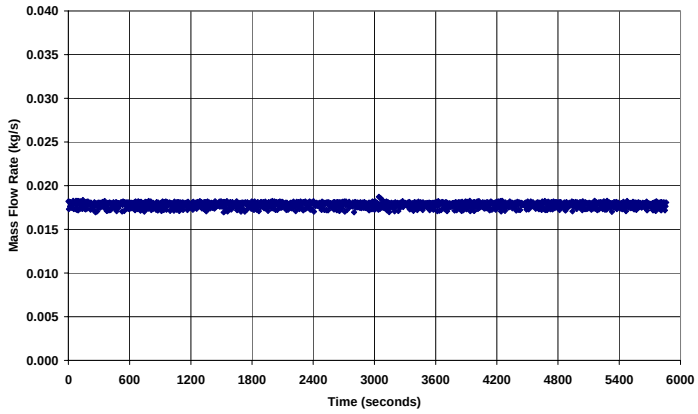

Slot Jet Fluid Temperatures
310 kPa, 15 degC Subcooled, 0.017 kg/s, 500 watt #1

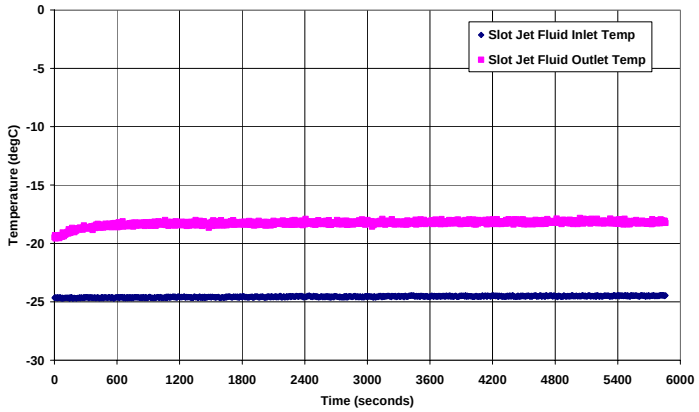

Ammonia Flow Loop Pressures
310 kPa, 15 degC Subcooled, 0.017 kg/s, 500 watt #1

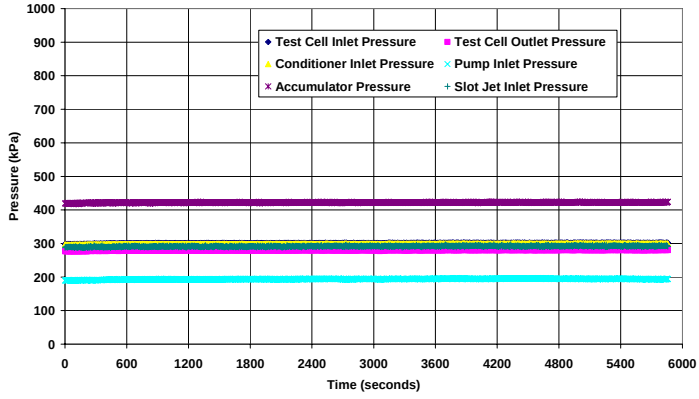

Slot Jet Surface Temperatures
310 kPa, 15 degC Subcooled, 0.017 kg/s, 500 watt #1

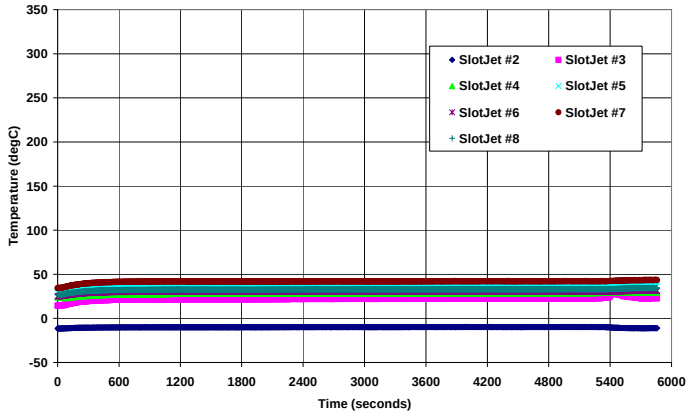

Heater Neck Temperatures
310 kPa, 15 deg Subcooled, 0.017 kg/s, 500 watt #1

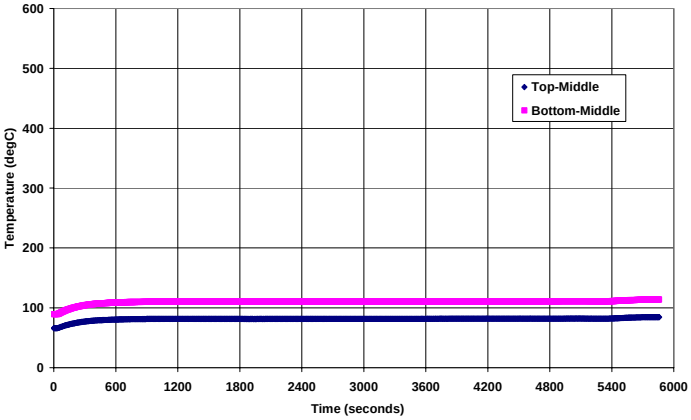

Heater Neck Heat Flux & Test Cell Watt Input
310 kPa, 15 degC Subcooled, 0.017 kg/s, 500 watt #1

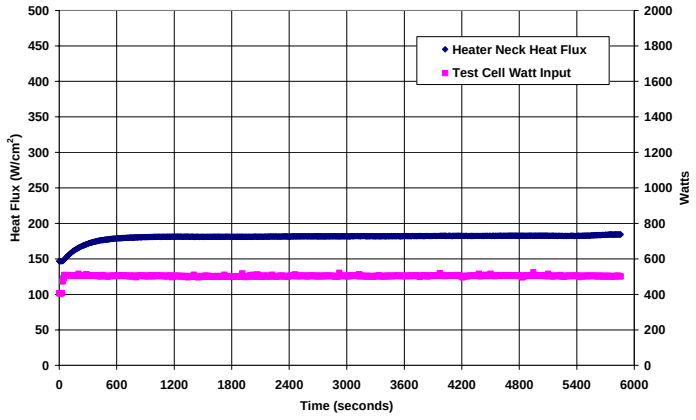

310 kPa, 15 degC Subcooled, 0.017 kg/s, 600 watt #1

Mass Flow Rate
310 kPa, 15 degC Subcooled, 0.017 kg/s, 600 watt #1

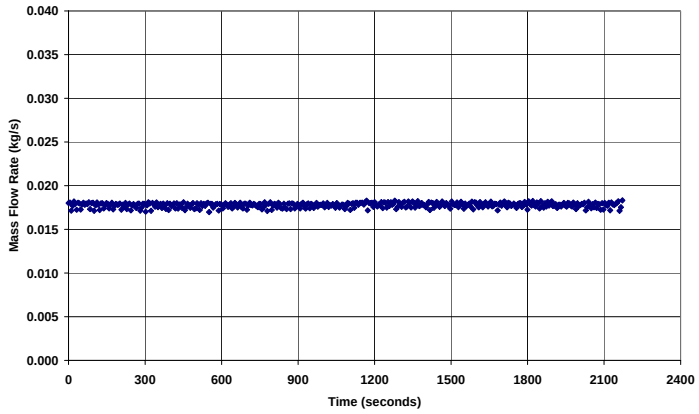

Slot Jet Fluid Temperatures
310 kPa, 15 degC Subcooled, 0.017 kg/s, 600 watt #1

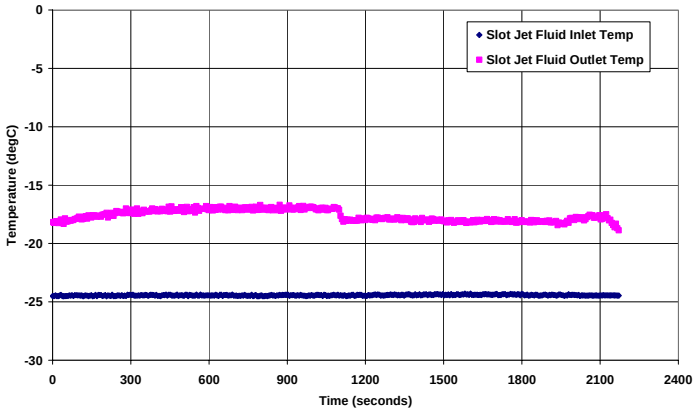

Ammonia Flow Loop Pressures
310 kPa, 15 degC Subcooled, 0.017 kg/s, 600 watt #1

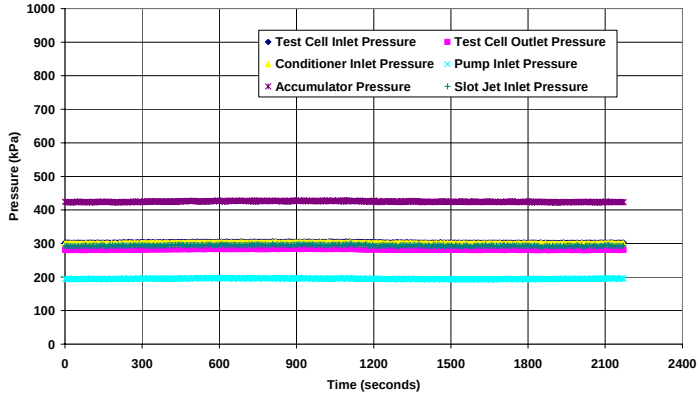

Slot Jet Surface Temperatures
310 kPa, 15 degC Subcooled, 0.017 kg/s, 600 watt #1

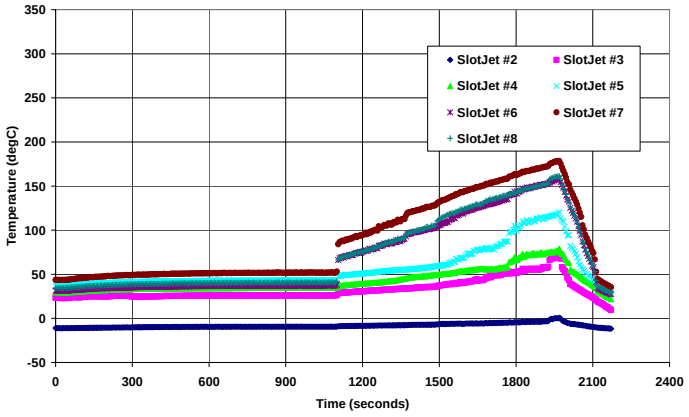

Heater Neck Temperatures
310 kPa, 15 deg Subcooled, 0.017 kg/s, 600 watt #1

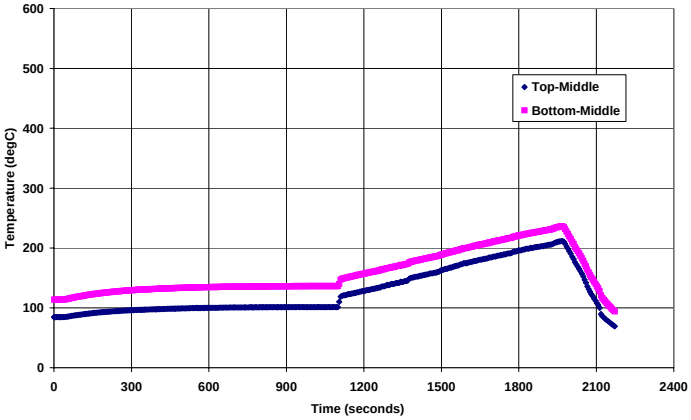

Heater Neck Heat Flux & Test Cell Watt Input
310 kPa, 15 degC Subcooled, 0.017 kg/s, 600 watt #1

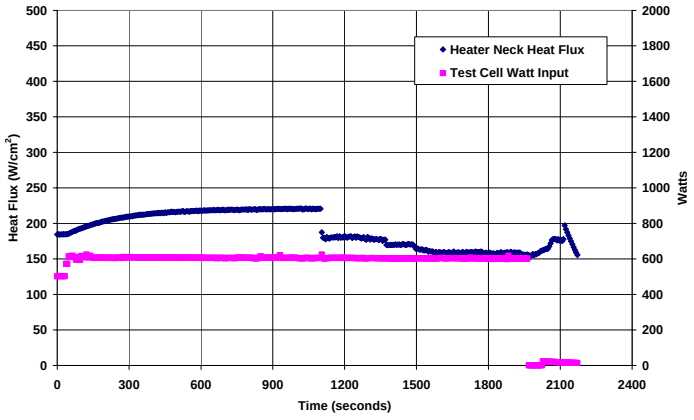

310 kPa, 15 degC Subcooled, 0.017 kg/s, 100 watt #2

Mass Flow Rate
310 kPa, 15 degC Subcooled, 0.017 kg/s, 100 watt #2

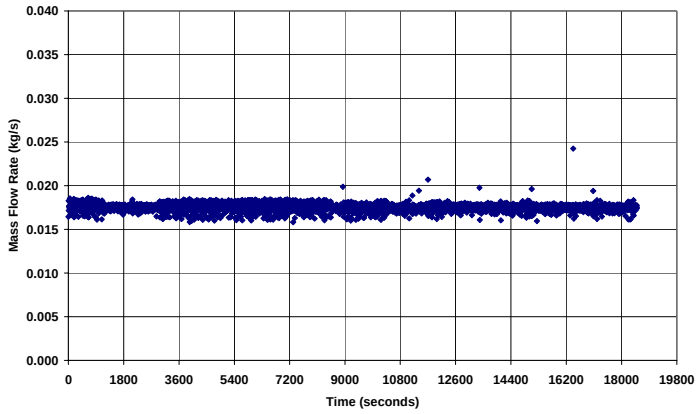

Slot Jet Fluid Temperatures
310 kPa, 15 degC Subcooled, 0.017 kg/s, 100 watt #2

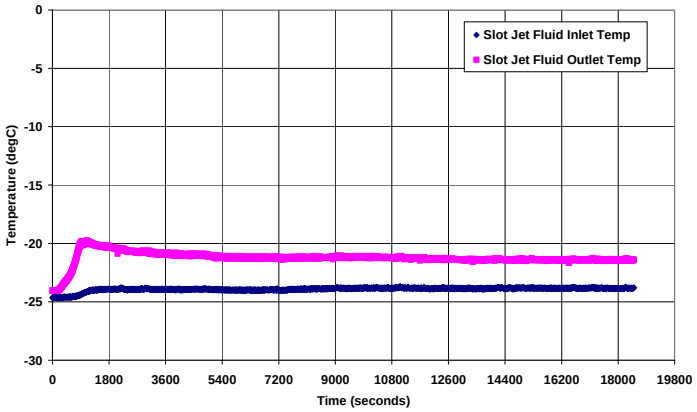

Ammonia Flow Loop Pressures
310 kPa, 15 degC Subcooled, 0.017 kg/s, 100 watt #2

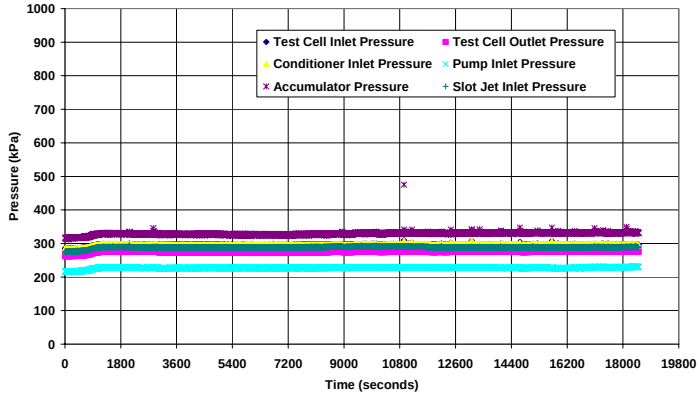

Slot Jet Surface Temperatures
310 kPa, 15 degC Subcooled, 0.017 kg/s, 100 watt #2

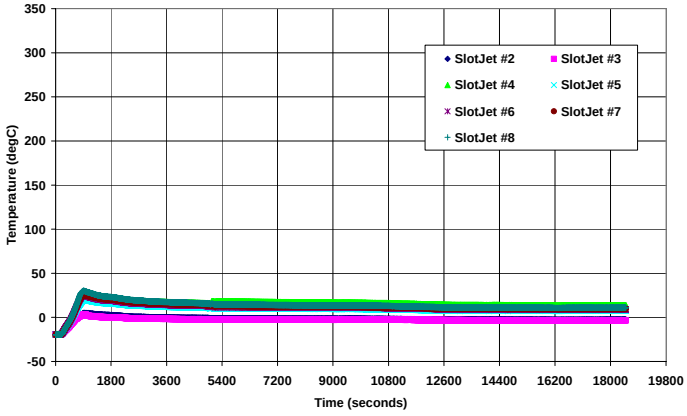

Heater Neck Temperatures
310 kPa, 15 deg Subcooled, 0.017 kg/s, 100 watt #2

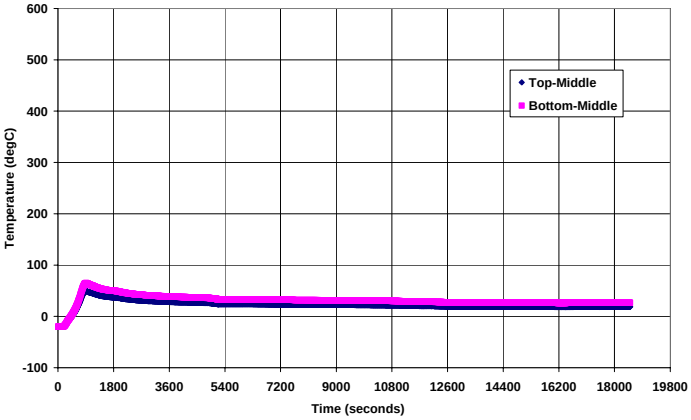

Heater Neck Heat Flux & Test Cell Watt Input
310 kPa, 15 degC Subcooled, 0.017 kg/s, 100 watt #2

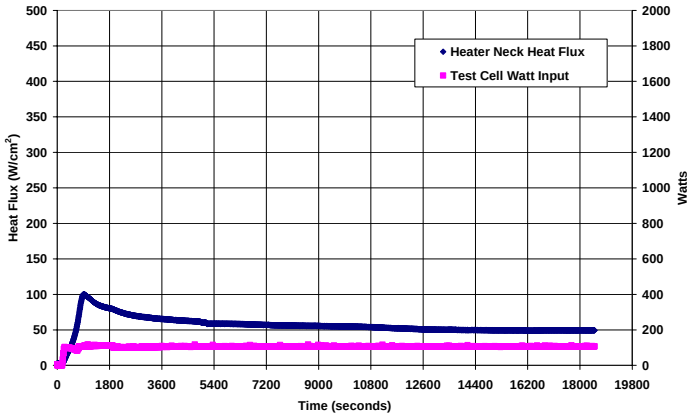

310 kPa, 15 degC Subcooled, 0.017 kg/s, 200 watt #2

Mass Flow Rate
310 kPa, 15 degC Subcooled, 0.017 kg/s, 200 watt #2

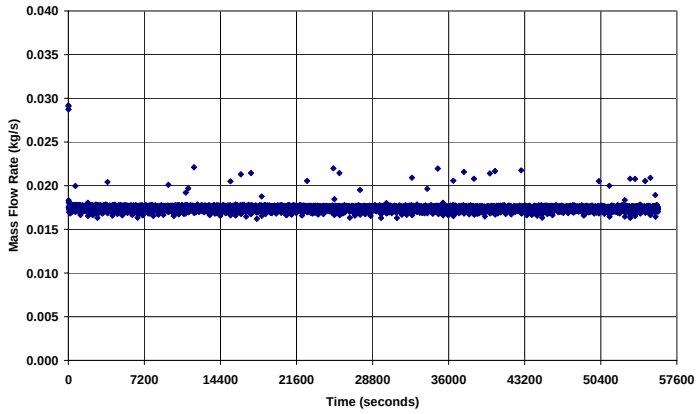

Slot Jet Fluid Temperatures
310 kPa, 15 degC Subcooled, 0.017 kg/s, 200 watt #2

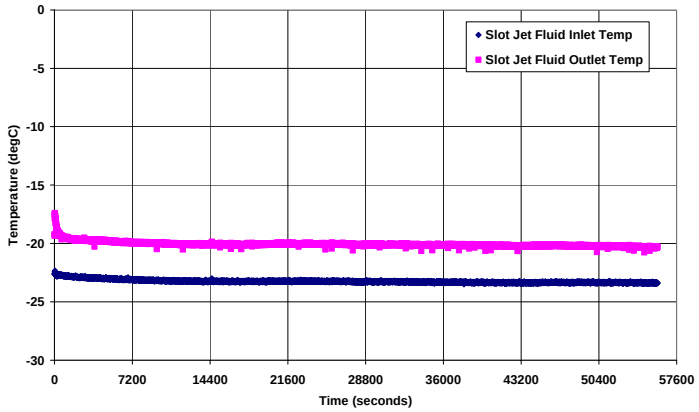

Ammonia Flow Loop Pressures
310 kPa, 15 degC Subcooled, 0.017 kg/s, 200 watt #2

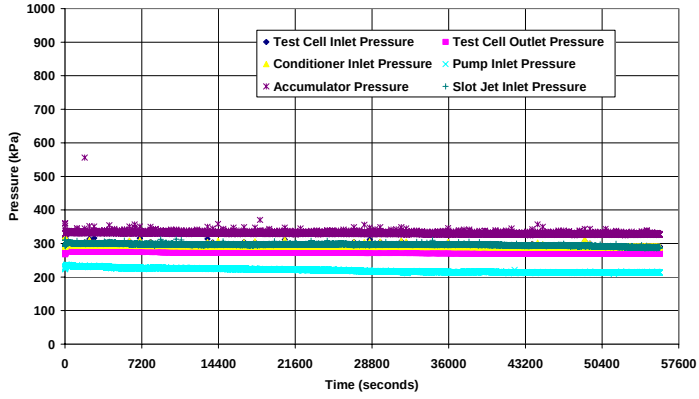

Slot Jet Surface Temperatures
310 kPa, 15 degC Subcooled, 0.017 kg/s, 200 watt #2

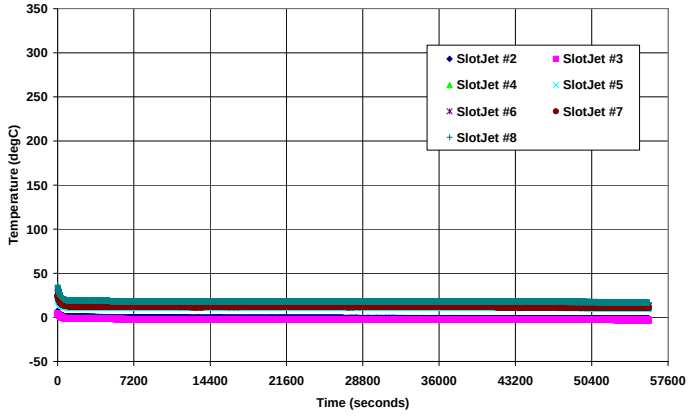

Heater Neck Temperatures
310 kPa, 15 deg Subcooled, 0.017 kg/s, 200 watt #2

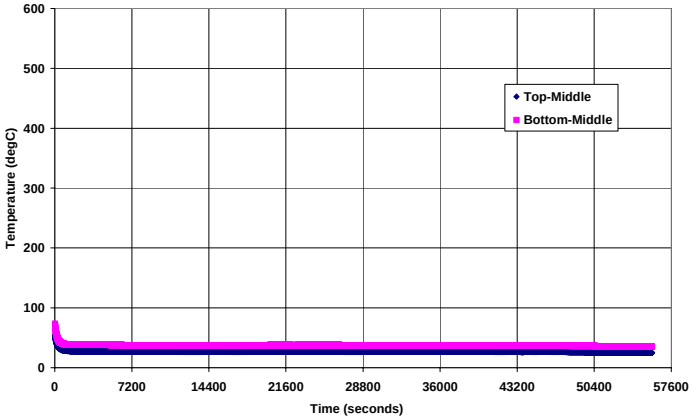

Heater Neck Heat Flux & Test Cell Watt Input
310 kPa, 15 degC Subcooled, 0.017 kg/s, 200 watt #2

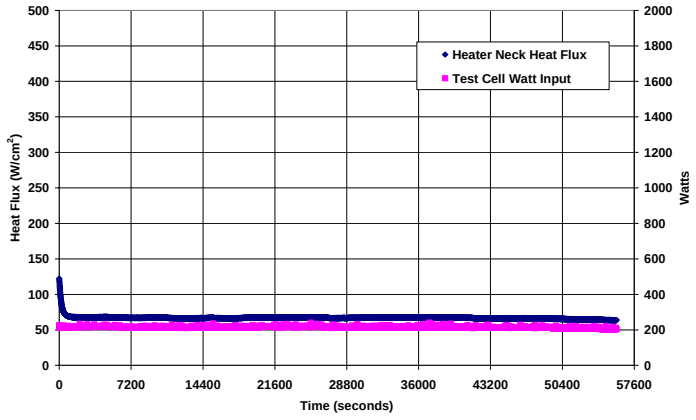

310 kPa, 15 degC Subcooled, 0.017 kg/s, 300 watt #2

Mass Flow Rate
310 kPa, 15 degC Subcooled, 0.017 kg/s, 300 watt #2

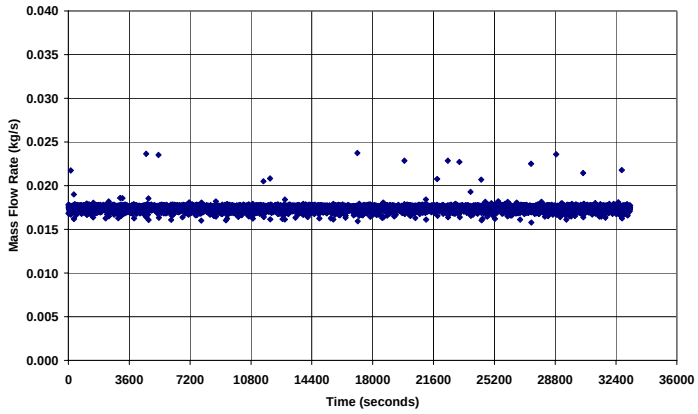

Slot Jet Fluid Temperatures
310 kPa, 15 degC Subcooled, 0.017 kg/s, 300 watt #2

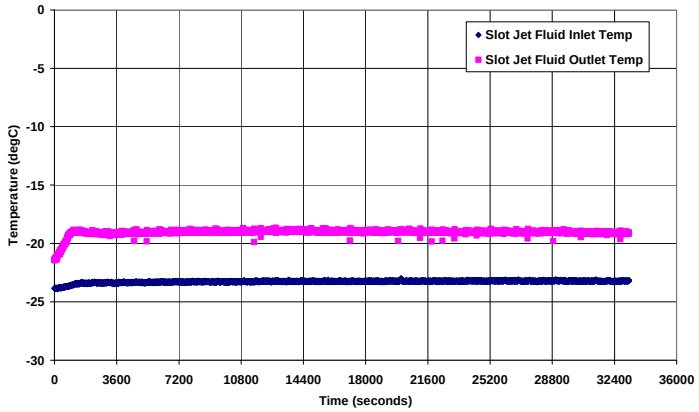

Ammonia Flow Loop Pressures
310 kPa, 15 degC Subcooled, 0.017 kg/s, 300 watt #2

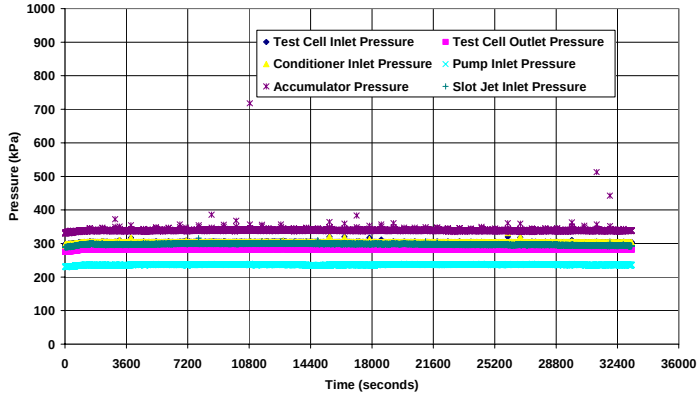

Slot Jet Surface Temperatures
310 kPa, 15 degC Subcooled, 0.017 kg/s, 300 watt #2

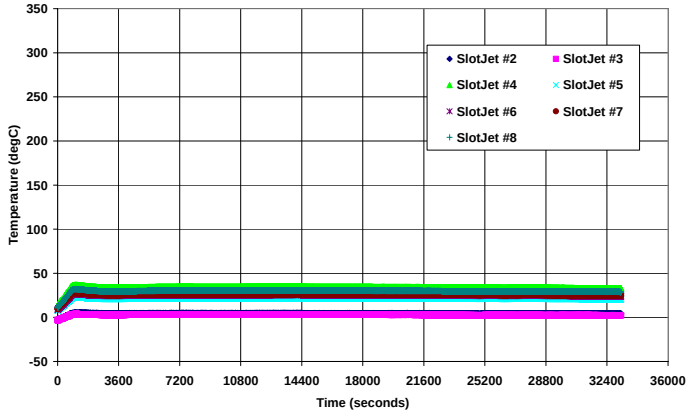

Heater Neck Temperatures
310 kPa, 15 deg Subcooled, 0.017 kg/s, 300 watt #2

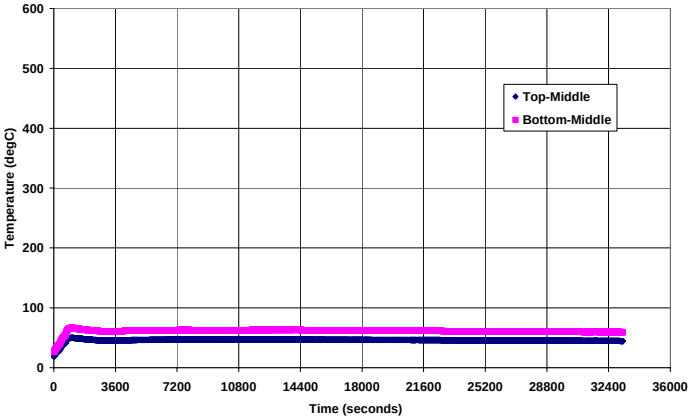

Heater Neck Heat Flux & Test Cell Watt Input
310 kPa, 15 degC Subcooled, 0.017 kg/s, 300 watt #2

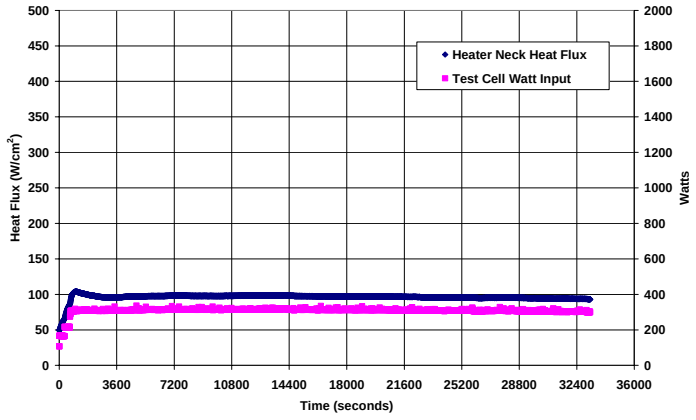

310 kPa, 15 degC Subcooled, 0.017 kg/s, 500 watt #2

Mass Flow Rate
310 kPa, 15 degC Subcooled, 0.017 kg/s, 500 watt #2

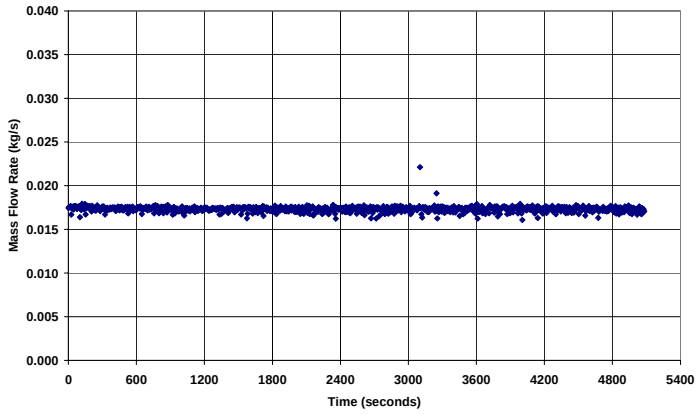

Slot Jet Fluid Temperatures
310 kPa, 15 degC Subcooled, 0.017 kg/s, 500 watt #2

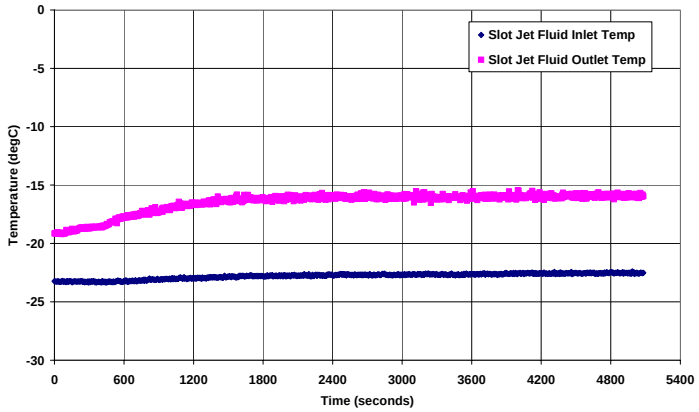

Ammonia Flow Loop Pressures
310 kPa, 15 degC Subcooled, 0.017 kg/s, 500 watt #2

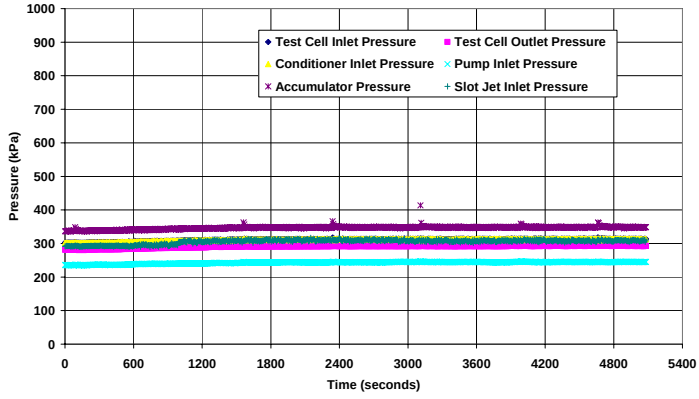

Slot Jet Surface Temperatures
310 kPa, 15 degC Subcooled, 0.017 kg/s, 500 watt #2

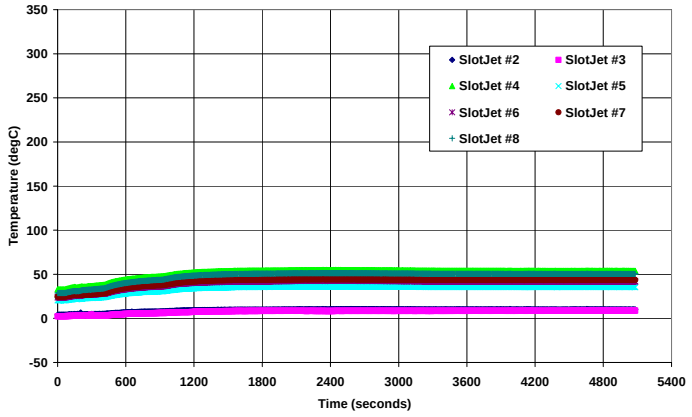

Heater Neck Temperatures
310 kPa, 15 deg Subcooled, 0.017 kg/s, 500 watt #2

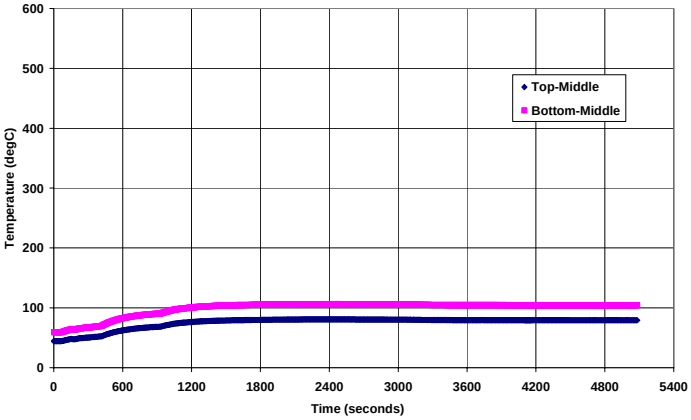

Heater Neck Heat Flux & Test Cell Watt Input
310 kPa, 15 degC Subcooled, 0.017 kg/s, 500 watt #2

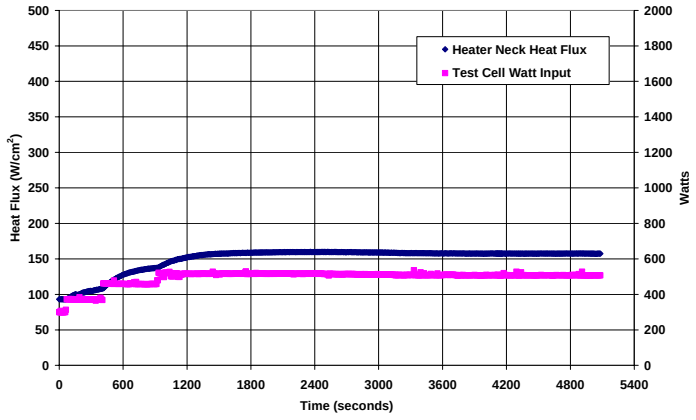

310 kPa, 15 degC Subcooled, 0.017 kg/s, 600 watt #2

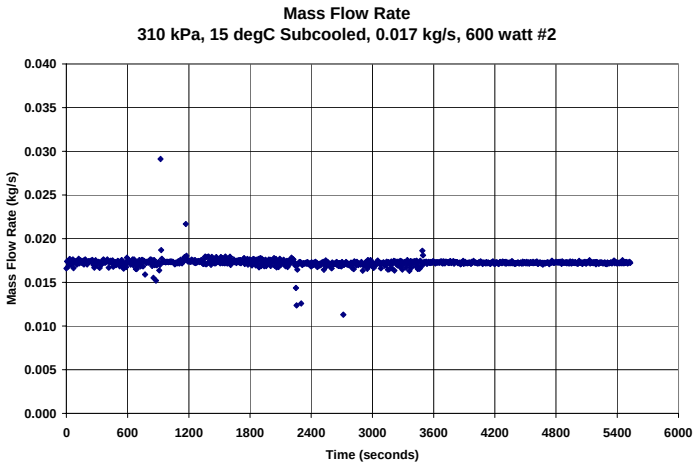

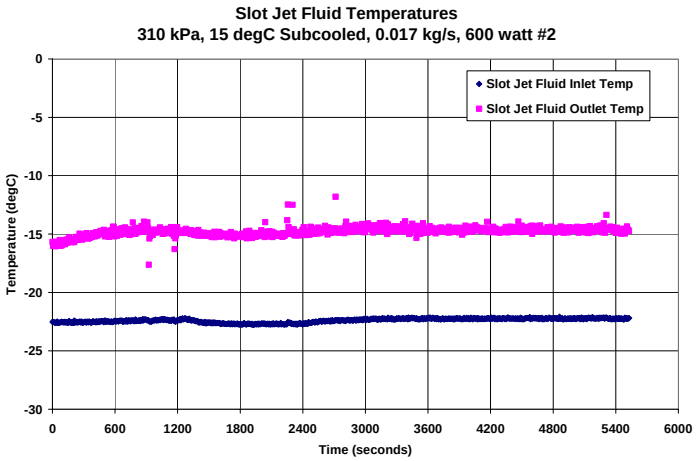

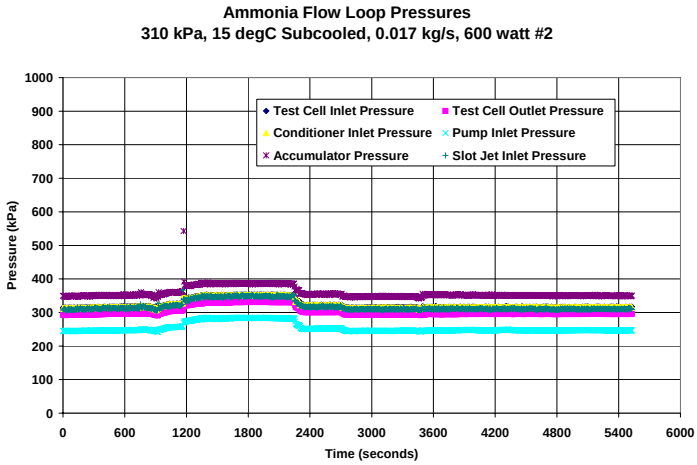

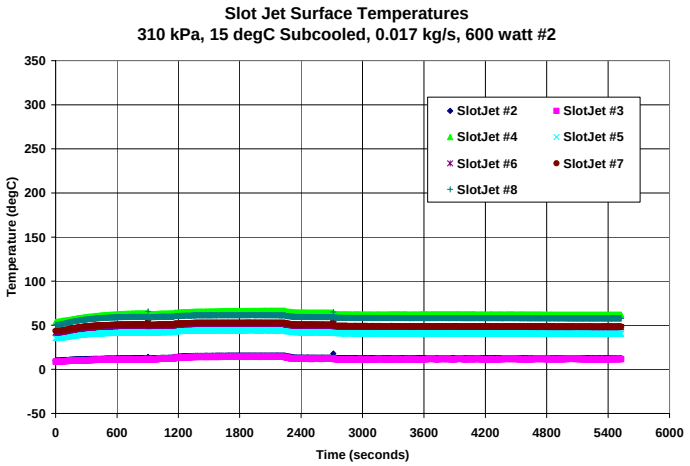

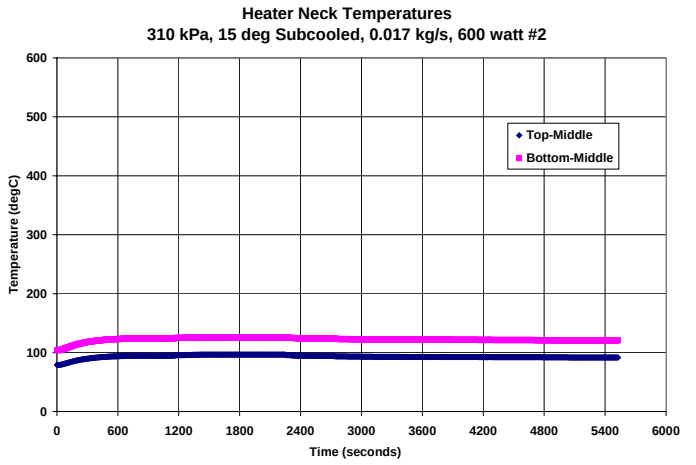

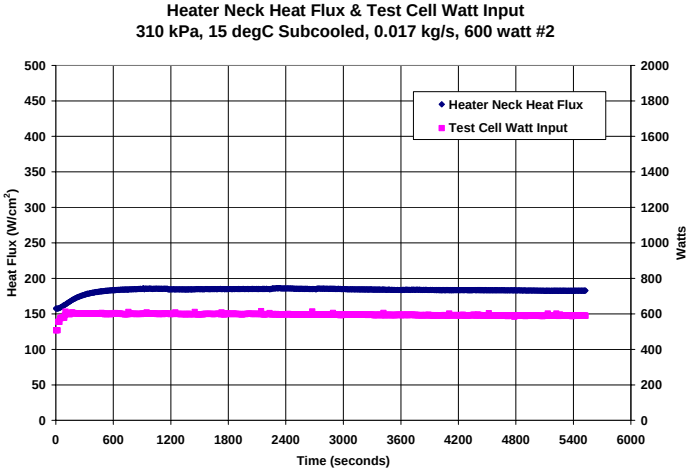

310 kPa, 15 degC Subcooled, 0.017 kg/s, 700 watt #2.1

Mass Flow Rate
310 kPa, 15 degC Subcooled, 0.017 kg/s, 700 watt #2.1

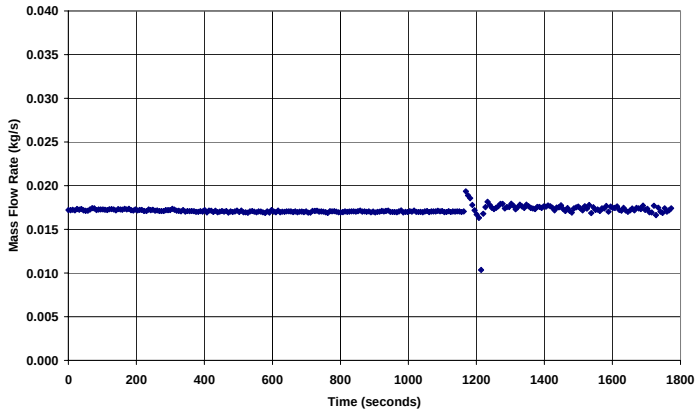

Slot Jet Fluid Temperatures
310 kPa, 15 degC Subcooled, 0.017 kg/s, 700 watt #2.1

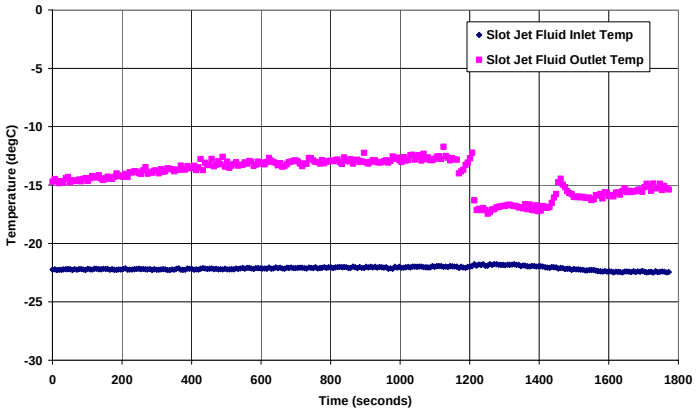

Ammonia Flow Loop Pressures
310 kPa, 15 degC Subcooled, 0.017 kg/s, 700 watt #2.1

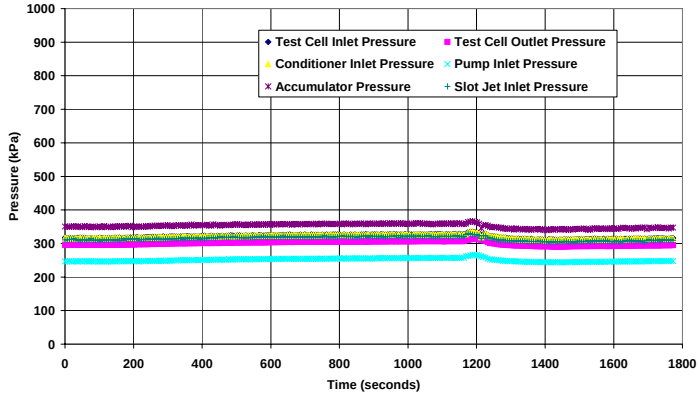

Slot Jet Surface Temperatures
310 kPa, 15 degC Subcooled, 0.017 kg/s, 700 watt #2.1

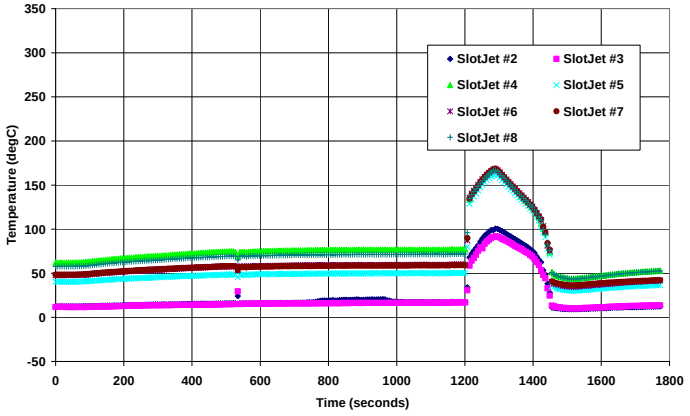

Heater Neck Temperatures
310 kPa, 15 deg Subcooled, 0.017 kg/s, 700 watt #2.1

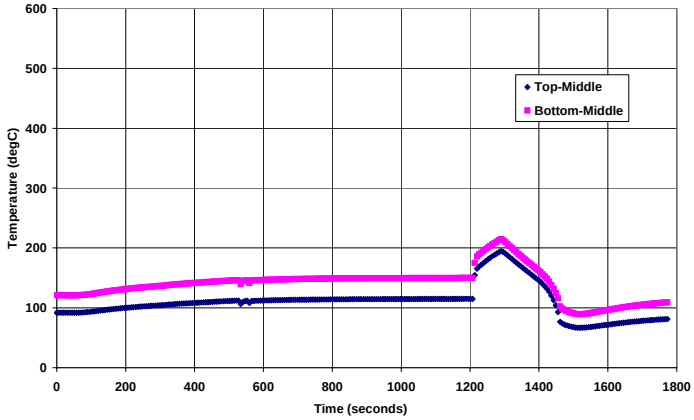

Heater Neck Heat Flux & Test Cell Watt Input
310 kPa, 15 degC Subcooled, 0.017 kg/s, 700 watt #2.1

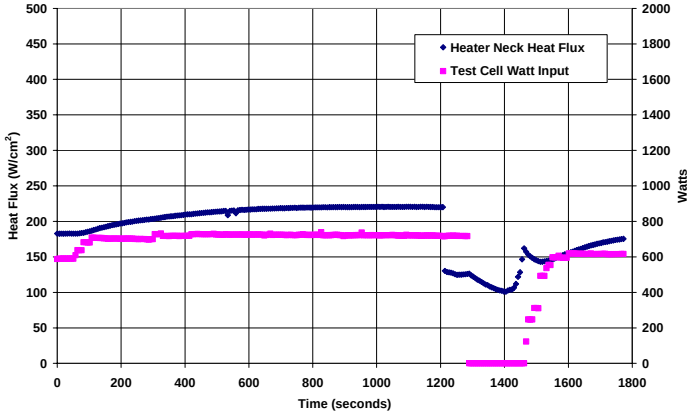

310 kPa, 15 degC Subcooled, 0.017 kg/s, 700 watt #2.2

Mass Flow Rate
310 kPa, 15 degC Subcooled, 0.017 kg/s, 700 watt #2.2

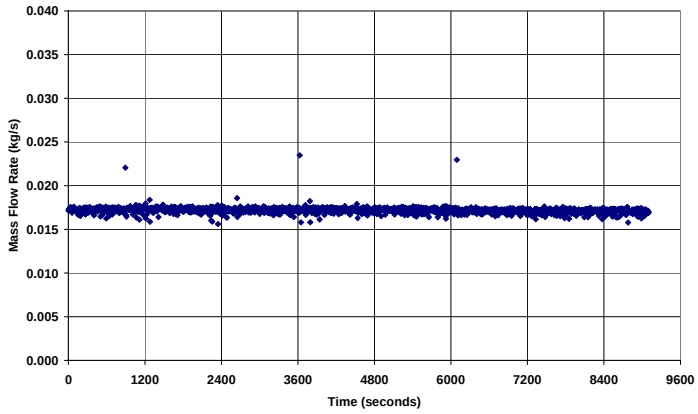

Slot Jet Fluid Temperatures
310 kPa, 15 degC Subcooled, 0.017 kg/s, 700 watt #2.2

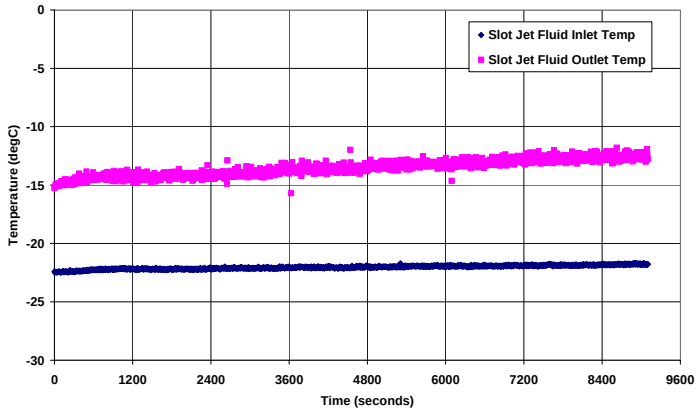

Ammonia Flow Loop Pressures
310 kPa, 15 degC Subcooled, 0.017 kg/s, 700 watt #2.2

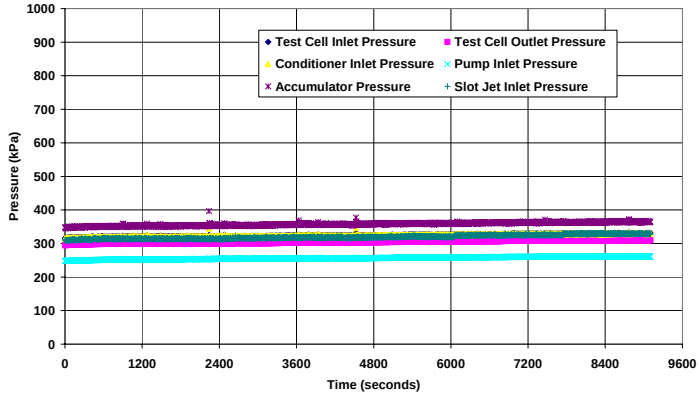

Slot Jet Surface Temperatures
310 kPa, 15 degC Subcooled, 0.017 kg/s, 700 watt #2.2

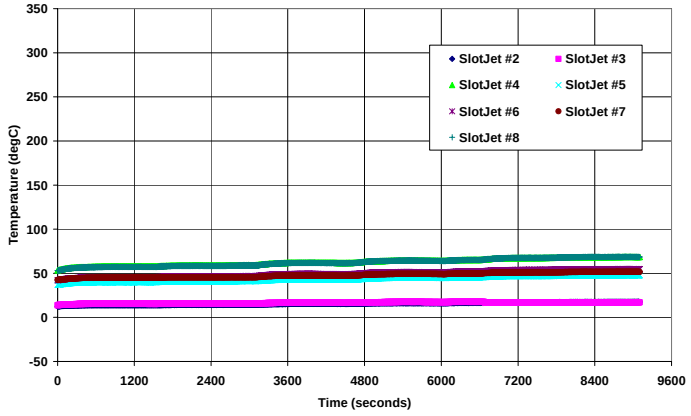

Heater Neck Temperatures
310 kPa, 15 deg Subcooled, 0.017 kg/s, 700 watt #2.2

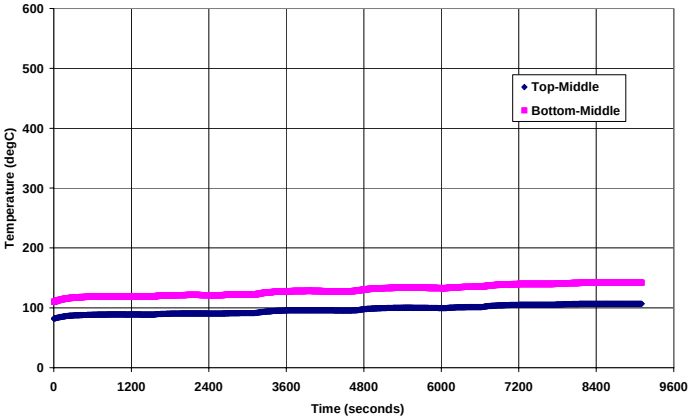

Heater Neck Heat Flux & Test Cell Watt Input
310 kPa, 15 degC Subcooled, 0.017 kg/s, 700 watt #2.2

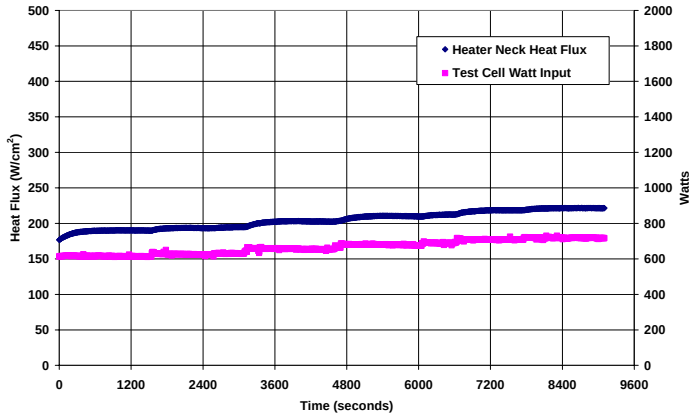

310 kPa, 15 degC Subcooled, 0.017 kg/s, 800 watt #2.1

Mass Flow Rate
310 kPa, 15 degC Subcooled, 0.017 kg/s, 800 watt #2.1

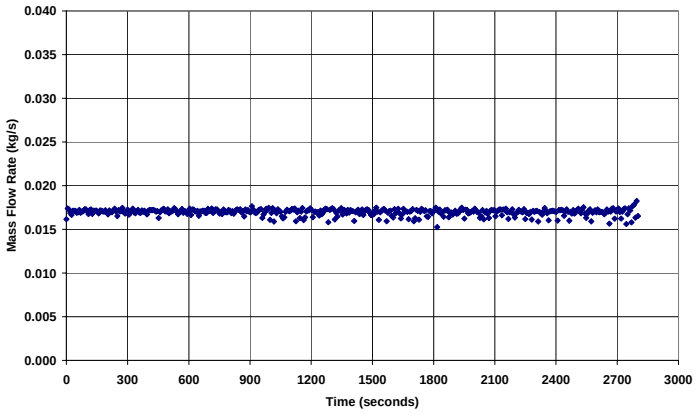

Slot Jet Fluid Temperatures
310 kPa, 15 degC Subcooled, 0.017 kg/s, 800 watt #2.1

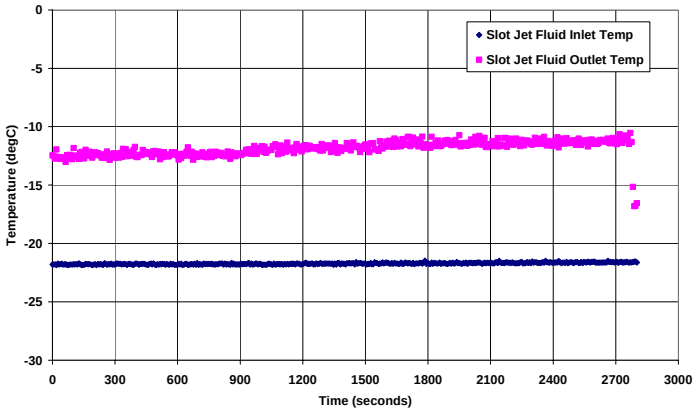

Ammonia Flow Loop Pressures
310 kPa, 15 degC Subcooled, 0.017 kg/s, 800 watt #2.1

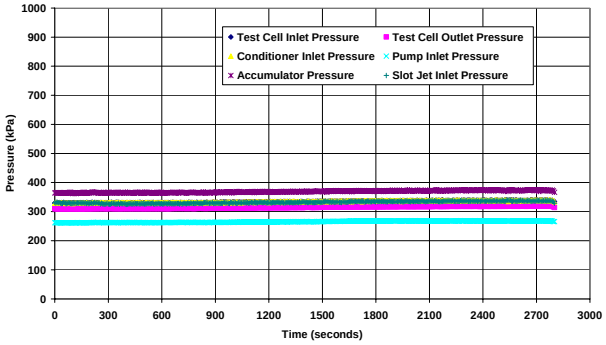

Slot Jet Surface Temperatures
310 kPa, 15 degC Subcooled, 0.017 kg/s, 800 watt #2.1

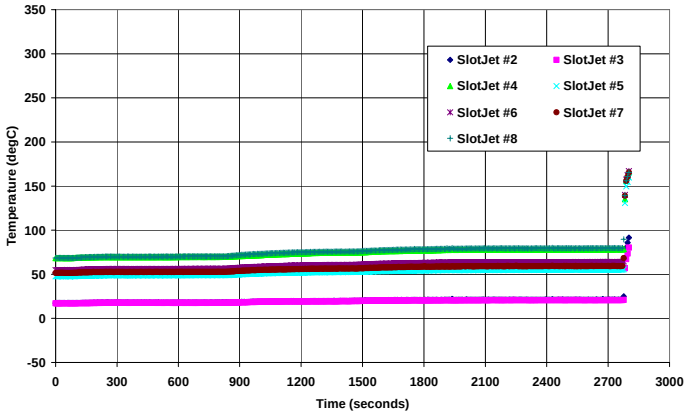

Heater Neck Temperatures
310 kPa, 15 deg Subcooled, 0.017 kg/s, 800 watt #2.1

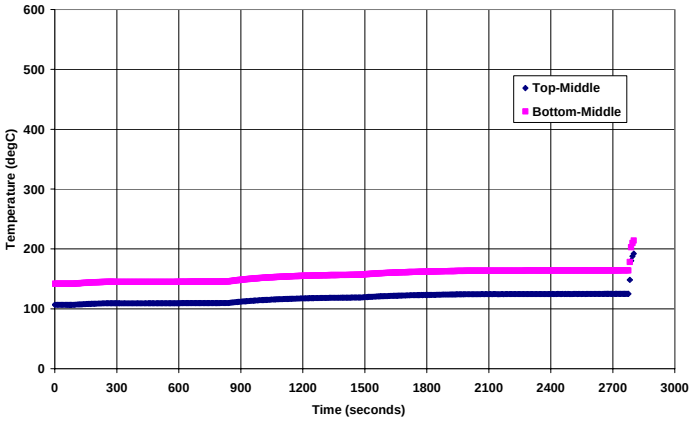

Heater Neck Heat Flux & Test Cell Watt Input
310 kPa, 15 degC Subcooled, 0.017 kg/s, 800 watt #2.1

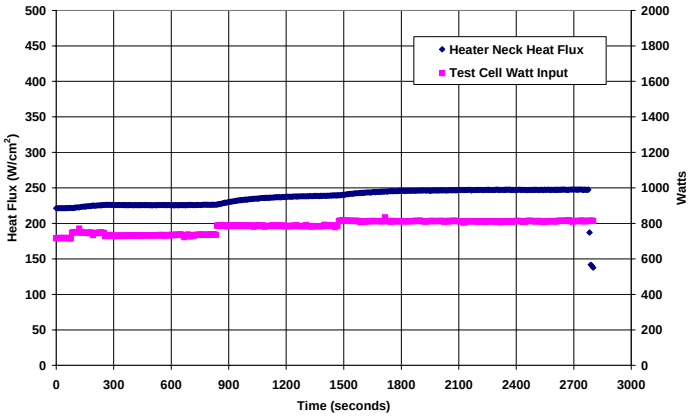

310 kPa, 15 degC Subcooled, 0.017 kg/s, 800 watt #2.2 (800 watt #2.1 Continued)

Mass Flow Rate
310 kPa, 15 degC Subcooled, 0.017 kg/s, 800 watt #2.2
(800 watt #2.1 Continued)

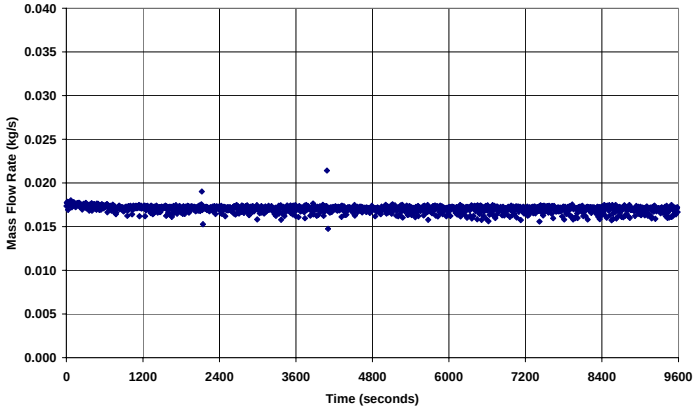

Slot Jet Fluid Temperatures
310 kPa, 15 degC Subcooled, 0.017 kg/s, 800 watt #2.2
(800 watt #2.1 Continued)

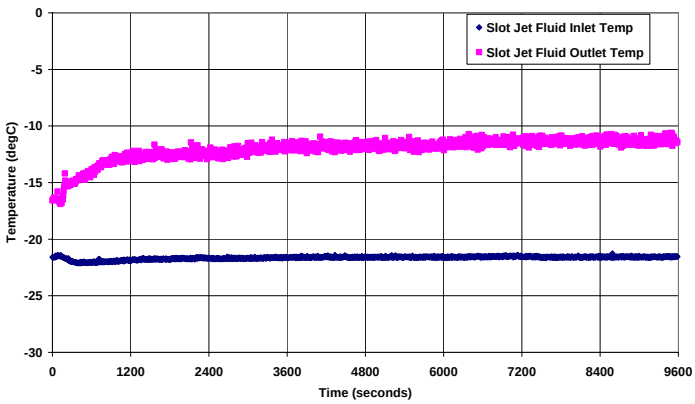

Ammonia Flow Loop Pressures
310 kPa, 15 degC Subcooled, 0.017 kg/s, 800 watt #2.2
(800 watt #2.1 Continued)

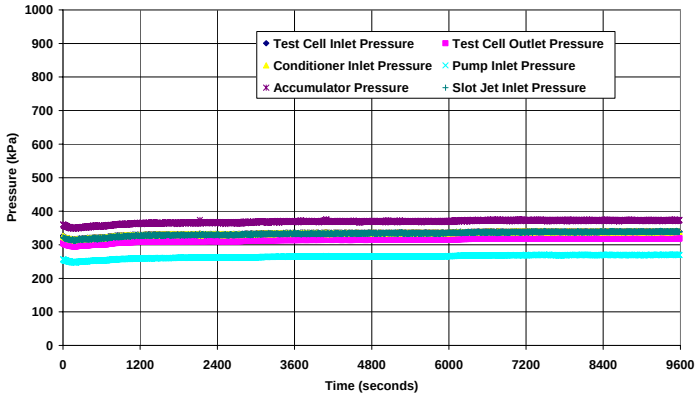

Slot Jet Surface Temperatures
310 kPa, 15 degC Subcooled, 0.017 kg/s, 800 watt #2.2
(800 watt #2.1 Continued)

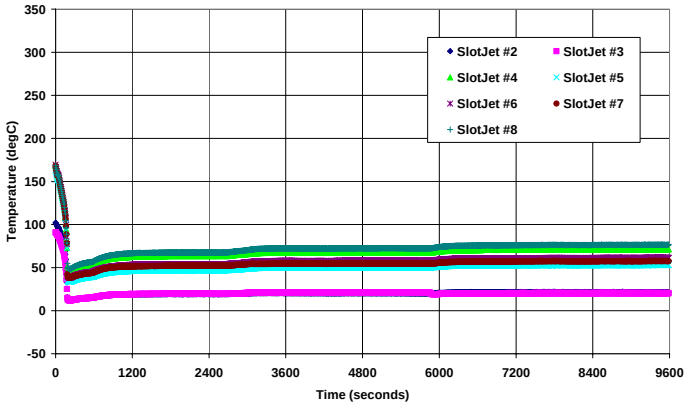

Heater Neck Temperatures
310 kPa, 15 deg Subcooled, 0.017 kg/s, 800 watt #2.2
(800 watt #2.1 Continued)

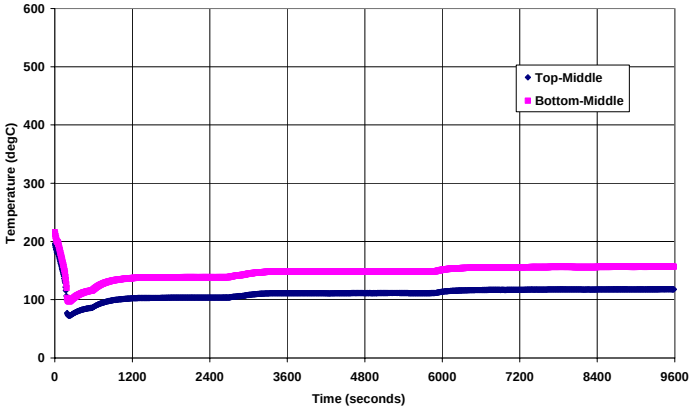

Heater Neck Heat Flux & Test Cell Watt Input
310 kPa, 15 degC Subcooled, 0.017 kg/s, 800 watt #2.2
(800 watt #2.1 Continued)

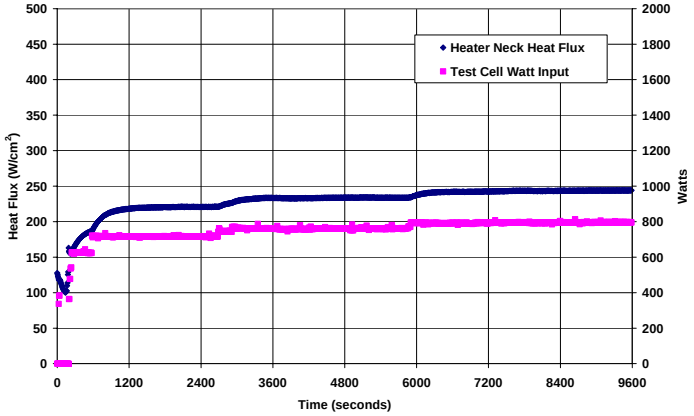

310 kPa, 15 degC Subcooled, 0.017 kg/s, 800 watt #2.3

Mass Flow Rate
310 kPa, 15 degC Subcooled, 0.017 kg/s, 800 watt #2.3

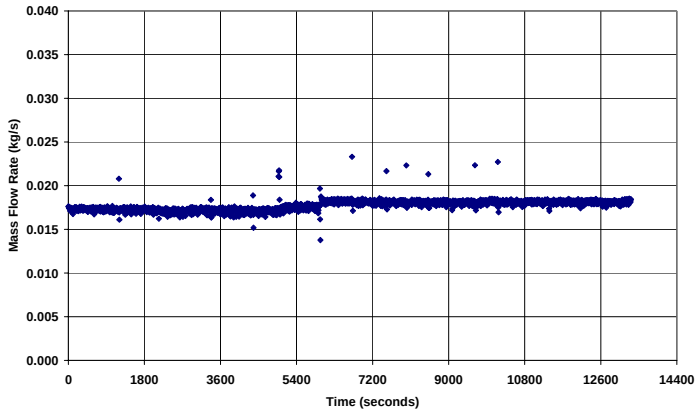

Slot Jet Fluid Temperatures
310 kPa, 15 degC Subcooled, 0.017 kg/s, 800 watt #2.3

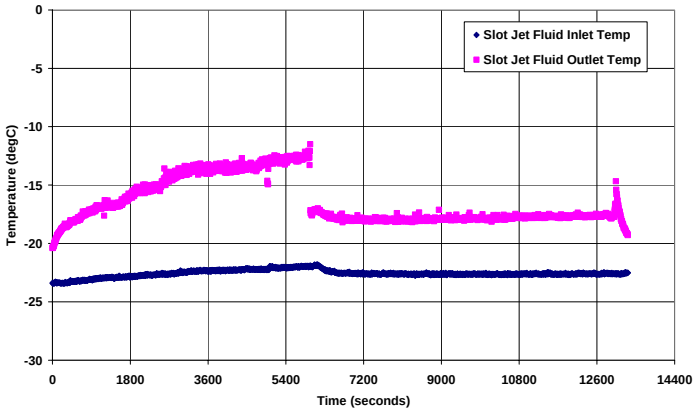

Ammonia Flow Loop Pressures
310 kPa, 15 degC Subcooled, 0.017 kg/s, 800 watt #2.3

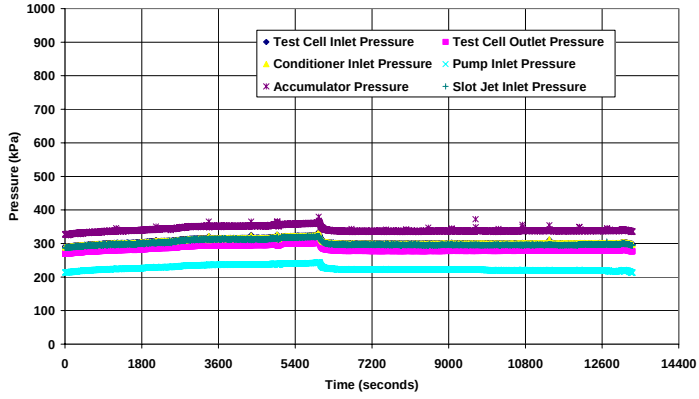

Slot Jet Surface Temperatures
310 kPa, 15 degC Subcooled, 0.017 kg/s, 800 watt #2.3

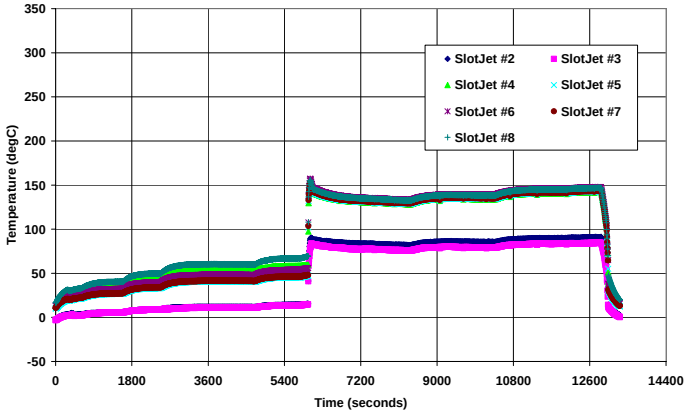

Heater Neck Temperatures
310 kPa, 15 deg Subcooled, 0.017 kg/s, 800 watt #2.3

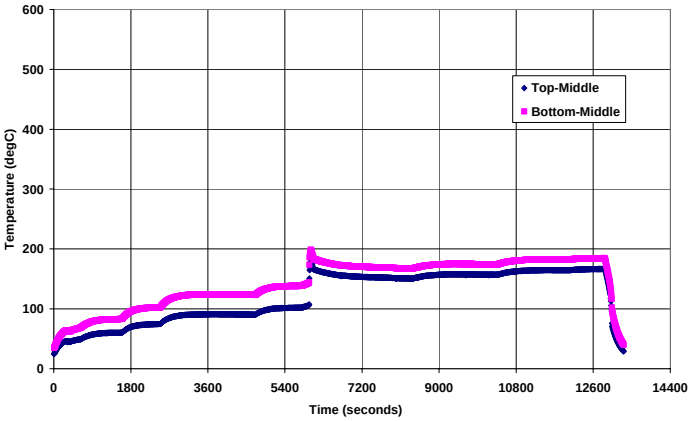

Heater Neck Heat Flux & Test Cell Watt Input
310 kPa, 15 degC Subcooled, 0.017 kg/s, 800 watt #2.3

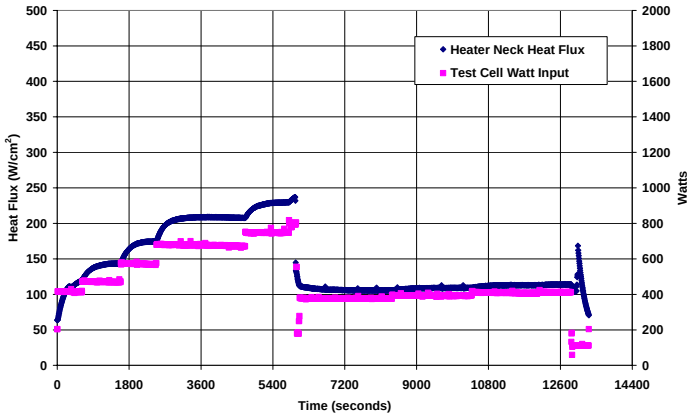

310 kPa, 15 degC Subcooled, 0.017 kg/s, 820 watt #2

Mass Flow Rate
310 kPa, 15 degC Subcooled, 0.017 kg/s, 820 watt #2

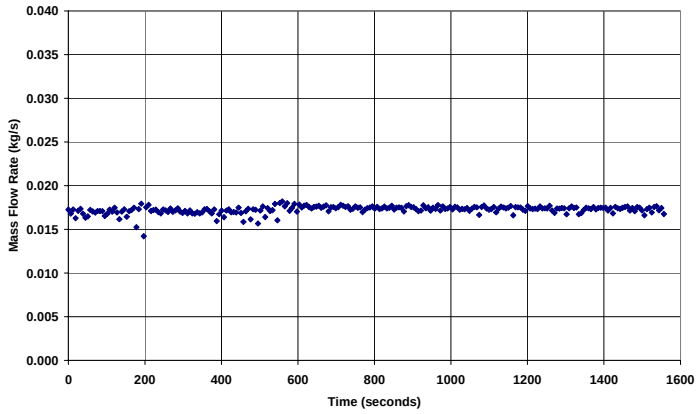

Slot Jet Fluid Temperatures
310 kPa, 15 degC Subcooled, 0.017 kg/s, 820 watt #2

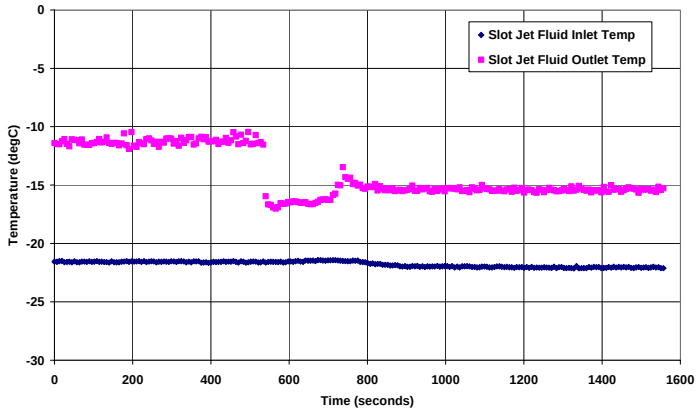

Ammonia Flow Loop Pressures
310 kPa, 15 degC Subcooled, 0.017 kg/s, 820 watt #2

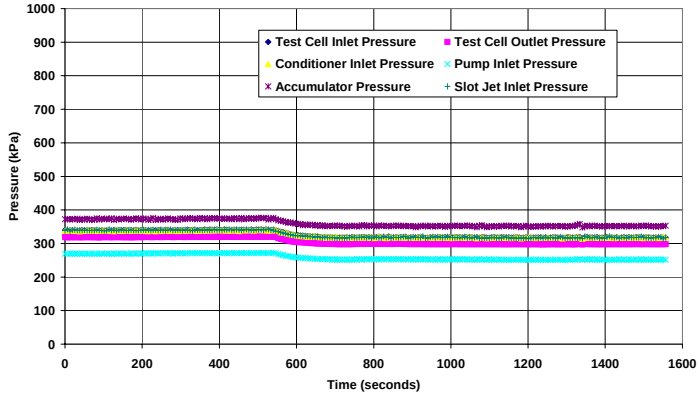

Slot Jet Surface Temperatures
310 kPa, 15 degC Subcooled, 0.017 kg/s, 820 watt #2

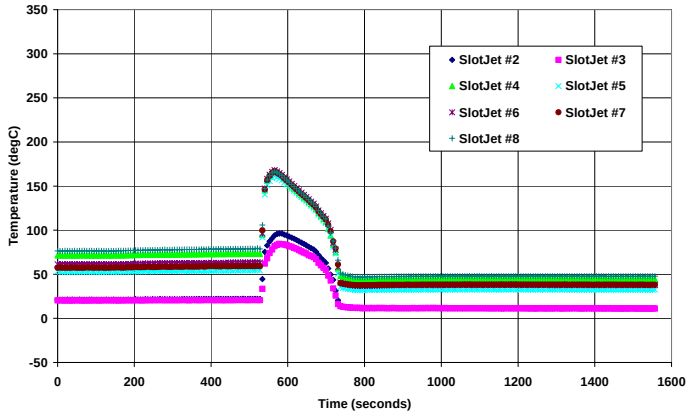

Heater Neck Temperatures
310 kPa, 15 deg Subcooled, 0.017 kg/s, 820 watt #2

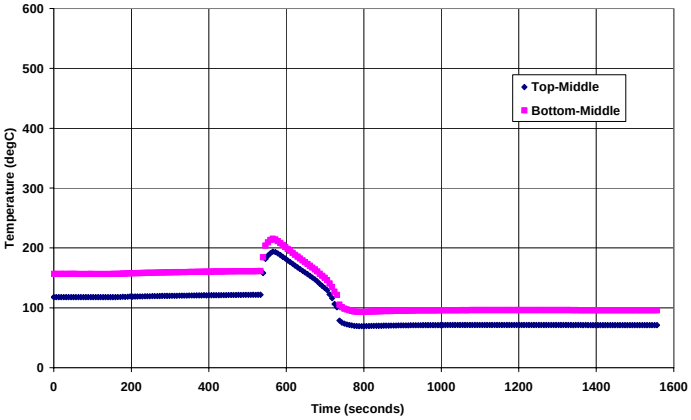

Heater Neck Heat Flux & Test Cell Watt Input
310 kPa, 15 degC Subcooled, 0.017 kg/s, 820 watt #2

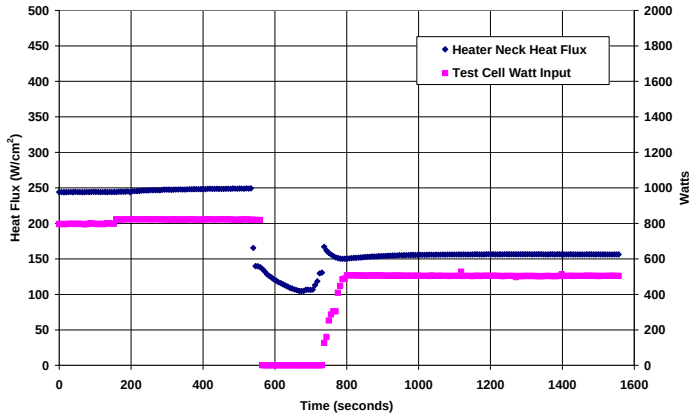

310 kPa, 15 degC Subcooled, 0.029 kg/s, 200 watt

Mass Flow Rate
310 kPa, 15 degC Subcooled, 0.029 kg/s, 200 watt

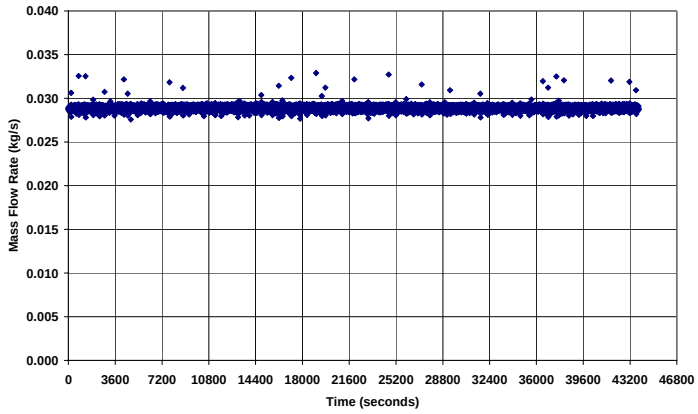

Slot Jet Fluid Temperatures
310 kPa, 15 degC Subcooled, 0.029 kg/s, 200 watt

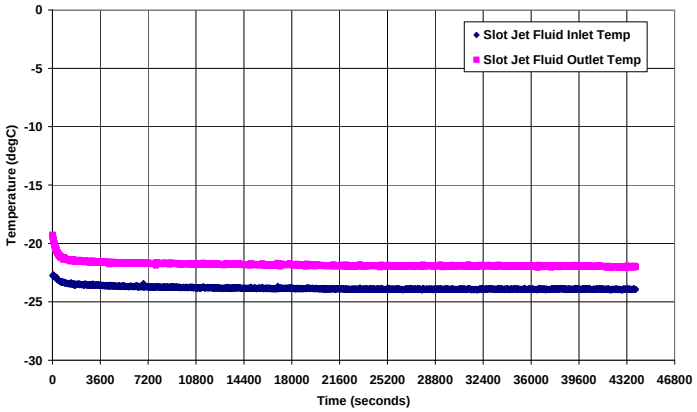

Ammonia Flow Loop Pressures
310 kPa, 15 degC Subcooled, 0.029 kg/s, 200 watt

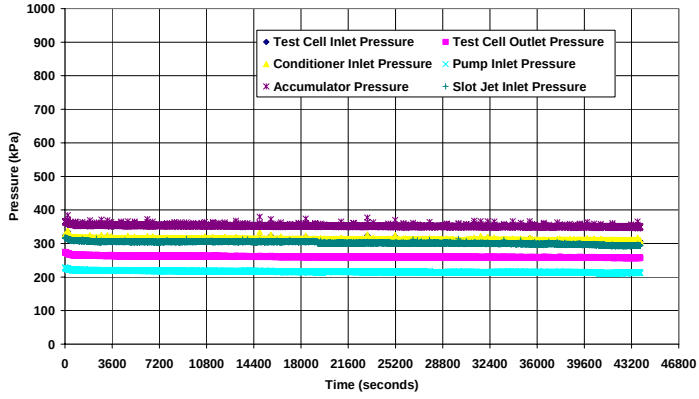

Slot Jet Surface Temperatures
310 kPa, 15 degC Subcooled, 0.029 kg/s, 200 watt

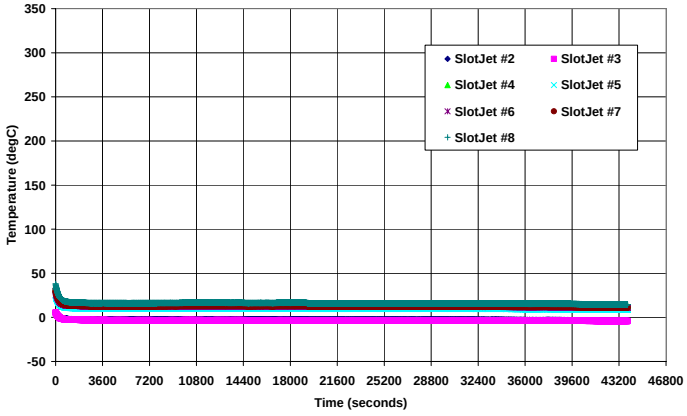

Heater Neck Temperatures
310 kPa, 15 deg Subcooled, 0.029 kg/s, 200 watt

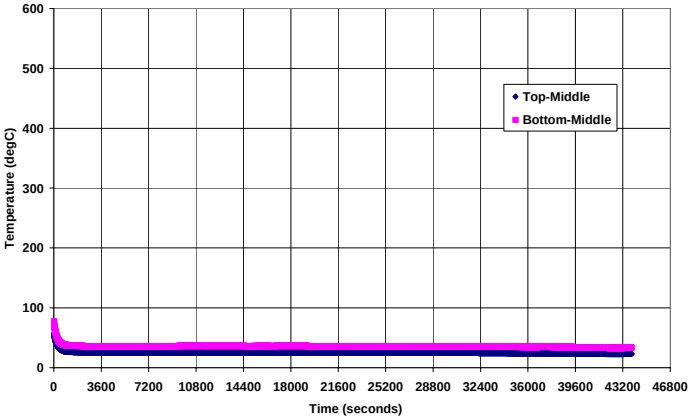

Heater Neck Heat Flux & Test Cell Watt Input
310 kPa, 15 degC Subcooled, 0.029 kg/s, 200 watt

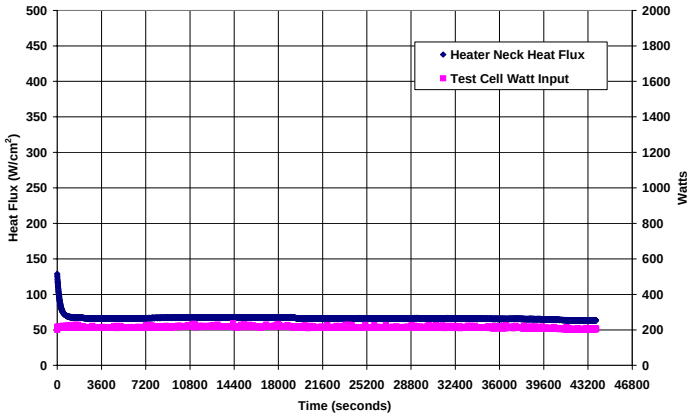

310 kPa, 15 degC Subcooled, 0.029 kg/s, 300 watt

Mass Flow Rate
310 kPa, 15 degC Subcooled, 0.029 kg/s, 300 watt

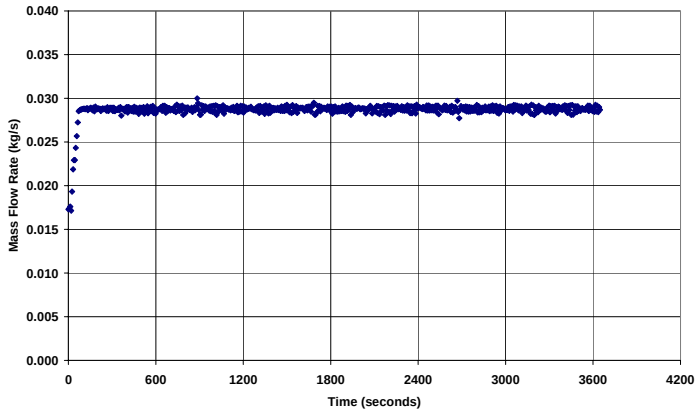

Slot Jet Fluid Temperatures
310 kPa, 15 degC Subcooled, 0.029 kg/s, 300 watt

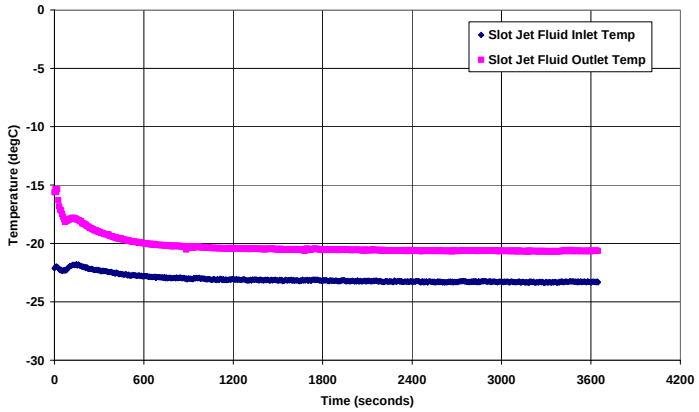

Ammonia Flow Loop Pressures
310 kPa, 15 degC Subcooled, 0.029 kg/s, 300 watt

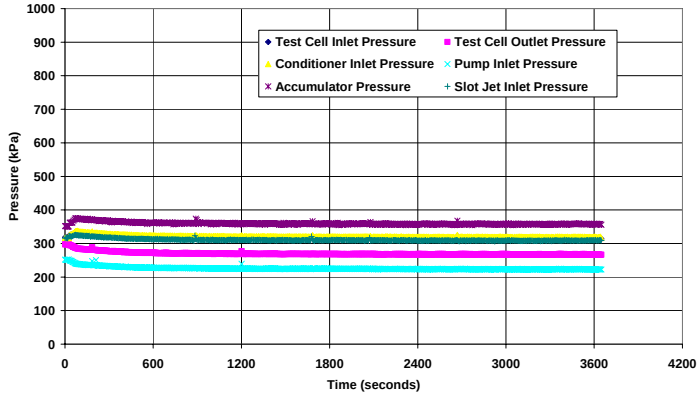

Slot Jet Surface Temperatures
310 kPa, 15 degC Subcooled, 0.029 kg/s, 300 watt

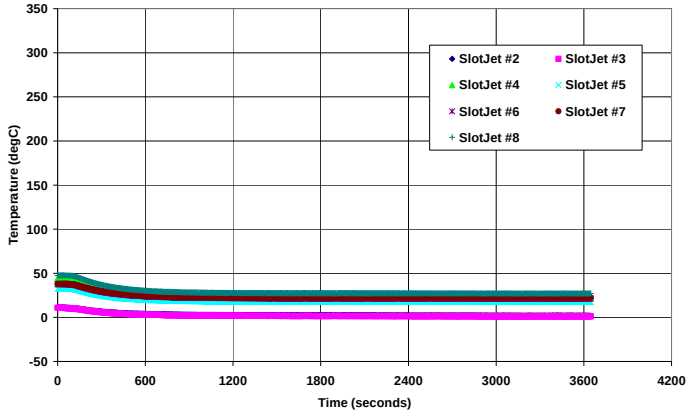

Heater Neck Temperatures
310 kPa, 15 deg Subcooled, 0.029 kg/s, 300 watt

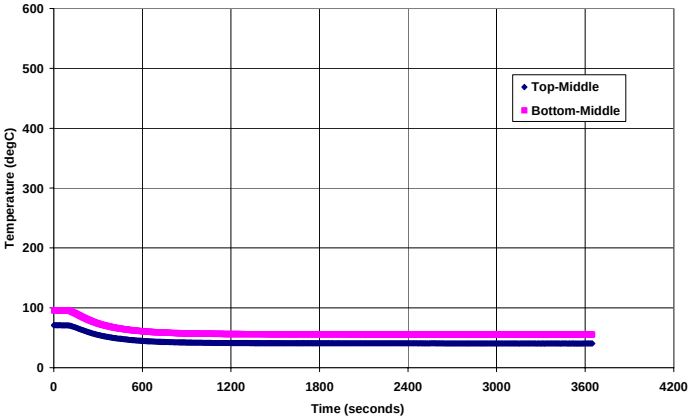

Heater Neck Heat Flux & Test Cell Watt Input
310 kPa, 15 degC Subcooled, 0.029 kg/s, 300 watt

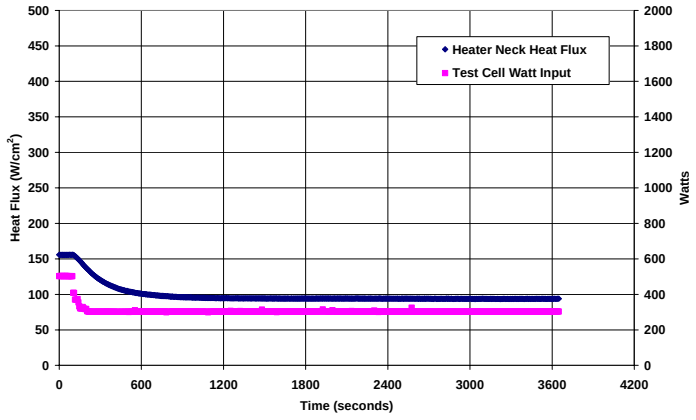

310 kPa, 15 degC Subcooled, 0.029 kg/s, 400 watt

Mass Flow Rate
310 kPa, 15 degC Subcooled, 0.029 kg/s, 400 watt

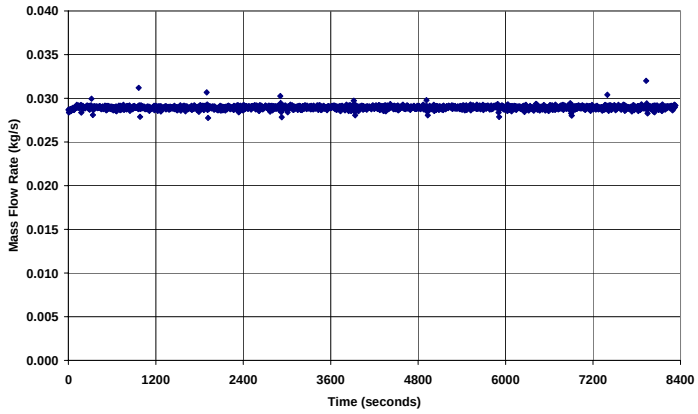

Slot Jet Fluid Temperatures
310 kPa, 15 degC Subcooled, 0.029 kg/s, 400 watt

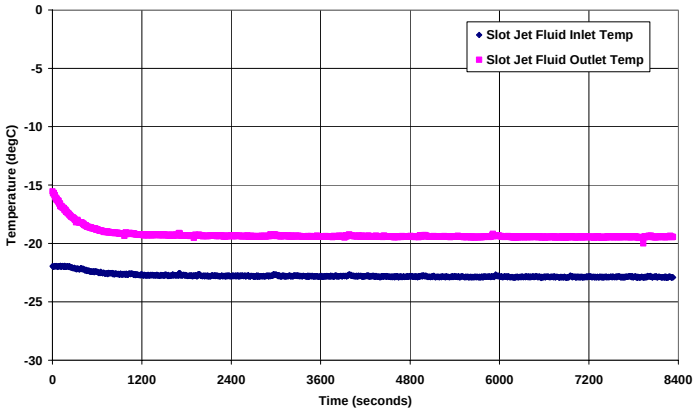

Ammonia Flow Loop Pressures
310 kPa, 15 degC Subcooled, 0.029 kg/s, 400 watt

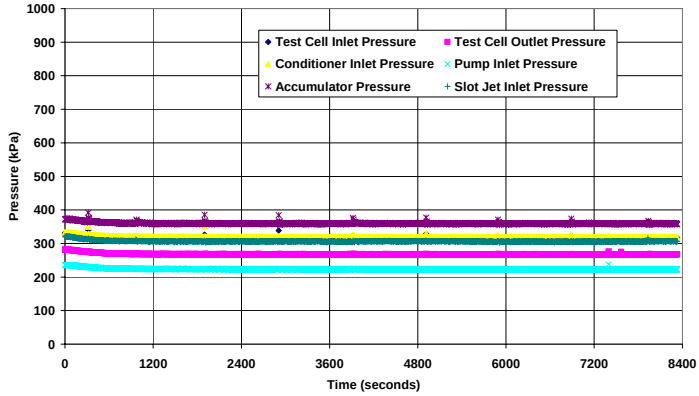

Slot Jet Surface Temperatures
310 kPa, 15 degC Subcooled, 0.029 kg/s, 400 watt

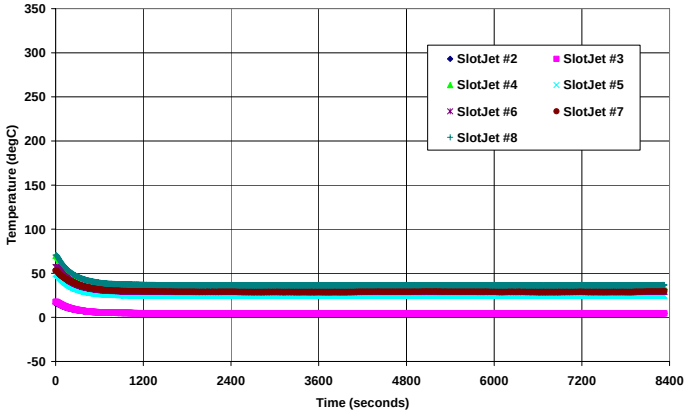

Heater Neck Temperatures
310 kPa, 15 deg Subcooled, 0.029 kg/s, 400 watt

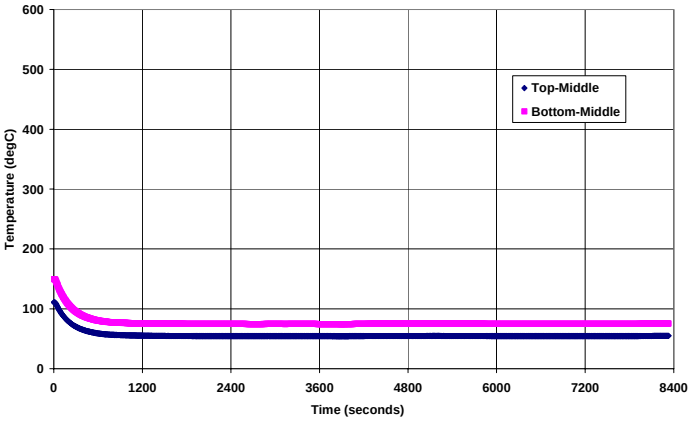

Heater Neck Heat Flux & Test Cell Watt Input
310 kPa, 15 degC Subcooled, 0.029 kg/s, 400 watt

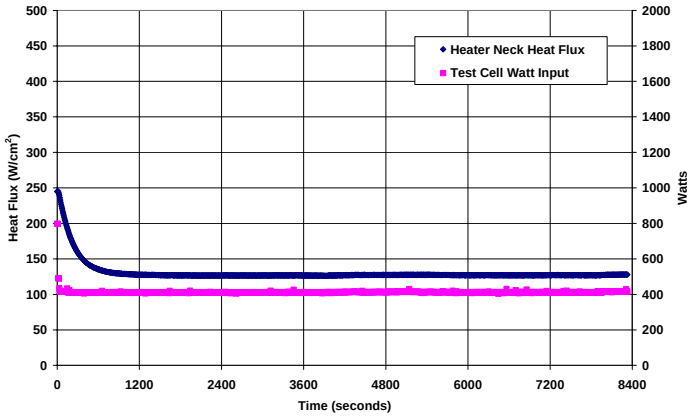

310 kPa, 15 degC Subcooled, 0.029 kg/s, 500 watt

Mass Flow Rate
310 kPa, 15 degC Subcooled, 0.029 kg/s, 500 watt

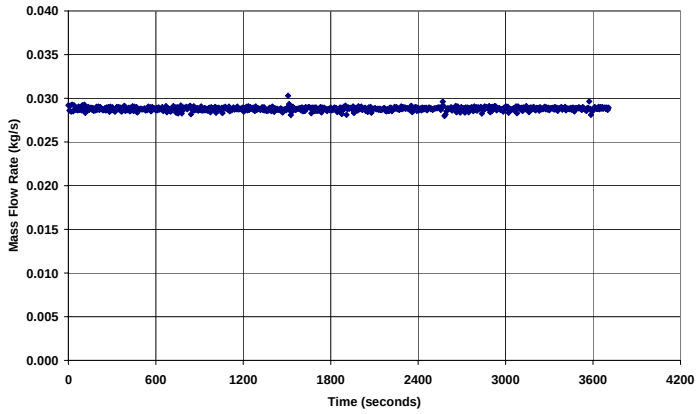

Slot Jet Fluid Temperatures
310 kPa, 15 degC Subcooled, 0.029 kg/s, 500 watt

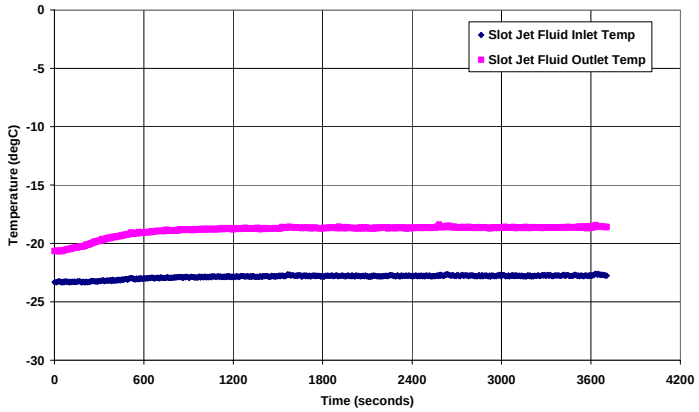

Ammonia Flow Loop Pressures
310 kPa, 15 degC Subcooled, 0.029 kg/s, 500 watt

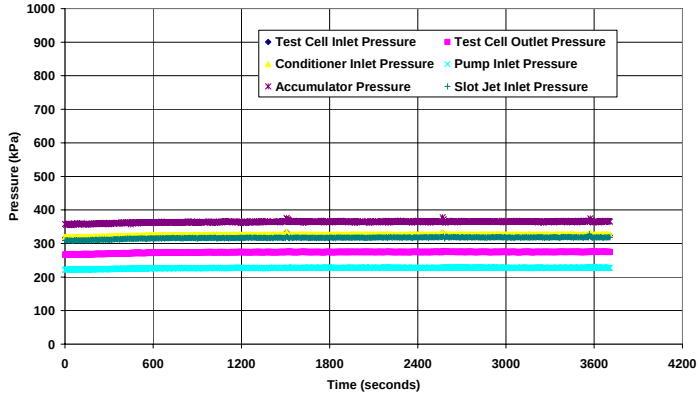

Slot Jet Surface Temperatures
310 kPa, 15 degC Subcooled, 0.029 kg/s, 500 watt

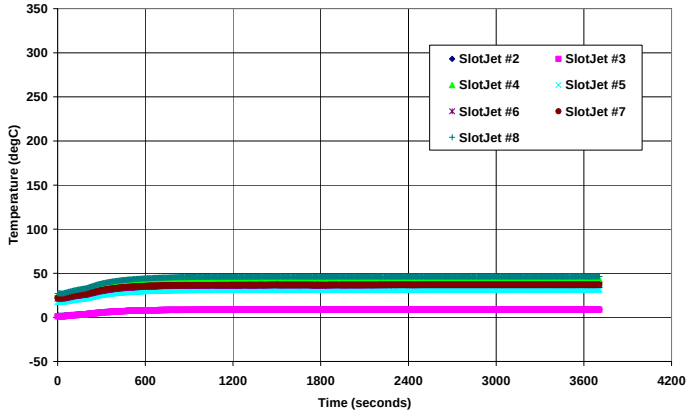

Heater Neck Temperatures
310 kPa, 15 deg Subcooled, 0.029 kg/s, 500 watt

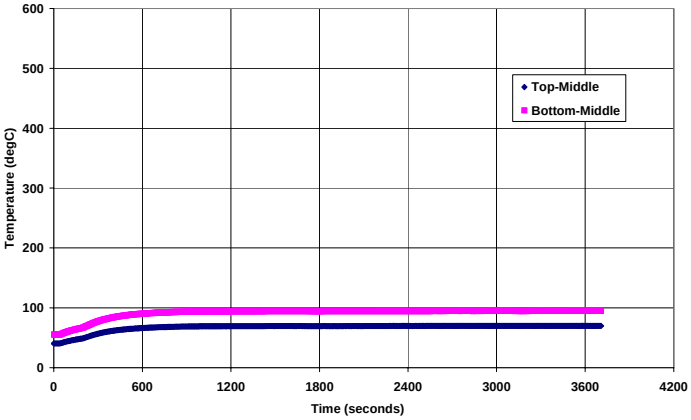

Heater Neck Heat Flux & Test Cell Watt Input
310 kPa, 15 degC Subcooled, 0.029 kg/s, 500 watt

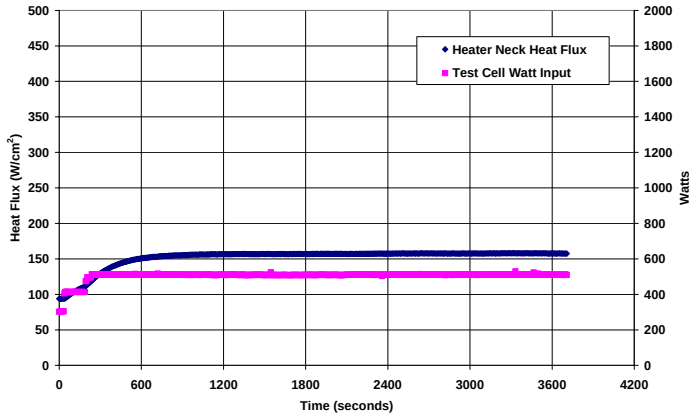

310 kPa, 15 degC Subcooled, 0.029 kg/s, 600 watt

Mass Flow Rate
310 kPa, 15 degC Subcooled, 0.029 kg/s, 600 watt

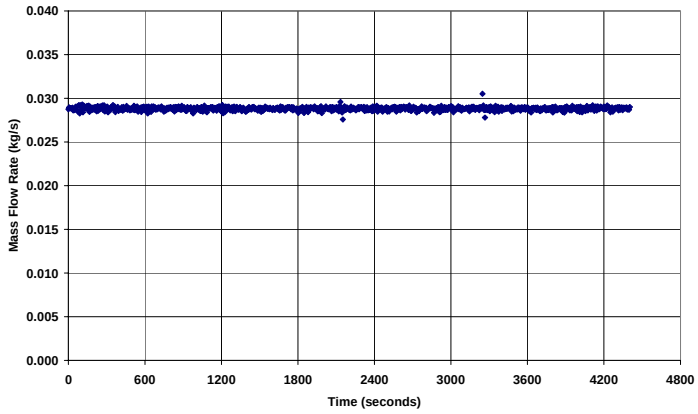

Slot Jet Fluid Temperatures
310 kPa, 15 degC Subcooled, 0.029 kg/s, 600 watt

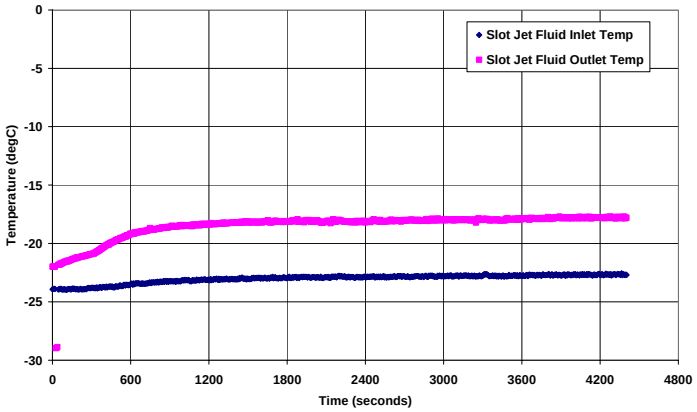

Ammonia Flow Loop Pressures
310 kPa, 15 degC Subcooled, 0.029 kg/s, 600 watt

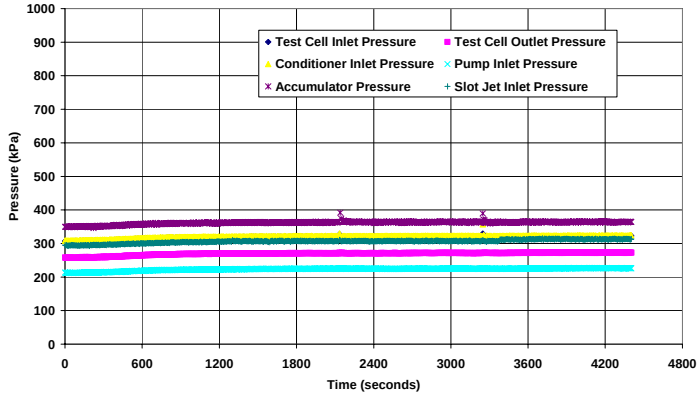

Slot Jet Surface Temperatures
310 kPa, 15 degC Subcooled, 0.029 kg/s, 600 watt

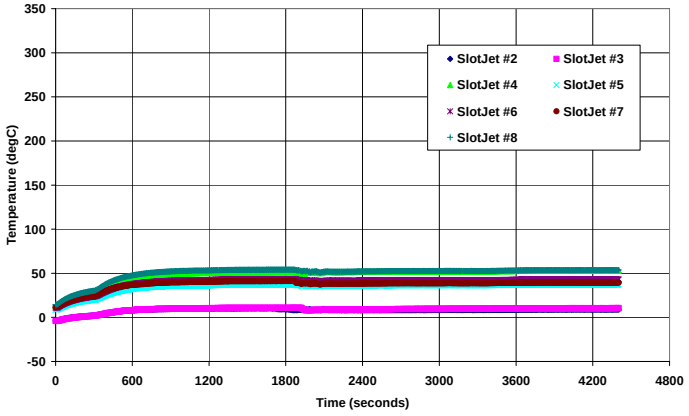

Heater Neck Temperatures
310 kPa, 15 deg Subcooled, 0.029 kg/s, 600 watt

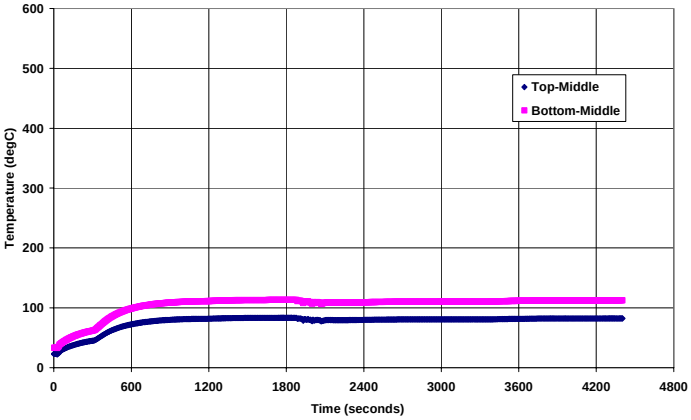

Heater Neck Heat Flux & Test Cell Watt Input
310 kPa, 15 degC Subcooled, 0.029 kg/s, 600 watt

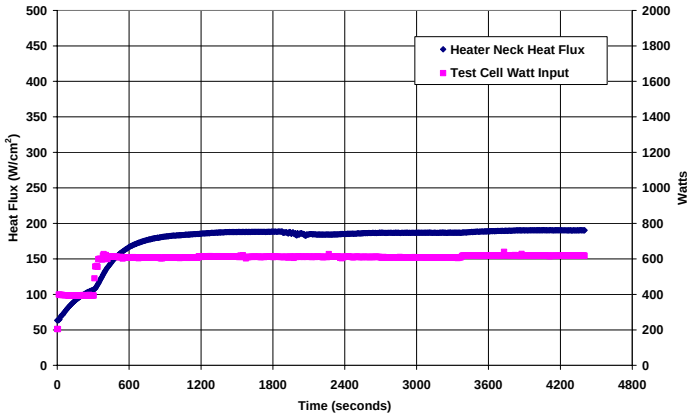

310 kPa, 15 degC Subcooled, 0.029 kg/s, 700 watt

Mass Flow Rate
310 kPa, 15 degC Subcooled, 0.029 kg/s, 700 watt

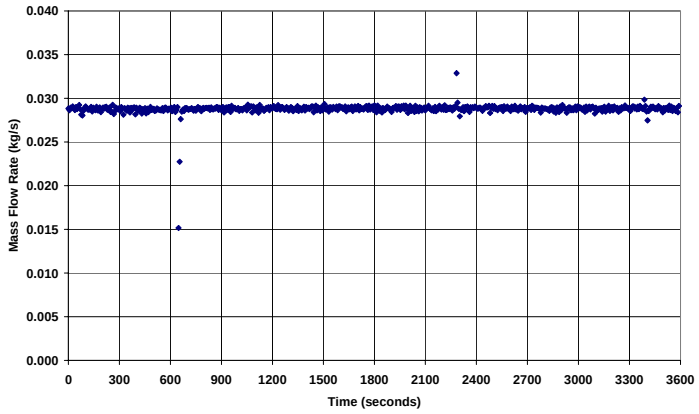

Slot Jet Fluid Temperatures
310 kPa, 15 degC Subcooled, 0.029 kg/s, 700 watt

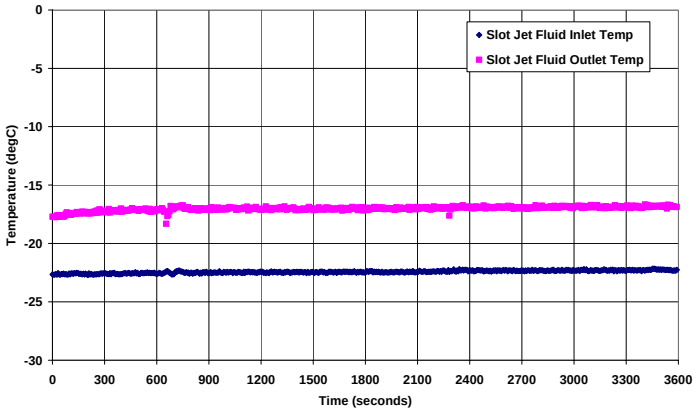

Ammonia Flow Loop Pressures
310 kPa, 15 degC Subcooled, 0.029 kg/s, 700 watt

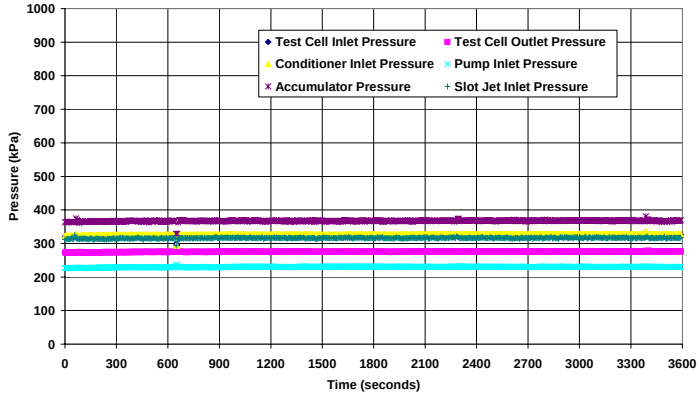

Slot Jet Surface Temperatures
310 kPa, 15 degC Subcooled, 0.029 kg/s, 700 watt

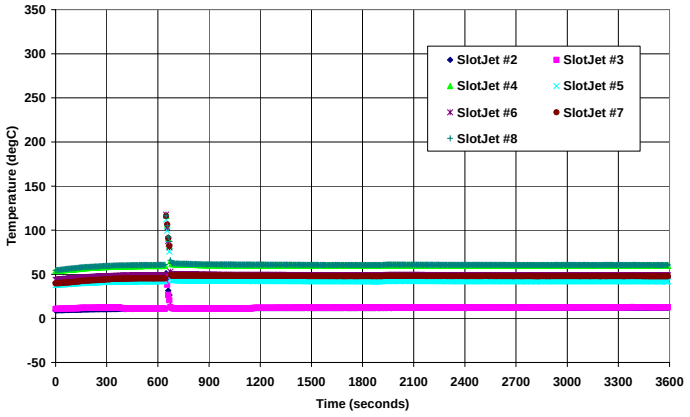

Heater Neck Temperatures
310 kPa, 15 deg Subcooled, 0.029 kg/s, 700 watt

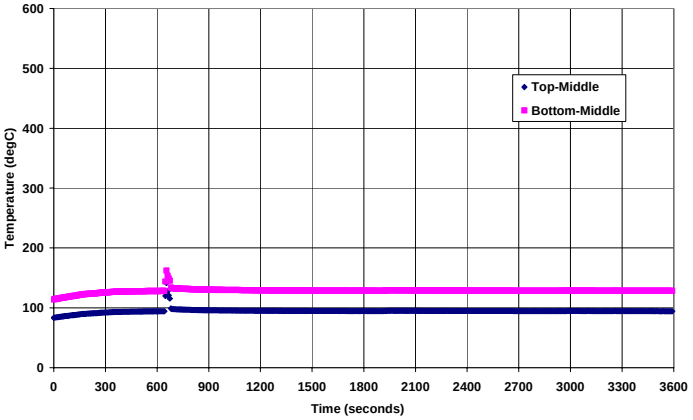

Heater Neck Heat Flux & Test Cell Watt Input
310 kPa, 15 degC Subcooled, 0.029 kg/s, 700 watt

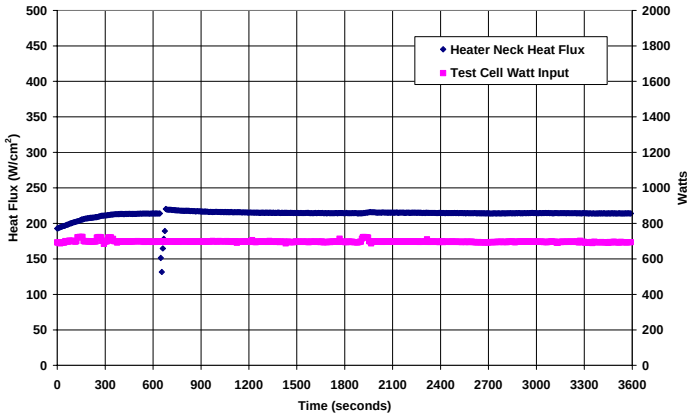

310 kPa, 15 degC Subcooled, 0.029 kg/s, 800 watt

Mass Flow Rate
310 kPa, 15 degC Subcooled, 0.029 kg/s, 800 watt

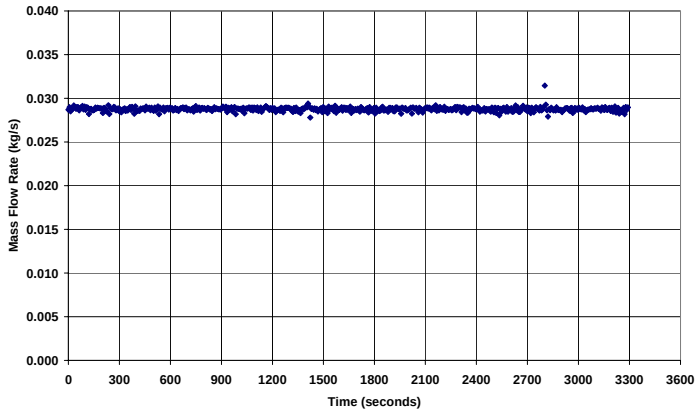

Slot Jet Fluid Temperatures
310 kPa, 15 degC Subcooled, 0.029 kg/s, 800 watt

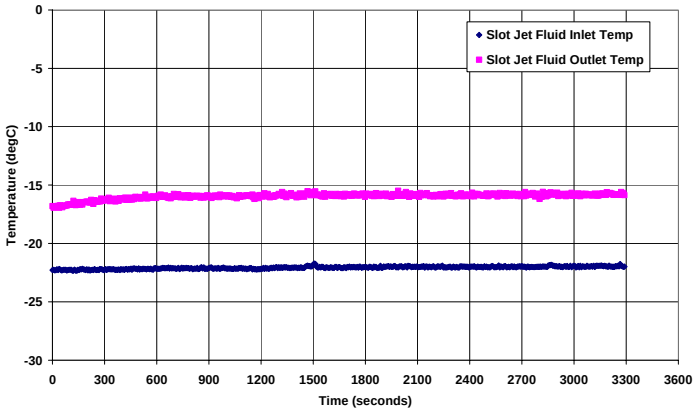

Ammonia Flow Loop Pressures
310 kPa, 15 degC Subcooled, 0.029 kg/s, 800 watt

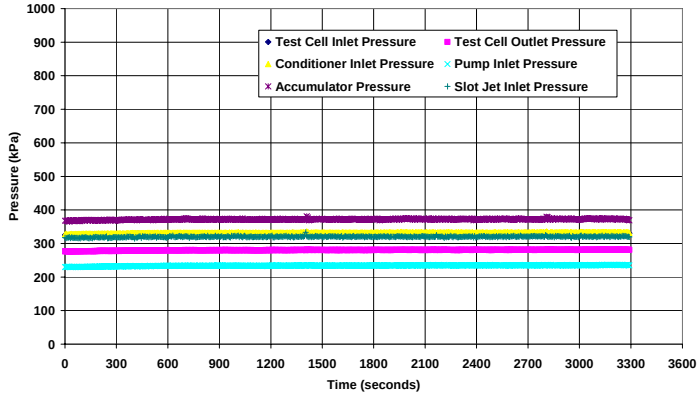

Slot Jet Surface Temperatures
310 kPa, 15 degC Subcooled, 0.029 kg/s, 800 watt

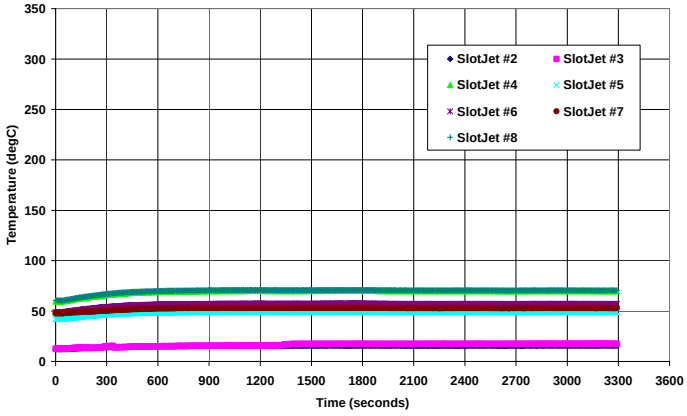

Heater Neck Temperatures
310 kPa, 15 deg Subcooled, 0.029 kg/s, 800 watt

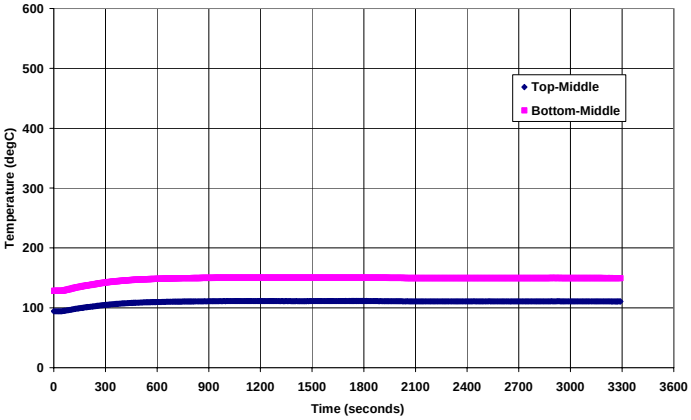

Heater Neck Heat Flux & Test Cell Watt Input
310 kPa, 15 degC Subcooled, 0.029 kg/s, 800 watt

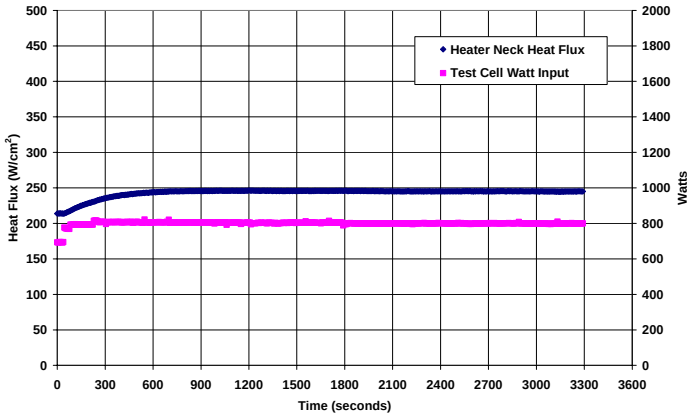

310 kPa, 15 degC Subcooled, 0.029 kg/s, 900 watt

Mass Flow Rate
310 kPa, 15 degC Subcooled, 0.029 kg/s, 900 watt

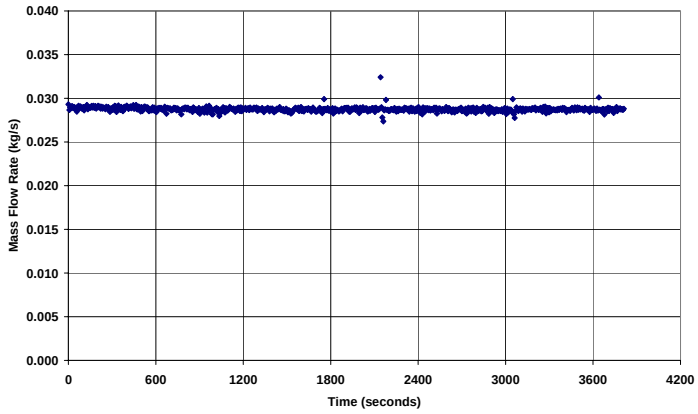

Slot Jet Fluid Temperatures
310 kPa, 15 degC Subcooled, 0.029 kg/s, 900 watt

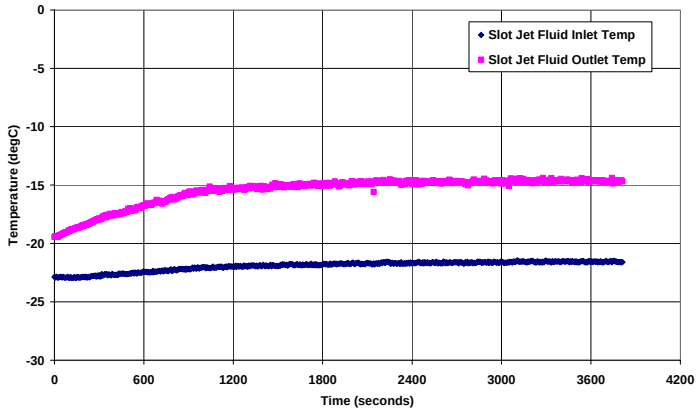

Ammonia Flow Loop Pressures
310 kPa, 15 degC Subcooled, 0.029 kg/s, 900 watt

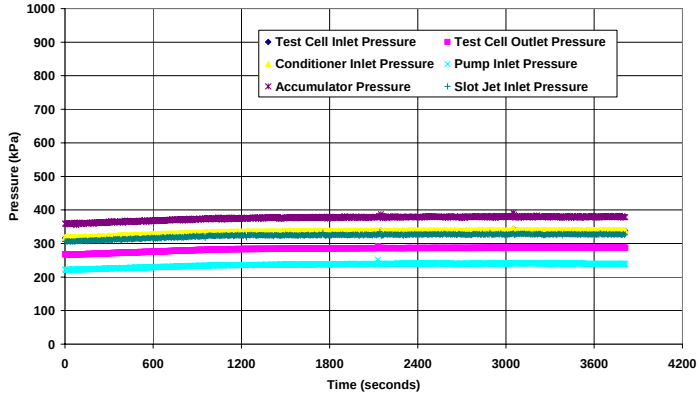

Slot Jet Surface Temperatures
310 kPa, 15 degC Subcooled, 0.029 kg/s, 900 watt

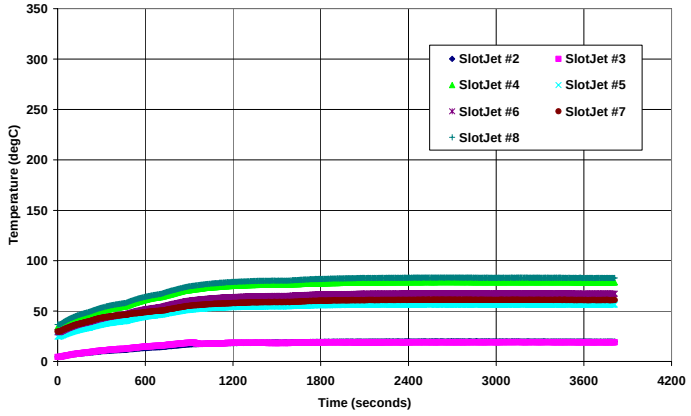

Heater Neck Temperatures
310 kPa, 15 deg Subcooled, 0.029 kg/s, 900 watt

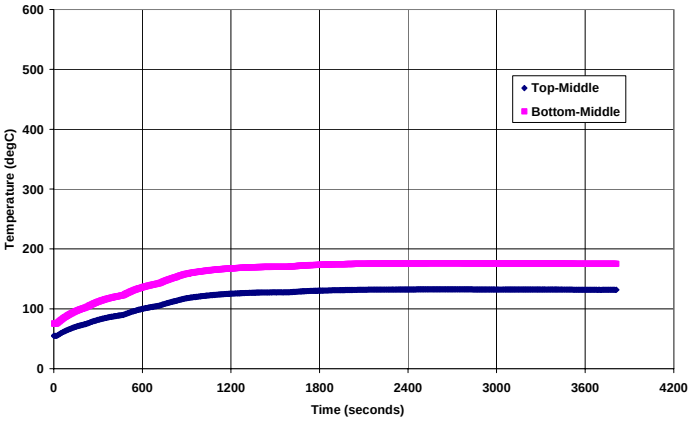

Heater Neck Heat Flux & Test Cell Watt Input
310 kPa, 15 degC Subcooled, 0.029 kg/s, 900 watt

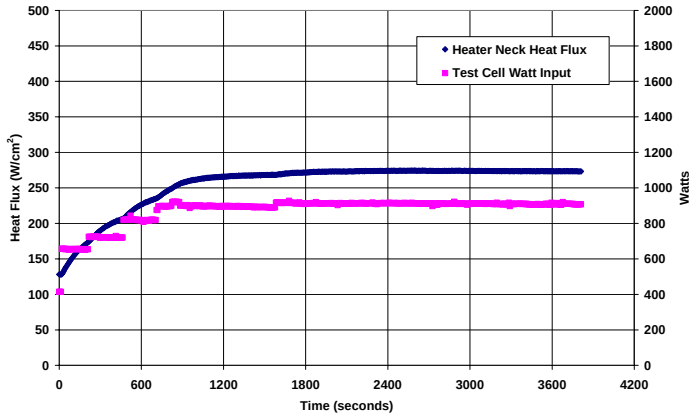

310 kPa, 15 degC Subcooled, 0.029 kg/s, 1000 watt

Mass Flow Rate
310 kPa, 15 degC Subcooled, 0.029 kg/s, 1000 watt

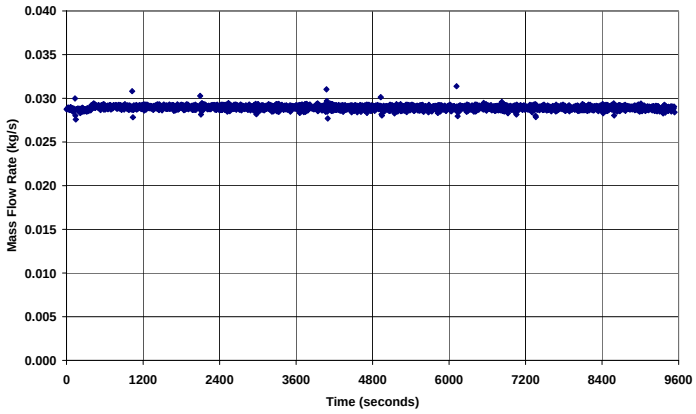

Slot Jet Fluid Temperatures
310 kPa, 15 degC Subcooled, 0.029 kg/s, 1000 watt

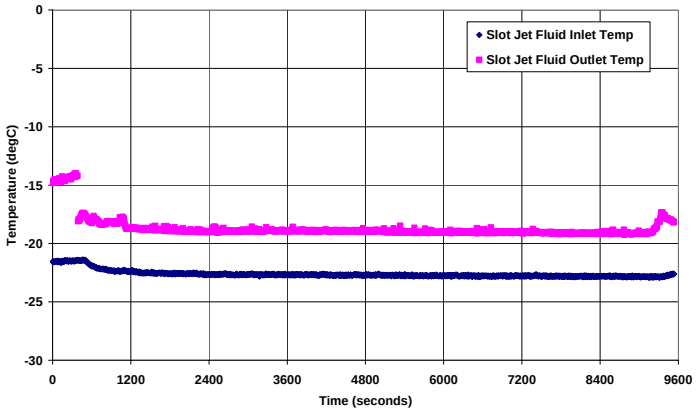

Ammonia Flow Loop Pressures
310 kPa, 15 degC Subcooled, 0.029 kg/s, 1000 watt

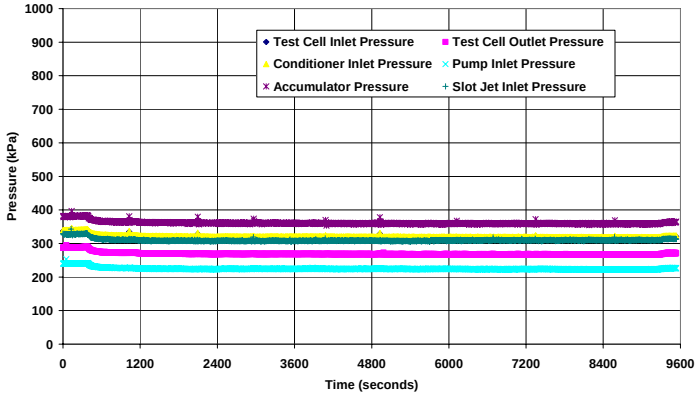

Slot Jet Surface Temperatures
310 kPa, 15 degC Subcooled, 0.029 kg/s, 1000 watt

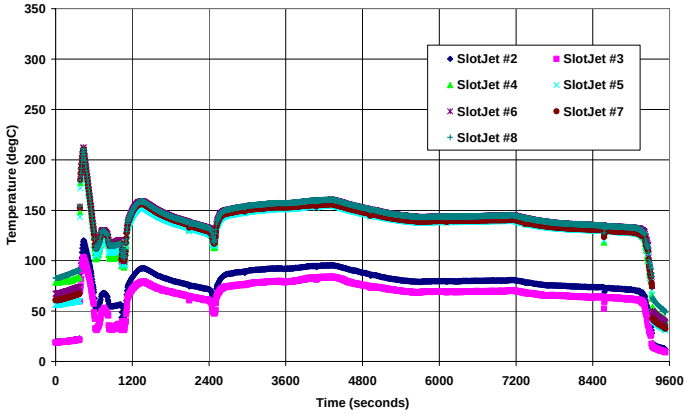

Heater Neck Temperatures
310 kPa, 15 deg Subcooled, 0.029 kg/s, 1000 watt

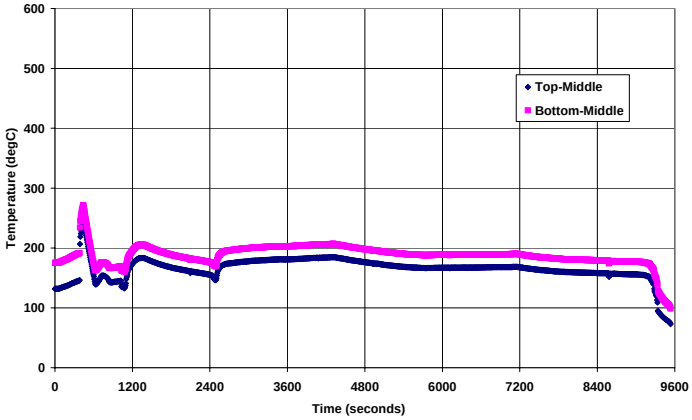

Heater Neck Heat Flux & Test Cell Watt Input
310 kPa, 15 degC Subcooled, 0.029 kg/s, 1000 watt

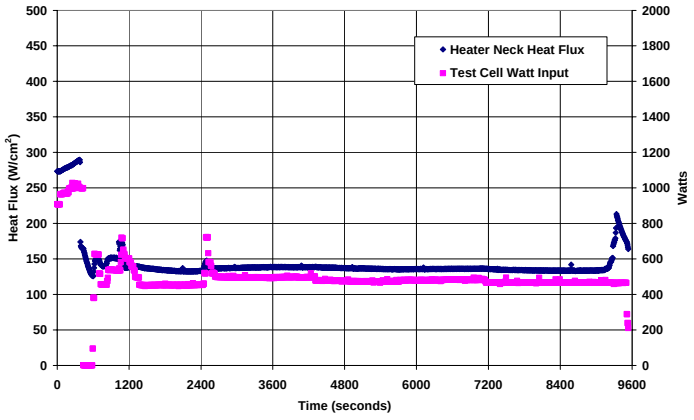

410 kPa, 20 degC Subcooled, 0.01 kg/s, 300 watt

Mass Flow Rate
410 kPa, 20 degC Subcooled, 0.01 kg/s, 300 watt

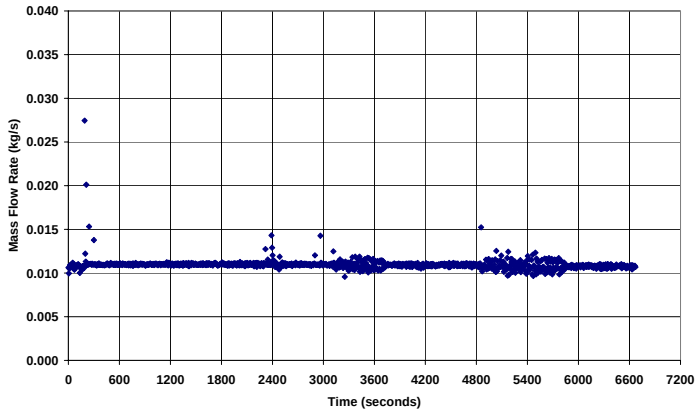

Slot Jet Fluid Temperatures
410 kPa, 20 degC Subcooled, 0.01 kg/s, 300 watt

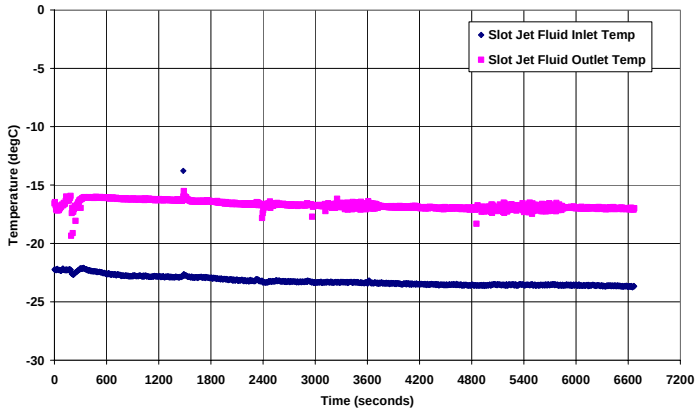

Ammonia Flow Loop Pressures
410 kPa, 20 degC Subcooled, 0.01 kg/s, 300 watt

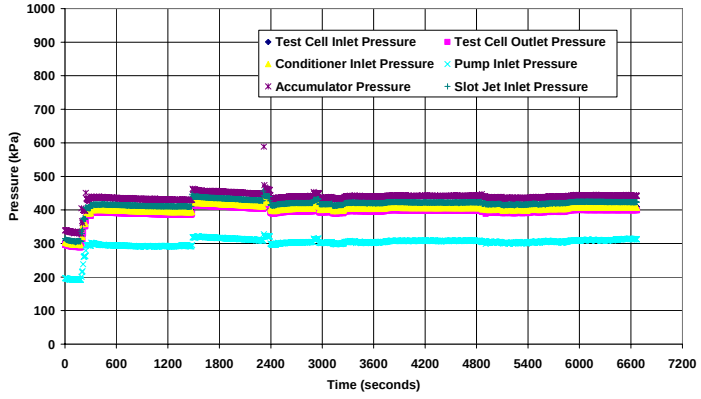

Slot Jet Surface Temperatures
410 kPa, 20 degC Subcooled, 0.01 kg/s, 300 watt

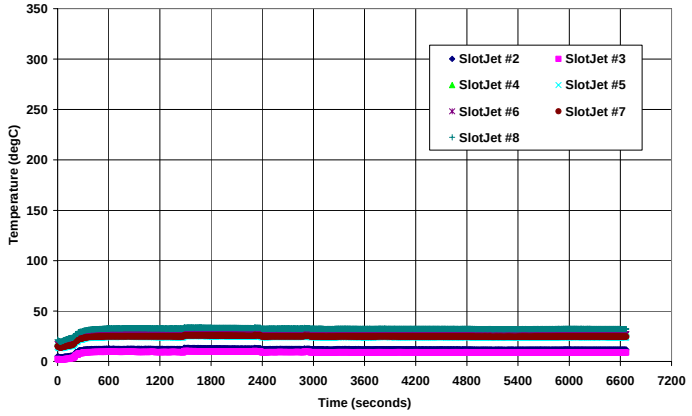

Heater Neck Temperatures
410 kPa, 20 deg Subcooled, 0.01 kg/s, 300 watt

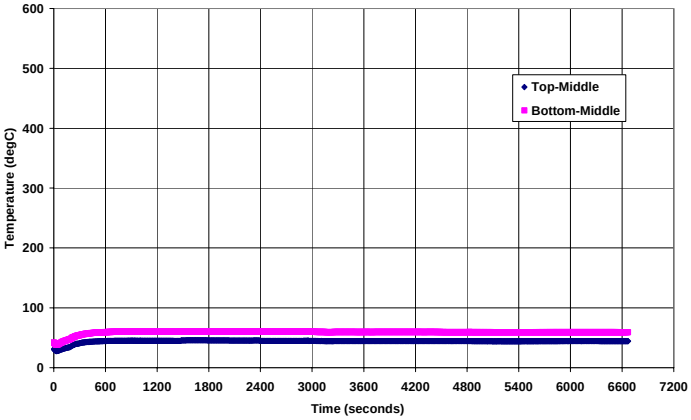

Heater Neck Heat Flux & Test Cell Watt Input
410 kPa, 20 degC Subcooled, 0.01 kg/s, 300 watt

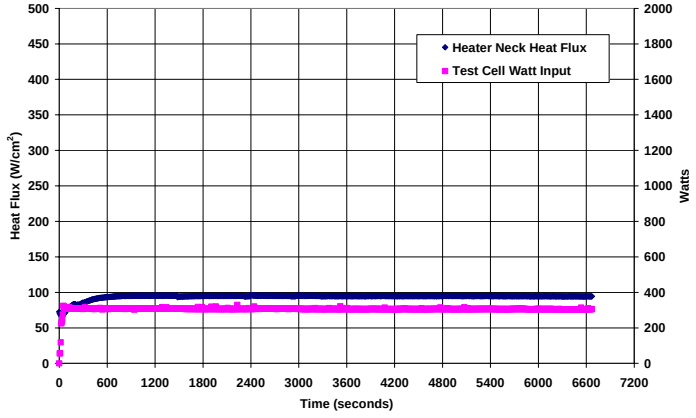

410 kPa, 20 degC Subcooled, 0.01 kg/s, 400 watt

Mass Flow Rate
410 kPa, 20 degC Subcooled, 0.01 kg/s, 400 watt

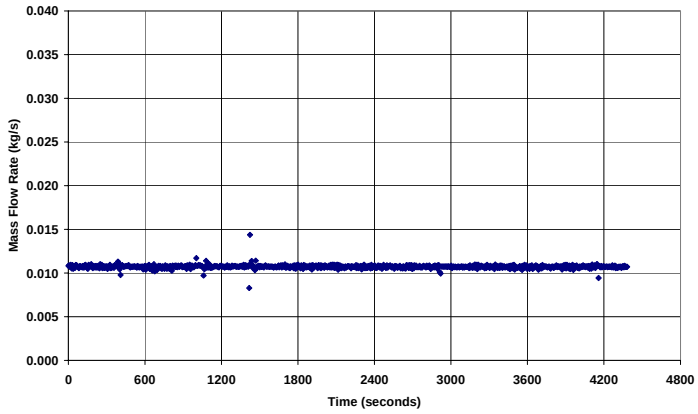

Slot Jet Fluid Temperatures
410 kPa, 20 degC Subcooled, 0.01 kg/s, 400 watt

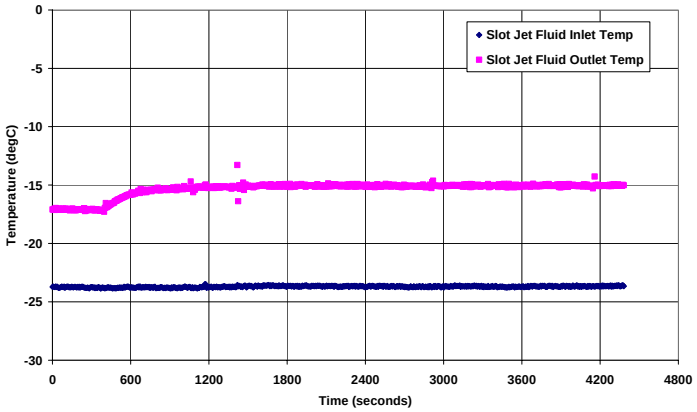

Ammonia Flow Loop Pressures
410 kPa, 20 degC Subcooled, 0.01 kg/s, 400 watt

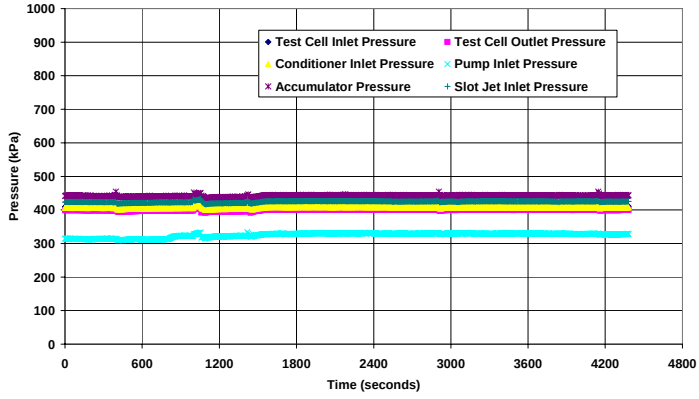

Slot Jet Surface Temperatures
410 kPa, 20 degC Subcooled, 0.01 kg/s, 400 watt

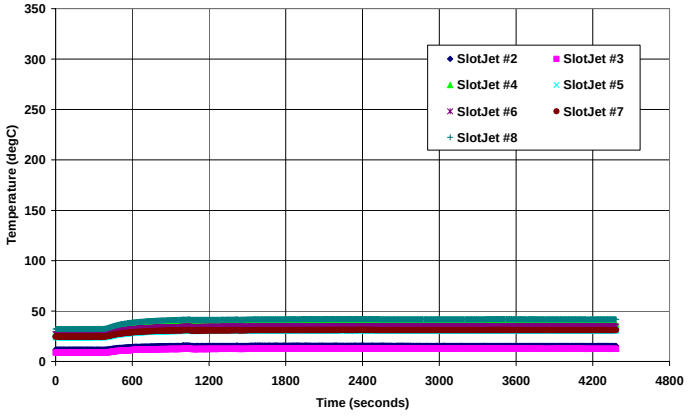

Heater Neck Temperatures
410 kPa, 20 deg Subcooled, 0.01 kg/s, 400 watt

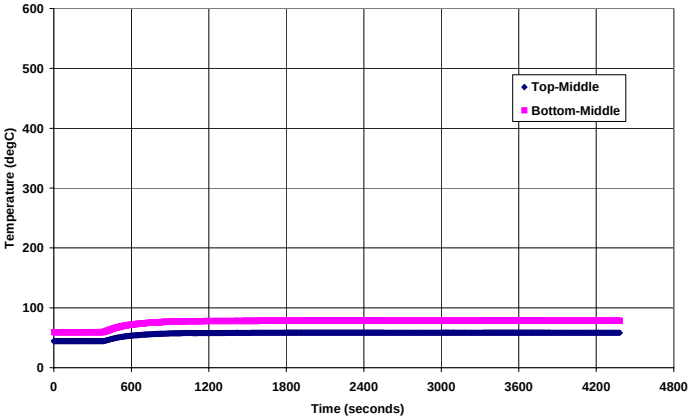

Heater Neck Heat Flux & Test Cell Watt Input
410 kPa, 20 degC Subcooled, 0.01 kg/s, 400 watt

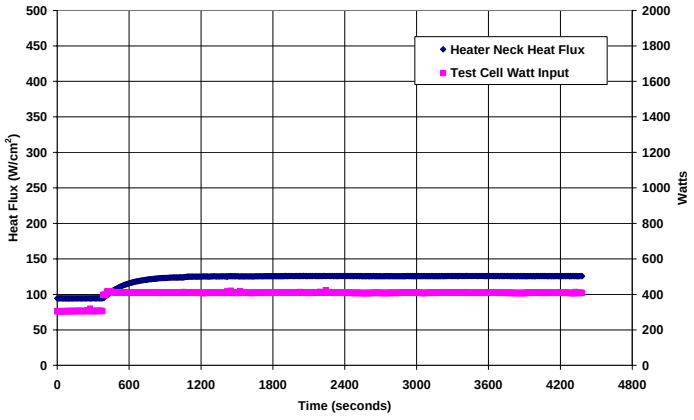

410 kPa, 20 degC Subcooled, 0.01 kg/s, 500 watt

Mass Flow Rate
410 kPa, 20 degC Subcooled, 0.01 kg/s, 500 watt

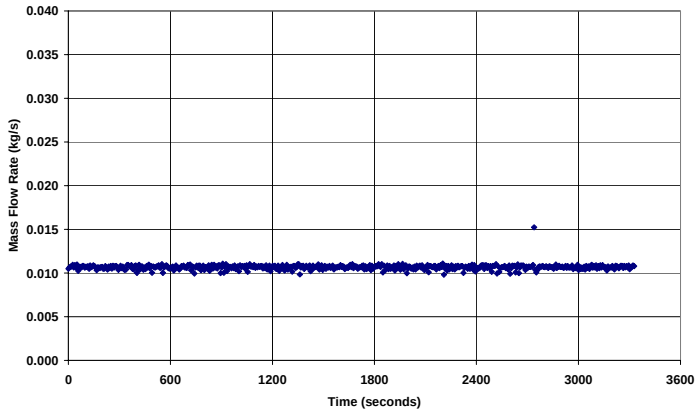

Slot Jet Fluid Temperatures
410 kPa, 20 degC Subcooled, 0.01 kg/s, 500 watt

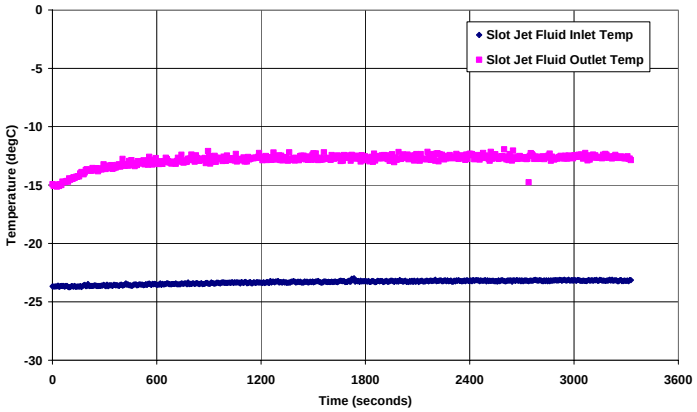

Ammonia Flow Loop Pressures
410 kPa, 20 degC Subcooled, 0.01 kg/s, 500 watt

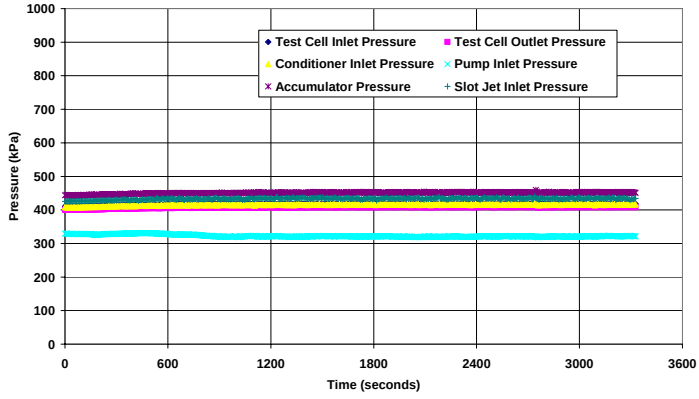

Slot Jet Surface Temperatures
410 kPa, 20 degC Subcooled, 0.01 kg/s, 500 watt

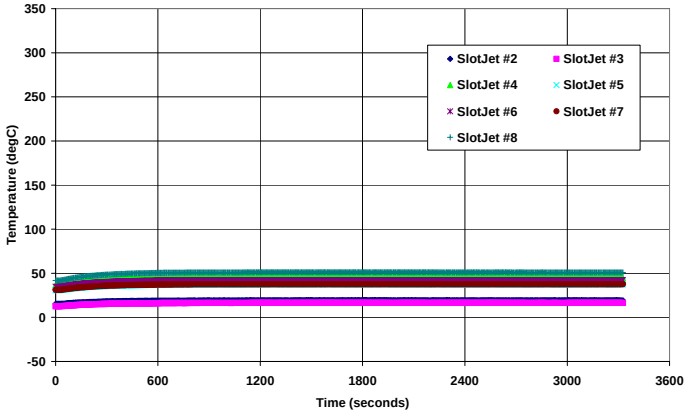

Heater Neck Temperatures
410 kPa, 20 deg Subcooled, 0.01 kg/s, 500 watt

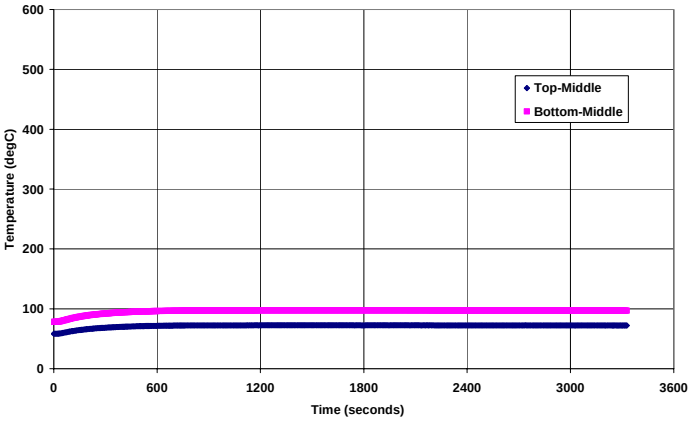

Heater Neck Heat Flux & Test Cell Watt Input
410 kPa, 20 degC Subcooled, 0.01 kg/s, 500 watt

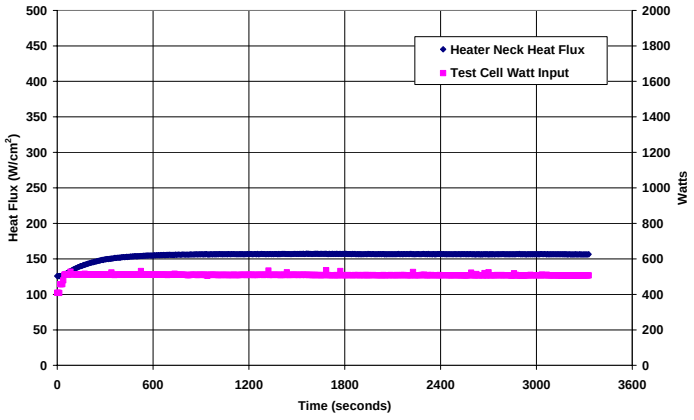

410 kPa, 20 degC Subcooled, 0.01 kg/s, 600 watt

Mass Flow Rate
410 kPa, 20 degC Subcooled, 0.01 kg/s, 600 watt

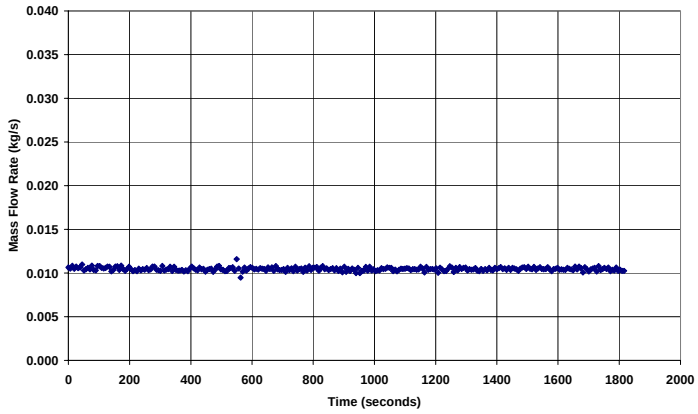

Slot Jet Fluid Temperatures
410 kPa, 20 degC Subcooled, 0.01 kg/s, 600 watt

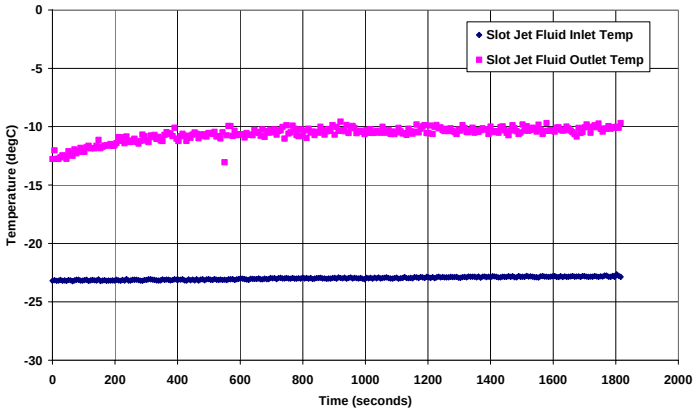

Ammonia Flow Loop Pressures
410 kPa, 20 degC Subcooled, 0.01 kg/s, 600 watt

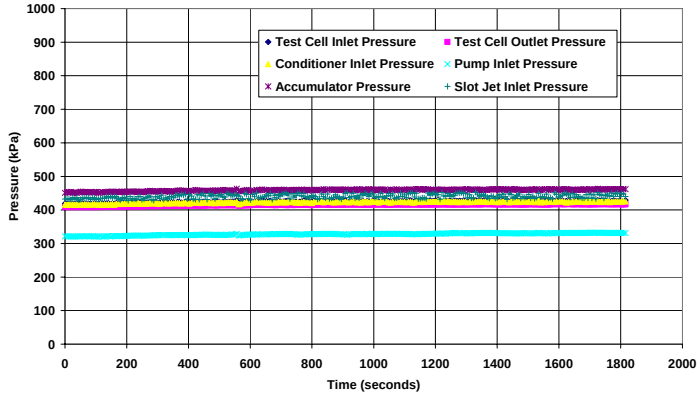

Slot Jet Surface Temperatures
410 kPa, 20 degC Subcooled, 0.01 kg/s, 600 watt

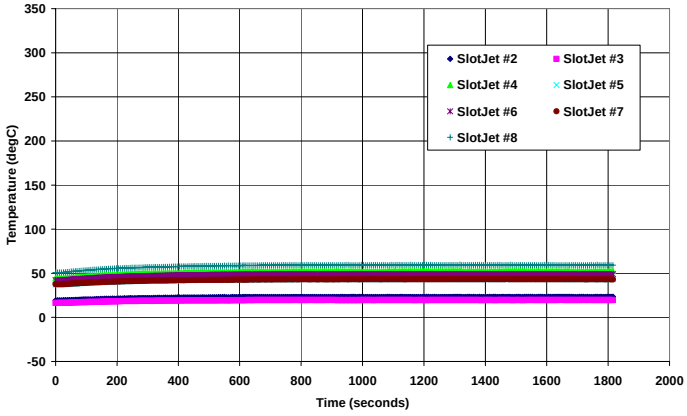

Heater Neck Temperatures
410 kPa, 20 deg Subcooled, 0.01 kg/s, 600 watt

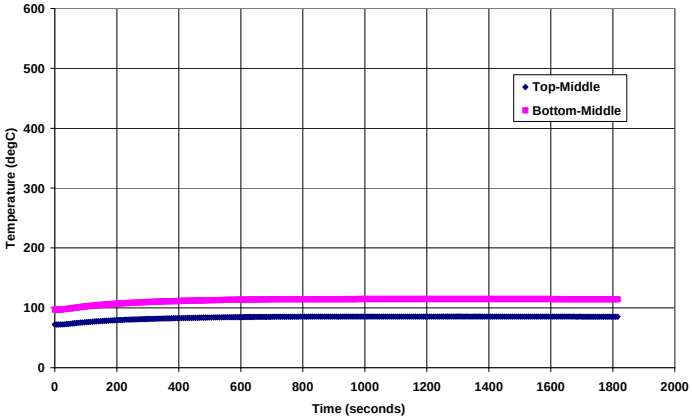

Heater Neck Heat Flux & Test Cell Watt Input
410 kPa, 20 degC Subcooled, 0.01 kg/s, 600 watt

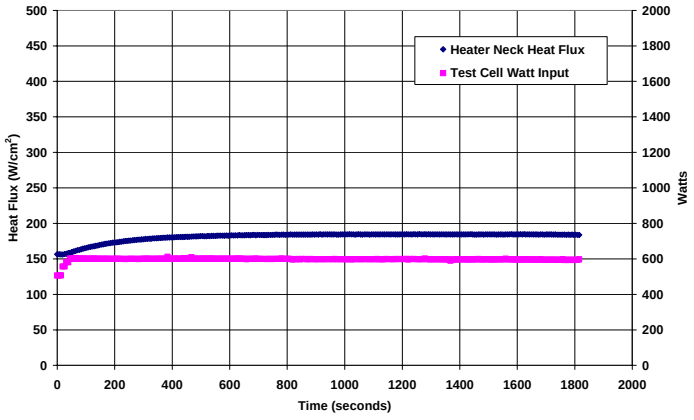

410 kPa, 20 degC Subcooled, 0.01 kg/s, 650 watt

Mass Flow Rate
410 kPa, 20 degC Subcooled, 0.01 kg/s, 650 watt

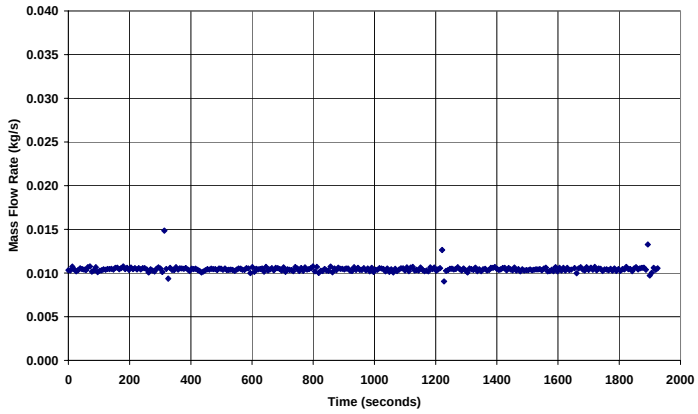

Slot Jet Fluid Temperatures
410 kPa, 20 degC Subcooled, 0.01 kg/s, 650 watt

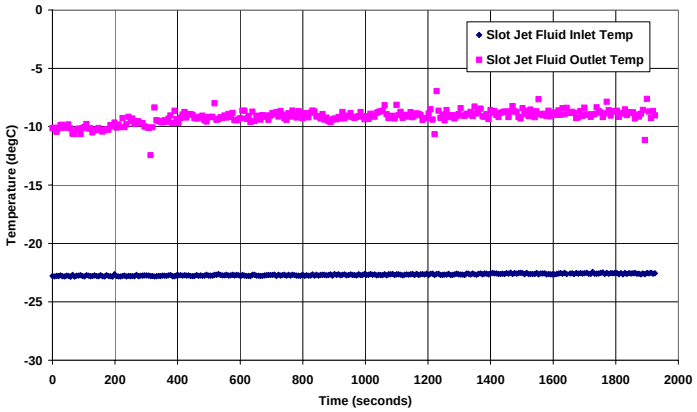

Ammonia Flow Loop Pressures
410 kPa, 20 degC Subcooled, 0.01 kg/s, 650 watt

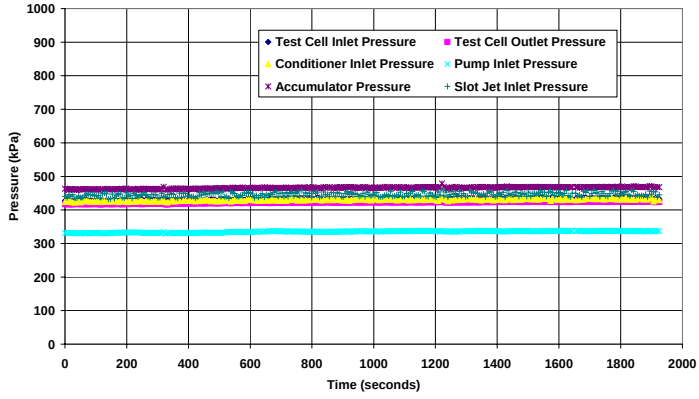

Slot Jet Surface Temperatures
410 kPa, 20 degC Subcooled, 0.01 kg/s, 650 watt

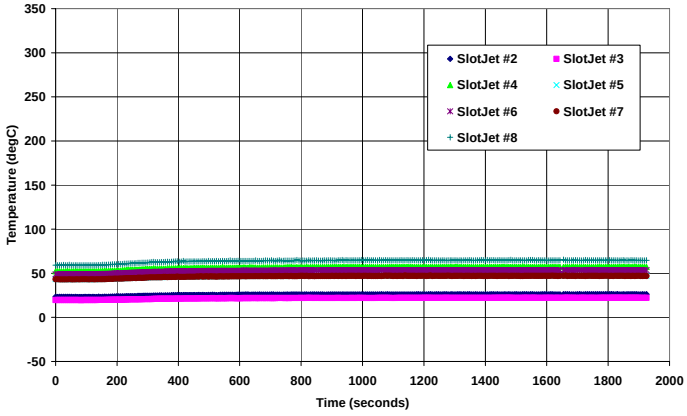

Heater Neck Temperatures
410 kPa, 20 deg Subcooled, 0.01 kg/s, 650 watt

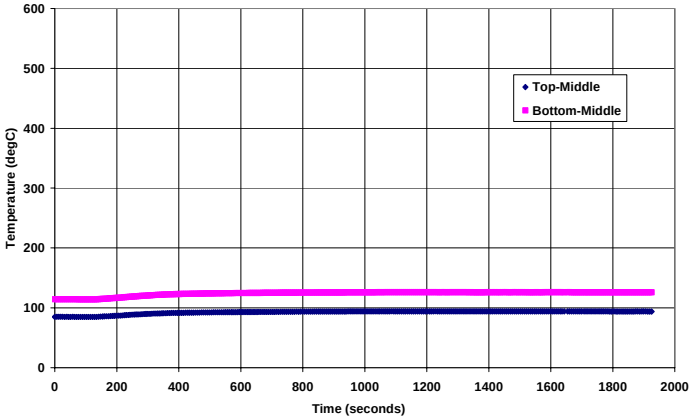

Heater Neck Heat Flux & Test Cell Watt Input
410 kPa, 20 degC Subcooled, 0.01 kg/s, 650 watt

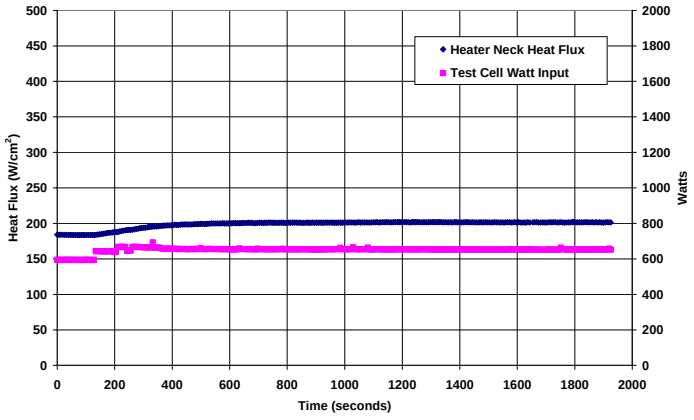

410 kPa, 20 degC Subcooled, 0.01 kg/s, 700 watt

Mass Flow Rate
410 kPa, 20 degC Subcooled, 0.01 kg/s, 700 watt

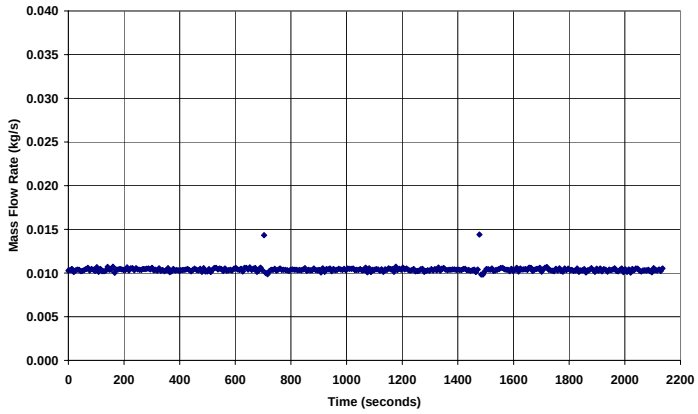

Slot Jet Fluid Temperatures
410 kPa, 20 degC Subcooled, 0.01 kg/s, 700 watt

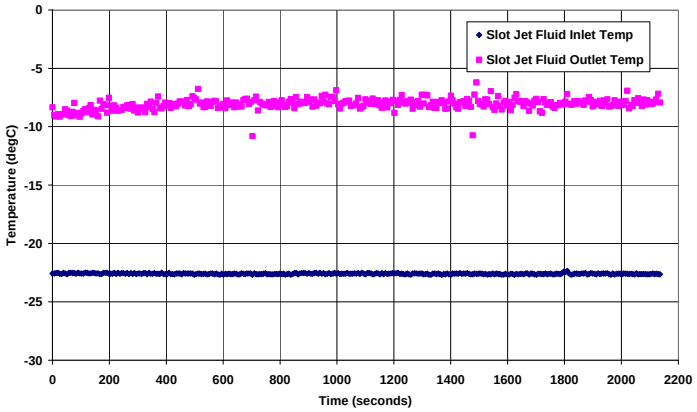

Ammonia Flow Loop Pressures
410 kPa, 20 degC Subcooled, 0.01 kg/s, 700 watt

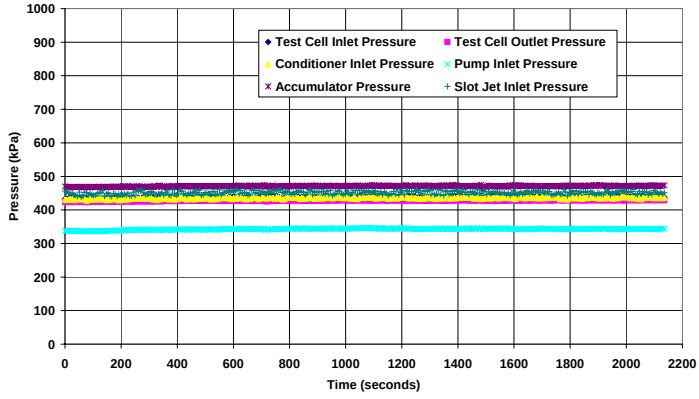

Slot Jet Surface Temperatures
410 kPa, 20 degC Subcooled, 0.01 kg/s, 700 watt

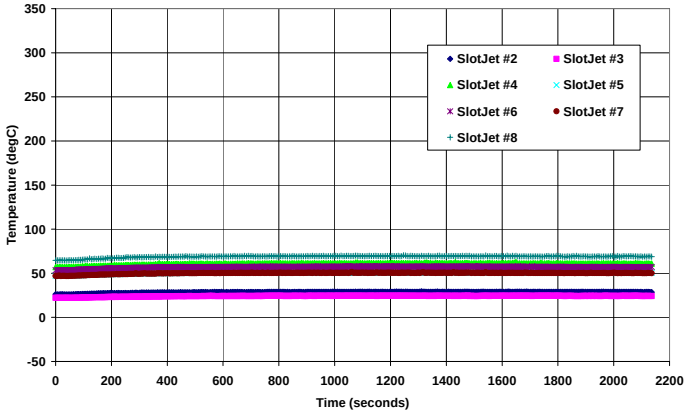

Heater Neck Temperatures
410 kPa, 20 deg Subcooled, 0.01 kg/s, 700 watt

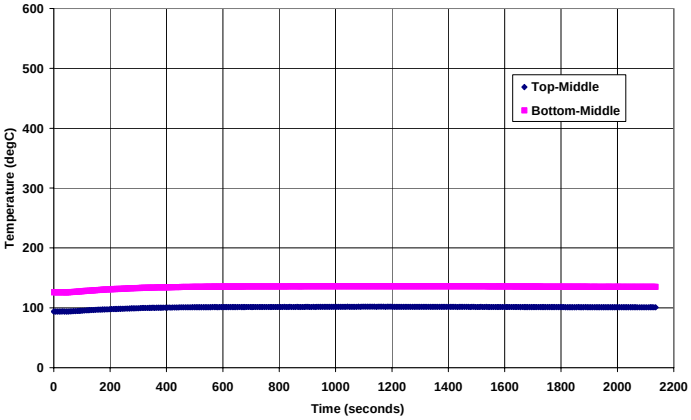

Heater Neck Heat Flux & Test Cell Watt Input
410 kPa, 20 degC Subcooled, 0.01 kg/s, 700 watt

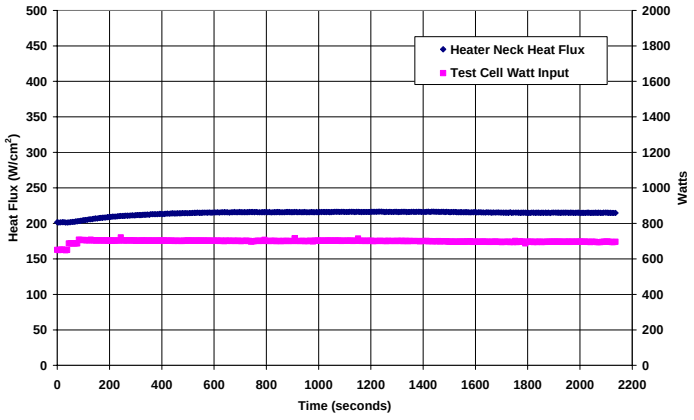

410 kPa, 20 degC Subcooled, 0.01 kg/s, 750 watt

Mass Flow Rate
410 kPa, 20 degC Subcooled, 0.01 kg/s, 750 watt

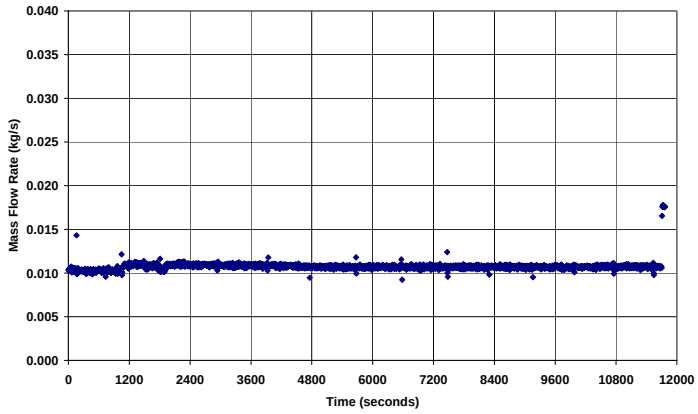

Slot Jet Fluid Temperatures
410 kPa, 20 degC Subcooled, 0.01 kg/s, 750 watt

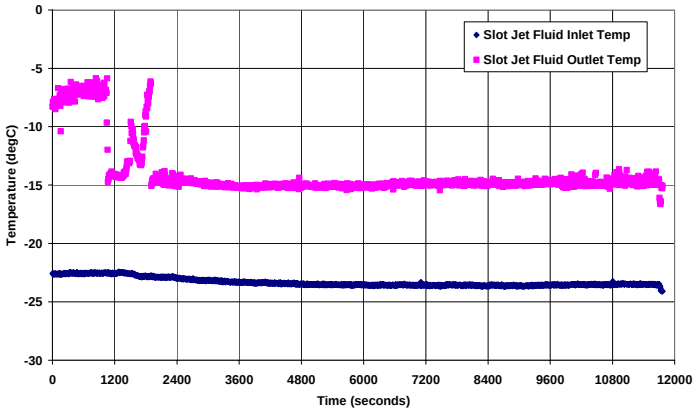

Ammonia Flow Loop Pressures
410 kPa, 20 degC Subcooled, 0.01 kg/s, 750 watt

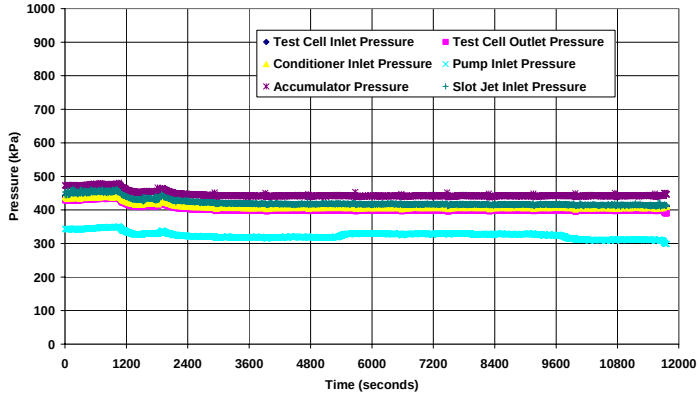

Slot Jet Surface Temperatures
410 kPa, 20 degC Subcooled, 0.01 kg/s, 750 watt

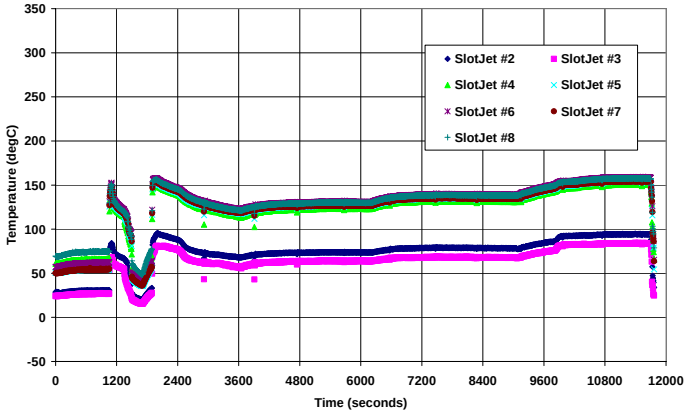

Heater Neck Temperatures
410 kPa, 20 deg Subcooled, 0.01 kg/s, 750 watt

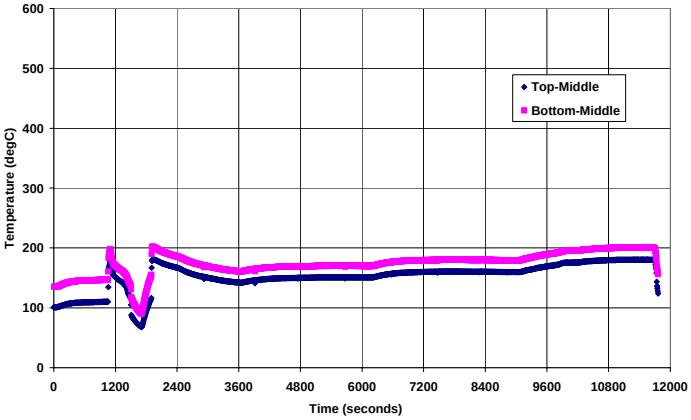

Heater Neck Heat Flux & Test Cell Watt Input
410 kPa, 20 degC Subcooled, 0.01 kg/s, 750 watt

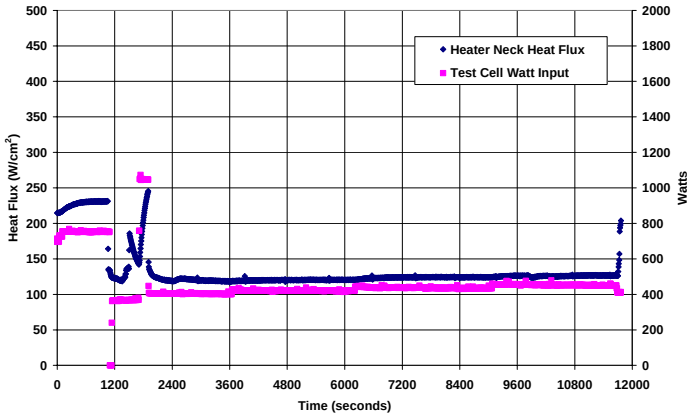

410 kPa, 20 degC Subcooled, 0.017 kg/s, 100 watt

Mass Flow Rate
410 kPa, 20 degC Subcooled, 0.017 kg/s, 100 watt

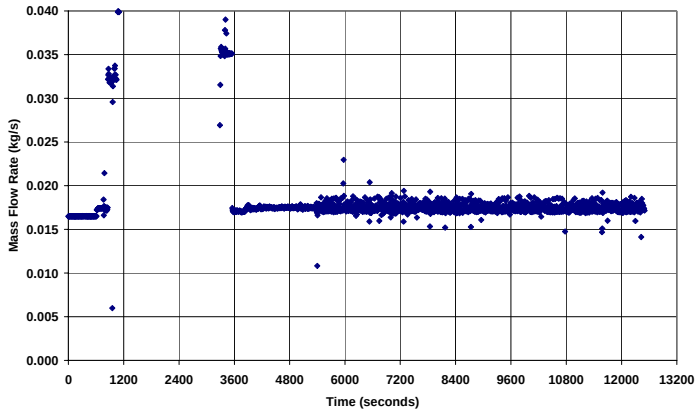

Slot Jet Fluid Temperatures
410 kPa, 20 degC Subcooled, 0.017 kg/s, 100 watt

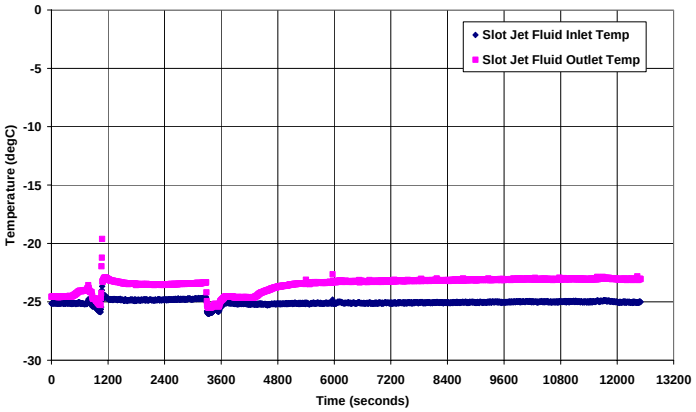

Ammonia Flow Loop Pressures
410 kPa, 20 degC Subcooled, 0.017 kg/s, 100 watt

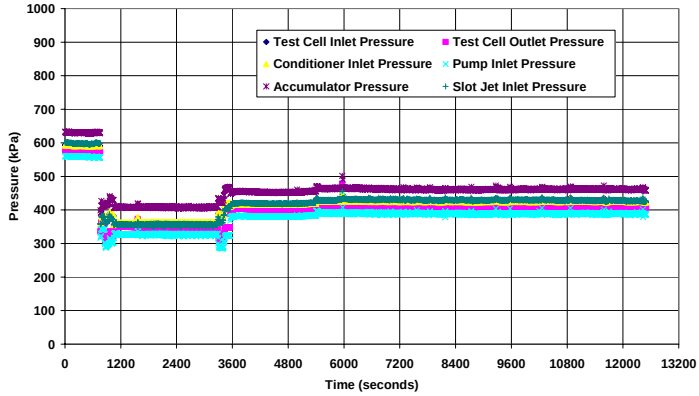

Slot Jet Surface Temperatures
410 kPa, 20 degC Subcooled, 0.017 kg/s, 100 watt

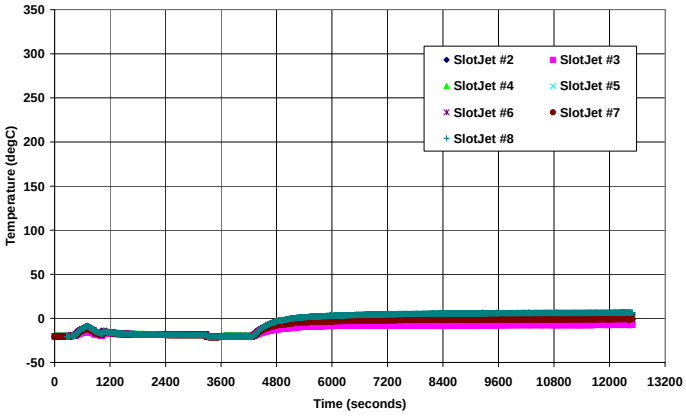

Heater Neck Temperatures
410 kPa, 20 deg Subcooled, 0.017 kg/s, 100 watt

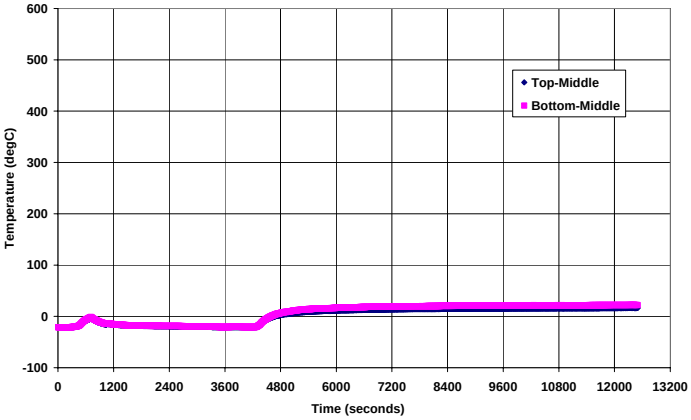

Heater Neck Heat Flux & Test Cell Watt Input
410 kPa, 20 degC Subcooled, 0.017 kg/s, 100 watt

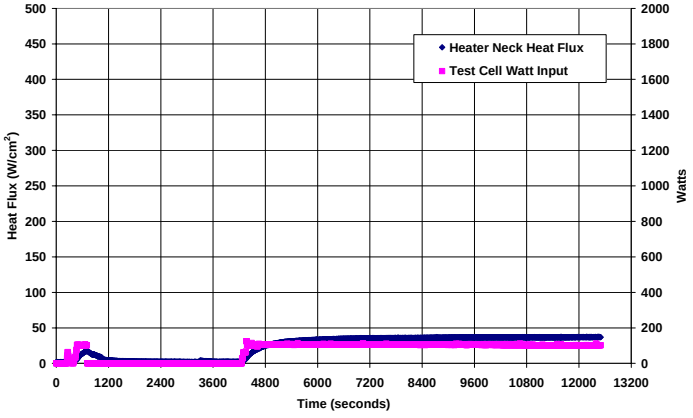

410 kPa, 20 degC Subcooled, 0.017 kg/s, 300 watt

Mass Flow Rate
410 kPa, 20 degC Subcooled, 0.017 kg/s, 300 watt

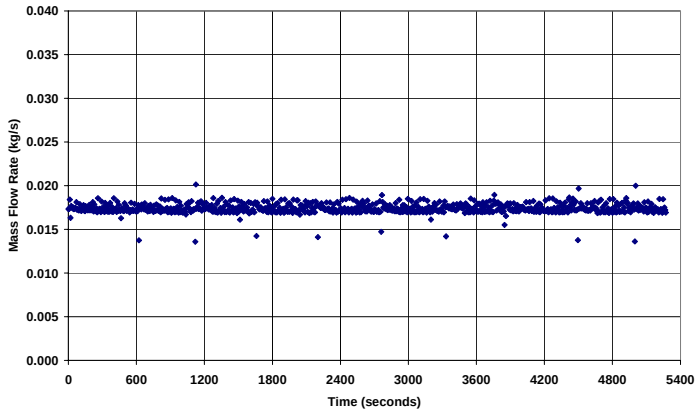

Slot Jet Fluid Temperatures
410 kPa, 20 degC Subcooled, 0.017 kg/s, 300 watt

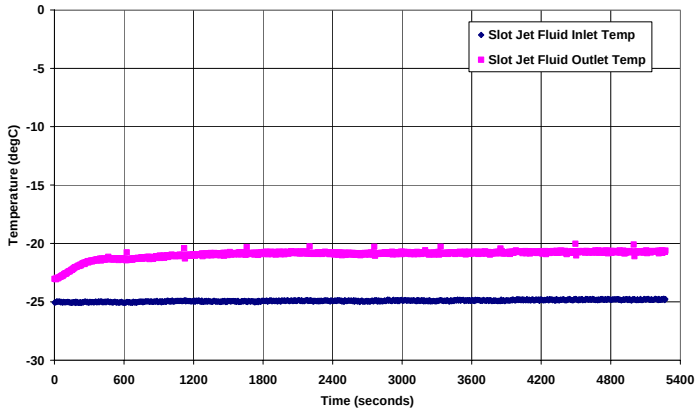

Ammonia Flow Loop Pressures
410 kPa, 20 degC Subcooled, 0.017 kg/s, 300 watt

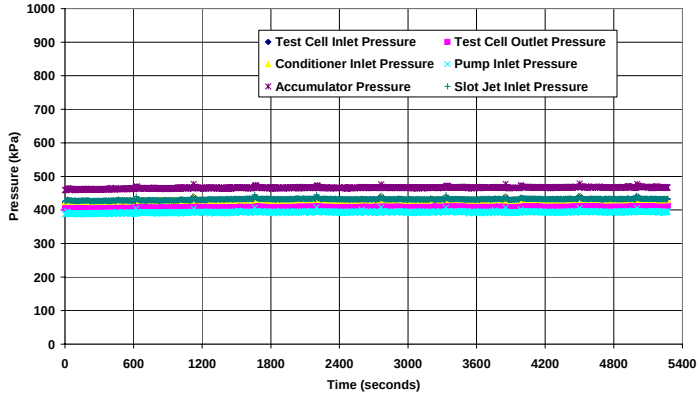

Slot Jet Surface Temperatures
410 kPa, 20 degC Subcooled, 0.017 kg/s, 300 watt

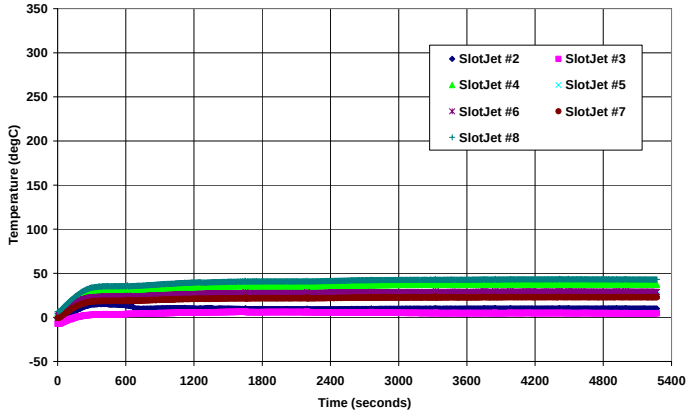

Heater Neck Temperatures
410 kPa, 20 deg Subcooled, 0.017 kg/s, 300 watt

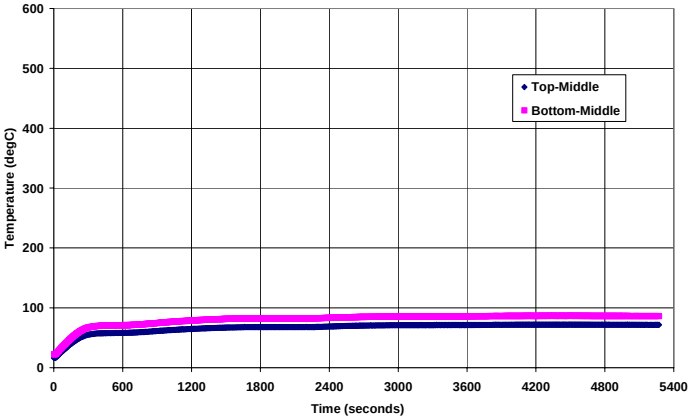

Heater Neck Heat Flux & Test Cell Watt Input
410 kPa, 20 degC Subcooled, 0.017 kg/s, 300 watt

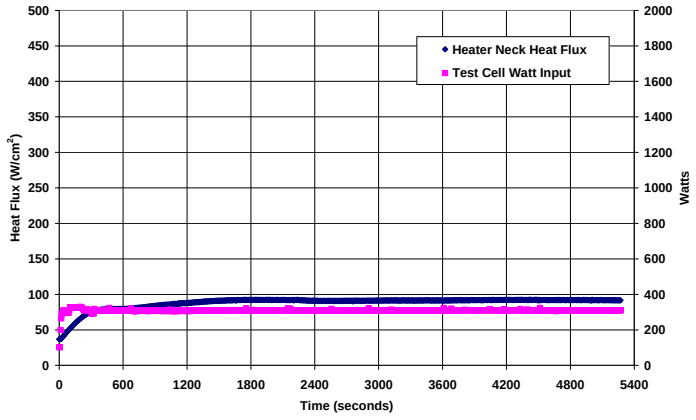

410 kPa, 20 degC Subcooled, 0.017 kg/s, 500 watt

Mass Flow Rate
410 kPa, 20 degC Subcooled, 0.017 kg/s, 500 watt

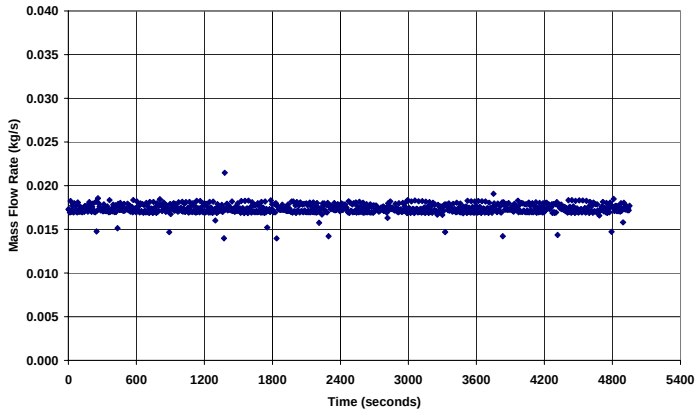

Slot Jet Fluid Temperatures
410 kPa, 20 degC Subcooled, 0.017 kg/s, 500 watt

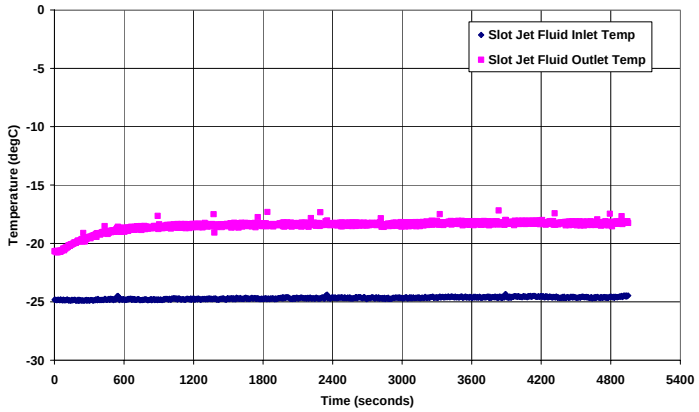

Ammonia Flow Loop Pressures
410 kPa, 20 degC Subcooled, 0.017 kg/s, 500 watt

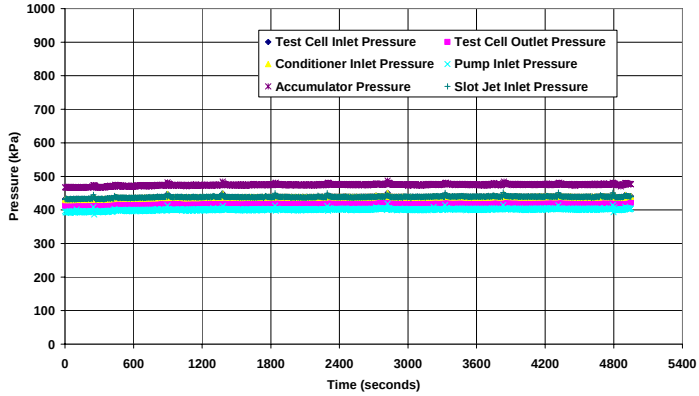

Slot Jet Surface Temperatures
410 kPa, 20 degC Subcooled, 0.017 kg/s, 500 watt

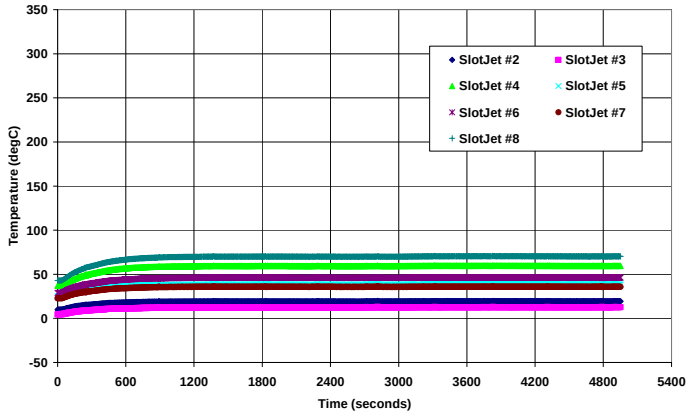

Heater Neck Temperatures
410 kPa, 20 deg Subcooled, 0.017 kg/s, 500 watt

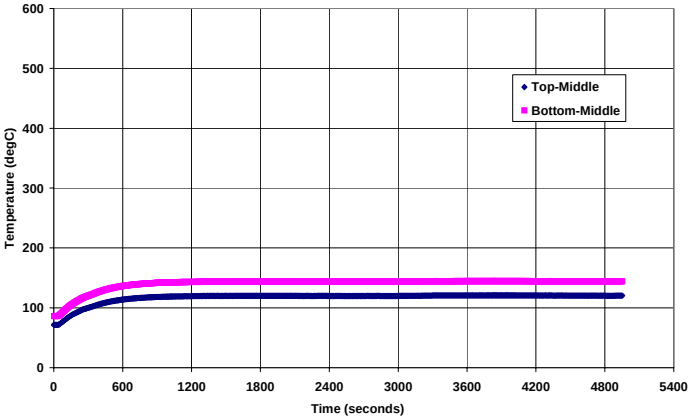

Heater Neck Heat Flux & Test Cell Watt Input
410 kPa, 20 degC Subcooled, 0.017 kg/s, 500 watt

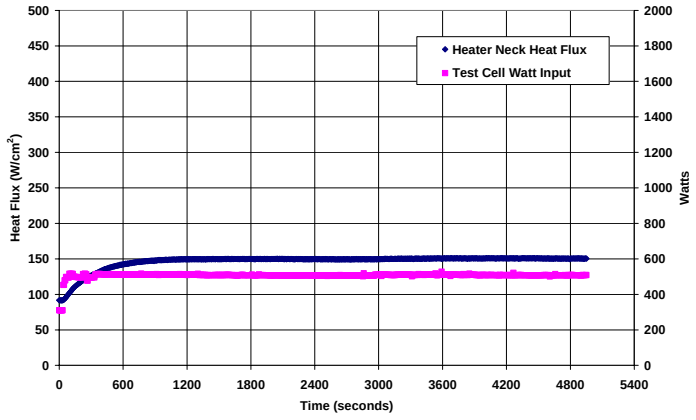

410 kPa, 20 degC Subcooled, 0.017 kg/s, 600 watt

Mass Flow Rate
410 kPa, 20 degC Subcooled, 0.017 kg/s, 600 watt

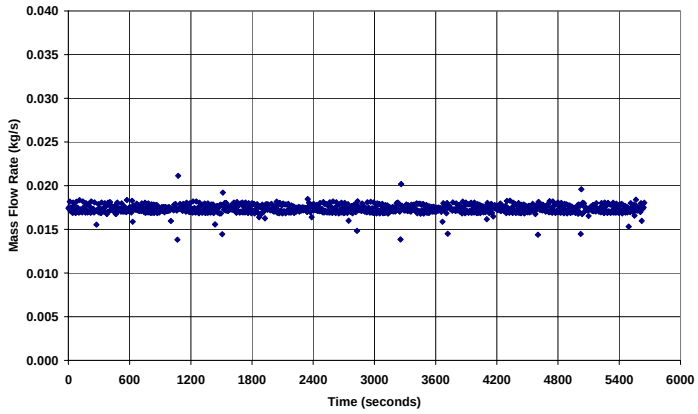

Slot Jet Fluid Temperatures
410 kPa, 20 degC Subcooled, 0.017 kg/s, 600 watt

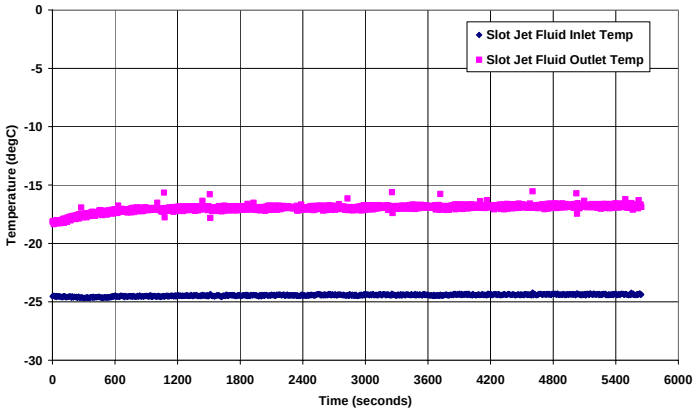

Ammonia Flow Loop Pressures
410 kPa, 20 degC Subcooled, 0.017 kg/s, 600 watt

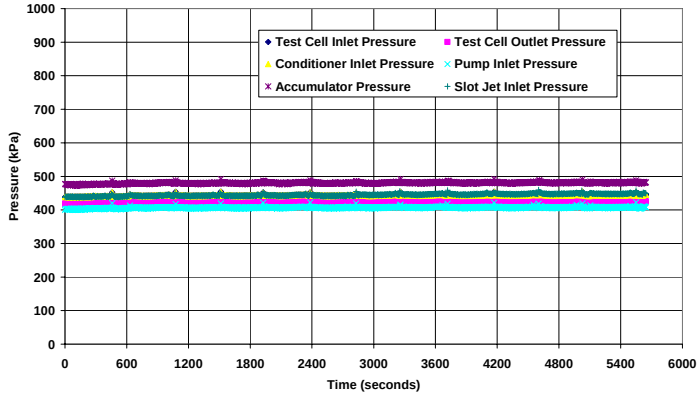

Slot Jet Surface Temperatures
410 kPa, 20 degC Subcooled, 0.017 kg/s, 600 watt

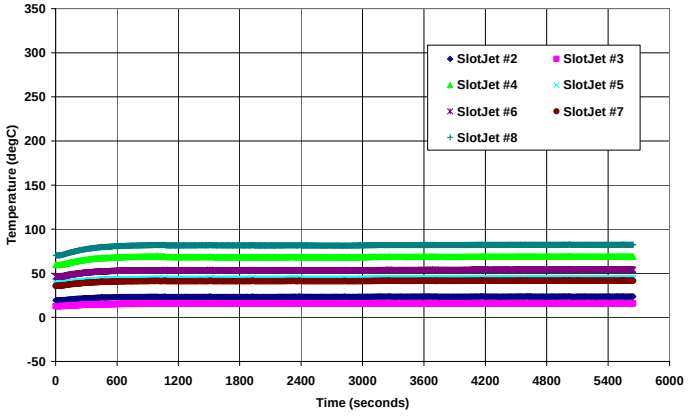

Heater Neck Temperatures
410 kPa, 20 deg Subcooled, 0.017 kg/s, 600 watt

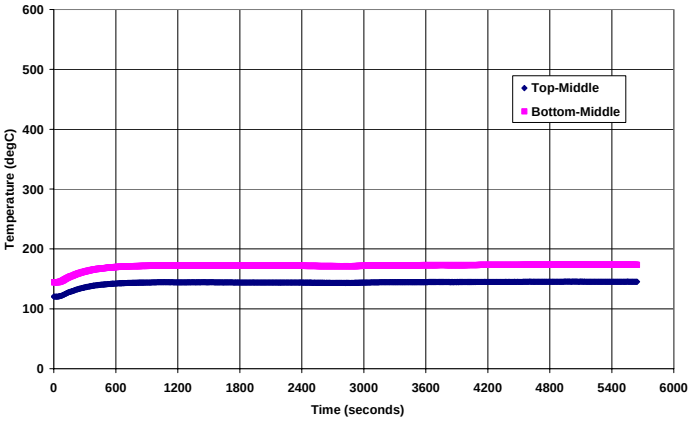

Heater Neck Heat Flux & Test Cell Watt Input
410 kPa, 20 degC Subcooled, 0.017 kg/s, 600 watt

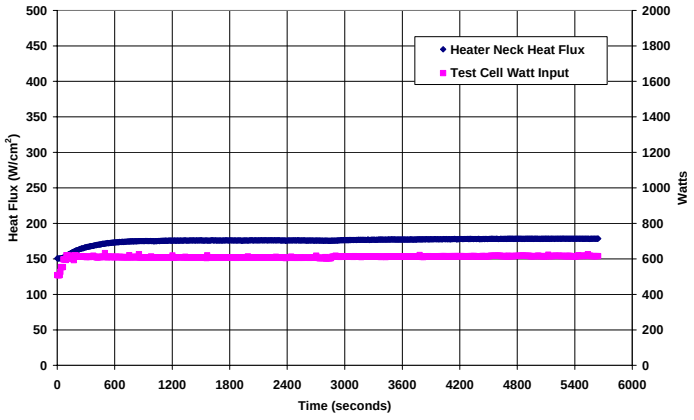

.

410 kPa, 20 degC Subcooled, 0.017 kg/s, 700 watt

Mass Flow Rate
410 kPa, 20 degC Subcooled, 0.017 kg/s, 700 watt

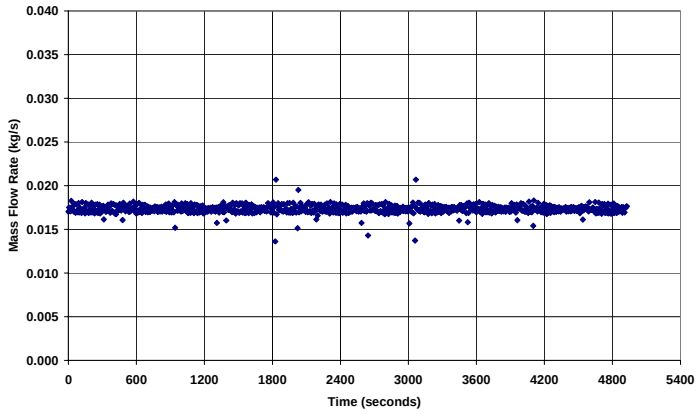

Slot Jet Fluid Temperatures
410 kPa, 20 degC Subcooled, 0.017 kg/s, 700 watt

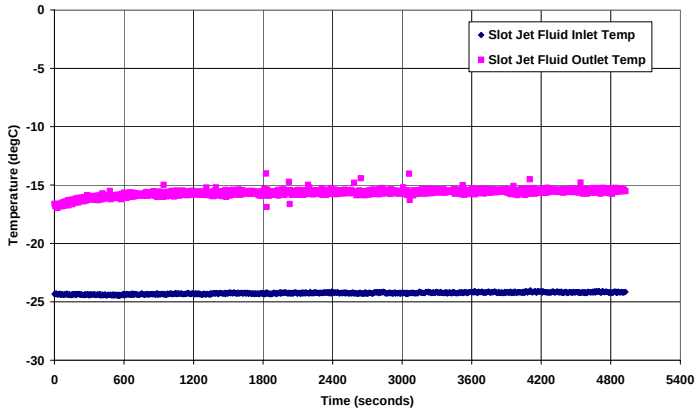

Ammonia Flow Loop Pressures
410 kPa, 20 degC Subcooled, 0.017 kg/s, 700 watt

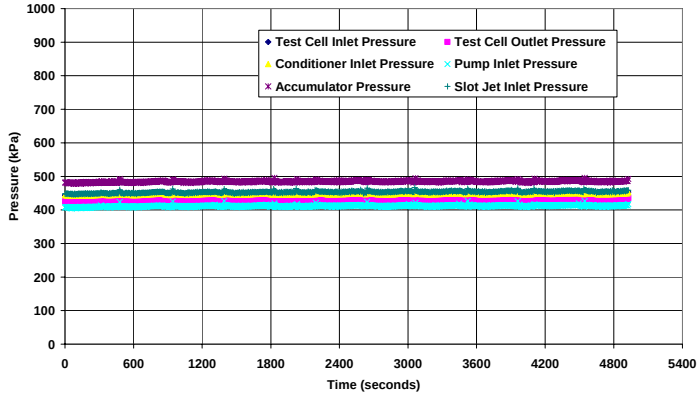

Slot Jet Surface Temperatures
410 kPa, 20 degC Subcooled, 0.017 kg/s, 700 watt

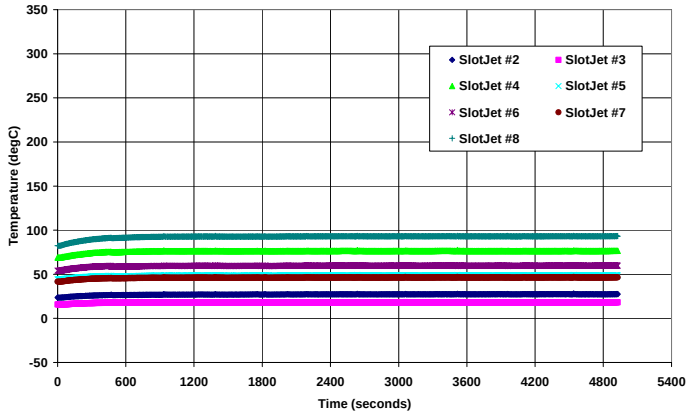

Heater Neck Temperatures
410 kPa, 20 deg Subcooled, 0.017 kg/s, 700 watt

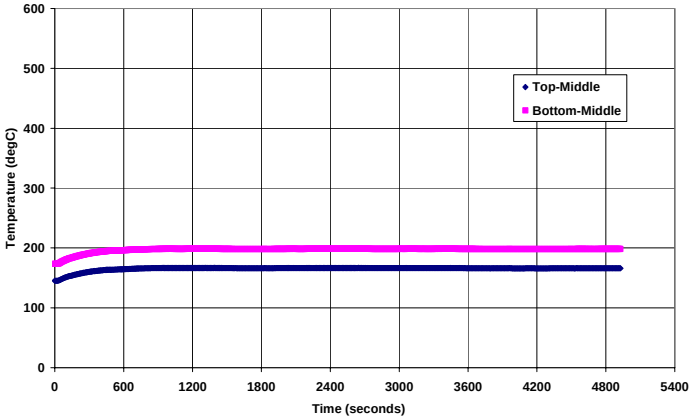

Heater Neck Heat Flux & Test Cell Watt Input
410 kPa, 20 degC Subcooled, 0.017 kg/s, 700 watt

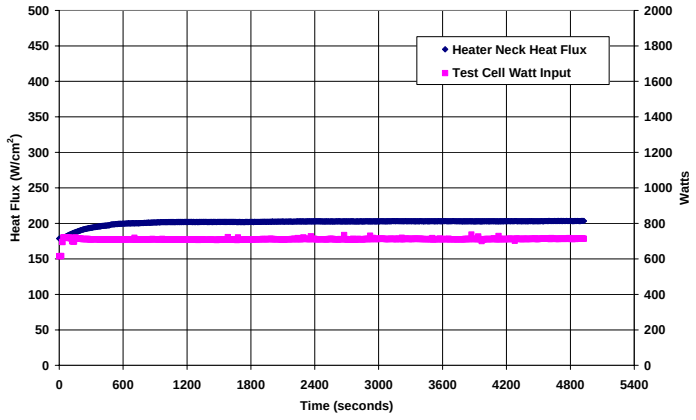

410 kPa, 20 degC Subcooled, 0.017 kg/s, 800 watt

Mass Flow Rate
410 kPa, 20 degC Subcooled, 0.017 kg/s, 800 watt

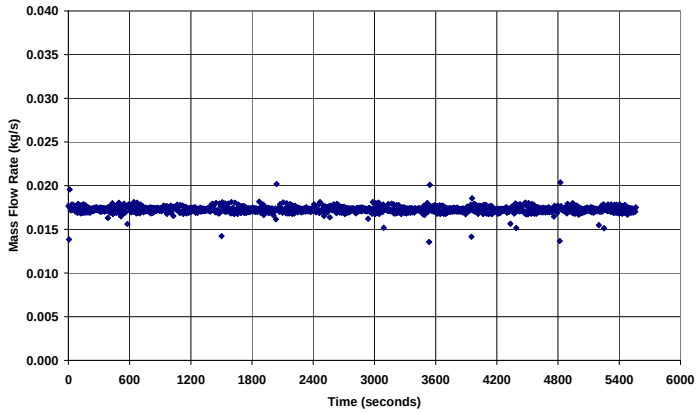

Slot Jet Fluid Temperatures
410 kPa, 20 degC Subcooled, 0.017 kg/s, 800 watt

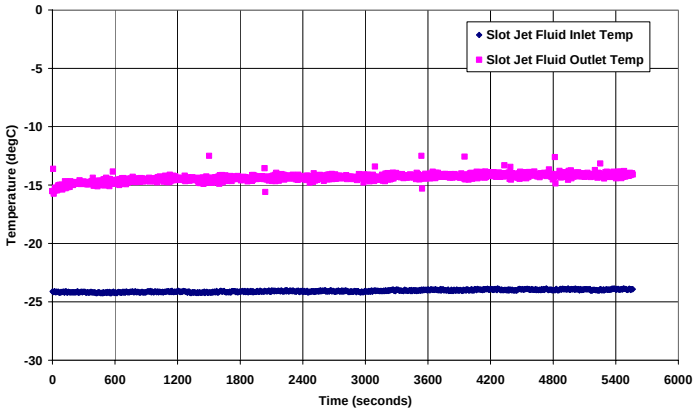

Ammonia Flow Loop Pressures
410 kPa, 20 degC Subcooled, 0.017 kg/s, 800 watt

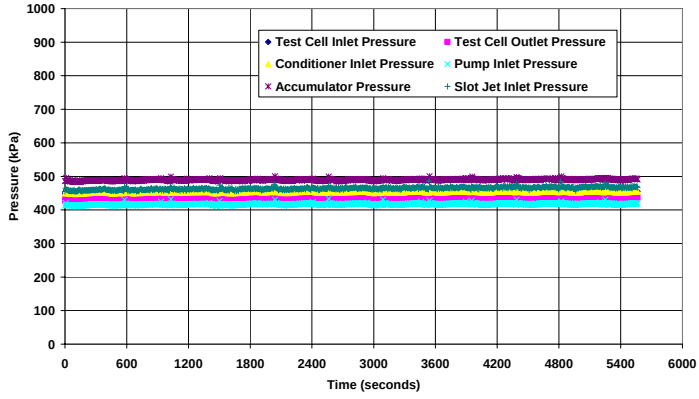

Slot Jet Surface Temperatures
410 kPa, 20 degC Subcooled, 0.017 kg/s, 800 watt

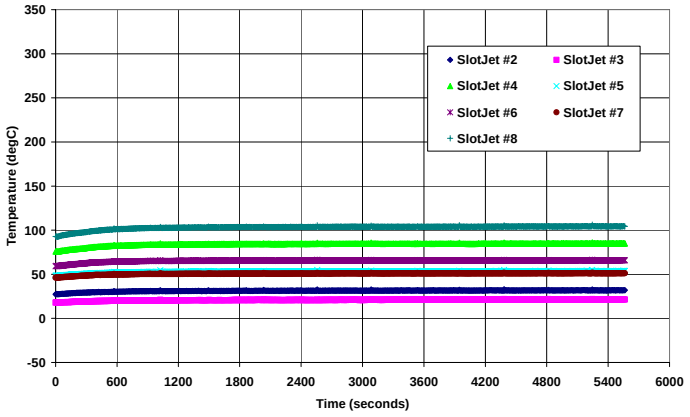

Heater Neck Temperatures
410 kPa, 20 deg Subcooled, 0.017 kg/s, 800 watt

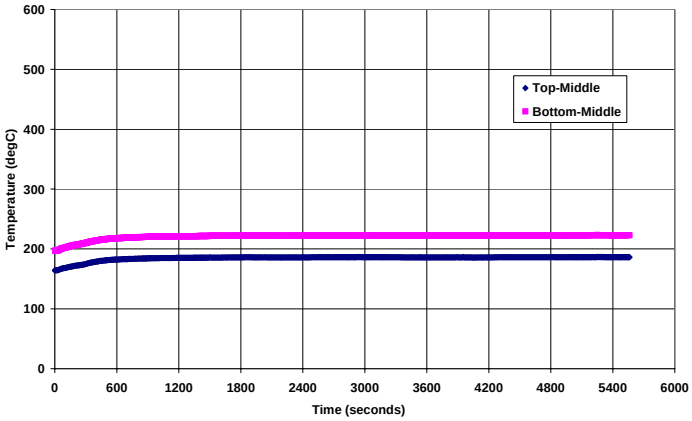

Heater Neck Heat Flux & Test Cell Watt Input
410 kPa, 20 degC Subcooled, 0.017 kg/s, 800 watt

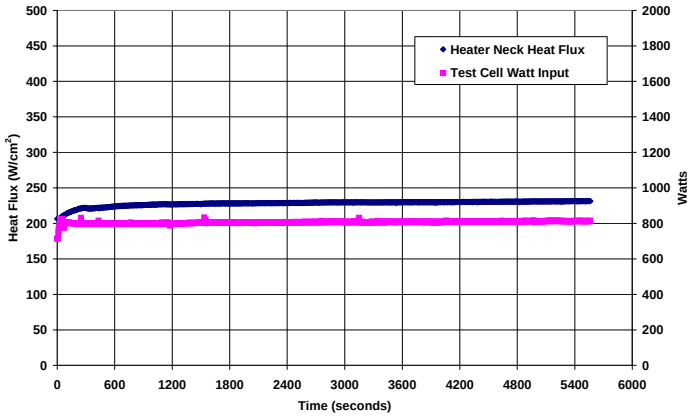

410 kPa, 20 degC Subcooled, 0.017 kg/s, 900 watt

Mass Flow Rate
410 kPa, 20 degC Subcooled, 0.017 kg/s, 900 watt

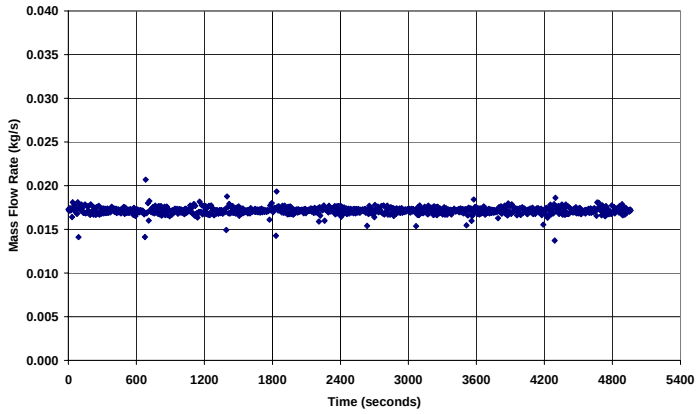

Slot Jet Fluid Temperatures
410 kPa, 20 degC Subcooled, 0.017 kg/s, 900 watt

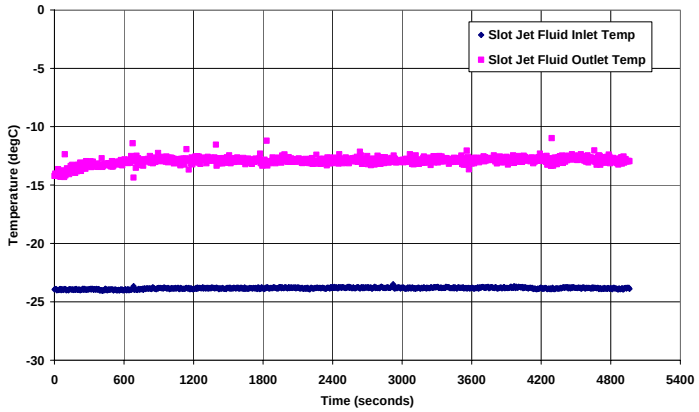

Ammonia Flow Loop Pressures
410 kPa, 20 degC Subcooled, 0.017 kg/s, 900 watt

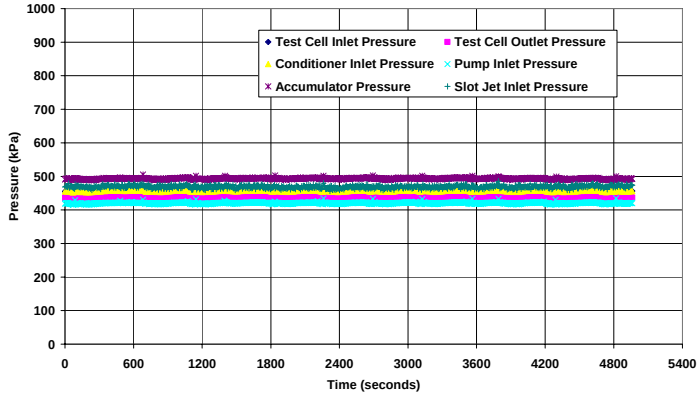

Slot Jet Surface Temperatures
410 kPa, 20 degC Subcooled, 0.017 kg/s, 900 watt

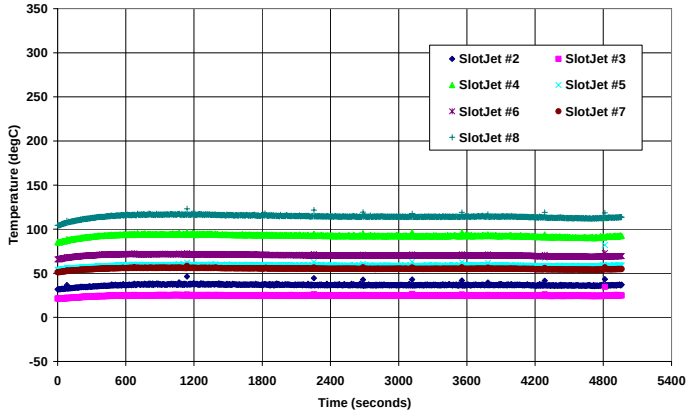

Heater Neck Temperatures
410 kPa, 20 deg Subcooled, 0.017 kg/s, 900 watt

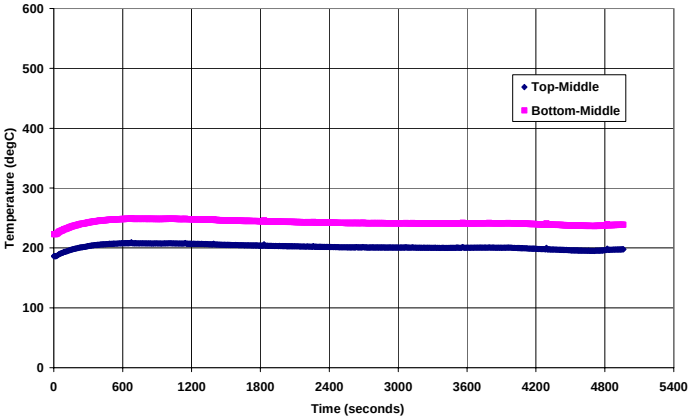

Heater Neck Heat Flux & Test Cell Watt Input
410 kPa, 20 degC Subcooled, 0.017 kg/s, 900 watt

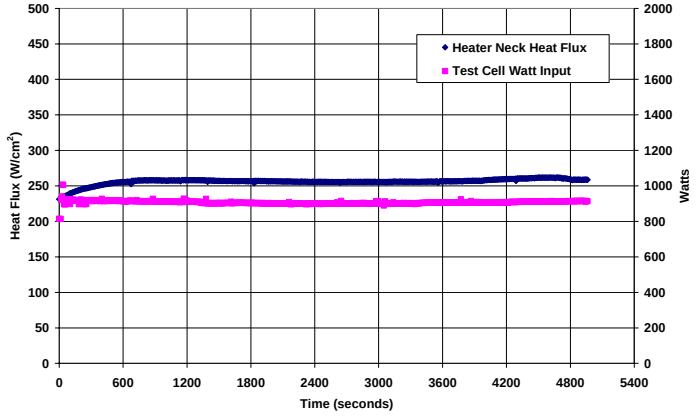

410 kPa, 20 degC Subcooled, 0.017 kg/s, 1000 watt

Mass Flow Rate
410 kPa, 20 degC Subcooled, 0.017 kg/s, 1000 watt

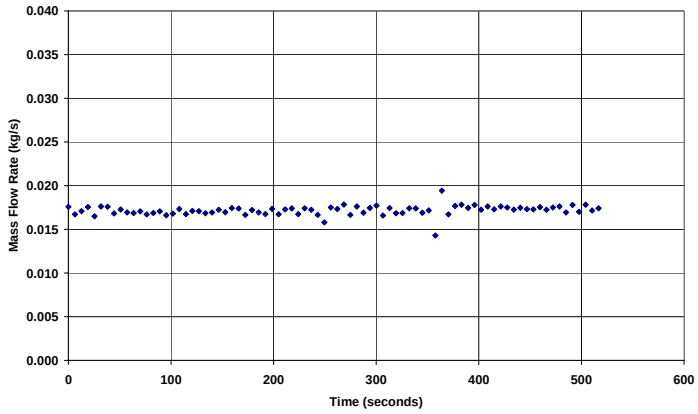

Slot Jet Fluid Temperatures
410 kPa, 20 degC Subcooled, 0.017 kg/s, 1000 watt

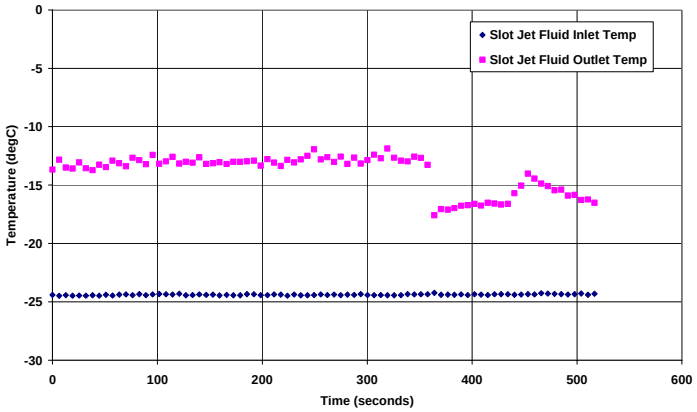

Ammonia Flow Loop Pressures
410 kPa, 20 degC Subcooled, 0.017 kg/s, 1000 watt

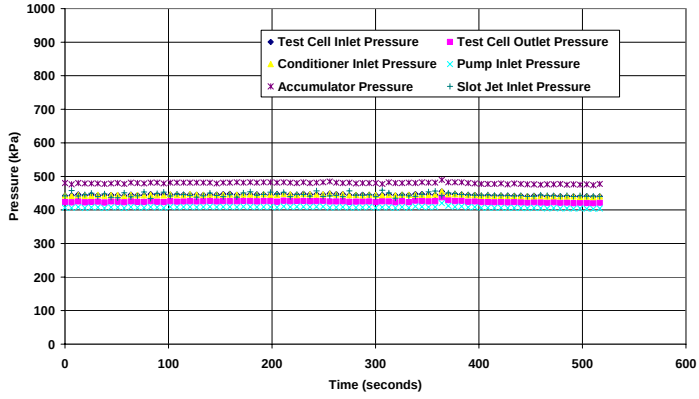

Slot Jet Surface Temperatures
410 kPa, 20 degC Subcooled, 0.017 kg/s, 1000 watt

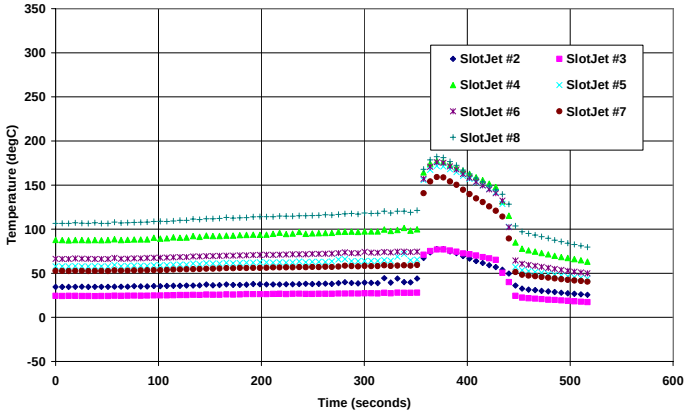

Heater Neck Temperatures
410 kPa, 20 deg Subcooled, 0.017 kg/s, 1000 watt

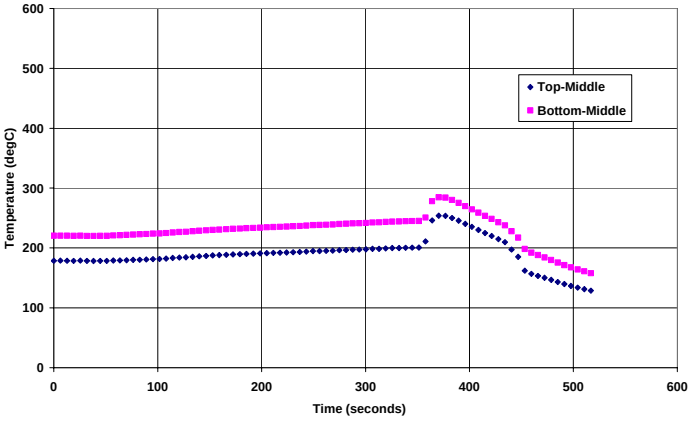

Heater Neck Heat Flux & Test Cell Watt Input
410 kPa, 20 degC Subcooled, 0.017 kg/s, 1000 watt

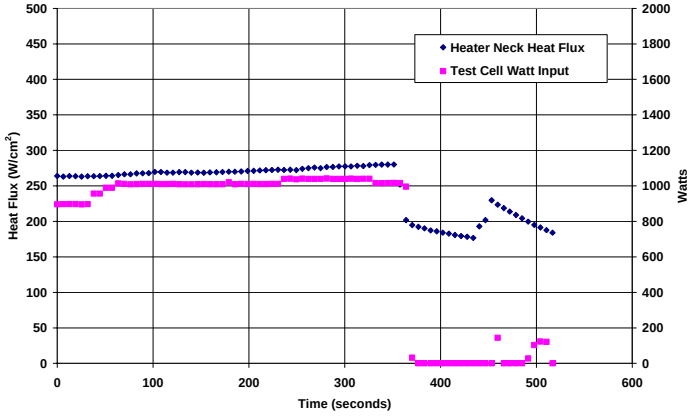

410 kPa, 20 degC Subcooled, 0.029 kg/s, 100 watt

Mass Flow Rate
410 kPa, 20 degC Subcooled, 0.029 kg/s, 100 watt

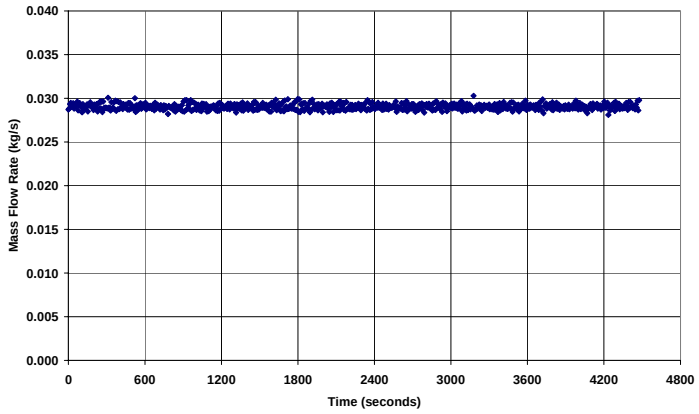

Slot Jet Fluid Temperatures
410 kPa, 20 degC Subcooled, 0.029 kg/s, 100 watt

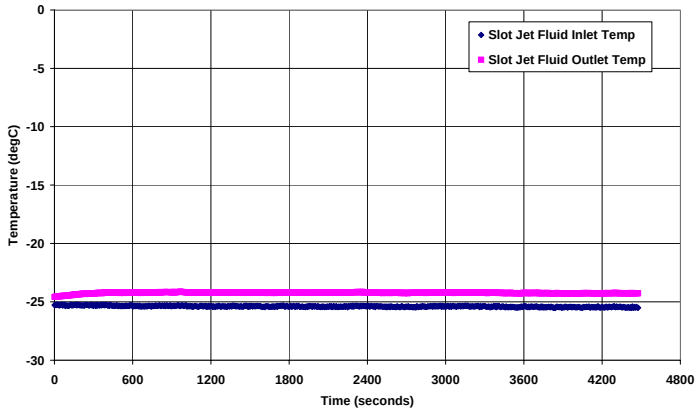

Ammonia Flow Loop Pressures
410 kPa, 20 degC Subcooled, 0.029 kg/s, 100 watt

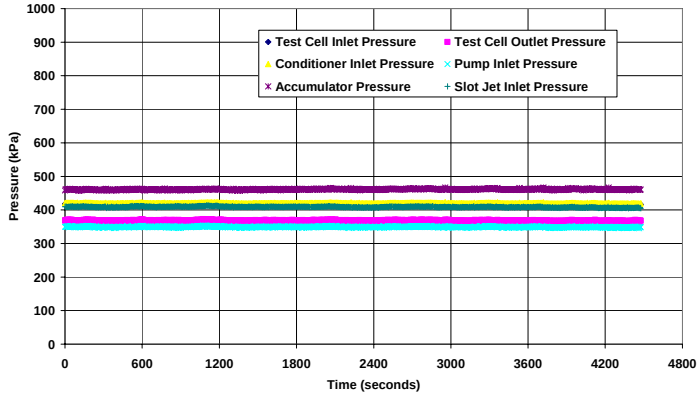

Slot Jet Surface Temperatures
410 kPa, 20 degC Subcooled, 0.029 kg/s, 100 watt

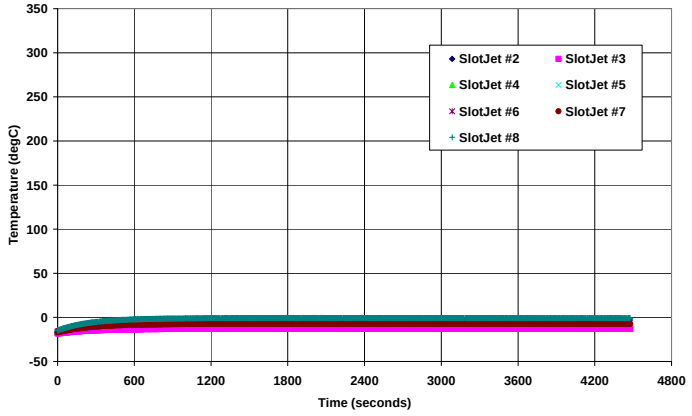

Heater Neck Temperatures
410 kPa, 20 deg Subcooled, 0.029 kg/s, 100 watt

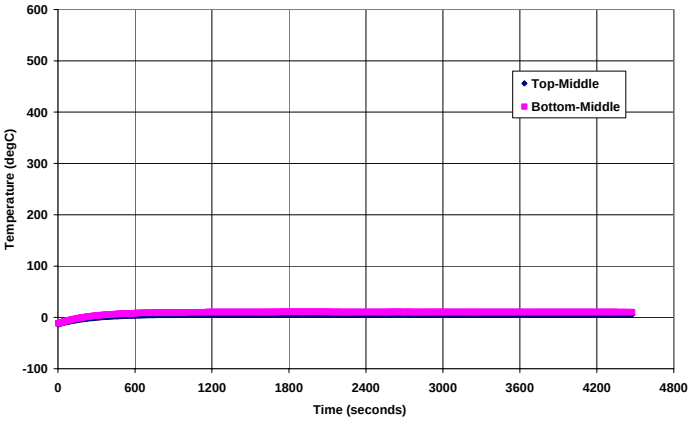

Heater Neck Heat Flux & Test Cell Watt Input
410 kPa, 20 degC Subcooled, 0.029 kg/s, 100 watt

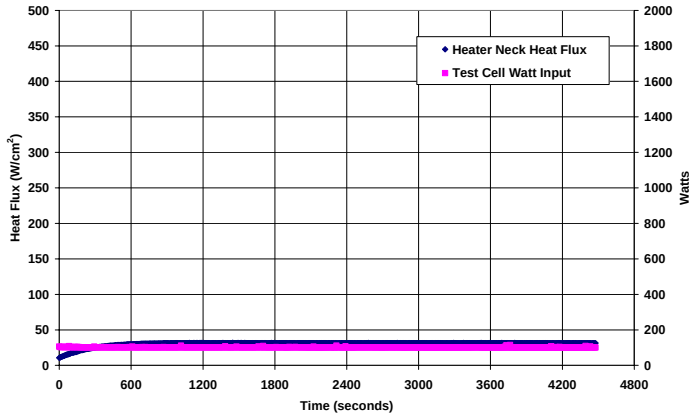

410 kPa, 20 degC Subcooled, 0.029 kg/s, 300 watt

Mass Flow Rate
410 kPa, 20 degC Subcooled, 0.029 kg/s, 300 watt

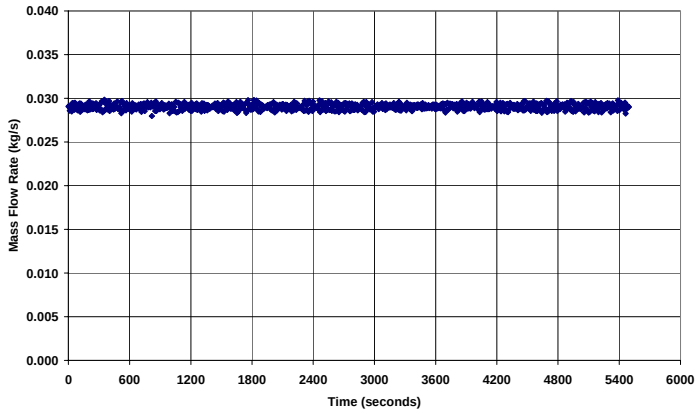

Slot Jet Fluid Temperatures
410 kPa, 20 degC Subcooled, 0.029 kg/s, 300 watt

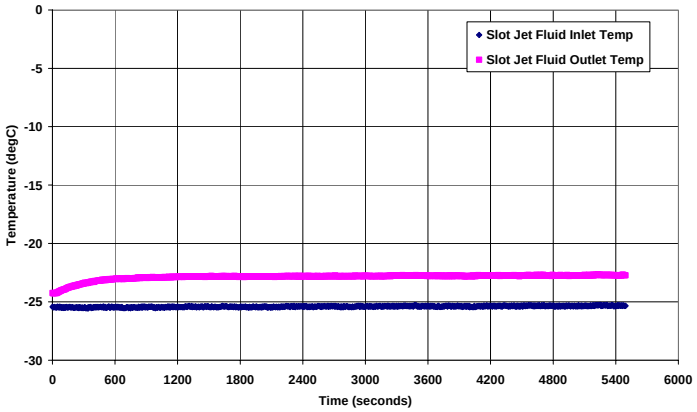

Ammonia Flow Loop Pressures
410 kPa, 20 degC Subcooled, 0.029 kg/s, 300 watt

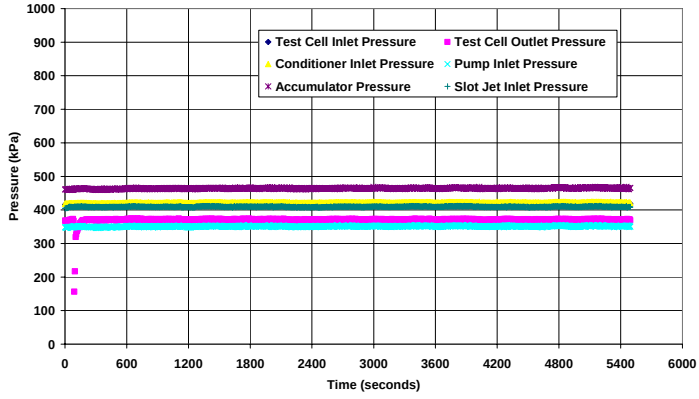

Slot Jet Surface Temperatures
410 kPa, 20 degC Subcooled, 0.029 kg/s, 300 watt

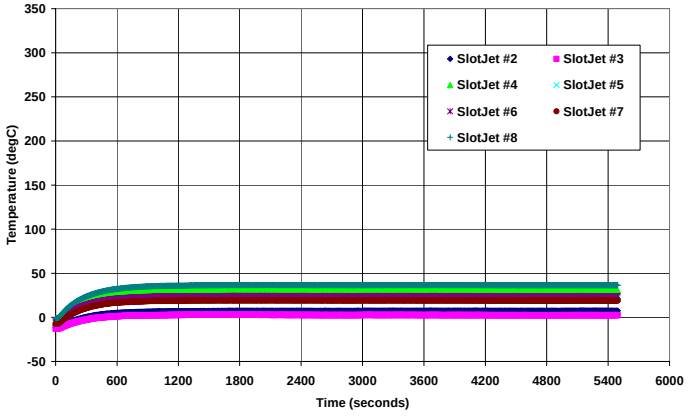

Heater Neck Temperatures
410 kPa, 20 deg Subcooled, 0.029 kg/s, 300 watt

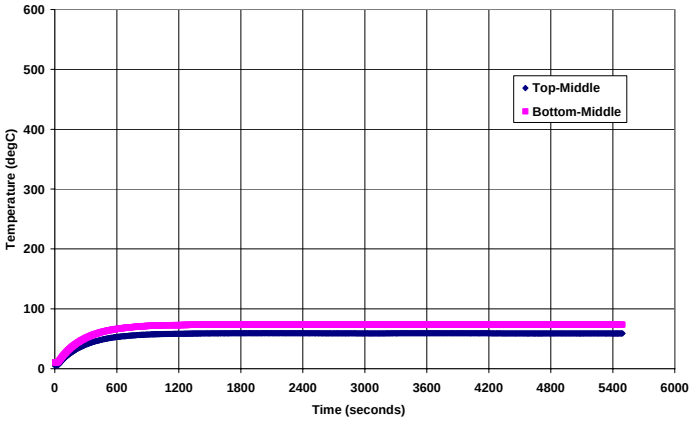

Heater Neck Heat Flux & Test Cell Watt Input
410 kPa, 20 degC Subcooled, 0.029 kg/s, 300 watt

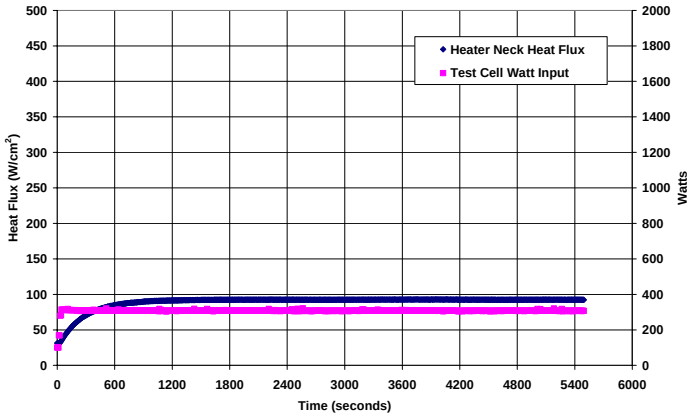

410 kPa, 20 degC Subcooled, 0.029 kg/s, 500 watt

Mass Flow Rate
410 kPa, 20 degC Subcooled, 0.029 kg/s, 500 watt

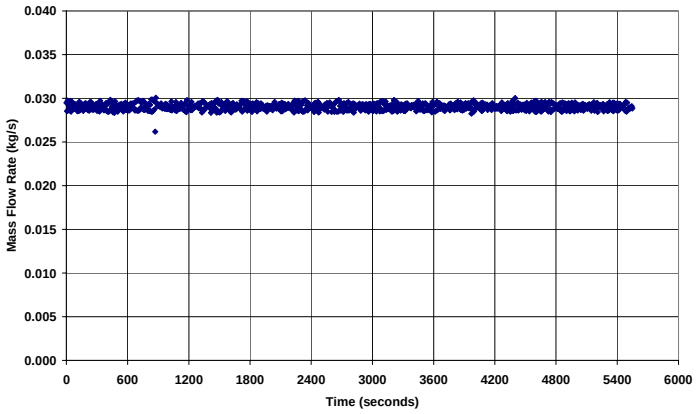

Slot Jet Fluid Temperatures
410 kPa, 20 degC Subcooled, 0.029 kg/s, 500 watt

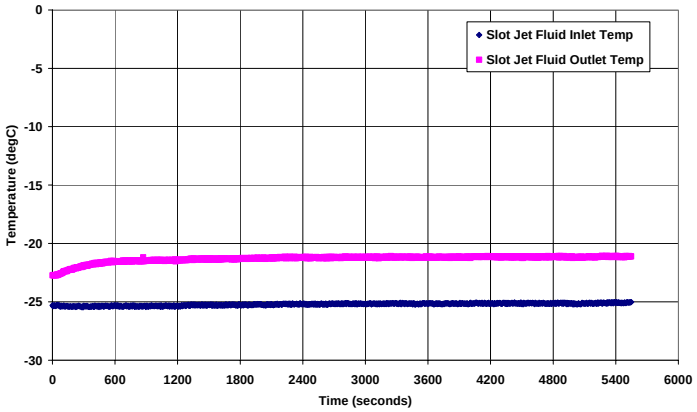

Ammonia Flow Loop Pressures
410 kPa, 20 degC Subcooled, 0.029 kg/s, 500 watt

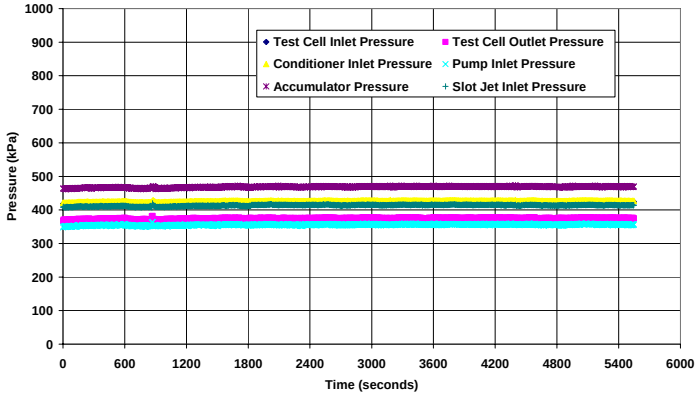

Slot Jet Surface Temperatures
410 kPa, 20 degC Subcooled, 0.029 kg/s, 500 watt

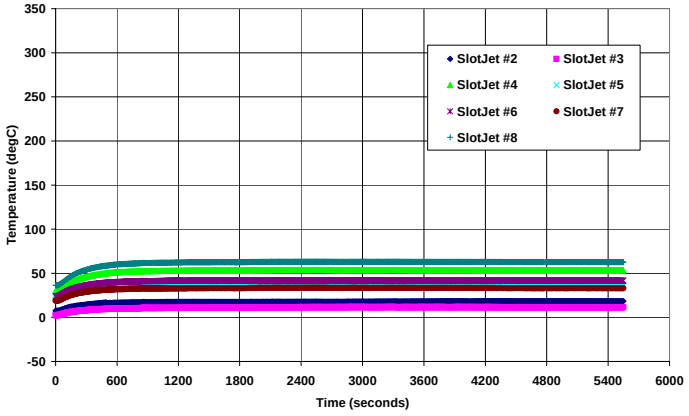

Heater Neck Temperatures
410 kPa, 20 deg Subcooled, 0.029 kg/s, 500 watt

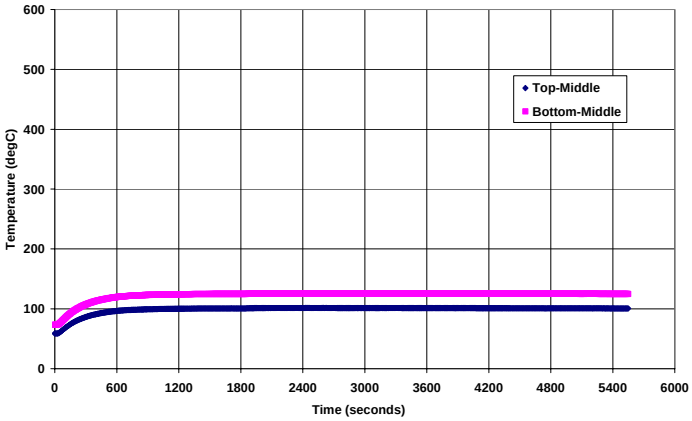

Heater Neck Heat Flux & Test Cell Watt Input
410 kPa, 20 degC Subcooled, 0.029 kg/s, 500 watt

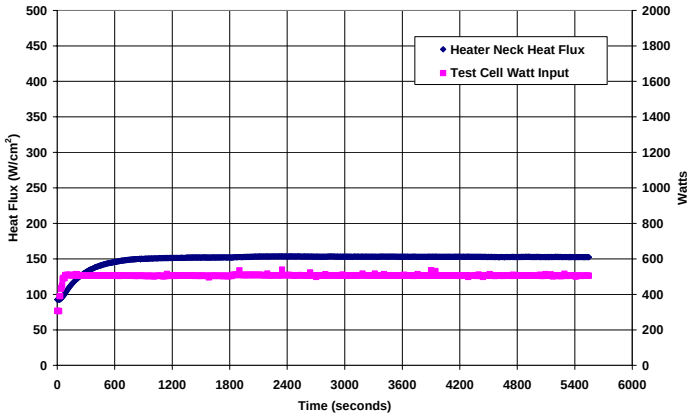

410 kPa, 20 degC Subcooled, 0.029 kg/s, 700 watt

Mass Flow Rate
410 kPa, 20 degC Subcooled, 0.029 kg/s, 700 watt

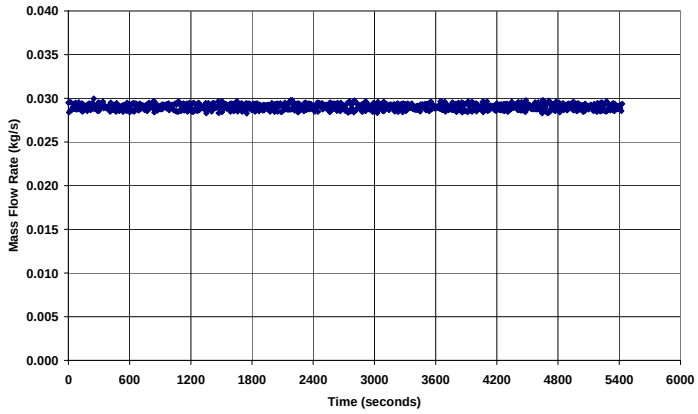

Slot Jet Fluid Temperatures
410 kPa, 20 degC Subcooled, 0.029 kg/s, 700 watt

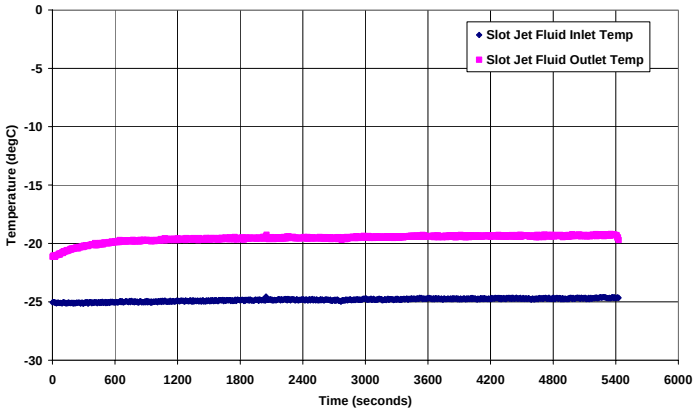

Ammonia Flow Loop Pressures
410 kPa, 20 degC Subcooled, 0.029 kg/s, 700 watt

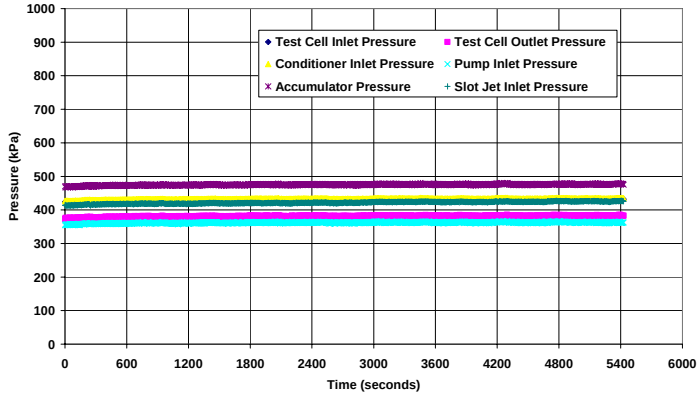

Slot Jet Surface Temperatures
410 kPa, 20 degC Subcooled, 0.029 kg/s, 700 watt

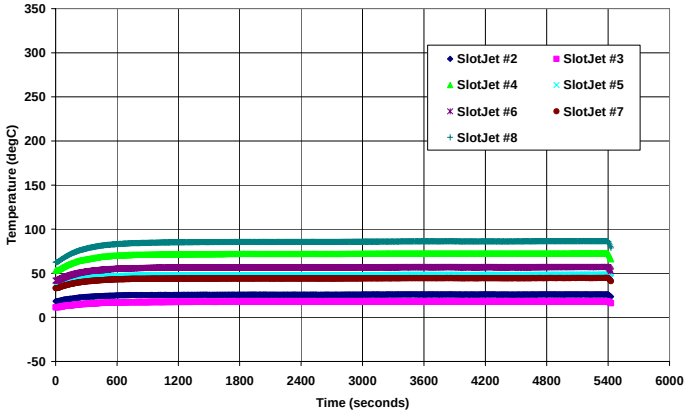

Heater Neck Temperatures
410 kPa, 20 deg Subcooled, 0.029 kg/s, 700 watt

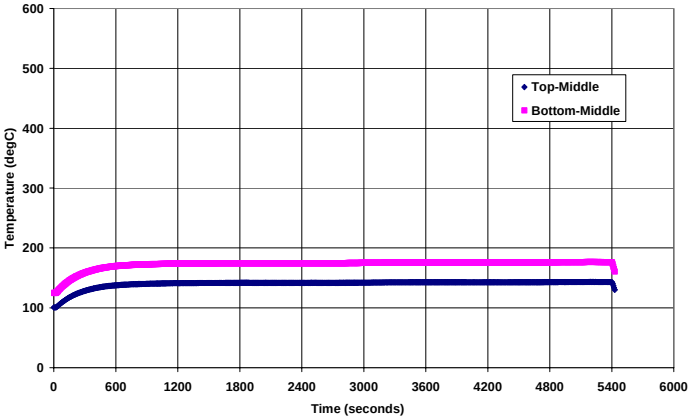

Heater Neck Heat Flux & Test Cell Watt Input
410 kPa, 20 degC Subcooled, 0.029 kg/s, 700 watt

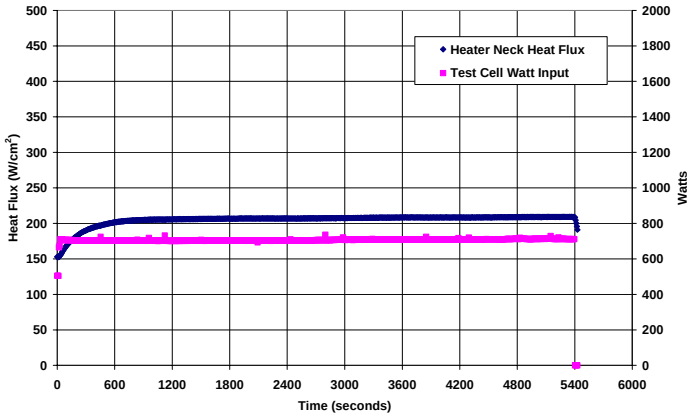

410 kPa, 20 degC Subcooled, 0.029 kg/s, 900 watt

Mass Flow Rate
410 kPa, 20 degC Subcooled, 0.029 kg/s, 900 watt

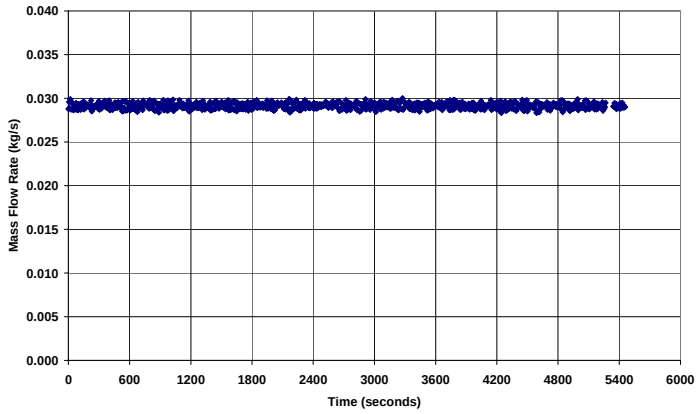

Slot Jet Fluid Temperatures
410 kPa, 20 degC Subcooled, 0.029 kg/s, 900 watt

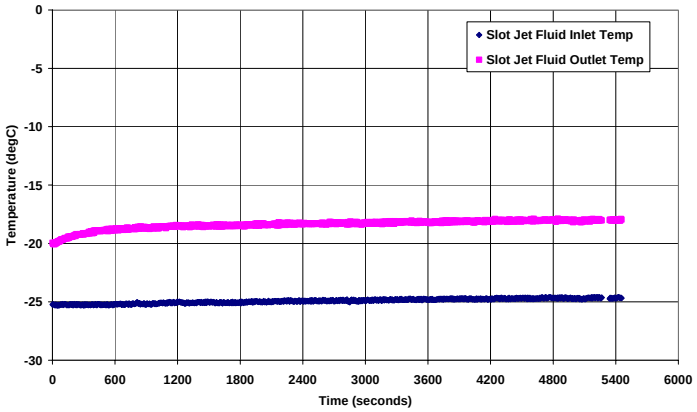

Ammonia Flow Loop Pressures
410 kPa, 20 degC Subcooled, 0.029 kg/s, 900 watt

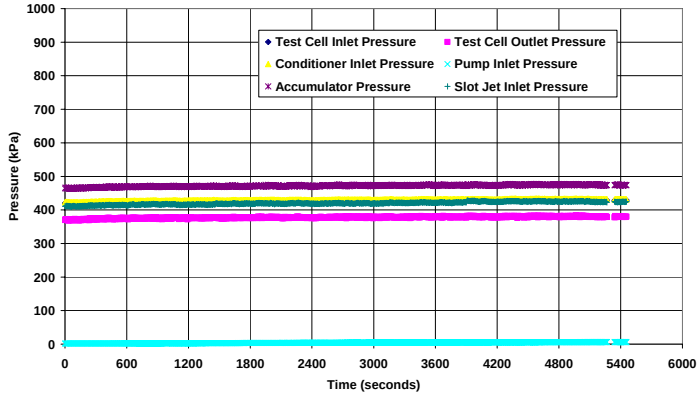

Slot Jet Surface Temperatures
410 kPa, 20 degC Subcooled, 0.029 kg/s, 900 watt

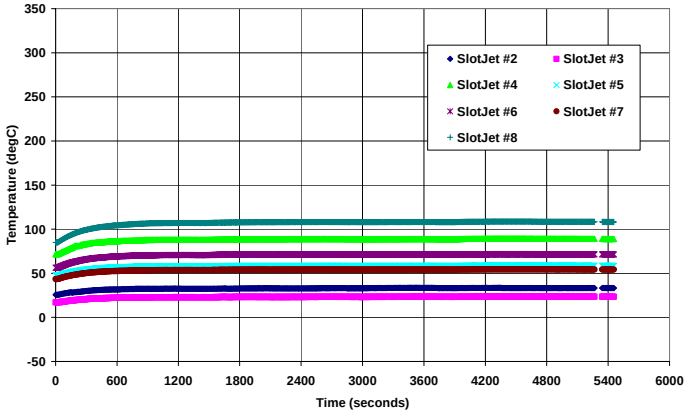

Heater Neck Temperatures
410 kPa, 20 deg Subcooled, 0.029 kg/s, 900 watt

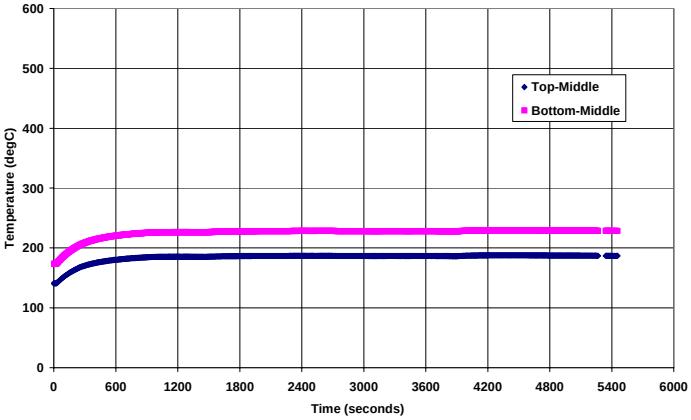

Heater Neck Heat Flux & Test Cell Watt Input
410 kPa, 20 degC Subcooled, 0.029 kg/s, 900 watt

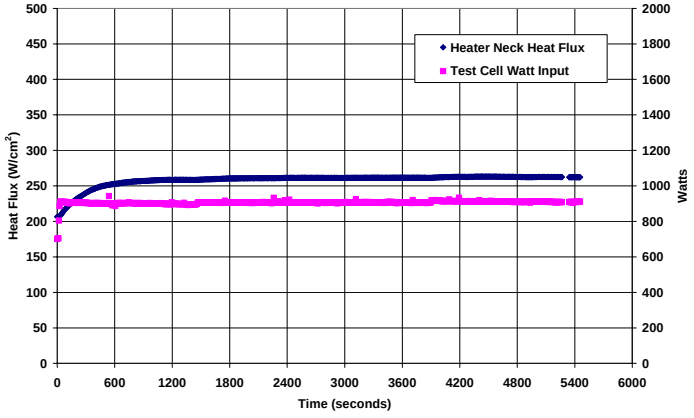

410 kPa, 20 degC Subcooled, 0.029 kg/s, 1000 watt

Mass Flow Rate
410 kPa, 20 degC Subcooled, 0.029 kg/s, 1000 watt

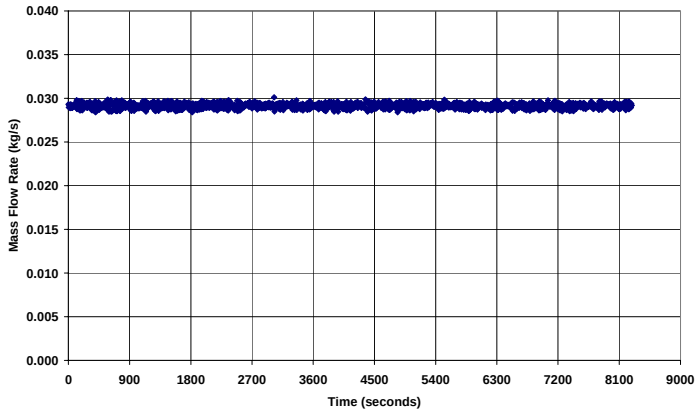

Slot Jet Fluid Temperatures
410 kPa, 20 degC Subcooled, 0.029 kg/s, 1000 watt

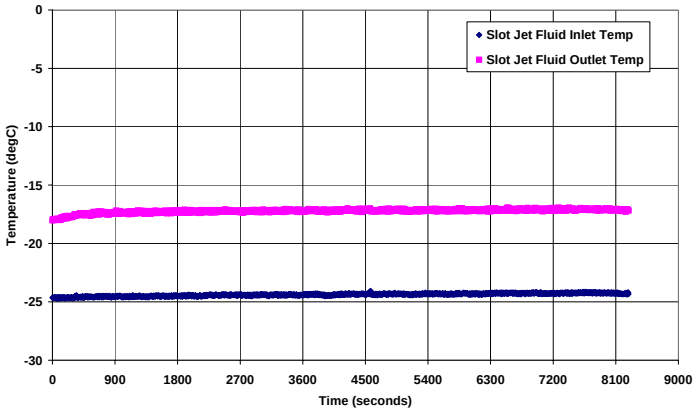

Ammonia Flow Loop Pressures
410 kPa, 20 degC Subcooled, 0.029 kg/s, 1000 watt

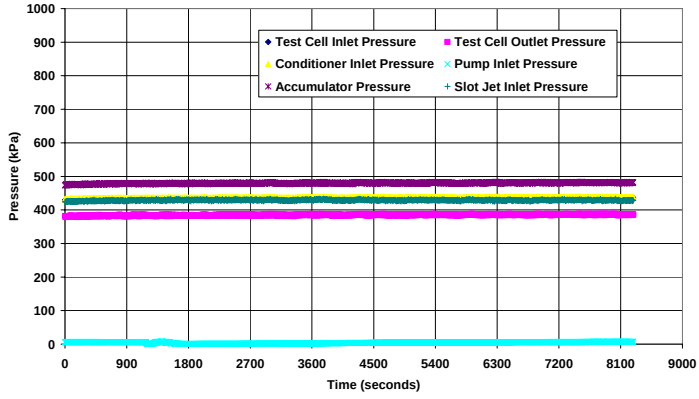

Slot Jet Surface Temperatures
410 kPa, 20 degC Subcooled, 0.029 kg/s, 1000 watt

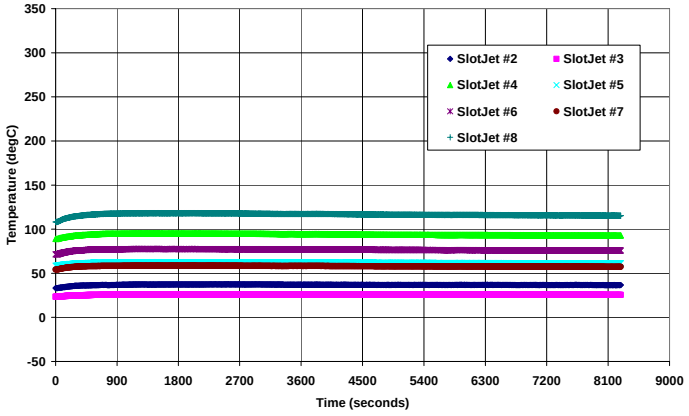

Heater Neck Temperatures
410 kPa, 20 deg Subcooled, 0.029 kg/s, 1000 watt

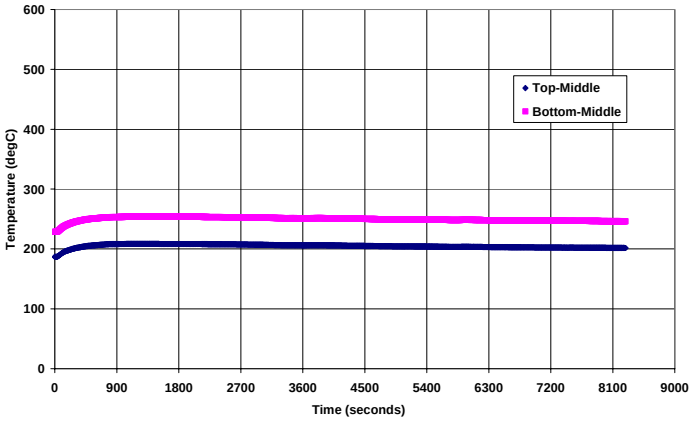

Heater Neck Heat Flux & Test Cell Watt Input
410 kPa, 20 degC Subcooled, 0.029 kg/s, 1000 watt

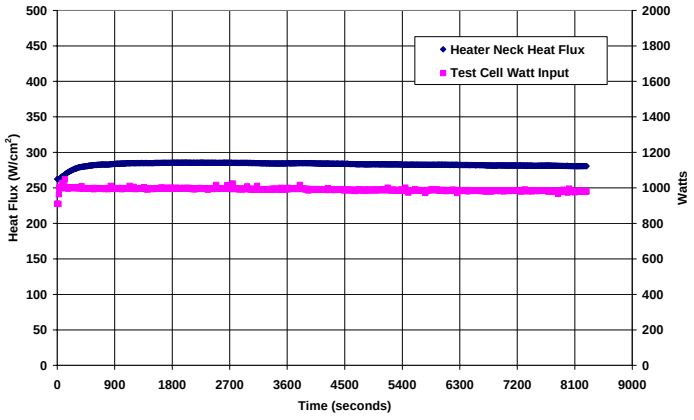

410 kPa, 20 degC Subcooled, 0.029 kg/s, 1100 watt

Mass Flow Rate
410 kPa, 20 degC Subcooled, 0.029 kg/s, 1100 watt

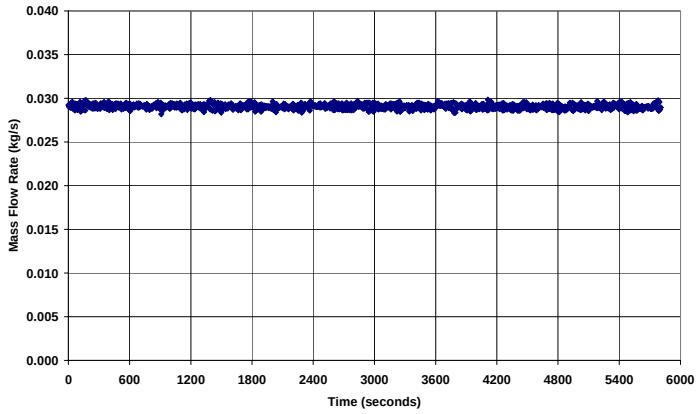

Slot Jet Fluid Temperatures
410 kPa, 20 degC Subcooled, 0.029 kg/s, 1100 watt

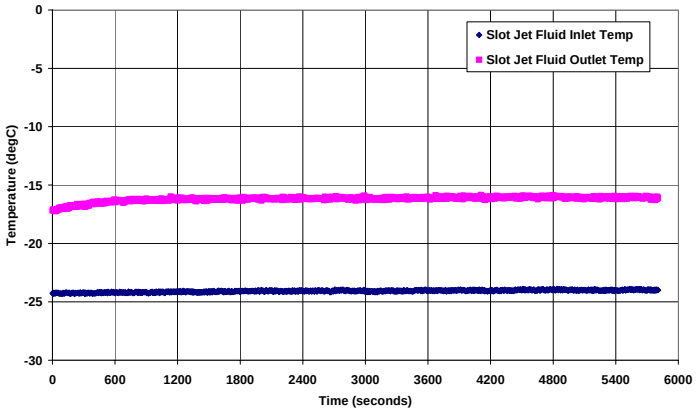

Ammonia Flow Loop Pressures
410 kPa, 20 degC Subcooled, 0.029 kg/s, 1100 watt

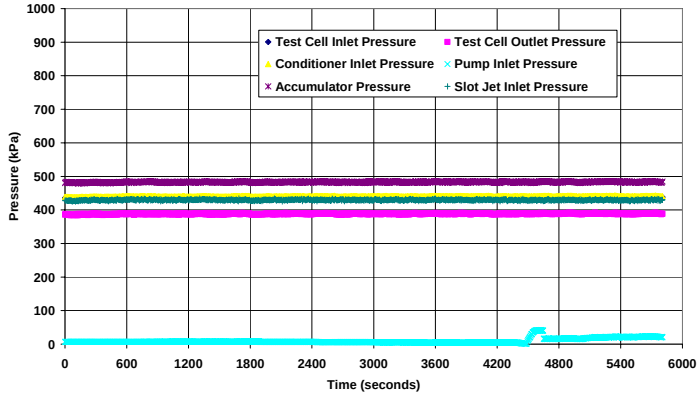

Slot Jet Surface Temperatures
410 kPa, 20 degC Subcooled, 0.029 kg/s, 1100 watt

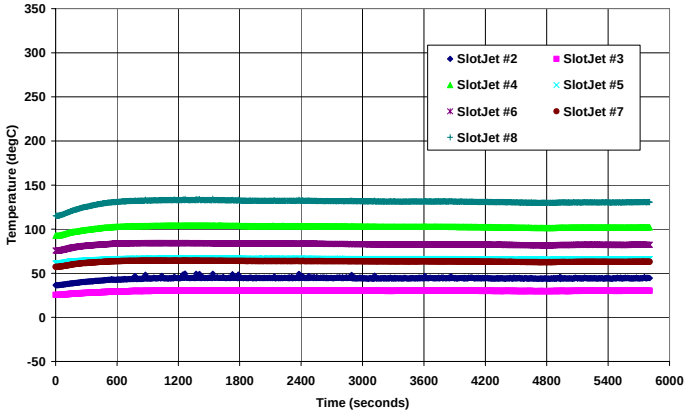

Heater Neck Temperatures
410 kPa, 20 deg Subcooled, 0.029 kg/s, 1100 watt

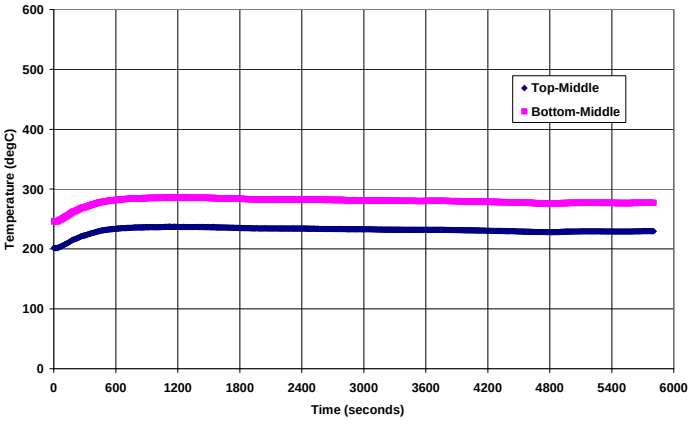

Heater Neck Heat Flux & Test Cell Watt Input
410 kPa, 20 degC Subcooled, 0.029 kg/s, 1100 watt

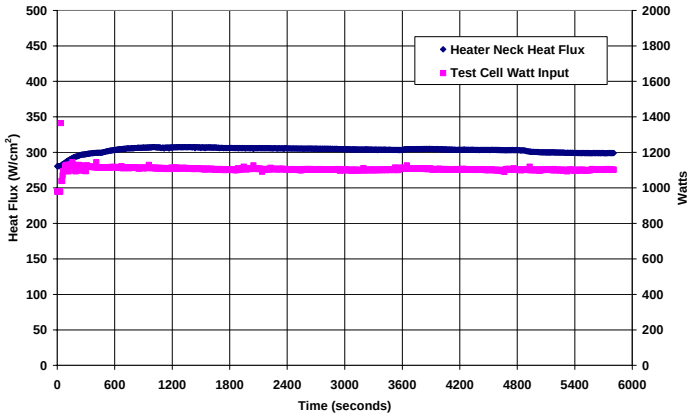

410 kPa, 20 degC Subcooled, 0.029 kg/s, 1200 watt

Mass Flow Rate
410 kPa, 20 degC Subcooled, 0.029 kg/s, 1200 watt

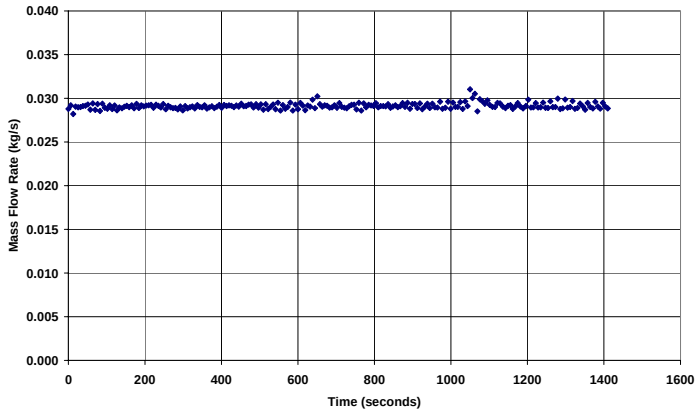

Slot Jet Fluid Temperatures
410 kPa, 20 degC Subcooled, 0.029 kg/s, 1200 watt

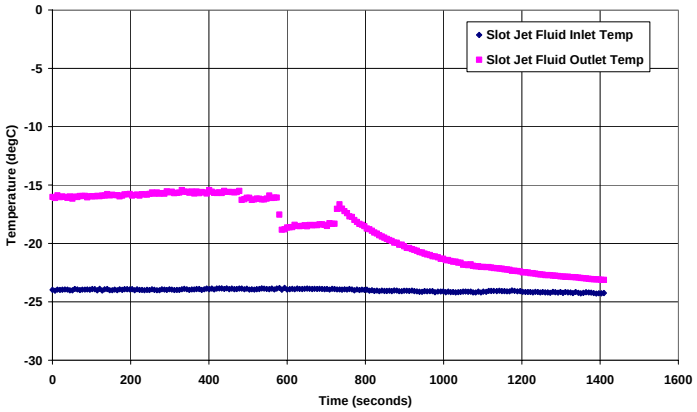

Ammonia Flow Loop Pressures
410 kPa, 20 degC Subcooled, 0.029 kg/s, 1200 watt

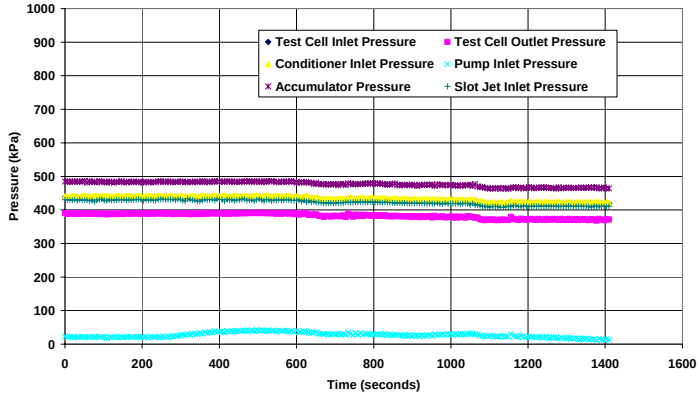

Slot Jet Surface Temperatures
410 kPa, 20 degC Subcooled, 0.029 kg/s, 1200 watt

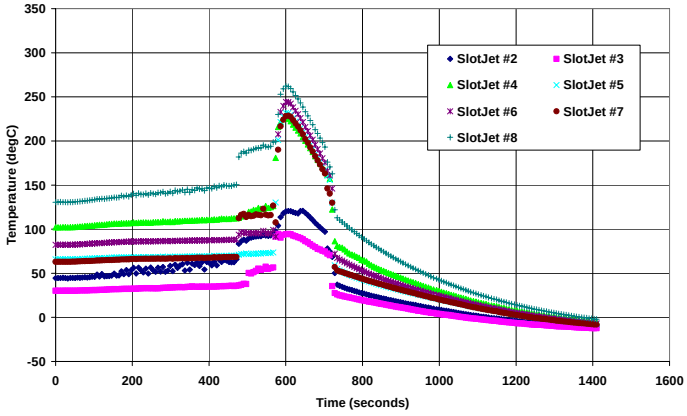

Heater Neck Temperatures
410 kPa, 20 deg Subcooled, 0.029 kg/s, 1200 watt

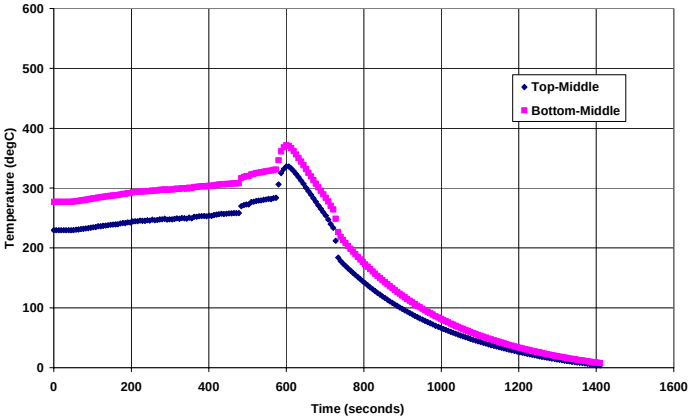

Heater Neck Heat Flux & Test Cell Watt Input
410 kPa, 20 degC Subcooled, 0.029 kg/s, 1200 watt

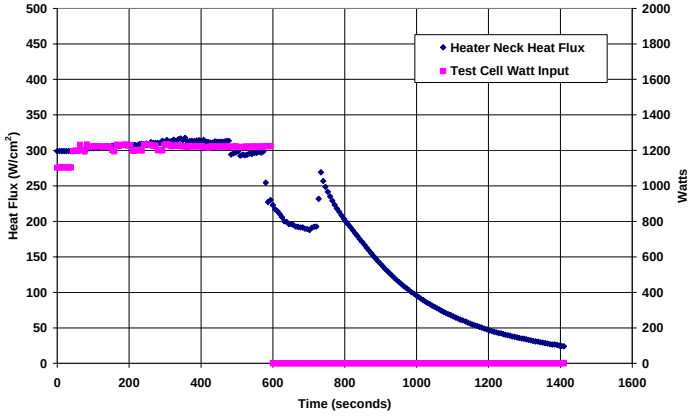

790 kPa, 40 degC Subcooled, 0.01 kg/s, 100 watt

Mass Flow Rate
790 kPa, 40 degC Subcooled, 0.01 kg/s, 100 watt

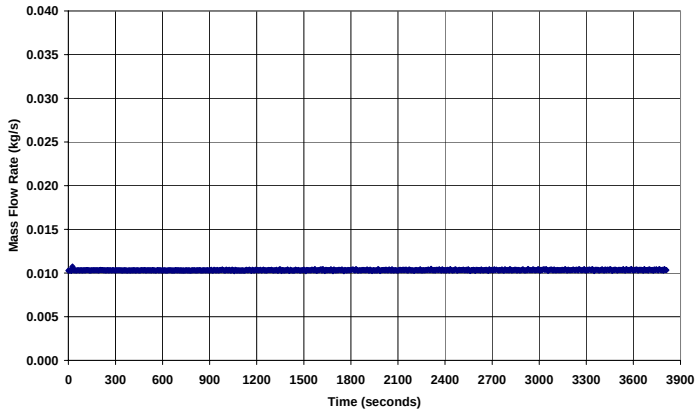

Slot Jet Fluid Temperatures
790 kPa, 40 degC Subcooled, 0.01 kg/s, 100 watt

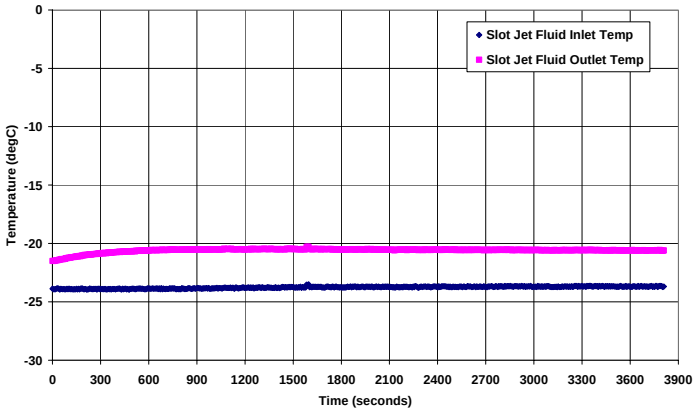

Ammonia Flow Loop Pressures
790 kPa, 40 degC Subcooled, 0.01 kg/s, 100 watt

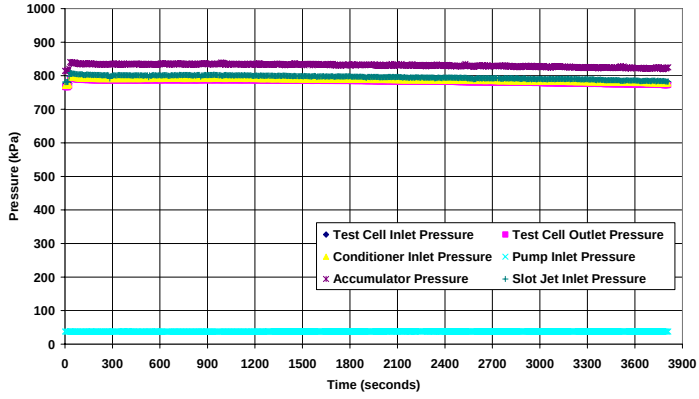

Slot Jet Surface Temperatures
790 kPa, 40 degC Subcooled, 0.01 kg/s, 100 watt

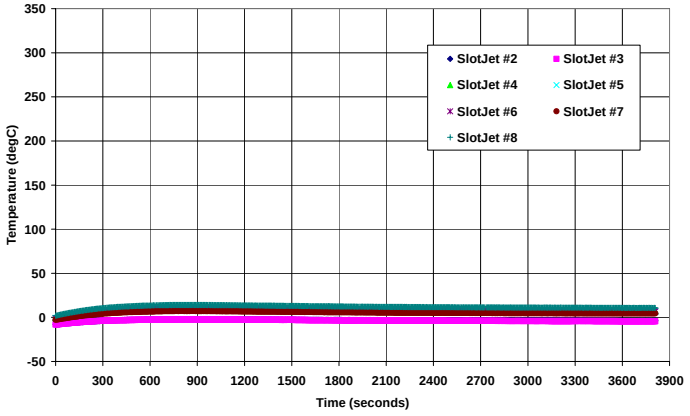

Heater Neck Temperatures
790 kPa, 40 deg Subcooled, 0.01 kg/s, 100 watt

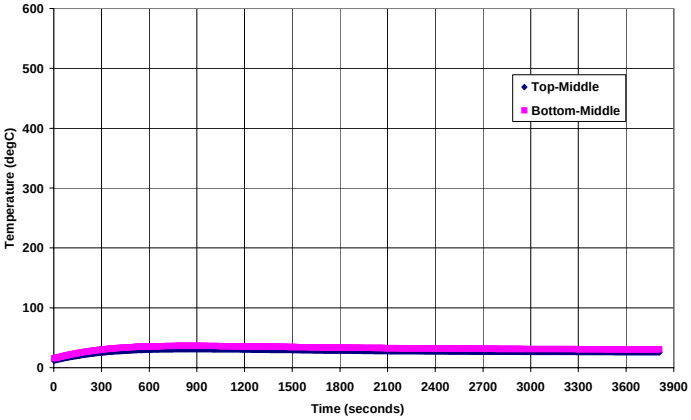

Heater Neck Heat Flux & Test Cell Watt Input
790 kPa, 40 degC Subcooled, 0.01 kg/s, 100 watt

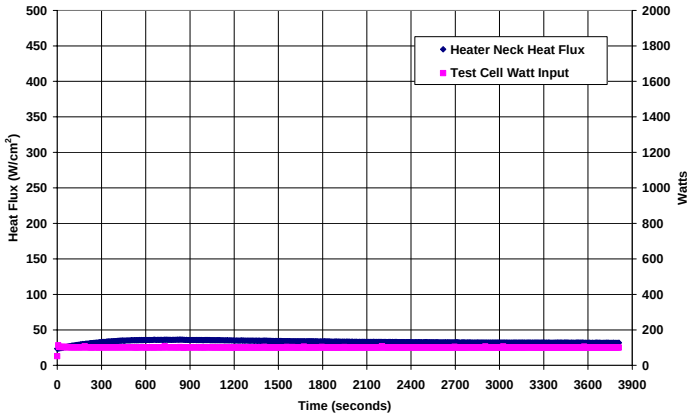

790 kPa, 40 degC Subcooled, 0.01 kg/s, 200 watt

Mass Flow Rate
790 kPa, 40 degC Subcooled, 0.01 kg/s, 200 watt

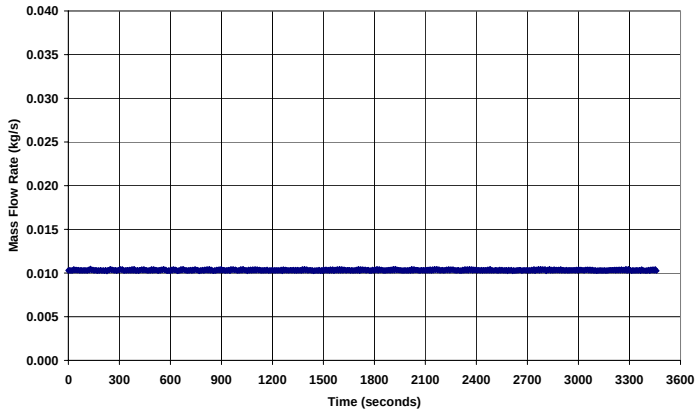

Slot Jet Fluid Temperatures
790 kPa, 40 degC Subcooled, 0.01 kg/s, 200 watt

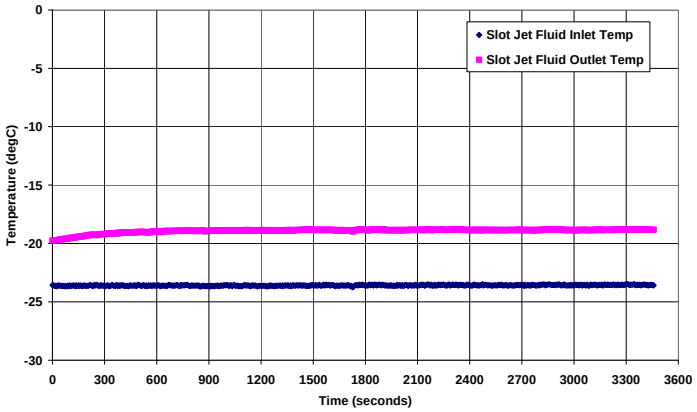

Ammonia Flow Loop Pressures
790 kPa, 40 degC Subcooled, 0.01 kg/s, 200 watt

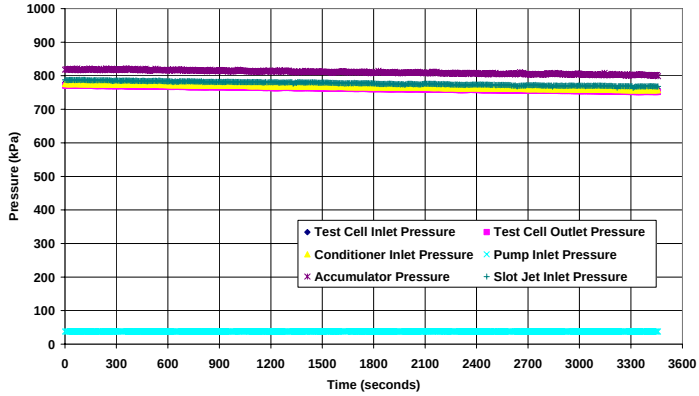

Slot Jet Surface Temperatures
790 kPa, 40 degC Subcooled, 0.01 kg/s, 200 watt

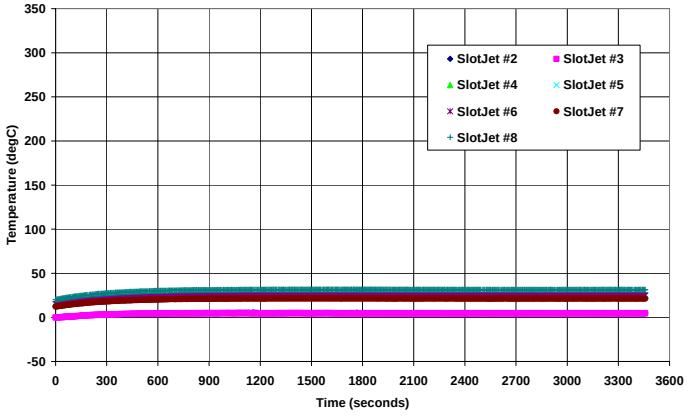

Heater Neck Temperatures
790 kPa, 40 deg Subcooled, 0.01 kg/s, 200 watt

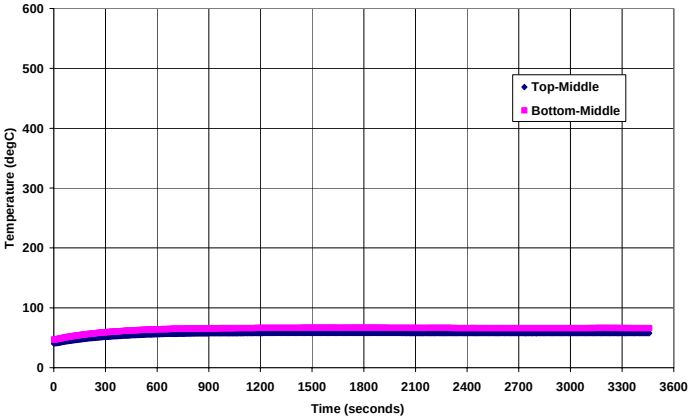

Heater Neck Heat Flux & Test Cell Watt Input
790 kPa, 40 degC Subcooled, 0.01 kg/s, 200 watt

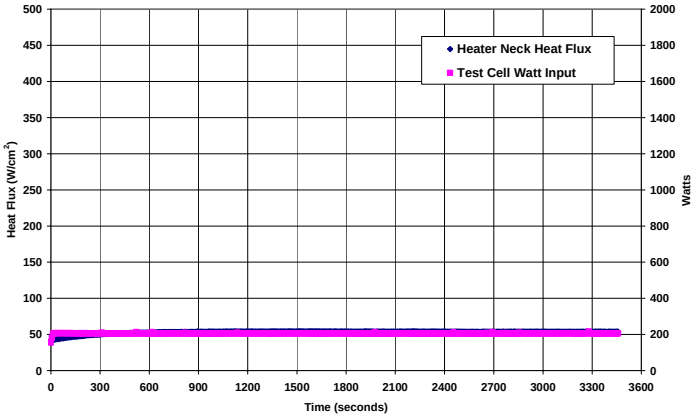

790 kPa, 40 degC Subcooled, 0.01 kg/s, 300 watt

Mass Flow Rate
790 kPa, 40 degC Subcooled, 0.01 kg/s, 300 watt

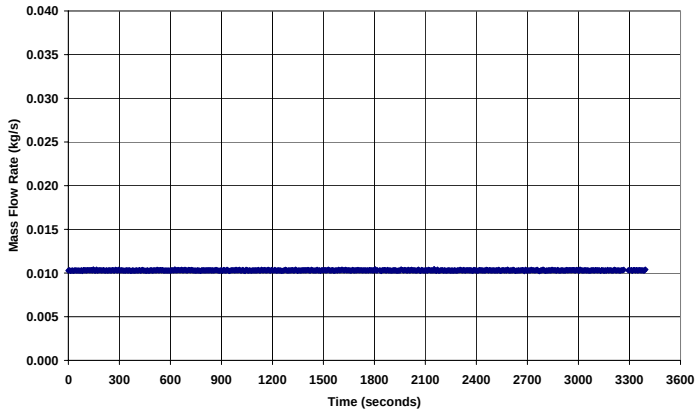

Slot Jet Fluid Temperatures
790 kPa, 40 degC Subcooled, 0.01 kg/s, 300 watt

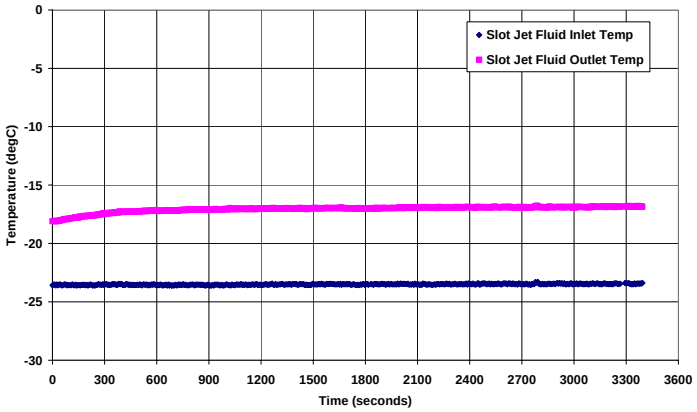

Ammonia Flow Loop Pressures
790 kPa, 40 degC Subcooled, 0.01 kg/s, 300 watt

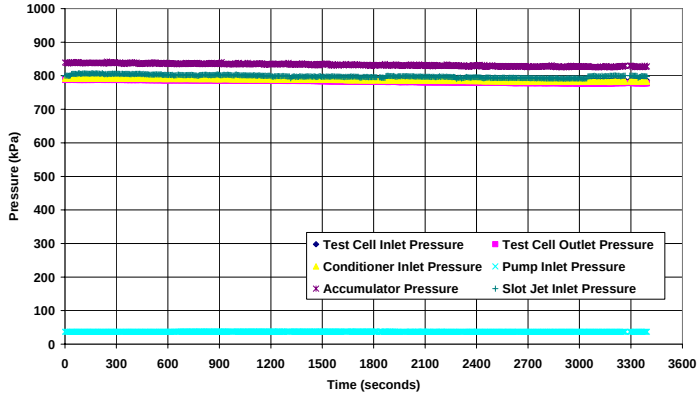

Slot Jet Surface Temperatures
790 kPa, 40 degC Subcooled, 0.01 kg/s, 300 watt

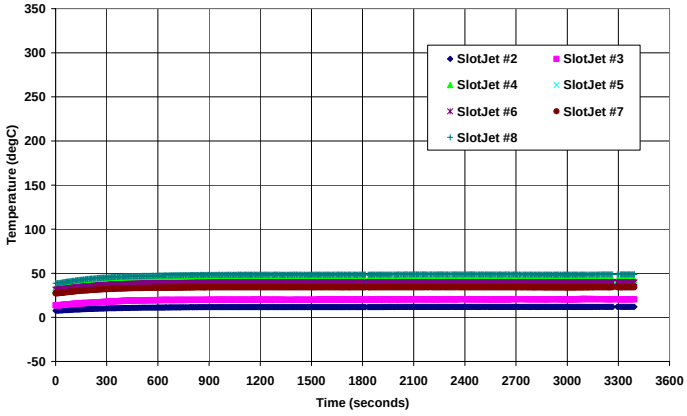

Heater Neck Temperatures
790 kPa, 40 deg Subcooled, 0.01 kg/s, 300 watt

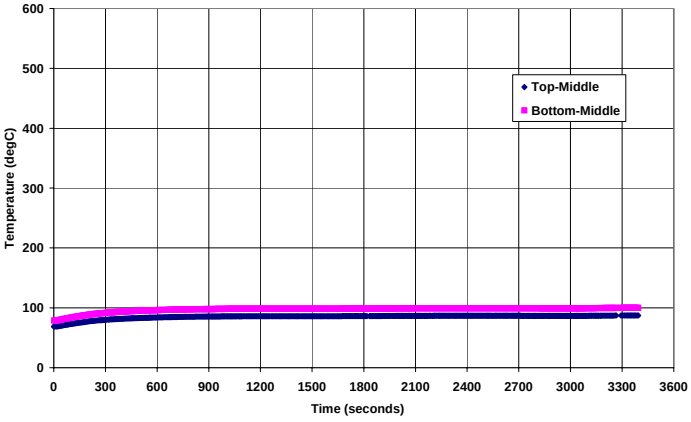

Heater Neck Heat Flux & Test Cell Watt Input
790 kPa, 40 degC Subcooled, 0.01 kg/s, 300 watt

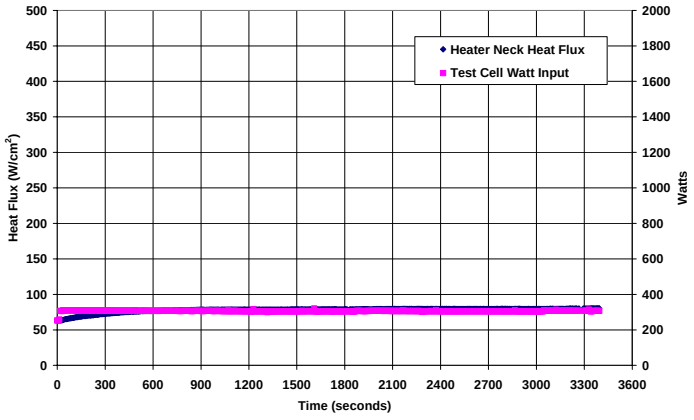

790 kPa, 40 degC Subcooled, 0.01 kg/s, 400 watt

Mass Flow Rate
790 kPa, 40 degC Subcooled, 0.01 kg/s, 400 watt

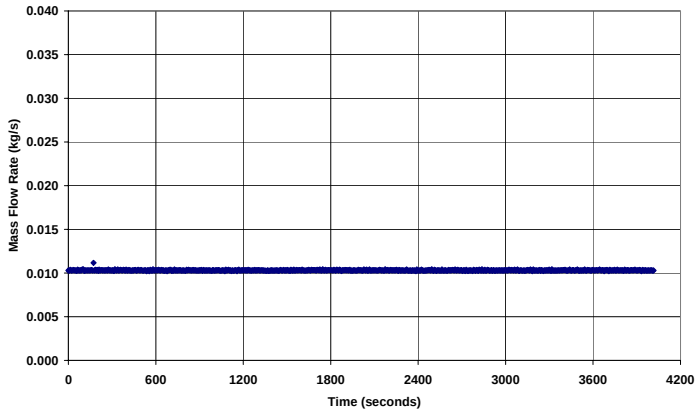

Slot Jet Fluid Temperatures
790 kPa, 40 degC Subcooled, 0.01 kg/s, 400 watt

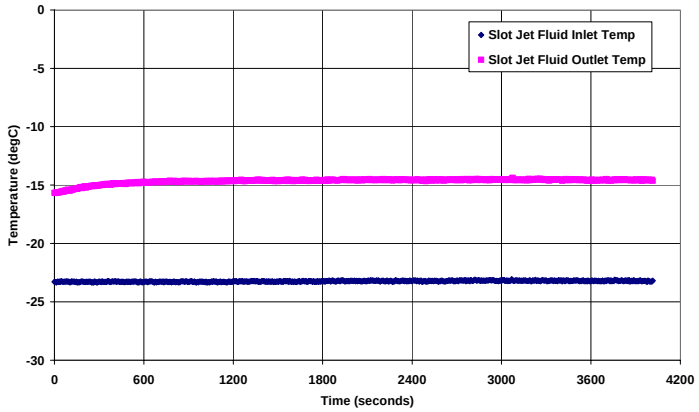

Ammonia Flow Loop Pressures
790 kPa, 40 degC Subcooled, 0.01 kg/s, 400 watt

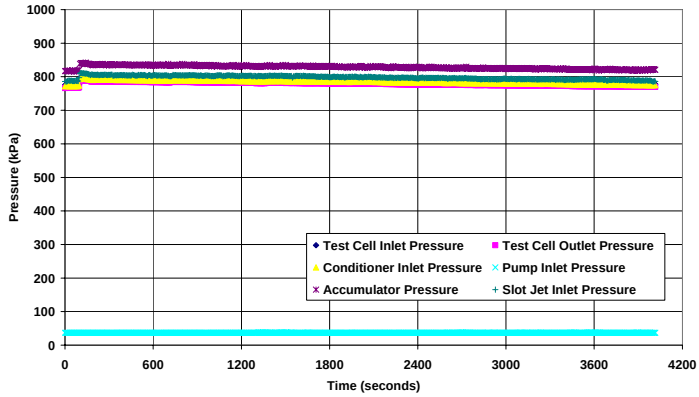

Slot Jet Surface Temperatures
790 kPa, 40 degC Subcooled, 0.01 kg/s, 400 watt

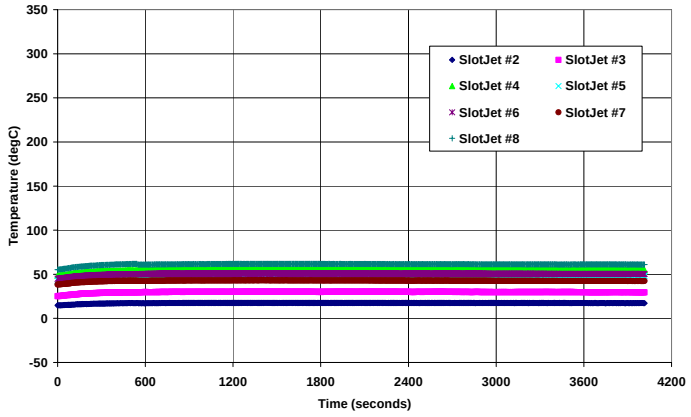

Heater Neck Temperatures
790 kPa, 40 deg Subcooled, 0.01 kg/s, 400 watt

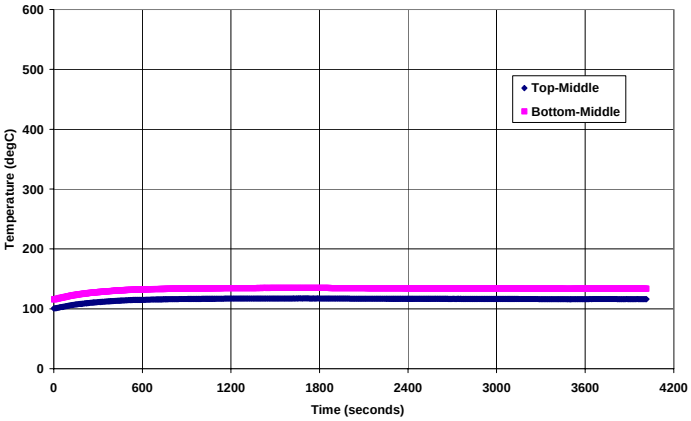

Heater Neck Heat Flux & Test Cell Watt Input
790 kPa, 40 degC Subcooled, 0.01 kg/s, 400 watt

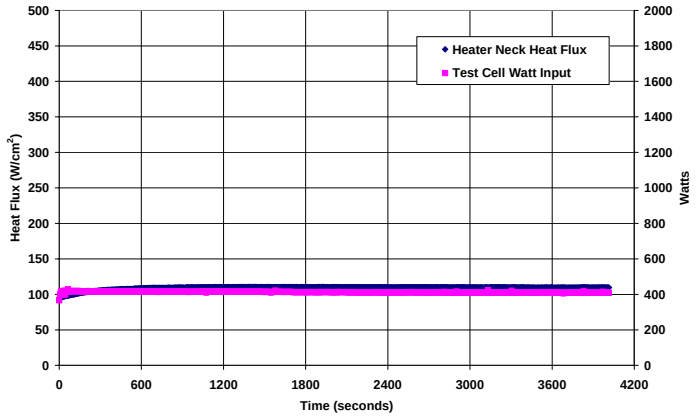

790 kPa, 40 degC Subcooled, 0.01 kg/s, 500 watt

Mass Flow Rate
790 kPa, 40 degC Subcooled, 0.01 kg/s, 500 watt

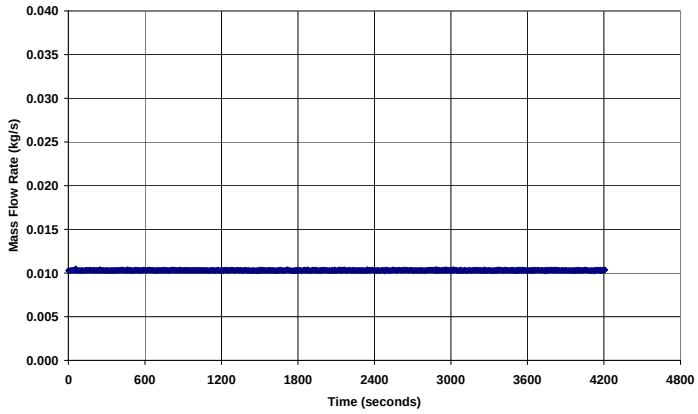

Slot Jet Fluid Temperatures
790 kPa, 40 degC Subcooled, 0.01 kg/s, 500 watt

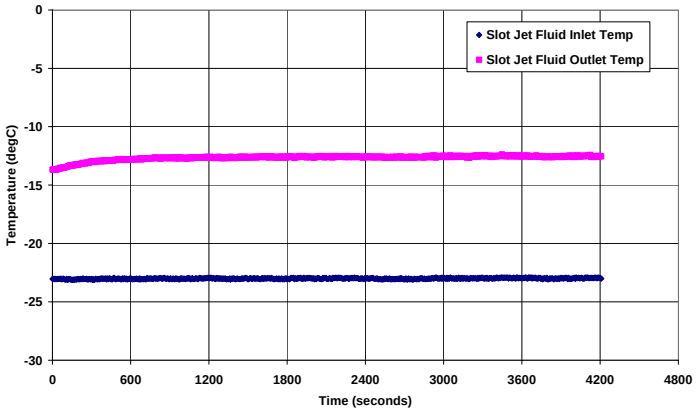

Ammonia Flow Loop Pressures
790 kPa, 40 degC Subcooled, 0.01 kg/s, 500 watt

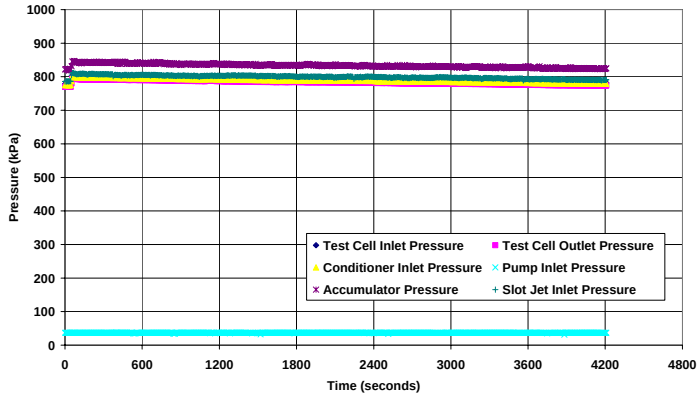

Slot Jet Surface Temperatures
790 kPa, 40 degC Subcooled, 0.01 kg/s, 500 watt

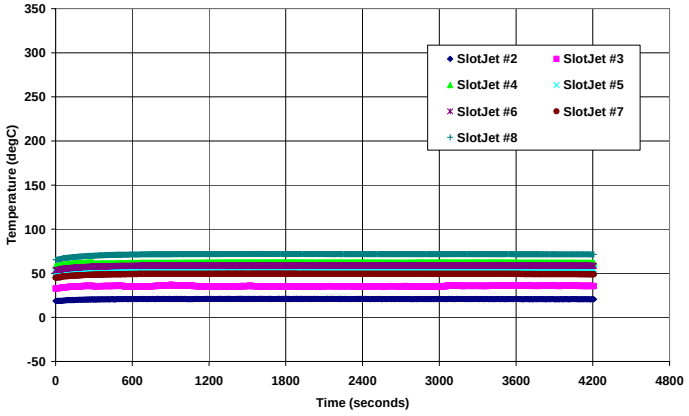

Heater Neck Temperatures
790 kPa, 40 deg Subcooled, 0.01 kg/s, 500 watt

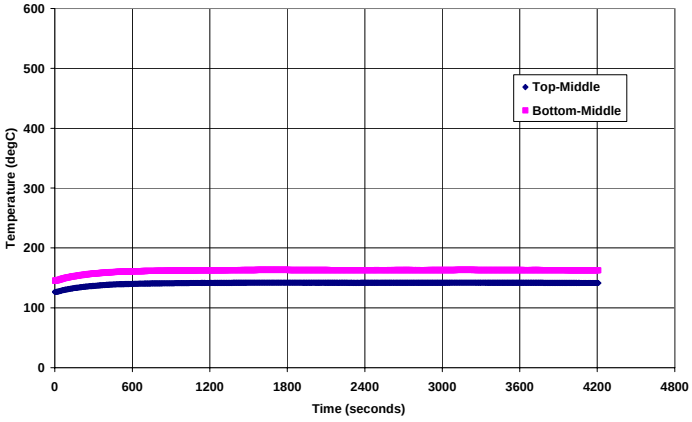

Heater Neck Heat Flux & Test Cell Watt Input
790 kPa, 40 degC Subcooled, 0.01 kg/s, 500 watt

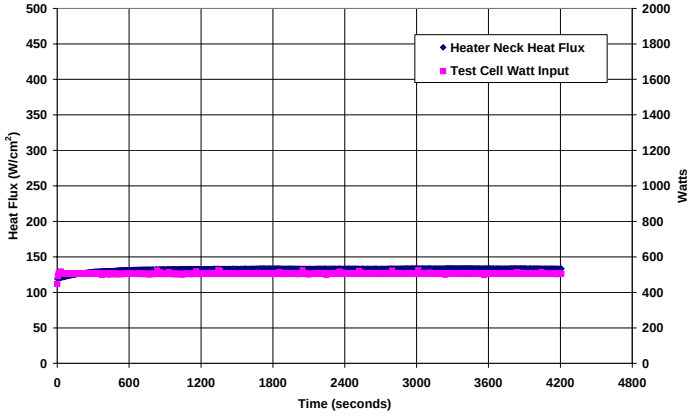

790 kPa, 40 degC Subcooled, 0.01 kg/s, 600 watt

Mass Flow Rate
790 kPa, 40 degC Subcooled, 0.01 kg/s, 600 watt

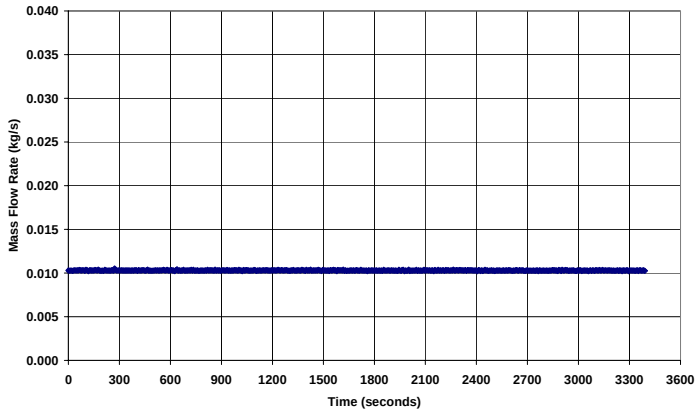

Slot Jet Fluid Temperatures
790 kPa, 40 degC Subcooled, 0.01 kg/s, 600 watt

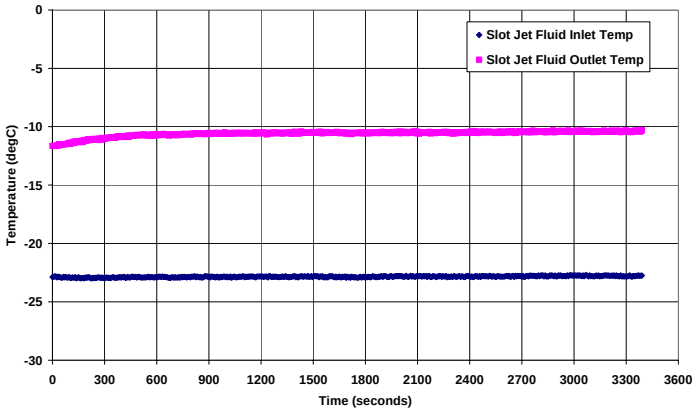

Ammonia Flow Loop Pressures
790 kPa, 40 degC Subcooled, 0.01 kg/s, 600 watt

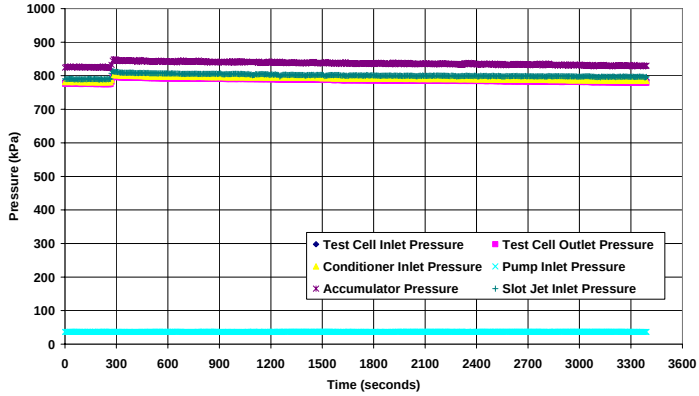

Slot Jet Surface Temperatures
790 kPa, 40 degC Subcooled, 0.01 kg/s, 600 watt

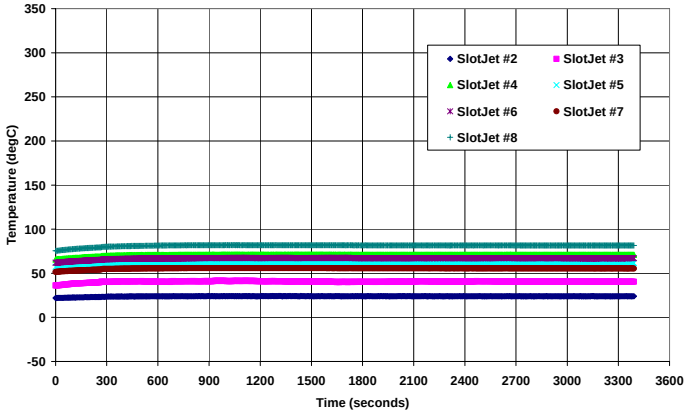

Heater Neck Temperatures
790 kPa, 40 deg Subcooled, 0.01 kg/s, 600 watt

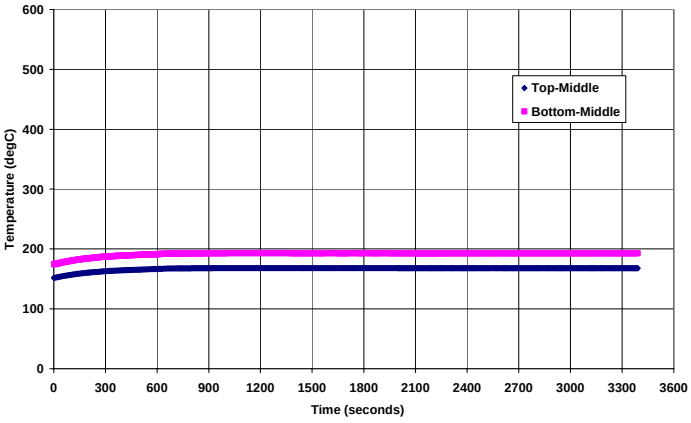

Heater Neck Heat Flux & Test Cell Watt Input
790 kPa, 40 degC Subcooled, 0.01 kg/s, 600 watt

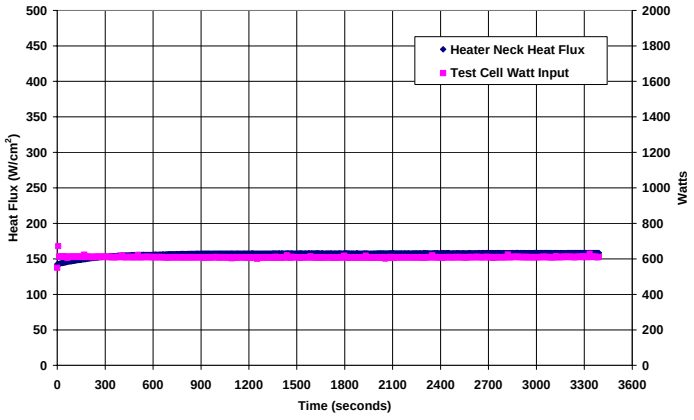

790 kPa, 40 degC Subcooled, 0.01 kg/s, 700 watt

Mass Flow Rate
790 kPa, 40 degC Subcooled, 0.01 kg/s, 700 watt

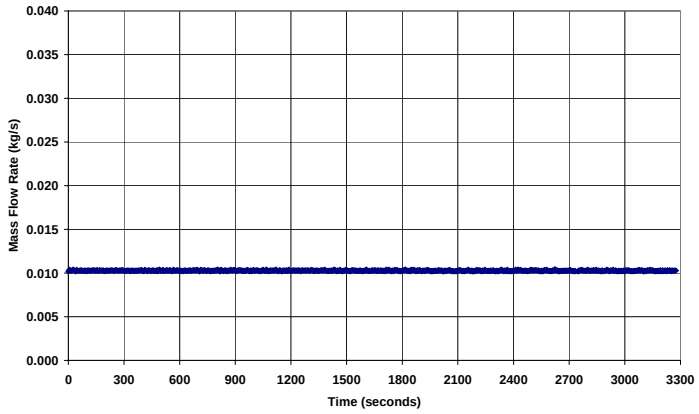

Slot Jet Fluid Temperatures
790 kPa, 40 degC Subcooled, 0.01 kg/s, 700 watt

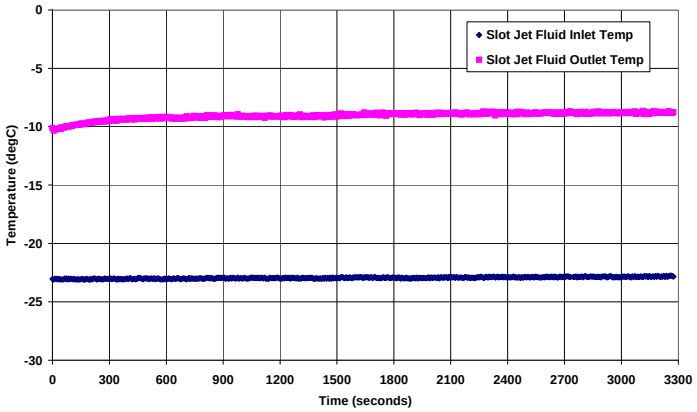

Ammonia Flow Loop Pressures
790 kPa, 40 degC Subcooled, 0.01 kg/s, 700 watt

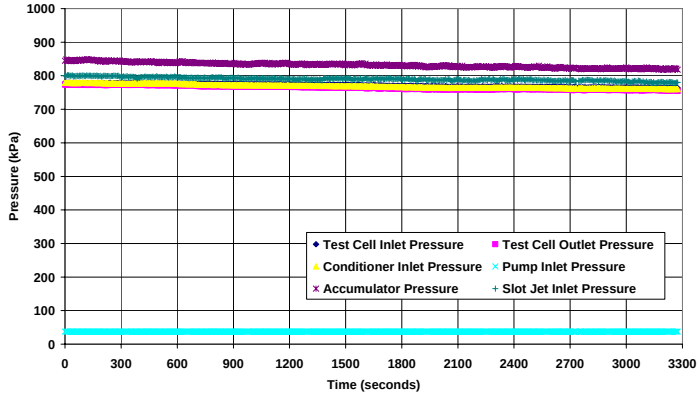

Slot Jet Surface Temperatures
790 kPa, 40 degC Subcooled, 0.01 kg/s, 700 watt

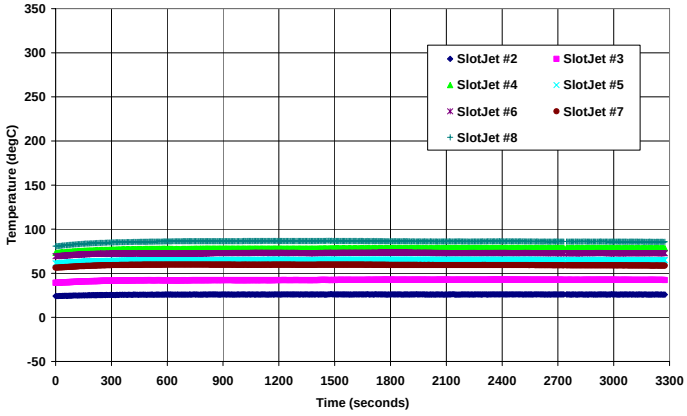

Heater Neck Temperatures
790 kPa, 40 deg Subcooled, 0.01 kg/s, 700 watt

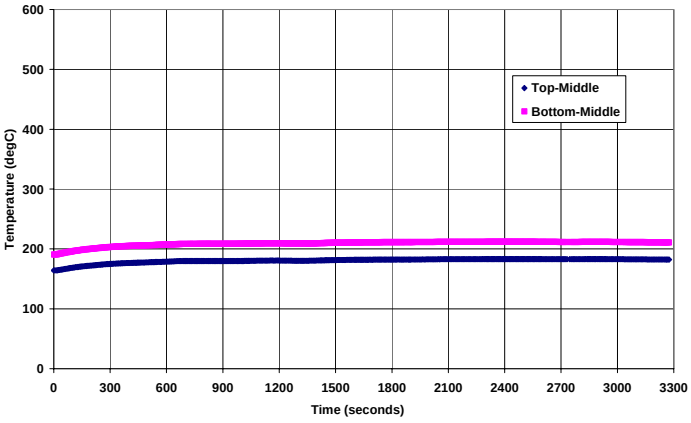

Heater Neck Heat Flux & Test Cell Watt Input
790 kPa, 40 degC Subcooled, 0.01 kg/s, 700 watt

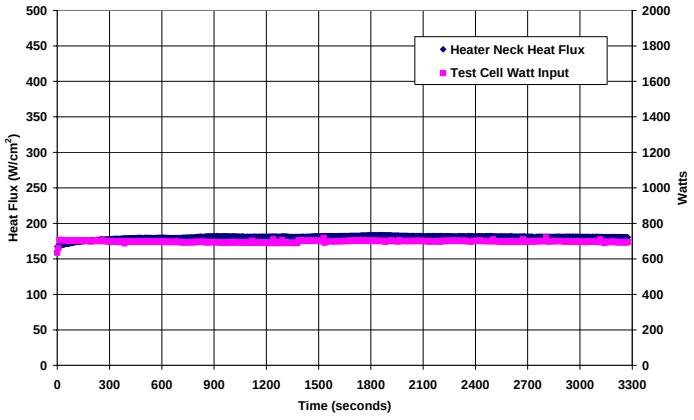

790 kPa, 40 degC Subcooled, 0.01 kg/s, 800 watt

Mass Flow Rate
790 kPa, 40 degC Subcooled, 0.01 kg/s, 800 watt

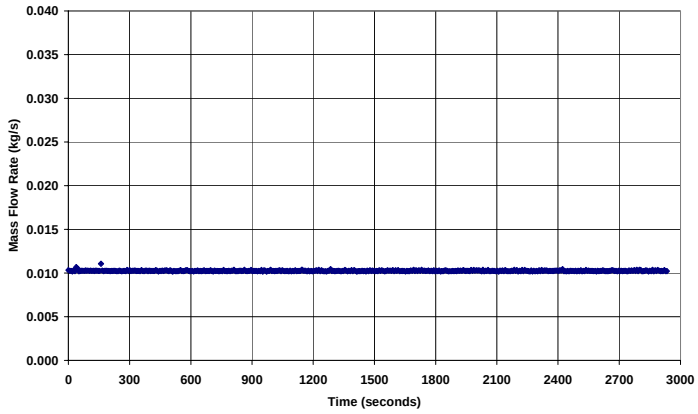

Slot Jet Fluid Temperatures
790 kPa, 40 degC Subcooled, 0.01 kg/s, 800 watt

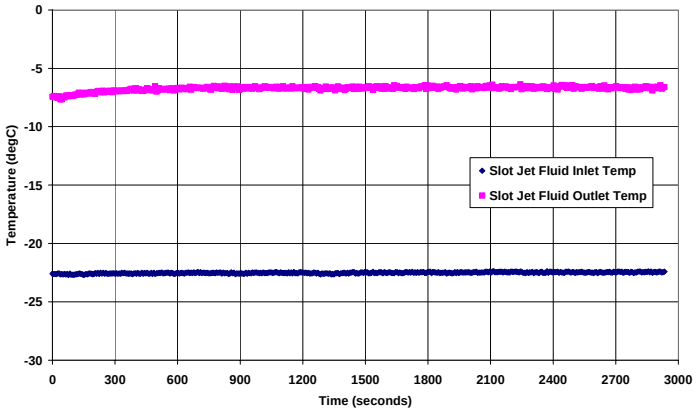

Ammonia Flow Loop Pressures
790 kPa, 40 degC Subcooled, 0.01 kg/s, 800 watt

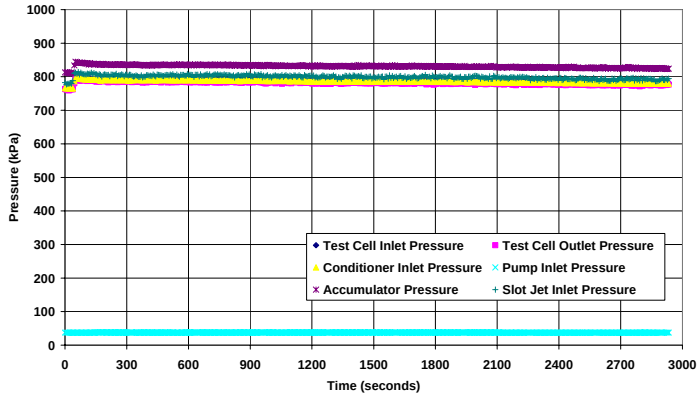

Slot Jet Surface Temperatures
790 kPa, 40 degC Subcooled, 0.01 kg/s, 800 watt

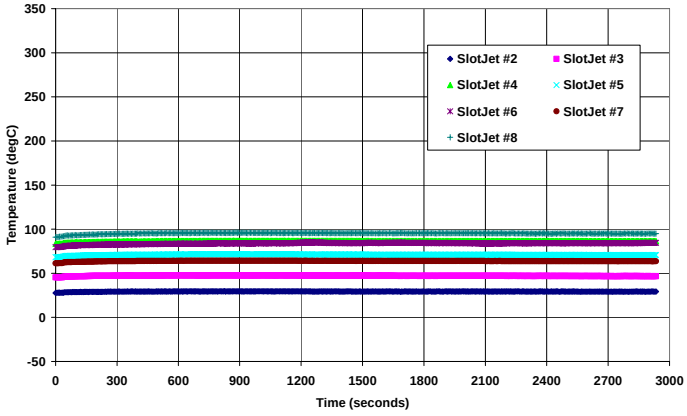

Heater Neck Temperatures
790 kPa, 40 deg Subcooled, 0.01 kg/s, 800 watt

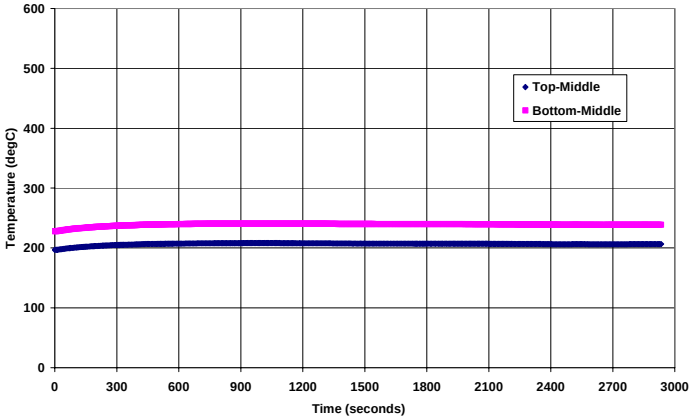

Heater Neck Heat Flux & Test Cell Watt Input
790 kPa, 40 degC Subcooled, 0.01 kg/s, 800 watt

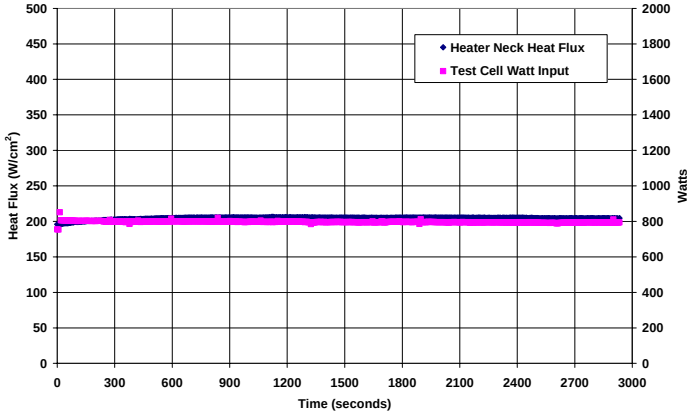

790 kPa, 40 degC Subcooled, 0.01 kg/s, 900 watt

Mass Flow Rate
790 kPa, 40 degC Subcooled, 0.01 kg/s, 900 watt

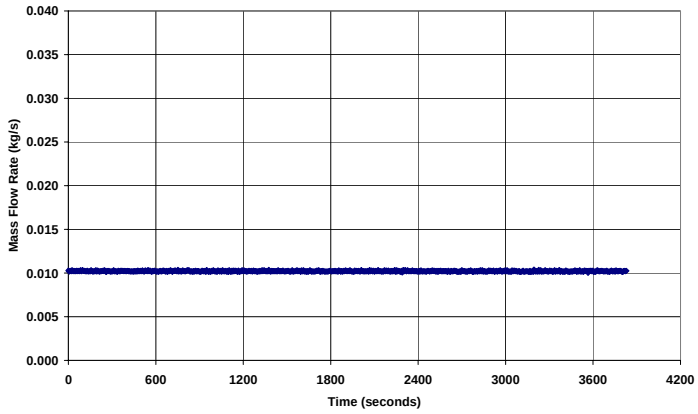

Slot Jet Fluid Temperatures
790 kPa, 40 degC Subcooled, 0.01 kg/s, 900 watt

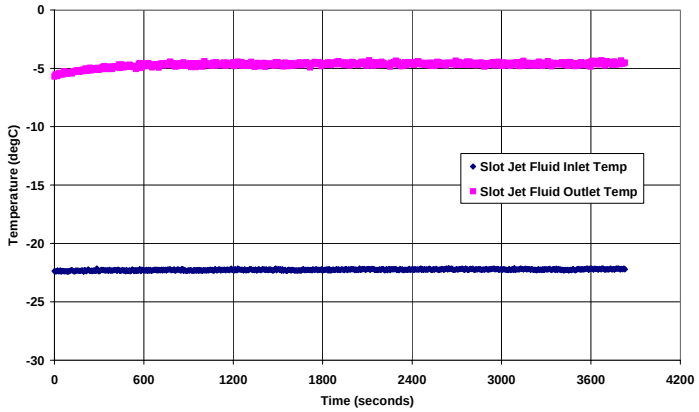

Ammonia Flow Loop Pressures
790 kPa, 40 degC Subcooled, 0.01 kg/s, 900 watt

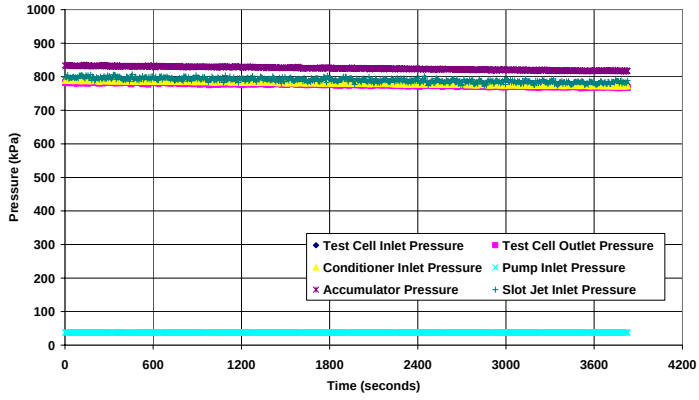

Slot Jet Surface Temperatures
790 kPa, 40 degC Subcooled, 0.01 kg/s, 900 watt

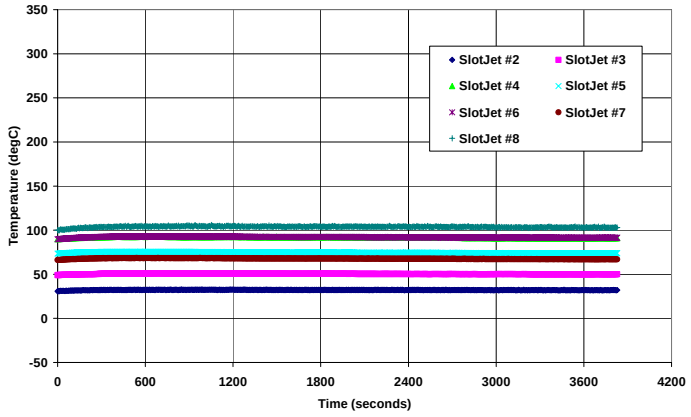

Heater Neck Temperatures
790 kPa, 40 deg Subcooled, 0.01 kg/s, 900 watt

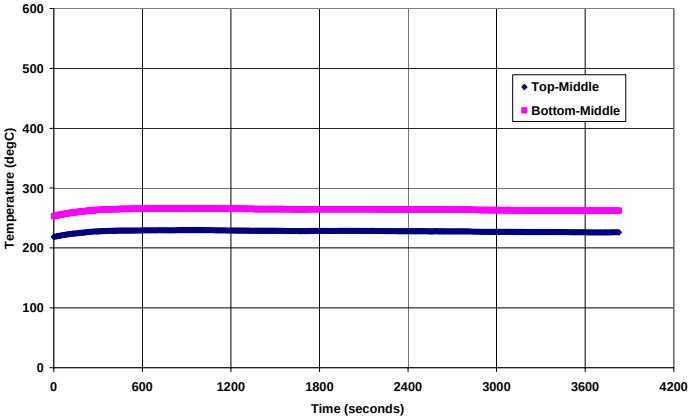

Heater Neck Heat Flux & Test Cell Watt Input
790 kPa, 40 degC Subcooled, 0.01 kg/s, 900 watt

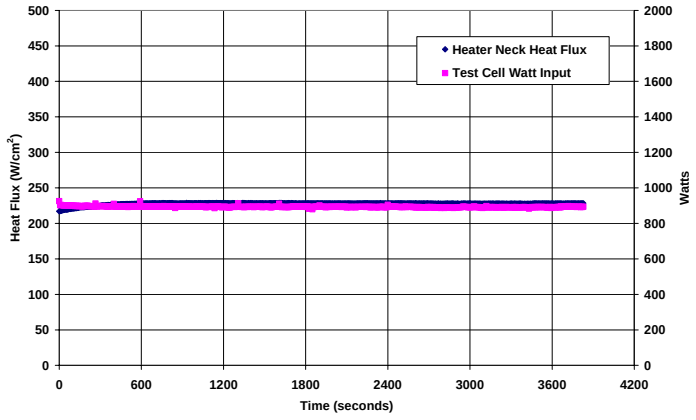

790 kPa, 40 degC Subcooled, 0.01 kg/s, 1000 watt

Mass Flow Rate
790 kPa, 40 degC Subcooled, 0.01 kg/s, 1000 watt

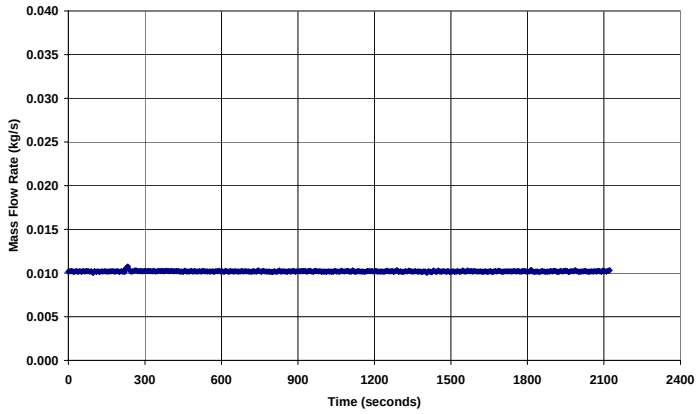

Slot Jet Fluid Temperatures
790 kPa, 40 degC Subcooled, 0.01 kg/s, 1000 watt

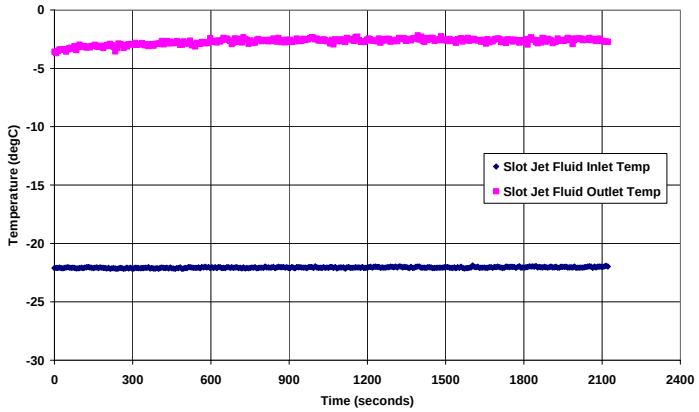

Ammonia Flow Loop Pressures
790 kPa, 40 degC Subcooled, 0.01 kg/s, 1000 watt

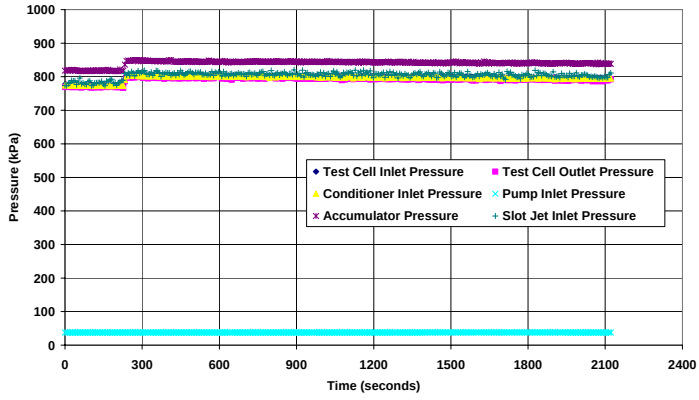

Slot Jet Surface Temperatures
790 kPa, 40 degC Subcooled, 0.01 kg/s, 1000 watt

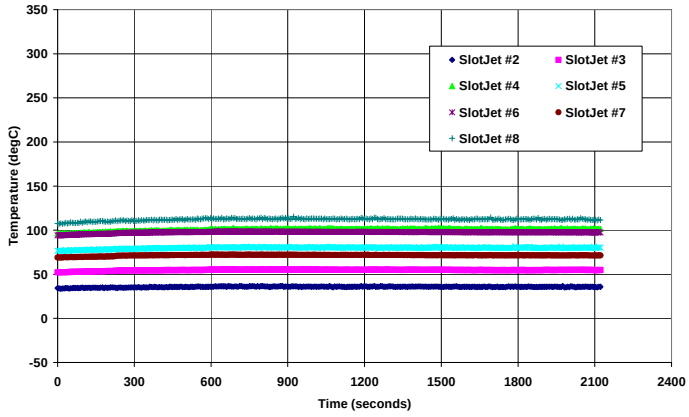

Heater Neck Temperatures
790 kPa, 40 deg Subcooled, 0.01 kg/s, 1000 watt

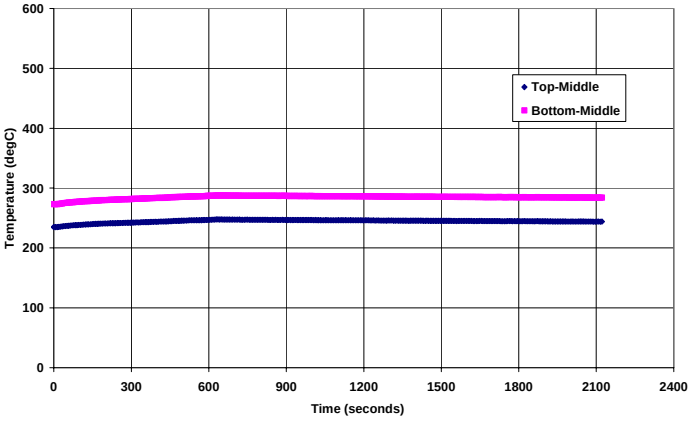

Heater Neck Heat Flux & Test Cell Watt Input
790 kPa, 40 degC Subcooled, 0.01 kg/s, 1000 watt

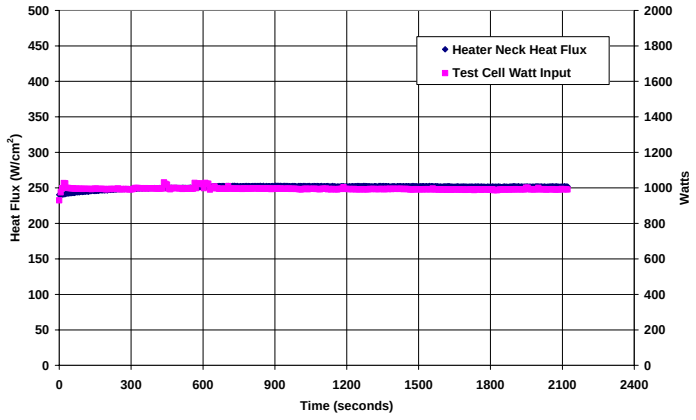

790 kPa, 40 degC Subcooled, 0.01 kg/s, 1050 watt

Mass Flow Rate
790 kPa, 40 degC Subcooled, 0.01 kg/s, 1050 watt

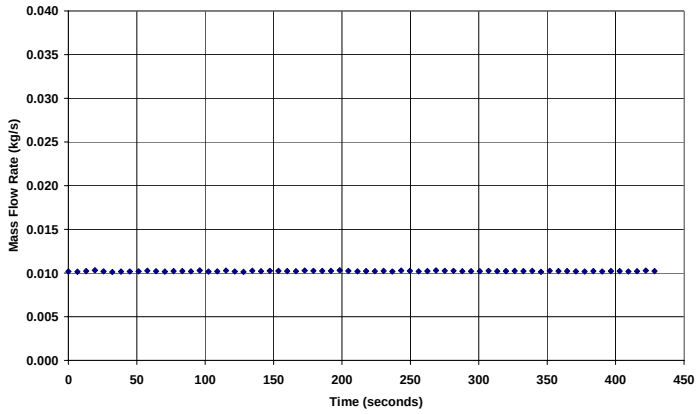

Slot Jet Fluid Temperatures
790 kPa, 40 degC Subcooled, 0.01 kg/s, 1050 watt

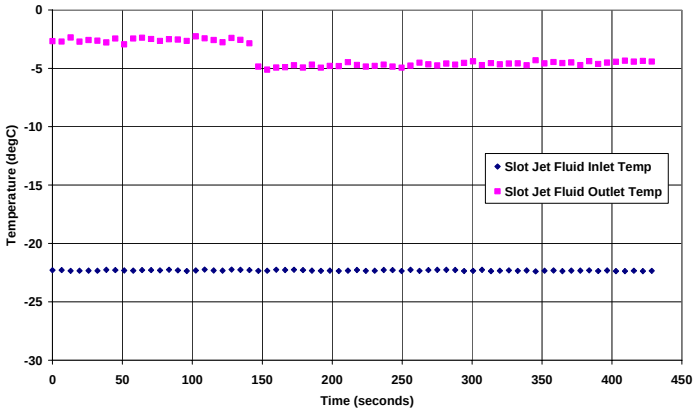

Ammonia Flow Loop Pressures
790 kPa, 40 degC Subcooled, 0.01 kg/s, 1050 watt

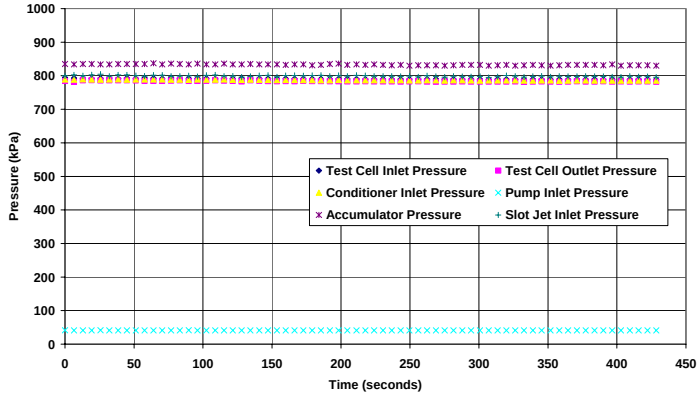

Slot Jet Surface Temperatures
790 kPa, 40 degC Subcooled, 0.01 kg/s, 1050 watt

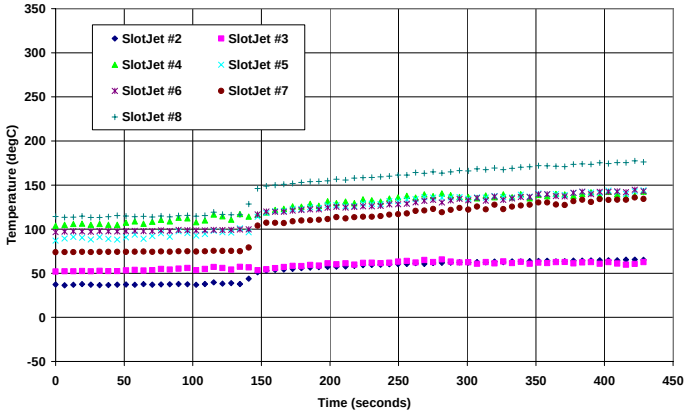

Heater Neck Temperatures
790 kPa, 40 deg Subcooled, 0.01 kg/s, 1050 watt

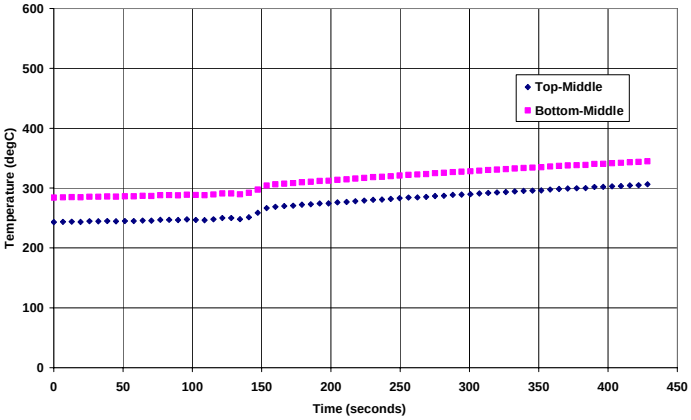

Heater Neck Heat Flux & Test Cell Watt Input
790 kPa, 40 degC Subcooled, 0.01 kg/s, 1050 watt

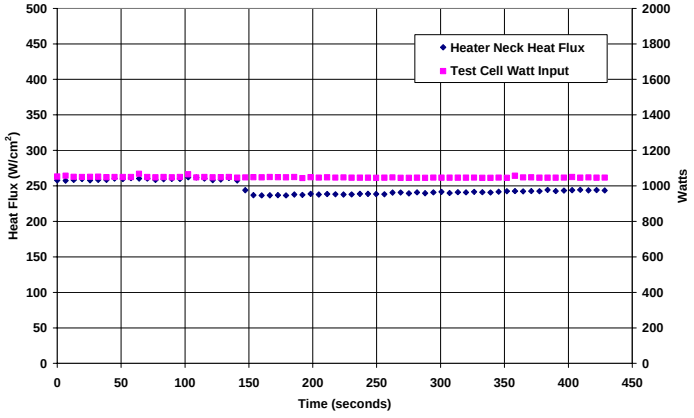

790 kPa, 40 degC Subcooled, 0.017 kg/s, 100 watt

Mass Flow Rate
790 kPa, 40 degC Subcooled, 0.017 kg/s, 100 watt

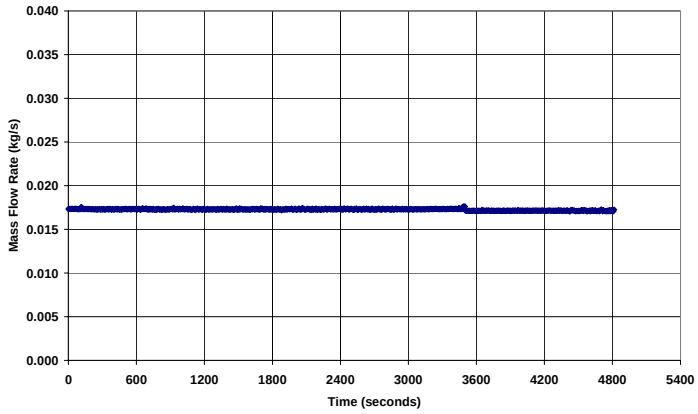

Slot Jet Fluid Temperatures
790 kPa, 40 degC Subcooled, 0.017 kg/s, 100 watt

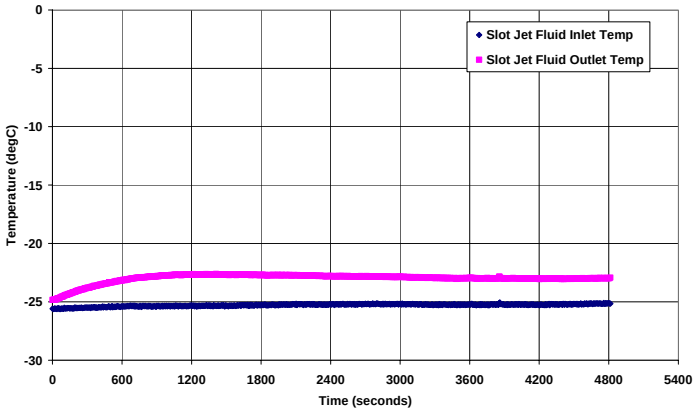

Ammonia Flow Loop Pressures
790 kPa, 40 degC Subcooled, 0.017 kg/s, 100 watt

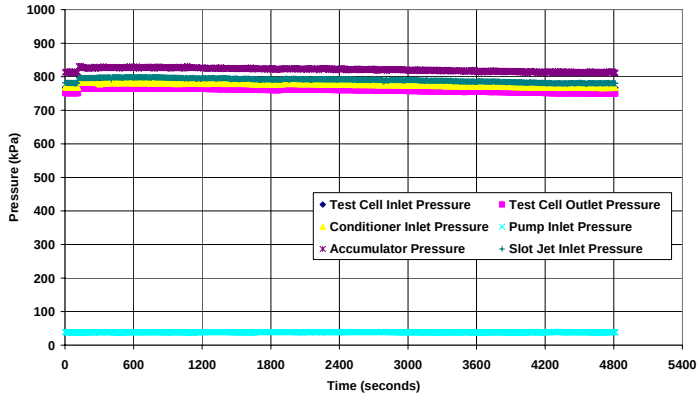

Slot Jet Surface Temperatures
790 kPa, 40 degC Subcooled, 0.017 kg/s, 100 watt

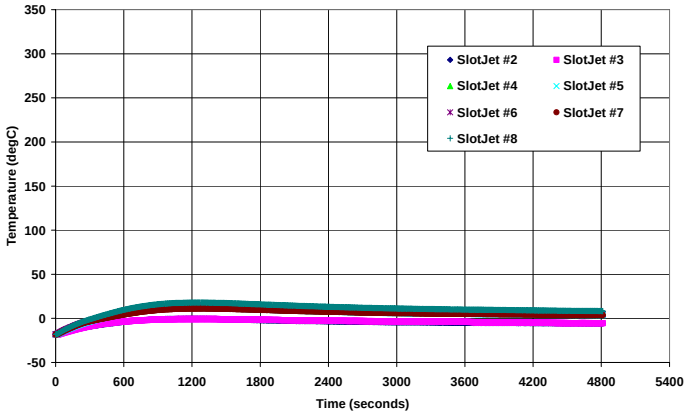

Heater Neck Temperatures
790 kPa, 40 deg Subcooled, 0.017 kg/s, 100 watt

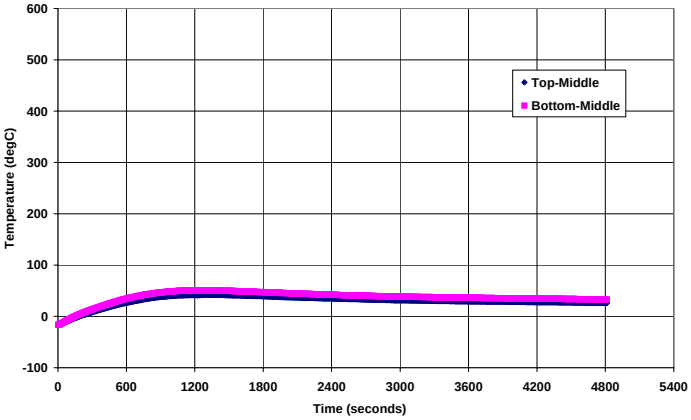

Heater Neck Heat Flux & Test Cell Watt Input
790 kPa, 40 degC Subcooled, 0.017 kg/s, 100 watt

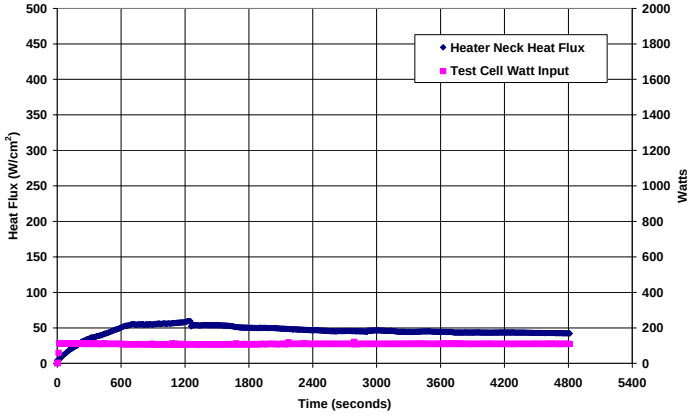

790 kPa, 40 degC Subcooled, 0.017 kg/s, 300 watt

Mass Flow Rate
790 kPa, 40 degC Subcooled, 0.017 kg/s, 300 watt

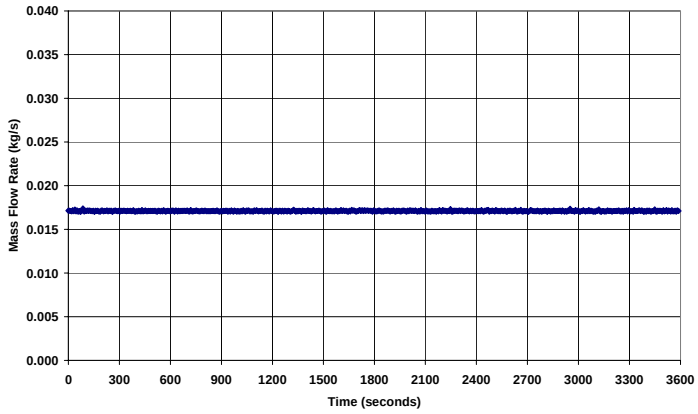

Slot Jet Fluid Temperatures
790 kPa, 40 degC Subcooled, 0.017 kg/s, 300 watt

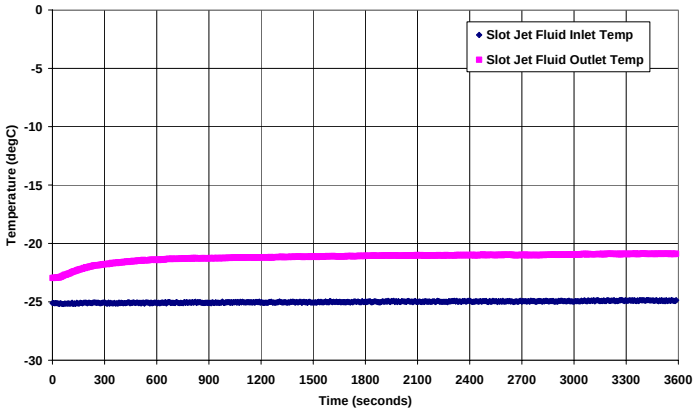

Ammonia Flow Loop Pressures
790 kPa, 40 degC Subcooled, 0.017 kg/s, 300 watt

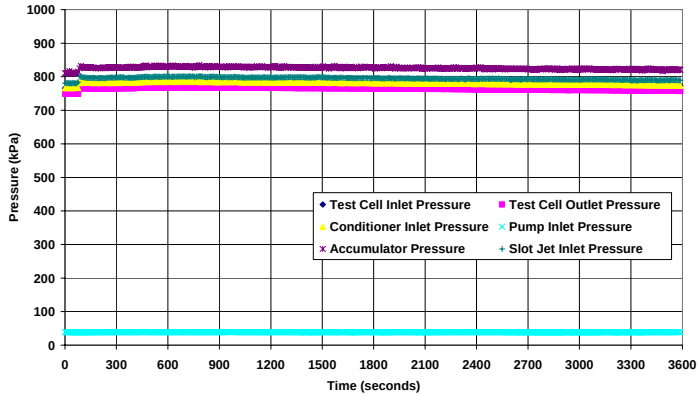

Slot Jet Surface Temperatures
790 kPa, 40 degC Subcooled, 0.017 kg/s, 300 watt

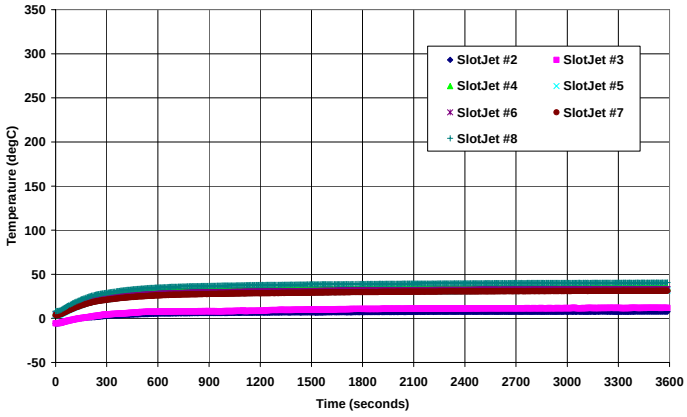

Heater Neck Temperatures
790 kPa, 40 deg Subcooled, 0.017 kg/s, 300 watt

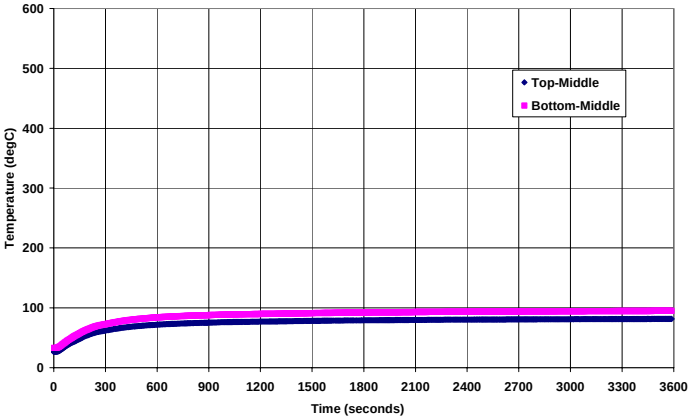

Heater Neck Heat Flux & Test Cell Watt Input
790 kPa, 40 degC Subcooled, 0.017 kg/s, 300 watt

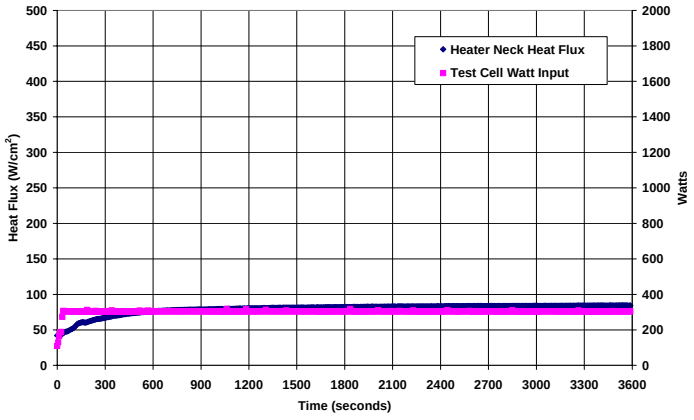

790 kPa, 40 degC Subcooled, 0.017 kg/s, 500 watt

Mass Flow Rate
790 kPa, 40 degC Subcooled, 0.017 kg/s, 500 watt

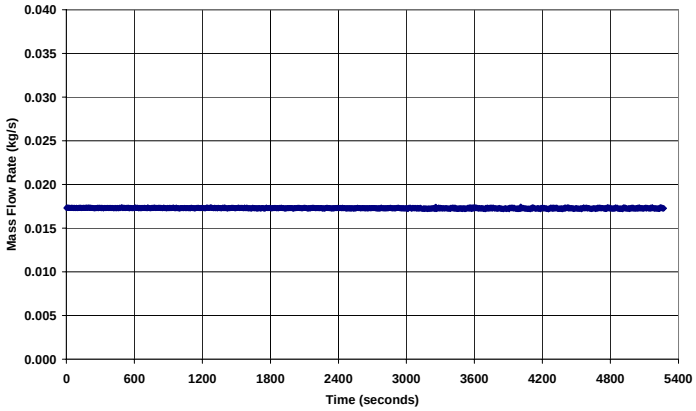

Slot Jet Fluid Temperatures
790 kPa, 40 degC Subcooled, 0.017 kg/s, 500 watt

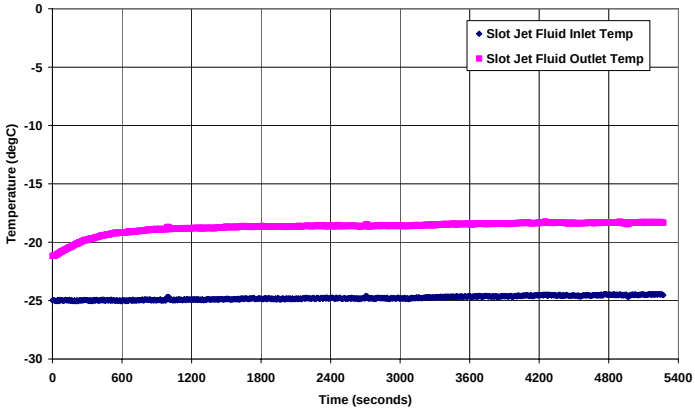

Ammonia Flow Loop Pressures
790 kPa, 40 degC Subcooled, 0.017 kg/s, 500 watt

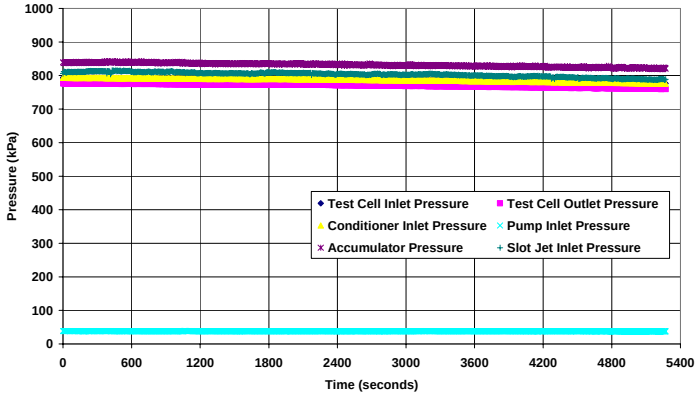

Slot Jet Surface Temperatures
790 kPa, 40 degC Subcooled, 0.017 kg/s, 500 watt

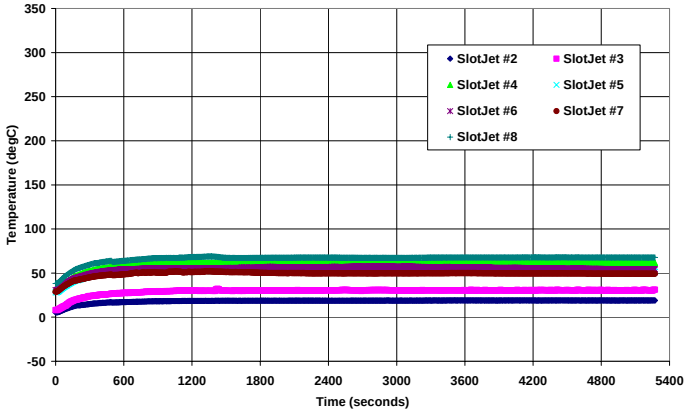

Heater Neck Temperatures
790 kPa, 40 deg Subcooled, 0.017 kg/s, 500 watt

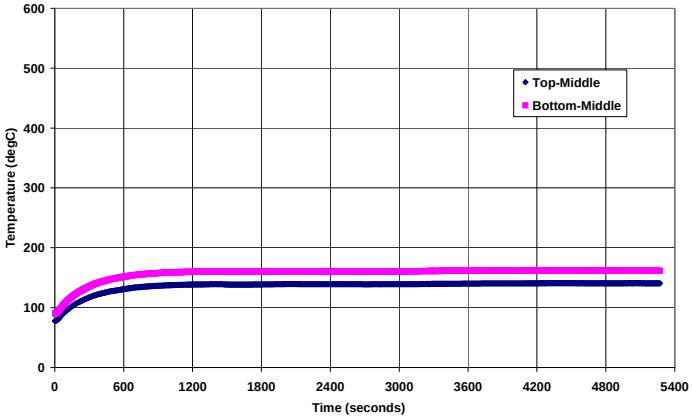

Heater Neck Heat Flux & Test Cell Watt Input
790 kPa, 40 degC Subcooled, 0.017 kg/s, 500 watt

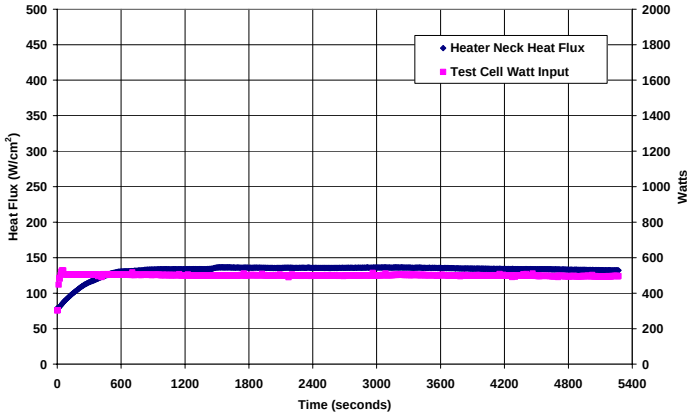

790 kPa, 40 degC Subcooled, 0.017 kg/s, 700 watt

Mass Flow Rate
790 kPa, 40 degC Subcooled, 0.017 kg/s, 700 watt

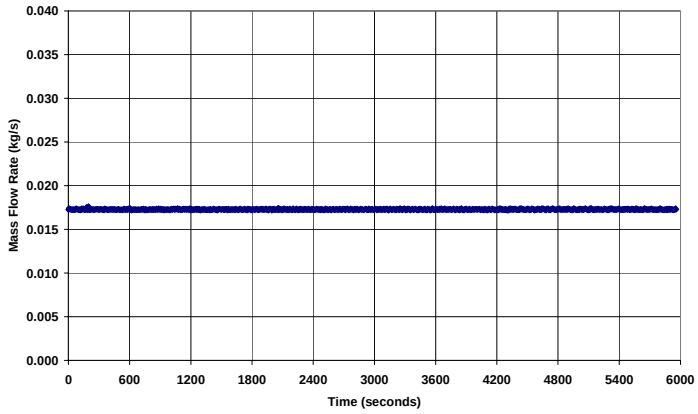

Slot Jet Fluid Temperatures
790 kPa, 40 degC Subcooled, 0.017 kg/s, 700 watt

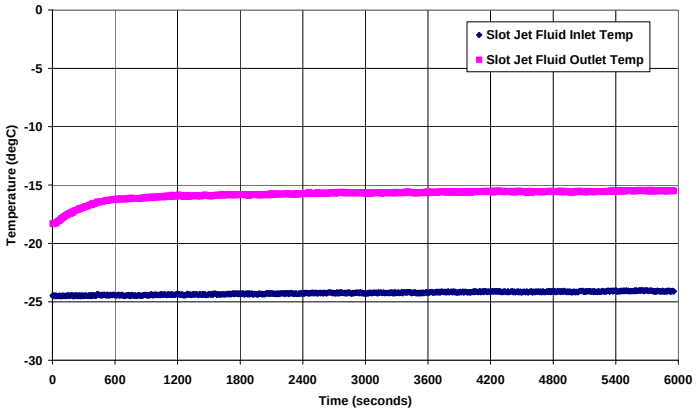

Ammonia Flow Loop Pressures
790 kPa, 40 degC Subcooled, 0.017 kg/s, 700 watt

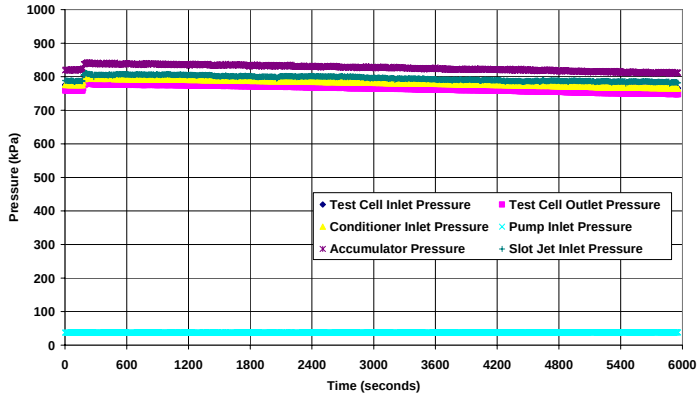

Slot Jet Surface Temperatures
790 kPa, 40 degC Subcooled, 0.017 kg/s, 700 watt

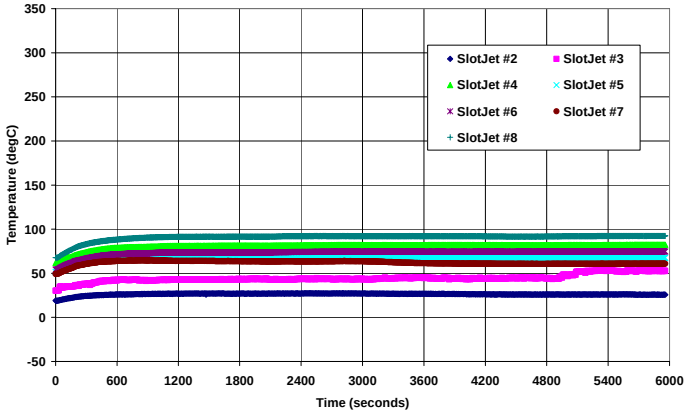

Heater Neck Temperatures
790 kPa, 40 deg Subcooled, 0.017 kg/s, 700 watt

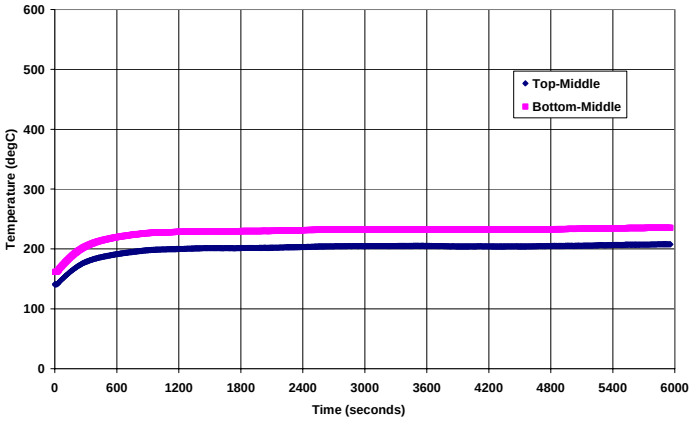

Heater Neck Heat Flux & Test Cell Watt Input
790 kPa, 40 degC Subcooled, 0.017 kg/s, 700 watt

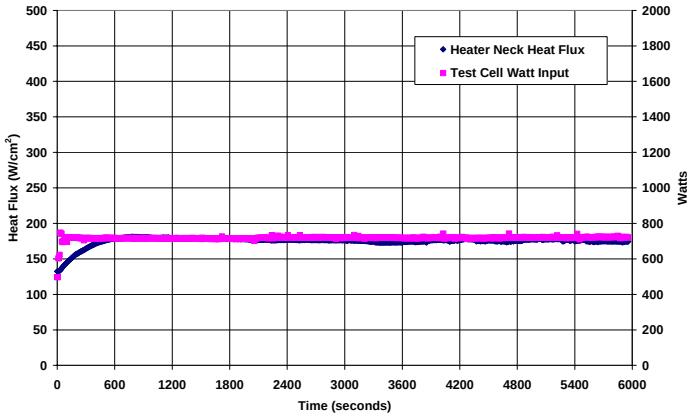

790 kPa, 40 degC Subcooled, 0.017 kg/s, 900 watt

Mass Flow Rate
790 kPa, 40 degC Subcooled, 0.017 kg/s, 900 watt

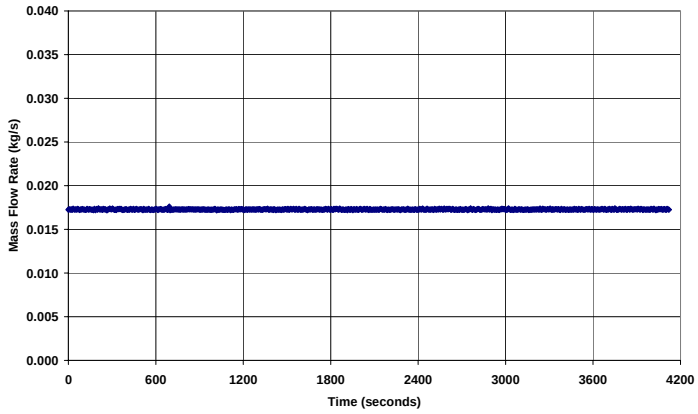

Slot Jet Fluid Temperatures
790 kPa, 40 degC Subcooled, 0.017 kg/s, 900 watt

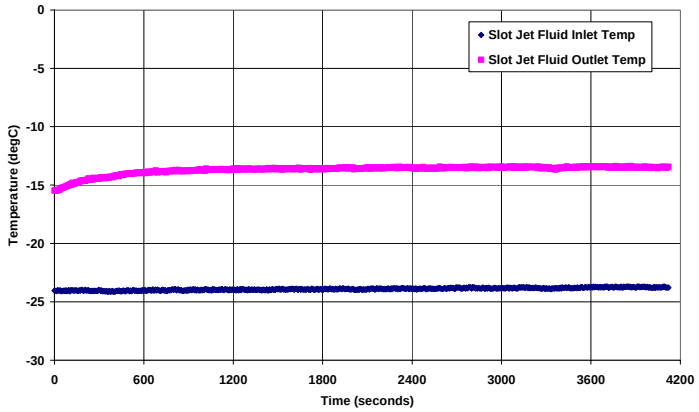

Ammonia Flow Loop Pressures
790 kPa, 40 degC Subcooled, 0.017 kg/s, 900 watt

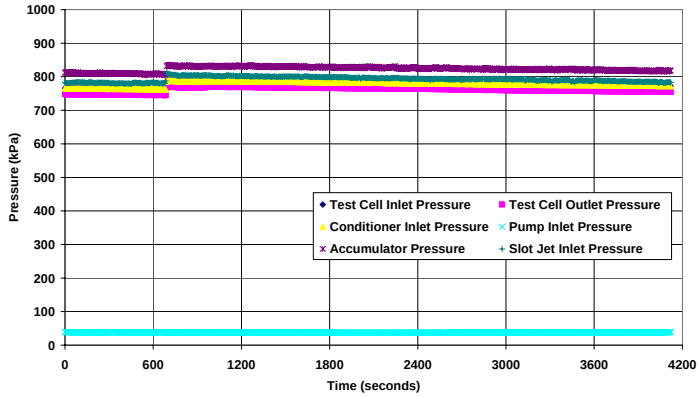

Slot Jet Surface Temperatures
790 kPa, 40 degC Subcooled, 0.017 kg/s, 900 watt

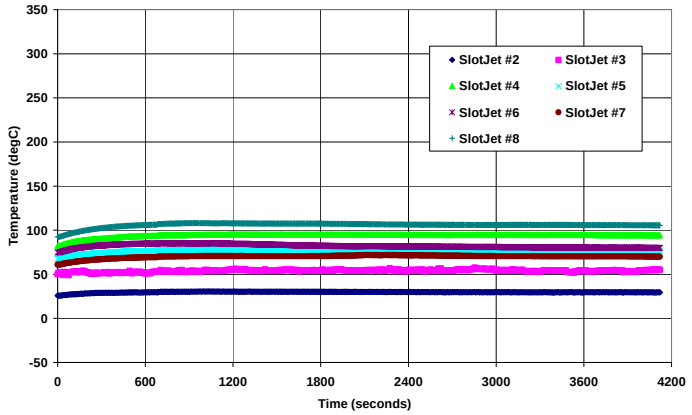

Heater Neck Temperatures
790 kPa, 40 deg Subcooled, 0.017 kg/s, 900 watt

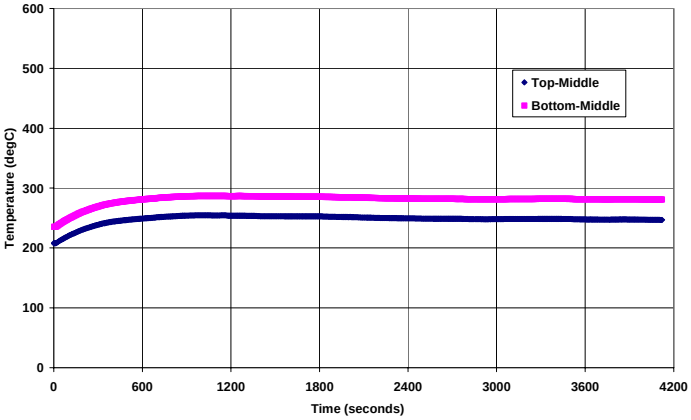

Heater Neck Heat Flux & Test Cell Watt Input
790 kPa, 40 degC Subcooled, 0.017 kg/s, 900 watt

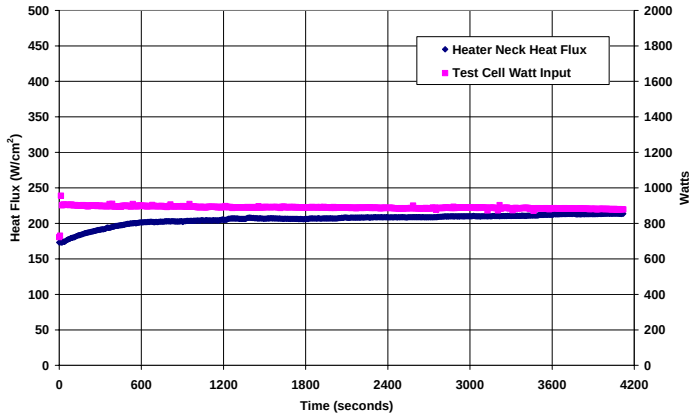

790 kPa, 40 degC Subcooled, 0.017 kg/s, 1100 watt

Mass Flow Rate
790 kPa, 40 degC Subcooled, 0.017 kg/s, 1100 watt

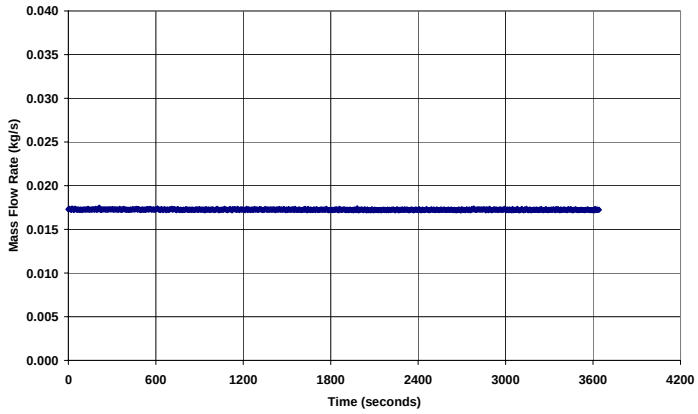

Slot Jet Fluid Temperatures
790 kPa, 40 degC Subcooled, 0.017 kg/s, 1100 watt

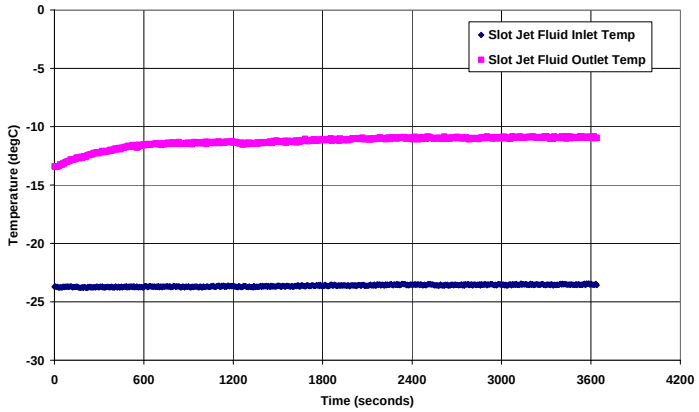

Ammonia Flow Loop Pressures
790 kPa, 40 degC Subcooled, 0.017 kg/s, 1100 watt

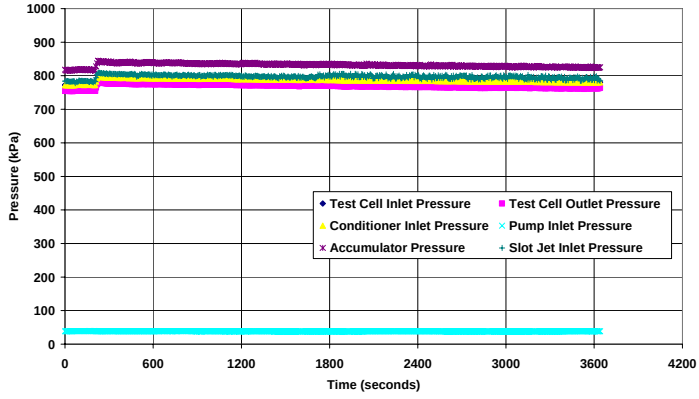

Slot Jet Surface Temperatures
790 kPa, 40 degC Subcooled, 0.017 kg/s, 1100 watt

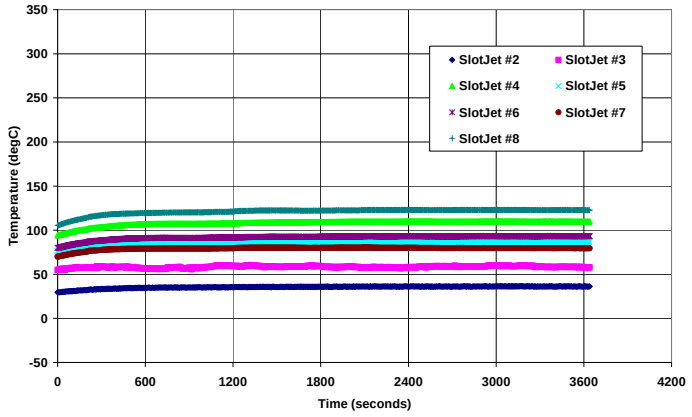

Heater Neck Temperatures
790 kPa, 40 deg Subcooled, 0.017 kg/s, 1100 watt

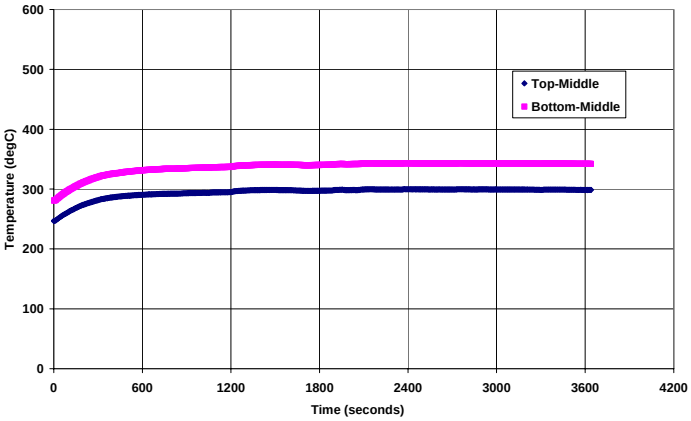

Heater Neck Heat Flux & Test Cell Watt Input
790 kPa, 40 degC Subcooled, 0.017 kg/s, 1100 watt

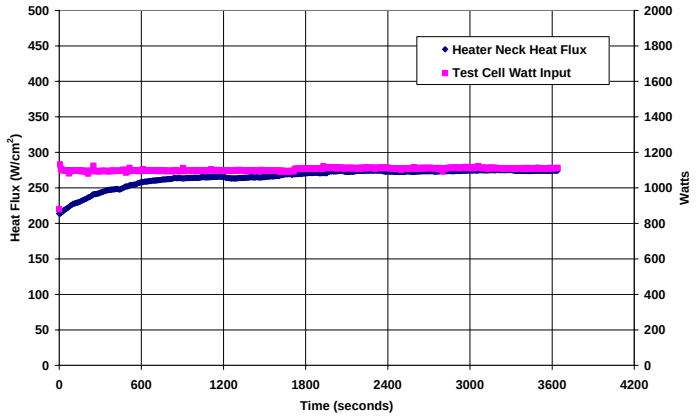

790 kPa, 40 degC Subcooled, 0.017 kg/s, 1200 watt

Mass Flow Rate
790 kPa, 40 degC Subcooled, 0.017 kg/s, 1200 watt

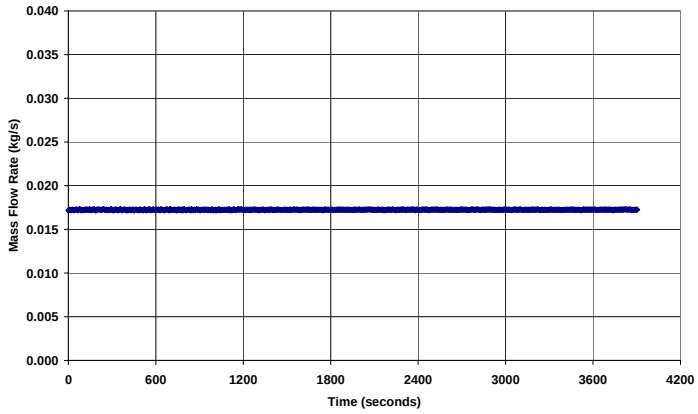

Slot Jet Fluid Temperatures
790 kPa, 40 degC Subcooled, 0.017 kg/s, 1200 watt

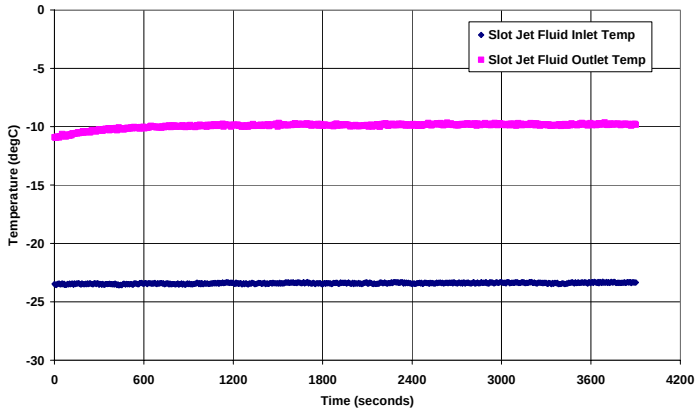

Ammonia Flow Loop Pressures
790 kPa, 40 degC Subcooled, 0.017 kg/s, 1200 watt

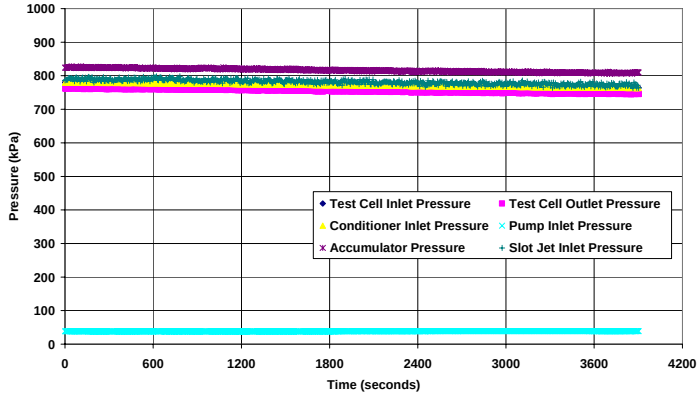

Slot Jet Surface Temperatures
790 kPa, 40 degC Subcooled, 0.017 kg/s, 1200 watt

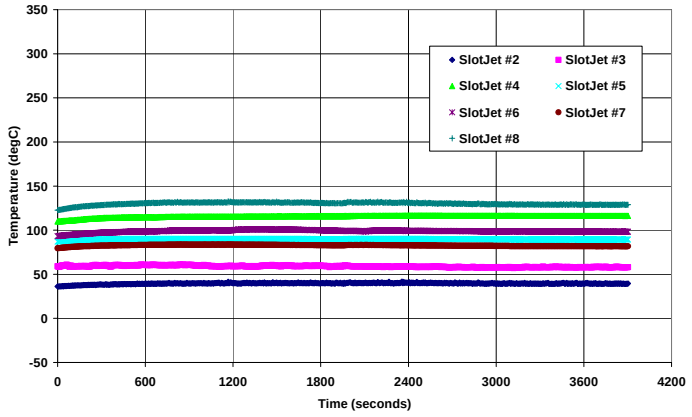

Heater Neck Temperatures
790 kPa, 40 deg Subcooled, 0.017 kg/s, 1200 watt

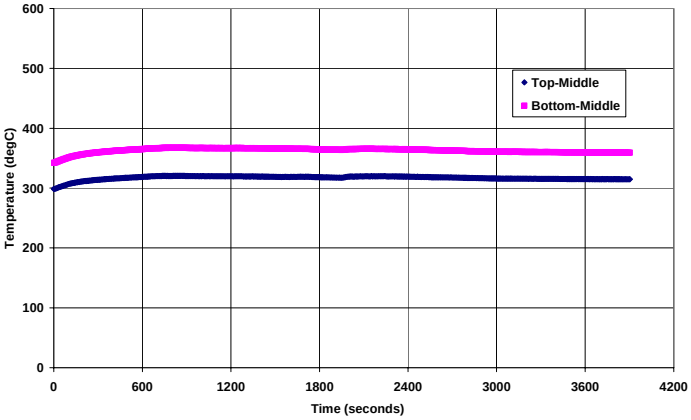

Heater Neck Heat Flux & Test Cell Watt Input
790 kPa, 40 degC Subcooled, 0.017 kg/s, 1200 watt

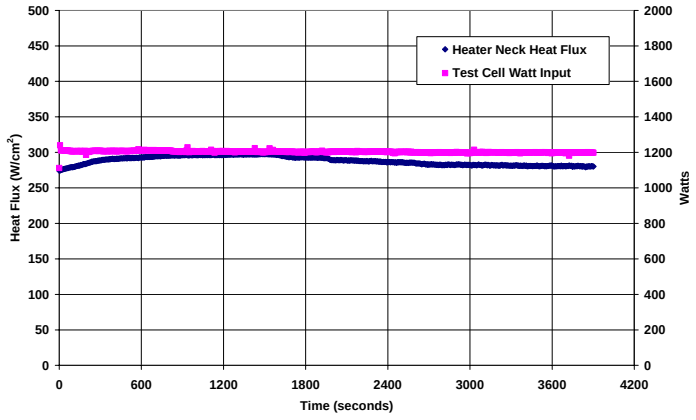

790 kPa, 40 degC Subcooled, 0.017 kg/s, 1300 watt

Mass Flow Rate
790 kPa, 40 degC Subcooled, 0.017 kg/s, 1300 watt

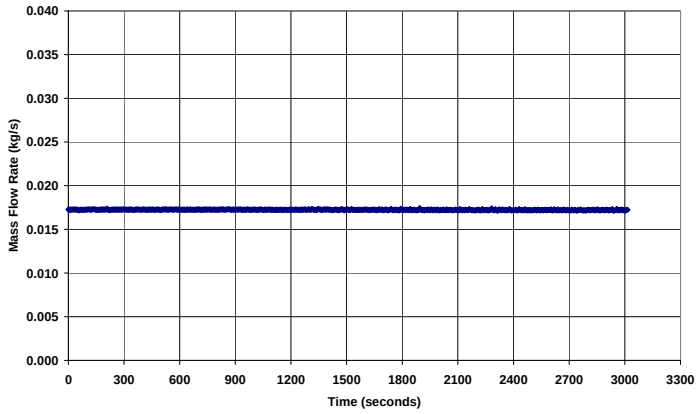

Slot Jet Fluid Temperatures
790 kPa, 40 degC Subcooled, 0.017 kg/s, 1300 watt

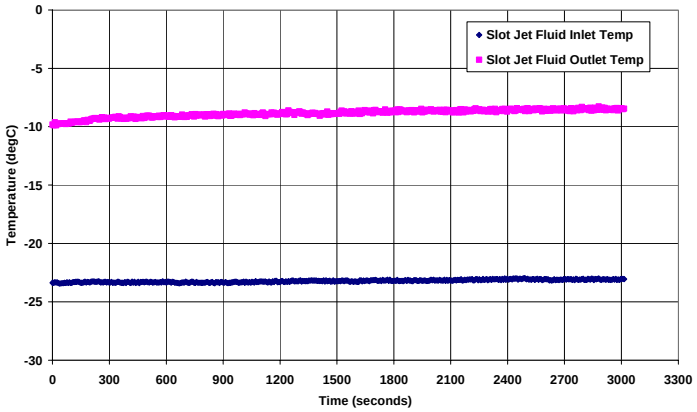

Ammonia Flow Loop Pressures
790 kPa, 40 degC Subcooled, 0.017 kg/s, 1300 watt

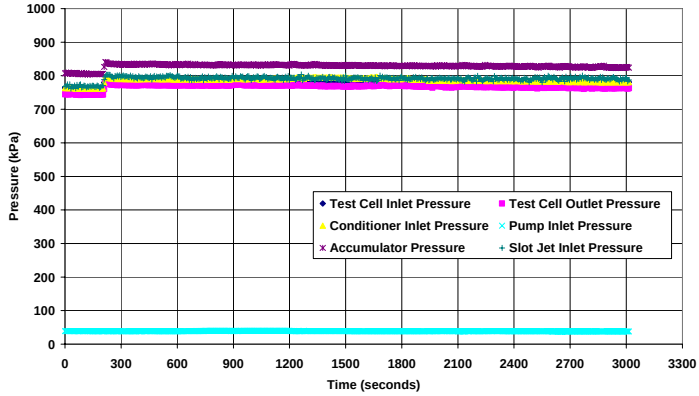

Slot Jet Surface Temperatures
790 kPa, 40 degC Subcooled, 0.017 kg/s, 1300 watt

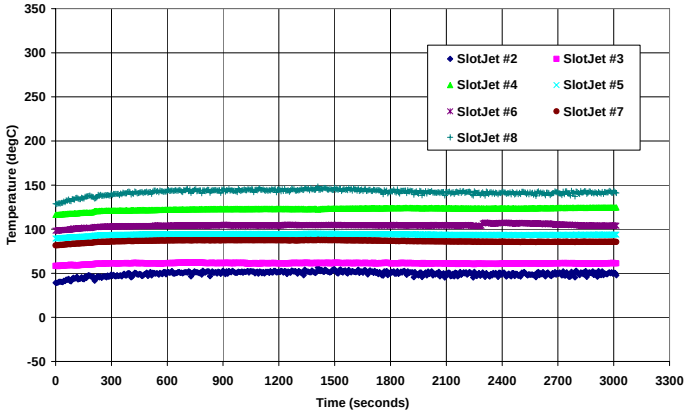

Heater Neck Temperatures
790 kPa, 40 deg Subcooled, 0.017 kg/s, 1300 watt

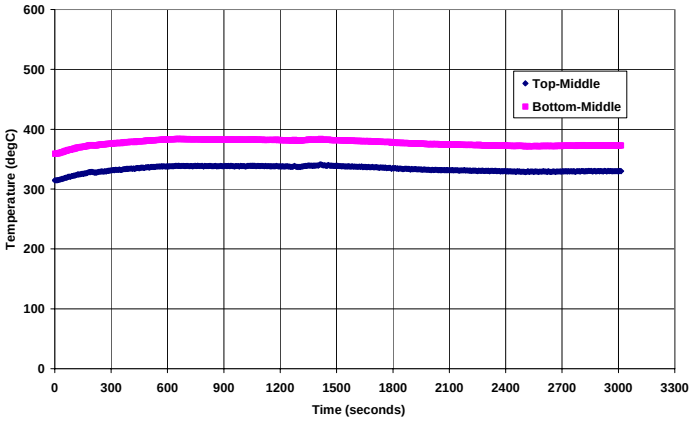

Heater Neck Heat Flux & Test Cell Watt Input
790 kPa, 40 degC Subcooled, 0.017 kg/s, 1300 watt

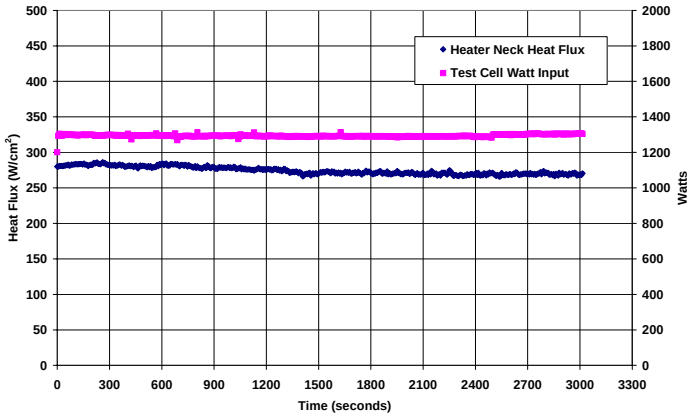

790 kPa, 40 degC Subcooled, 0.017 kg/s, 1400 watt

Mass Flow Rate
790 kPa, 40 degC Subcooled, 0.017 kg/s, 1400 watt

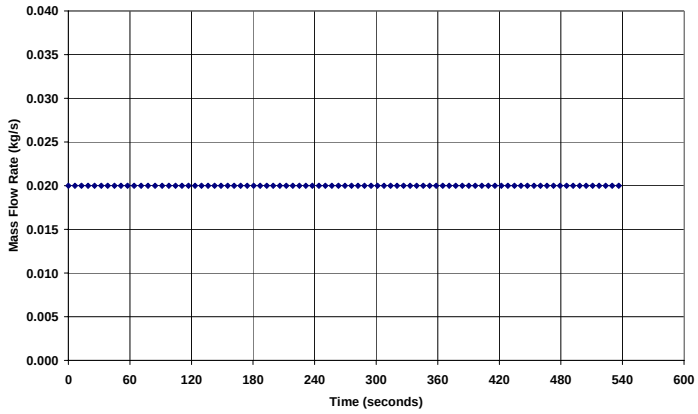

Slot Jet Fluid Temperatures
790 kPa, 40 degC Subcooled, 0.017 kg/s, 1400 watt

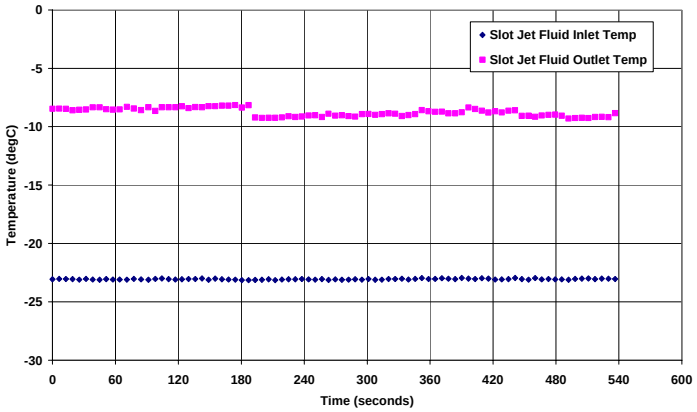

Ammonia Flow Loop Pressures
790 kPa, 40 degC Subcooled, 0.017 kg/s, 1400 watt

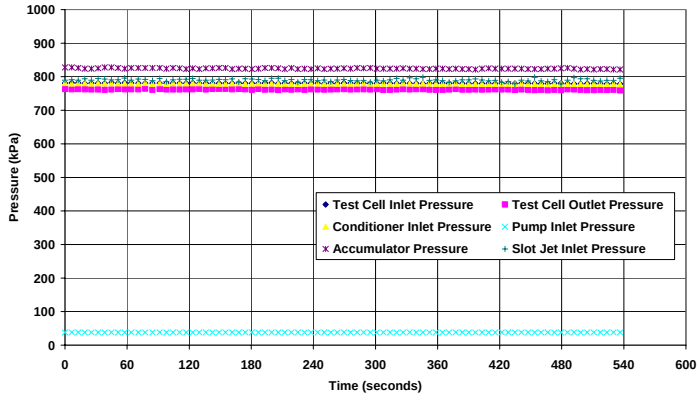

Slot Jet Surface Temperatures
790 kPa, 40 degC Subcooled, 0.017 kg/s, 1400 watt

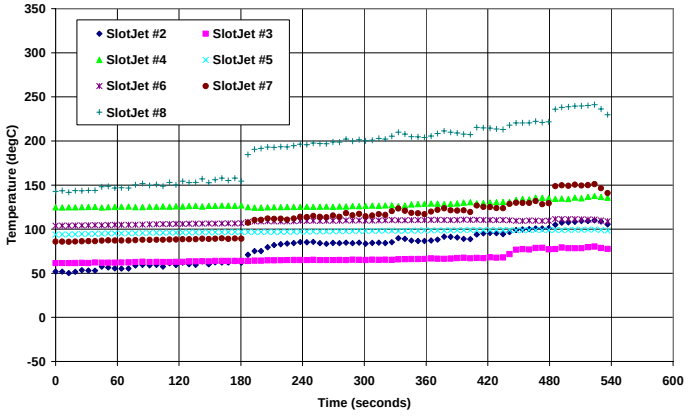

Heater Neck Temperatures
790 kPa, 40 deg Subcooled, 0.017 kg/s, 1400 watt

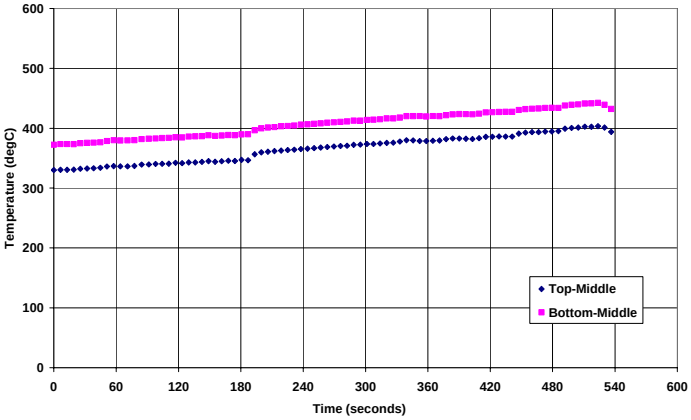

Heater Neck Heat Flux & Test Cell Watt Input
790 kPa, 40 degC Subcooled, 0.017 kg/s, 1400 watt

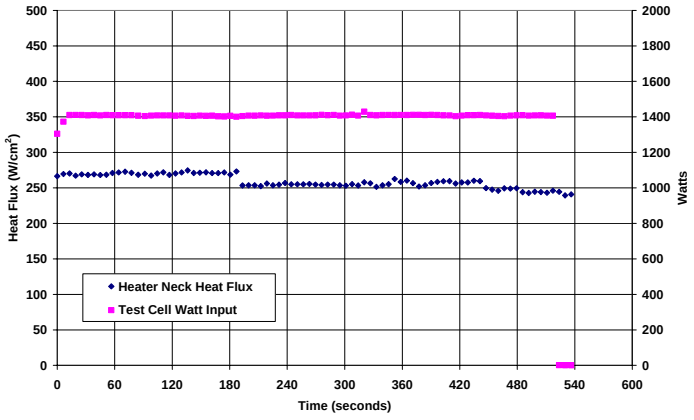

790 kPa, 40 degC Subcooled, 0.029 kg/s, 100 watt

Mass Flow Rate
790 kPa, 40 degC Subcooled, 0.029 kg/s, 100 watt

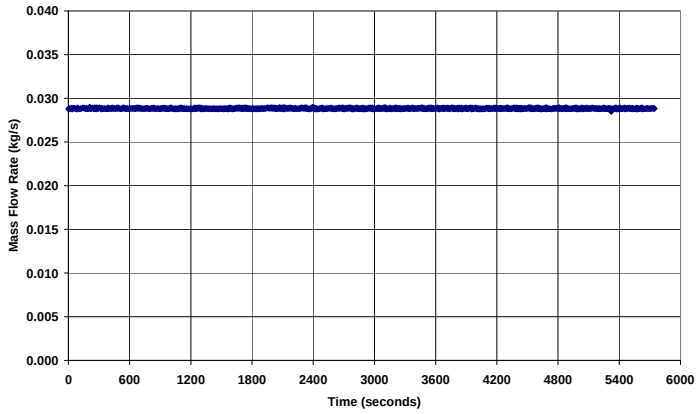

Slot Jet Fluid Temperatures
790 kPa, 40 degC Subcooled, 0.029 kg/s, 100 watt

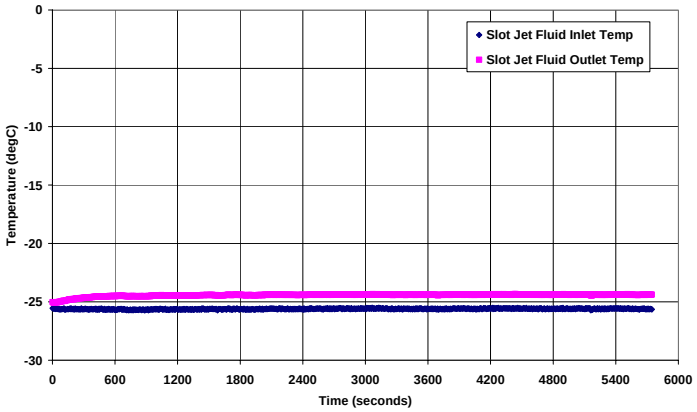

Ammonia Flow Loop Pressures
790 kPa, 40 degC Subcooled, 0.029 kg/s, 100 watt

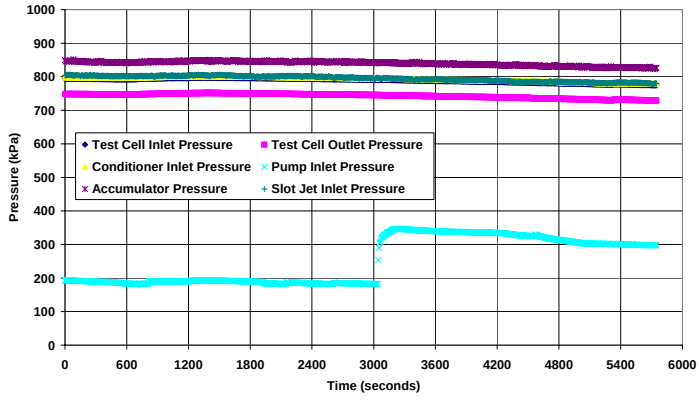

Slot Jet Surface Temperatures
790 kPa, 40 degC Subcooled, 0.029 kg/s, 100 watt

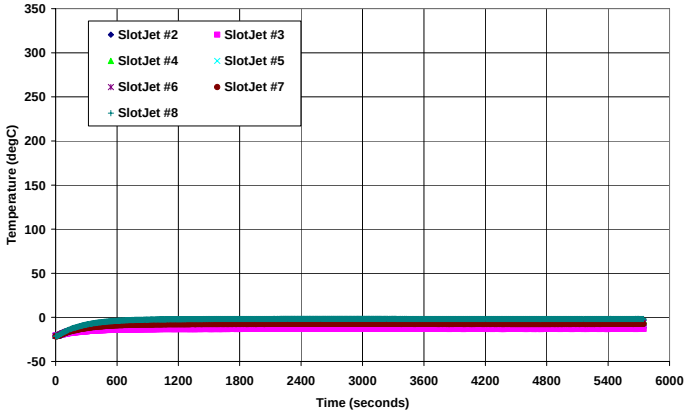

Heater Neck Temperatures
790 kPa, 40 deg Subcooled, 0.029 kg/s, 100 watt

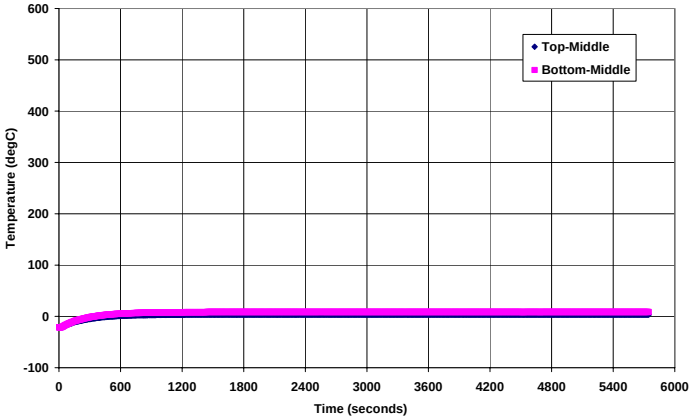

Heater Neck Heat Flux & Test Cell Watt Input
790 kPa, 40 degC Subcooled, 0.029 kg/s, 100 watt

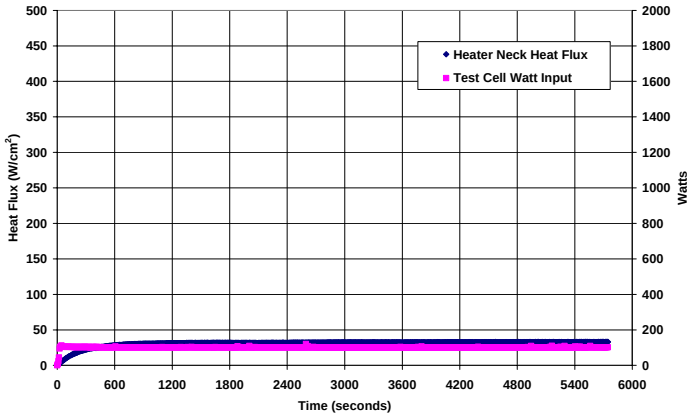

790 kPa, 40 degC Subcooled, 0.029 kg/s, 300 watt

Mass Flow Rate
790 kPa, 40 degC Subcooled, 0.029 kg/s, 300 watt

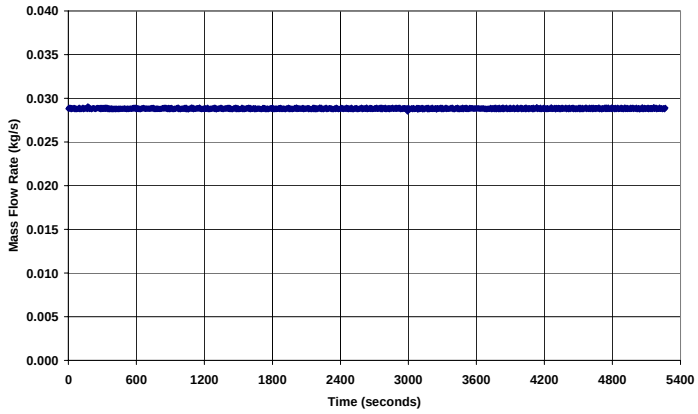

Slot Jet Fluid Temperatures
790 kPa, 40 degC Subcooled, 0.029 kg/s, 300 watt

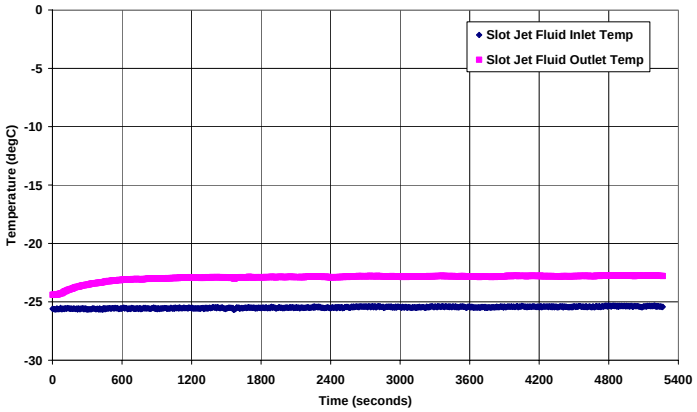

Ammonia Flow Loop Pressures
790 kPa, 40 degC Subcooled, 0.029 kg/s, 300 watt

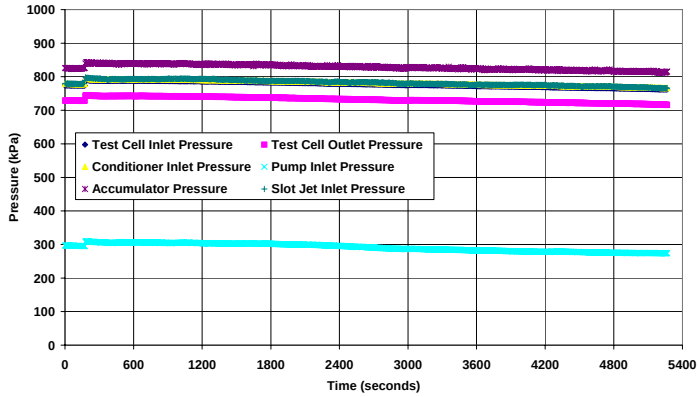

Slot Jet Surface Temperatures
790 kPa, 40 degC Subcooled, 0.029 kg/s, 300 watt

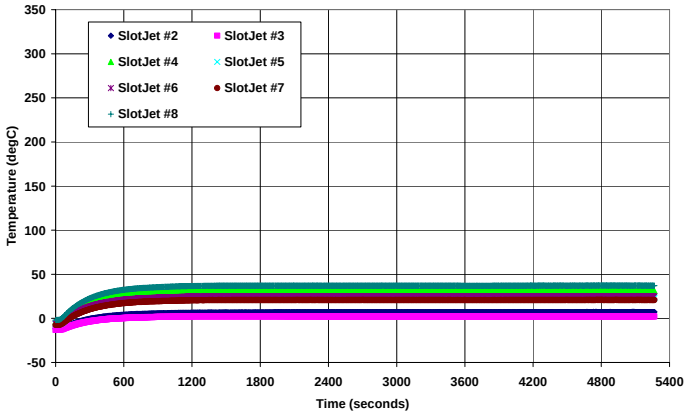

Heater Neck Temperatures
790 kPa, 40 deg Subcooled, 0.029 kg/s, 300 watt

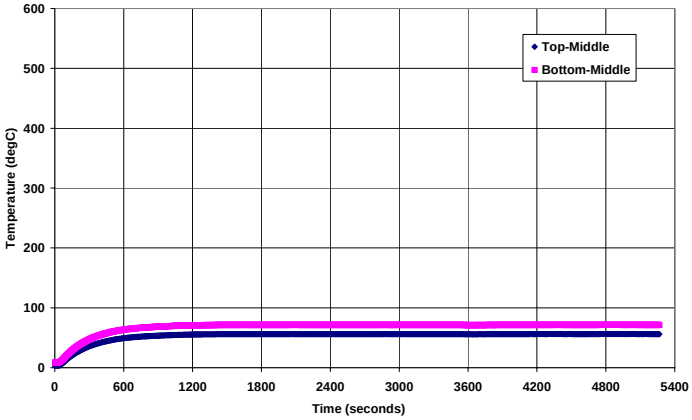

Heater Neck Heat Flux & Test Cell Watt Input
790 kPa, 40 degC Subcooled, 0.029 kg/s, 300 watt

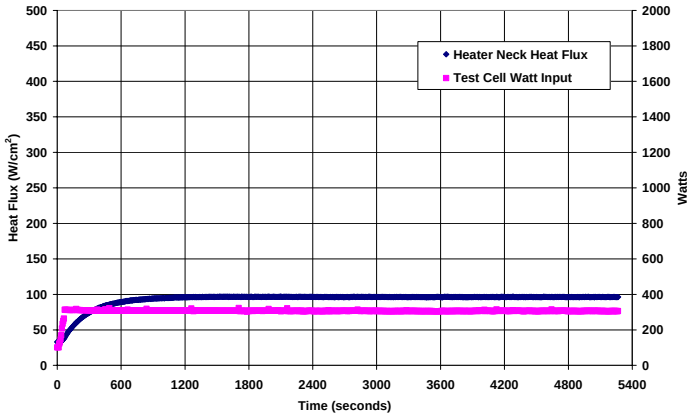

790 kPa, 40 degC Subcooled, 0.029 kg/s, 500 watt

Mass Flow Rate
790 kPa, 40 degC Subcooled, 0.029 kg/s, 500 watt

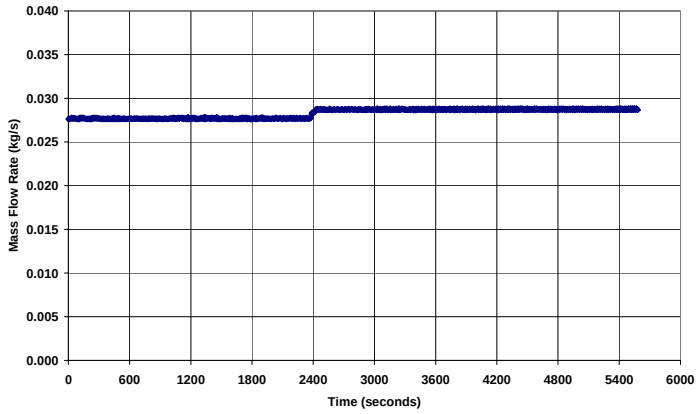

Slot Jet Fluid Temperatures
790 kPa, 40 degC Subcooled, 0.029 kg/s, 500 watt

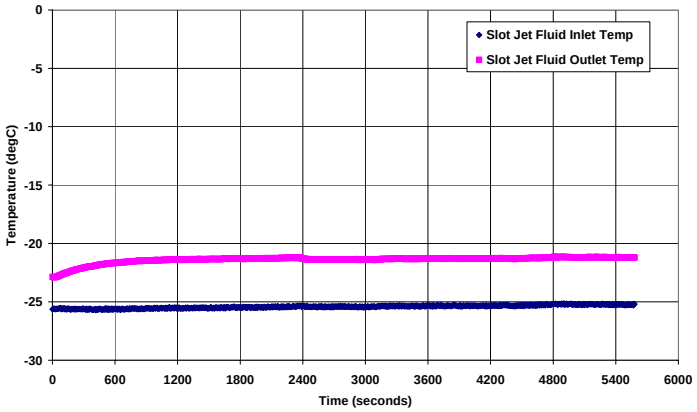

Ammonia Flow Loop Pressures
790 kPa, 40 degC Subcooled, 0.029 kg/s, 500 watt

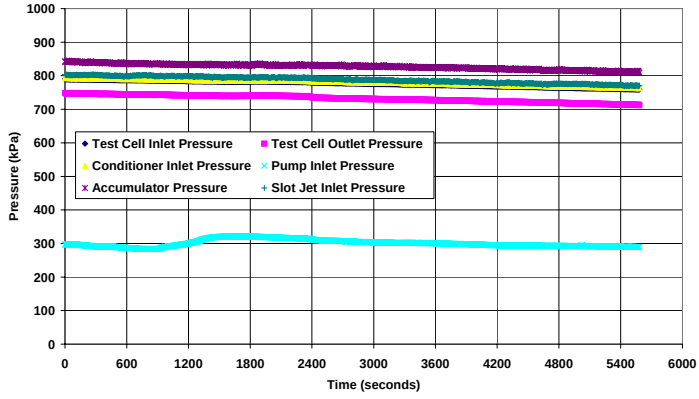

Slot Jet Surface Temperatures
790 kPa, 40 degC Subcooled, 0.029 kg/s, 500 watt

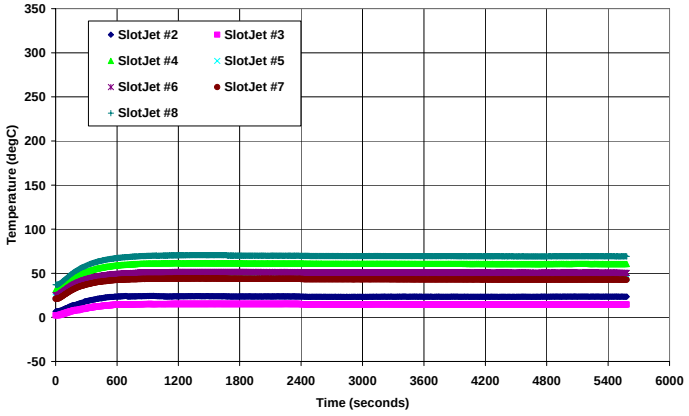

Heater Neck Temperatures
790 kPa, 40 deg Subcooled, 0.029 kg/s, 500 watt

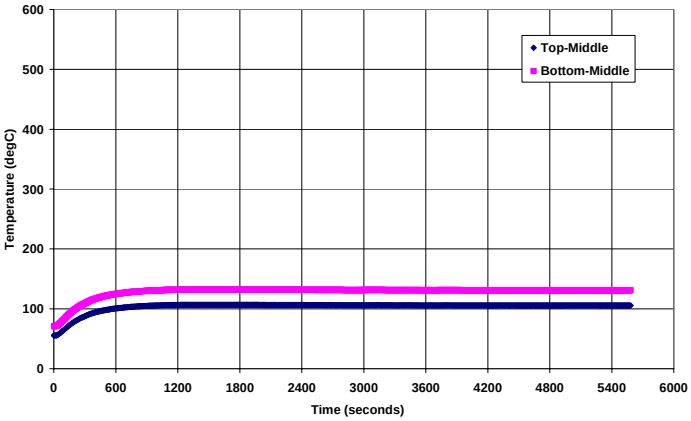

Heater Neck Heat Flux & Test Cell Watt Input
790 kPa, 40 degC Subcooled, 0.029 kg/s, 500 watt

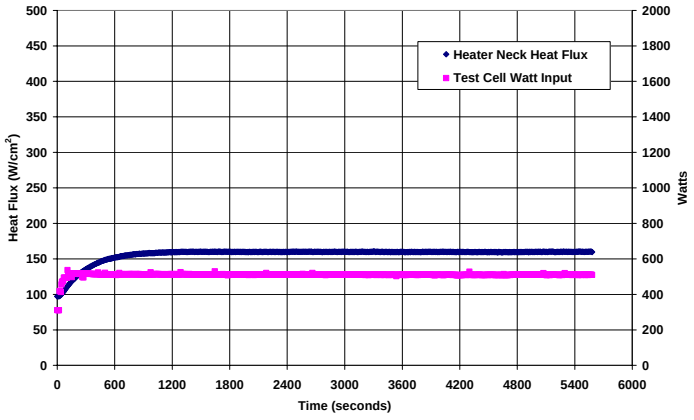

790 kPa, 40 degC Subcooled, 0.029 kg/s, 700 watt

Mass Flow Rate
790 kPa, 40 degC Subcooled, 0.029 kg/s, 700 watt

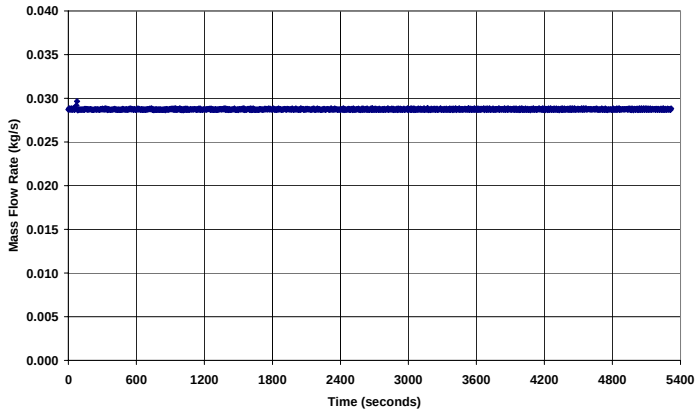

Slot Jet Fluid Temperatures
790 kPa, 40 degC Subcooled, 0.029 kg/s, 700 watt

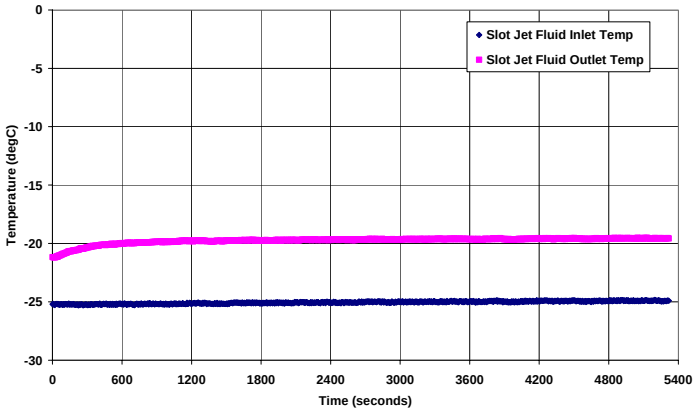

Ammonia Flow Loop Pressures
790 kPa, 40 degC Subcooled, 0.029 kg/s, 700 watt

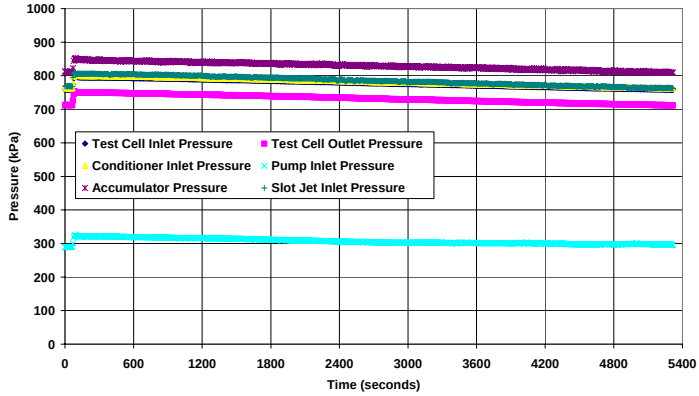

Slot Jet Surface Temperatures
790 kPa, 40 degC Subcooled, 0.029 kg/s, 700 watt

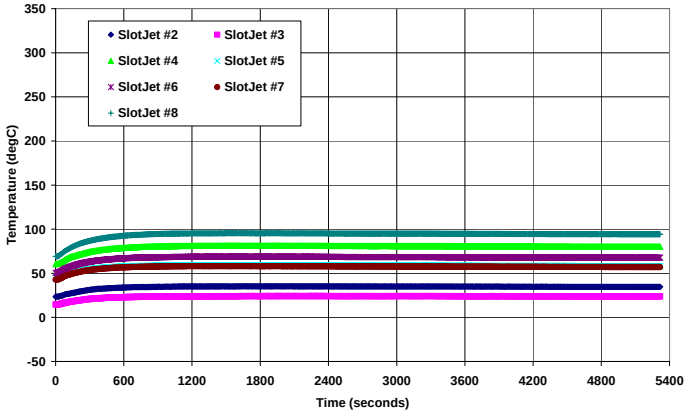

Heater Neck Temperatures
790 kPa, 40 deg Subcooled, 0.029 kg/s, 700 watt

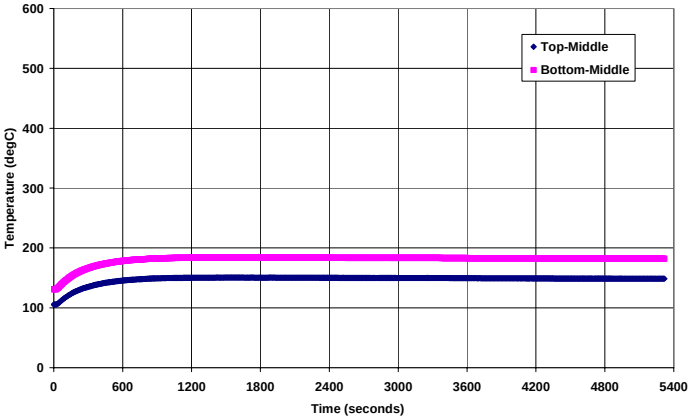

Heater Neck Heat Flux & Test Cell Watt Input
790 kPa, 40 degC Subcooled, 0.029 kg/s, 700 watt

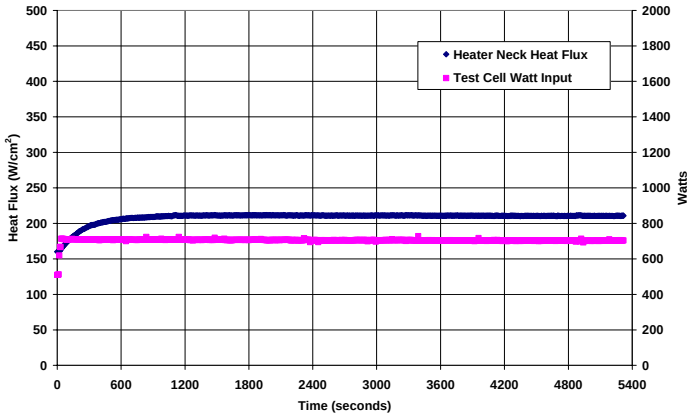

790 kPa, 40 degC Subcooled, 0.029 kg/s, 900 watt

Mass Flow Rate
790 kPa, 40 degC Subcooled, 0.029 kg/s, 900 watt

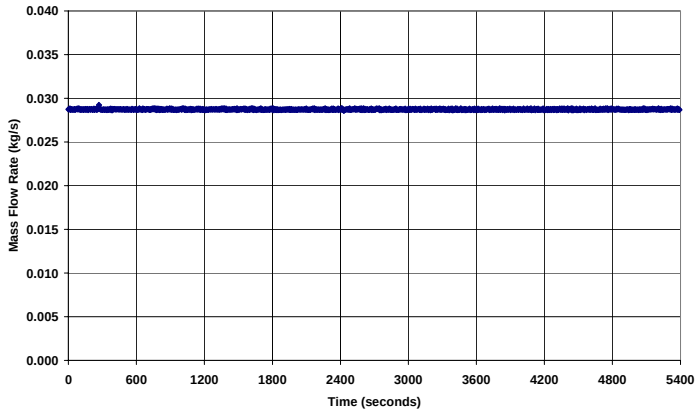

Slot Jet Fluid Temperatures
790 kPa, 40 degC Subcooled, 0.029 kg/s, 900 watt

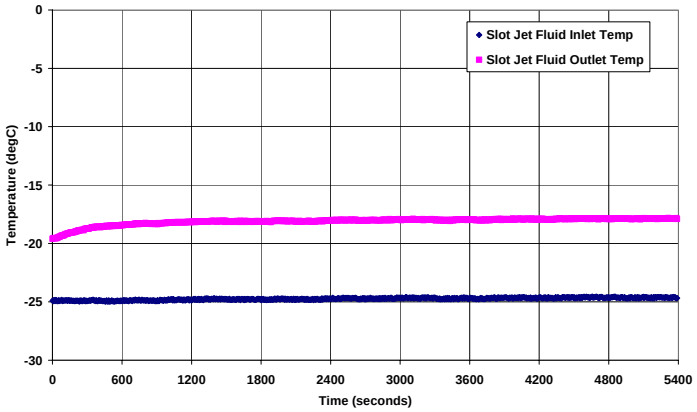

Ammonia Flow Loop Pressures
790 kPa, 40 degC Subcooled, 0.029 kg/s, 900 watt

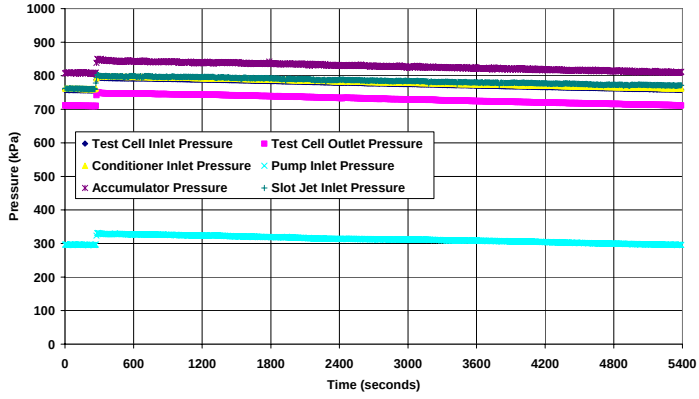

Slot Jet Surface Temperatures
790 kPa, 40 degC Subcooled, 0.029 kg/s, 900 watt

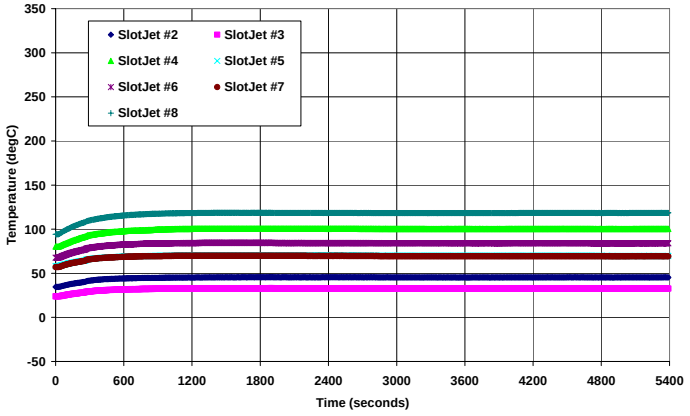

Heater Neck Temperatures
790 kPa, 40 deg Subcooled, 0.029 kg/s, 900 watt

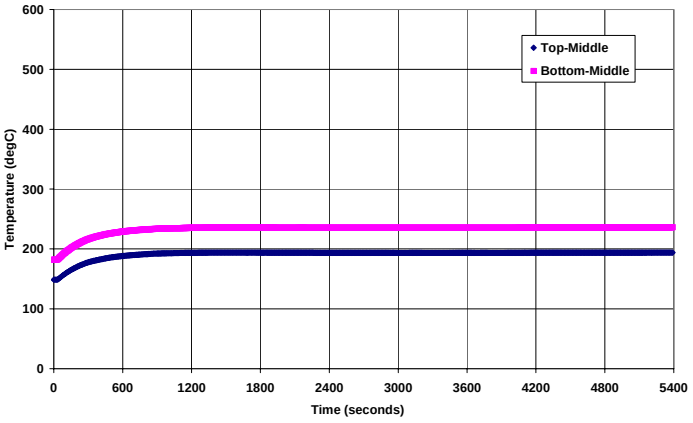

Heater Neck Heat Flux & Test Cell Watt Input
790 kPa, 40 degC Subcooled, 0.029 kg/s, 900 watt

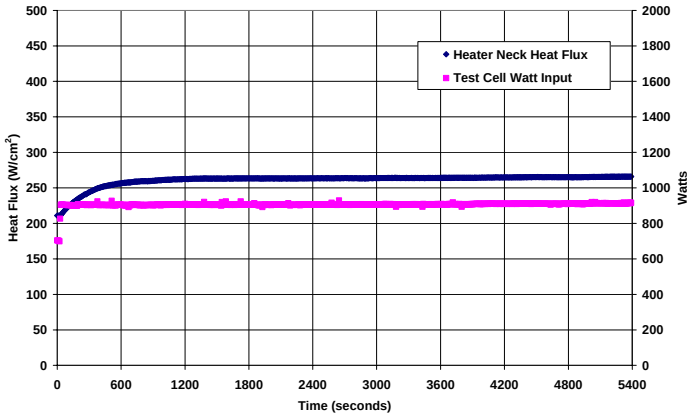

790 kPa, 40 degC Subcooled, 0.029 kg/s, 1000 watt

Mass Flow Rate
790 kPa, 40 degC Subcooled, 0.029 kg/s, 1000 watt

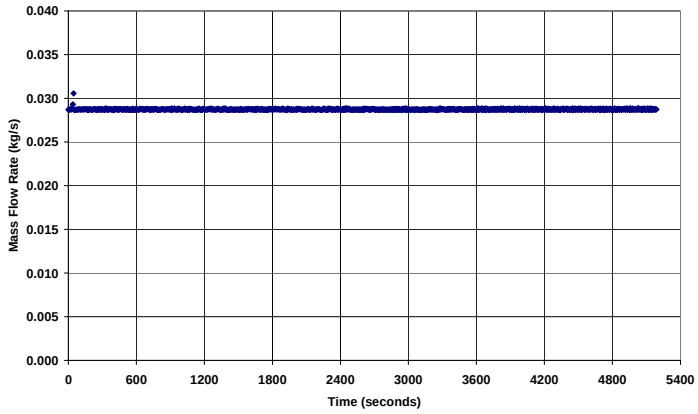

Slot Jet Fluid Temperatures
790 kPa, 40 degC Subcooled, 0.029 kg/s, 1000 watt

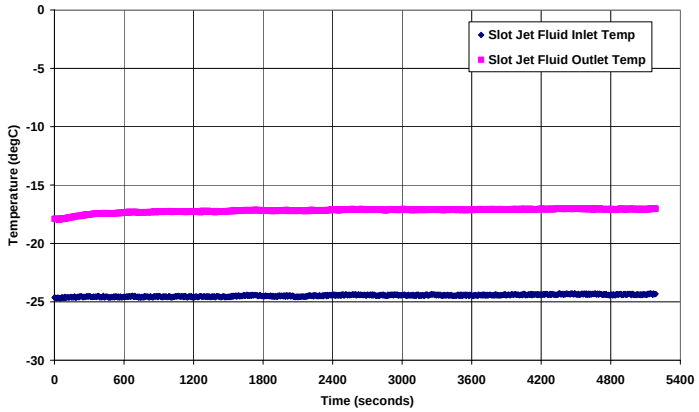

Ammonia Flow Loop Pressures
790 kPa, 40 degC Subcooled, 0.029 kg/s, 1000 watt

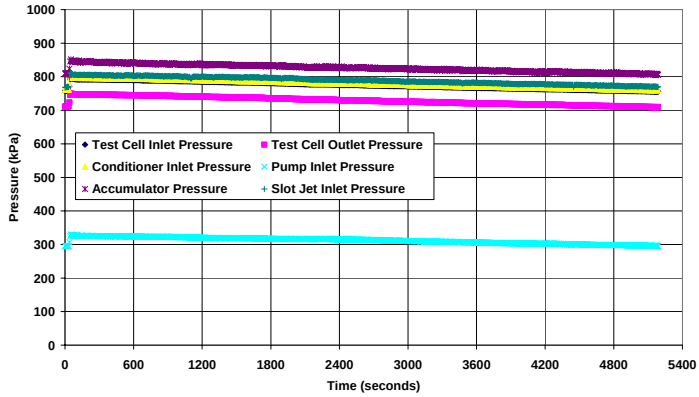

Slot Jet Surface Temperatures
790 kPa, 40 degC Subcooled, 0.029 kg/s, 1000 watt

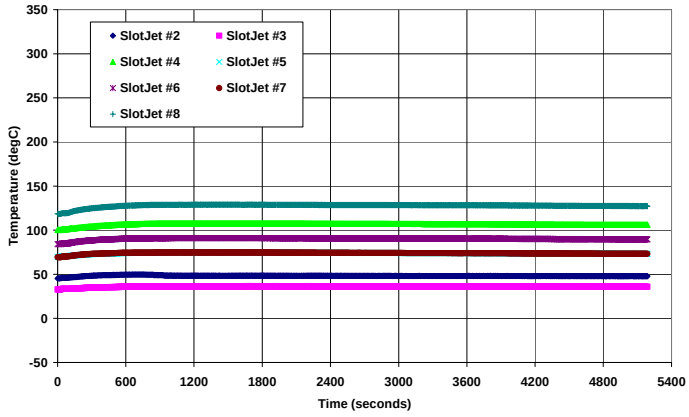

Heater Neck Temperatures
790 kPa, 40 deg Subcooled, 0.029 kg/s, 1000 watt

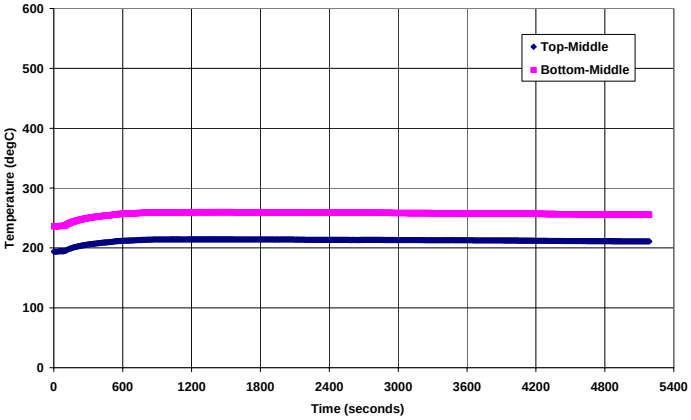

Heater Neck Heat Flux & Test Cell Watt Input
790 kPa, 40 degC Subcooled, 0.029 kg/s, 1000 watt

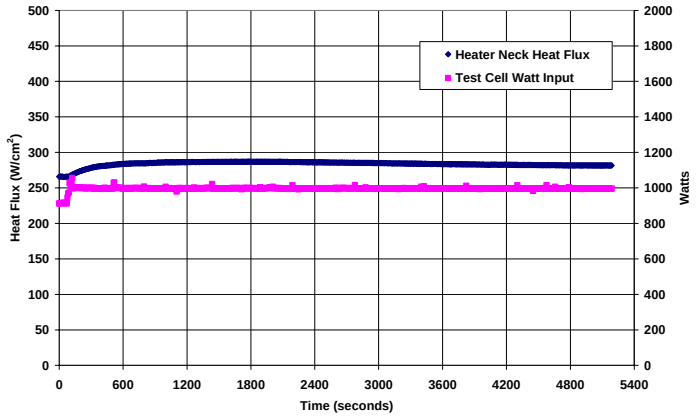

790 kPa, 40 degC Subcooled, 0.029 kg/s, 1100 watt

Mass Flow Rate
790 kPa, 40 degC Subcooled, 0.029 kg/s, 1100 watt

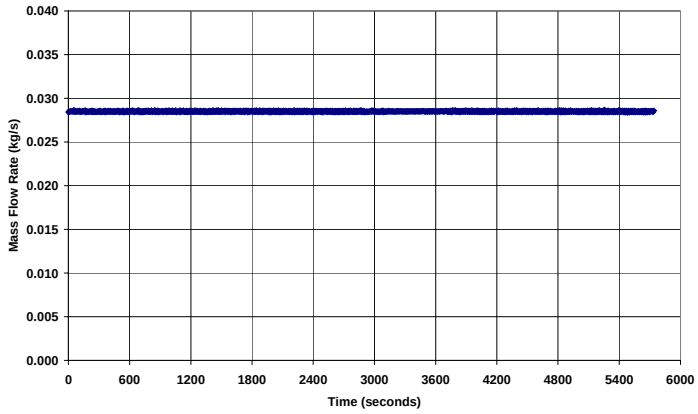

Slot Jet Fluid Temperatures
790 kPa, 40 degC Subcooled, 0.029 kg/s, 1100 watt

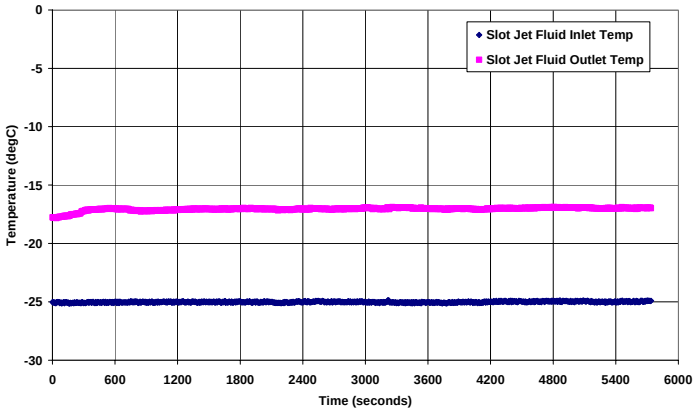

Ammonia Flow Loop Pressures
790 kPa, 40 degC Subcooled, 0.029 kg/s, 1100 watt

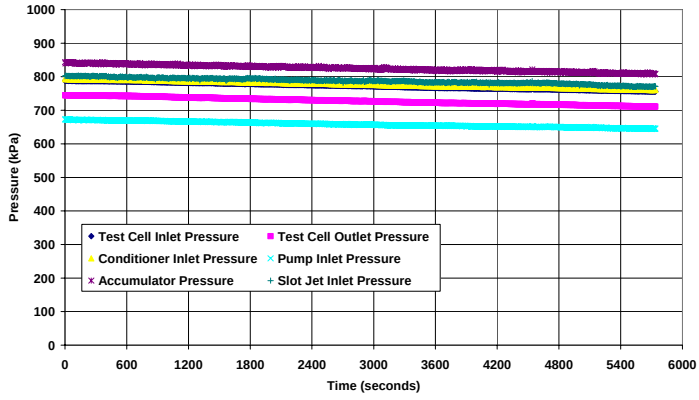

Slot Jet Surface Temperatures
790 kPa, 40 degC Subcooled, 0.029 kg/s, 1100 watt

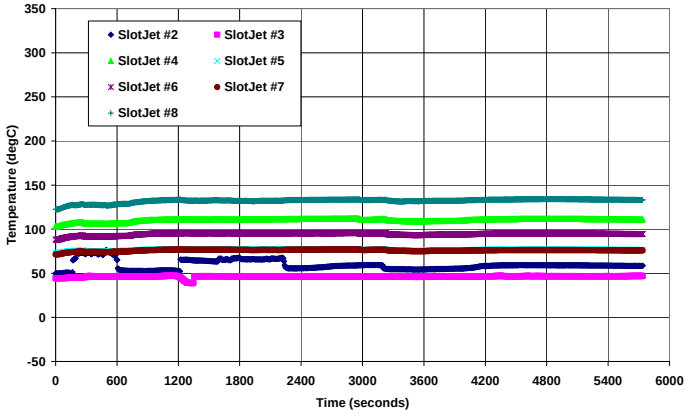

Heater Neck Temperatures
790 kPa, 40 deg Subcooled, 0.029 kg/s, 1100 watt

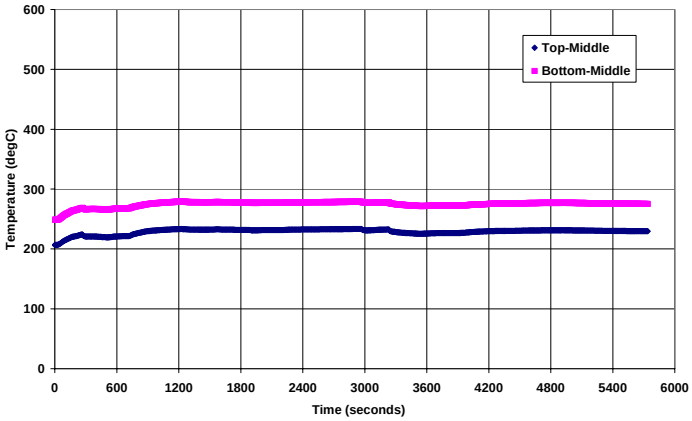

Heater Neck Heat Flux & Test Cell Watt Input
790 kPa, 40 degC Subcooled, 0.029 kg/s, 1100 watt

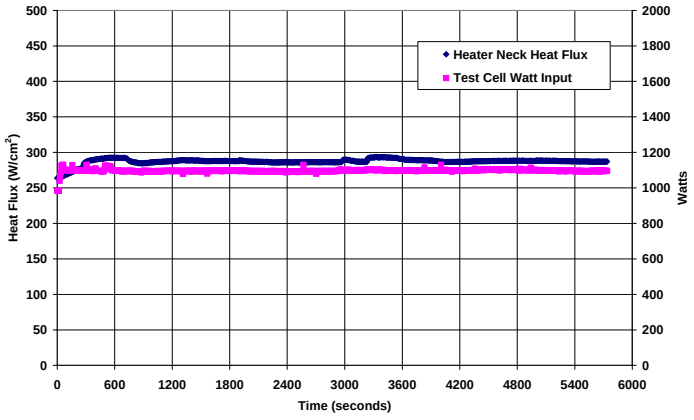

790 kPa, 40 degC Subcooled, 0.029 kg/s, 1200 watt

Mass Flow Rate
790 kPa, 40 degC Subcooled, 0.029 kg/s, 1200 watt

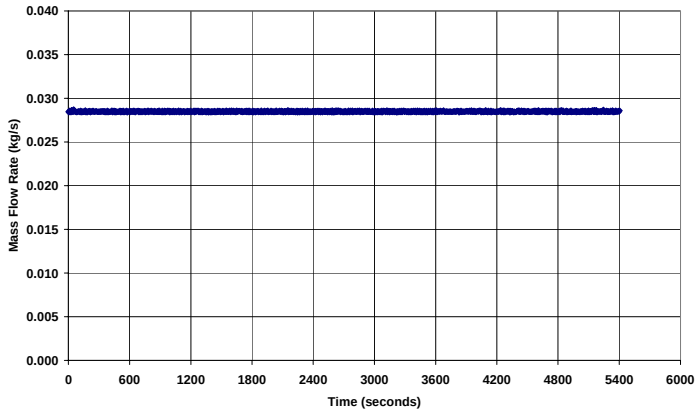

Slot Jet Fluid Temperatures
790 kPa, 40 degC Subcooled, 0.029 kg/s, 1200 watt

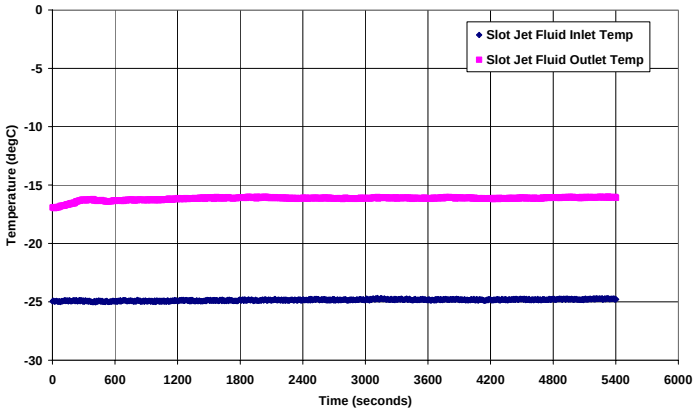

Ammonia Flow Loop Pressures
790 kPa, 40 degC Subcooled, 0.029 kg/s, 1200 watt

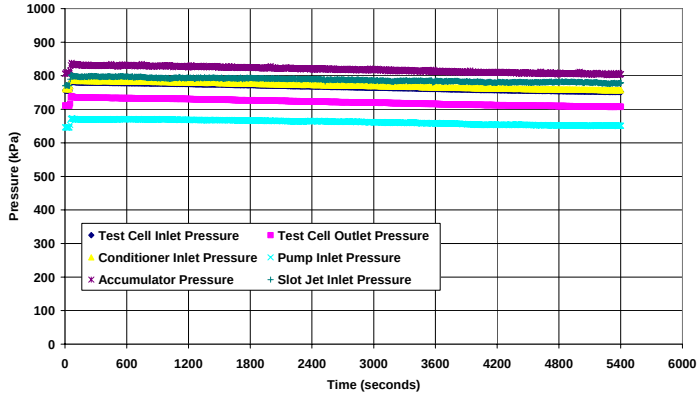

Slot Jet Surface Temperatures
790 kPa, 40 degC Subcooled, 0.029 kg/s, 1200 watt

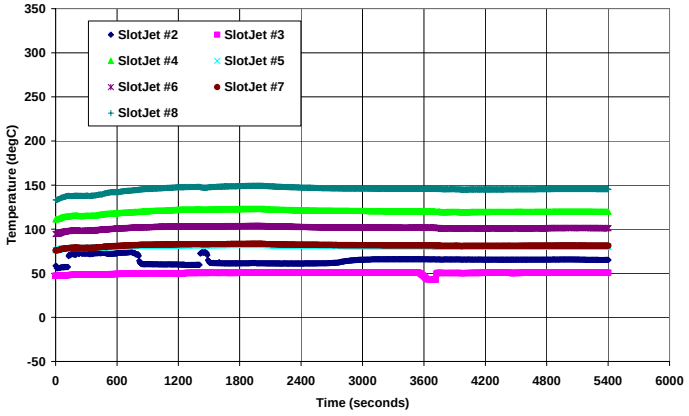

Heater Neck Temperatures
790 kPa, 40 deg Subcooled, 0.029 kg/s, 1200 watt

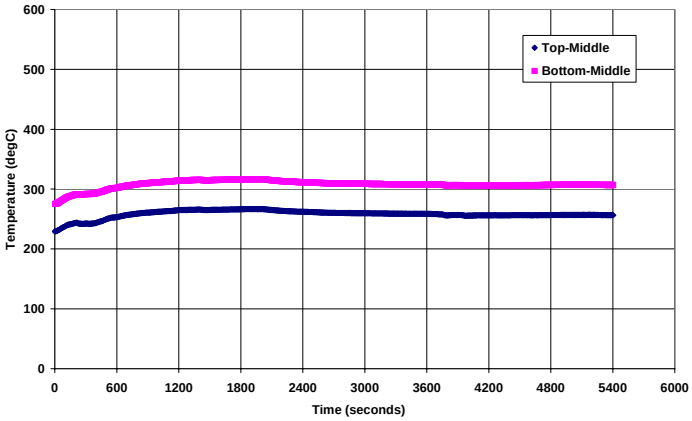

Heater Neck Heat Flux & Test Cell Watt Input
790 kPa, 40 degC Subcooled, 0.029 kg/s, 1200 watt

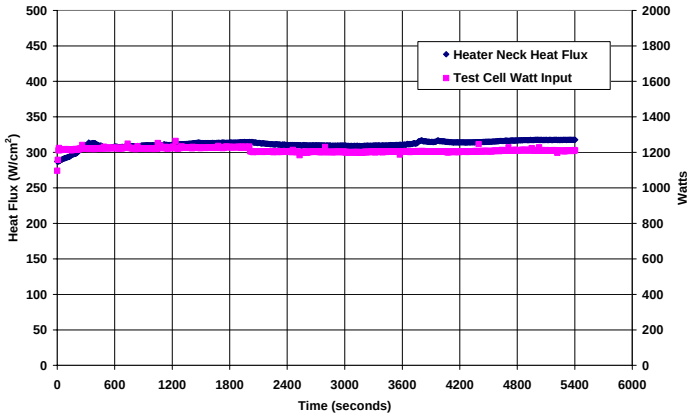

790 kPa, 40 degC Subcooled, 0.029 kg/s, 1300 watt

Mass Flow Rate
790 kPa, 40 degC Subcooled, 0.029 kg/s, 1300 watt

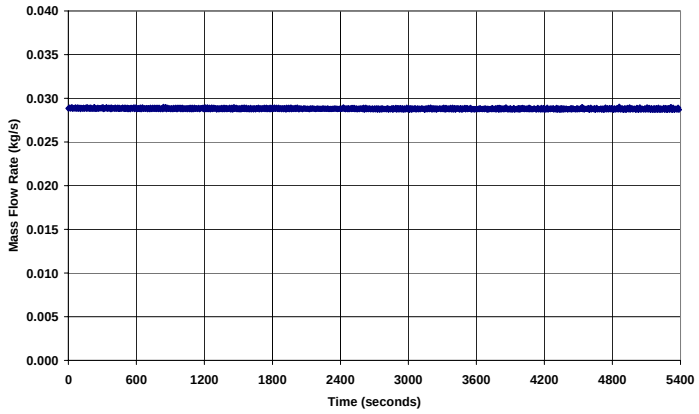

Slot Jet Fluid Temperatures
790 kPa, 40 degC Subcooled, 0.029 kg/s, 1300 watt

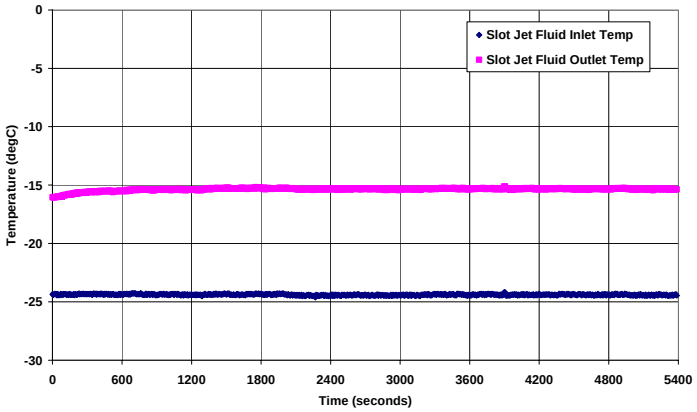

Ammonia Flow Loop Pressures
790 kPa, 40 degC Subcooled, 0.029 kg/s, 1300 watt

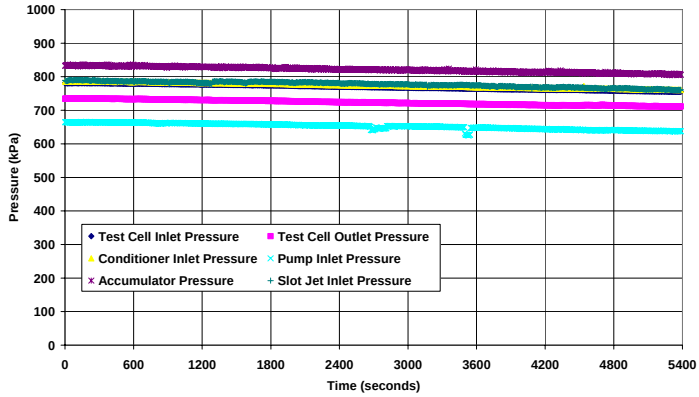

Slot Jet Surface Temperatures
790 kPa, 40 degC Subcooled, 0.029 kg/s, 1300 watt

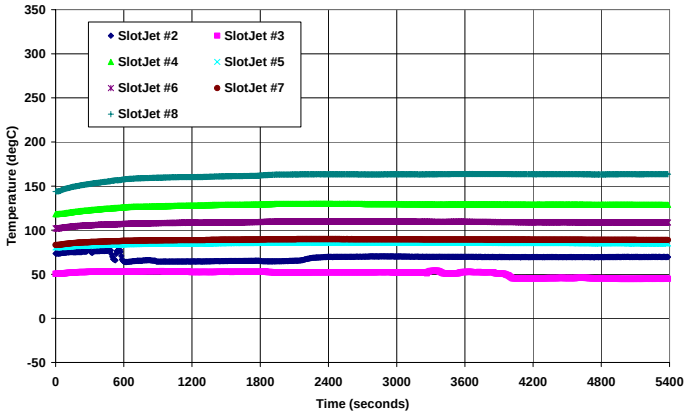

Heater Neck Temperatures
790 kPa, 40 deg Subcooled, 0.029 kg/s, 1300 watt

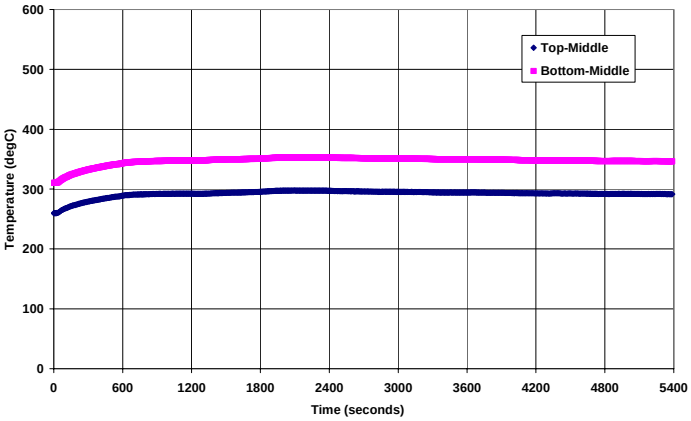

Heater Neck Heat Flux & Test Cell Watt Input
790 kPa, 40 degC Subcooled, 0.029 kg/s, 1300 watt

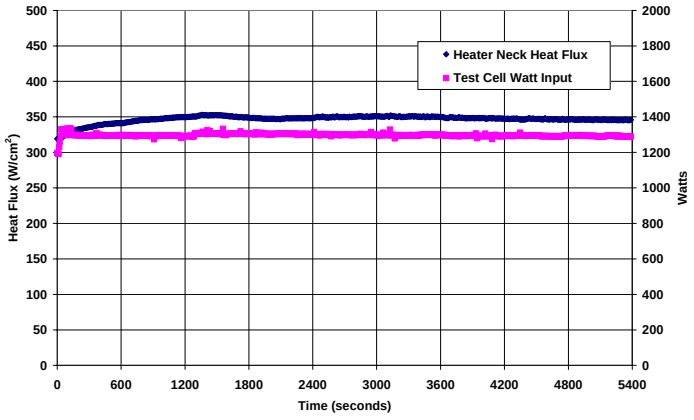

790 kPa, 40 degC Subcooled, 0.029 kg/s, 1400 watt

Mass Flow Rate
790 kPa, 40 degC Subcooled, 0.029 kg/s, 1400 watt

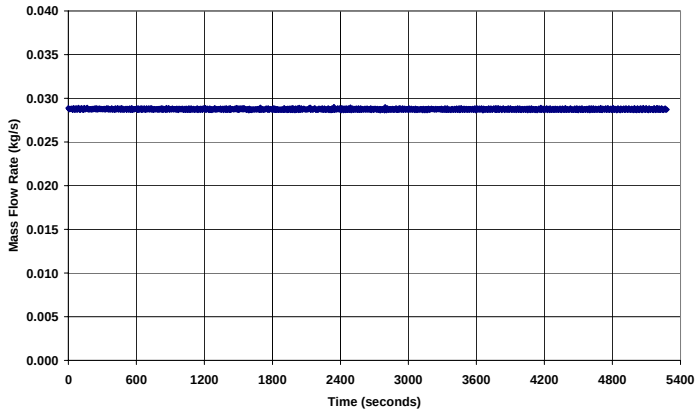

Slot Jet Fluid Temperatures
790 kPa, 40 degC Subcooled, 0.029 kg/s, 1400 watt

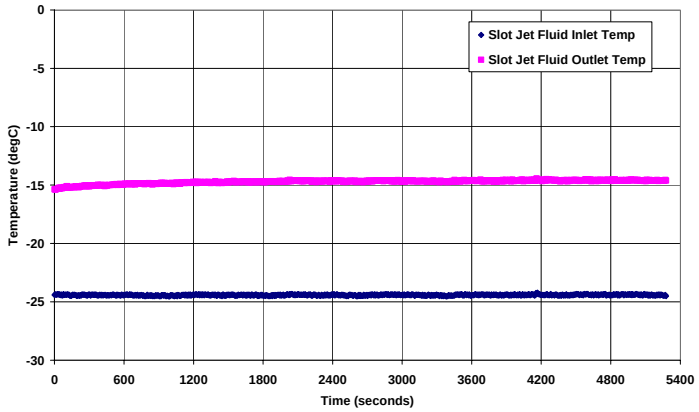

Ammonia Flow Loop Pressures
790 kPa, 40 degC Subcooled, 0.029 kg/s, 1400 watt

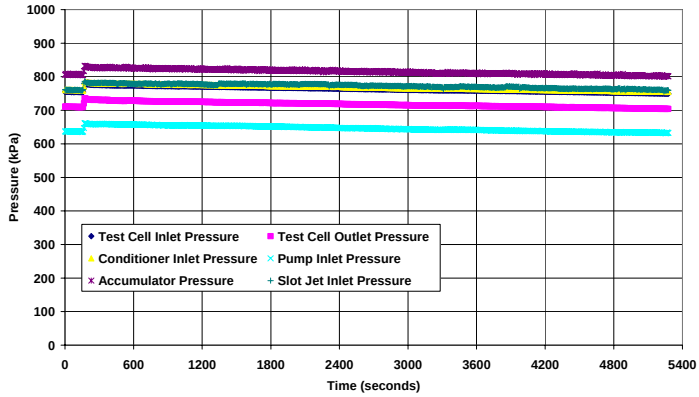

Slot Jet Surface Temperatures
790 kPa, 40 degC Subcooled, 0.029 kg/s, 1400 watt

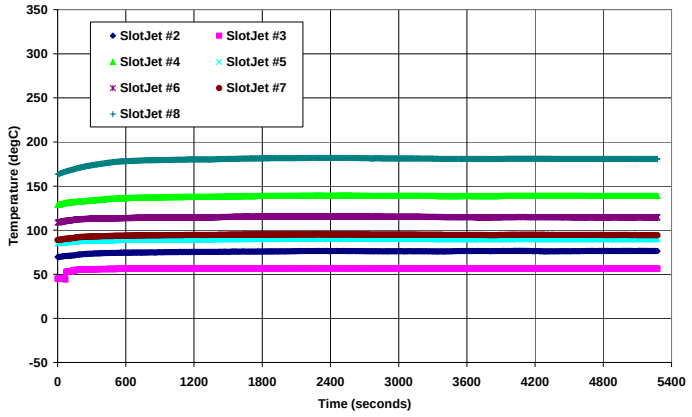

Heater Neck Temperatures
790 kPa, 40 deg Subcooled, 0.029 kg/s, 1400 watt

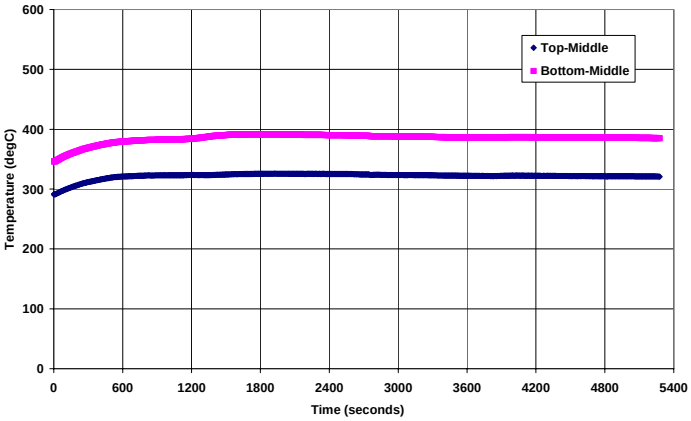

Heater Neck Heat Flux & Test Cell Watt Input
790 kPa, 40 degC Subcooled, 0.029 kg/s, 1400 watt

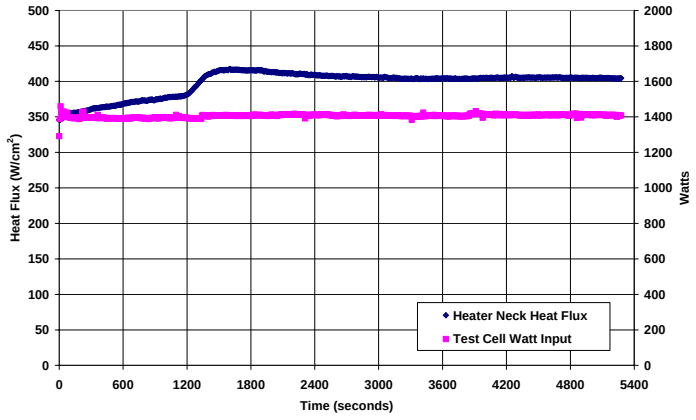

790 kPa, 40 degC Subcooled, 0.029 kg/s, 1500 watt

Mass Flow Rate
790 kPa, 40 degC Subcooled, 0.029 kg/s, 1500 watt

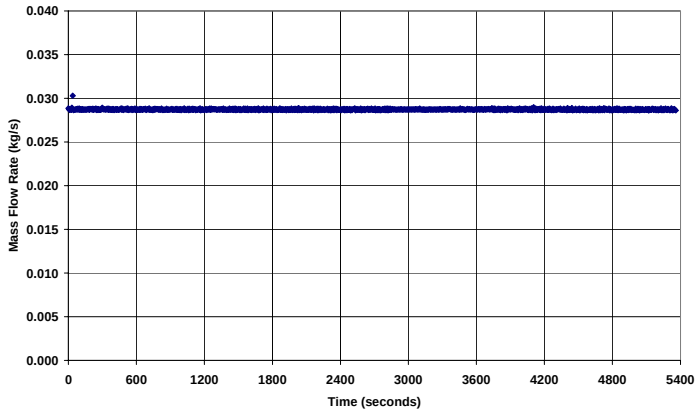

Slot Jet Fluid Temperatures
790 kPa, 40 degC Subcooled, 0.029 kg/s, 1500 watt

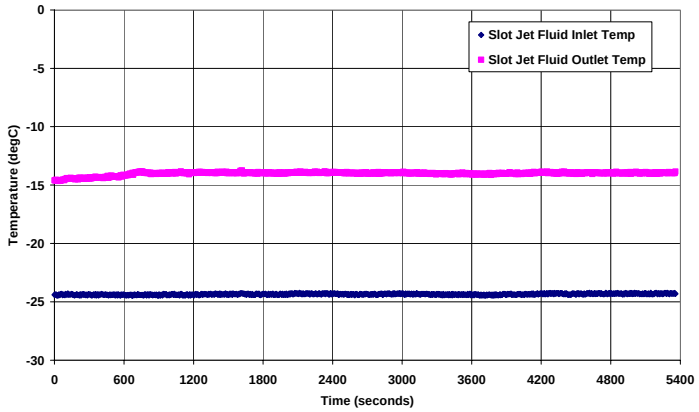

Ammonia Flow Loop Pressures
790 kPa, 40 degC Subcooled, 0.029 kg/s, 1500 watt

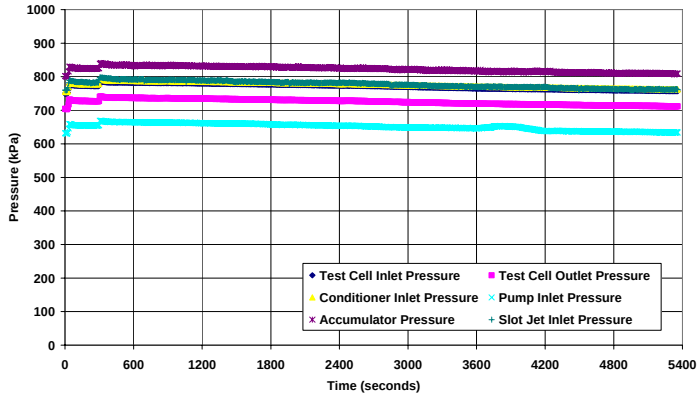

Slot Jet Surface Temperatures
790 kPa, 40 degC Subcooled, 0.029 kg/s, 1500 watt

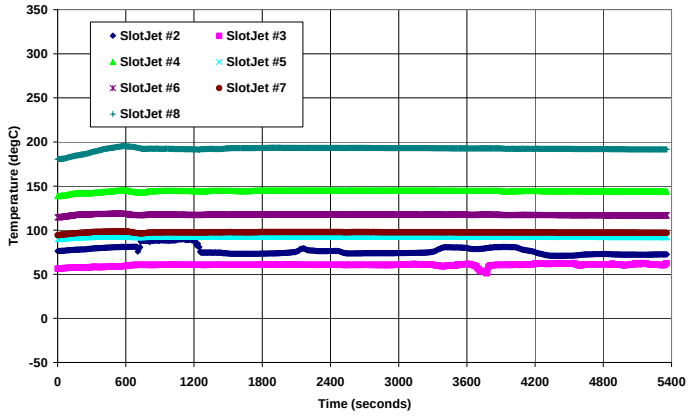

Heater Neck Temperatures
790 kPa, 40 deg Subcooled, 0.029 kg/s, 1500 watt

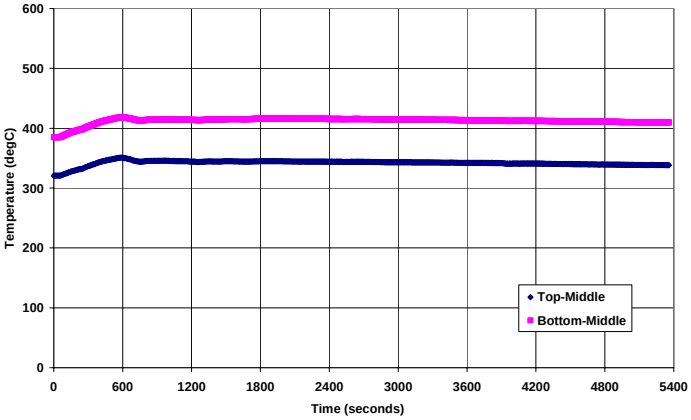

Heater Neck Heat Flux & Test Cell Watt Input
790 kPa, 40 degC Subcooled, 0.029 kg/s, 1500 watt

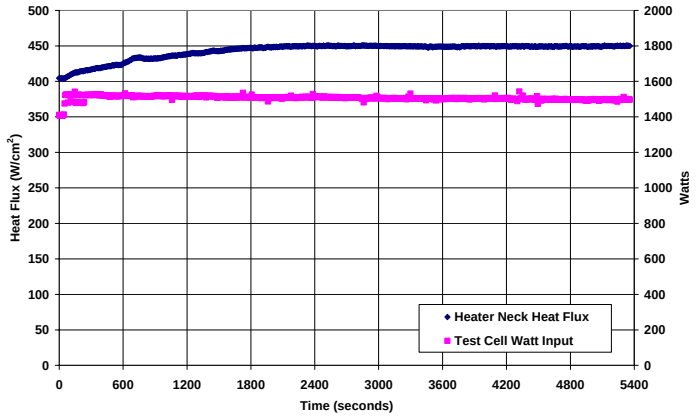

790 kPa, 40 degC Subcooled, 0.029 kg/s, 1600 watt

Mass Flow Rate
790 kPa, 40 degC Subcooled, 0.029 kg/s, 1600 watt

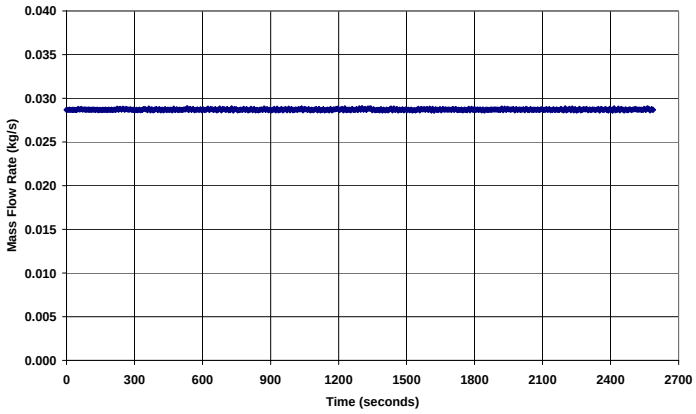

Slot Jet Fluid Temperatures
790 kPa, 40 degC Subcooled, 0.029 kg/s, 1600 watt

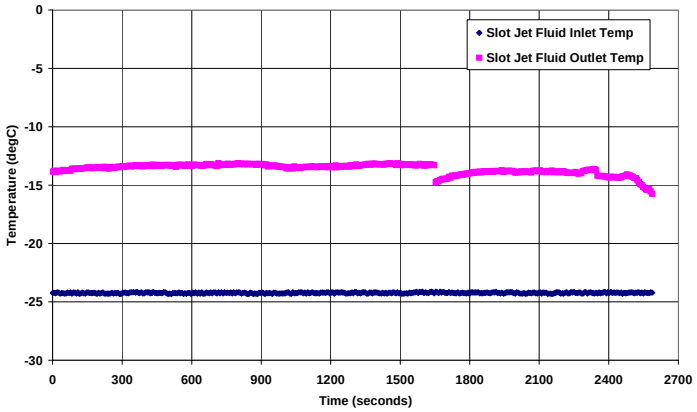

Ammonia Flow Loop Pressures
790 kPa, 40 degC Subcooled, 0.029 kg/s, 1600 watt

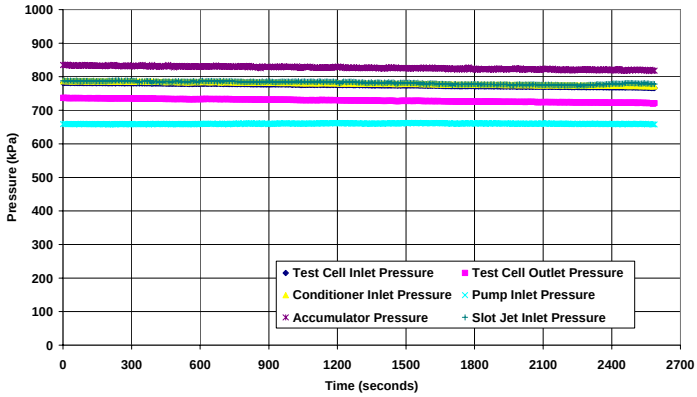

Slot Jet Surface Temperatures
790 kPa, 40 degC Subcooled, 0.029 kg/s, 1600 watt

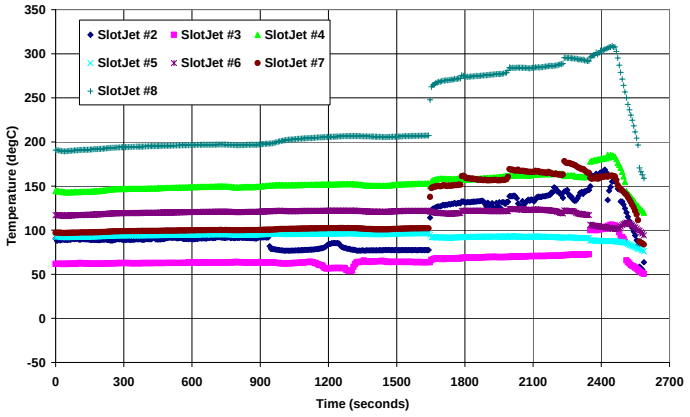

Heater Neck Temperatures
790 kPa, 40 deg Subcooled, 0.029 kg/s, 1600 watt

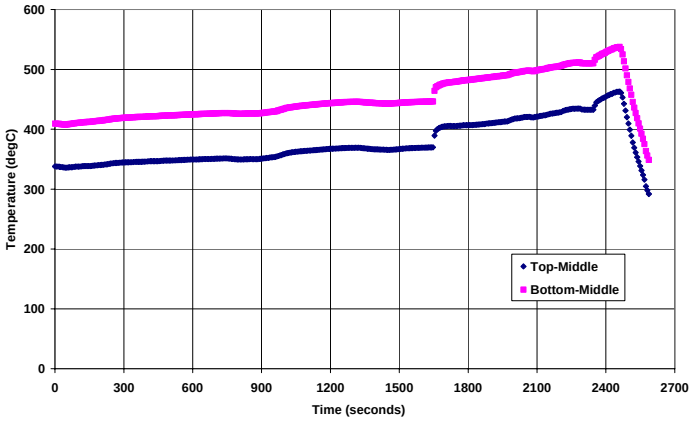

Heater Neck Heat Flux & Test Cell Watt Input
790 kPa, 40 degC Subcooled, 0.029 kg/s, 1600 watt